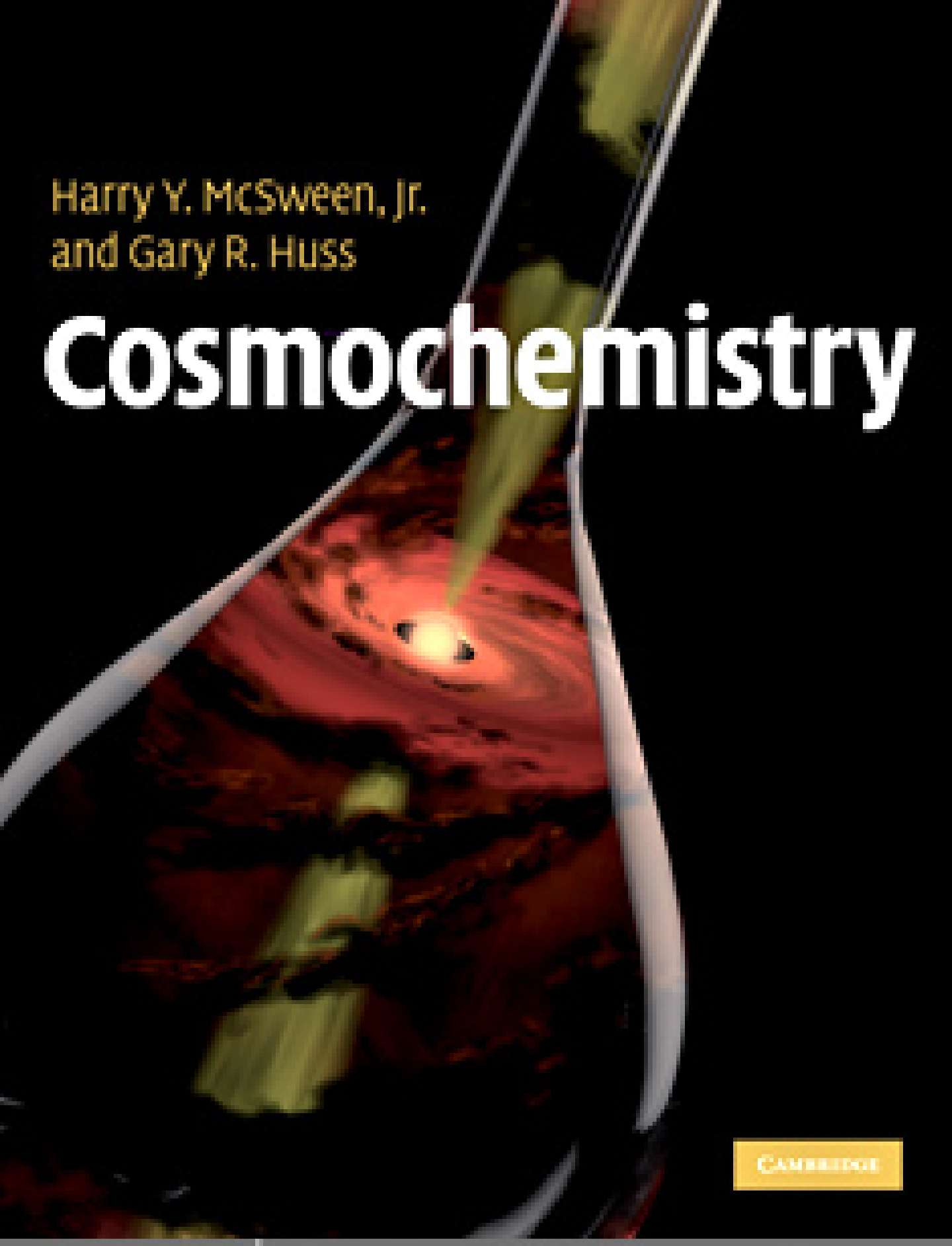

CAMBRIDGE www.cambridge.org/9780521878623

This page intentionally left blank

Cosmochemistry

How did the solar system's chemical composition arise and evolve?

This textbook provides the answers in the first interdisciplinary introduction to cosmochemistry. It makes this exciting and evolving field accessible to undergraduate and graduate students from a range of backgrounds, including geology, chemistry, astronomy, and physics.

The authors – two established research leaders who have helped pioneer developments in the field – provide a complete background to cosmochemical processes and discoveries, enabling students outside geochemistry to fully understand and explore the solar system's composition.

Topics covered include:

- synthesis of nuclides in stars
- partitioning of elements between solids, liquids and gas in the solar nebula
- overviews of the chemistry of extraterrestrial materials
- isotopic tools used to investigate processes such as planet accretion and element fractionation
- chronology of the early solar system
- geochemical exploration of planets.

Boxes provide basic definitions and mini-courses in mineralogy, organic chemistry, and other essential background information for students. Review questions and additional reading for each chapter encourage students to explore cosmochemistry further.

HARRY (Hap) Y. McSWEEN Jr. is Chancellor's Professor at the University of Tennessee. He has conducted research on cosmochemistry for more than three decades and was one of the original proponents of the hypothesis that some meteorites are from Mars. He has been a co-investigator for four NASA spacecraft missions and serves on numerous advisory committees for NASA and the US National Research Council. Dr. McSween has written or edited four books on meteorites and planetary science, and coauthored a textbook in geochemistry. He is a former president and Fellow of the Meteoritical Society, a Fellow of the American Academy of Arts and Sciences, recipient of the Leonard Medal, and has an asteroid named for him.

GARY HUSS is a Research Professor and Director of the W. M. Keck Cosmochemistry Laboratory at the Hawai'i Institute for Geophysics and Planetology, University of Hawai'i at Mānoa. In more than three decades of research on cosmochemistry, he was among the first

to study presolar grains, the raw materials for the solar system. He presently studies the chronology of the early solar system. He comes from a family of meteorite scientists: his grandfather, H. H. Nininger, has been called the father of modern meteoritics, and his father, Glenn Huss, and grandfather were responsible for recovering over 500 meteorites previously unknown to science. Dr. Huss is a former president and Fellow of the Meteoritical Society and also has an asteroid named for him.

Cosmochemistry

Harry Y. McSween, Jr.
University of Tennessee, Knoxville

Gary R. Huss
University of Hawai'i at Mānoa

CAMBRIDGE
UNIVERSITY PRESS

CAMBRIDGE UNIVERSITY PRESS
Cambridge, New York, Melbourne, Madrid, Cape Town, Singapore,
São Paulo, Delhi, Dubai, Tokyo

Cambridge University Press
The Edinburgh Building, Cambridge CB2 8RU, UK

Published in the United States of America by Cambridge University Press, New York

www.cambridge.org
Information on this title: www.cambridge.org/9780521878623

First published in print format 2010

ISBN-13 978-0-511-72968-3 eBook (NetLibrary)

ISBN-13 978-0-521-87862-3 Hardback

For Sue and Jackie

Contents

Preface

Cosmochemistry provides critical insights into the workings of our local star and its companions throughout the galaxy, the origin and timing of our solar system's birth, and the complex reactions inside planetesimals and planets (including our own) as they evolve. Much of the database of cosmochemistry comes from laboratory analyses of elements and isotopes in our modest collections of extraterrestrial samples. A growing part of the cosmochemistry database is gleaned from remote sensing and *in situ* measurements by spacecraft instruments, which provide chemical analyses and geologic context for other planets, their moons, asteroids, and comets. Because the samples analyzed by cosmochemists are typically so small and valuable, or must be analyzed on bodies many millions of miles distant, this discipline leads in the development of new analytical technologies for use in the laboratory or flown on spacecraft missions. These technologies then spread to geochemistry and other fields where precise analyses of small samples are important.

Despite its cutting-edge qualities and newsworthy discoveries, cosmochemistry is an orphan. It does not fall within the purview of chemistry, geology, astronomy, physics, or biology, but is rather an amalgam of these disciplines. Because it has no natural home or constituency, cosmochemistry is usually taught (if it is taught at all) directly from its scientific literature (admittedly difficult reading) or from specialized books on meteorites and related topics. In crafting this textbook, we attempt to remedy that shortcoming. We have tried to make this subject accessible to advanced undergraduate and graduate students with diverse academic backgrounds, although we do presume some prior exposure to basic chemistry. This goal may lead to uneven treatment of some subjects, and our readers should understand that our intended audience is broad.

Cosmochemistry is advancing so rapidly that we can only hope to provide a snapshot of the discipline as it is currently understood and practiced. We have found even that to be a challenge, because we could not hope to possess expertise in all the subjects encompassed by this discipline. We have drawn heavily on the contributions of many colleagues, especially those who educate by writing thoughtful reviews. That assistance is gratefully acknowledged through our annotated suggestions for further reading at the end of each chapter.

The topics covered in the chapters of this book include the following, in this order:

- An introduction to how cosmochemistry developed, and to how it differs from geochemistry
- A review of the characteristics and behaviors of elements and nuclides
- A discussion of how elements are synthesized within stars, and how the chemistry of the galaxy has evolved over time

- An assessment of the abundances of elements and isotopes in the solar system
- A description of presolar grains, and how they constrain stellar nucleosynthesis and processes in interstellar space
- An introduction to meteorites and lunar samples
- An evaluation of processes that have fractionated elements and isotopes in interstellar space, in the solar nebula, and within planetary bodies
- An explanation of how radioactive isotopes are used to quantify solar system history
- A synthesis of the radiometric age of the solar system and the ages of its constituents
- An assessment of the most volatile materials – organic matter, noble gases, and ices
- A survey of the chemistry of anhydrous planetesimals and the samples we have of them
- A survey of the chemistry of ice-bearing comets and asteroids and the samples we have of them
- Examples of modern geochemical exploration of planetary bodies – the Moon and Mars
- A review of the formation of the solar system, from the perspective of cosmochemistry
- An Appendix describing some important analytical methods used in cosmochemistry

More-established disciplines are taught using tried-and-true methods and examples, the results of generations of pedagogical experimentation. Cosmochemistry does not yet offer that. Most of those who dare to teach cosmochemistry, including the authors of this book, have never actually been students in a cosmochemistry course. In the authors' case, we have learned from a handful of scientists who have guided our introduction to the field, including Calvin Alexander, Bob Pepin, Ed Anders, Jim Hays, Dick Holland, Ian Hutcheon, Klaus Keil, Roy Lewis, Dimitri Papanastassiou, Jerry Wasserburg, and John Wood. We hope that this book on cosmochemistry will guide other students and their teachers as they explore together this emerging, interdisciplinary subject, and that they will enjoy the experience as much as we have.

1 Introduction to cosmochemistry

Overview

Cosmochemistry is defined, and its relationship to geochemistry is explained. We describe the historical beginnings of cosmochemistry, and the lines of research that coalesced into the field of cosmochemistry are discussed. We then briefly introduce the tools of cosmochemistry and the datasets that have been produced by these tools. The relationships between cosmochemistry and geochemistry, on the one hand, and astronomy, astrophysics, and geology, on the other, are considered.

What is cosmochemistry?

A significant portion of the universe is comprised of elements, ions, and the compounds formed by their combinations – in effect, chemistry on the grandest scale possible. These chemical components can occur as gases or superheated plasmas, less commonly as solids, and very rarely as liquids.

Cosmochemistry is the study of the chemical composition of the universe and the processes that produced those compositions. This is a tall order, to be sure. Understandably, cosmochemistry focuses primarily on the objects in our own solar system, because that is where we have direct access to the most chemical information. That part of cosmochemistry encompasses the compositions of the Sun, its retinue of planets and their satellites, the almost innumerable asteroids and comets, and the smaller samples (meteorites, interplanetary dust particles or "IDPs," returned lunar samples) derived from them. From their chemistry, determined by laboratory measurements of samples or by various remote-sensing techniques, cosmochemists try to unravel the processes that formed or affected them and to fix the chronology of these events. Meteorites offer a unique window on the *solar nebula* – the disk-shaped cocoon of gas and dust that enveloped the early Sun some ~4.57 billion years ago, and from which planetesimals and planets accreted (Fig. 1.1).

Within some meteorites are also found minuscule presolar grains, providing an opportunity to analyze directly the chemistry of interstellar matter. Some of these tiny grains are pure samples of the matter ejected from dying stars and provide constraints on our understanding of how elements were forged inside stars before the Sun's birth. Once formed, these

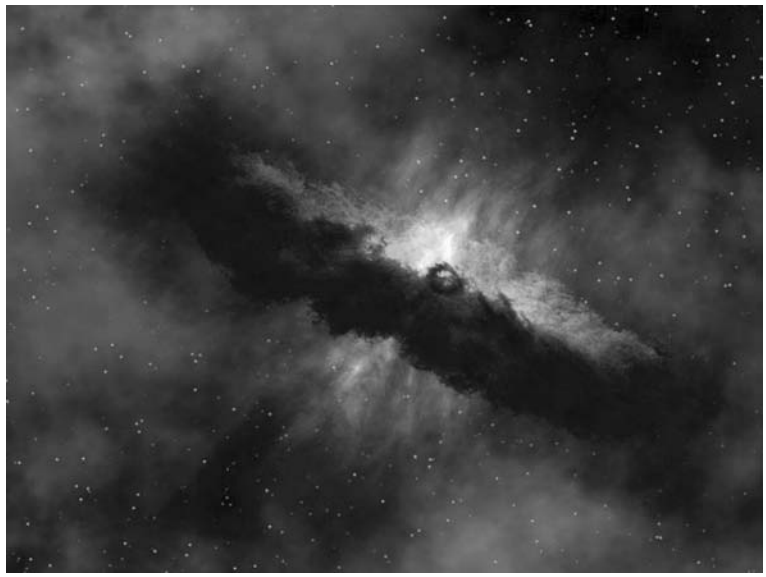

Fig. 1.1 **An artist's conception of the solar nebula, surrounding the violent young Sun. Figure courtesy of NASA.**

grains were released to the *interstellar medium* (ISM), the space between the stars. The ISM is filled primarily by diffuse gases, mostly hydrogen and helium, but with oxygen, carbon, and nitrogen contributing about 1% by mass and all the other elements mostly in micrometer-size dust motes. Much of the chemistry in the ISM occurs within relatively dense molecular clouds, where gas densities can reach 10^3 to 10^6 particles per cm^3, high by interstellar standards (but not by our everyday experience – Earth's atmosphere has $\sim 3 \times 10^{19}$ atoms per cm^3 at sea level). These clouds are very cold, with temperatures ranging from 10 to 100 K, so interstellar grains become coated with ices. Reactions between ice mantles and gas molecules produced organic compounds that can be extracted from meteorites and identified by their bizarre isotopic compositions. Many dust grains were undoubtedly destroyed in the ISM, but some hardy survivors were incorporated into the nebula when the molecular cloud collapsed, and thence were accreted into meteorites.

Processes that occur inside stars, in interstellar space, and within the solar nebula have no counterparts in our terrestrial experience. They can be studied or inferred from astronomical observations and astrophysical theory, but cosmochemical analyses of materials actually formed or affected by these processes provide constraints and insights that remote sensing and theory cannot. Our terrestrial experience places us on firmer ground in deciphering the geologic processes occurring on the Earth's Moon. In studying lunar rocks and soils, we can use familiar geochemical tools developed for understanding the Earth. We have also measured the chemical compositions of some other planetary bodies or their smaller cousins, geologically processed planetesimals, using telescopes or instruments on spacecraft. In some cases, we even have meteorites ejected during impacts onto these bodies. Chemical measurements (whether from laboratory analyses of samples or *in situ* analyses of rocks and soils by orbiting or landed spacecraft) add quantitative

dimensions to our understanding of planetary science. All extraterrestrial materials are fair game for cosmochemistry.

Geochemistry versus cosmochemistry

Traditionally, cosmochemistry has been treated as a branch of *geochemistry* – usually defined as the study of the chemical composition of the Earth. Geochemistry focuses on the chemical analysis of terrestrial materials, as implied by the prefix "geo," and geochemistry textbooks commonly devote only a single chapter to cosmochemistry, if the subject is introduced at all. However, the line between geochemistry and cosmochemistry has always been somewhat fuzzy. The most prominent technical journal in this discipline, *Geochimica et Cosmochimica Acta*, has carried both names since its inception in 1950. The burgeoning field of planetary geochemistry appropriates the "geo" prefix, even though its subject is not Earth. A broader and more appropriate definition of geochemistry might be the study of element and isotope behavior during geologic processes, such as occur on and within the Earth and other planets, moons, and planetesimals. Using this definition, we will include *planetary geochemistry* as an essential part of our treatment of cosmochemistry.

It is worth noting, though, that the geochemical and cosmochemical behaviors of elements do show some significant differences. A geochemical perspective of the periodic table is illustrated in Figure 1.2 (adapted from Railsback, 2003). As depicted, this diagram is decidedly Earth-centric, but the controls on element behavior during geologic processes apply to other bodies as well. Determining relative elemental abundances is an important part of geochemistry, and the relative abundances of elements in the Earth's crust vary over many orders of magnitude. Crustal abundances are illustrated in Figure 1.2, because most geochemical data are based on readily accessible samples of the crust. Geochemistry is also concerned with determining the composition of the Earth's interior – its mantle and core – and a more comprehensive figure would include those abundances as well. Very few native elements (pure elements not chemically bound to any others) occur naturally in the Earth, so Figure 1.2 distinguishes elements that occur commonly as cations or anions (positively and negatively charged particles, respectively), which allows them to combine into compounds (minerals), to be dissolved in natural fluids, or to occur in melts (magmas) at high temperatures. The elements in Figure 1.2 are also grouped by their so-called *geochemical affinities*: lithophile (rock-loving) elements tend to form silicates or oxides (the constituents of most rocks), siderophile (iron-loving) elements combine with iron into metal alloys, chalcophile (sulfur-loving) elements react with sulfur to form sulfides, and atmophile elements tend to form gases and reside in the atmosphere. Many elements exhibit several affinities, depending on conditions, so the assignments illustrated in Figure 1.2 offer only a rough approximation of the complexity of element geochemical behavior. Finally, an important part of geochemistry takes advantage of the fact that most elements exist in more than one isotopic form. Measuring isotopic abundances has great value as a geochemical tool, and the most commonly used isotope systems are illustrated by heavy boxes in Figure 1.2. Stable isotopes of some light elements provide information on sources of elements, the conditions under

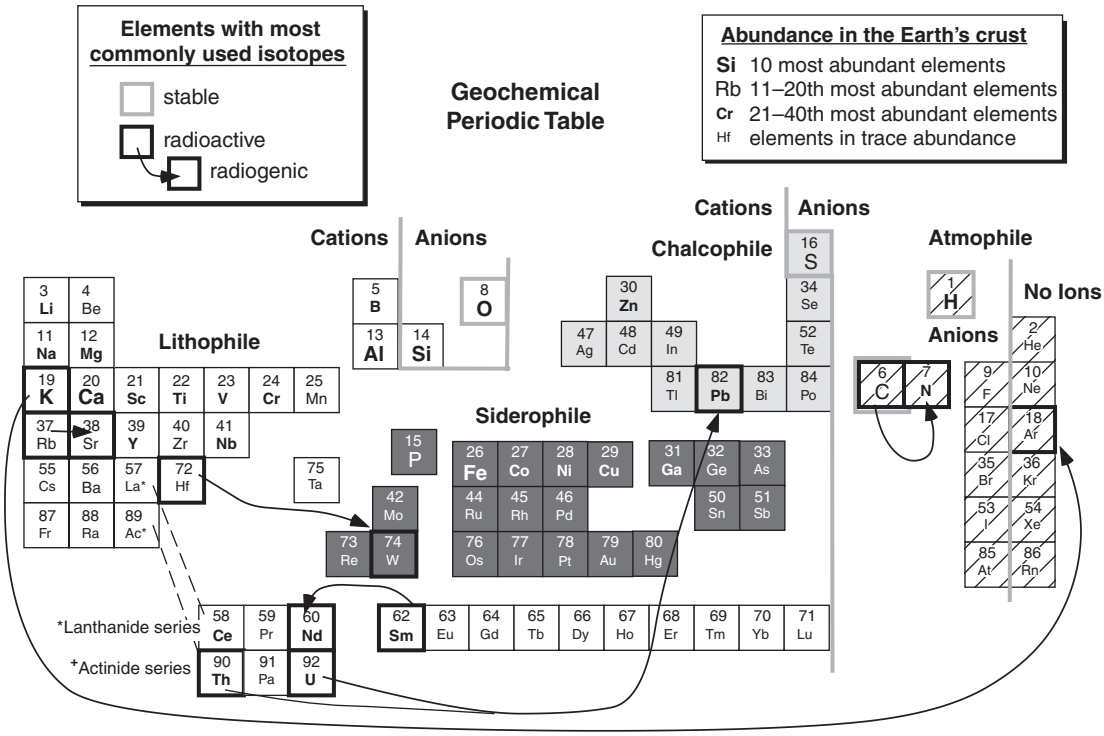

Fig. 1.2 A geochemical periodic table, illustrating controls on element behavior during geologic processes. Abundances of elements in the Earth's crust are indicated by symbol sizes. Cations and anions are usually combined into minerals. Elements having affinities for silicate or oxide minerals (lithophile), metal (siderophile), sulfide minerals (chalcophile), and non-rock (atmophile) phases are identified. Elements having stable isotopes that are commonly used in geochemistry are shown as boxes with bold gray outlines. Radioactive and radiogenic isotopes used for chronology are shown by boxes with bold black outlines and arrows showing decay relationships.

which minerals form, and the processes that separate isotopes from each other. Unstable (radioactive) nuclides and their decay products (radiogenic nuclides) similarly constrain element sources and geologic processes, as well as permit the ages of rocks and events to be determined. The isotopic compositions of many other elements in terrestrial materials are now being analyzed, and a future Figure 1.2 will certainly expand the list of commonly used isotopic systems.

By way of contrast, Figure 1.3 illustrates a cosmochemical perspective of the periodic table. The element abundances shown in this figure are atomic concentrations in the Sun (relative to the abundance of silicon), as best we can determine them. The Sun comprises >99.8% of the mass of solar system matter, so solar composition is approximately equivalent to the average solar system (often incorrectly called "cosmic") composition. The behavior of elements in space is governed largely by their volatility, which we quantify by specifying the temperature interval where elements change state from a gas to a solid on cooling. (The liquid state is not generally encountered at the very low pressures of space; liquids tend to be more common in geochemistry than cosmochemistry.) All elements

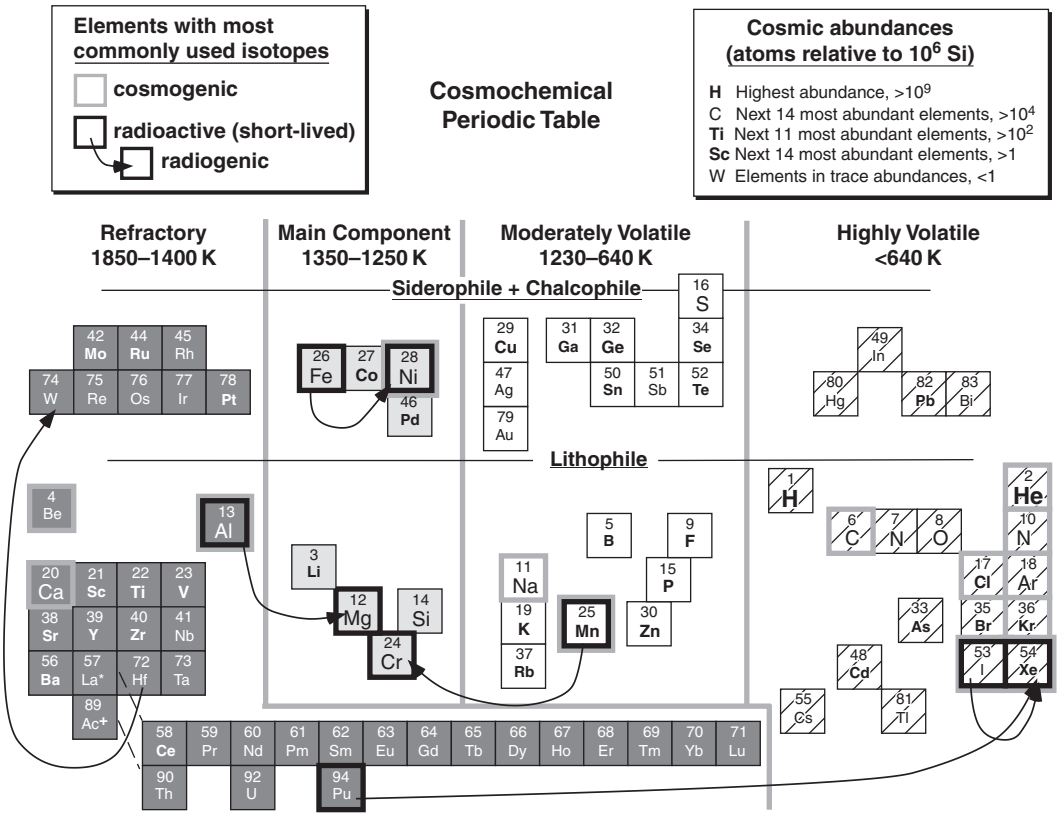

Fig. 1.3 A cosmochemical periodic table, illustrating the behavior of elements in chondritic meteorites. Cosmic abundances are indicated by symbol sizes. Volatilities of elements reflect the temperatures at which 50% of each element would condense into a solid phase from a gas of solar composition. As in Figure 1.2, the chemical affinities of each element, lithophile for silicates and oxides, siderophile for metals, and chalcophile for sulfides, are indicated. Some of the most highly volatile phases may have remained uncondensed in the nebula. Stable, radioactive, and radiogenic isotopes used in cosmochemistry are indicated by bold outlines, as in Figure 1.2. Abundances and 50% condensation temperatures are from tabulations by Lodders and Fegley (1998).

occur as gases at high enough temperatures, and they either condense at lower temperatures to form solid minerals or ices, or react with already condensed phases to form other solid phases. Some elements condense at such low temperatures that they effectively remain as gases. Thermodynamic data can be used to predict the temperatures at which solid phases become more stable than their components in a gas of solar composition. Assignment of elements to the various refractory and volatile groups in Figure 1.3 is based on the temperature at which 50% of each element has condensed into solid phases. It is convenient in cosmochemistry to identify elements according to the kinds of minerals into which they condense – lithophile, siderophile, and chalcophile. Some volatile elements only condense at very low temperatures to form ices, or do not condense at all. Also illustrated in Figure 1.3 are the most commonly used isotope systems in cosmochemistry; the complete list is considerably longer than for geochemistry, and would include stable isotopes measured in

presolar grains in meteorites, cosmogenic nuclides formed by interaction with cosmic rays in space, and now-extinct radioactive isotopes that existed in the early solar system.

Comparison of Figures 1.2 and 1.3 reveals that the chemical behavior of an element may differ depending on whether it is in a geochemical or cosmochemical environment. This book's topics will refer to both figures in understanding the compositions of extraterrestrial materials. In cosmochemistry we are concerned with the origin and behavior of elements in space, whereas in planetary geochemistry we focus on their behavior once they are accreted into bodies that undergo geologic (usually thermal) processing. Planetary geochemistry follows more or less the same rules as on the Earth, although these rules must be modified to accommodate different geologic conditions or starting compositions. And the geochemical consequences of biology, so important on Earth, do not apply on other worlds, so far as we can determine presently.

Beginnings of cosmochemistry (and geochemistry)

Philosophical foundations

The philosophical foundations of cosmochemistry date to the last half of the eighteenth century when Immanuel Kant (1724–1804) and Pierre-Simon Marquis de Laplace (1749–1827) put forward comprehensive models for the origin of the solar system. Kant's model, published in 1755, started with the Sun at the center of a gaseous nebula. In order for this cocoon of gas and dust to be stable in the gravitational field of the Sun, the nebula had to rotate about the Sun. Kant suggested that the matter in the disk would segregate into large bodies that would become the planets. This segregation would take place slowly, with each body developing into a miniature version of the solar system. Kant showed that the rotation of the planets and their satellites would be in the same sense as their revolution around the Sun. In 1796, Laplace published a model that started with the primordial Sun occupying the entire volume now occupied by the planetary orbits. This hot, luminous "solar nebula" rotated as a rigid body so that linear velocity was greatest at the outer edge. As the nebula cooled and contracted, it rotated faster to preserve angular momentum. When centrifugal force exceeded gravitation attraction, a ring was left behind. This process was repeated many times and the rings contracted to form planets. During the nineteenth century, these two models became intertwined into a "nebular hypothesis" that was generally accepted in some form until the beginning of the twentieth century. Ideas based on these models, such as a hot solar nebula, have remained part of mainstream cosmochemical thought until very recently.

Meteorites and microscopy

Meteorites (Fig. 1.4) are central to cosmochemistry, because they are our most accessible source of extraterrestrial samples. Though people have seen stones falling from the sky for

Fig. 1.4 **Broken surface of the Allende meteorite, a chondrite that fell in Mexico in 1969. Note the abundant round chondrules and white calcium–aluminum inclusions.**

thousands of years, the fact that meteorites actually fall was not acknowledged by the European and American scientific establishments until early in the nineteenth century. Credit for putting meteorites on the scientific map generally goes to Ernst Chladni (1756–1827). In a 63-page book with the long title (translated from German) *On the Origin of the Mass of Iron Found by Pallas and of Other Similar Iron Masses, and on a Few Natural Phenomena Connected Therewith*, published in 1794, Chladni laid out a case based on historical records of observed falls that stone and iron masses enter the Earth's atmosphere from space and form fireballs as they plunge through the atmosphere. These ideas contradicted two strongly held beliefs by his scientific contemporaries: rocks and masses of metal do not fall from the sky, and no small bodies exist in space beyond the Moon. However, during the next five years, four falls of stony meteorites were witnessed and widely reported in Europe. Chemist Edward Howard (1774–1816) and mineralogist Jacques-Louis de Bournon (1751–1825) carried out a series of chemical and mineralogical analyses of stones said to have fallen from the sky and found that they were similar in texture and composition and significantly different from terrestrial rocks. The publication of these findings in early 1802 was followed by the fall in 1803 of nearly 3000 stones at L'Aigle in Normandy, France. These events provided evidence to support Chladni's claims, and meteorites entered the realm of scientific study.

A major step in understanding meteorites came with Henry Clifton Sorby's (1826–1908) development of the petrographic microscope in the mid-1800s. Using this instrument, thin sections (paper-thin slices of rock, mounted on glass slides) are observed by passing polarized light through them from below, providing a means of identifying minerals and observing the textures of rocks. Sorby soon turned his attention to a type of meteorite called *chondrites*, describing the round droplets of solidified melt in them (called "chondrules,"

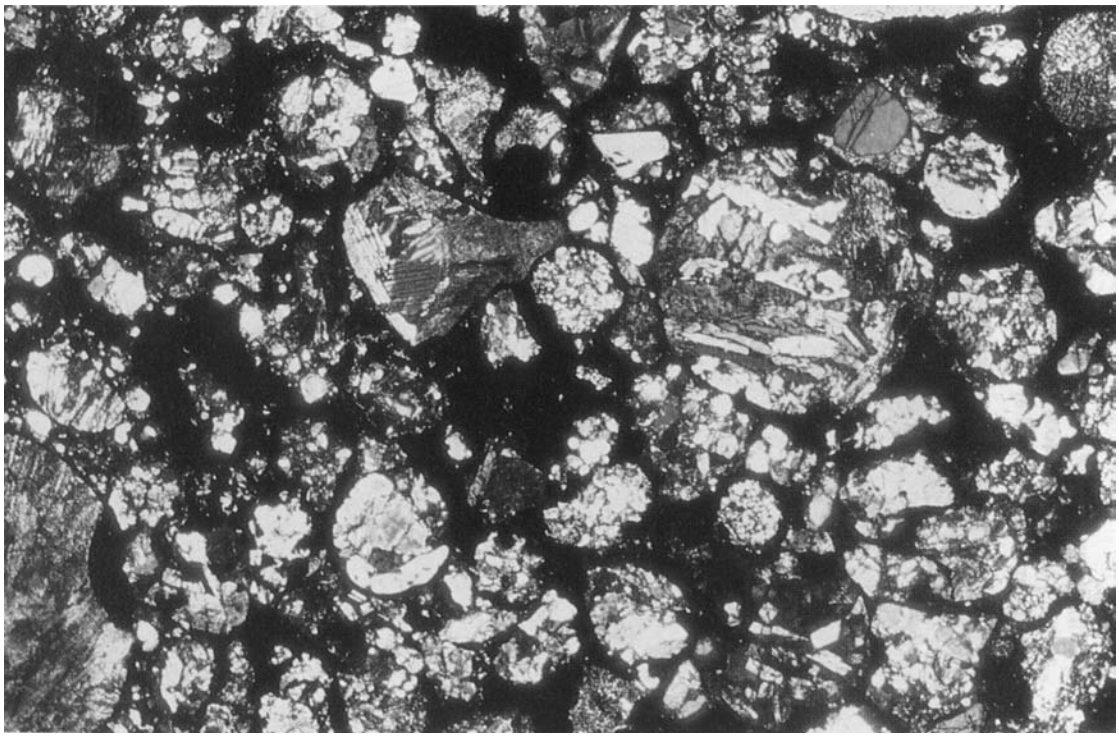

Fig. 1.5 Transmitted-light photomicrograph of the Tieschitz chondritic meteorite. Horizontal field of view is ~3.5 mm. The rounded, millimeter-size chondrules contain crystals of olivine and pyroxene, and the chondrules are set in a fine-grained, opaque matrix.

after the Greek *chondros* for "grains" or "seeds") as drops of a fiery rain (Fig. 1.5). Chondrites will be described in detail in Chapter 6.

A significant part of meteoritics literature focuses on petrographic description and classification. This does not usually make for exciting reading, but an orderly classification is essential for interpreting the chemical compositions of meteorites and recognizing relationships among them. Beginning in the 1860s, Gustav Rose (1798–1873) at the University Museum of Berlin and Nevil Story-Maskelyne (1823–1911) at the British Museum developed meteorite taxonomies based on microscope observations. Gustav Tschermak (1836–1927) later refined Rose's classification, and Aristides Brezina (1848–1909) refined the Rose-Tschermak classification, which reached its final form in 1904. This classification was based on mineralogy, because at the time there were few chemical analyses of meteorites and those that existed were of uneven quality. George Prior (1862–1936) devised a simpler mineralogical classification for chondrites in 1920. Prior's major mineralogical subdivisions for meteorites are still used today, but his system has been supplanted by one devised by Randall Van Schmus and John Wood (1967) that separates primary characteristics of meteorites, such as bulk composition, from secondary characteristics, such as degree of metamorphic or aqueous alteration. We will discuss meteorite classification in detail in Chapter 6.

Box 1.1 Lockyer and the discovery of helium in the Sun

Joseph Lockyer (1836–1920) was one of the pioneers of solar spectroscopy. In examining the spectra of solar prominences in 1869, Lockyer noticed an absorption line that he could not identify. Reasoning that it represented an element not present on Earth, he proposed a new element – helium, from the Greek word *helios* for Sun. This idea failed to achieve acceptance from Lockyer's scientific colleagues until a gas having the same mysterious spectral line was found 25 years later in rocks. The helium in terrestrial uranium ore formed as a decay product of radioactive uranium. Thus, this abundant element was first discovered in the Sun, rather than in the laboratory. Lockyer's cosmochemical discovery was recognized by the British government, which created a solar physics laboratory for him. Lockyer also founded the scientific journal *Nature*, which he edited for 50 years.

In the late 1800s, after decades of work on the spectroscopy of stars, Lockyer developed his "meteoritic hypothesis". According to this idea, meteorites were the primary dust of the universe. Nebulae observed by astronomers were interpreted as swarms of meteorites bound together through gravitation and interacting much like atoms in a gas. Lockyer postulated that the solar system and other objects had formed from these meteorite swarms (Lockyer, 1890). Although the original hypothesis was soon abandoned, the idea that meteorites might be chemically primitive materials that sample the cosmos was not far off the mark.

Spectroscopy and the compositions of stars

In the early nineteenth century, determining the compositions of stars posed a fundamental hurdle for astronomy. The French philosopher Auguste Compte (1798–1857) confidently asserted that never, by any means, would we be able to study the chemical compositions of celestial bodies. But spectroscopy soon proved him wrong. Spectroscopes attached to telescopes were used to spread out starlight into its component wavelengths. The spectra of stars and of the Sun showed numerous narrow, dark gaps where particular wavelengths were missing. These gaps (absorption lines) are due to the various chemical elements in a star's outer layers absorbing light emanating from the hotter interior. Each element absorbs (or emits) light at specific wavelengths characteristic of its electronic structure.

Identifying the elements present in the Sun and stars from their spectra was one thing, but determining their relative abundances was quite another. The solar absorption lines for iron are particularly prominent, leading astronomers to believe that iron was the most abundant element in the Sun, as it is in the Earth and in many meteorites. Princeton astronomer Henry Russell (1877–1957) even conjectured that if the Earth's crust were heated to the temperature of the Sun, its spectrum would resemble the solar spectrum. It took until the 1920s before the establishment of a clear understanding of how spectra arise, permitting evaluation of the true compositions of the Sun and stars. The key to understanding stellar spectra was discovered in 1925 by Cecilia Payne (1900–79). She showed that the spectral lines arose from the excitation of the electrons surrounding the atomic nucleus and that the energy

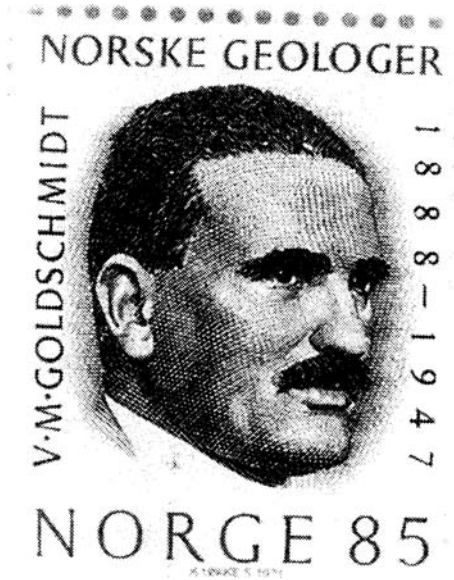

Fig. 1.6 Victor Goldschmidt, as pictured on a Norwegian postage stamp issued in 1974.

levels of the electrons were a function of stellar temperature. When temperature was taken into account, the abundances of elements in stars were shown to be nearly the same in a variety of stars in spite of their having different spectra. Her work also showed that hydrogen and helium are the most abundant elements in the Sun and other stars. This last result was not immediately widely accepted and was downplayed in her published thesis. But by 1930, her work had completely supplanted previous interpretations and modern spectroscopy was born.

Solar system element abundances

The term "cosmochemistry" apparently derives from the work of Victor Goldschmidt (Fig. 1.6), who is often described as the father of geochemistry. This is yet another crossover and, in truth, Goldschmidt also established cosmochemistry as a discipline. In 1937 he published a *cosmic* abundance table based on the proportions of elements in meteorites. He used the term "cosmic" because, like his contemporaries, he believed that meteorites were interstellar matter. Chemist William Harkins (1873–1951) had formulated an earlier (1917) table of elemental abundances – arguably the first cosmochemistry paper, although he did not use that term. As explained in Chapter 3, the term *solar system* abundance is now preferred over cosmic abundance, although the terms are often used interchangeably.

Goldschmidt and his colleagues in Germany, and later in Norway (where he escaped the grasp of the Nazis in World War II), analyzed and compiled a wealth of chemical data on

terrestrial rocks and meteorites. The compositions of terrestrial rocks have been modified by partial melting (leaving some components behind as residues) and by fractional crystallization (where crystals are segregated from the melt, causing the liquid's composition to change). However, Goldschmidt recognized that chondrites have not experienced wholesale melting and thereby escaped geologic processing. They are basically cosmic sediments – physical mixtures of nebular matter whose chemical abundances have remained unchanged since they formed. To obtain accurate compositions using the then-new analytical technique of emission spectrography, Goldschmidt separated chondrites into their more readily measurable silicate, metal, and sulfide components and analyzed each in turn. Consequently, he was able to determine how various elements were partitioned among these coexisting phases (he invented the descriptive terms lithophile, siderophile, and chalcophile to describe their geochemical affinities). He then calculated what he called the "cosmic abundances" of 66 elements by using the weighted means of element concentrations in meteorite silicate (10 parts), metal (2 parts), and sulfide (1 part). At about the same time, astronomers began using the Sun's spectra to estimate elemental abundances. It soon became apparent that solar elemental abundances were similar to Goldschmidt's cosmic (chondritic) abundances, except that the meteorites were depleted in the most volatile elements like hydrogen and helium. Cosmic abundances (more properly called solar system abundances) are a cornerstone of cosmochemistry because they represent the raw material from which the solar system formed.

Isotopes and nuclear physics

Isotopes were recognized at the beginning of the twentieth century as a result of studies of radioactivity. Careful studies found three naturally occurring radioactive decay series, the thorium, uranium, and actinium series, all of which ended with stable lead. The existence of isotopes was confirmed in 1911 when Fredrick Soddy (1877–1956) measured the atomic masses of lead obtained from uranium-rich and thorium-rich ores and showed that they were different. During this same period, J. J. Thompson (1856–1940) discovered that ions accelerated through an electric field would adopt different parabolic trajectories depending upon their masses. Thompson's student, Francis Aston (1877–1945) used this principle to design several different mass spectrographs, which separated particles by mass/charge ratio and recorded the output on photographic plates. By 1920, Aston was reporting the presence and relative abundance isotopes of numerous elements, including oxygen, neon, argon, krypton, xenon, and mercury (e.g. Aston, 1920). In 1922, he received the Nobel Prize in chemistry for his work on isotopes using a mass spectrograph. However, an understanding of the structure of the atom had to await the discovery of the neutron in 1930.

During the 1930s, further technological advances permitted detailed studies of the masses and relative abundances of the isotopes. Modern mass spectrometers designed by Alfred Nier (1911–94) at the University of Minnesota had greater mass-resolving power and were more sensitive than any built previously. Nier made accurate measurements of the isotopic abundances of argon, potassium, zinc, rubidium, and cadmium and, in the process, discovered ^{40}K, which would later become an important isotope for dating rocks. He also did

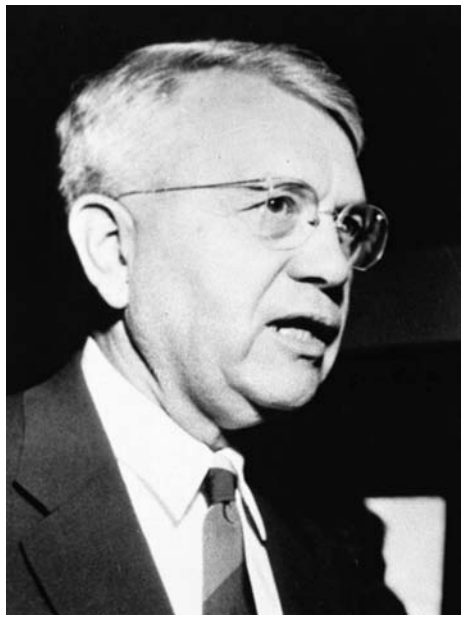

Fig. 1.7 Harold Urey, one of the fathers of cosmochemistry. Figure courtesy of NASA.

pioneering work on the development of uranium-lead and thorium-lead dating. Nier's determinations of the isotopic compositions of many elements in natural materials are still the standard against which many other measurements are made.

In 1940, Nier successfully separated ^{235}U from ^{238}U using a mass spectrometer, providing an enabling technology for the Manhattan Project. During World War II, many of the top nuclear physicists worked on the development of the atomic bomb. The fascinating story of these years and their effect upon the participants is beyond the scope of this book. But as war ended, many of them turned their attention away from the tools of war to understanding our world and universe, and their knowledge became available to cosmochemistry.

The leading figure in cosmochemistry during the 1950s and 1960s was Harold Urey (1893–1981). Urey (Fig. 1.7) was one of the first practitioners of cosmochemistry as we understand it today. He was awarded the Nobel Prize in chemistry in 1934 for his work on deuterium and heavy water. During the war, he and his colleagues developed the gaseous diffusion method for separating ^{235}U from ^{238}U. After the war, he became a professor at the University of Chicago, where he did pioneering work using the $^{18}O/^{16}O$ ratio in paleoclimate research, developed theories about the origin of the elements and their abundance in stars, pointed out the importance of short-lived radionuclides such as ^{26}Al, investigated the origins of life on Earth, and made many other contributions. He was a leader in developing the scientific rationale for returning samples from the Moon.

During World War II, Hans Suess (1909–93) was part of a team of German scientists working on heavy water. In 1950, he immigrated to the United States. His work with Urey on nucleosynthesis and the abundances of the elements is a cornerstone of cosmochemistry. In 1965, along with Heinrich Wänke, he proposed that the extremely high noble gas contents

in some chondritic meteorites were due to the implantation of solar wind. He also did pioneering work on climate research and ^{14}C dating. Together, Suess and Urey (1956) published the first table of cosmic abundances to include the abundances of the isotopes.

The new knowledge of nuclear physics affected cosmochemistry in another way. A classic paper by astrophysicists Margaret and Geoffrey Burbidge (husband and wife), William Fowler, and Fred Hoyle (this paper was so influential that it has come to be known by scientists simply as "B^2FH") and a similar contribution by Allister Cameron, both published in 1957, provided the theoretical basis for understanding how elements are produced in stars, as described in Chapter 3.

Radiometric dating using long-lived radionuclides came into its own in the 1940s and 1950s with the advent of better mass spectrometers. The uranium isotope decay scheme was first shown to be useful as a geochronometer by Fritz Houtermans and Arthur Holmes in 1946. The first accurate determination of the age of the Earth was made in 1956 by Clair Patterson, who used the uranium–lead method to date meteorites. The ^{40}K–^{40}Ar decay scheme was shown to be a useful chronometer for meteorites by Gerald Wasserburg in his doctoral thesis, completed in 1954. The first age determination by the ^{87}Rb–^{87}Sr method was published by Hahn *et al*. (1943), and the method came into wide use in the 1950s. Application to meteorites peaked in the late 1960s and 1970s, in conjunction with work on the lunar samples.

Short-lived radionuclides are those with half-lives sufficiently short that any atoms present in the early solar system would have completely decayed away. In 1960, John Reynolds found the first clear evidence that short-lived nuclides were present in the form of large excesses of ^{129}Xe, the decay product of short-lived ^{129}I, in chondritic meteorites. This discovery showed that elements had been synthesized in stars shortly before the formation of the solar system. A more important short-lived radionuclide, ^{26}Al, was demonstrated to have been present in meteorites by Typhoon Lee and coworkers in 1977. This isotope is particularly significant, as it is thought to have been a potent source of heating for asteroids and planets early in solar system history. A variety of other short-lived isotopes have now been confirmed in meteorites and are the basis for high-resolution chronometry of the early solar system.

Nuclides formed by nuclear reactions induced by high-energy cosmic rays are called cosmogenic. Cosmogenic isotopes are more common in meteorites than on the Earth, because our planet's atmosphere screens out most cosmic rays. However, meteorites traveling in space are heavily irradiated by cosmic rays, and the production of cosmogenic isotopes can be used to estimate the times since the meteorites were liberated from their parent asteroids (these times are called cosmic-ray exposure ages). The first meteorite exposure ages were measured in the late 1950s. Since that time, thousands of meteorite exposure ages have been estimated using a variety of cosmogenic nuclides, and new modeling techniques have allowed the interpretation of complex irradiation histories.

In 1956, John Reynolds pioneered a new and highly sensitive method for measuring noble gases, which effectively created the field of noble gas geochemistry and cosmochemistry. Noble gases have many isotopes and, because they do not bond with rock-forming elements, they have very low abundances in most materials. Thus, additions from decay of radioactive nuclides or cosmic ray interactions are easy to detect. Noble gases also exhibit different elemental and isotopic ratios in meteorites, reflecting different processes operating

in the early solar system. In addition, isotopic anomalies that could not be explained by any processes known to be operating in the solar system were found in xenon (discovered by John Reynolds and Grenville Turner in 1964) and neon (discovered by David Black and Robert Pepin in 1969) extracted from meteorites. These noble gases provided the first hints that presolar grains might have survived in the nebula, although they were not widely recognized at the time.

The pursuit of the carriers of exotic noble gas isotopes by Edward Anders and colleagues at the University of Chicago and in other laboratories eventually led to the isolation of presolar grains from meteorites. The approach used by Anders involved laborious tracking of the exotic noble gas carriers through steps of increasingly harsh chemical dissolutions and physical separations. His reward was a small amount of diamond dust, the first isolated presolar grains. These tiny mineral grains provide a window on the very creation of elements in stars. Other presolar grains, all bearing some distinctive isotopic fingerprint, have now been isolated from meteorites. Like diamond, the other common presolar grains (graphite, silicon carbide) are made of carbon, reflecting its high cosmic abundance and the refractory nature of these minerals. However, a number of other kinds of presolar grains have also been found, as discussed in Chapter 5.

Space exploration and samples from other worlds

The launch of Sputnik by the Soviet Union in 1957 changed the world forever. The immediate impact was to change the nature of the Cold War by demonstrating the feasibility of intercontinental ballistic missiles. But Sputnik also raised the curtain on the scientific exploration of space and on visiting and obtaining samples from other solar system bodies. The first target was the Moon. Close-up images of the Moon were provided by the US Ranger missions, which impacted the Moon in 1964 and 1965. The first lunar chemical data were provided by Soviet Luna and American Surveyor spacecraft in 1966. The first manned landing on the Moon was the Apollo 11 mission, which landed in Mare Tranquilitatis in 1969. Five more Apollo missions followed, before the program was abruptly terminated.

The return of 382 kg of lunar rocks and soils from six sites on the Moon's nearside by Apollo astronauts (Fig. 1.8) and 326 g by Soviet Luna robotic landers in the 1970s provided a bonanza of new extraterrestrial materials for cosmochemistry. The intense interest in these samples encouraged a considerable expansion of laboratory techniques and capabilities. Fortuitously, two large meteorites (the Allende and Murchison chondrites) fell in 1969, just as the new laboratories were gearing up for lunar sample return. The new analytical techniques were applied to these meteorites, initially as a means of demonstrating capability. But the two chondrites turned out to be incredibly interesting in their own right and provided a new impetus to the study of all types of extraterrestrial materials. Because lunar samples were so precious, many groups simultaneously analyzed the same rocks, and competition forced the quality of analyses to new heights. Lunar rocks were especially useful because mapping by telescopes and orbiting spacecraft provided the geologic context for these samples. Lunar soils allowed wider sampling of rock types, because the soils consist of rock particles thrown tremendous distances by impacts. In addition, lunar soils contained

Fig. 1.8 Lunar soil samples being collected by an Apollo astronaut. Figure courtesy of NASA.

implanted solar wind particles, providing a window on solar element abundances. A decade after the Apollo program ended, the first lunar meteorites were recognized. While the Apollo and Luna samples were collected from a geographically restricted (<5%) area of the Moon, the ~60 distinct lunar meteorites are thought to provide a more representative sampling.

Remote sensing of the Moon by spacecraft complemented the return of samples. Using X-ray fluorescence spectrometers (XRF), the Apollo 15 and 16 service modules obtained orbital measurements of aluminum, silicon, and magnesium at a spatial resolution of ~50 km. In 1994, the Clementine orbiter mapped the surface reflectance of the Moon at 11 wavelengths with spatial resolutions of 100–300 m. These multispectral images have been used to infer mineralogy as well as the abundances of iron and titanium. The Lunar Prospector orbiter in 1997–8 used a gamma-ray spectrometer (GRS) to obtain global maps of the abundances of iron and thorium at 15 km spatial resolution and potassium and titanium at 60 km resolution. Additional GRS data for oxygen, magnesium, aluminum, silicon, calcium, and uranium were obtained at 150 km resolution, and a neutron spectrometer measured hydrogen concentrations in lunar soils.

The first close-up images of the planet Mars were returned by the Mariner 4 spacecraft, which flew by the planet in 1964. Mariners 6 and 7 flew past Mars in 1969, returning more images, and Mariner 8 was the first spacecraft to go into orbit around Mars in 1971. The Viking missions landed two spacecraft on Mars in 1976. Viking landers took high-resolution images of their landing sites and gathered data on the composition of the atmosphere and surface soils.

In 1979, a handful of unusual meteorites, all igneous rocks, were hypothesized to be Mars samples. This controversial idea was based primarily on their young crystallization ages (1.3 billion years or younger), because it was difficult to envision how melting could occur

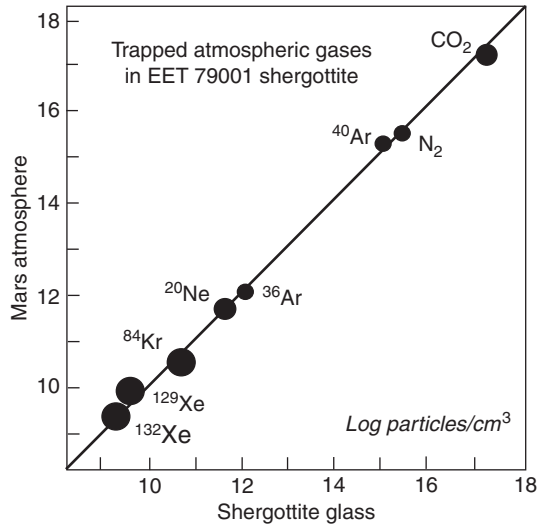

Fig. 1.9 **Comparison of trapped gases in impact-melt glass in the EET 79001 Martian meteorite with the composition of the Martian atmosphere as measured by Viking landers. This remarkable agreement is the evidence that convinced most planetary scientists that SNC meteorites came from Mars.**

on small asteroids so late in solar system history. The idea found wide acceptance several years later when trapped gases in these meteorites were found to have chemical compositions identical to the Martian atmosphere, as measured by Viking landers (Fig. 1.9). The discovery of lunar meteorites in Antarctica, identified by comparing them with Apollo samples, proved that rocks could be ejected from one body and travel to another. For the first time, rocks from another planet were available for direct geochemical analyses. The chemical compositions of these meteorites – shergottites, nakhlites, chassignites, commonly abbreviated as "SNCs" – have provided a wealth of new insights into geochemical processes on Mars.

More recently, analyses of Martian rocks and soils were obtained using alpha particle X-ray spectrometers (APXS) on the Mars Pathfinder rover in 1997 and two Mars Exploration Rovers in 2004–10 (Fig. 1.10). Several of the rocks investigated by the MER rovers turned out to be meteorites. The mineralogy of Martian surface materials has been determined by a thermal emission spectrometer (TES) on the Mars Global Surveyor orbiting spacecraft at spatial resolutions of a few tens of km. Abundances of iron, potassium, thorium, silicon, calcium, and chlorine have also been determined by a gamma-ray spectrometer on the Mars Odyssey orbiter, and the abundances of other elements await better counting statistics. A neutron spectrometer determined concentrations of hydrogen in the Martian subsurface.

Several Soviet Venera and Vega spacecraft landed on the surface of Venus in the early 1980s, and survived for a few minutes before succumbing to the stifling heat. X-ray fluorescence chemical analyses for a number of major elements in surface samples were reported. Chemical and isotopic analyses of the Venus atmosphere were made by Pioneer Venus, Venera, and other orbiters.

Aspects of the chemical composition of the atmospheres of Jupiter, Saturn, Uranus, and Neptune were measured by the Voyager and Galileo spacecraft in the 1980s and 1990s,

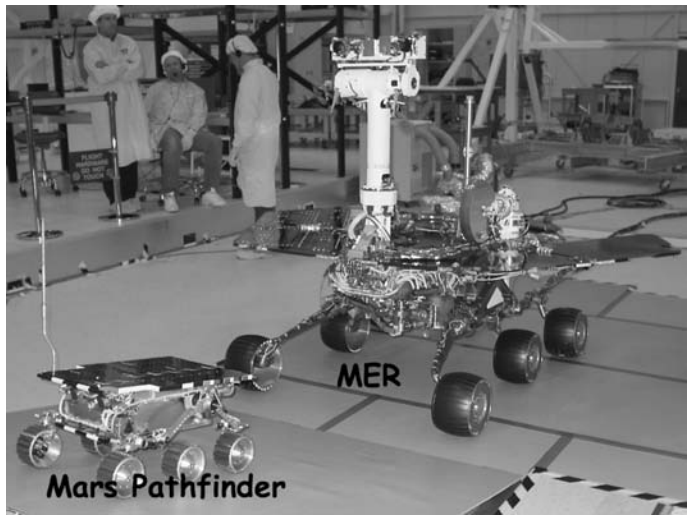

Fig. 1.10 **The Mars Pathfinder rover (flight spare) pictured with one of the Mars Exploration Rovers (MER) during assembly.**

respectively. The atmosphere of Titan, the largest satellite of Saturn, was analyzed by the Cassini spacecraft. Most of what is known or inferred about the compositions of satellites of the giant planets is based on the spectra of sunlight reflected from their surfaces.

The Mariner 10 spacecraft flew by Mercury and photographed one side of the planet in 1975. Mercury was not visited again until the Messenger spacecraft flew past the planet in 2008. As this is being written, the spacecraft is in orbit around the Sun. It will fly past Mercury two more times before finally going into orbit around the planet in 2011. In addition to high-resolution imagery of the entire planet, Messenger will acquire compositional and mineralogical information about the planet, study its magnetic field, and investigate the composition of its very thin atmosphere.

The only *in situ* chemical data for asteroids are from the NEAR Shoemaker spacecraft, which orbited 433 Eros in 2000–1, and from the Japanese Hayabusa spacecraft, which visited 25143 Itokawa in 2003. NEAR obtained numerous measurements of the surface composition using X-ray fluorescence and gamma-ray spectrometers, and Hayabusa carried an XRF. The magnesium/silicon and aluminum/silicon ratios for both asteroids are consistent with the compositions of chondrites. However, sulfur is depleted in Eros relative to chondritic compositions, possibly due to devolatilization by impacts or small degrees of melting.

Spacecraft missions have visited five comets and have provided some spectacular images of the comet nuclei and data on their chemical and mineralogical compositions. In 1985, NASA's ICE spacecraft passed through the tail of Comet Giacobini-Zinner. In 1986, five spacecraft visited comet IP/Halley (Halley's comet). The Soviet Vega 1 and Vega 2 probes sent images of the nucleus, and the European Giotto probe made a close pass by the nucleus. All three of these probes had mass spectrometers that returned data on the composition of dust expelled from the comet. Two Japanese probes also visited comet IP/Halley. Comet

Grigg-Skjellerup was visited by the Giotto spacecraft in 1989. NASA's demonstration spacecraft DS1 imaged the nucleus of Comet Borrelly in 2001.

More ambitious comet missions have flown recently. The Deep Impact mission went to comet Temple 1, arriving in 2005. Deep Impact released a large impactor that crashed into the comet and then studied the material that was released using spectrometers and cameras. Information on the chemical composition and mineralogy of the comet showed that it contains both low-temperature and high-temperature materials. The Stardust mission visited comet Wild 2 in 2004. In addition to taking some spectacular images, the spacecraft brought samples of comet dust back to Earth in 2006.

New sources of extraterrestrial materials

For many years, cosmochemistry depended on the chance discovery of meteorites – either witnessed "falls" and serendipitous "finds," or the dogged determination of a few private collectors who systematically searched for them. That changed in 1969, when Japanese explorers in Antarctica led by Masaru Yoshida stumbled onto meteorites exposed on bare ice. American geologist William Cassidy immediately recognized an opportunity, and with support from the National Science Foundation he mounted a joint expedition with the Japanese to the Allan Hills region of Antarctica in 1977 to recover meteorites. This was the first of many expeditions, sponsored by the National Science Foundation and headed first by Cassidy and later by Ralph Harvey, that have returned to Antarctica every year to collect meteorites (Fig. 1.11). The Japanese have operated a parallel field program in

Fig. 1.11 Collection of a meteorite frozen in Antarctic ice. Photograph courtesy of R. Harvey.

the Yamato Mountains region of Antarctica. Other countries, including Italy, the countries comprising the European Space Agency, and China have also sent meteorite-collecting expeditions to Antarctica. All together, these expeditions have recovered well over 20 000 meteorites (including paired specimens), which have significantly increased the number of meteorite falls available to science. Among the meteorites returned by these expeditions were the first lunar meteorites and several other previously unknown meteorite types.

Meteorites fall onto the Antarctic continent and become frozen into the ice. Glaciers, carrying this treasure trove of meteorites, constantly creep downslope towards the edges of the continent. Wherever the flow of glaciers is obstructed by mountains, their movement stagnates and layers of ice are removed by wind ablation, exposing meteorites in great concentrations. The American expeditions collect the meteorites and send them to the former Lunar Receiving Laboratory at NASA's Johnson Space Center in Houston, where they are cut into pieces and allocated to scientists all over the world. Japanese expeditions return their samples to the National Institute for Polar Research for curation and allocation.

About the same time that meteorites were found in Antarctica, an important collection of meteorites was being put together in Roosevelt County, New Mexico. Over a period from 1966 to 1972, several meteorite hunters collected ~140 meteorite specimens representing about 100 separate fall events. This collection demonstrated another way for nature to concentrate meteorites. The meteorites in Roosevelt County were found in "blowout" areas where up to a meter of soil had been blown away by wind, leaving meteorites in plain view on the hardpan surface. Based on this experience, systematic and successful searches of desert areas in Western Australia have been carried out. Subsequently, the deserts of North Africa have turned out to be especially prolific sources of meteorites. The shifting desert sands expose meteorites that have accumulated over thousands of years. The meteorites are collected by nomads and sold to western collectors. Although most desert meteorites are weathered to some degree, new and rare meteorite classes have been discovered.

In 1974, astronomer Donald Brownlee began collecting interplanetary dust particles (IDPs) in the stratosphere using collectors on the leading edges of airfoils on high-altitude aircraft. These tiny particles would normally melt during their deceleration through the atmosphere, but they are captured at high altitude before they melt. IDPs appear to be materials from asteroids and from comets. Similar particles have also been collected frozen in polar ice.

The Genesis spacecraft collected solar wind particles during two years in orbit. The solar collectors were returned to Earth in 2005, but unfortunately a parachute failed to open and the sample container ruptured during its hard landing. Although the collector devices were damaged by the impact and there was significant contamination, valuable data on the Sun's composition have been, and continue to be, obtained from the damaged collectors.

In 2006, the Stardust spacecraft returned samples of the comet Wild 2 to Earth. These tiny particles were expelled from the comet nucleus and captured in aerogel (a highly porous medium that can snag speeding cometary grains) when the spacecraft flew through the coma at high speed. Even though the deceleration caused many particles to melt or vaporize, some mineral grains were preserved intact, and element signatures have been measured along the tracks formed by vaporized grains.

Organic matter and extraterrestrial life?

Some meteorites, known as carbonaceous chondrites, contain several percent of carbon-bearing compounds, primarily organic molecules. The earliest characterizations of organic matter in chondritic meteorites were attempted in the late 1800s. Researchers speculated that the organic material was probably extraterrestrial in origin. However, interest soon died and, curiously, not a single paper appeared on meteoritic organic matter between 1899 and 1953. However, interest in extraterrestrial organic compounds intensified in the 1960s, when Bartholomew Nagy and his colleagues published a series of papers claiming that carbonaceous chondrites contained biogenic hydrocarbons and "organized elements" that resembled fossilized algae. However, it was soon shown that the organic material was terrestrial contamination, a problem that continues to plague organic cosmochemistry. The large amounts of meteoritic material available from the fall of the Murchison chondrite in 1969 generated considerable activity in determining both the structures and relative abundances of organic compounds and their stable isotope compositions. Subsequent work has provided important new constraints on the processes that formed organic compounds in the ISM, the solar nebula, and meteorite parent bodies, as described in Chapter 10.

Since ancient times, philosophers have wondered whether life on Earth was seeded from elsewhere in the universe, an idea known as "panspermia." It is generally agreed that meteorites and comets contain pre-biotic compounds that could have provided the raw material for life on Earth. A more contentious question is whether the comets might actually contain microscopic organisms, as proposed by Hoyle and Wickramasinghe (1981). This hypothesis has not been taken seriously by most scientists, although it is hard to disprove.

In 1996, David McKay and coworkers published a paper that claimed to show evidence for life in the Martian meteorite ALH84001 (Fig. 1.12). One of the lines of evidence involved organic compounds found in this meteorite. This paper generated tremendous interest and controversy and resulted in the creation of a new NASA research initiative to study astrobiology. Intense study has provided non-biological explanations for all the original claims. Nonetheless, the intense astrobiology research effort generated by the 1996 study is still going strong.

The tools and datasets of cosmochemistry

In this section, we briefly review the tools used by cosmochemists and the datasets that have been acquired over the years. The tools identified below are described in more detail in the Appendix at the end of this book. Drawing on the data gained from these tools and on the intellectual framework of cosmochemistry, we can formulate key questions and define research protocols to answer those questions. Although the datasets and intellectual framework are intimately intertwined, one must always keep in mind that good data always trump theoretical models.

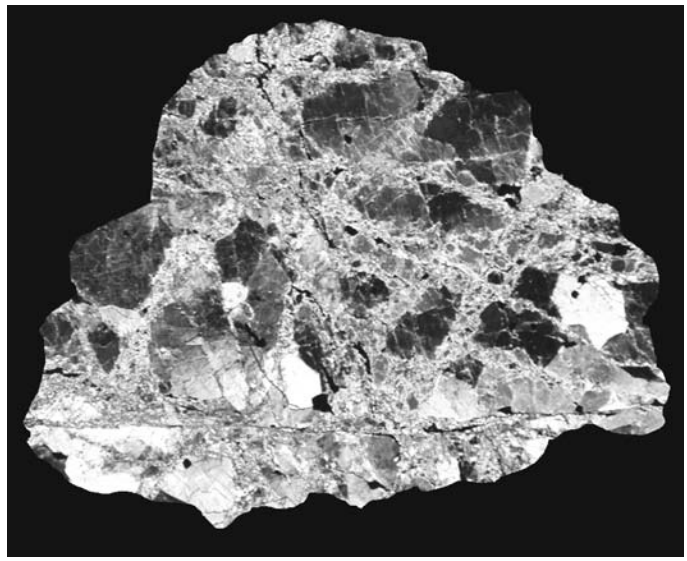

Fig. 1.12 Photomicrograph of the ALH84001 Martian meteorite, field of view = 1.3 cm. Large, broken grains of pyroxene form this breccia. This sample created a stir when it was proposed to contain evidence for extraterrestrial life. Image from Lauretta and Kilgore (2005), with permission.

Laboratory and spacecraft analyses

Mineralogy and petrography

The most basic information about any object is obtained by examining it with our own senses. What does it look like? How heavy is it? Is it solid or crumbly? A powerful extension of these senses is the petrographic microscope, used to examine slices of rocks and meteorites that are thin enough to transmit light. A skilled petrographer can identify minerals based on their interactions with polarized light. Meteorite classification is heavily based on mineralogical and textural characteristics of the samples. Petrography has also played a major role in inferring the history of the Moon from lunar samples and of Mars from Martian meteorites.

Minerals can also be identified by remote sensing, using spectroscopy. Reflectance spectra have absorption bands in the visible and near-infrared region caused by electronic transitions, commonly of iron in certain crystal sites. Thermal emission spectra are produced when solar energy is absorbed by minerals and re-emitted at thermal infrared wavelengths. Both types of spectra can be diagnostic for specific minerals, and spectroscopic measurements are made using telescopes and instruments on orbiting or landed spacecraft.

Mineral chemistry

Prior to the 1960s, mineral compositions were determined either by wet chemical analyses of mineral separates or by reference to an extensive database of the optical properties of

minerals as functions of their compositions. With the development of the electron microprobe, it became possible to measure directly the chemical composition of each mineral in a thin section. The energy dispersive X-ray detector available on most scanning electron microscopes can also provide *in situ* chemical analyses of minerals. Certain mineral compositions can also be determined from spectroscopy.

Bulk-rock chemistry (major and minor elements)

During the nineteenth century and the first half of the twentieth century, bulk chemical compositions of meteorites were determined by wet chemistry techniques. The most reliable bulk chemical datasets were compiled by Hugo Wiik and Eugene Jarosewich. During the second half of the twentieth century, new methods were established to determine chemical compositions. X-ray fluorescence analysis was used extensively during the 1950s and 1960s. In this technique a beam of X-rays excites electrons in the sample, which loses this energy by re-emitting X-rays that are unique to each element. X-ray fluorescence has also been used to analyze a few elements on the lunar surface from orbit, and a more complete analysis of soils on Mars by Viking landers in 1975. During the 1960s, this technique was largely supplanted by neutron activation analysis. In this technique, small samples are placed into a nuclear reactor, and neutrons from the reactor interact with the elements in the sample to produce radioactive isotopes. The sample is then removed from the reactor and the radioactive isotopes decay, emitting characteristic gamma rays, which are then counted to determine the chemical composition. Neutron activation analysis can detect 74 elements, but unfortunately, silicon, a dominant element in most cosmochemical samples, cannot be directly measured. Today datasets based on this technique provide a cornerstone for ideas about meteorites and lunar samples.

Gamma-ray and neutron spectrometers on orbiting spacecraft have been used to determine elemental abundances in surface samples from the Moon, Mars, and one asteroid. Gamma rays are produced by nuclear transitions, such as occur during interactions of surface materials with solar cosmic rays. The energy of gamma rays identifies specific nuclei, which can be translated into the abundances of a handful of elements, including hydrogen. Accurate major and minor element abundances in Mars rocks and soils have also been determined by alpha particle X-ray spectrometers on three rovers. Alpha particles (^{4}He nuclei) produced by radioactive decay bombard a sample, producing X-rays that are characteristic of specific elements.

Trace element abundances

The distributions of trace elements between minerals and within a suite of related rocks provide powerful tools for constraining the origin and history of rocks and meteorites. Trace-element abundances for rocks typically are part of the data set collected when determining bulk compositions. Trace element compositions of minerals require more powerful techniques such as the ion microprobe or the laser-ablation inductively coupled plasma mass spectrometer (ICPMS).

Potassium and thorium, which normally occur in minor or trace abundances, have been determined in surface materials on the Moon, Mars, and an asteroid by gamma-ray spectroscopy from orbiting spacecraft.

Chronology

Radiometric age dating utilizes the constant decay rates of radioactive (unstable) isotopes to determine how much time has passed since an object formed. Long-lived radionuclides (those for which some of the primordial abundance is still present in the solar system) provide absolute ages of objects relative to today. Short-lived, now-extinct radionuclides provide high-resolution relative ages for objects that formed in the earliest epochs of solar system history. Mass spectrometry is the main tool for determining ages by radiometric dating.

Radiometric dating is not the only method of determining age relationships. Relative ages can be determined by examining the textural relationships between various objects. For example, an object enclosed by another object must have formed earlier. Some complex relative chronologies can be developed based on textural observations. A rock formation that overlies another rock formation must have formed after the formation upon which it lies. A melt that contains a mineral grain unrelated to the melt must have formed after the mineral grain that it contains. Combined with radiometric dating, detailed chronologies can and have been developed for solar system materials.

Cosmic-ray exposure dating is used to determine how long a meteorite traveled through space as a small object on the way to the Earth from its parent asteroid, or how long a material was exposed on the surface of a planet (or the Moon) during its history. Exposure to high-energy cosmic rays alters the isotopic chemistry of the target material, and measurement of the products of these interactions can be used to determine cosmic-ray exposure ages.

Stable isotope compositions

Chemical and physical processes affect the stable isotopes of an element differently because of slight variations in the energy levels of the electrons caused by different numbers of neutrons in the nucleus of each isotope. These slight differences result in mass-dependent fractionations (changes in relative abundances of the isotopes) that are characteristic of the process. For example, during precipitation of a mineral from a fluid, the isotopic composition of the mineral will differ slightly from that of the fluid. The magnitude of the difference is typically temperature dependent, so the compositions of the liquid and the mineral can be used to define the temperature at which the mineral formed. This is an example of mass fractionation during an equilibrium process. As another example, if a melt evaporates into empty space, the isotopic composition of the melt will favor heavier isotopes as lighter isotopes are preferentially lost. The isotopic composition of the residual melt will be proportional to the amount of evaporation. This is an example of kinetic isotope fractionation. As with radiometric dating, the primary tool for this type of analysis is the mass spectrometer.

Organic compounds

Organic molecules are identified by a variety of techniques, after they have been extracted from chondrites using liquid solvents or stepwise heating. Mass spectrometers can separate many compounds and identify them by their masses. Other techniques identify reactive functional groups or specific structural types of molecules.

Cosmochemical theory

A powerful theoretical tool for cosmochemical models is *thermodynamics*. This formalism considers a system in a state of *equilibrium*, a consequence of which is that observable properties of a system undergo no net change with time. (We offer a somewhat more rigorous discussion of thermodynamics in Chapter 7). The tools of thermodynamics are not useful for asking questions about a system's evolutionary history. However, with the appropriate equations, we are able to estimate what a system at equilibrium would look like under any environmental conditions. The methods of thermodynamics allow the use of temperature and pressure, plus the system's bulk composition, to predict which minerals will be stable and in what relative amounts they will be present. In this way, the thermodynamic approach to a cosmochemical system can help us measure its stability and predict the direction in which it will change if environmental parameters change.

The cosmochemistry literature often contains discussions of equilibrium condensation from a gas of solar composition. During the 1960s through 1980s, the intellectual framework for these discussions was a hot, monotonically cooling solar nebula (recall the Laplace model mentioned earlier). However, the discovery in chondrites of isotopic anomalies that could not have survived in the gaseous state and grains that existed in interstellar space prior to the formation of the solar system showed that this simple model for the early solar system was not correct. Cosmochemists still refer to condensates, and the previous work still provides important constraints for understanding solar system bodies. However, the application of these principles is generally in reference to a local environment or specific situation rather than a global environment like a hot solar nebula. We are also now more aware that thermodynamics reveals nothing about the pathways to the final states that we observe, and that similar compositions can result from condensation or evaporation.

In the planetary geochemical literature, there are also extensive discussions about the thermodynamics of crystallizing melts. Sophisticated programs have been developed to model the compositions of the minerals that crystallize from a cooling liquid as well as changes in the residual melt.

A third way in which thermodynamics can be used is to invert the measured major, minor, and trace element compositions of coexisting minerals to estimate the temperature, pressure, and oxidation state under which they formed. Valid results can only be obtained if the system was truly in equilibrium at the inferred conditions and the minerals did not subsequently change composition. Nevertheless, this is a powerful way to infer the formation conditions of various solar-system materials.

An alternative way of studying a system is to examine its *kinetics*. Using kinetics, we can study the pathways along which a system may evolve between states of thermodynamic equilibrium and determine the rates of change of system properties along those pathways. Cosmochemical systems can evolve along a variety of pathways, some of which are more efficient than others. In a kinetic study, the task is often to determine which of the competing pathways is dominant.

Cosmochemists are interested in determining not only what should happen in a real system (the thermodynamic answer) but also how it is most likely to have happened (the kinetic answer). The two are intimately linked. While the focus of thermodynamics is on the end states of a system – before and after a change has taken place – a kinetic treatment sheds light on what happens between the end states. Where possible, it is advantageous to keep both approaches in mind.

Theories of the origin of the solar system and of the formation and evolution of the bodies within it provide the intellectual framework for detailed investigations of processes and events in the early solar system. The hot solar nebula theory provided the basis for much of the scientific discussion of the 1960s through the 1980s. These theories are often based primarily on work in fields other than cosmochemistry as we have defined it. For example, observations made by astronomers tell us about the environments in which stars form. Modelers describe the gravitational collapse of dense cores in molecular clouds to form protostars and accretion disks. Dynamicists model the evolution of planetary systems starting with the solar nebula and continuing through the formation of the planets and evolution of the distribution of asteroids and icy bodies as we see them today. Input from these and other fields generate global models that provide the often unstated framework for cosmochemistry. Cosmochemists must be familiar with these broad ideas, but must also test them against observations from their own research. The observations are the ultimate arbiter of a successful theory.

Relationship of cosmochemistry to other disciplines

It should be clear from the above discussions that cosmochemistry is a highly interdisciplinary subject that draws on aspects of astronomy, astrophysics, physics, chemistry, geology, and perhaps eventually even biology. Understanding the formation of the elements requires consideration of the astrophysical settings in which nucleosynthesis occurs – stars, supernovae, and the interstellar medium. Astronomy provides direct observations of these settings, as well as spectroscopic data on chemical abundances that complement chemical analyses of presolar grains in meteorites. Astrophysics provides the theoretical predictions of relative abundances of nuclides produced in various stellar settings that can be tested by the chemical and isotopic compositions of presolar grains. Hypotheses about the formation of organic molecules in interstellar space can be evaluated by studying organic matter in meteorites. Spectroscopic elemental abundances measured in the Sun can be compared with element ratios in bulk chondritic meteorites, and the agreement allows measured chondritic abundances to be substituted for those elements without measurable solar spectral lines. Astrophysical calculations of changes in the composition of the Sun over time can be tested

by analyzing solar wind gases implanted into soils on the Moon and asteroids. Nowhere in science is there a better example of synergy between disparate disciplines.

Likewise, planetary geochemistry cannot be interpreted without understanding its geologic context. Geologic processes on Mars and the Moon can be inferred from spacecraft imagery, and the conditions under which they occur can be determined by *in situ* measurements. Element behavior during melting and crystallization can be inferred by analyzing Martian and lunar meteorites and returned lunar samples. The timing of major geologic events and the ages of mantle reservoirs can be defined by radiogenic isotope measurements. Geochemistry and geology provide complementary ways of assessing how planets work.

Small bodies such as asteroids and comets contain primordial material but may also have experienced heating and impacts. Metamorphism (mineralogical and textural changes wrought by heat and shock) can blur or even destroy the cosmochemical and chronological records in meteorites, and it is essential to catalog these geologic processes so that we can interpret the records correctly. Melting and sequestering of siderophile elements in some asteroid cores produced iron meteorites, analyses of which shed light on an inaccessible region of our own planet. Astronomical observations and spectroscopy of asteroids complement direct measurements of their chemical compositions by analyses of meteorites.

In this book, we will explore cosmochemistry and planetary geochemistry, usually in the context of astronomy, geology, and physics. In this way we hope to illuminate how the abundances and chemical behaviors of elements and isotopes are critical to understanding the formation and inner workings of the Earth's neighboring planets, the processes that shaped the early solar system, the chronology of major events, and the origin of the elemental building blocks of the Universe.

Questions

1. How does cosmochemistry relate to other, more well-known disciplines such as geology, chemistry, or astronomy?
2. Distinguish between the following terms: lithophile, siderophile, chalcophile, atmophile.
3. How do element behaviors in the solar nebula or in interstellar space differ from those in planets?
4. Who was Victor Goldschmidt and what role did he play in the development of geochemistry and cosmochemistry?
5. What are some of the sample sets that are available to cosmochemists?
6. List five techniques by which elemental and isotopic abundances can be measured.

Suggestions for further reading

Burke, J. G. (1986) *Cosmic Debris: Meteorites in History.* Berkeley: University of California Press, 445 pp. The most authoritative account of the long history of meteorites and the early development of meteorite research.

Davis, A. M., editor (2004) *Treatise on Geochemistry, Volume 1: Meteorites, Comets, and Planets*. Oxford: Elsevier Pergamon, 737 pp. A comprehensive and up-to-date set of excellent review chapters of cosmochemistry topics by authorities in the field. This volume covers many of the subjects of the present book, but at a more technical level.

Lauretta, D. S. and McSween, H. Y., Jr., editors (2006) *Meteorites and the Early Solar System II*. Tucson: University of Arizona Press, 943 pp. Another comprehensive, modern collection of reviews by prominent meteoriticists – everything you want to know about meteorites is here, but the chapters are at an advanced technical level.

References

Aston, F. W. (1920) Isotopes and atomic weights. *Nature*, **105**, 617–619.

Black, D. C. and Pepin, R. O. (1969) Trapped neon in meteorites II. *Earth and Planetary Science Letters*, **6**, 395–405.

Burbidge, E. M., Burbidge, G. R., Fowler, W. A. and Hoyle, F. (1957) Synthesis of elements in stars. *Reviews of Modern Physics*, **29**, 547–650.

Cameron, A. G. W. (1957) *Stellar Evolution, Nuclear Astrophysics, and Nucleogenesis* (CRL-41; AECL-454). Chalk River, Ontario: Atomic Energy of Canada, Ltd.

Hahn, O., Strassman, F., Mattauch, J. and Ewald, H. (1943) Geologische Altersbestimmungen mit der Strontiummethode. *Chemische Zeitung*, **67**, 55–56.

Holmes, A. (1946) An estimate of the age of the Earth. *Nature*, **157**, 680–684.

Houtermans, F. G. (1946) Die Isotopenhäufigkeiten im natürlichen Blei und das Alter den Urans. *Naturwissenschaften*, **33**, 186–186, 219.

Hoyle, F. and Wickramasinghe, C. (1981) Where microbes boldly went. *New Scientist*, **91**, 412–415.

Lauretta, D. S. and Killgore, M. (2005) *A Color Atlas of Meteorites in Thin Section*. Tucson: Golden Retriever Press, 301 pp.

Lee, T., Papanastassiou, D. A. and Wasserburg, G. J. (1977) Aluminum-26 in the early solar system: Fossil or fuel? *Astrophysical Journal Letters*, **211**, L107–L110.

Lockyer, J. N. (1890) *The Meteoritic Hypothesis*. New York: MacMillan and Co., 560 pp.

Lodders, K. and Fegley, B., Jr. (1998) *The Planetary Scientist's Companion*. New York: Oxford University Press, 371 pp.

McKay, D. S., Gibson, E. K., Thomas-Keprta, K. L. *et al*. (1996) Search for past life on Mars: Possible relic biogenic activity in Martian meteorite ALH 84001. *Science*, **273**, 924–930.

Patterson, C. C. (1956) Age of meteorites and the Earth. *Geochimica et Cosmochimica Acta*, **10**, 230.

Railsback, L. B. (2003) An earth scientist's periodic table of the elements and their ions. *Geology*, **31**, 737–740.

Reynolds, J. H. (1960) Determination of the age of the elements. *Physical Reviews Letters*, **4**, 8–10.

Reynolds, J. H. and Turner, G. (1964) Rare gases in the chondrite Renazzo. *Journal of Geophysical Research*, **49**, 3263–3281.

Suess, H. E. and Urey, H. C. (1956) Abundances of the elements. *Reviews of Modern Physics*, **28**, 53–74.

Van Schmus, W. R. and Wood, J. A. (1967) A chemical–petrologic classification for the chondritic meteorites. *Geochimica et Cosmochimica Acta*, **31**, 747–765.

Wasserburg, G. J. and Hayden, R. J. (1955) Age of meteorites by the ^{40}Ar–^{40}K method. *Physics Review*, **97**, 86–87.

2 Nuclides and elements: the building blocks of matter

Overview

In order to understand the origin of the elements, their relative abundances, their interactions, and the processes that produced the objects that we observe today in the solar system and in the universe as a whole, it is necessary to have a basic knowledge of the building blocks and structure of matter. Cosmochemists operate at the boundaries between traditional fields of physics, chemistry, geology, and astronomy. In this chapter, we will review some basic nuclear physics to provide a background for understanding the origin and abundances of the elements. Fundamentals of radioactive decay and isotope cosmochemistry will be presented. We will also review some basic chemistry to provide a background for discussions of chemical processes in later chapters.

Elementary particles, isotopes, and elements

At the simplest level, an *atom* consists of a nucleus composed of protons and neutrons surrounded by a cloud of electrons. A neutral atom consists of an equal number of protons (positively charged) and electrons (negatively charged) and a similar number of neutrons. Protons and neutrons have nearly equivalent masses, while electrons are much smaller, $^1/_{1836}$ times the mass of a proton (Table 2.1). An *ion* is an atom that has either lost or gained one or more electrons, giving it a positive or negative charge. The chemical properties of an element are governed by the number of electrons and the ease with which they are lost or gained. The atomic weights and abundances of the elements are governed by the composition and physics of the nucleus.

Each element consists of between one and ten stable *isotopes*. Isotopes of an element have the same number of protons, which defines the element, but differ in the number of neutrons in the nucleus. For example, oxygen has eight protons and either eight, nine, or ten neutrons. The isotopes of oxygen are ^{16}O, ^{17}O, and ^{18}O, with the numbers referring to the total number of protons + neutrons in the nucleus. The atomic number, Z, which is unique to each element, is the number of protons in the nucleus (equal to the number of electrons in the neutral atom). The atomic mass, A, is the number of protons plus the number of neutrons, N, in the nucleus ($A = Z + N$). Isotopes can either be stable or unstable (radioactive), and the

Table 2.1 Constituents of an atom and other particles

Particle	Symbol	Location in Atom	Mass	Charge
Proton	p	nucleus	938.256 MeV = 1.673×10^{-24} g = 1.00728 *u*	+1
Neutron	n	nucleus	939.550 MeV = 1.675×10^{-24} g = 1.00866 *u*	0
Electron	β-	cloud around nucleus	0.511 MeV = 9.110×10^{-28} g	−1
Gamma	γ	emitted in nuclear reaction	0	0
Neutrino	η	emitted in nuclear reaction	very small	0

isotopes resulting from radioactive decay are said to be radiogenic. Natural samples contain 266 stable isotopes comprising 81 elements along with 65 radioactive isotopes of these and nine additional elements. (When discussing the isotopes of more than one element, the term *nuclide* is typically used.) In addition, more than 1650 nuclides and 22 elements not found on Earth have been created in the laboratory with nuclear reactors and particle accelerators. Most of the man-made isotopes are very short-lived. Most probably exist briefly in special natural settings, such as in an exploding supernova, but we typically have no way of detecting them. Radioactive technetium, which does not exist in the solar system, has been identified in the spectra of highly evolved low-mass stars.

The notation used for isotopes, ions, and chemical compounds is illustrated by this example: $^{16}O_2^0$. The number to the upper left of the element symbol gives the isotope number in atomic mass units. The number to the upper right of the element symbol gives its charge, with 0 referring to a neutral atom, +, 2+, 3+, −, 2−, 3− referring to its degree and sign of ionization. The number to the lower right gives the number of atoms present in a molecule. When reading the symbol for an isotope, one should always say the element name first, then the isotope number. For example, say oxygen-16, not 16-O. A concern when this convention was adopted was that people might say the isotope number first, rather than the element. As you will see as you gain experience in cosmochemistry, this concern was well founded.

The masses of the isotopes are described in cosmochemistry using atomic mass units, or *amu*. The official unit of measure, the *unified atomic mass unit* (abbreviated *u*) or *Dalton* (abbreviated *Da*), is defined as $^1/_{12}$ of the mass of one atom of ^{12}C, and thus is approximately equal to the mass of a proton or a neutron. Thus, the mass of ^{16}O, which consists of eight protons and eight neutrons, is approximated as 16 *u* and that of ^{18}O, which has two additional neutrons, is approximated as 18 *u*. The exact masses are slightly less than the sum of the masses of the individual protons and neutrons. This is because the potential energy of a bound stable nucleus is lower than that of its constituent parts. Albert Einstein showed that mass and energy are related by the famous equation, $E = mc^2$, where c is the velocity of light. When a nucleus forms, the potential energy of the dispersed components is converted to heat, which can be lost from the system as the system cools. As a result, the cooled system has a lower mass than the constituent protons and neutrons did before the nucleus was bound together. Thus the atomic mass of the ^{16}O atom is 15.9994 *u* rather than 16.12752 *u*, which is the sum of 8 protons and 8 neutrons. The mass "deficit" is the nuclear binding energy.

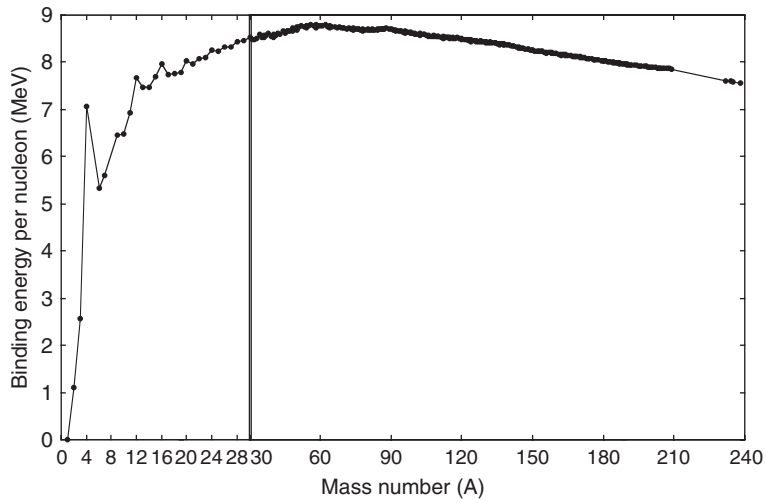

Fig. 2.1 **Binding energy per nucleon (total nuclear binding energy divided by the number of protons and neutrons in the nucleus) plotted against atomic mass number, A. The highest binding energy per nucleon (= highest stability) is found for elements near iron (mass ~56). Nuclear binding energy can be released by combining light nuclei into heavier ones (fusion) or by splitting heavier nuclei into lighter ones (fission). Note the local peaks and valleys in binding energy among the light nuclei. The region of lower binding energy per nucleon between mass numbers 4 and 12 helps to explain the low abundance of lithium, beryllium, and boron.**

Figure 2.1 shows the nuclear binding energy per nucleon (the protons and neutrons in the nucleus) as a function of nuclear mass number for the stable isotopes. Notice that the binding energy per nucleon increases rapidly from H to D (^{2}H) to ^{3}He to ^{4}He. This is because the attractive force between the nucleus and each additional proton or neutron exceeds the additional electrostatic repulsion between the positively charged protons. This trend generally continues through ^{23}Na, although some nuclear configurations between mass 4 and mass 12 are not energetically favored. For elements between ^{24}Mg and Xe (masses 124–136), the binding energy per nucleon is approximately constant, although it continues to increase slowly to ^{62}Ni, the most tightly bound nucleus. This is because the nucleus has become large enough that the nuclear force associated with a proton or neutron at one edge of the nucleus no longer extends completely across its width. For all nuclei with masses $\leq^{62}$Ni, the addition of a proton or neutron releases energy, the energy of fusion. For example, combining four protons to form a ^{4}He nucleus releases about 7 MeV of energy per nucleon, or a total of 28 MeV.

For isotopes with masses greater than ^{62}Ni, the *total* binding energy of the nucleus continues to increase, but the binding energy *per nucleon* decreases slowly with the addition of a proton or neutron until Xe. Thereafter, adding a proton or neutron significantly reduces the binding energy per nucleon. The heaviest stable nuclide is ^{209}Bi. All heavier nuclides are unstable and decay by α-emission or fission to smaller nuclides, releasing energy as the system achieves a more stable configuration. For example, the splitting of a ^{238}U nucleus into two ^{119}Pd nuclei releases a total energy of 240 MeV. In some cases, the decay occurs

almost instantaneously after the nuclide forms, while in others, such as ^{232}Th, ^{235}U, and ^{238}U, the nuclei are almost stable and their half-lives against decay are measured in hundreds of millions to tens of billions of years. The energy released when a heavy isotope fissions is the energy that powers nuclear power stations. The awesome destructive power of an atomic bomb comes from the instantaneous release of binding energy of uranium or plutonium through a neutron-induced-fission chain reaction. The even-more-powerful hydrogen bomb uses the energy of fusion.

The *atomic mass of an isotope* (A) should not be confused with the *atomic weight of an element*, which is the abundance-weighted average value of the various stable isotope masses of an element. For example, oxygen, which is composed of 99.757% ^{16}O, 0.038% ^{17}O (16.9991 *u*), and 0.205 ^{18}O (17.9992 *u*), has an atomic weight of 15.9994, and chlorine, which is composed of 75.78% ^{35}Cl (34.9689 *u*) and 24.22% ^{37}Cl (36.9659 *u*), has an atomic weight of 35.453. The atomic weights of most elements are constant to a very high precision in natural materials because the relative abundances of the isotopes are always the same to high precision. Exceptions to this rule are elements with radioactive or radiogenic isotopes, whose isotopic abundances change with time, and very small mass-dependent isotope fractionations caused by physical and biological processes. The latter are the basis for stable-isotope geochemistry. Why should the mixture of isotopes always be the same for each of the elements? The answer to this question has profound implications for how one views the origin of the solar system, and we will discuss it extensively in later chapters. There is one caveat to this general rule, however. Samples of elements that have been processed by humans can have highly anomalous isotopic compositions and thus unusual atomic weights.

Chart of the nuclides: organizing elements by their nuclear properties

The Chart of the Nuclides©™ provides a very useful way to organize the large number of different nuclides. The chart, a publication of Lockheed Martin, is available through their website at www.ChartOfTheNuclides.com. Analogous compilations are also available from other sources. The chart plots the atomic number, Z, against the number of neutrons, N. For each nuclide, the chart gives the symbol and mass number, the isotopic abundance (or the half-life if it is radioactive), the atomic mass, and a number of other nuclear properties, some of which will be discussed below. Naturally occurring radioactivities are identified, as are members of natural radioactive decay chains. Especially stable nuclides, such as those with closed neutron or proton shells, the so-called "magic numbers," are identified. A schematic version of the Chart of the Nuclides is shown in Figure 2.2.

The Chart of the Nuclides reveals several important features of matter. The stable nuclides lie along a trend that starts at close to 45 degrees, corresponding to approximately equal numbers of protons and neutrons, but becomes shallower as N and Z increase. This reflects the extra neutrons required to stabilize the nucleus against the electrostatic repulsion between the positively charged protons. When the nuclides become too large, the forces

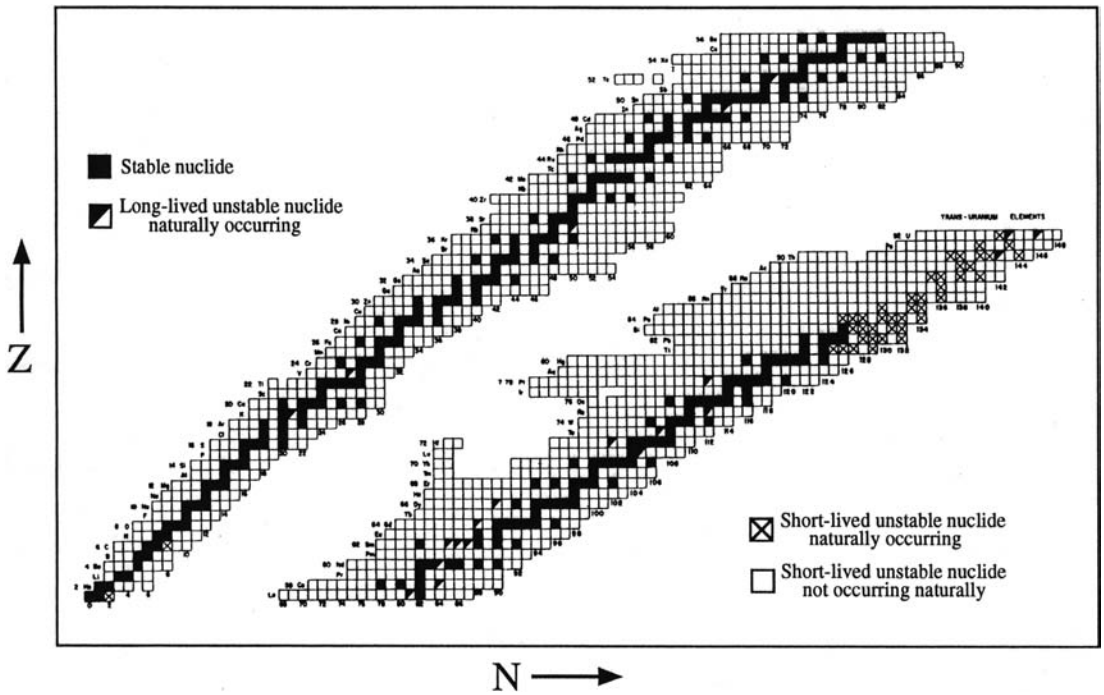

Fig. 2.2 Schematic presentation of the Chart of the Nuclides, which plots Z (number of protons) versus N (number of neutrons). Stable isotopes, shown in black, define a narrow band within a wider band of unstable nuclides. In general, elements with even Z are more abundant and have more isotopes than elements with odd Z. Among the isotopes of a given element, those with even N are more abundant than those with odd N.

holding them together can no longer overcome the electrostatic forces trying to drive them apart, and they are unstable. On either side of the array of stable isotopes are many unstable isotopes that have either too many protons (those on the left) or too many neutrons (those on the right) (Fig. 2.2). These nuclides must eliminate their excess protons and neutrons. They eliminate neutrons by emitting an electron from the nucleus (β-decay) and they eliminate excess protons by either emitting a positron (positron decay) or by a proton capturing an electron to become a neutron (electron capture). The nuclides move toward the so-called "valley of β stability," where the nuclides are stable against β-decay, positron decay, and electron capture.

Look closely at the distribution of stable elements in Figure 2.2. For some values of Z there is only one stable isotope, whereas for others, there are many isotopes. In fact, there are 20 stable elements that have only one isotope, elements such as ^{9}Be, ^{19}F, ^{23}Na, ^{27}Al, ^{31}P, ^{45}Sc, ^{51}V, and ^{55}Mn. For all of these, Z is an odd number. A detailed view of a portion of the Chart of the Nuclides (Fig. 2.3) shows that for even-Z elements with several isotopes, the even-numbered isotopes are more abundant than the odd-numbered isotopes. In fact, many of the odd-numbered isotopes are unstable. For odd-Z elements with multiple isotopes, the even-numbered isotopes are typically unstable. Now look at columns of constant N. For

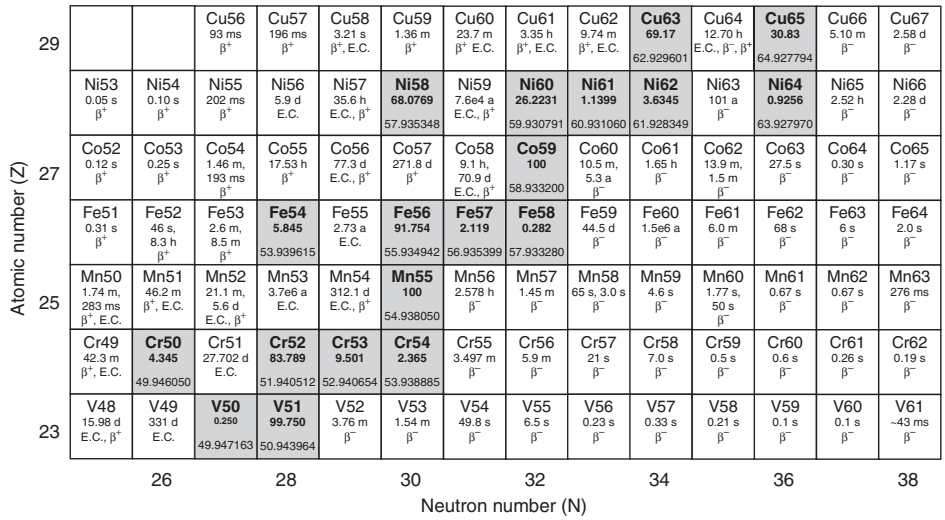

Fig. 2.3 **Detailed view of a portion of the Chart of the Nuclides. Stable isotopes are shaded. For stable nuclides, isotopic abundances are given below the element symbol and isotopic masses are given at the bottom of the square. Half-lives of the unstable nuclides are given, along with their decay modes.**

some values of N there is only one stable isotope, while for others there are several. Again, nuclides with an even number of neutrons are more common, and Figure 2.3 shows that the odd-N nuclides are either unstable or have low abundances relative to other isotopes of the same element. The Chart of the Nuclides does not contain sufficient information to evaluate the relative abundances of isotopes with odd N and variable Z because only the relative abundances of the isotopes within an element are shown, not the absolute abundances. Nuclides whose boxes join at the corners to make diagonal lines running from the upper left to the lower right on the diagram have the same mass number and are called *isobars*. In Figure 2.3, there are several cases where two stable nuclides have the same mass number: ^{54}Cr and ^{54}Fe, ^{58}Fe and ^{58}Ni, and ^{64}Ni and ^{64}Zn. Nuclides that are the only isotope of an element never have another stable nuclide on their isobar. These patterns can be understood in terms of how the protons and neutrons in the nucleus are arranged.

Neutrons and protons reside in shells in the nucleus, each of which contains a specific number of protons or neutrons. This structure is broadly analogous to the shells that control the distribution of electrons, which will be discussed in some detail below. When protons or neutrons in a shell are paired, the structure is more energetically favored. This is why nuclei with even numbers of protons or neutrons are more stable than those with odd numbers. Table 2.2 summarizes the abundances of nuclides with different nuclear configurations. As one might suspect from looking at the Chart of the Nuclides, the most stable configuration is to have even numbers of both protons and neutrons. Having an even number of either protons or neutrons is also an energetic advantage. But for nuclides with both unpaired protons and unpaired neutrons, the nucleus is typically unstable. The four stable nuclides with unpaired protons and neutrons are all among the lightest nuclides.

Table 2.2 Numbers of stable nuclides as a function of nuclear configuration

A	Z	N	Number of Stable Nuclides
Even	Even	Even	159
Odd	Even	Odd	53
Odd	Odd	Even	50
Even	Odd	Odd	4

A nucleus is even more stable when the proton or neutron shells are full, again analogous to the electron shell structure we will discuss below. Nuclides with these configurations are more tightly bound than their neighbors and are said to be "magic." These magic numbers occur at 2, 8, 20, 28, 50, 82, and 126. Because neutrons and protons have separate shells, a nuclide can have a full proton shell and a partially filled neutron shell, or vice versa. If neutrons and protons both have filled shells, the nuclide is said to be "doubly magic." Stable nuclei that are doubly magic are ^{4}He, ^{16}O, ^{40}Ca, ^{48}Ca, and ^{208}Pb. There are other doubly magic nuclei that are not stable because of the imbalance in the number of protons and neutrons (e.g. ^{56}Ni, ^{78}Ni, ^{100}Sn, ^{132}Sn). One version of the shell theory predicts that a nuclide with 114 protons and 184 neutrons should also be doubly magic, producing a so-called "island of stability" well beyond the heaviest stable nuclide. Nuclides of this mass would not be stable, but would exist for longer than neighboring configurations, perhaps long enough to be detected. Although nuclides with 114–118 protons have been produced, they had too few neutrons, so as yet there is no experimental verification of the island of stability (Hofmann and Münzenberg, 2000).

Radioactive elements and their modes of decay

The 65 naturally occurring radioactive isotopes generally fall into three categories, depending upon their *half-lives* (the time it takes for half of the atoms present to decay). (1) Many of the longer-lived radioactive isotopes were produced during nucleosynthesis and have sufficiently long half-lives that the atoms have not all decayed yet. Examples include ^{40}K, ^{87}Sr, ^{232}Th, ^{235}U, and ^{238}U. (2) Some radioactive isotopes are continuously produced in the Earth's atmosphere, in rocks at the surface of planetary bodies or in meteoroids, and in space by collisions between high-energy cosmic rays and stable isotopes. The collisions break the stable isotope into smaller fragments, some of which are radioactive. Such nuclides are said to be *cosmogenic*, and the reactions that produce them are called spallation reactions. An example is the cosmogenic isotope ^{14}C, which is used to date archeological finds. It is produced from ^{14}N in the Earth's atmosphere. 3) The third category of radioactive nuclide consists of isotopes produced by naturally occurring radioactive chains. For example, when an atom of ^{238}U decays, it passes through radioactive ^{234}Th, ^{234}Pa, ^{234}U, ^{230}Th, ^{226}Ra, ^{222}Rn, ^{218}Po, and several other isotopes before it finally ends up as stable ^{206}Pb. The

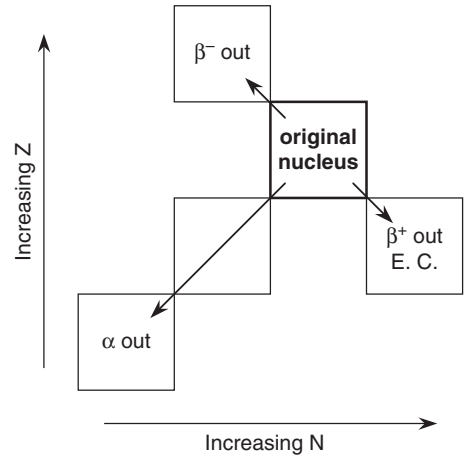

Fig. 2.4 **Effects of different modes of radioactive decay on the position of an isotope on the Chart of the Nuclides. Beta-decay, which changes a neutron to a proton, moves the nuclide up and to the left. Positron decay or electron capture, which changes a proton into a neutron, moves the nuclide down and to the right. And α-decay, which is the emission of a ^{4}He nucleus, moves the nuclide down and to the left.**

intermediate isotopes have half-lives ranging from a few hours to almost 10^5 years, too short for there to be any contribution from stellar nucleosynthesis in solar system materials. These species are also too heavy to be produced in significant amounts by cosmic-ray-induced spallation reactions.

Radioactive decay occurs by several pathways, as illustrated in Figure 2.4. Beta-decay (β^-), emission of an electron by the nucleus, converts a neutron to a proton and increases Z by one without changing A. Isotopes of interest to cosmochemistry that decay only by β-decay include ^{3}H, ^{10}Be, ^{14}C, ^{36}Cl, ^{60}Fe, and ^{87}Rb. Positron decay (β^+) and electron capture (E.C.) both convert a proton to a neutron. Although the two processes differ in nuclear detail, both reduce Z by one without changing A (Fig. 2.4). Isotopes that decay by one or both of these processes include ^{22}Na, ^{26}Al, ^{41}Ca, and ^{53}Mn. The isotope ^{40}K, which is important for radiometric dating, decays by β-decay to ^{40}Ca and by positron decay to ^{40}Ar. Radioactive isotopes can also decay by emission of an α-particle, which consists of two protons and two neutrons (α-decay). This decreases Z by two and A by four (Fig. 2.4). Alpha-decay is the primary mode of decay for heavy radioactive isotopes. The decay series for actinides such as ^{232}Th, ^{235}U, and ^{238}U consist primarily of α-decays, punctuated by occasional β-decay to keep the resulting daughter isotopes close to the valley of β stability.

Isotopes heavier than about 230 *u* can also decay by spontaneous fission. In spontaneous fission, the nucleus splits into two smaller nuclei. The split is typically asymmetrical, leaving fragments of different Z. Spontaneous fission is a minor decay pathway for naturally occurring isotopes such as ^{232}Th, ^{235}U, and ^{238}U. A more efficient pathway for fission to occur is for the nucleus to first absorb a neutron. The extra neutron triggers the nucleus to split. The process is called neutron-induced fission, and it is this process that is utilized for nuclear reactors and weapons. It is possible for neutron-induced fission to occur naturally.

Spontaneous fission typically releases neutrons, which can then be absorbed by other atoms. If the concentration of fissionable nuclei is high enough, the released neutrons can trigger additional fission reactions. The process can be further enhanced if a moderating material such as water is present to slow down the ejected neutrons, making them easier to capture. In 1956, P. K. Kuroda speculated that early in Earth's history, when the relative abundance of ^{235}U was higher, a deposit of natural uranium and water might generate a self-sustaining nuclear chain reaction – a natural nuclear reactor. Such a deposit, called Oklo, was found in the African Gabon Republic in 1972 (Cowan, 1976). It was recognized because the uranium in the deposit had a very low abundance of ^{235}U, which had been destroyed by neutron-induced fission in the self-sustaining reactor.

The decay of radioactive nuclides is used to determine the chronology of events from the earliest epochs of the solar system to recent times. The usefulness of radiometric dating depends critically on the constancy of radioactive decay rates. There are a number of observations that confirm that decay rates do not change with time. For example, radionuclides used to date rocks and minerals over the age of the solar system decay by all of the above mechanisms (e.g. ^{40}K by β-decay and electron capture, ^{87}Rb by electron capture, ^{147}Sm and ^{232}Th by α-decay, ^{187}Re by β-decay, ^{235}U and ^{238}U by alpha decay and spontaneous fission). In spite of these differences, dates obtained from different decay systems are consistent for rocks and minerals formed at various times over the ~4.57 billion year history of the solar system. For decay rates to vary and produce this result, the decay rates would have to vary in concert, which would require several different nuclear properties to vary in such a way as to maintain the illusion of constancy. Astronomy provides another line of evidence. Supernovae are known to produce large quantities of radioactive isotopes, the decay of which drives the light curves observed from Earth. Supernovae that exploded billions of years ago but whose light is only now reaching Earth show the same characteristic light curves as supernovae that exploded a few million years ago. Thus, the decay of newly formed radioactivities has followed the same laws for billions of years. These and other lines of direct evidence show that the laws of nuclear physics, and thus the decay constants of radioactive isotopes, have remained constant within tight limits since the universe formed.

As the ability to measure decay rates and as the understanding of the laws of physics have improved, a few exceptions to the rule of constant decay rates have been identified. However, these exceptions are effectively irrelevant to cosmochronology. For example, in the interior of stars, where temperatures exceed 100 million degrees and pressures reach millions of atmospheres, the stabilities of atomic nuclei change dramatically. For example, the half-life of ^{60}Fe can decrease from 1.5 million years in normal space to a few minutes in the interior of a massive star (Limongi and Chieffi, 2006). If the temperatures and pressures become high enough, the atomic structure breaks down completely and the material degenerates into a tightly packed ball of neutrons, a neutron star. But because matter that can be dated by radioactive decay must exist in the same form from the time of its origin until it is dated, we need not worry about what would happen if it found itself in the interior of a star.

One radioactive decay pathway, electron capture, has been found to have a minor dependence on external conditions of relevance to cosmochemistry. The rate at which an electron in the cloud surrounding the nucleus is captured by a proton to make a neutron is

proportional to the probability of an electron ending up close to the nucleus. Changes in the electron distribution can potentially change the electron capture rate. Such changes can be produced by chemical bonding, high pressure, low temperature, superconductivity, and strong electric and magnetic fields (Huh, 1999; Liu and Huh, 2000). However, *ab-initio* calculations of the decay rate of ^{40}K under high pressure predict an increase of only ~0.025% (2.5 parts in 10^4) at 25 Gpa (giga Pascal) (Lee and Steinle-Neumann, 2008), and a measurement performed on ^{83}Rb, which, like ^{87}Rb decays by electron capture, showed no measurable change in decay rate at 42 GPa. The extremely small changes in electron-capture rate that occur under cosmochemically relevant conditions have no effect on ages obtained using radiochronometers.

The periodic table: organizing elements by their chemical properties

Credit for constructing the periodic table of the elements (Fig. 2.5) is generally given to Dmitri Mendeleev, a professor at St. Petersburg University. While writing a textbook on inorganic chemistry, he noticed patterns in the properties and atomic weights of elements such as Cl–K–Ca, Br–Rb–Sr, and I–Cs–Ba. He then attempted to identify similar patterns for all of the 63 known elements. The result of his work was his statement of the periodic law and his classic paper, *On the Relationship of the Properties of the Elements to their Atomic Weights*, published in 1869. At the time that Mendeleev developed his periodic table, the experimentally determined atomic weights of the elements were not always accurate. He found that 17 elements had to be moved to new positions in the table from those indicated by their accepted atomic weights. In most cases, the new positions were confirmed by subsequent measurements of atomic weight. There were also some gaps in his table, and from those gaps Mendeleev predicted the existence of additional elements. For example, he predicted elements that he called eka-aluminum, eka-boron, and eka-silicon, which were eventually found and renamed gallium, scandium, and germanium. The discovery of the element argon by Lord Rayleigh in 1895 was not predicted by the periodic table, and in fact there was no place for it in the table. A few years later, William Ramsey suggested that argon be placed between chlorine and potassium in a family with helium. Based on this suggestion, he accurately predicted the existence and properties of neon.

In the modern periodic table (Fig. 2.5), the elements are arranged in order of increasing atomic number and then in horizontal rows called periods and vertical columns called groups. Members of each group have similar physical and chemical properties. Group 1A elements are called the alkali metals, Group 2A elements are the alkaline earths, Group 7A elements are the halogens, etc. Figure 2.6 illustrates some of the properties that vary periodically with atomic numbers. For example, atomic radius peaks at Z = 3 (Li), [12 (Mg)], 19 (K), 37 (Rb), 55 (Cs), and 87 (Fr). With the exception of magnesium, all are members of Group 1A of the periodic table. Ionization energy peaks at 2 (He), 10 (Ne), 18 (Ar), 36 (Kr), 54 (Xe), and 86 (Rn), all of which are noble gases and members of Group 8A. Likewise, the melting points and boiling points of the elements vary periodically with

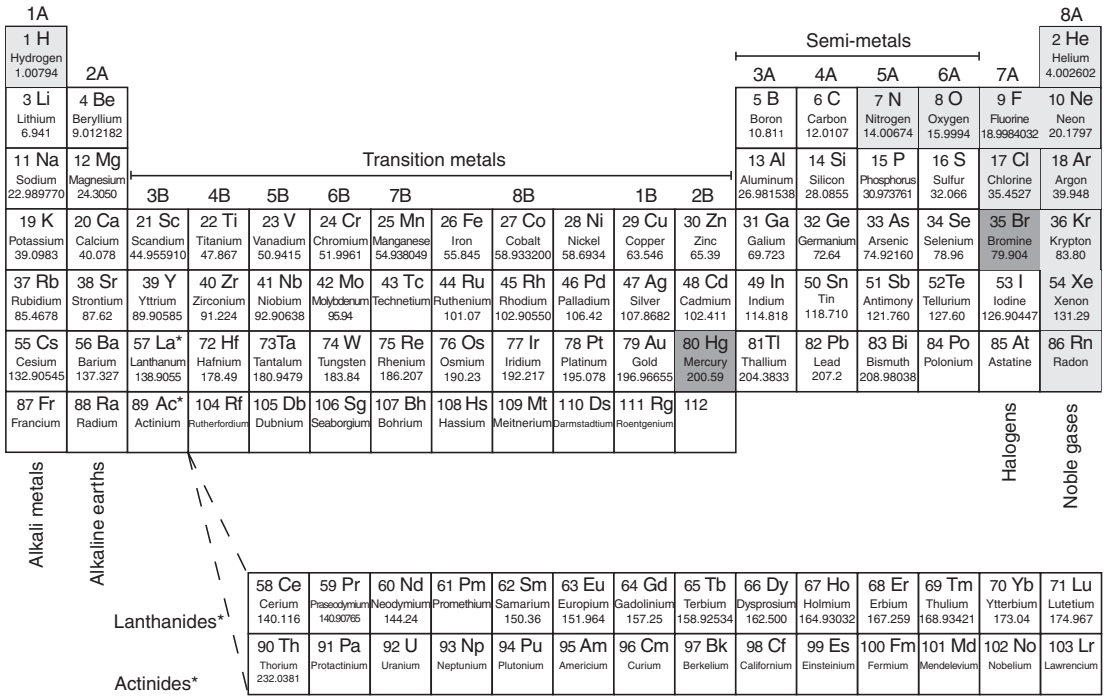

1 H Hydrogen 1.00794																	2 He Helium 4.002602
3 Li Lithium 6.941	4 Be Beryllium 9.012182											5 B Boron 10.811	6 C Carbon 12.0107	7 N Nitrogen 14.00674	8 O Oxygen 15.9994	9 F Fluorine 18.9984032	10 Ne Neon 20.1797
11 Na Sodium 22.989770	12 Mg Magnesium 24.3050											13 Al Aluminum 26.981538	14 Si Silicon 28.0855	15 P Phosphorus 30.973761	16 S Sulfur 32.066	17 Cl Chlorine 35.4527	18 Ar Argon 39.948
19 K Potassium 39.0983	20 Ca Calcium 40.078	21 Sc Scandium 44.955910	22 Ti Titanium 47.867	23 V Vanadium 50.9415	24 Cr Chromium 51.9961	25 Mn Manganese 54.938049	26 Fe Iron 55.845	27 Co Cobalt 58.933200	28 Ni Nickel 58.6934	29 Cu Copper 63.546	30 Zn Zinc 65.39	31 Ga Galium 69.723	32 Ge Germanium 72.64	33 As Arsenic 74.92160	34 Se Selenium 78.96	35 Br Bromine 79.904	36 Kr Krypton 83.80
37 Rb Rubidium 85.4678	38 Sr Strontium 87.62	39 Y Yttrium 89.90585	40 Zr Zirconium 91.224	41 Nb Niobium 92.90638	42 Mo Molybdenum 95.94	43 Tc Technetium	44 Ru Ruthenium 101.07	45 Rh Rhodium 102.90550	46 Pd Palladium 106.42	47 Ag Silver 107.8682	48 Cd Cadmium 102.411	49 In Indium 114.818	50 Sn Tin 118.710	51 Sb Antimony 121.760	52 Te Tellurium 127.60	53 I Iodine 126.90447	54 Xe Xenon 131.29
55 Cs Cesium 132.90545	56 Ba Barium 137.327	57 La* Lanthanum 138.9055	72 Hf Hafnium 178.49	73 Ta Tantalum 180.9479	74 W Tungsten 183.84	75 Re Rhenium 186.207	76 Os Osmium 190.23	77 Ir Iridium 192.217	78 Pt Platinum 195.078	79 Au Gold 196.96655	80 Hg Mercury 200.59	81 Tl Thallium 204.3833	82 Pb Lead 207.2	83 Bi Bismuth 208.98038	84 Po Polonium	85 At Astatine	86 Rn Radon
87 Fr Francium	88 Ra Radium	89 Ac* Actinium	104 Rf Rutherfordium	105 Db Dubnium	106 Sg Seaborgium	107 Bh Bohrium	108 Hs Hassium	109 Mt Meitnerium	110 Ds Darmstadtium	111 Rg Roentgenium	112						

58 Ce Cerium 140.116	59 Pr Praseodymium 140.90765	60 Nd Neodymium 144.24	61 Pm Promethium	62 Sm Samarium 150.36	63 Eu Europium 151.964	64 Gd Gadolinium 157.25	65 Tb Terbium 158.92534	66 Dy Dysprosium 162.500	67 Ho Holmium 164.93032	68 Er Erbium 167.259	69 Tm Thulium 168.93421	70 Yb Ytterbium 173.04	71 Lu Lutetium 174.967
90 Th Thorium 232.0381	91 Pa Protactinium	92 U Uranium	93 Np Neptunium	94 Pu Plutonium	95 Am Americium	96 Cm Curium	97 Bk Berkelium	98 Cf Californium	99 Es Einsteinium	100 Fm Fermium	101 Md Mendelevium	102 No Nobelium	103 Lr Lawrencium

Fig. 2.5 **Periodic table of the elements. Elements are designated by their atomic number and symbol. The atomic weights are given for the stable elements and those with long-lived radioactive isotopes. Elements consisting of short-lived, naturally occurring radioactive isotopes are shown without atomic weights. Elements that are not known from nature, but which have been made in accelerators are shown in gray type. The elements in white boxes are solids at room temperature, those in dark gray boxes are liquids, and those in light gray boxes are gases.**

atomic number (Fig. 2.6c, d). As we have already noted in the case of magnesium, the periodicity of the properties of the elements is not always perfectly correlated with the atomic number. This reflects the details of the forces that hold the atoms together and the order in which the electron shells are filled.

The use of atomic number rather than atomic weight, as in Mendeleev's original table, dates to the discovery that the characteristic X-ray lines emitted by the elements are a strict function of the atomic number, Z. Electrons of an element that have been excited to a higher energy level lose the excess energy by emitting X-rays of specific frequency (= energy). The most energetic of these lines are called the K-series, the next the L-series, then the M-series, and so on. Measuring the intensities of these lines is the basis for electron microprobe analysis of the chemical compositions of minerals (Appendix). In 1913–14, Henry Mosley studied these X-ray lines and showed that the square-root of the X-ray energy (= hν, Planck's constant times frequency) is proportional to Z (Fig. 2.7). He concluded that the order of the elements in the periodic table should be based on Z. This insight changed the positions of some elements in the table, because atomic weights depend on the number and relative abundances of the different isotopes of an element, whereas the periodic properties of the elements and the X-ray frequencies depend on the number of protons and electrons in the

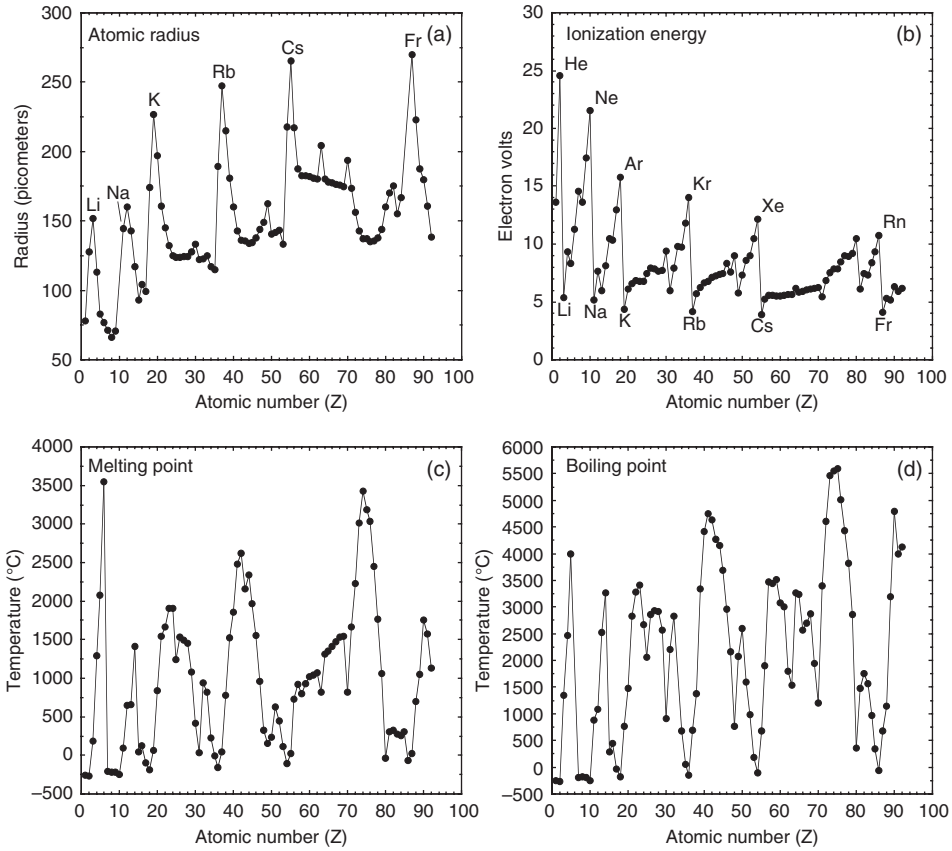

Fig. 2.6 **Properties of the elements as a function of atomic number (Z). Ionization energy (a) and atomic radius (b) directly reflect the atomic structure of the atoms. Other properties, such as melting point (c) and boiling point (d), are controlled indirectly by atomic structure through the bonding between atoms.**

atom. Note, for example, that tellurium, which has eight stable isotopes, has a higher atomic weight than the element with the next higher atomic number, iodine, which has a single isotope. With the new ordering, the elements still missing from the periodic table could now be predicted with certainty. In 1913, seven gaps still existed in the periodic table among the elements between H (Z=1) and U (Z=92). These gaps were at Z=43, 61, 72, 75, 85, 87, and 91. All have now been identified, but three, technetium (43), promethium (61), and astatine (85), are radioactive.

The chemical properties of an element are functions of the number and distribution of its electrons around the nucleus. In 1913, Niels Bohr devised a model for the atom that successfully explained why atomic spectra consist of discrete lines, not only in X-rays, as discussed above, but also in visible light. Building on the ideas of quantum mechanics, he postulated that the angular momentum of an orbiting electron can only have certain fixed values. If so, then the orbital energy associated with any electron cannot vary continuously, but can only have discrete quantum values. He described a series of spherical shells at fixed

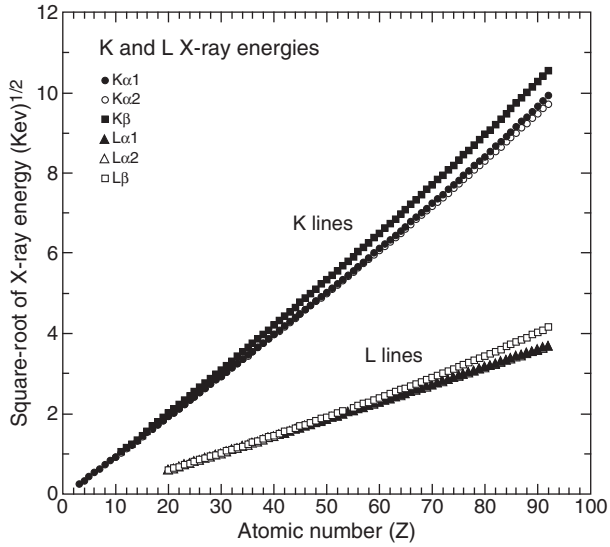

Fig. 2.7 **The K and L X-ray energies of the elements plotted as a function of atomic number (Z). The tight relationship between the square-root of the X-ray energy (or frequency) and atomic number led to the modern ordering of elements in the periodic table according to Z and shows that the table is now complete.**

distances from the nucleus. However, chemical physicists soon created a better model that uses the language of wave equations. In 1926, Erwin Schrödinger proposed a model incorporating not only a single quantum number, as Bohr had suggested, but three others as well. Schrödinger's equations describe geometrical charge distributions (atomic orbitals) that are unique for each combination of quantum numbers. The electrical charge that corresponds to each electron is not ascribed to an orbiting particle, as in Bohr's model. Instead, you can think of each electron as being spread over the entire orbital, which is a complex three-dimensional figure.

The *principle quantum number*, n, which can take integral values from 1 to infinity, describes the effective volume of an orbital. Chemists commonly use the word *shell* to refer to all orbitals with the same value of n, because each increasing value of n defines a layer of electron density that is farther from the nucleus.

The orbital *angular momentum quantum number*, l, describes the shape of the region occupied by an electron. Depending on the value of n, a particular electron can have values of l that range from zero to $n-1$. If $l = 0$, the orbital described by Schrödinger's equations is spherical and is given the shorthand symbol s. If $l = 1$, the orbital looks like one of those in Figure 2.8 and is called a p orbital. Orbitals with $l = 2$ (d orbitals) are shown in Figure 2.9. The $l = 3$ orbitals (f orbitals) have shapes that are not easy to illustrate in a flat drawing.

The third quantum number, m_l, describes the orientation of the electron orbital relative to an arbitrary direction. Because an external magnetic field (such as might be induced by a neighboring atom) provides a convenient reference direction, m_l is usually called the *magnetic orbital quantum number*. It can take an integral value from $-l$ to l.

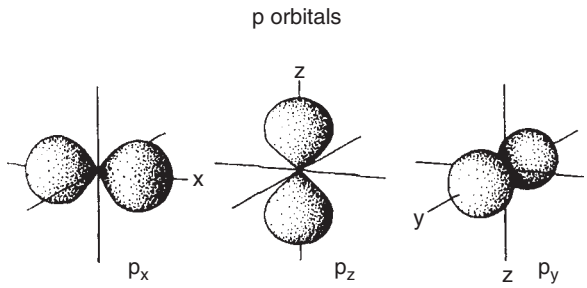

Fig. 2.8 The three p orbitals in any electron shell have figure-eight shapes, oriented along Cartesian x, y, and z axes centered on the atomic nucleus.

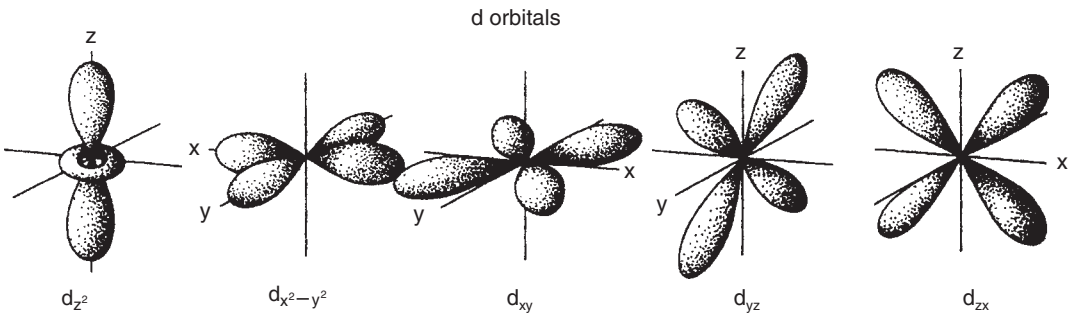

Fig. 2.9 Three of the d orbitals (d_{xy}, d_{yz}, and d_{zx}) in any electron shell have four lobes, oriented between the Cartesian axes. A fourth ($d_{x^2-y^2}$) also has four lobes, which lie along the x and y axes. The fifth (d_{z^2}) has lobes parallel to the z axis and a ring of charge density in the x-y plane.

The fourth quantum number, m_s, does not describe an orbital itself, but imagines the electron as a particle within the orbital spinning around its own polar axis. In doing so, the electron becomes a tiny magnet with a north and south pole. The *magnetic spin quantum number*, m_s, can be either positive or negative depending on whether the electron's magnetic north pole points up or down relative to an outside magnetic reference.

Each orbital can therefore contain no more than two electrons, with opposite spin quantum numbers. This rule, which affects the order in which electrons may fill orbitals, is known as the *Pauli exclusion principle*. Table 2.3 summarizes the configuration of electron orbitals for the first three shells. The orbitals are labeled with the numerical value of n and a letter corresponding to the value of l (s, p, d, f . .). As you can see from Table 2.3, the $n = 1$ shell can hold up to two electrons, both in the s orbital, the $n = 2$ shell can hold up to eight electrons (2 in the s and 6 in the p orbital), the $n = 3$ can hold up to 18 electrons (2 s, 6 p, and 10 d), and the $n = 4$ shell can hold up to 32 electrons (2 s, 6 p, 10 d, and 14 f). The lowest energy orbitals are occupied first. So for hydrogen, which has one electron, the electron resides in the 1s orbital. For lithium, which has three electrons, two are in the 1s orbital and the third is in the 2s orbital. For silicon (Z = 14), there are two electrons in 1s, two electrons in 2s, six electrons in 2p, two electrons in 3s, and two electrons in 3p.

Table 2.3 Configuration of electrons in orbitals

		n	l	m_l	m_s
K shell	1s orbital	1	0	0	+
2 s electrons		1	0	0	−
L shell	2s orbital	2	0	0	+
2 s, 6 p electrons		2	0	0	−
	2p orbitals	2	1	−1	+
		2	1	−1	−
		2	1	0	+
		2	1	0	−
		2	1	1	+
		2	1	1	−
M shell	3s orbital	3	0	0	+
2 s, 6 p, 10 d electrons		3	0	0	−
	3p orbitals	3	1	−1	+
		3	1	−1	−
		3	1	0	+
		3	1	0	−
		3	1	1	+
		3	1	1	−
	3d orbitals	3	2	−2	+
		3	2	−2	−
		3	2	−1	+
		3	2	−1	−
		3	2	0	+
		3	2	0	−
		3	2	1	+
		3	2	1	−
		3	2	2	+
		3	2	2	−
N shell	4s, 4p, 4d, 4f orbitals				
2 s, 6 p, 10 d, 14 f electrons					

The layout of the periodic table (Fig. 2.5) reflects the shell structure of the electrons. Hydrogen and helium have only K-shell electrons. The elements in row two have K and L-shell electrons, with the 1s orbitals always filled and the 2s and 2p orbitals filled in succession. Those in row three have K and L-shell electrons, with 1s, 2s, and 2p orbitals filled, and the 3s and 3p orbitals are filled in succession. Elements in the fourth row have K, L, and M-shell electrons, with the 1s, 2s, 3s, 2p, and 3p orbitals completely filled. After the 4s orbitals are filled, the 3d orbitals are filled, giving the transition metals. Then come the 4p orbitals. Row five is filled in an analogous fashion. In row six, the lanthanides, which fit between lanthanum and hafnium, reflect the appearance of the N-shell electrons, which fill the f orbitals. Row seven, which contains the actinides, also has K, L, M, and N-shell electrons.

The periodic behavior of the elements now makes sense. The noble gases, which are positioned at the right side of the periodic table, have completely filled electron shells and thus have little or no tendency to form chemical bonds. The alkali metals, which have only one s electron in the outermost shell, can easily lose that electron and become a positive ion. In contrast, the halogens are only one electron short of having filled out shells, and they often acquire an extra electron and become a negative ion. Note that the ionization energy, the energy required to remove one electron from an atom, increases from left to right across the periodic table, peaking with the noble gases (Fig. 2.6b). Electronegativity, which is the tendency to acquire another electron, also increases across the periodic table, but peaks with the halogens. The noble gases have very low electronegativities because they have filled electron shells.

Chemical bonding

The interactions between elements in nature and in the laboratory are manifestations of the chemical bonding between the elements. The nature of chemical bonds between elements is a direct result of their electron configurations. The outermost unfilled shells of electrons surrounding the nucleus generate the various types of bonds, and the electrons that create the bonds are known as the *valence electrons*. The valence of an atom is defined as the number of hydrogen-atom equivalents that could combine in that molecule. For example, the sodium in NaCl has a valence of +1, while the magnesium in MgO has a valence of +2. The chlorine and oxygen in these compounds have valences of −1 and −2, respectively. In this section we briefly review the different types of chemical bonding to provide the basics for later discussions. Detailed discussions of chemical bonding are available elsewhere (e.g. Roher, 2001).

An *ionic bond* is formed between a metal and a non-metal by the electrostatic attraction between two oppositely charged ions. A metal donates one or more electrons, forming a positive ion (cation). The donated electrons enter the non-metal, filling vacancies in the outer electron shell and creating a negative ion (anion). The resulting electrostatic attraction between the positively and negatively charged ions forms the bond. An example is common table salt, sodium chloride. Sodium, an alkali metal, has one 3s electron in its outermost (valence) shell, while chlorine, a halogen, has one empty spot in its 3p shell. Sodium donates an electron to chlorine, giving both of them closed-shell electron configurations. The positively charged sodium ion then bonds to the negatively charged chlorine ion in an ionic bond. The charge of an ion in a stable ionic compound is governed by the balance between the energy required to remove ions from the metal (ionization energy) and the energy released when the electron is added to the nonmetal, plus the energy released by bringing the ions together to form a bond. In general, the ionization energy is lower when removing electrons from the outer shell that has only one electron (e.g. Na^+, K^+, Ag^+) or when the resulting ion has a filled outer shell (e.g. Mg^{2+}, Ca^{2+}, Zn^{2+}), although other configurations do form ionic bonds.

Compounds with ionic bonds tend to have high melting points and boiling points because of the strong electrostatic attractions between the ions. They also tend to be soluble in water

because the positive and negative ions form dative covalent and hydrogen bonds, respectively, with the water molecules (see below).

Covalent bonds are characterized by the sharing of pairs of electrons between atoms. For example, a hydrogen atom has one electron. A more stable structure can be formed if two hydrogen atoms come together and share their electrons so that each has the paired electron structure of the helium atom. Two hydrogen atoms can also form covalent bonds with oxygen, which has room for two more electrons in the valence shell. Both oxygen and hydrogen thus achieve a more stable electronic structure. Covalent bonds can form between atoms of the same element or between different elements. But the atoms must have similar electronegativity. Because the electrons are shared, the bonding is delocalized, and the strength of the bond depends on the angular relationship between atoms in a molecule. Silicon dioxide (SiO_2) is a covalently bonded compound. Silicon has two 3p electrons, and oxygen has four 2p electrons out of the stable configuration of six. If each oxygen atom shares two electrons with silicon, the oxygen atoms reach the energetically more favorable stable configuration of six 2p electrons, and silicon, by sharing a total of four electrons with two oxygen atoms also reaches the stable configuration of six 3p electrons. Of course there are more than three atoms in a crystal of quartz, so the oxygen atoms each share electrons with two silicon atoms and the silicon atoms each share electrons with four oxygen atoms to generate an infinite structure. Carbon can share up to four electrons in covalent bonding. Carbon has two 2s and two 2p electrons, so the energy levels of the four electrons are not the same. However, when carbon bonds with four hydrogen atoms to form methane or four other carbon atoms to form diamond, the bonds are identical. Both methane and diamond are very energetically stable relative to the separate atoms. To form these molecules, the orbitals are hybridized to four identical orbitals pointing to the apexes of a tetrahedron. These sp3 hybrid orbitals allow the carbon and hydrogen atoms in methane and the carbon atoms in diamond to achieve energetically favorable configurations. Other types of hybridization involving s, p, and d orbitals are also possible.

Covalently bonded substances tend to be hard and to have high melting and boiling points, reflecting the bond strength. They do not conduct electricity because the electrons are tightly held between the atoms and are not free to move. They are insoluble in water and organic solvents because the attractions between the solvent molecules and the atoms in the covalently bonded substances are much weaker than the covalent bonds.

Metallic bonds are characterized by sharing of valence electrons among many atoms, so the bonding electrons are highly delocalized and are free to move around. For example, a sodium atom has one unpaired 3s electron. When sodium atoms come together, the close packing of atoms means that each sodium atom touches eight other sodium atoms. The 3s electron is shared with all eight of the adjacent atoms. In a piece of sodium metal, the molecular orbitals produced by the overlapping of the 3s orbitals extend over the whole piece of metal, so the electrons are not associated with any specific sodium atom. In magnesium, there are two 3s electrons for each atom, so in magnesium metal there are twice as many electrons in the molecular orbitals. This increases the strength of the bonding, as does the higher charge of each magnesium nucleus. Thus magnesium has a higher melting point than sodium. Because the electrons are delocalized, metallic bonds are non-polar.

Metals tend to have high melting and boiling points due to the strength of the metallic bond. The strength depends on the number of electrons that each atom provides to the sea of electrons and on the packing of the atoms in the structure. Group I metals have relatively low melting and boiling points because each atom contributes only one atom to the bond and because the atoms are relatively large and the packing in the structure is inefficient. Metals conduct electricity well because the delocalized electrons are free to move around, and they conduct heat well because the electrons can transfer the heat energy as they move through the metal. Metals are both malleable (can be formed into sheets) and ductile (can be pulled into wires) because the atoms can move easily past one another into new positions.

Van der Waals forces are intermolecular forces that are much weaker than the chemical bonding that results from sharing or exchanging electrons. Some molecules have more electrons on one end than on the other and thus form a permanent dipole. The positive end of one such molecule is attracted to the negative end of another such molecule. Many molecules have, on average, a symmetrical configuration of electrons and so are not permanent dipoles. However, the electrons are constantly in motion, and at any one instant, more of them may be on one side of the molecule than the other. At that moment, the molecule is a dipole and can attract another molecule. Furthermore, the attraction of the temporary dipole can cause the electrons in the other molecule to move toward the positive end of the temporary dipole, creating a second dipolar molecule. The electrons continue to move, so the polarity of the dipole is constantly changing. The electrons in the nearby molecules follow the dance of the strongest dipole, and the synchronous temporary dipoles result in a permanent attraction between the molecules. This latter type of dipole attraction is known as dispersion forces.

These two types of interaction, dipole–dipole and dispersion forces, determine properties such as the boiling point and melting point of molecular solids and of atoms such as the noble gases. In general, the melting and boiling points increase with increasing size of the molecule or atom because there are more electrons in the atom, resulting in a stronger dipole attraction.

Hydrogen bonds are intermolecular bonds that form between molecules consisting of hydrogen and some of the most electronegative elements (e.g. N, O, F, Cl). The electronegative atoms have one or sets of paired electrons in their outermost shells. These lone pairs align themselves around the nucleus on the opposite side from the hydrogen atoms. The electrons from the hydrogen atoms are strongly attracted to the electronegative atom, so the net result is a highly polar molecule. Because of this strong polarity, when water molecules come close together, the positively charged hydrogen is strongly attracted to the lone pairs of the electronegative atoms in the adjacent molecule. The attraction is not as strong as in a true covalent bond. Hydrogen bonds are about $^1/_{10}$ the strength of the average covalent bond, but they are significantly stronger than the dipole–dipole attraction of van der Waals forces (Jeffrey, 1997).

Chemical and physical processes relevant to cosmochemistry

The basic chemical properties of elements described above play key roles in the physical and chemical properties that cosmochemists investigate in their research.

-Box 2.1 The unique chemical bonding of water and its cosmochemical consequences

Water is a unique substance that plays a major role in geochemistry and cosmochemistry and is a critical component of life. The physical properties of water control the environment on the Earth's surface and have played significant roles in the history of other planets, comets, and asteroids. Most plants and animals are about 60% water by volume, and most biological reactions involve water. It is no exaggeration to say that water is the key to our existence.

A water molecule consists of two hydrogen atoms bonded to one oxygen atom. The angle of 104.5° between the bonds of the two hydrogen atoms means that water is a permanent dipole, with more positive charge on the side of the hydrogen atoms and more negative charge on the side of the oxygen atom. Water molecules can also make hydrogen bonds. In its liquid state, the molecules interact through both dipole bonds and hydrogen bonds; the structure is semi-ordered. When water freezes, all of the molecules link up with hydrogen bonds to make a highly ordered structure. The unique properties of water are manifestations of the two kinds of bonding.

Water is known as a *universal solvent*. Substances that carry a net electrical charge across a molecule will dissolve in water. This includes both ionic compounds and polar covalent molecules. The water molecules dissolve a substance by pulling the molecules apart due to the dipole charge on each water molecule. With an ionic substance such as NaCl, the water molecules surround the Na^+ atoms with the negatively charged oxygen ends pointing inward, and surround the Cl^- atoms with the positively charged H atoms pointing inward. Substances that do not have a net electrical charge across a molecule, such as oil molecules, will not dissolve in water. This property has important implications for the compositions of fluids in planets and planetesimals.

Water has a *high specific heat*, which means that it takes a lot of energy to heat it. Water thus acts as a powerful thermal buffer in the Earth's climate, absorbing heat from the atmosphere during the heat of the day and releasing it at night.

Water has a much *higher boiling point* than it would otherwise have due to the effects of hydrogen bonding. Extrapolating the boiling points of the compounds of hydrogen with column 6A of the periodic table (H_2Te, H_2Se, H_2S) suggests that in the absence of hydrogen bonding, water would boil at about −90° C, making it a gas at room temperature.

Water is one of only a handful of substances, out of the more than 15 million known, that *expands when it freezes*. The density of liquid water at 0 °C is 0.9998 g cm^{-3}, whereas ice has a density of 0.9167 g cm^{-3} at 0 °C. In order to achieve a regular structure where each oxygen is covalently bonded to two hydrogen atoms and hydrogen-bonded to two other hydrogen atoms, the space between the oxygen atoms must increase (Fig. 2.10). This property is critically important for life on Earth. When water freezes, the ice floats on the top of the water. Most lakes and oceans are cooler at the bottom than at the top because colder water is more dense. If ice were denser than water and sank to the bottom of a lake or ocean, it would probably never melt because there are no efficient ways of getting heat to the bottom. Our planet would probably be an icy snowball.

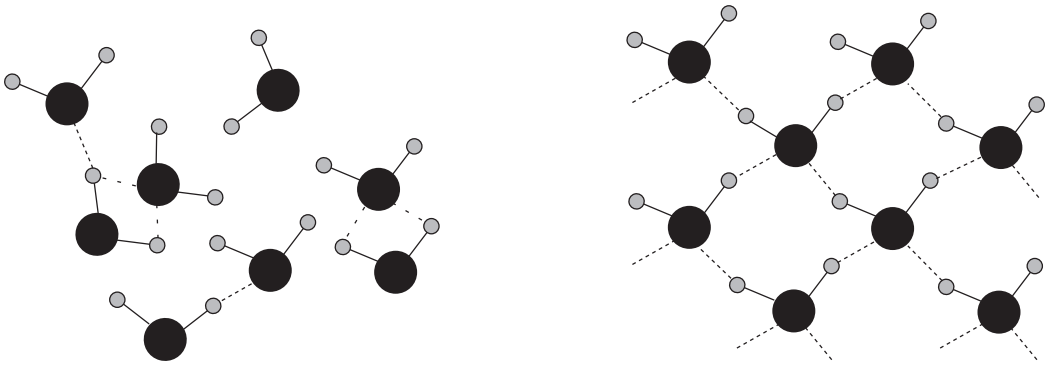

Fig. 2.10 **Schematic diagram of the structures of liquid and frozen water. Black circles represent oxygen atoms, and smaller gray circles represent hydrogen atoms. As water freezes, the molecules link up with hydrogen bonds (dashed lines) to form an open structure that is less dense than liquid water.**

Water has *high surface tension*. It tends to form drops rather than to spread out as a thin film over a surface. This is because the attractive forces between water molecules are larger than the attraction between the water and the surface in most cases. Molecules inside a drop are equally attracted to surrounding water molecules in all directions. However at the surface, there are no water molecules on one side, so a molecule experiences attractions on the sides and toward the interior of the drop. This tends to minimize the surface area of a drop and creates an effect like an elastic membrane on the water surface. The distinction between surface molecules and interior molecules is particularly great in water because of the hydrogen bonding. High surface tension allows water drops to cling to surfaces, allows large waves to form, and can help move water and the dissolved nutrients from plant roots to the leaves.

Water exists on the surface of the Earth as a solid, liquid, and gas. This permits the hydrologic cycle to operate and move water from the oceans to the tops of the highest mountains, where water is stored as snow and ice to be released later in the year. Having a temperature in the range where water can exist in all three forms may be a key ingredient for a planet to have life. On the surface of Mars, water exists only in solid and vapor forms.

Evaporation and condensation

When the elements are ejected from the stars where they were produced, they are in the gas phase. Subsequently, they combine in various chemical compounds and most condense as solids. The nature of those compounds and their behavior in the various environments encountered on their way to becoming part of the solar system can, in principle, be determined from the basic chemical properties of the elements. Evaporation and condensation are also important in the solar system and have played a defining role in determining the properties of planets, moons, asteroids, and the meteorites derived from them, comets, dust

grains, and all other solar system materials, as discussed in Chapter 7. Cosmochemists have spent a lot of effort quantifying the evaporation and condensation behavior of the elements and the compounds that they form.

Melting and crystallization

The interiors of planets, moons, and many asteroids either are, or have been in the past, molten. The behavior of molten silicates and metal is important in understanding how a planet or moon evolved from an undifferentiated collection of presolar materials into the differentiated object we see today. Basaltic volcanism is ubiquitous on the terrestrial planets and many asteroids. A knowledge of atomic structure and chemical bonding is necessary to understand how basaltic melts are generated and how they crystallize. Melting and crystallization are also important processes in the formation of chondrules, tiny millimeter-sized spherical objects that give chondritic meteorites their name. The melting, crystallization, and sublimation of ices are dominant processes in the histories of the moons of the outer planets, comets, asteroids, and probably of the Earth.

Dissolution and precipitation of solids from solution

When water, the universal solvent, is present on a planet, an asteroid, or in a meteorite, a wide variety of chemical reactions take place that can completely alter the mineralogy and chemistry of an object. Some meteorites show extensive evidence of aqueous alteration. To understand the conditions under which the alteration occurred, one must be able to infer the amount, composition, and temperature of the fluids from the minerals that they produced.

Solid-state diffusion

Elements also move around within solids. This motion is typically very slow, but over time it turns a rock composed of a disequilibrium assemblage of materials produced at high and low temperatures into an assemblage where all phases are in equilibrium. Understanding the nature and extent of these solid-state processes is critical to understanding and quantifying the histories of meteorites, asteroids, comets, and planets.

Isotope effects from chemical and physical processes

Chemical processes such as evaporation and condensation, precipitation of a mineral from a fluid phase, or diffusion can cause small changes in the relative abundances of the isotopes of the elements involved. These small isotopic shifts, which are typically a few parts in a thousand, are the basis for stable isotope geochemistry and cosmochemistry.

Isotopes of an element behave slightly differently in chemical, physical, and biological processes because of the differences in their masses. As a consequence, many processes can cause the relative proportions of the isotopes to change (to become *fractionated*) relative to the starting composition. There are two basic ways in which isotopes can become

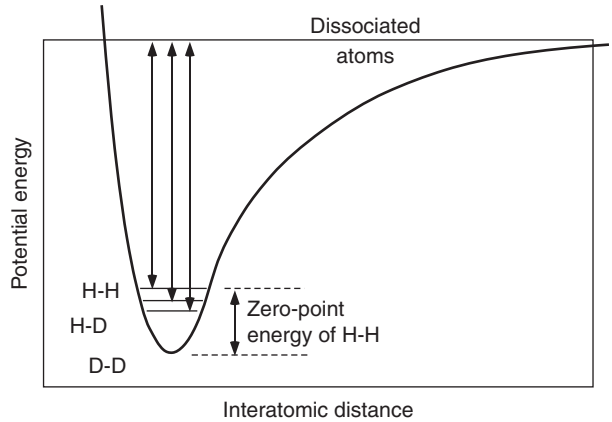

Fig. 2.11 **Potential energy curve for diatomic hydrogen. Shown are the zero-point energies of the $^{1}H-^{1}H$, $^{1}H-^{2}D$, and $^{2}D-^{2}D$ molecules. The zero-point energy of the $^{2}D-^{2}D$ molecule sits deeper in the potential energy well than the other two molecules, so it has a higher dissociation energy and a stronger bond.**

fractionated. Equilibrium processes partition the isotopes among the phases involved without any changes in conditions. At equilibrium, the forward and reverse reactions are in balance, but that does not mean that the isotope compositions of the phases are the same. When a light isotope is substituted for a heavy isotope, the internal energy of a molecule changes slightly. Consider the diatomic molecule, H_2. The two atoms will have an average distance from one another that balances the attractive force between the two atoms as they share electrons and the repulsive force between the two positively charged protons. The atoms behave as a harmonic oscillator and vibrate at a characteristic frequency. At absolute zero, the energy of the molecule is given by

$$E = \frac{1}{2}\, hv \tag{2.1}$$

where h is Planck's constant and v is the vibrational frequency. This is the *zero-point energy.* When a deuterium atom is substituted for a hydrogen atom, the frequency decreases, producing a corresponding decrease in the zero-point energy of the molecule. This decrease corresponds to an increase in the strength of the bond between the atoms. Figure 2.11 shows schematically the potential energy curve for hydrogen and the zero-point energies of the H_2, HD, and D_2 molecules. The D_2 molecule has the strongest bond. In general, equilibrium fractionation between two phases decreases with increasing temperature (proportional to $1/T^2$), the degree of fractionation is larger for lighter elements because there is a greater relative mass difference between the isotopes, and the heavy isotope is preferentially partitioned into the site with the stiffest (strongest and/or shortest) chemical bonds. Because of the temperature dependence, isotopic shifts between phases at equilibrium can be used as geothermometers.

The second way in which isotopes can be fractionated is via kinetic processes. Kinetic isotope effects are associated with fast, incomplete, or unidirectional processes such as

evaporation, diffusion, dissociation reactions, and biological reactions. Isotopic effects produced by diffusion and evaporation are due to differences in translational velocity between different isotopic forms of molecules as they move through a phase or cross a phase boundary. The kinetic energy of a molecule is given by

$$K.E. = \frac{1}{2}mv^2 \tag{2.2}$$

where m is the mass of the molecule and v is its velocity. Under a given set of conditions, the kinetic energy of molecules of the same compound but with different isotopic configuration will be the same. In order for this to be true, the difference in mass caused by the presence of different isotopes must be counteracted by a difference in velocity. The lighter molecule will move faster. In cosmochemistry, kinetic mass fractionation via evaporation, diffusion, and dissociation reactions is widely observed and is useful for constraining the conditions and processes that produced the objects that we have to study. We will consider some isotopic fractionations of cosmochemical interest in Chapter 7.

Because isotopic changes caused by chemical processes are so small, the isotopic data are typically reported as deviations in parts per thousand from a standard composition. For example, the shift in the $^{13}C/^{12}C$ ratio relative to a standard is given in "delta" notation by:

$$\delta^{13}C = \left[\left(\frac{\left(^{13}C/^{12}C\right)_{meas}}{\left(^{13}C/^{12}C\right)_{std}}\right) - 1\right] \times 1000 \tag{2.3}$$

These "delta" values (read "delta C-13", or "delta carbon-13") are typically given in parts per thousand ("permil", ‰). For historical reasons, carbon stable isotopes are reported relative to the PDB (Pee Dee Belemnite, a fossil) or the equivalent VPDB (Vienna PDB) standard. Oxygen and hydrogen stable isotopes are reported relative to SMOW (Standard Mean Ocean Water) or the equivalent VSMOW (Vienna SMOW). The VPDB and VSMOW standards are preferred, not only because the original standards, PDB and SMOW, are no longer available, but also because they imply that the measurements have been calibrated according to international conventions.

In cosmochemistry, we use stable-isotope fractionations to study evaporation and condensation in the solar nebula, aqueous processes on asteroids, and even ion–molecule reactions to form organic molecules in interstellar clouds. The oxygen isotopes also show large mass-*independent* shifts that may be related either to chemical or physical processes or to incomplete mixing of the products of nucleosynthesis. These topics will be covered in detail in later chapters.

Summary

In this chapter, we introduced the constituents and structure of the atom and showed that elements typically have several isotopes (same number of protons but different numbers of neutrons). Using the Chart of the Nuclides, we briefly discussed the distribution and stability of the isotopes. Radioactive isotopes were introduced, and we mentioned that they can be used for dating of geological and cosmochemical events. We then discussed the periodic

table and showed that the physical and chemical properties of the elements are derived from the number and arrangement of the electrons. The different types of chemical bonding were introduced. The range of chemical and physical processes that can be understood from basic chemical principles was discussed. Finally, we showed that physical, chemical, and biological processes can produce small shifts in the isotopic compositions of the elements and that these shifts can be used to study the processes that caused them.

The contents of this chapter will be the foundation of all subsequent discussions. Your depth of understanding of each of these subjects will grow as you continue through the book, but it is critical to have a grasp of these basic ideas before moving ahead. In the next chapter we will discuss the origin of the elements via nucleosynthesis in stars.

Questions

1. What is nuclear binding energy? What are the two main ways it can be released? Which of these is currently powering our Sun?
2. When discussing stable and radioactive isotopes, what is meant by the "valley of β stability"?
3. What are the four modes of radioactive decay?
4. In order to use radioactive decay of an element for a chronometer, the decay constant must not have changed with time. How do we know that this is true?
5. What are the five main types of chemical bonds? Give two important properties of each type.
6. Why is water such an important compound in geochemistry and cosmochemistry? What are some of its properties?

Suggestions for further reading

Baum, E. M., Knox, H. D. and Miller, T. R., editors (2002) *Chart of the Nuclides*, 16th edn. Lockheed Martin: Knolls Atomic Power Laboratory, 88 pp. Everything you might want to know about nuclides in one convenient place.

References

Cowan, G. A. (1976) A natural fission reactor. *Scientific American*, **235**, 36–47.

Hofmann, S. and Münzenberg, G. (2000) The discovery of the heaviest elements. *Reviews of Modern Physics*, **72**, 733–767.

Huh, C.-A. (1999) Dependence of the decay rate of ^{7}Be on chemical forms. *Earth and Planetary Science Letters*, **171**, 325–328.

Jeffrey, G. A. (1997) *An Introduction to Hydrogen Bonding*. New York: Oxford University Press, 303 pp.

Kuroda, P. K. (1956) On the nuclear physical stability of the uranium minerals. *Journal of Chemical Physics*, **25**, 781–782.

Lee, K. K. M. and Steinle-Neumann, G. (2008) *Ab-initio* study of the effects of pressure and chemistry on the electron-capture radioactive decay constants of ^{7}Be, ^{22}Na, and ^{40}K. *Earth and Planetary Science Letters*, **267**, 626–628.

Limongi, M. and Chieffi, A. (2006) The nucleosynthesis of ^{26}Al and ^{60}Fe in solar metallicity stars extending in mass from 11 to 120 solar masses: the hydrostatic and explosive contributions. *Astrophysical Journal*, **647**, 483–500.

Liu, L. and Huh, C.-A. (2000) Effect of pressure on the decay rate of ^{7}Be. *Earth and Planetary Science Letters*, **180**, 163–167.

Roher, G. S. (2001) *Structure and Bonding in Crystalline Materials*. Cambridge: Cambridge University Press, 552 pp.

Sharp, Z. (2007) *Principles of Stable Isotope Geochemistry*. Upper Saddle River, New Jersey: Pearson Prentice Hall, 344 pp.

3 Origin of the elements

Overview

Several processes were responsible for producing the current inventory of elements in the cosmos. Hydrogen, helium, and some lithium were created in the Big Bang, a massive explosion that is thought to have produced the universe. Elements heavier than hydrogen and helium, known as *metals* in astronomy, were produced in stars by processes collectively called *stellar nucleosynthesis*. The chemical elements other than hydrogen and helium in our solar system are the result of nucleosynthesis that occurred in stars that lived and died before the solar system formed. These processes involve fusion of light elements into heavy elements, sometimes at modest rates as stars evolve and sometimes at furious rates in stellar explosions. Significant amounts of a few rare elements, such as lithium, beryllium, and boron, were created via spallation reactions, in which collisions between highly energetic cosmic rays (typically protons or helium ions) and atoms break up the heavier nuclides into lighter fragments. And, of course, some nuclides have been produced by decay of radioactive nuclides. In this chapter, we will review these processes and discuss the evolution of the elemental abundances with time in the universe and the galaxy.

In the beginning

The cosmological model that best explains the origin of the universe is the *Big Bang*. According to this model, the universe began at a finite time in the past and at a discrete point in space, expanded from a hot dense initial state of very small size, and continues to expand to this day. The framework for the model comes from Albert Einstein's Theory of General Relativity. In 1922, Alexander Friedman, a Russian cosmologist and mathematician, derived a series of equations based on General Relativity indicating that the universe might be expanding, contrary to the then popular idea of a static universe. In 1927, Belgian physicist and Catholic priest Georges Lemaître independently derived similar equations. In 1929, American astronomer Edwin Hubble published the results of a decade of observations showing that the distances to far-away galaxies were proportional to the red-shift of the light received from them. The red-shift is the lengthening of the wavelength of light caused by rapid movement away from the observer (the Doppler shift). Thus, Hubble's

observations imply that galaxies are receding from us at speeds proportional to their distance. Lemaître's "hypothesis of the primeval atom", published in 1931, combined the theoretical and observational work into the first version of the Big Bang model.

The Big Bang model

The Big Bang model has become much more sophisticated over the >75 years since it was first articulated. Readable summaries of the main features of the Big Bang model are given by Hawking (1988) and Wienberg (1993). Mathematical models break down when describing the initial state of the universe, so the earliest stages are subject to considerable uncertainty. Immediately after the Big Bang, the universe consisted of an incredibly high energy density of unimaginable temperature and pressure and was expanding and cooling very rapidly. Approximately 10^{-35} seconds into the expansion, the universe went through a phase of exponential expansion, known as *cosmic inflation*, driven by a poorly understood negative-pressure vacuum energy density. During this inflationary period, the observable universe originated in a small region, explaining why the Universe appears flat, homogeneous, and isotropic, as assumed by the Cosmological Principle, a fundamental assumption of the Big Bang. Cosmic inflation also explains the origin of large-scale structure in the cosmos, which is the manifestation of quantum fluctuations in the microscopic inflationary region magnified to cosmic size.

After inflation stopped, the universe consisted of a quark–gluon plasma containing all of the elementary particles. From this point on, detailed, self-consistent mathematical models describe the evolution of the universe. Temperatures were so high that motions of particles were near the speed of light, and particle–antiparticle pairs of all kinds were being continuously created and destroyed in collisions. At some point, an unknown process known as baryogenesis violated the conservation of baryon number (protons and neutrons are baryons), leading to a very small (one part in 30 million) excess of quarks and leptons over antiquarks and antileptons. This led to the predominance of matter over antimatter in the present universe. As the universe continued to expand and cool, various symmetry-breaking phase transitions put the fundamental forces of physics and the parameters of elementary particles into their present form.

After about 10^{-11} seconds, particle energies had dropped to values that can be attained in particle physics experiments. At $\sim 10^{-6}$ seconds, quarks and gluons combined to form baryons (protons and neutrons). The small excess of quarks over antiquarks led to a small excess of baryons over antibaryons. Because the temperature was no longer high enough to create new proton–antiproton pairs, a mass annihilation occurred, leaving just one in 10^{10} of the original protons and neutrons and none of their antiparticles. At about 1 second, a similar process happened for electrons and positrons. After these annihilations, the energy density of the universe was dominated by photons.

A few minutes into the expansion, when the temperature had dropped to $\sim 10^{9}$ degrees, neutrons combined with protons to form deuterium and helium nuclei. Most protons remained uncombined as hydrogen nuclei. As the universe continued to cool, the rest mass energy density of matter (gravity) came to exceed the energy density of the photons

(electromagnetic radiation). After about 379 000 years, electrons and nuclei combined into atoms, mostly hydrogen, and the universe became transparent to light. Over the next ~10^9 years, slightly denser regions of the nearly uniformly distributed matter gravitationally attracted nearby matter and began to form gas clouds, stars, galaxies, and other astronomical structures observable today.

Three types of matter exist in the universe today: cold dark matter (matter that cannot be detected by electromagnetic radiation), hot dark matter (dark matter traveling near the speed of light, often considered to be neutrinos), and baryonic matter (normal chemical elements). The dominant form of matter today appears to be cold dark matter, with the two other types of matter making up less the ~18% of the universe. Observations also indicate that ~72% of the total energy density in today's universe is in the form of dark energy, a mysterious form of energy that cannot be directly detected. Dark energy is postulated to explain an apparent acceleration of the expansion of the universe over the last few billion years.

Observational evidence

The Big Bang model is based on three lines of observational evidence. The first is Hubble's original observations relating distance to red-shift and to the speed of receding galaxies. This relationship is described by the Hubble Constant. The second is the cosmic microwave background, which is the electromagnetic radiation left over from the Big Bang that can be measured today. The third is the relative abundances of hydrogen, helium, and lithium in the universe. Their abundances are in good agreement with specific predictions of the Big Bang model.

The Hubble Constant

Astronomers use a variety of methods to determine the distance to objects in the universe. One of the most effective is the "standard candle" provided by Type Ia supernovae. These supernovae originate in a binary star system when a white dwarf star accretes matter from its companion. When the white dwarf reaches the Chandrasekhar limit of 1.4 solar masses, a thermonuclear runaway occurs that completely disrupts the star in a cataclysmic explosion that makes the supernova as bright as an entire galaxy. Because Type Ia supernovae occur in stars with similar masses and because the nuclear burning affects the entire star, they all have essentially the same intrinsic brightness and their apparent brightness observed from Earth can be used to derive the distance to the supernova.

A measure of the speed at which a galaxy is traveling relative to the Earth can be obtained by looking at the spectrum of electromagnetic radiation (including visible light) arriving at Earth from that galaxy. When an observer is moving relative to the source of waves, the frequency of the waves changes, becoming longer if the distance between the observer and the source is increasing and becoming shorter if the distance is decreasing. This Doppler shift is commonly observed when a vehicle sounding a siren approaches, passes, and moves away from an observer. A higher pitch is heard as the vehicle approaches and a lower pitch is

heard as it moves away. The same phenomenon is observed with electromagnetic radiation. A star emits a characteristic spectrum that depends on the mass and stage of evolution of the star. Lines appear in the spectrum due to absorption by atoms in the stellar atmosphere. When the star is moving away from the Earth, the entire spectrum, including the absorption lines, is shifted to longer (redder) wavelengths. The spectrum is said to be *red-shifted*. A star moving toward the Earth will have a spectrum shifted toward shorter (bluer) wavelengths. Such a spectrum is said to be *blue-shifted*. The same is true for galaxies, if they are far enough away. Nearby galaxies have spectra that are dominated by the effects of rotation, with the side of the galaxy where stars are moving toward the Earth being blue-shifted and the side where they are moving away being red-shifted.

Hubble's crucial observation was that, in every direction one looks, the farther away a galaxy is, the more the light from that galaxy is red-shifted. If the red shift is a Doppler shift, this implies that the farther away the galaxy is, the faster it is moving away from us. The most reasonable explanation for this observation is that the universe is uniformly expanding everywhere. The current best estimate for the Hubble Constant, which describes the rate of expansion, is ~70.8 km s^{-1} megaparsec^{-1}, with an uncertainty of ~5.6%.

Cosmic microwave background

During the initial stages after the Big Bang, all of the particles and photons in the universe were in full thermal equilibrium. Under these conditions the electromagnetic radiation had a blackbody spectrum. Electrons and atomic nuclei (mostly protons) were unbound, and photons were continuously scattered by the electrons, making the early universe opaque to light. When the temperature fell due to expansion to a few thousand Kelvin, electrons and nuclei began to combine to form atoms. Scattering of photons ceased and the radiation became decoupled from the matter. Photons could travel unimpeded. As the universe expanded and cooled, the energy of the photons was red-shifted. Now, this primordial radiation falls into the microwave region of the electromagnetic spectrum and corresponds to a temperature of ~3 K. This radiation, which permeates the universe, was accidentally discovered in 1964 by Arno Penzias and Robert Wilson, who were conducting diagnostic observations at Bell Laboratories using a new microwave receiver. Penzias and Wilson were awarded the Nobel Prize for their discovery.

Big Bang nucleosynthesis

The outlines of Big Bang nucleosynthesis were laid out with the calculations of Ralph Alpher and George Gamow in the 1940s. Together with Hans Bethe, they published the seminal paper (Alpher, Bethe, and Gamow, 1948) outlining the theory of light-element production in the early universe. Big Bang nucleosynthesis began about 3 minutes after the Big Bang, when the universe had cooled sufficiently to permit protons and neutrons to combine into stable nuclei. The nuclear physics of Big Bang nucleosynthesis is well understood because the temperatures involved (~10^9 K) are found in the interiors of stars. As long as the universe was hot enough, protons and neutrons easily transformed into each other and the abundance ratio was determined by their relative masses, with about one

neutron for every seven protons. Helium-4 is more stable than free neutrons and protons and so has a strong tendency to form. However, formation of ^{4}He requires an intermediate step, which is the formation of deuterium (^{2}H), consisting of a proton and a neutron. Deuterium is only marginally stable, and two deuterium atoms will easily combine to form ^{4}He. But until the universe became cool enough so that the mean energy per particle was lower than the binding energy of deuterium, significant amounts of deuterium could not build up. This is known as the deuterium bottleneck. Production of significant ^{4}He had to wait until the temperature of the universe became low enough for deuterium to be stable ($T = 10^{9}$ K). At this point a burst of nucleosynthesis occurred, but soon thereafter, at about 20 minutes after the Big Bang, the universe had become too cool for any fusion reactions to occur. This froze in the abundances before the nuclear reactions could go to completion. From this point on, the abundances were fixed, except for decay of radioactive nuclides, until stars formed and stellar nucleosynthesis began. Big Bang nucleosynthesis did not produce elements heavier than beryllium because there are no stable nuclides with five or eight nucleons. In stars, this bottleneck is bypassed when three ^{4}He atoms combine to form ^{12}C (the triple-alpha process, see below). But by the time enough ^{4}He had built up, the temperature of the universe was too low for this process to operate efficiently, so it made a negligible contribution to Big Bang nucleosynthesis. The Big Bang model predicts mass abundances of ~75% ^{1}H, ~25% ^{4}He (~8.3% by number), ~0.01% ^{2}D (~0.005% by number), and trace amounts (~10^{-10}) of ^{3}He, ^{6}Li, ^{7}Li, ^{9}Be, and perhaps ^{10}B and ^{11}B. Radioactive species such as ^{3}H (tritium), ^{7}Be, ^{10}Be, and shorter-lived species were produced, but decayed away.

There is good agreement between observations and the predictions of Big Bang synthesis. The abundances of H, ^{4}He, ^{3}He, and deuterium, match the predictions very well. For ^{7}Li, observations and predictions match within about a factor of two. It is likely that the main uncertainty for ^{7}Li is in the nuclear physics of its synthesis. This level of agreement represents an impressive success of modern cosmology.

Nucleosynthesis in stars

There are several lines of evidence that nucleosynthesis takes place in stars. The compositions of the outer envelopes of evolved low- and intermediate-mass stars show enhancements of the products of nuclear reactions (hydrogen and helium burning and *s*-process nucleosynthesis, as defined below). The ejecta of supernovae (stellar explosions) are highly enriched in short-lived radioactive nuclides that can only have been produced either just before or during the explosion. At the other extreme, low-mass stars in globular clusters, which apparently formed shortly after the universe formed, are deficient in metals (elements heavier than hydrogen and helium) because they formed before heavy elements were synthesized.

The energy released by nuclear reactions provides the power that causes stars, including our Sun, to shine. The realization that stars are fueled by nuclear reactions was key to understanding the long lifetimes of stars and to reconciling the age of the Sun with the age of the Earth (see Box 3.1). The energy budget of a star represents a balance between

Box 3.1 The age of the universe, the solar system, and the Earth

In Europe, by the middle of the nineteenth century, the age of the cosmos and of our own planet were no longer the purview of religious scholars, but had become topics that could be addressed by the methodology of science. Charles Lyell, in his *Principles of Geology*, published in three volumes from 1830 to 1833, argued that the scientific way to understand the history of the Earth was to invoke only those processes that can be observed acting today (e.g. erosion, earthquakes, volcanic eruptions). Based on this approach, there was no reason to adopt any specific age of the Earth, but there was also no reason to believe that the Earth is particularly young. By the end of the nineteenth century, geological estimates based on processes such as transport of salt by rivers to the oceans or deposition of sediments were yielding ages of ~100 million years. When Charles Darwin published his *On the Origin of Species* in 1859, he suggested, based on the time he thought was necessary for species to evolve into what they are today, that the Earth was on the order of 300 million years old.

Physicists were also worrying about the age of the Earth. During the latter part of the nineteenth century, William Thomson, also known as Lord Kelvin, was studying heat conduction in solids. He calculated initially that the Earth must have been molten ~100 million years ago, but by the end of the nineteenth century, Lord Kelvin and Hermann von Helmholtz had reduced this estimate to ~24 million years. They assumed that there were no sources of heat within the Earth. Lord Kelvin further calculated that if the Sun's energy was derived simply from the conversion of gravitational potential energy to heat, it should be only ~20 million years old. Also in the late nineteenth century, George Darwin worked extensively on the theory of tidal dissipation and calculated that the time required for the Moon's orbit to evolve from the time when the Moon had separated from the molten spinning Earth until it reached its present state would require a little more than 54 million years. These estimates were much shorter than the times inferred from geological reasoning. Geology and physics were giving different results, and because physics was considered a more "fundamental" science, physicists, at least, thought that there must be something wrong with the geological interpretation.

The discovery of radium in 1902 by Marie and Pierre Curie changed the rules of the game. Radioactive decay of radium in the Earth's crust was shown to provide approximately enough heat to keep the Earth from cooling. This removed the main constraint requiring a young Earth. Radioactivity also provided a means to date rocks. In 1904, Ernest Rutherford used U–He dating to estimate a rock to be 500 million years old. The next year, J. W. Strutt estimated the U–He age of a thorianite at 2.4 billion years, but admitted that some of the helium might have come from thorium. The U–He ages were soon shown to be unreliable for most rocks because helium escapes by diffusion. Over the next 15 years, isotopes were discovered and the radioactive decay series of uranium was sorted out. By 1920, Arthur Holmes used more reliable dates for old minerals to estimate that the Earth's crust was probably ~2 billion years old. In 1936, Alfred Nier and his colleagues used the ^{235}U–^{207}Pb and ^{238}U–^{206}Pb decay series and an estimate for primordial lead derived from a galena to derive an age for a monazite of 2.57 billion years. In 1946, Fredrich Houtermans and Arthur Holmes showed that the decay of uranium to lead could be used to determine the age of the Earth. Their initial results gave an age for the Earth of 2.9 to 3.35 billion years. In 1956, Clair Patterson used the U–Pb system and an estimate of the composition of the initial lead of the solar system, based on measurements of uranium-free

troilite (FeS) from the Canyon Diablo meteorite, to show that the age of the Earth was 4.55±0.07 billion years. The currently accepted age of the Earth is within error of Patterson's measured value.

The Sun was getting older too. During the early 1900s, Arthur Eddington, George Gamov, Subrahmanyan Chandrasekhar, and others were developing a quantitative theory of nuclear fusion. In 1920, Eddington suggested that the Sun was powered by the fusion of hydrogen to helium. However, his calculations indicated that the Sun should be 20 orders of magnitude brighter than it is. The resolution of this problem came from a better understanding of nuclear physics. In 1926, Gamow derived what is now called the Gamow factor, a quantum-mechanical formula that gave the probability of bringing two nuclei sufficiently close together for the strong nuclear force to overcome the electrostatic repulsion of the Coulomb barrier and allow the atoms to fuse. The Gamov factor was used in the following decades to derive the rate at which nuclear reactions would proceed at the temperatures believed to exist in the stellar interiors. Once this was understood, the Sun could be shown to have enough fuel to shine at its current luminosity for ~10 billion years.

Essentially all theories of the formation of the solar system since those of Immanuel Kant (1755, *Allgemeine Naturgeschichte un Theorie des Himmels*) and Pierre LaPlace (1796, *Exposition du system du monde*) have assumed that the Earth and Sun formed at approximately the same time. Our modern view holds that the solar system formed 4.568 billion years ago in a single event and that the Sun is about half way through its life.

But as the inferred ages for the Earth and the Sun were increasing, a new problem arose. The Earth seemed to be older than the universe. In 1929, astronomer Edwin Hubble showed that there is a linear relationship between the distances of nebula (=galaxies) and the speed at which they are moving away from us, estimated from the red shifts of spectral lines. From his observations, he estimated that the universe had expanded from a very small space to its current size in 1.8 to 2 billion years (this was the beginning of the Big Bang theory). As the age of the Earth crept up to ~3 billion years, the problem became acute. The conflict was resolved gradually starting in the early 1950s, when astronomers began revising their distance scale based on new observations until the age of the universe reached its present value of ~13.5 billion years.

gravitational compression and pressure exerted by the thermal energy in the stellar core. An increase in pressure due to compression produces a higher temperature as the stellar material is confined into a smaller area. This in turn increases the nuclear reaction rate, which increases the thermal pressure in the stellar material, balancing the compression. This balance, known as hydrostatic equilibrium, is maintained until the energy source at the core of the star is exhausted.

There are several bodies of information that feed into our understanding of stellar nucleosynthesis. We will start with a discussion of the classification of stars, their masses and mass distributions, and their lifetimes. From this information we can assess the relative importance of different types of stars to the nucleosynthesis of the elements in our solar system and in the galaxy. We will then discuss the life cycles of stars to give a framework for the discussion of nucleosynthesis processes. Next, we will review the nuclear pathways

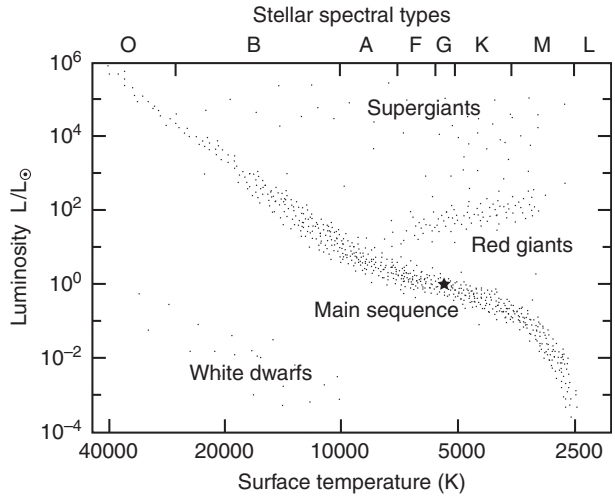

Fig. 3.1 **Herzsprung–Russell diagram plotting stellar luminosity in units of solar luminosity ($L/L_\odot$) versus surface temperature (bottom) and spectral type (top). Most stars lie in a band extending from the upper left to the lower right of the diagram, called the main sequence. The black star represents the Sun. Main sequence stars convert hydrogen to helium in their cores. Stars in other portions of the diagram are mostly stars that have evolved off the main sequence and are using elements other than hydrogen for fuel. Pre-main sequence stars plot above the main sequence.**

involved in stellar nucleosynthesis and the elements that they produce. And finally, we will show how stellar nucleosynthesis has driven the chemical evolution of the galaxy, producing matter with the chemical composition of our solar system.

Classification, masses, and lifetimes of stars

An important tool for classifying stars is the Herzsprung–Russell (or H–R) diagram, which is a plot of stellar luminosity (variously plotted as luminosity, absolute bolometric magnitude, apparent visual magnitude, etc.) versus effective surface temperature (variously plotted as temperature, color index B–V, or spectral class). An example of such a diagram is shown in Figure 3.1. The brightest stars (highest luminosity) are at the top, and the hottest stars (highest surface temperature) are on the left. The band that goes from the upper left to the lower right is the *main sequence*, containing ~90% of all stars. These stars are converting hydrogen to helium in their cores. This *hydrogen-burning* stage is the longest stage in a star's lifetime. The Sun (shown as a star in Fig. 3.1) is a main sequence star of spectral class G2. The spectral characteristics of main sequence stars are listed at the top of Figure 3.1 and are summarized in the Harvard Spectral Classification of Stars (Table 3.1). Note that the brightest, hottest stars (O and B stars) have lifetimes on the main sequence of only a few million years, whereas a cooler dimmer star such as our Sun has a main sequence lifetime of roughly 10 billion years.

The details of stellar nucleosynthesis are a strong function of stellar mass (see below). Stars range in mass from ~0.08 to ~120 solar masses (abbreviated $M_\odot$). The low-mass

Table 3.1 Harvard spectral classification of stars

Spectral type (color)	Atmospheric temperature (K)	Spectral features	$M/M_\odot$	$R/R_\odot$	$L/L_\odot$	Main sequence lifetime
O (blue)	>30 000 K	Weak H (Balmer) lines, He^+ features, strong UV continuum	20–60	9–15	90 000–800 000	10–1 Myr
B (blue-white)	10 000–30 000 K	Medium H lines, neutral He absorption	3–18	3.0–8.4	95–52 000	400–11 Myr
A (white)	7400–10 000 K	Strong H lines, some features of heavy elements	1.8–3.0	1.7–2.7	8–55	3 Gyr–400 Myr
F (yellow-white)	6000–7400 K	Medium H lines	1.1–1.8	1.2–1.6	2.0–6.5	7–3 Gyr
G (yellow)	5250–6000 K	Weak H lines, Ca^+ H&K lines, Na D lines	0.8–1.1	0.85–1.1	0.66–1.5	7–15 Gyr
K (orange)	4000–5250 K	Very weak H lines, Ca^+, Fe, strong molecules such as CH, CN	0.4–0.8	0.65–0.80	0.10–0.42	17 Gyr
M (red)	2600–3850 K	Very weak H lines, molecules (e.g. TiO_2), very red continuum	0.08–0.4	0.17–0.63	0.001–0.08	56 Gyr
L			<0.08			

$M/M_\odot$ is the mass of the star in units of solar masses, $R/R_\odot$ is the radius in units of solar radii, and $L/L_\odot$ is the luminosity in units of solar luminosity and lifetimes are in millions (Myr) or billions (Gyr) of years.
The spectral classes are further subdivided into ten categories given by numbers 0–9, with luminosity, color, temperature, and stellar mass increasing from 0 to 9.

end, ~80 times the mass of Jupiter, is the smallest size that can sustain hydrogen burning. Stars larger than ~120 $M_\odot$ are thought either not to form or to be very unstable because they exceed the Eddington limit, where the radiation pressure on the gas balances the gravitational attraction and either prevents further accretion of gas onto the star or actually drives off the outer layers. A famous example of such a massive star, Eta Carinae, is located 7000–8000 light years from Earth.

The lifetime of a star is also a strong function of its mass. Stars shine because of a balance between the force of gravity, which tends to make the star contract, and heat from nuclear reactions, which tends to make the star expand. This hydrostatic equilibrium is maintained as long as there is enough nuclear energy to balance the gravitational attraction. The more massive the star, the faster it must burn its nuclear fuel to maintain hydrostatic equilibrium. Figure 3.2 plots the lifetime of a star against its mass. Note that stars having the mass of the Sun live for ~10 billion years, but high-mass stars live and die within a few million years.

In order to understand the production of the chemical elements with time in our galaxy (galactic chemical evolution), it is necessary to understand the relative contributions of stars of different masses to the galactic inventory. Therefore, in addition to how long stars of a

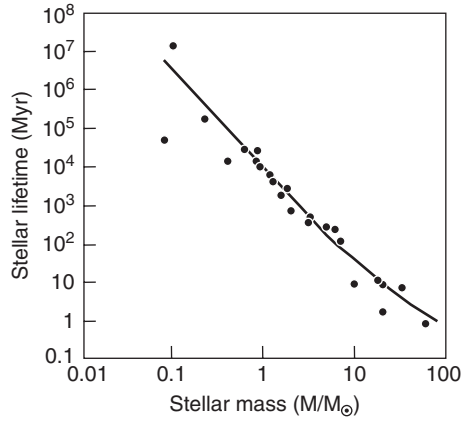

Fig. 3.2 Lifetimes of stars are a strong function of stellar mass. The lifetimes of low-mass stars (<0.9 $M_\odot$) exceed the age of the galaxy. In contrast, massive stars (>10 $M_\odot$) live fast and die young, expending their nuclear fuel in <10 million years. The change in slope of the trend for high-mass stars is due to mass loss, which significantly lowers their masses over their lifetimes.

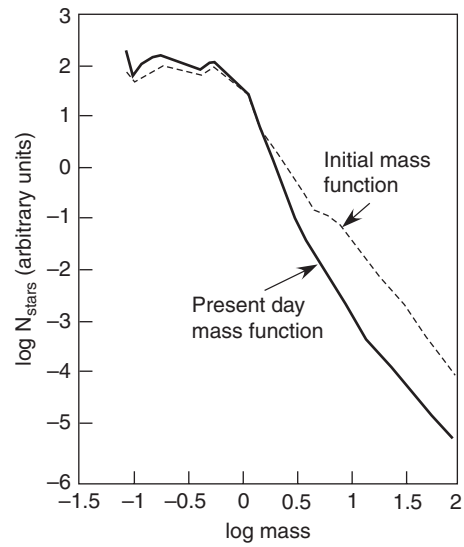

Fig. 3.3 Present-day mass function (PDMF) of stars in the galaxy compared to the initial mass function (IMF). PDMF is the number of stars of a given mass in the galaxy today, whereas IMF is the number of stars of a given mass produced in a single episode of star formation. The difference in the two curves at high stellar mass reflects absence of the stars that have exhausted their nuclear fuel and died over galactic history from the PDMF. After Basu and Rana (1992).

given mass will live, we need to know the number of stars of each mass. By counting up the stars of different spectral types, we can estimate the numbers of stars of each mass in the galaxy today. The *present day mass function* (PDMF) is illustrated in Figure 3.3. But what we really want to know is how many stars of each mass have formed over the history of

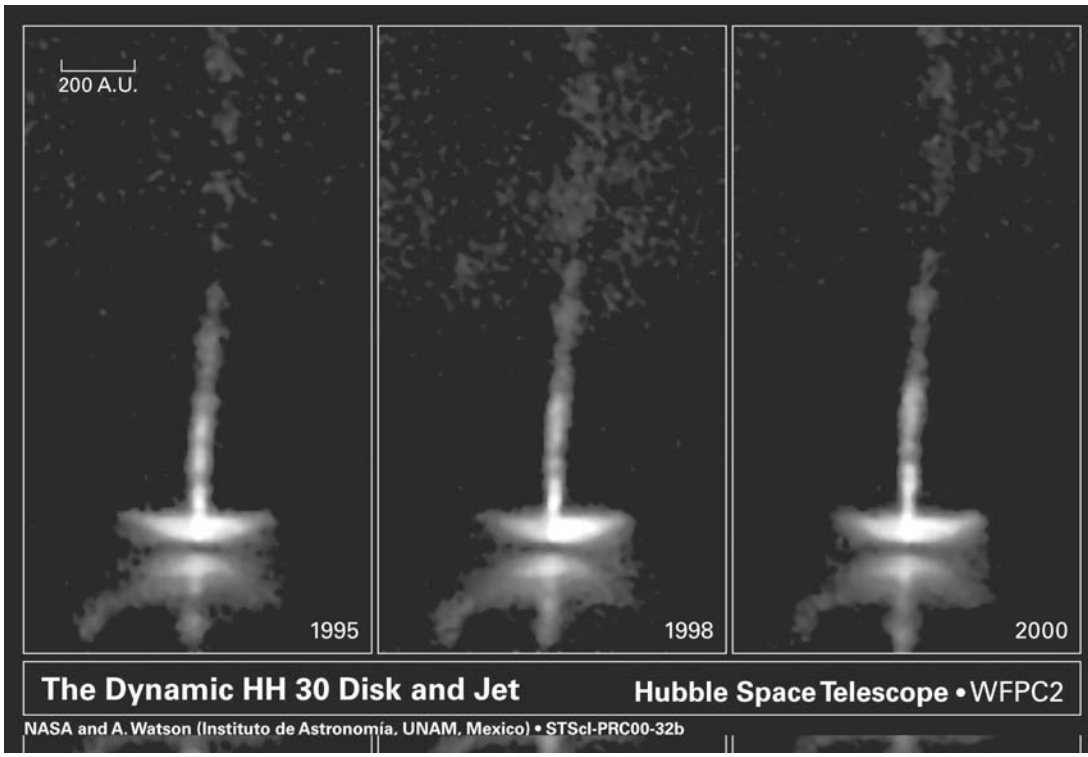

Fig. 3.4 Images of a bipolar jet from a protostar taken by the Hubble space telescope. Evolution of the jet with time is visible between the three images.

the galaxy. The *initial mass function* (IMF) of stars is the distribution of stellar masses in a single star formation event in a given volume in the galaxy (Kroupa, 2002). It is determined by correcting the PDMF for those stars that have exhausted their nuclear fuel and have exploded as supernovae or have become white dwarfs (see below). The IMF is compared to the PDMF in Figure 3.3. Note that the two curves are the same for low-mass stars, for which even the oldest have not yet exhausted their nuclear fuel. But for high-mass stars, the IMF is significantly higher than the PDMF, reflecting the fact that most of the high-mass stars that formed in the galaxy have long ago exhausted their fuel and died. These are the stars that have contributed the heavy elements to the galaxy. The initial mass function has been very reproducible over the age of the galaxy, and it provides the basis for modeling galactic chemical evolution.

The life cycles of stars

The life cycle of stars begins in cold dark molecular clouds. A particularly dense region in the cloud may become gravitationally unstable and collapse. As the density increases, the temperature rises due to the conversion of gravitational potential energy to thermal energy.

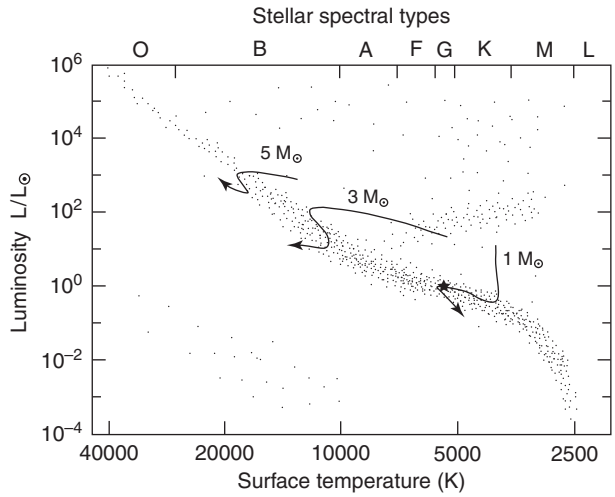

Fig. 3.5 **Tracks followed by 1, 3, and 5 $M_\odot$ pre-main sequence stars as they evolve toward the main sequence are shown on an H–R diagram. Pre-main sequence stars shine primarily by conversion of gravitational potential energy to heat, although energy released by burning of deuterium and other elements also plays a role.**

The central region quickly contracts to form a protostar. Differential motions cause the cloud core to rotate, and material arriving later joins the star through an accretion disk. Processes within the disk and ejection of material from the protostar via polar jets are mechanisms by which angular momentum is removed from the system, aiding accretion of the protostar (Fig. 3.4). As the protostar contracts and heats up, hydrogen and helium are ionized, and the protostar evolves toward hydrostatic equilibrium. During this period, the protostar becomes completely convective and has a very high luminosity. As low-mass protostars evolve, luminosity decreases substantially, but the surface temperature remains about the same. Low-mass protostars follow a nearly vertical track on the H–R diagram called the Hayashi Track toward the main sequence (Fig. 3.5). Higher-mass stars move down and/or to the left to join the main sequence (Fig. 3.5).

A protostar first begins to shine by radiating gravitational potential energy, with half of the released energy going into increasing the temperature in the star and half being radiated into space. But, as the star approaches the main sequence, fusion reactions begin. When the core temperature reaches ~10^6 degrees, hydrogen begins to combine with deuterium to make ^{3}He. The reaction is $^1H + {}^2D \Rightarrow {}^3He + \gamma$, where γ is a gamma ray. Reactions such as this are generally written $^2D(p,\gamma)^3He$ (see Box 3.2). But the deuterium is soon exhausted because of its low initial abundance in the star, so deuterium burning only slows the contraction somewhat. Proton reactions also occur with lithium, beryllium, and boron as the temperature passes through a few million degrees. But as with deuterium, the fuel is soon exhausted, and the protostar continues to contract. Fusion of hydrogen must begin before enough energy is released to stabilize the star against further contraction. As the protostar approaches hydrostatic equilibrium, its position on the H–R diagram drops to slightly below the main sequence (Fig. 3.5).

Box 3.2 Convention for writing nuclear reactions

Nuclear reactions can be described quickly and clearly using the following convention. A reaction of the form

$$A + B \rightarrow C + D \quad \text{is typically written} \quad A(B,C)D$$

where A and D are nuclides and B and C are typically light particles such as a neutron (n), proton (p), α-particle (α), electron or positron (designated by β^- or β^+), a photon (designated by γ, or a neutrino (designated by ν). As an example, neutron-capture reactions such as

$$^{48}Ti + n \rightarrow {}^{49}Ti + \gamma \quad \text{would be written} \quad {}^{48}Ti(n,\gamma)\,{}^{49}Ti$$

Reactions involving protons such as

$$^{25}Mg + p \rightarrow {}^{26}Al + \gamma \quad \text{would be written} \quad {}^{25}Mg(p,\gamma)\,{}^{26}Al$$

Reactions with alpha particles (helium nuclei) such as

$$^{12}C + \alpha \rightarrow {}^{16}O + \gamma \quad \text{would be written} \quad {}^{12}C(\alpha,\gamma)^{16}O$$

More complicated reactions can also be written using this formalism. For example, the reactions of carbon burning, where two carbon atoms fuse to make heavier elements, are written

$$^{12}C(^{12}C,\alpha)^{20}Ne \quad \text{and} \quad {}^{12}C(^{12}C,\gamma)^{24}Mg$$

and a chain of reactions can also be written using this convention. For example, the reactions that make up the CNO cycle can be written

$$^{12}C(p,\gamma)^{13}N(,\beta^+\nu)^{13}C(p,\gamma)^{14}N(p,\gamma)^{15}O(,\beta^+\nu)^{15}N(p,\alpha)^{12}C$$

In this chain, ^{12}C captures a proton and emits a gamma ray to become ^{13}N, which spontaneously decays by emitting a positron and a neutrino to become ^{13}C, which captures a proton and emits a gamma ray to become ^{15}O, which spontaneously decays to ^{15}N, which captures a proton and emits an α-particle to become ^{12}C.

Using this convention, almost any nuclear reaction can be written clearly and concisely.

The nuclear reaction that finally stabilizes the structure of the protostar is the fusion of two protons to form a deuterium atom, a positron, and a neutrino ($^1H(p,\beta^+\nu)^2D$). This reaction becomes important at a temperature of a few million degrees. The newly produced deuterium then burns to ^3He, which in turn burns to ^4He in the *proton–proton chain*. The proton–proton chain is the main source of nuclear energy in the Sun. With the initiation of hydrogen burning in the core, a star settles into a stable configuration, in which gravitational contraction is balanced by the thermal energy of hydrogen fusion, and joins the main sequence. The star will spend most of its life on the main sequence, during which time it will slowly increase in luminosity, moving back across the main sequence on the H–R diagram (Fig. 3.1).

The end of hydrogen burning in the core marks the end of a star's life on the main sequence. Figure 3.6 summarizes the stages of evolution of low- to intermediate-mass stars

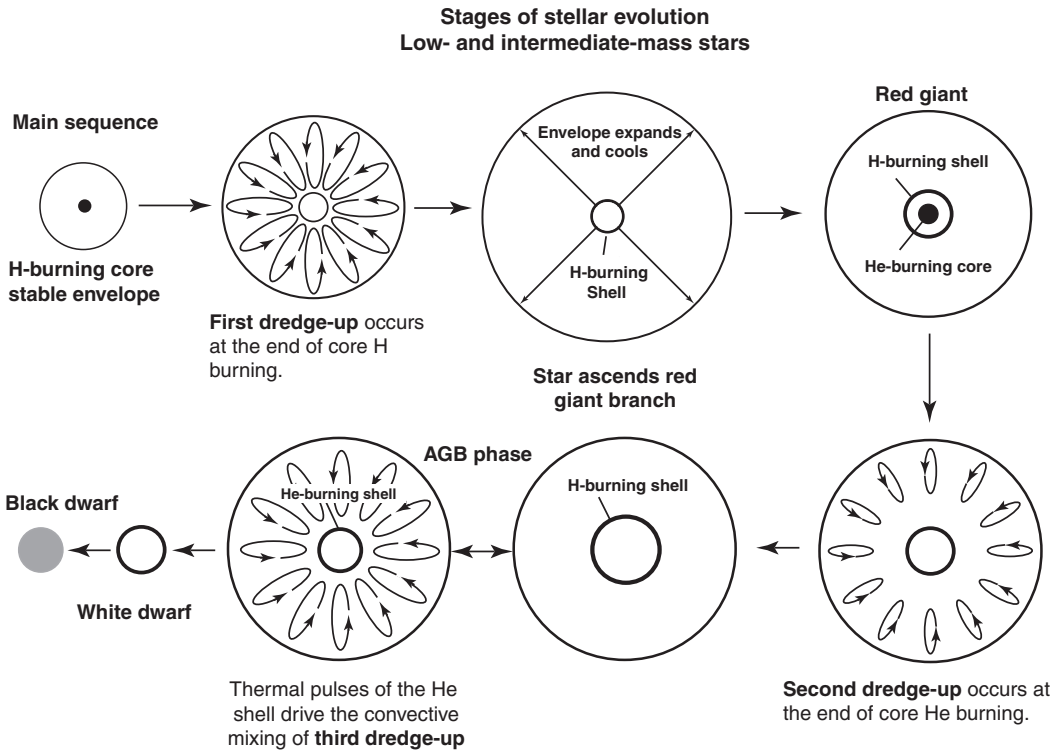

Fig. 3.6 **Stages of stellar evolution for low-and intermediate-mass stars. As the star exhausts its hydrogen fuel and leaves the main sequence, the helium core contracts and heats up, and the resulting thermal instability mixes the products of partial hydrogen burning throughout the stellar envelope (first dredge-up). The star expands and the surface cools. Hydrogen burning continues in a shell around the core, and the star ascends the red giant branch (see Fig. 3.7). When the core is hot enough, helium burning is initiated and the star returns to a stable configuration, the red giant stage. When helium is exhausted in the core, the core again contracts. The envelope becomes convective again in the second dredge-up. Core contraction continues, along with shell hydrogen burning, which leaves behind a region dominated by helium outside of the core. When the temperature gets high enough, the helium ignites and burns in a runaway "flash" that again disrupts the thermal structure of the star. Convection in the envelope brings products of helium burning and *s*-process nucleosynthesis to the surface in one of many cycles of the third dredge-up. The star is now an AGB star. The surface of the star heats up as the hydrogen shell burns toward the surface, and toward the end of the AGB phase, a planetary nebula is emitted. Then the nuclear fuel runs out and the star cools and contracts to become a white dwarf and eventually a black dwarf.**

from the main sequence to the end of nuclear burning. When the hydrogen in the core has been converted to helium, the core contracts because it is no longer supported by nuclear burning and heats up due to compression. The thermal instability introduced by the cessation of core hydrogen burning causes the outer 70–80% of the star to become convective. The convection mixes throughout the envelope the products of partial hydrogen burning that took place at the base of the stratified envelope during the main sequence. This mixing event is known as the first dredge-up, because this is the first time that nucleosynthesis products appear at the stellar surface. Because of the increasing temperature and pressure in the

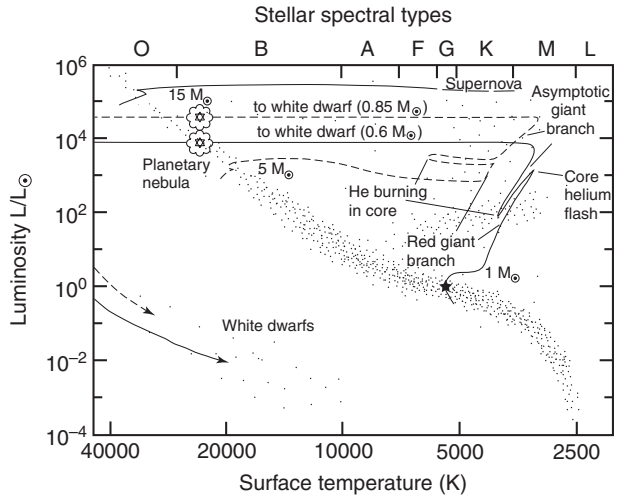

Fig. 3.7 **H–R diagram with tracks followed by 1, 5, and 15 $M_\odot$ stars as they leave the main sequence after hydrogen burning ends in their cores. Energy is provided by a series of different nuclear fuels, with more elements involved in nuclear reactions in higher-mass stars. Low-mass stars ascend the red giant branch until core helium burning begins. The star heats up and moves back toward the main sequence. At the end of core helium burning, the star again moves upward along the asymptotic giant branch. As the hydrogen shell burns toward the stellar surface, the star heats up and moves to the left across the upper part of the diagram, ejecting its envelope via a strong wind. The ejected gas and dust eventually are illuminated as a planetary nebula. Shortly thereafter the star exhausts its fuel and burning ceases. The star moves down the diagram to become a white dwarf. Intermediate-mass stars follow a similar progression, but they tend to cool more during the red giant stage, moving right across the diagram. Massive stars move right across the top of the diagram, becoming supergiants before ending their lives with type II supernova explosions.**

hydrogen rich zone just outside of the helium core, hydrogen burning resumes in a shell around the hydrogen-depleted core. The shell gradually moves outward, consuming the hydrogen as it goes, and the star heats up. The envelope expands greatly during this period due to increasing thermal pressure and the outer envelope of the star cools. The star is now a red giant and on the Herzprung-Russell diagram has moved up and to the right of its position on the main sequence (Fig. 3.7).

Eventually, the core becomes hot enough for helium to begin to fuse into carbon. In low-mass stars, core helium burning begins with a helium flash. After the helium flash, fusion in the core settles down to a balance between thermal pressure and gravitation compression. The star contracts, its surface temperature increases and it moves back toward the main sequence in the H–R diagram (Fig. 3.7). For intermediate-mass stars, this track is called the horizontal branch. This stage, during which helium is converted to carbon and oxygen in the core via the “triple alpha process” and hydrogen fuses to helium in the hydrogen shell outside of the core, lasts about 10% as long as the main sequence.

The red giant stage ends when helium in the core is exhausted. Again the core contracts and the thermal structure of the star becomes unstable. Convective mixing again reaches down toward the layers that have experienced nuclear burning. This mixing event is

known as the second dredge-up. In low-mass stars, the convection is not deep enough to bring newly synthesized material to the surface, but in stars of greater than 4–5 $M_{\odot}$, the mixing encounters the hydrogen shell and nucleosynthesis products are again dredged up. As the mixing subsides, the hydrogen shell is again established and the core slowly contracts and heats up. A zone of helium builds up between the hydrogen shell and the carbon-rich core.

When the temperature gets high enough, the helium outside the core ignites and burns in a runaway "flash," creating a thermal pulse that mixes the material from the helium shell and the intershell region between the hydrogen and helium shells. The star then readjusts its structure to radiate the energy produced, and the convective envelope reaches down into the material mixed by the thermal pulse and brings the products of helium burning and s-process nucleosynthesis to the surface. This mixing event is known as the third dredge-up. The helium flash terminates quickly due to exhaustion of helium and the star settles down again with only the hydrogen shell burning to supply energy. The hydrogen shell burns outward, leaving behind a hydrogen-depleted, helium-rich region. The interior of the star contracts and heats up, eventually triggering another helium shell flash and another third dredge-up mixing event. This sequence repeats from 10 to 100 times depending on the mass of the star. On a Herzsprung–Russell diagram, low- and intermediate-mass stars move back toward the red giant branch, approaching it asymptotically (Fig. 3.7). Such stars are known as asymptotic giant branch (AGB) stars. Herwig (2005) gives a detailed review of the evolution of AGB stars, and Busso *et al*. (1999) give a good review of nucleosynthesis in these stars.

During the AGB phase, the stars eject matter in strong stellar winds that increase in intensity with time. Towards the end of the AGB stage, the surface temperature of the star begins to increase as the hydrogen shell gets closer to the surface. The star moves to the left across the H–R diagram (Fig. 3.7). The surface temperature of the star can exceed 25 000 K and the brightness can be several thousand times the solar luminosity. The flux of ionizing photons increases with the surface temperature and begins to excite the dust that condensed in the earlier winds. The radiation flux begins to illuminate the surrounding dust shell, making a *planetary nebula* that is visible from Earth. The surface temperature of the star continues to rise, reaching a maximum of >100 000 K, and the planetary nebula reaches peak illumination. This planetary nebula stage lasts about 10 000 years, after which the nuclear fuel is exhausted. The luminosity and temperature of the central star decrease and the star contracts, shining from gravitational and stored energy only and eventually becoming a *white dwarf*. The core continues to contract until it is supported by *electron degeneracy*. In a normal gas, compression to a higher density occurs by squeezing out the space between the atoms. In a degenerate gas, this process has reached its limit and the electrons become essentially incompressible. White dwarfs are very hot, very small, faint stars. They form a diagonal band across the lower left of the H–R diagram, roughly parallel to the main sequence (Fig. 3.7). White dwarfs have masses ranging from slightly larger than the Sun to considerably smaller, but have radii ranging from about 0.01 to 0.001 times that of the Sun (roughly the size of the Earth). They have exhausted all of the nuclear fuel and are no longer generating energy. They are cooling and contracting and after several hundred billion years, will become cold *black dwarfs*.

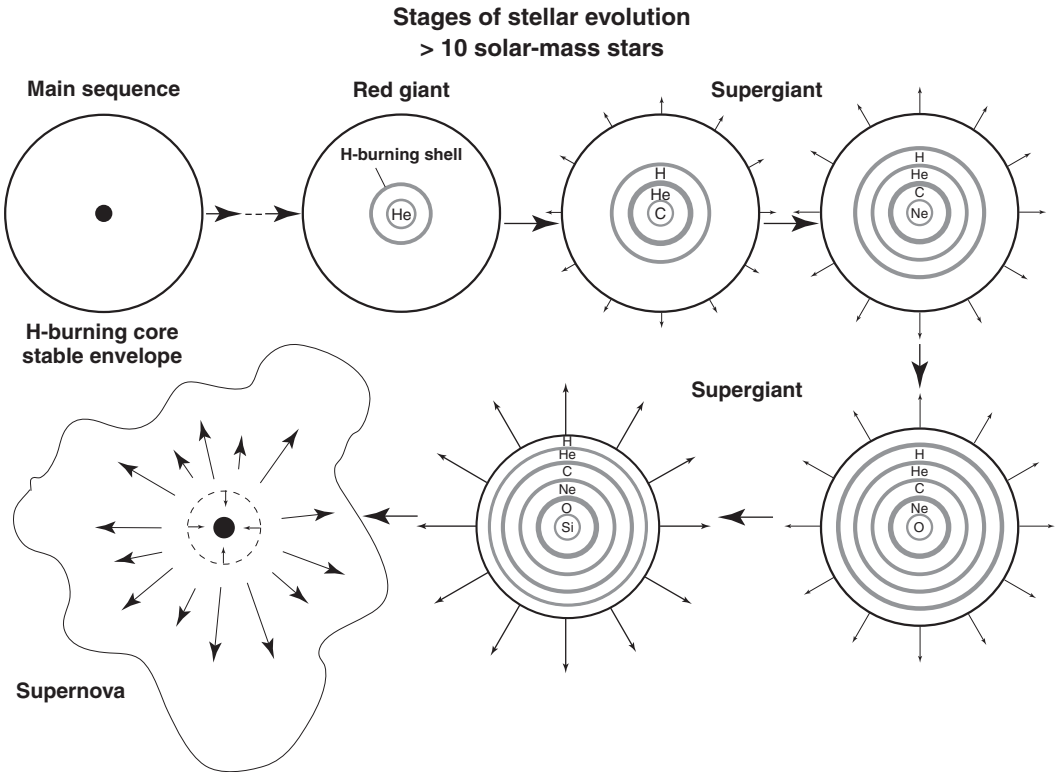

Fig. 3.8 Stages of stellar evolution for stars of >10 $M_\odot$. The initial stages of burning in a massive star are analogous to those in low- and intermediate-mass stars (Fig. 3.6). But after helium is exhausted in the core, the star burns a series of new fuels, predominantly carbon, neon, oxygen, and silicon in the core. As each fuel is exhausted in the core, it begins to burn in a shell around the core, creating an onion-shell structure with each layer containing products of different nucleosynthetic burning. When silicon has been consumed in the core, there is no more nuclear fuel to support the star against gravity and it collapses catastrophically. The result is a type II supernova explosion that ejects the outer and intermediate layers of the star, returning newly synthesized elements to the galaxy. The interior zones collapse back on the remnant, which can be either a neutron star or, if the progenitor was >25 $M_\odot$, a black hole.

For stars between ~4 $M_\odot$ and ~8 $M_\odot$, the core temperature is high enough to initiate carbon burning. An inert core of oxygen, magnesium, and neon accumulates. After ~1000 years, the star runs out of carbon and the core cools and contracts. This occurs at the end of the AGB stage at a point when the star is emitting massive winds. These stars also generate planetary nebulae before cooling and contracting to become O–Ne–Mg white dwarfs.

Figure 3.8 summarizes the stages of post-main-sequence evolution of stars of >10 solar masses ($M_\odot$). The early part of this evolution is similar to that for low- and intermediate-mass stars. But in stars with masses >10 $M_\odot$, the nuclear burning does not stop with hydrogen, helium, and carbon. In these stars, once the carbon in the core is exhausted, gravity causes the core to contract and heat up sufficiently to initiate neon burning, followed in turn by oxygen burning, magnesium burning, and silicon burning (Fig. 3.8). These stages

are increasingly rapid because less and less energy is being released, until a core of iron is produced. Fusion reactions cannot proceed further because nuclear reactions no longer supply energy; instead they require energy to proceed (cf. Fig. 2.1). The iron core of the star builds up very quickly to the 1.4 $M_\odot$ Chandrasekhar limit, the maximum mass that can be supported by electron degeneracy. This happens in about a day in a 25 $M_\odot$ star. The temperature in the core reaches 10 billion degrees. The iron nuclei disintegrate into protons and electrons. This requires energy, so the core cools. The very high pressure in the core causes the electrons and protons to combine into neutrons, a process that releases a blast of neutrinos. The neutrinos carry away a tremendous amount of energy from the core and the neutrons collapse to nuclear density ($>10^{17}$ g cm^{-3}), shrinking the neutron core to a tiny fraction of its previous size almost instantaneously. The neutrons now form a degenerate gas (neutron degeneracy is broadly analogous to electron degeneracy, the neutrons cannot move in spite of their high energy and they behave like matter at near 0 K). The surrounding layers are no longer supported and collapse onto the neutron ball at supersonic speed. The infalling material bounces off of the neutron core and a shock wave is created, which along with the neutrinos released from the core, eject the outer layers of the star at speeds of 10 000 to 20 000 km s^{-1}. The star explodes as a type II core-collapse supernova, with a luminosity of 10^8 times the solar luminosity. Most supernovae leave behind a neutron star, with a radius of a few kilometers and a mass similar to that of the Sun, rotating as fast as 30 times per second (these are observed as pulsars). If the mass left behind by the explosion is high enough, the remaining material may collapse into a black hole. The mass cut that seems to separate these two outcomes is ~25 $M_\odot$.

The stars destined to become type II supernovae are the supergiants that occupy the top of the H–R diagram (Fig. 3.7). Supergiants have very high luminosities and appear in all spectral classes. These are all very massive stars that have two or more shells of nuclear burning. These stars are often losing mass at a tremendous rate. Stars of >~33 $M_\odot$ may lose their entire envelopes through massive stellar winds and become Wolf Rayette stars. These unusual stars have newly synthesized material at their surfaces. They also eventually become core-collapse supernovae. Supernovae are classified spectroscopically. Those without hydrogen in their spectra are type I supernovae and those with hydrogen are type II supernovae. Because stars of <33 $M_\odot$ retain their hydrogen envelope, they form type II supernovae. Wolf Rayette stars explode as type Ib (no hydrogen but helium in the spectrum) or Ic (no hydrogen or helium in the spectrum) core-collapse supernovae. Supernova explosions are responsible for most of the elements heavier than hydrogen and helium in the galaxy.

Roughly 40% of the objects in the galaxy are binary star systems (or stated another way, 80% of stars have companions). In many cases one member of the system is significantly larger than the other and evolves more quickly. The more-evolved star becomes a white dwarf and when the envelope of the other star expands during the red giant stage, the outer portion is gravitationally pulled onto the white dwarf. The transferred material is compressed and heated and eventually an explosive fusion reaction in triggered. If the explosive reaction only involves the surface layers of the star, a nova results. But if the accretion triggers explosive nuclear burning of the carbon-oxygen core, the star is completely disrupted as a type Ia supernova explosion. Novae and type Ia contribute newly synthesized elements to the galaxy.

Stellar nucleosynthesis processes

Hydrogen burning

The dominant source of nuclear energy powering a star is the conversion of hydrogen to helium. There are two main ways of doing this: (1) proton–proton chains; and (2) CNO cycles. Both methods have the net result of converting four hydrogen atoms into a ^{4}He atom, releasing 26.73 MeV of energy per ^{4}He atom. The reactions must change two protons into two neutrons through either electron capture or positron emission, so two neutrinos are emitted for each ^{4}He created.

Proton–proton chains

In first generation stars, those that consist almost entirely of hydrogen and helium, and in stars of later generations where the core temperature is less than ~20 million degrees ($M \leq M_{\odot}$), hydrogen burns to helium via the proton–proton chains. The simplest chain, and the one activated at the lowest temperature (~5 million degrees), is called PPI. Three reactions are involved. In the first step, two protons fuse to form a ^{2}He atom, which immediately emits a positron (β^{+}) to form a deuterium atom and a neutrino [^{1}H(p,$\beta^{+}\nu$)^{2}D]. This reaction is very slow and controls the rate of the PPI chain. Deuterium then quickly combines with a proton to form ^{3}He (^{2}D(p,γ)^{3}He), and two ^{3}He nuclei combine to form ^{4}He and two hydrogen atoms [^{3}He(^{3}He,2p)^{4}He].

Helium-3 can also react with ^{4}He to make ^{7}Be, which then captures an electron to form ^{7}Li and a neutrino [^{3}He(α,γ)^{7}Be(β^{-},ν)^{7}Li]. Lithium-7 then captures a proton and the resulting ^{8}Be nucleus breaks up into two ^{4}He atoms, one more than was present initially [^{7}Li(p,α)^{4}He]. This is the PPII chain, and it becomes more important as the star ages and ^{4}He becomes more abundant, and as temperature increases beyond ~15 million degrees inside the star.

Beryllium-7 also reacts via two branches. Instead of capturing an electron to become ^{7}Li, ^{7}Be can react with a proton to form ^{8}B plus a gamma ray. ^{8}B emits an electron and neutrino to form ^{8}Be, which then breaks up into two ^{4}He atoms [^{7}Be(p,γ)^{8}B(β^{+} ν)^{8}Be* (α)^{4}He]. This is the PPIII chain. PPIII becomes important at temperatures above ~25 million degrees.

CNO cycles

Most stars are second-, third-, or higher, generation stars that contain elements heavier than hydrogen and helium produced by the earlier generations of stars. In these stars, hydrogen is converted to helium by several reactions that use atoms of carbon, nitrogen, and oxygen as catalysts, the CNO cycles. Schematic representations of the three main CNO cycles are shown in Figure 3.9. The CN I cycle is the first to operate efficiently as temperature rises. It consists of the following sequence of reactions (see Box 3.2):

$$^{12}\mathrm{C}(\mathrm{p},\gamma)^{13}\mathrm{N}(,\beta^{+}\nu)^{13}\mathrm{C}(\mathrm{p},\gamma)^{14}\mathrm{N}(\mathrm{p},\gamma)^{15}\mathrm{O}(,\beta^{+}\nu)^{15}\mathrm{N}(\mathrm{p},\alpha)^{12}\mathrm{C}$$

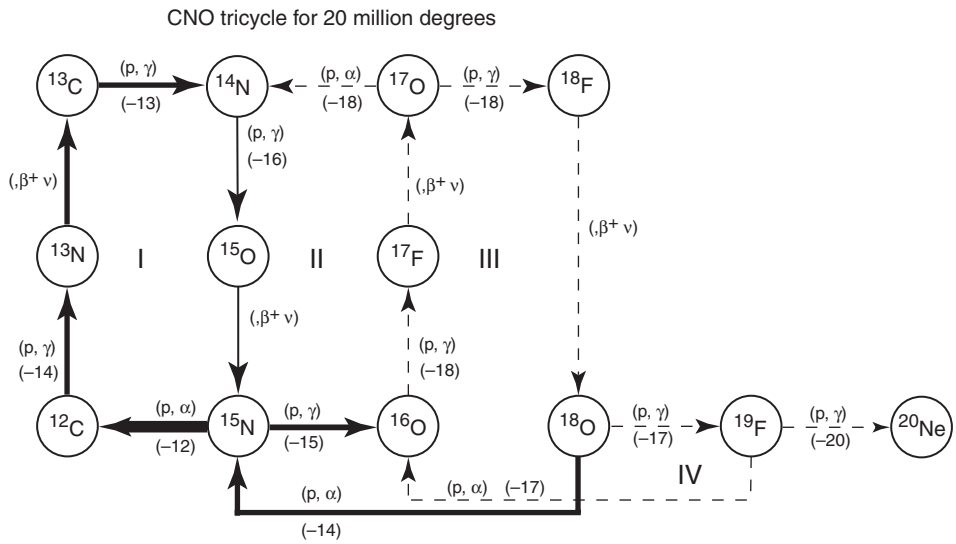

Fig. 3.9 **Schematic representation of catalytic hydrogen burning via the CNO tricycle. The arrows show the paths that catalyst nuclei follow. The sizes of the arrows are proportional to the reaction rates, so large arrows represent fast reactions with a high throughput. The type of reaction and the exponent of the reaction rate at 20 million degrees are shown for each reaction. At this relatively low temperature, the (,β^+ ν) reactions are effectively instantaneous (to avoid cluttering the diagram, they are shown with the same size arrow as the reaction feeding them). The cycles labeled I, II, and III each consume four protons and produce an α-particle (^{4}He nucleus), with the original species returned to start a new cycle. The net result of extensive CNO cycling, in addition to converting hydrogen to helium, is to convert most of the CNO nuclei to ^{14}N. After Rolfs and Rodney (1988), with reaction rates from Caughlan and Fowler (1988).**

The (,β^+ ν) reactions are essentially instantaneous and so are much faster than the other reactions at the temperatures in low- and intermediate-mass stars. The fastest proton reaction in this series is ^{15}N(p,α)^{12}C, while the slowest reaction is ^{14}N(p,γ)^{15}O. As a result, extensive CN cycling converts much of the ^{15}N, ^{12}C, and ^{13}C into ^{14}N. In the CN cycle, ^{12}C is destroyed more rapidly than ^{13}C by about a factor of three. In the solar composition, ^{12}C is 89 times more abundant than ^{13}C, so initially more ^{13}C is produced from the destruction of ^{12}C than is destroyed by proton reactions. The ^{12}C/^{13}C ratio decreases until it reaches an equilibrium value equal to the inverse of the reaction rates, where as much ^{13}C is being destroyed as is being produced. From this point on the ^{12}C/^{13}C ratio remains the same as carbon is gradually converted to ^{14}N.

The CNO bicycle, consisting of the CN I and CNO II loops in Figure 3.9, becomes important as the temperature increases. A small fraction of the ^{15}N is lost from the CN cycle via ^{15}N(p,γ)^{16}O. The relative importance of the two cycles is governed by the factor of ~1000 difference in the rates of the two ^{15}N reactions. The rate of the ^{16}O(p,γ)^{17}F reaction is very much slower than the reactions in the CN cycle, but ^{16}O is a factor of ~5000 more abundant than ^{15}N, so the rates at which the ^{15}N and ^{16}O reactions process nuclei through the CNO II cycle are similar. However, because the CNO II cycle is a factor of ~1000 slower than the CN cycle, it contributes little to the energy budget of the star.

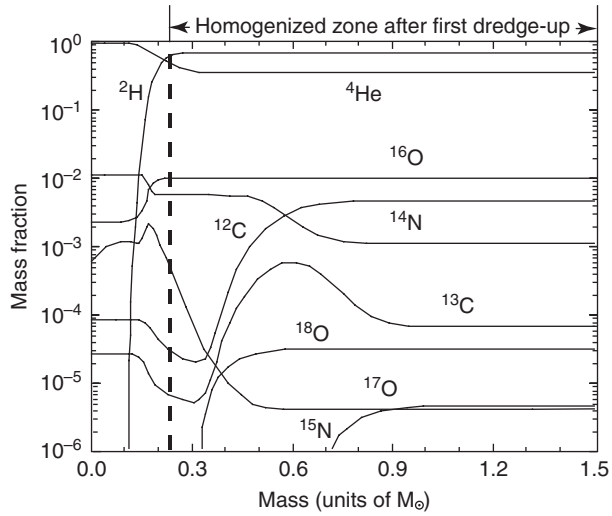

Fig. 3.10 **Schematic cross-section of a 1.5 $M_\odot$ star showing concentrations of various nuclei as a function of depth within the star at the end of its main sequence lifetime. The position within the star is given in units of mass normalized to the solar mass, with zero being the center and 1.5 $M_\odot$ being the surface of the star. The outer portion of the star from ~1 $M_\odot$ to the surface has the initial abundances of the nuclei because this portion of the star was never hot enough for nuclear burning. The region from 0.25 to 1.0 $M_\odot$ is the zone of partial hydrogen burning where the CNO cycle dominates. In this region, ^{15}N, ^{18}O, and ^{12}C are depleted, ^{13}C, ^{17}O and ^{14}N are enriched, and ^{16}O is essentially unchanged. The region from the center to ~0.12 $M_\odot$ is the hydrogen-exhausted core. With the end of core hydrogen burning, the outer envelope becomes convective down to ~0.22 solar masses, mixing the partially processed lower envelope material to the surface in the so-called first dredge-up. The resulting composition is the mass-weighted average of the material between the vertical dashed line and 1.5 $M_\odot$. After Dearborn (1992).**

There are additional cycles involving the CNO isotopes that also produce ^{4}He. ^{18}O is rapidly converted to ^{15}N via ^{18}O(p,α)^{15}N. Initially this dumps most of the original ^{18}O nuclei into the CN cycle. But the ^{18}O is slowly replaced via the CNO III cycle from ^{16}O via ^{16}O(p,γ)^{17}F(,β^{+}ν)^{17}O(p,γ)^{18}F(,β^{+}ν)^{18}O, and the ^{16}O nuclei are largely replaced through two pathways, ^{18}O(p,γ)^{19}F(p,α)^{16}O and ^{18}O(p,α)^{15}N(p,γ)^{16}O. A few nuclei escape from the CNO tricycle through ^{19}F to be synthesized into ^{20}Ne and heavier elements.

Figure 3.10 shows the abundances of hydrogen, helium, and the CNO isotopes as a function of stellar radius in a 1.5 $M_\odot$ star at the end of the main sequence. The horizontal axis represents the position within the star (in units of mass, a rather quirky astrophysics convention). The center of the star is on the left and the surface is on the right. The lines on the diagram show the mass fraction of each isotope at each position inside the star. For example, at the surface of the star, most of the mass consists of hydrogen, helium is the next most abundant, followed by ^{16}O, ^{12}C, ^{14}N, and so forth. The starting composition of this hypothetical star, and the composition that remains at the stellar surface, is the same as that of our Sun.

In the center of the star, all of the hydrogen has been converted to helium, and most of the CNO nuclei have been converted to ^{14}N. The small amount of carbon that still remains

has a $^{12}C/^{13}C$ ratio of ~3, and oxygen has a $^{17}O/^{16}O$ ratio almost 1000 times higher than in the starting composition. However, this portion of the star contains only ~15% of the mass. Outside of this helium core, hydrogen burning has not gone to completion. The temperature inside the star increases as a function of depth, and the nuclear reaction rates increase very strongly as a function of temperature. Between ~0.2 and 0.9 $M_\odot$, partial hydrogen burning has modified the initial composition of the star. With increasing depth, the first effects are seen in ^{15}N, which has the fastest reaction rate at all temperatures. Below 0.9 $M_\odot$, ^{15}N is depleted relative to the starting composition, and below 0.7 $M_\odot$, its abundance is a tiny fraction of its initial abundance, sustained only by CNO cycling. In contrast, ^{13}C, which is fed by the high-abundance isotope ^{12}C, initially builds up in abundance until the destruction rate of ^{13}C in CNO cycling matches that of ^{12}C. Below this point, the $^{12}C/^{13}C$ ratio stabilizes at ~3 and both isotopes are converted to ^{14}N. At a depth of ~0.5 $M_\odot$, the ^{18}O abundance drops as it is burned to ^{15}N in the CNO III cycle. But note that the ^{16}O abundance remains essentially unchanged until just outside the helium core. Compare the depths at which the abundance of each isotope begins to change with the relative reaction rates shown in Figure 3.9.

As hydrogen is exhausted in the stellar core, the energy source supporting the star is removed and the core contracts. Because the thermal balance has been disturbed, the thin convective layer at the surface of the star reaches down and mixes the products of partial hydrogen burning throughout the envelope. This mixing is the first dredge-up, described earlier. At the end of the first dredge-up, the envelope is enriched in ^{14}N and ^{17}O compared to the starting composition, and is depleted in ^{14}N and ^{18}O. The carbon abundance is lower, and the $^{12}C/^{13}C$ ratio has decreased from ~89 in a solar composition to ~40. These changes are diagnostic of hydrogen burning at temperatures below ~50 million degrees. As temperatures rise, proton captures on other nuclei become increasingly important, resulting in minor production of heavier isotopes.

Hydrogen burning at temperatures far in excess of those reached in the interiors of ordinary main-sequence stars can occur in a variety of astrophysical settings, including nova or supernova outbursts. In these environments, temperatures of 10^8 to 10^9 degrees may occur. At such temperatures, the reaction rates become fast enough that ^{13}N, ^{15}O, and the other β-unstable nuclei survive long enough to be burned by proton reactions before they can β-decay (Fig. 3.11). This is known as hot CNO or explosive hydrogen burning. For temperatures up to ~2×10^8 K ($T_9 = 0.2$), the cycle

$$^{12}C(p,\gamma)^{13}N(p,\gamma)^{14}O(,\beta^+\nu)^{14}N(p,\gamma)^{15}O(,\beta^+\nu)^{15}N(p,\alpha)^{12}C$$

dominates. This is the likely energy source for classical novae. At higher temperatures, other sequences of reactions come into play (Fig. 3.11), but these are not major energy producers.

Helium burning

After hydrogen burning ends in the core, a hydrogen burning-shell forms outside of the helium core. The helium core becomes more massive until it is compressed to temperatures and pressures high enough to initiate helium burning. Combining two α-particles

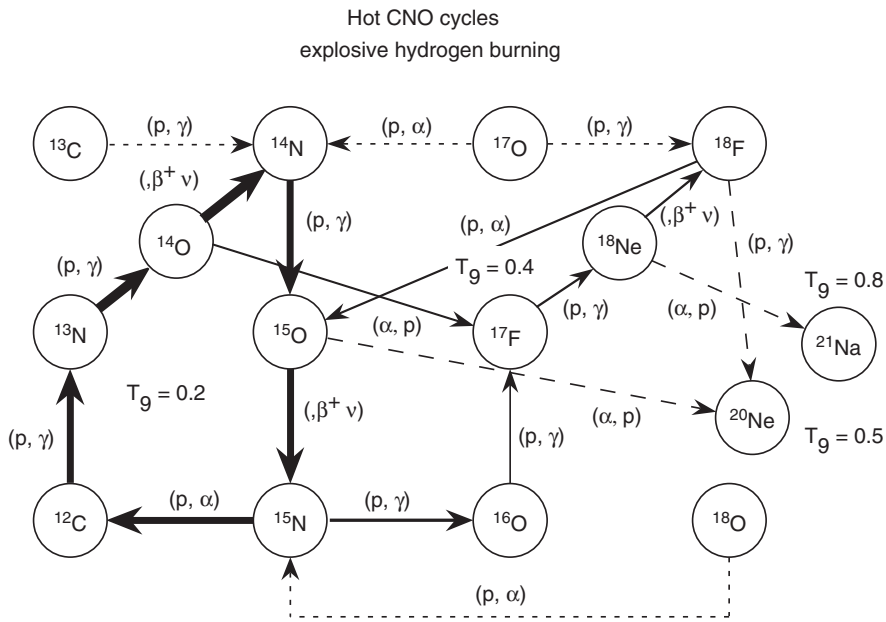

Fig. 3.11 **Schematic representation of hot hydrogen burning via the CNO tricycle. Branching is shown for four different temperatures designated using the symbol T_9, which means 10^9 K. Widths of arrows are proportional to reaction rate. At temperatures >10^8 K, the proton reaction rates on ^{13}C, ^{15}O, ^{17}F, and ^{18}F begin to compete effectively with the (,β^+ ν) reactions. Isotopes such as ^{13}C and ^{15}N are bypassed and a different equilibrium is established. If this equilibrium is quenched, such as in a nova explosion, the unstable nuclei β-decay to their respective stable daughters, resulting in low ^{12}C/^{13}C and ^{14}N/^{15}N, and ^{12}C/^{16}O can be greater than one, very different from the outcome of normal CNO burning. After Champaign and Wiescher (1992).**

(^{4}He nuclei) produces ^{8}Be, which has a lifetime of ~10^{-16} seconds. The lack of stable nuclei at masses 5 and 8 is the primary reason that heavier nuclei were not produced during the Big Bang. Carbon-12 can, in theory, form via a simultaneous collision between three α-particles, but the likelihood of this occurring in a star is much too low to explain the production of ^{12}C. However, in the helium core of a star, a steady-state abundance of ^{8}Be builds up:

$$\alpha + \alpha \Leftrightarrow {}^8\mathrm{Be}$$

Production of ^{12}C occurs via the interaction between ^{8}Be and an α-particle:

$$^8\mathrm{Be}(\alpha,\gamma)^{12}\mathrm{C}$$

Because three α-particles combine to form ^{12}C, this process is known as the "triple-alpha" process. Oxygen-16 is also produced during helium burning through the reaction ^{12}C(α,γ)^{16}O.

This reaction apparently proceeds more slowly than the production reaction for ^{12}C, so the resulting carbon–oxygen core is probably richer in ^{12}C than ^{16}O. In principle, α-capture can continue, producing ^{20}Ne, ^{24}Mg, ^{28}Si, and so on. However, this does not happen due to the increasingly high Coulomb barrier that prevents these reactions under quiescent conditions.

Quiescent burning of heavy isotopes

Quiescent burning of heavier isotopes takes place in the cores of stars and in shells surrounding the core (Fig. 3.8). *Carbon burning* requires temperatures of ~500 million degrees and densities of about 3×10^6 gcm^{-3}. Such temperatures are reached only in stars more massive than ~8–10 $M_\odot$. Carbon burning consists of several reactions, the most important of which are $^{12}C(^{12}C,2\alpha)^{16}O$, $^{12}C(^{12}C,\alpha)^{20}Ne$, $^{12}C(^{12}C,\gamma)^{24}Mg$, and $^{12}C(^{12}C,p)^{23}Na$. Light particles (n, p, α-particle) released during carbon burning can be captured by other species to synthesize minor amounts of many elements. In the core of a 25 $M_\odot$ star, carbon burning lasts about 600 years. Near the end of the carbon-burning phase, carbon can begin to interact with oxygen and neon as well.

The next reaction to proceed efficiently is $^{20}Ne(\alpha,\gamma)^{24}Mg$. The *neon-burning* phase lasts only ~1 year in a 25 $M_\odot$ star, and at the end of this stage, the composition of the stellar core is now primarily ^{16}O with some ^{24}Mg. As temperature and density rise, *oxygen burning* takes place as oxygen reacts with itself to produce silicon and sulfur, along with isotopes of argon, calcium, chlorine, potassium, and other elements up to approximately scandium. The reaction network is quite complex. This stage lasts about 6 months in a 25 $M_\odot$ star.

The ultimate stage of quiescent nuclear burning is *silicon burning*. However, rather than ^{28}Si reacting with itself, silicon burns with the aid of photodisintegration. The number of photons present increases as the fourth power of the temperature, so by the time oxygen burning ends, the silicon nuclei are sitting in a sea of high-energy γ-ray photons. Photodisintegration plays a major role in all subsequent nucleosynthesis. During silicon burning, α-particles, protons, and neutrons are ejected from stable nuclei to be used in further synthesis. Nucleii up to and slightly beyond the iron peak are produced. Production of nuclei beyond the iron peak requires more energy than is released by adding more particles to the nuclei, so for the most part, nucleosynthesis terminates, leaving an iron core. The silicon-burning stage lasts for about a day in a 25 $M_\odot$ star.

Synthesis of elements heavier than iron

The main mechanism by which nuclides beyond the iron peak are produced is by neutron capture. The basic processes involved in neutron capture were laid out by Burbidge, Burbidge, Hoyle, and Fowler (1957) (this classic paper is commonly known as B^2FH). The common ingredient in these processes is the capture of a neutron by a nucleus, increasing the atomic mass by one unit. If the resulting nucleus is stable, it remains an isotope of the original element. If not, the atom β-decays (a neutron emits an electron and becomes a proton) and becomes an isotope of the next heavier element. Any isotope, whether stable or unstable, can capture another neutron. The rate of capture compared to the rate of decay leads to two basic end-member processes, the *s*-process and the *r*-process. The *s*-process is capture of neutrons on a time scale that is slow compared to the rate of β-decay. The *r*-process is neutron capture on such a rapid time scale that many neutrons can be captured before β-decay occurs.

The s-*process* occurs during the AGB stage in low and intermediate mass stars, when the hydrogen shell is burning outward from the core and the helium shell repeatedly ignites,

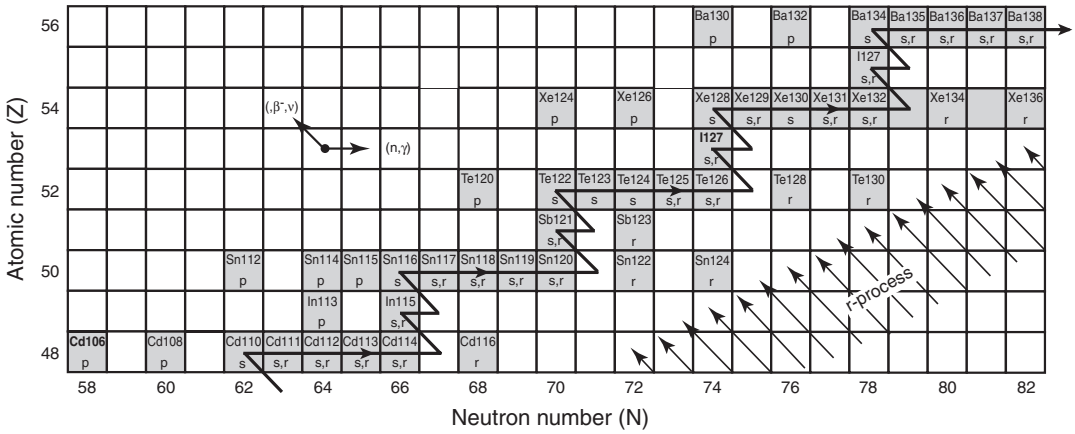

Fig. 3.12 **Portion of the Chart of the Nuclides showing *s*-process and *r*-process pathways. The *s*-process pathway, shown by the dark line in the center of the valley of β-stability, shows how a nuclide that successively captures individual neutrons would evolve. Each added neutron moves the nuclide to the right on the diagram, until it reaches an unstable nuclide, in which case it will β-decay to the stable nuclide with a higher Z. In contrast, in situations where nuclides capture neutrons very rapidly (*r*-process), they will be driven far to the right of the valley of β-stability until the timescale for neutron capture matches that for β-decay. They will then move to higher Z and capture more neutrons until they either reach a size that causes them to fission (break) into smaller nuclei (which can then capture more neutrons) or until the neutrons disappear, in which case they will β-decay back to the first stable isotope along paths of constant A (arrows).**

generating third dredge-up mixing events. It can also occur in massive stars during analogous stages. There are two main reactions that provide the neutrons to drive the *s*-process, $^{13}C(\alpha,n)^{16}O$ and $^{22}Ne(\alpha,n)^{25}Mg$. Both reactions require α-particles (^{4}He nuclei). The $^{13}C(\alpha,n)^{16}O$ reaction operates primarily in the intershell region between the hydrogen and helium shells while the helium shell is quiescent. The $^{22}Ne(\alpha,n)^{25}Mg$ reaction is marginally activated during the helium-shell flash. Because the neutrons from the two reactions are released at different temperatures, the details of the *s*-process nucleosynthesis that results are different and provide a probe of nucleosynthesis in stars.

The *s*-process is responsible for approximately half of the isotopes heavier than iron. Figure 3.12 is a portion of the Chart of the Nuclides with the *s*-process path highlighted. The *s*-process path defines the center of the region of the stable isotopes on the Chart of the Nuclides (*valley of β-stability)*. When the *s*-process is activated, the stable isotopes acquire neutrons and move to the right (constant Z) until the resulting nuclide is unstable and β-decays to become an isotope of the next heavier element. As the process continues, the isotopes that do not capture neutrons very efficiently (said to have low *neutron-capture cross-sections*) build up, while those with high neutron-capture cross-sections are depleted. If the neutron fluence (total number of neutrons available) is high enough, the abundances of the isotopes approach a steady state, where the abundances of isotopes of similar mass are proportional to the inverse of the neutron-capture cross-sections.

Explosive nucleosynthesis

Explosive nucleosynthesis occurs under conditions where temperature and density are changing rapidly with time, either due to the passage of a shock wave or because of a runaway explosion. We highlight some of the more important processes here.

Explosive hydrogen burning occurs via the hot CNO cycle in nova explosions when the density of hydrogen accreted to a white dwarf or neutron star from a binary companion reaches a critical density of ~10^3 g cm^{-3}. The resulting thermonuclear runaway powers the nova explosion. Explosive hydrogen burning also occurs in core-collapse supernovae as the shock wave passes through the hydrogen-rich envelope.

Explosive helium burning occurs in supernova explosions when the shock wave passes through helium-rich layers. If the layer has a sufficiently high ^{22}Ne abundance, the passage of the shock wave triggers the ^{22}Ne(α,n)^{25}Mg reaction, which releases a burst of neutrons. This neutron burst drives the stable seed nuclei to the neutron-rich side of the valley of β-stability.

Explosive oxygen, carbon, and neon burning occur in the oxygen-rich layers of massive stars during the passage of the supernova shock wave. The passage of the shock generates temperatures near 3 billion degrees. A key product is ^{28}Si, but some iron-group elements are also produced. In layers that are heated to less than 3 billion degrees, photodisintegration reactions [(γ,p), (γ,n), (γ,α)] on stable nuclei produce nuclei on the neutron-deficient side of the valley of β-stability. Outside the layer that experiences explosive oxygen burning, conditions are appropriate for explosive carbon and neon burning. Explosive carbon burning via the reactions, ^{12}C(^{12}C,2α)^{16}O, ^{12}C(^{12}C,α)^{20}Ne, ^{12}C(^{12}C,γ)^{24}Mg, and ^{12}C(^{12}C,p)^{23}Na, is also the underlying energy source for type Ia supernova.

The r-*process* is the process of rapid neutron-capture nucleosynthesis and is responsible for about half of the isotopes heavier than iron. It occurs when rapidly expanding material contains heavy seed nuclei in the presence of a high density of neutrons. The time scale for neutron capture in the *r*-process is so fast that nuclides are driven far to the neutron-rich side of the valley of β-stability (Fig. 3.12). When the neutron source is removed, the isotopes β-decay along paths of constant A back toward the valley of β-stability, following the arrows on Figure 3.12, until they reach a stable configuration. An analogous *p*-process may also operate in which a nucleus captures protons and moves up and to the left on Figure 3.12 before decaying back toward the valley of β-stability. The low-abundance isotopes to the left of the valley of β-stability that are bypassed by the *s*-process may be produced either by the supposed *p*-process or by photodisintegration reactions such as those described above.

The exact mechanism and site of the *r*-process are not well understood, although core-collapse supernovae are likely sites. There are two peaks in the solar system *r*-process abundances, one at A = ~130 and one at A = ~195. A single *r*-process cannot produce this distribution, so multiple *r*-process sites are indicated. Spectroscopic studies of very metal-poor stars, which formed during the first billion years after the Big Bang, also show evidence of multiple *r*-process sites. These observations suggest that the elements from ~90 < A < ~110 (called CPR elements because they are thought to be produced by charged particle reactions), the elements from ~110 < A <~130 (the light *r*-process elements), and the heavy *r*-process elements (A > ~130) have different mechanisms of production and arise from different sources. The production of the CPR elements is

relatively well understood. These elements appear to be produced in the neutrino-driven winds generated by the formation of a neutron star during a type II supernova explosion. This process occurs in all supernovae from progenitors of <25 $M_\odot$. But the current understanding of this process indicates that there are too few neutrons to drive a true *r*-process (Qian and Woosley, 1996). The processes by which the true *r*-process elements form are not known, but the observations of metal-poor stars provide a good indication of their source stars. The source for *r*-process elements of the first peak (~110 < A < ~130) appears to be supernovae of 12–25 $M_\odot$. The heavy *r*-process elements likely come from core-collapse supernovae of progenitor stars of $\leq$11 $M_\odot$. Stars of >25 $M_\odot$ probably generate black holes as remnants rather than neutron stars. It is likely that these stars do not produce *r*-process elements, either because there is no neutron star to drive the process or because any such elements that are produced fall back into the black hole and are not returned to interstellar space. A summary of the current state of knowledge about the *r*-process is given by Qian and Wasserburg (2007).

Other ways to produce new isotopes

In addition to the processes of stellar nucleosynthesis, there are two other ways in which isotopes are produced. One is *radioactive decay*. Many of the nuclides produced by explosive nucleosynthesis are unstable and decay to stable nuclei with timescales ranging from a fraction of a second to billions of years. Those with very short half-lives decayed completely into their stable daughter isotopes before any evidence of their existence was recorded in objects from our solar system. However, radioactive nuclei from stellar nucleosynthesis that have half-lives of >100 000 years left a record in solar system materials. For those with half-lives of more than ~50 million years some of the original nuclei from the earliest epoch are still present in the solar system today. The ultimate fate of all radioactive nuclides is to decay to their stable daughter nuclides. Thus, the only real distinction between isotopes produced by stellar nucleosynthesis and those produced by decay of radioactive nuclides produced by stellar nucleosynthesis is the time scale of their decay. We choose to make a distinction, however, because radioactive nuclides are extremely useful to cosmochemists. They provide us with chronometers with which to construct the sequence of events that led to the solar system we live in, and they provide us with probes of stellar nucleosynthesis and the environment in which our solar system formed. These topics appear throughout this book and will be discussed in detail in Chapters 8, 9, and 14.

Nuclides produced by irradiation

Irradiation of matter by high-energy particles, primarily protons and α-particles, can change one isotope into another. These high-energy particles are typically called *cosmic rays*, and they can originate either in the Sun or in a variety of environments elsewhere in the galaxy. Spallation reactions are those in which a nucleus is split by an incoming cosmic ray into two or more smaller nuclides. Much of the lithium, beryllium, and boron in the galaxy is produced by cosmic-ray-induced spallation on abundant species such as ^{12}C, ^{16}O, ^{20}Ne, ^{24}Mg, and ^{28}Si. Spallation reactions often release neutrons, which can then be captured by

other nuclides. In the outer meter or so of asteroids and other solid objects, these secondary neutrons from spallation reactions in the surface layer can produce measurable changes in the isotopic compositions of the constituent elements. These spallation and neutron-capture reactions provide the basis for another type of chronometer that is useful to cosmochemists (see Chapter 9).

Origin of the galaxy and galactic chemical evolution

So far in this chapter, we have considered the origin of the universe, nucleosynthesis of hydrogen and helium in the Big Bang, and the origin of the other elements through stellar nucleosynthesis, radioactive decay, and cosmic-ray irradiation. In this section, we will discuss the formation of the galaxy and the evolution of the composition of the galaxy due to nucleosynthesis in stars (galactic chemical evolution).

The first galaxies began to appear about 1 billion years after the Big Bang. They formed through gravitational attraction working on very small density variations in the universe left over from the Big Bang. The origins of our galaxy, the Milky Way, extend back to this early period. When the first stars formed, our galaxy had not yet accumulated into a disk. Instead its matter was spread out over a very large region. This matter had a clumpy distribution and moved randomly. The halo stars, stars with very low abundances of metals that form an irregular cloud or halo around the galaxy, date from this period. As gravity pulled the clumps of gas together, the overall net angular momentum caused it to flatten into a relatively thin, rotating galactic disk, leaving the halo stars behind. The increase in gas density initiated a new round of star formation within the disk. Much of the growth of the galaxy appears to have occurred relatively early, but it took some time to reach its current mass. We know this because star formation is strongly coupled to the amount of gas present. The IMF of stars forming in the young galaxy should have been very similar to that observed today (Fig. 3.3). The lowest-mass stars that formed in the galaxy are still present today, but they are less abundant than one would predict if the galaxy had its present mass 12 billion years ago. This means that infall of metal-free gas was spread out in time. Merging of galaxies within clusters of galaxies is still relatively common in the universe, and the Milky Way may have also swallowed up several smaller galaxies over its ~12 billion-year history.

Star formation in our galaxy began very early and has closely tracked the abundance of gas. The earliest stars formed from very low-metallicity gas. The most massive stars burned through their nuclear fuel within a few million years and exploded as supernovae, returning much of their mass to the galaxy in the form of heavy elements, the metals. These metals were incorporated into a new generation of stars, the most massive of which again quickly expended their nuclear fuel and exploded as supernovae. The mass of gas in the galaxy at any time was thus a balance between infalling metal-poor gas falling into the galaxy, the gas consumed in making stars, and the gas returned to the galaxy from stars that have completed their life cycle. Because the low- and intermediate-mass stars have such long lifetimes (Fig. 3.2), they sequester gas and do not contribute to galactic chemical evolution. As time passes, lower-mass stars do begin to return newly synthesized material to the galaxy. At the

present galactic age of ~12 billion years, stars with masses as low as 0.9 $M_\odot$ are contributing to galactic chemical evolution. But when the solar system formed, ~4.57 billion years ago, first-generation stars less massive than ~1.3 $M_\odot$ were still on the main sequence.

The style of galactic nucleosynthesis changed dramatically with time. In the earliest epochs, massive stars were the only contributors, so explosive nucleosynthesis dominated. In addition, because the galactic gas had very low metallicity, only some of the reactions discussed earlier in this chapter were available. In very low-metallicity stars, hydrogen burning must take place via the proton–proton chains because there were no CNO isotopes available to catalyze CNO burning. In low-metallicity massive stars, hydrogen burns to ^{4}He, ^{4}He burns to ^{12}C and ^{16}O, ^{12}C burns to ^{16}O, ^{20}Ne, ^{24}Mg, and ^{23}Na, ^{20}Ne burns to ^{24}Mg, ^{16}O burns to ^{28}Si, ^{32}S, ^{36}Ar, ^{40}Ca, and ^{44}Ca, and finally ^{28}Si burns to make iron group elements along with some minor isotopes of lighter elements. Isotopes that can be produced in stars consisting initially only of hydrogen and helium are called *primary isotopes*. The core-collapse supernovae of the earliest generations of massive stars ejected the major isotopes of the elements from carbon to titanium into the interstellar medium. The iron-group elements were not efficiently ejected and fell back onto the neutron stars or black holes.

Once the primary isotopes had built up in abundance, then the full range of reactions discussed above became available and nuclides such as ^{13}C, ^{15}N, ^{17}O, ^{18}O, ^{19}F, ^{21}Ne, ^{22}Ne, ^{25}Mg, ^{26}Mg, and so on, were produced by reactions between primary isotopes and protons and neutrons. Isotopes that require the presence of metals in the initial composition of the star in order to be efficiently synthesized are *secondary isotopes*. Abundances of primary isotopes built up rapidly in the early universe via synthesis in massive stars. Secondary isotopes initially built up more slowly, but their rate of synthesis increased as metallicity increased.

After ~2 billion years, when stars of <8 $M_\odot$ began to reach the end of their lifetimes, type Ia supernovae began to contribute to the elemental budget of the galaxy. Because a type Ia supernova completely disrupts the star, it efficiently ejects iron-group elements. The iron group elements thus built up more slowly than the elements from carbon to titanium.

Recent modeling based on the lifetimes of stars, their IMF, the star formation rate as a function of time, and nucleosynthesis processes have succeeded in matching reasonably well the abundances of the elements in the solar system and in the galaxy as a whole (e.g. Timmes *et al.*, 1995). These models are still very primitive and do not include nucleosynthesis in low and intermediate-mass stars. But the general agreement between model predictions and observations indicates that we understand the basic principles of galactic chemical evolution.

Summary

In this chapter, we reviewed the broad outlines of the Big Bang model for the origin of the universe and discussed some of the supporting observations. We showed that the Big Bang gave rise to hydrogen, helium, and some lithium, beryllium, and boron, but that other elements were produced primarily in stars. The rest of the elements were synthesized in stars via the nuclear reactions that cause the stars to shine. To understand stellar nucleosynthesis, it is necessary to understand the characteristics of stars. Astronomers use

the Herzsprung–Russell diagram (Fig. 3.1) and the color spectrum of the light emitted by the stars (Table 3.1) to classify and characterize stars. Stars range in mass from 0.08 to ~120 $M_{\odot}$. There are many more low-mass stars than intermediate-mass stars, and many more intermediate-mass stars than massive stars (Fig. 3.3). The rate of nuclear burning within a star, and thus the lifetimes of stars, are a strong function of stellar mass. Low-mass stars the size of the Sun or smaller, shine for in excess of 10 billion years. Massive stars live fast and die young, expending their nuclear fuel in as little as a few million years.

For most of their lifetimes, stars are powered by hydrogen burning, which turns hydrogen into helium. Hydrogen burning can take place through either the proton–proton chains or through CNO burning. Once hydrogen has been exhausted in the stellar core, the star passes through a series of stages during which power generation moves to helium burning, and in more-massive stars, on to carbon burning, neon burning, oxygen burning, and silicon burning. Each of these processes generates new elements. Synthesis of elements heavier than iron requires energy, so the buildup of heavier elements occurs either through the *s*-process, which takes place during alternate hydrogen-shell and helium-shell burning, or through explosive nucleosynthesis, which includes the *r*-process. Newly synthesized elements are returned to the interstellar medium to be incorporated into the next generation of stars through massive stellar winds during the late stages of the stars' lives, or through stellar explosions, such as supernovae and novae. One of the great triumphs of human intellectual endeavor is the level of detail that we have reached in our understanding of these processes.

In the final section of this chapter, we discussed the formation of galaxies and the formation and chemical evolution of the Milky Way. This sequence of events set the stage for the formation of the solar system. In Chapter 4, we will look at the resulting abundances of the elements and isotopes, both in the solar system and in the galaxy. The solar system abundances of the elements are a fundamental constraint for understanding the Sun, the planets, and the smaller bodies in the solar system.

Questions

1. What was the Big Bang? What is some of the observational evidence that supports this model?
2. What is a Herzsprung–Russell diagram and how is it used?
3. What is the initial mass function (IMF) of stars and how and why is it different from the present day mass function (PDMF)?
4. What are the main nuclear reactions that power main sequence stars? What happens when this energy source is exhausted?
5. What are the dominant processes that produced the elements heavier than iron? Give the basic outlines of how each one works.
6. How would you identify a star that formed in early in galactic history? List two important characteristics of such a star?
7. Why did massive stars dominate nucleosynthesis early the history of the galaxy?

Suggestions for further reading

Brush, S. G. (1987) Cooling spheres and accumulating lead: the history of attempts to date the Earth's formation. *The Science Teacher*, **54**, 29–34. A summary by a leading science historian.

Busso, M., Gallino, R. and Wasserburg, G. J. (1999) Nucleosynthesis in asymptotic giant branch stars: relevance for galactic enrichment and solar system formation. *Annual Reviews of Astronomy and Astrophysics*, **37**, 239–309. A good review of nucleosynthesis in low- and intermediate-mass stars.

Hawking, S. W. (1988) *A Brief History of Time*. New York, NY: Bantam Books, 198 pp. A readable but authoritative book about cosmology and the Big Bang written by one of the leading scientists in the field.

Herwig, F. (2005) Evolution of asymptotic giant branch stars. *Annual Reviews of Astronomy and Astrophysics*, **43**, 435–479. An excellent discussion of the evolution of AGB stars.

Weinberg, S. (1993) *The First Three Minutes*. New York, NY: Basic Books, 191 pp. Nobel prize-winning physicist Weinberg discusses the very beginnings of the universe in this influential book. It is a bit more detailed and challenging than Hawking's book, but provides more detail about the Big Bang.

References

Alpher, R. A., Bethe, H. and Gamow, G. (1948) The origin of chemical elements. *Physical Review*, **73**, 803–804.

Basu, S. and Rana, N. C. (1992) Multiplicity-corrected mass function of main-sequence stars in the solar neighborhood. *Astrophysical Journal*, **393**, 373–384.

Burbidge, E. M., Burbidge, G. R., Fowler, W. A. and Hoyle, F. (1957) Synthesis of elements in stars. *Reviews of Modern Physics*, **29**, 547–650.

Caughlan, G. R. and Fowler, W. A. (1988) Thermonuclear reaction rates V. *Cosmic Data and Nuclear Data Tables*, **40**, 283–334.

Champaign, A. E. and Wiescher, M. (1992) Explosive hydrogen burning. *Annual Reviews of Nuclear and Particle Science*, **42**, 39–76.

Dearborn, D. S. P. (1992) Diagnostics of stellar evolution: the oxygen isotopes. *Physics Reports*, **210**, 367–382.

Kroupa, P. (2002) The initial mass function of stars: evidence for uniformity in variable systems. *Science*, **295**, 82–91.

Qian, Y.-Z. and Woosley, S. E. (1996) Nucleosynthesis in neutrino-driven winds. I. The physical conditions. *Astrophysical Journal*, **471**, 331–351.

Qian, Y.-Z. and Wasserburg, G. J. (2007) Where, oh where has the *r*-process gone? *Physics Reports*, **442**, 237–268.

Rolfs, C. E. and Rodney, W. S (1988) *Cauldrons in the Cosmos*. Chicago: University of Chicago Press, 561 pp.

Timmes, F. X., Woosley, S. E. and Weaver, T. A. (1995) Galactic chemical evolution: hydrogen through zinc. *Astrophysical Journal Supplement*, **98**, 617–658.

4 Solar system and cosmic abundances: elements and isotopes

Overview

In this chapter, we discuss the abundances of the elements and isotopes in the solar system. First, we look at the techniques used to determine solar system abundances, including spectroscopy of the stellar photosphere, measurements of solar wind, and analyses of chondritic meteorites. The solar system abundances of the elements and isotopes are then presented. These abundances are then compared to the abundances in the solar neighborhood of the galaxy and elsewhere. Finally, we introduce how solar system abundances provide a basis for much of what we do in cosmochemistry.

Chemistry on a grand scale

The bulk chemical composition of the solar system is an important cornerstone of our ideas about how the Sun formed, and how the various planets, asteroids, meteorites, and comets came to be as we see them today. In older literature, you will typically see the term "cosmic abundances." In more recent literature, this term is being replaced by "solar system abundances." This shift reflects an evolution of our understanding of the composition of the solar system and how it relates to that of the surrounding neighborhood and the galaxy as a whole. The terms have been interchangeable for most of the past century, and for most purposes in cosmochemistry, they still are. However, as we continue to learn about how the solar system came to be, it will become important to be specific about which composition we want to discuss. We will therefore discuss solar system abundances when talking about our solar system and will use cosmic abundances when talking about the abundances in a more general sense.

Historical perspective

Of what is the Universe made? This question has been the subject of serious scientific study for more than a century. One of the first papers on the subject, entitled "The relative

abundances of the chemical elements," was presented in 1889 before the Philosophical Society of Washington by Frank W. Clarke. In it, the following sentence appears: "An attempt was made in the course of this investigation to represent the relative abundances of the elements by a curve, taking their atomic weight for one set of ordinates. It was hoped that some sort of periodicity might be evident, but no such regularity appeared." Clarke was in the early stages of a career-long study of the chemical compositions of all types of terrestrial rocks and the Earth's crust. By the end of the 1800s, the chemical compositions of meteorites were well known, and spectroscopy had been used to infer (incorrectly as it turns out) the compositions of the Sun, stars, and comets. Based on these observations, Norman Lockyer published "The Meteoritic Hypothesis" in 1890 in which he proposed that "all self-luminous bodies in the celestial spaces are composed either of swarms of meteorites or of masses of meteoritic vapor produced by heat." While this sounds naïve today, one must remember that, at the time, scientists did not know that the extended "nebulae" that they observed with telescopes were, in fact, galaxies rather than diffuse gas, that comets were composed of ice, that stars were powered by nuclear reactions, and many of the other ideas that are the basis for our understanding of the cosmos. However, Lockyer's idea that the celestial space around the solar system consists of material with a composition similar to that of the solar system was profound and became one of these basic ideas. Lockyer had, in effect, proposed that the composition of the visible universe could be determined by measuring the compositions of meteorites.

The first half of the twentieth century saw major advances in understanding of the visible Universe and in gathering detailed information about chemical abundances. On the chemistry side, William Harkins showed in 1917 that elements with even atomic numbers are more abundant than those with odd atomic numbers. This fundamentally important observation became known as the Oddo-Harkins rule. In the 1920s and 1930s, Victor Goldschmidt compiled a huge database of chemical data on terrestrial rocks, meteorites, and their constituents. In 1937, he published a table of element abundances based on his meteorite data and a recipe of 10 parts silicates, 2 parts metal, and 1 part sulfide, as noted earlier in Chapter 1. He called his table the "cosmic abundances", because some contemporary astronomers believed that the meteorites came from interstellar space. He also recognized that chondritic meteorites had not been melted (although their constituent chondrules had) and thus had not experienced the chemical fractionations associated with partial melting and crystallization. Goldschmidt's table provided the cosmic abundances of 66 elements.

The next major step forward was taken by Suess and Urey (1956), who published a new table of cosmic abundances based on meteorite data, solar abundances, and theoretical arguments based on the growing understanding of nucleosynthesis. These authors found regularities in the elemental abundances that had eluded Clarke. But these regularities had nothing to do with the periodic table, which organizes the elements based on chemical behavior. Instead, the observed abundance patterns reflect the nucleosynthetic processes that created the elements. The odd–even effect could now be explained in terms of nuclear physics (see Chapter 2). Suess and Urey were able to interpolate abundances of elements that could not be directly measured (e.g. noble gases) based on the observation that the abundances of odd-mass-number nuclides vary smoothly with increasing mass number.

Their table included isotopic abundances as well as elemental abundances. Since the Suess and Urey table was published, subsequent work has primarily refined the determinations of the cosmic abundances through improved measurements of meteorites, a better understanding of which meteorites should be considered for this work, improved measurements of the solar composition, and a better understanding of nuclear physics.

In recent decades, spectroscopy has revealed that the elemental and isotopic abundances in the galaxy vary with radial position and that the Sun has a somewhat different composition than the molecular clouds and diffuse interstellar medium in the solar neighborhood. For this reason, we can no longer think of the solar system abundances as truly "cosmic" abundances.

How are solar system abundances determined?

Determining the composition of the solar system is a complicated undertaking. Our goal is to determine the *original* composition of the solar system, the composition of the material from which the solar system formed. As you will see in later chapters, if we know the current composition of a meteorite, planet, or other solar system object, and we know the composition of the material from which it was derived, we have a good chance of understanding the processes that operated to produce the current object. Over the ~4.57 billion years of solar system history, chemical and physical processes have segregated the elements from one another so that it is very difficult to obtain a representative sample of the solar system to measure. The challenge is to find material that has survived until today without significant modification.

The Sun contains >99.8% of the mass in the solar system, so to a very good first approximation, the composition of the Sun is the composition of the solar system. However, in addition to being rather hard to determine, the composition of the Sun has been evolving since the solar system formed. The nuclear reactions that power the Sun are transmuting elements into other elements, modifying the initial composition. Fortunately, most (but not all, see below) of these reactions are occurring deep in the Sun and the evidence has not yet appeared at the surface. Physical and chemical processes operating in the outer parts of the Sun have also caused the compositions of the outer layers to change somewhat relative to the starting composition. These changes are relatively small, however, and good theoretical models have been developed to account for them. So the Sun is a reasonable place to measure the original composition of the solar system. The Sun's composition can be measured spectroscopically, and the solar wind can be captured and analyzed. These techniques, and their advantages and disadvantages, will be discussed below.

The Earth and other planetary bodies have been heavily modified by planetary-scale differentiation, smaller scale melting and the resulting chemical fractionations, collisions that mix material with different histories, and other processes. Samples of these materials are thus not suitable for determining the solar system composition. More primitive objects, such as comets and chondritic meteorites, have compositions more similar to the composition of

the Sun. Until very recently, comets could only be measured spectroscopically when they passed close to the Sun and the signature tail of gas and dust formed. However, the process of forming the tail can fractionate the chemical elements from one another. We also have samples of comet dust in the form of interplanetary dust particles (IDPs) captured in the upper stratosphere, described in Chapter 12. But these particles are too small to be chemically representative of their cometary sources by themselves. They come from many different comets, each perhaps with a different history and composition, and we do not know how to reassemble them to obtain the original composition of even one comet. NASA's recent Stardust Mission, which returned samples from comet Wild2, solves some of these problems, but, while we have learned and will continue to learn a tremendous amount about the comet, it is not clear that an accurate bulk composition of the comet will be one of the results of this work. Chondritic meteorites are much more promising. They are bigger than comet particles, and we can measure their compositions very precisely in the laboratory. However, over the years it has become apparent that most meteorites are made up of material that has evolved chemically from the original solar system composition. Only one rare group of chondritic meteorites, the CI carbonaceous chondrites, have compositions that appear to be essentially unmodified from the original solar system composition. This is surprising, considering that the CI chondrites have experienced extensive mineralogical alteration on their parent body.

Our current level of understanding about the original composition of the solar system is the result of a boot-strap effort involving more than a century of gathering compositional data about the Sun, stars, other astronomical objects, the Earth, other planets, and meteorites; establishing relationships between objects; and developing increasingly sophisticated models of stellar nucleosynthesis and chemical and physical processes that operated in the early solar system.

Determining elemental abundances in the Sun

Spectroscopic observations of the Sun

Elements and molecules emit and absorb photons with characteristic energies. As a result, measurements of stars, comets, or other luminous bodies with a spectrograph, which permits the output to be measured as a function of wavelength, reveal numerous emission or absorption lines (Fig. 4.1). These lines can be used to infer the compositions of the objects. The first spectroscopic measurements of the Sun, stars, and other luminous objects were made in the last half of the nineteenth century. However, it wasn't until the late 1920s that relatively accurate elemental abundances for the Sun and the stars were determined (see Box 4.1).

It is now relatively easy to obtain detailed spectra of the Sun, but determining the Sun's chemical composition from such spectra requires a realistic model of the stellar atmosphere and a detailed understanding of how the lines are formed and interact to give the observed spectrum. The elemental abundances are not "observed," but are derived from

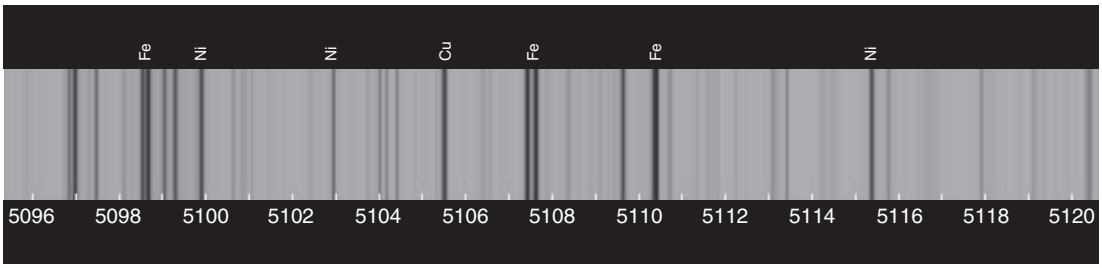

Fig. 4.1 **Portion of the high-spectral-resolution solar spectrum (2 milli-ångstroms resolution) recorded by Louis Delbouille in the 1970s at the observatory at the Jungfraujoch. The spectrum contains thousands of absorption lines that are used to determine the composition of the solar photosphere. The elements responsible for some of the stronger lines are noted at the top of the figure. The numbers at the bottom give wavelength in ångstroms. Image courtesy of Jean-Marie Malherbe.**

Box 4.1 **Cecilia Payne cracks the spectral code**

"The most brilliant Ph.D. thesis ever written in astronomy." This high praise was given by Otto Struve, Director of the Yerkes Observatory, to the thesis of Cecilia Payne, entitled, "Stellar Atmospheres." In her thesis, published in 1925, Payne provided the key to unlocking the mysteries of stellar spectroscopy, allowing for the first time accurate determinations of the compositions of stars from their spectral lines. Her methodology and conclusions were so ingenious and well founded that they were rapidly accepted and completely changed the nature of stellar spectroscopy. But history does not give her the acclaim that her discoveries deserve.

Payne was born in 1900 in Wendover, England, to an upper-class family. Her early education was in botany, physics, and chemistry, but her passion was astronomy. In 1922, she heard a lecture by Harlow Shapley, the director of the Harvard College Observatory. The lecture inspired her to seek admission to Harvard, and with strong recommendations from her mentors in England, including Sir Arthur Eddington, she was admitted and arrived on campus in 1923. Two years later, in 1925, she became the first student, male or female, to earn a Ph.D. from the Harvard College Observatory.

When Payne began her work in the 1920s, stellar spectroscopy was a very active area of research. Numerous elemental and molecular lines had been identified in stellar spectra. The lines observed in each star varied with the inferred temperature of the star, which was understood to mean that the elemental abundances varied with temperature. This body of data was the basis for the spectral typing of stars (O, B, A, F, G, K, M, L). However, the power source for stars was not understood and it was not clear why the composition of a star should be related to its temperature. In the 1920s, it was also widely believed that the Sun had the same composition as the Earth; models considered the Earth to have formed from the outer layers of the Sun. Payne used the new quantum mechanical understanding of atomic structure to show how and why the spectral lines of the different elements varied as a function of stellar spectral type. She demonstrated how the temperature of the stellar surface controls the spectral lines that are observed. Her analysis led to the conclusion that the chemical

composition of the starry universe is homogeneous, and that stars are composed almost entirely of hydrogen and helium. However, the latter result was not so readily accepted, as it went directly against conventional wisdom, and she downplayed it in her thesis. However, in 1929, Henry Russell published a paper entitled "On the composition of the Sun's atmosphere," where he argued on the basis of a new theoretical understanding of the physics of the hydrogen atom that the Sun's atmosphere must be hydrogen-rich. He did give credit to Payne's conclusions based on spectroscopy, but history gives credit to Russell for showing that the Sun is mostly hydrogen.

Why did Cecilia Payne not get credit for her groundbreaking work? It was not easy for a woman to work in science in the first half of the twentieth century. Those with exceptional talent were able to make exceptional contributions, but they often worked in obscurity. But this was only one factor – timing was also an issue. A person making a profound discovery is often well ahead of his or her time, and the importance of the new result is not recognized right away. The person who gets credit is the person who convinces the world of the correctness and importance of the result. In this case, that person was Russell. Although Payne's career was marked with slow promotions and low salaries, she valued immensely the joy of discovery. She encouraged the same single-minded purpose in her students, telling them, "Your reward will be the widening of the horizon as you climb. If you achieve that reward, you will ask no other."

Payne (later Payne-Gaposchkin) went on to have a brilliant academic career. Although she suffered many years of gender discrimination, she eventually became Harvard's first female full professor and chair of the Astronomy Department.

the observations, and uncertainties in models of the stellar atmosphere and of line formation are much greater than the uncertainties in the spectral measurements (Hill, 2001).

The last few years have seen a minor revolution in determining solar and stellar abundances (Asplund, 2005). Much of the previous work assumed that the spectral lines originate in local thermodynamic equilibrium (LTE), and the stellar atmosphere has been modeled in a single dimension. Since 2000, improved computing power has permitted three-dimensional modeling of the Sun's atmosphere and non-LTE treatment of line formation. The result has been significant shifts in inferred solar abundances.

In LTE modeling of line formation, the strength of a line can be straightforwardly predicted from a few properties of the line and the species that generate it, once a model atmosphere and continuous opacity are known everywhere. Non-LTE modeling does not assume anything, but calculates line strengths from first principles. In non-LTE modeling, everything depends on everything else, everywhere else. Thus many more inputs into the model and much more computational power are required. However, the resulting models of line formation are much more realistic, and presumably, more accurate.

The 3D modeling of the solar atmosphere permits an accurate representation of the "granularity" of the Sun's surface. Granularity is the term used to describe areas of convective upwelling of hot material and narrower regions of down-going cooler material (Fig. 4.2). Temperature modeling of the Sun's atmosphere must account for this granularity.

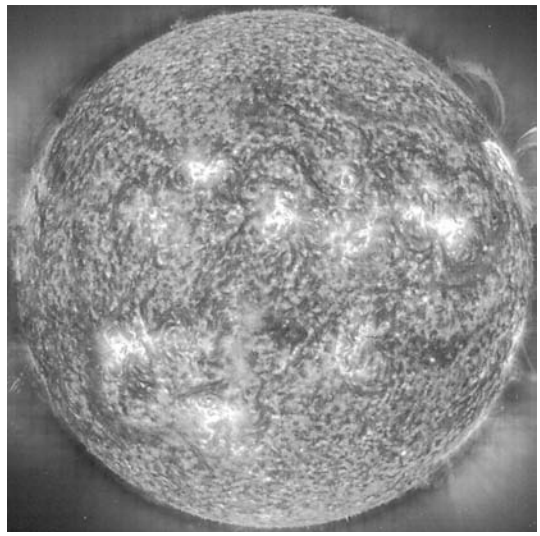

Fig. 4.2 **Image of the Sun taken by the SOHO spacecraft, showing the turbulent convection in the surface layers. Lighter areas are hotter and darker areas are cooler. Image courtesy of SOHO (ESA and NASA).**

The 3D modeling, accounting for departures from LTE and using improved atomic and molecular data, results in lower overall abundances of elements heavier than H and He. The resulting inferred solar metallicity is $Z = 0.012$ rather than earlier values of $Z = 0.017–0.0189$. [Metallicity, the mass fraction of elements other than hydrogen and helium, is typically denoted by the symbol Z, with X referring to the proportion of hydrogen and Y referring to the proportion of helium.] Table 4.1 compares inferred solar abundances from Anders and Grevesse (1989), estimated using the older methodology, with new abundances reported by Grevesse, Asplund, and Sauval (2007), which reflect this new modeling. As of this writing, it must be pointed out that the new lower abundances do not agree with the results of helioseismology (see Box 4.2), which matched the old abundances quite well (Basu and Antia, 2004). The 3D modeling of the Sun's granularity has resulted in much better matches of line widths and related properties, while at the same time showing that absorption lines should typically be stronger than modeled in the 1D case (consequently, fewer atoms are required to achieve the same absorption).

The composition of the Sun is not the same as it was when the constituent materials first came together to form a protostar. The initial stages of nuclear burning, which took place while the protostar was completely convective, burned ^{2}D to form ^{3}He, lowering the D/H ratio and raising the ^{3}He/^{4}He ratio. Lithium is depleted by a factor of ~160 in the Sun compared to meteoritic abundances, probably also due to nuclear reactions in the solar envelope, but the details of how this happened are not understood. Other than these changes, main sequence nucleosynthesis in the solar core and at the base of the solar envelope are burning hydrogen to form helium and modifying the abundances and isotopic compositions of the carbon, nitrogen, and oxygen. These effects will not appear at the surface until the Sun leaves the main sequence.

Table 4.1 Solar system abundances of the elements

	Mean CI chondrites		Solar photosphere		Solar system abundances	
	Lod*		A&G*	GAS*		
Element	ppm by weight	Atoms/10^6 Si	Atoms/10^{12} H	Atoms/10^{12} H	Atoms/10^6 Si	
1 H	21,015±1770	5.498×10^6	$\equiv 1.000 \times 10^{12}$	$\equiv 1.000 \times 10^{12}$	3.007×10^{10}	P
2 He	9.17×10^{-3}	0.6040	$[9.772 \times 10^{10}]$	$[8.511 \times 10^{10}]$	2.559×10^9	P
3 Li	1.46±0.03	55.47	14.45	11.22	55.47	M
4 Be	0.0252±0.005	0.7374	14.12	23.99	0.7374	M
5 B	0.713±0.072	17.32	(398)	501	17.32	M
6 C	35 180±4810	7.724×10^5	3.631×10^8	2.455×10^8	7.381×10^6	P
7 N	2940±20	5.535×10^4	1.122×10^8	6.026×10^7	1.812×10^6	P
8 O	458 200±5750	7.552×10^6	8.511×10^8	4.571×10^8	1.374×10^7	P
9 F	60.6±4.1	841.1	3.631×10^4	3.631×10^4	841.1	M
10 Ne	1.8×10^{-4}	2355×10^{-3}	$[1.23 \times 10^8]$	$[6.918 \times 10^7]$	2.080×10^6	P
11 Na	5010±33	5.747×10^4	2.138×10^6	1.479×10^6	5.097×10^4	A
12 Mg	95 870±780	1.040×10^6	3.802×10^7	3.388×10^7	1.029×10^6	A
13 Al	8500±130	8.308×10^4	2.951×10^6	2.344×10^6	7.678×10^4	A
14 Si	106 500±1250	$\equiv 1.000 \times 10^6$	3.548×10^7	3.326×10^7	$\equiv 1.000 \times 10^6$	
15 P	920±100	7833	2.818×10^5	2.291×10^5	7361	A
16 S	54 100±3650	4.449×10^5	1.621×10^7	1.380×10^7	4.449×10^5	M
17 Cl	704±10	5237	3.162×10^5	3.162×10^5	5237	M
18 Ar	1.33×10^{-3}	9.622×10^{-3}	$[3.63 \times 10^6]$	$[1.514 \times 10^6]$	1.025×10^5	T
19 K	530±24	3582	1.318×10^5	1.202×10^5	3598	A
20 Ca	9070±20	5.968×10^4	2.291×10^6	2.042×10^6	6.054×10^4	A
21 Sc	5.83±0.06	34.20	1259	1479	34.20	M
22 Ti	440±3	2422	9.772×10^4	7.943×10^4	2422	M
23 V	55.7±1.3	288.4	1.000×10^4	1.000×10^4	294.6	A
24 Cr	2590±80	1.313×10^4	4.677×10^5	4.365×10^5	1.313×10^4	A
25 Mn	1910±40	9168	2.454×10^5	2.454×10^5	9168	M
26 Fe	182 800±1470	8.632×10^5	4.677×10^7	2.818×10^7	8.553×10^5	A
27 Co	502±17	2246	8.318×10^4	8.318×10^4	2374	A
28 Ni	10 640±210	4.780×10^4	1.778×10^6	1.698×10^6	4.943×10^4	A
29 Cu	127±6	527.0	1.622×10^4	1.622×10^4	527.0	M
30 Zn	310±12	1250	3.981×10^4	3.981×10^4	1224	A
31 Ga	9.51±0.31	35.97	758.6	758.6	35.97	M
32 Ge	33.2±0.3	120.6	2570	3801	120.6	M
33 As	1.73±0.06	6.089	–	–	6.089	M
34 Se	19.7±0.4	65.79	–	–	65.79	M
35 Br	3.43±0.75	11.32	–	–	11.32	M
36 Kr	5.22×10^{-5}	1.643×10^{-4}	–	–	53.45	T
37 Rb	2.13±0.02	6.572	398.1	398.1	6.572	M
38 Sr	7.74±0.10	23.30	794.3	831.2	24.15	A
39 Y	1.53±0.12	4.538	173.8	162.2	4.708	A
40 Zr	3.96±0.11	11.45	398.1	380.2	11.44	A
41 Nb	0.265±0.016	0.7522	26.30	26.30	0.7715	A
42 Mo	1.02±0.11	2.804	83.18	83.18	2.653	A
44 Ru	0.692±0.044	1.806	69.18	69.18	1.943	A
45 Rh	0.141±0.002	0.3613	13.18	13.18	0.3788	A

Table 4.1 (cont.)

	Mean CI chondrites		Solar photosphere		Solar system abundances	
	Lod*		A&G*	GAS*		
Element	ppm by weight	Atoms/10^6 Si	Atoms/10^{12} H	Atoms/10^{12} H	Atoms/10^6 Si	
46 Pd	0.588±0.020	1.457	48.98	45.71	1.416	A
47 Ag	0.201±0.004	0.4913	(8.71)	(8.71)	0.4913	M
48 Cd	0.675±0.006	1.584	72.44	58.88	1.584	M
49 In	0.0788±0.002	0.1810	45.71	39.81	0.1810	M
50 Sn	1.68±0.04	3.733	100	100	3.733	M
51 Sb	0.152±0.009	0.3292	(10)	(10)	0.3292	M
52 Te	2.33±0.18	4.815	–	–	4.815	M
53 I	0.48±0.16	0.9975	–	–	0.9975	M
54 Xe	1.74×10^{-4}	3.495×10^{-4}	–	–	5.224	T
55 Cs	0.185±0.002	0.3671	–	–	0.3671	M
56 Ba	2.31±0.03	4.436	134.9	147.9	4.442	A
57 La	0.232±0.010	0.4405	16.60	13.49	0.4405	M
58 Ce	0.621±0.022	1.169	35.48	50.11	1.169	M
59 Pr	0.0928±0.0005	0.1737	5.12	3.80	0.1737	M
60 Nd	0.457±0.011	0.8355	31.62	28.18	0.8355	M
62 Sm	0.145±0.002	0.2542	10	10	0.2542	M
63 Eu	0.0546±0.0010	0.09475	3.23	3.31	0.0972	A
64 Gd	0.198±0.006	0.3321	13.18	12.88	0.3321	M
65 Tb	0.0356±0.0031	0.05907	(0.79)	(1.91)	0.05907	M
66 Dy	0.238±0.002	0.3862	12.59	13.80	0.3862	M
67 Ho	0.0562±0.0012	0.08986	(1.82)	(3.24)	0.08986	M
68 Er	0.162±0.008	0.2554	8.51	8.51	0.2554	M
69 Tm	0.0237±0.0014	0.03700	–	–	0.03700	M
70 Yb	0.163±0.005	0.2484	12.02	12.02	0.2484	M
71 Lu	0.0237±0.0002	0.03572	(5.75)	(1.15)	0.03572	M
72 Hf	0.115±0.006	0.1699	7.59	7.59	0.1699	M
73 Ta	0.0144±0.0001	0.02099	–	–	0.02099	M
74 W	0.089±0.007	0.1277	12.9	12.9	0.1277	M
75 Re	0.037±0.002	0.05254	–	–	0.05254	M
76 Os	0.486±0.007	0.6738	28.18	17.78	0.6738	M
77 Ir	0.470±0.005	0.6448	22.38	23.99	0.6448	M
78 Pt	1.004±0.064	1.357	63.10	–	1.357	M
79 Au	0.146±0.002	0.1955	10.2	10.2	0.1955	M
80 Hg	0.314±0.029	0.4128	–	–	0.4128	M
81 Tl	0.143±0.002	0.1845	7.94	7.94	0.1845	M
82 Pb	2.56±0.03	3.258	70.79	100	3.258	M
83 Bi	0.110±0.003	0.1388	–	–	0.1388	M
90 Th	0.0309±0.0030	0.03512	(1.3)	–	0.03512	M
92 U	0.0084±0.0080	9.306×10^{-3}	<0.34	<0.34	9.306×10^{-3}	M

* Lod = Lodders (2003), A&G = Anders and Grevese (1989), GAS = Grevese *et al*. (2007).

[] Indirect measurements: He from inversion of helioseismology; Ne, Ar from coronal Ne/O and Ar/O ratios

() Uncertainties greater than 25%.

P: photosphere, M: meteorites, A: average of photosphere and meteorites, T: theoretical abundance

Box 4.2 Helioseismology

Helioseismology is the study of oscillations in the Sun. It is broadly analogous to seismology on the Earth, except that on Earth the source of the seismic energy is typically a point source, such as an earthquake or an explosion. In the Sun, the energy comes from the convective zone near the surface where near-sound-speed convection produces strong acoustic waves. These waves make the Sun ring as though it were a bell being struck by a continuous rain of sand. There are three basic types of oscillations, each named for the restoring force that drives it. The *p-mode* or *acoustic waves* have pressure as their restoring force. The p-mode oscillations have frequencies >1 mHz and are very strong in the 2–4 mHz range, often referred to as "5-minute oscillations." [5 minutes per cycle is $^{1}/_{300}$ cycles per second or 3.33 mHz.] These are the waves that currently provide the most information. *Gravity waves* (*g-mode*) have gravity (buoyancy) as their restoring force and have frequencies of 0–0.4 mHz. They are confined to the interior of the Sun below the convective zone and are very difficult to observe from the surface. The *f-mode* or *surface gravity waves* occur at or near the photosphere (Christensen-Dalsgaard, 2002).

Helioseismic waves are detected by measuring the Doppler shift of lines in the solar spectrum due to vertical motion of the Sun's surface along the line of sight. With appropriate data-reduction techniques, the frequencies for global oscillations can be determined to an accuracy of 5 ppm. This extreme accuracy requires long-term, continuous observations that are best done by spacecraft such as the joint ESA/NASA SOHO spacecraft, which observes the Sun from the Lagrangian point where the Earth gravity balances that of the Sun.

Data reduction is done by a process called *inversion*. It is not possible to uniquely derive the structure of a body from first principles based on seismic data. Instead, a model of the structure must be assumed and then the predictions of the model are compared to the observations. The model is then adjusted until the predictions match the observations. The more precise the predictions, the better the model can be tested by the observations. Properties that can be investigated by helioseismic inversion include the density, pressure, sound speed, angular velocity, temperature, and composition.

Helioseismology has provided a wide range of information about the solar interior. The position of the base of the convective zone is precisely known at 0.287 of the distance from the surface to the center of the Sun. Inferred angular velocities show a strong dependence of velocity on latitude in the convective zone. The convective zone has circulation much like the outer layers of Jupiter or the Earth's atmosphere. In contrast, there is little variation in the underlying radiative zone. The boundary between the convective and radiative zones is quite sharp and is called the *tachocline*. This appears to be the region where the dynamo that generates the Sun's magnetic field must operate. Recent determinations of the helium abundance in the convective zone yield values for helium, Y, in the range 0.24–0.25, in good agreement with standard models, which predict a present-day value of 0.245. This number is lower than the initial value due to gravitational settling in the Sun. The metallicity, Z, of the solar photosphere inferred from helioseismology is very close to the 0.189 inferred from 1D models of the photosphere. The convective core has a radius of 0.25 times the solar radius and contains about half of the mass of the Sun. The solar structure inferred from the sound speed matches the structure predicted by the standard model of the Sun to better than 0.5%.

Also, a recent inversion of helioseismic data including special relativistic corrections to the equations of state claims a best-fit value for the age of the Sun of $t_{seis} = 4.57 \pm 0.11$ Ga (Bonanno, Schlattl, and Paternò, 2002).

Helioseismology has also pointed out some differences between the Sun and the standard models. Inferences of solar rotation rate in the solar interior show that the radiative solar interior rotates nearly uniformly, contrary to predictions. This implies that there is efficient transfer of angular momentum from the interior to the surface convective zone, from which it can be lost through the solar wind. There is a mismatch in sound speed between the prediction of the standard model and inferences from helioseismology for the region just below the convective zone. This is the region where the model predicts a strong gradient in hydrogen abundance due to gravitational settling of helium from the convective zone. The mismatch implies some extra mixing below the convective zone that smoothes out the gradient. Such mixing could also explain why the lithium abundance in the photosphere is ~160 times lower than expected from the abundance in CI meteorites. Extra mixing to a depth comparable to a temperature of $\sim 2.5 \times 10^6$ K, the temperature where lithium begins to burn, would explain both the low lithium abundance and the difference in sound speed.

Although the Sun may have accreted as a homogeneous body, elemental settling has occurred in the non-convecting region below the surface convective zone (Vauclair, 1998). Elemental segregation is the result of two kinds of processes. First, individual atoms want to move in the presence of a gravitational field, pressure or thermal gradient, radiative acceleration, or concentration gradient. Through these motions, heavier atoms tend to migrate toward the center of a star. Second, the motions of the atoms are slowed down due to collisions with other atoms. As a result, they share angular momentum in a random way. In our Sun, these processes result in compositional variations of about 10%. Variations of this magnitude are easily detected by helioseismology, and theoretical modeling matches the observations very well. It is not clear how the segregation of elements in the Sun beneath the surface convective zone affects surface abundances. As already mentioned, the new lower abundances of carbon, nitrogen, oxygen, and neon inferred for the solar photosphere are inconsistent with helioseismological modeling. One suggested solution is that the surface convective zone in the Sun has lower metallicity than the bulk Sun because it accreted hydrogen-rich gas from the nebula after the heavy elements had segregated into planets. However, as of this writing, neither this model nor any of several other models produce a good agreement between the new lower solar abundances of carbon, nitrogen, oxygen, and neon and the results of helioseismology (Castro *et al*., 2007).

We also know that processes that eject solar wind fractionate elements based on their first ionization potential, the energy necessary to ionize the element. Over time, ejection of solar wind that is fractionated relative to the bulk Sun changes the surface composition of the Sun, the part that we measure spectroscopically. There are theoretical models to account for this effect, but it introduces uncertainties into the inferred composition of the bulk Sun.

Collecting and analyzing the solar wind

The solar wind consists of charged particles emitted from the Sun's upper atmosphere. The hot ionized plasma in the corona is accelerated by the Sun's magnetic field. Like the Sun itself, the wind consists primarily of protons (ionized H atoms), but it also contains all the other elements in the Sun. Thus, if one could measure the composition of the solar wind, one might get an independent measurement of the composition of the Sun. However, this turns out to be harder than it might initially appear. The density of the solar wind is not very high, only about 3 atoms cm^{-3} at the Earth's orbit, most of it hydrogen. A solar-wind collector must be exposed for a long time to get enough atoms to measure. In addition, the process that accelerates the solar wind and ejects it from the solar surface fractionates the elements. The biggest fractionations follow the first ionization potential of the elements. Those elements that are easy to ionize are preferentially incorporated into the wind over those that are hard to ionize. Because it is so difficult to quantify these effects, measurements of the solar wind have been used primarily to determine the isotopic composition of the Sun (all isotopes of an element have the same ionization potential), and by extension, the solar system. However, recent studies of solar wind samples brought back by the Genesis Mission (see Box 4.3) suggest that isotopes may also be fractionated in the solar wind by a process called Coulomb drag.

Box 4.3 The Genesis Mission

The Genesis spacecraft was launched on August 8, 2001, with goals of obtaining precise measurements of the solar isotopic abundances and improving the determination of elemental abundances. The spacecraft contained three arrays of passive collectors and an electrostatic concentrator (Fig. 4.3). The collectors had to be very pure materials because the concentrations of solar-wind elements captured by the collectors were expected to be very low. Collector materials included metals (gold, germanium, and silicon), as well as sapphire (Al_2O_3) and diamond-like hydrocarbon. These different materials permitted all of the major elements of the solar wind to be collected and analyzed without interference from the collector materials. The solar wind is ejected from the Sun in several ways. The normal solar wind travels at speeds of ~300 km s^{-1} and has a density of ~3 particles cm^{-3} at the Earth's orbit. Coronal mass ejections are violent sporadic events that eject much more material at speeds of 1000 to 1500 km s^{-1}. The mission was designed to sample both types of solar wind.

An electrostatic concentrator was designed especially to get a good measurement of the oxygen isotopic composition of the Sun. Oxygen has distinct isotopic compositions in different solar system materials, but without knowing the overall isotopic composition of oxygen in the solar system, it is very difficult to infer the origin and meaning of these isotopic differences. A concentrator was necessary because the integrated oxygen fluence expected in a passive collector over the duration of the mission would have been insufficient to provide enough oxygen atoms for a precise isotopic measurement. The concentrator increased the oxygen concentration in the target material by a factor of ~30.

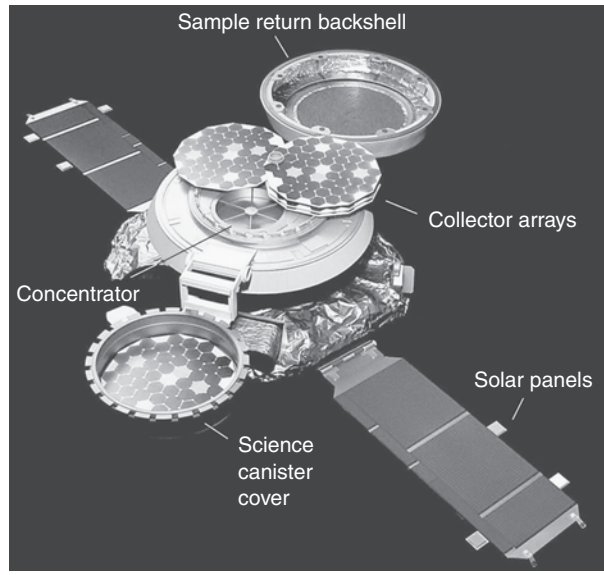

Fig. 4.3 **Genesis spacecraft with solar wind collectors deployed. Image courtesy of NASA/JPL-Caltech.**

The spacecraft traveled to a point outside of the Earth's magnetic field. It was stationed at the L1 Lagrangian Point, between the Earth and Moon, for 884 days while it collected solar wind. The spacecraft then returned to Earth on September 8, 2004. The mission plan was for a helicopter to snag the spacecraft out of the air while it descended on a parachute. Unfortunately the parachute failed to open and the spacecraft plummeted onto the Utah desert (Fig. 4.4).

The crash shattered many of the detectors into pieces a few millimeters across, and Utah dirt and dust from the spacecraft coated the pieces. But, while the crash of the spacecraft was a setback, all was not lost. The spacecraft and all of its pieces were carefully collected and returned to the Johnson Space Center in Houston. There, all the tools and skills of ground-based laboratories and scientists were applied to the problem of cleaning the collectors and making them suitable for analysis.

A solar wind mission has a major advantage over many other types of mission. The solar wind is implanted under the surface of the collectors, while the dirt and contamination are on the surface. After careful study, cleaning procedures were established that removed the surface contamination, and within a year of the landing, data on the isotopic composition of the solar wind were being published. The mission team is confident that all of the major mission objectives will be met. The main effect of the crash was simply to delay the publication of the results. One can even find a silver lining to the crash: sample curators no longer have to worry about subdividing the collectors to provide material to different labs. They have thousands of pieces that can be sent out for analysis. An important lesson from this mission is that if one can bring the samples back to Earth, the resources and ingenuity of dedicated people can perform miracles.

Fig. 4.4 **Genesis spacecraft shortly after its abrupt return to Earth. Image courtesy of the Genesis Mission, NASA.**

To measure the solar wind, one must find or make suitable solar wind collectors. The Earth is protected from the solar wind by its magnetic field, so the collectors must be outside of the influence of the Earth's magnetic field. The first measurements of the noble gases in the solar wind were made in a subclass of chondritic meteorites (originally called gas-rich), which are actually pieces of the surface regolith on the parent asteroid. The so-called solar noble gases in these meteorites show a much smaller elemental fractionation relative to the expected composition of the Sun than do other noble gas components trapped in meteorites and noble gases in the Earth's atmosphere. The gas-rich meteorites gave the first data on the isotopic compositions of the noble gases in the solar wind.

The Moon, which lies outside of the influence of the Earth's magnetic field, is another excellent solar wind collector. In fact, the Moon's surface is saturated with solar wind hydrogen and helium, which means that every time a new solar wind atom is implanted into the surface, it kicks out an atom that was previously implanted. The concentration of solar wind helium in the lunar surface is high enough for helium to be considered a potential resource for future lunar mining. Unfortunately, because the Moon's surface consists of rocks and minerals that contain lots of elements, these rocks are not suitable collectors for measuring the solar wind because, except for noble gases and nitrogen, one cannot distinguish the solar wind atoms from the atoms that originally made up the rock. Measurements of lunar soils give estimates of the isotopic compositions of nitrogen and noble gases in the Sun, but provide no information on relative abundances of the elements because of the fractionations associated with acceleration from the Sun, trapping in the lunar soils, and degassing over time as the soil is thermally cycled on the lunar surface.

The Apollo missions attempted to take advantage of the Moon's location outside of the Earth's magnetic field to capture solar wind in aluminum collectors. The collectors were deployed for the duration of each mission (from 10 to 45 hours) and provided information on the helium, neon, and argon isotopic compositions in the solar wind.

The NASA Genesis mission (see Box 4.3), launched in 2001, was designed to collect solar wind over a ~2.5-year period. Special collector materials were designed to be free of contaminants so that clean measurements of the isotopic compositions of trapped solar wind

elements would be possible. The spacecraft was stationed between the Earth and the Sun at a point where their gravities balance. The mission returned ~10^{20} atoms of solar wind (0.4 mg) to Earth. In spite of an unfortunate crash on return to Earth, the first results from analyzing the Genesis collectors have begun to appear and it is likely that the major objectives of the mission will eventually be met.

Determining chemical abundances in meteorites

Importance of CI chondrites

For over a century, it has been widely accepted that chondrites have primitive compositions, meaning that physical and chemical processes that formed the meteorites did not significantly change their elemental compositions. However, as analytical techniques improved, it became clear that all chondrites are not the same. In fact, at least 15 compositional groups can be identified among the chondrites (see Chapter 6). So then the question became, which group of chondrites is most representative of the bulk composition of the solar system? By the 1960s, it was clear that a small group of meteorites, the CI chondrites, have the most-primitive compositions. This conclusion comes from plots like Figure 4.5, which shows the

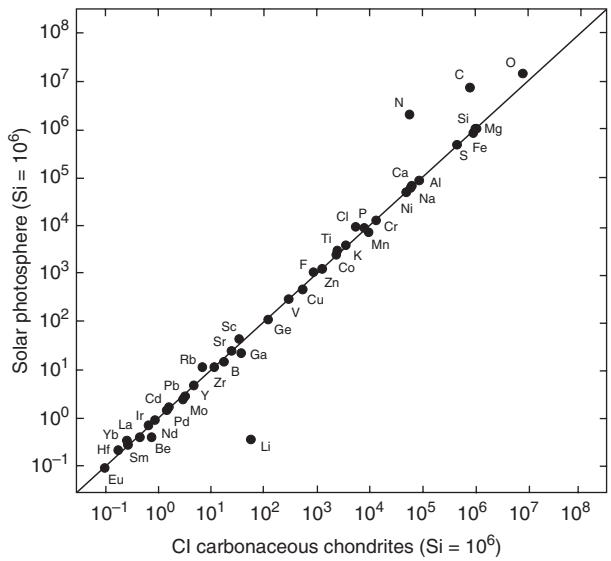

Fig. 4.5 Abundances of elements as determined in the solar photosphere are plotted against abundances in CI carbonaceous chondrites (both normalized to 10^6 atoms of silicon). The 45-degree line is the 1:1 line describing equal abundance in the two materials. Almost all elements fall within a few percent of the 1:1 line. The exceptions are elements that are gases or form gaseous compounds at room temperature (hydrogen, helium, nitrogen, carbon, oxygen, neon, argon, krypton, xenon), which are not effectively retained in the CI chondrites, and elements that have been destroyed by nucleosynthesis processes in the Sun over its lifetime. The close agreement between the two compositions indicates that CI chondrites acquired a representative sample of bulk solar system material.

photospheric abundances of the elements plotted against the abundances in CI chondrites. Elements that plot on the solid line on Figure 4.5 are present in the same abundance in the Sun and in CI chondrites. Except for those volatile elements that exist in the gas phase at room temperature (hydrogen, helium, oxygen, carbon, nitrogen, noble gases), and elements that were burned out of the Sun by the first stages of nuclear burning (e.g. Li), essentially all elements are present in the same relative abundance in the Sun and the CI chondrites. Figure 4.5 uses the best data available today, but plots based on earlier data have given the same basic picture since the 1960s.

Measuring CI abundances

A variety of techniques have been used to measure the bulk chemical compositions of CI chondrites and other meteorites.

Wet chemistry

The first technique to be used was wet chemistry. In this technique, a few grams of meteorite are dissolved in a variety of acids and the elements are separated based on their chemical properties. Approximately 15 major and minor elements can be determined by wet chemical techniques. Wet chemistry requires relatively large samples. This means that the sample used to determine the composition of a meteorite is likely to be representative of the entire meteorite. On the other hand, some meteorites are too small to allocate material for a wet chemical analysis. Fortunately, there are other methods that require less material. Because of the large sample requirements and because of the tedious nature of the analysis, no one is doing wet chemical analyses of meteorites any more. The best analyses were made during the 1950s through 1980s, especially by Hugo Wiik and Eugene Jarosewich (e.g. Jarosewich, 1990).

X-ray fluorescence

A second method of determining major and minor element abundances in meteorites is X-ray fluorescence analysis. In this method, a sample of meteorite is ground into a fine powder and irradiated by a monochromatic X-ray beam. The atoms in the sample absorb some of the X-rays, causing electrons to be ejected. The ejection of an electron causes other electrons to drop to lower energy levels to fill the vacancy, and characteristic X-rays are emitted. The X-ray energies are unique to each element and permit the chemical composition to be determined. X-ray fluorescence was used to determine the compositions of meteorites in the late 1950s and 1960s. If done correctly the compositions have the same accuracy as wet chemical analyses, but some of the measurements in the literature have problems with alkali elements.

Neutron activation analysis

Both wet chemistry and X-ray fluorescence require relatively large samples, typically at least a gram. As scientists prepared for the arrival of the Apollo lunar samples, they developed

techniques that could provide reliable chemical information on samples that were very much smaller, down to tens of milligrams. Wet chemistry and X-ray fluorescence also are not useful for determining the abundances of trace elements in meteorites, which can be extremely informative about the processes that produced a rock. The two techniques developed to meet these requirements were Instrumental Neutron Activation Analysis (INAA) and Radiochemical Neutron Activation Analysis (RNAA). In these techniques, a sample is placed in a nuclear reactor and irradiated with neutrons. This irradiation produces short-lived radioactive species. As the atoms of each radioactive species decay, they give off characteristic gamma rays, which can be counted. In INAA, the samples are counted directly with no additional processing. In RNAA, elements are separated to minimize interferences between gamma rays of similar energies. Up to 74 of the 92 elements can be detected by neutron activation analysis. Unfortunately, silicon, a key major element, is not one of them. If one can determine the abundances of the other elements with sufficient precision, the silicon abundance can be determined by difference. Neutron activation data are reported and discussed as ratios to a common major element thought not to fractionate in solar system processes, commonly magnesium. The small sample size requirement of neutron activation analysis is also its Achilles' heel. An analyst must always be sure to analyze a sample that is truly representative of the bulk material. In a chondritic meteorite, this sample size is on the order of a gram. Either a larger sample must be homogenized so a representative aliquot can be measured, or several measurements of different samples must be made and averaged appropriately to get a good analysis (Kallemeyn and Wasson, 1981).

Indirect methods of estimating abundances

As understanding of nuclear physics and stellar nucleosynthesis has improved, it has become possible to use that knowledge along with measured abundances to infer the solar system abundances of elements that cannot be directly measured, either by solar spectroscopy because their ionization potentials are too high, or in meteorites because they were not efficiently incorporated into the chondrites. In particular, the noble gases cannot be directly measured and must be inferred from theoretical considerations or other indirect means.

Helium

Although helium was first discovered through spectral observations of the Sun, the lines that were observed appear in the high-temperature corona. Helium does not appear in the spectrum of the solar photosphere, and it is very inefficiently retained in meteorites. Solar wind and solar energetic particles show highly variable helium abundances, and these are rather low when compared with helium values inferred from hot stars or from the H II regions (characterized by ionized hydrogen) in the interstellar medium. The best estimates for the helium abundance in the Sun come from two sources: (1) solar standard and non-standard models; and (2) inversion of helioseismic data. Standard models give a helium

abundance by mass in the protosolar cloud of Y = 0.27±0.01 (Christensen-Dalsgaard, 1998). Non-standard models, which take into account elemental migration over the age of the Sun (see below), give a solar helium abundance of Y = 0.275 (Gabriel, 1997). Inversion of helioseismic data give a smaller value, Y = 0.2485 as the helium abundance in the outer convective zone of the Sun (Basu and Antia, 2004). The best estimate for the abundance in the outer layers is thus Y = 0.2485 (He/H = 0.0851 by number). This is the value given in Table 4.1. The helium abundance of the bulk Sun at the time it formed is estimated to have been Y = 0.275 ± 0.01 (He/H = 0.098) (Grevesse and Sauval, 1998). The difference between this number and the current inferred abundance in the convective zone is due to elemental segregation over the age of the Sun.

Neon and argon

No spectral lines of neon and argon appear in the photospheric spectrum. The abundances of these elements come from measurements of the Ne/O and Ar/O ratios in coronal material and thus are relatively uncertain. Unfortunately, nucleosynthesis theory does not provide much guidance for either neon or argon.

Krypton and xenon

The abundances of krypton and xenon are determined exclusively from nucleosynthesis theory. They can be interpolated from the abundances of neighboring elements based on the observation that abundances of odd-mass-number nuclides vary smoothly with increasing mass numbers (Suess and Urey, 1956). The regular behavior of the *s*-process also provides a constraint (see Chapter 3). In a mature *s*-process, the relative abundances of the stable nuclides are governed by the inverse of their neutron-capture cross-sections. Isotopes with large cross-sections have low abundance because they are easily destroyed, while the abundances of those with small cross-sections build up. Thus, one can estimate the abundances of krypton and xenon from the abundances of *s*-only isotopes of neighboring elements (selenium, bromine, rubidium and strontium for krypton; tellurium, iodine, cesium, and barium for xenon).

Solar system abundances of the elements

Table 4.1 shows the solar system abundances of the elements as determined by the methods discussed above. For some elements, the photospheric abundances provide the best estimate, whereas for others, the meteorite data must be used. In some cases, the data are equally reliable and an average of the values determined from the solar photosphere and CI chondrites is used. The abundances of the noble gases come from indirect measurements or theoretical considerations. The method for determining each abundance is indicated in the far right column of Table 4.1.

You will note that two normalization conventions are used in Table 4.1. Astronomers like to calculate the abundances relative to 10^{12} atoms of hydrogen, whereas cosmochemists like to calculate abundances relative to 10^6 atoms of silicon. The two scales differ by a factor of 33.26. We give the data for CI chondrites and the final solar system abundances (second column from the right) using the cosmochemical scale (normalized to 10^6 silicon atoms), but we retain the astronomical scale for the photospheric data to facilitate comparison with the primary literature. Note that the photospheric values for many elements have changed significantly between the publication of Anders and Grevesse (1989) and Grevesse *et al*. (2007). As discussed above, these changes reflect the transition to 3D modeling coupled with relaxing the assumption of local thermodynamic equilibrium (LTE) and, to a lesser extent, improvements in the basic physical data for the Sun.

There are several basic features to note about the chemical abundances of the solar system. First, the Sun, and thus the solar system, consists dominantly of hydrogen and helium, with these two elements making up >98% of the mass of the solar system. Outside of the Sun, hydrogen and helium are found primarily in the gas-giant planets.

Second, lithium, beryllium, and boron have very low abundances. These elements are, for the most part, not made in stars and were not made efficiently in the Big Bang. They are produced via cosmic ray interactions. Nuclei of heavier atoms, when hit by fast moving protons or other nuclei, can break into pieces, including protons, neutrons, alpha particles, and heavier fragments. Some of these fragments are lithium, beryllium, and boron nuclei.

Third, carbon, nitrogen, and oxygen, the elements that catalyze hydrogen burning in the Sun, are relatively abundant in the solar system. Oxygen is somewhat more abundant than carbon; the C/O ratio is ~0.54. Because CO is a very stable molecule, most of the carbon and oxygen in the early solar system was tied up in CO. The excess oxygen that remained controlled the chemical environment of the early solar system.

Among the elements that make up rocks and minerals, silicon, magnesium, and iron are of almost equal abundance followed by sulfur, aluminum, calcium, sodium, nickel, and chromium. Two of the most common minerals in meteorites and in the terrestrial planets are olivine ($(Mg,Fe)_2SiO_4$) and pyroxene ($(Mg,Fe,Ca)SiO_3$). The composition obtained by averaging these two minerals is very similar to the bulk solar system composition, so it is really no surprise that they are so abundant.

Fifth, for elements heavier than iron, the abundances decrease in a regular way with increasing mass (there is a zig-zag structure superimposed upon this decrease that reflects nuclear properties, e.g. the Oddo-Harkins rule). This is because the elements of the iron peak (iron, nickel, cobalt) have the highest binding energies of all nuclides (cf. Fig. 2.1). For elements below iron, energy was released as protons and neutrons were added to smaller nuclei. However, for elements above iron, energy is required to force another proton or neutron into the nucleus. As nuclear mass increases, the binding energy per nucleon holding the nucleus together decreases until at a nuclear mass of ~200, many nuclear configurations are not stable at all. The heaviest naturally occurring nuclide in the solar system is ^{238}U, and the abundance of U is about one part in 10^8 of that of Si (Table 4.1).

Solar system abundances of the isotopes

Table 4.2 gives current estimates for the relative abundances of the isotopes in the solar system. The isotopic compositions of most elements, especially those that exist as solids, come from measurements of terrestrial materials. Because the Earth has experienced extensive melting and differentiation, it can be considered a homogeneous isotopic reservoir. However, each of the elements can experience both equilibrium and kinetically based isotopic fractionations during igneous, evaporative, and aqueous processes. The range of compositions introduced by such processes is small for most elements and so does not obscure the overall picture.

Why can one assume that the isotopic compositions of elements on the Earth are representative of the bulk solar system? This was not obvious in the beginning. Isotope-ratio measurements of meteorites made in the late 1950s appeared to show significant variations. However, within a few years, it was shown that those variations were due almost entirely to problems with the measurements, not to real variations in the samples. By the early 1960s enough measurements had been made to convince most scientists that in the material to which they had access, terrestrial rocks and meteorites, each element always had the same isotopic composition (except for small fractionations of stable isotopes and shifts

Table 4.2 Abundances of the isotopes in the solar system

Element	A	Atom %	Abundance	Process	Element	A	Atom %	Abundance	Process
1 H	1	99.99806	2.431×10^{10}			18	0.20004	28 270	He,N
	2	0.00194	4.716×10^{6}	U			100	1.413×10^{7}	
		100	2.431×10^{10}		9 F	19	100	841.1	N
2 He	3	0.016597	3.889×10^{5}	U,h?	10 Ne	20	92.9431	1.996×10^{6}	C
	4	99.983403	2.343×10^{9}	U,h		21	0.2228	4786	C,Ex
		100	2.343×10^{9}			22	6.8341	1.468×10^{5}	He,N
3 Li	6	7.589	4.21	X			100	2.148×10^{6}	
	7	92.411	51.26	U,x,h	11 Na	23	100	57 510	C,Ne,Ex
		100	55.47		12 Mg	24	78.992	8.057×10^{5}	N,Ex
4 Be	9	100	0.7374	X		25	10.003	1.020×10^{5}	Ne,Ex,C
5 B	10	19.82	3.433	X		26	11.005	1.123×10^{5}	Ne,Ex,C
	11	80.18	13.887	X			100	1.020×10^{6}	
		100	17.32		13 Al	27	100	84 100	Ne,Ex
6 C	12	98.8922	7.001×10^{6}	He	14 Si	28	92.22968	9.2230×10^{5}	O,Ex
	13	1.1078	78 420	H,N		29	4.68316	46 830	Ne,Ex
		100	7.079×10^{6}			30	3.08716	30 870	Ne,Ex
7 N	14	99.6337	1.943×10^{6}	H			100	1.000×10^{6}	
	15	0.3663	7143	H,N	15 P	31	100	8373	Ne,Ex
		100	1.950×10^{6}		16 S	32	95.018	4.227×10^{5}	O,Ex
8 O	16	99.7628	1.410×10^{7}	He		33	0.75	3340	Ex
	17	0.0372	5260	N,H		34	4.215	18 750	O,Ex

Table 4.2 (cont.)

Element	A	Atom %	Abundance	Process	Element	A	Atom %	Abundance	Process
	36	0.017	76	Ex,Ne,S	27 Co	59	100	2323	E,C
		100	4.449×10^5		28 Ni	58	68.0769	32 541	E,Ex
17 Cl	35	75.771	3968	Ex		60	26.2231	12 532	E
	37	24.229	1269	Ex,C,S		61	1.1399	545	E,Ex,C
		100	5237			62	3.6345	1737	E,Ex,O
18 Ar	36	84.5946	86 710	Ex		64	0.9256	442	Ex
	38	15.3808	15 765	O,Ex			100	47 800	
	40	0.0246	25	S,Ne	29 Cu	63	69.174	364.5	Ex,C
	40*		*24*			65	30.826	162.5	Ex
		100	102 500				100	527.0	
19 K	39	93.25811	3443	Ex	30 Zn	64	48.63	596	Ex,E
	40	0.011672	0.431	S,Ex,Ne		66	27.9	342	E
	40*		*5.37*			67	4.10	50.3	E,S
	41	6.73022	248.5	Ex		68	18.75	230	E,S
		100	3692			70	0.62	7.6	E,S
20 Ca	40	96.941	60 947	Ex			100	1226	
	42	0.647	407	Ex,O	31 Ga	69	60.1079	21.62	S,e,r
	43	0.135	84.9	Ex,C,S		71	39.8921	14.35	S,e,r
	44	2.086	1311	Ex,S			100	35.97	
	46	0.004	2.5	Ex,C,Ne	32 Ge	70	21.234	25.6	S,e
	48	0.187	118	E,Ex		72	27.662	33.4	S,e,r
		100	62 870			73	7.717	9.3	e,s,r
21 Sc	45	100	34.20	Ex,Ne,E		74	35.943	43.3	e,s,r
22 Ti	46	8.249	200	Ex		76	7.444	9.0	E
	47	7.437	180	Ex			100	120.6	
	48	73.72	1785	Ex	33 As	75	100	6.089	R,s
	49	5.409	131	Ex	34 Se	74	0.889	0.58	P
	50	5.185	126	E		76	9.366	6.16	S,p
		100	2422			77	7.635	5.02	R,s
23 V	50	0.2497	0.720	Ex,E		78	23.772	15.64	R,s
	51	99.7503	287.68	Ex		80	49.607	32.64	R,s
		100	288.4			82	8.731	5.74	R
24 Cr	50	4.3452	559	Ex			100	65.79	
	52	83.7895	10 775	Ex	35 Br	79	50.686	5.74	R,s
	53	9.5006	1222	Ex		81	49.314	5.58	R,s
	54	2.3647	304	E			100	11.32	
		100	12 860		36 Kr	78	0.362	0.20	P
25 Mn	55	100	9168	Ex,E		80	2.33	1.28	S,p
26 Fe	54	5.845	48 980	Ex		82	11.65	6.43	S
	56	91.754	768 900	Ex,E		83	11.55	6.37	R,s
	57	2.119	17 760	E,Ex		84	56.90	31.38	R,S
	58	0.282	2360	He,E,C		86	17.21	9.49	S,r
		100	838 000				100	55.15	

Table 4.2 (cont.)

Element	A	Atom %	Abundance	Process	Element	A	Atom %	Abundance	Process
37 Rb	85	72.1654	4.743	R,s	47 Ag	107	51.8392	0.2547	R,s
	87	27.8346	1.829	S		109	48.1608	0.2366	R,s
	87*		*1.951*				100	0.4913	
		100	6.572		48 Cd	106	1.25	0.01980	P
38 Sr	84	0.5551	0.13124	P		108	0.89	0.01410	P
	86	9.8168	2.32069	S		110	12.49	0.198	S
	87	7.3771	1.7439	S		111	12.8	0.203	R,S
	87*		*1.62181*			112	24.13	0.382	S,R
	88	82.2510	19.4441	S,r		113	12.22	0.194	R,S
		100	23.64			114	28.73	0.455	S,R
39 Y	89	100	4.608	S		116	7.49	0.119	R
40 Zr	90	51.452	5.830	S			100	1.584	
	91	11.223	1.272	S	49 In	113	4.288	0.0078	p,s,r
	92	17.146	1.943	S		115	95.712	0.173	R,S
	94	17.38	1.969	S			100	0.181	
	96	2.799	0.317	R	50 Sn	112	0.971	0.03625	P
		100	11.33			114	0.659	0.02460	P,s
41 Nb	93	100	0.7554	S		115	0.339	0.1265	p,s,r
42 Mo	92	14.8362	0.386	P		116	14.536	0.5426	S,r
	94	9.2466	0.241	P		117	7.676	0.2865	R,S
	95	15.9201	0.414	R,s		118	24.223	0.9042	S,r
	96	16.6756	0.434	S		119	8.585	0.3205	S,R
	97	9.5551	0.249	R,s		120	32.593	1.2167	S,R
	98	24.1329	0.628	R,s		122	4.629	0.1728	R
	100	9.6335	0.251	R		124	5.789	0.2161	R
		100	2.601				100	3.733	
44 Ru	96	5.542	0.1053	P	51 Sb	121	57.213	0.1883	R,s
	98	1.8688	0.0355	P		123	42.787	0.1409	R
	99	12.7579	0.242	R,s			100	0.3292	
	100	12.5985	0.239	S	52 Te	120	0.096	0.0046	P
	101	17.06	0.324	R,s		122	2.603	0.1253	S
	102	31.5519	0.599	R,S		123	0.908	0.0437	S
	104	18.621	0.354	R		124	4.816	0.2319	S
		100	1.900			125	7.139	0.3437	R,s
45 Rh	103	100	0.3708	R,s		126	18.952	0.9125	R,S
46 Pd	102	1.02	0.0146	P		128	31.687	1.526	R
	104	11.14	0.160	S		130	33.799	1.627	R
	105	22.33	0.320	R,s			100	4.815	
	106	27.33	0.392	R,S	53 I	127	100	0.9975	R
	108	26.46	0.380	R,S	54 Xe	124	0.129	0.00694	P
	110	11.72	0.168	R		126	0.112	0.00602	P
		100	1.435			128	2.23	0.120	S

Table 4.2 (cont.)

Element	A	Atom %	Abundance	Process	Element	A	Atom %	Abundance	Process
	129	27.46	1.480	R			100	0.2542	
	130	4.38	0.236	S	63 Eu	151	47.81	0.04548	R,s
	131	21.80	1.175	R		153	52.19	0.04965	R,s
	132	26.36	1.421	R,s			100	0.09513	
	134	9.66	0.521	R	64 Gd	152	0.2029	0.00067	P,s
	136	7.87	0.424	R		154	2.1809	0.00724	S
		100	5.391			155	14.7998	0.04915	R,s
55 Cs	133	100	0.3671	R,s		156	20.4664	0.06797	R,s
56 Ba	130	0.1058	0.00460	P		157	15.6518	0.05198	R,s
	132	0.1012	0.00440	P		158	24.8347	0.08248	R,s
	134	2.417	0.1052	S		160	21.8635	0.07261	R
	135	6.592	0.2868	R,s			100	0.3321	
	136	7.853	0.3417	S	65 Tb	159	100	0.05907	R
	137	11.232	0.4887	S,r	66 Dy	156	0.056	0.000216	P
	138	71.699	3.120	S		158	0.096	0.000371	P
		100	4.351			160	2.34	0.00904	S
57 La	138	0.09017	0.000397	P		161	18.91	0.0730	R
	138*		*0.000401*			162	25.51	0.0985	R,s
	139	99.90983	0.4401	S,r		163	24.9	0.0962	R
		100	0.4405			164	28.19	0.1089	R,S
58 Ce	136	0.186	0.00217	P			100	0.3862	
	138	0.251	0.00293	P	67 Ho	165	100	0.08986	R
	138*		*0.00293*		68 Er	162	0.137	0.000350	P
	140	88.449	1.0340	S,r		164	1.609	0.004109	P,S
	142	11.114	0.1299	R		166	33.61	0.08584	R,s
		100	1.169			167	22.93	0.05856	R
59 Pr	141	100	0.1737	R,S		168	26.79	0.06842	R,S
60 Nd	142	27.16	0.22689	S		170	14.93	0.03813	R
	143	12.19	0.1018631	R,S			100	0.2554	
	143*		*0.1007121*		69 Tm	169	100	0.0370	R,s
	144	23.83	0.1990728	S,R	70 Yb	168	0.13	0.000323	P
	145	8.30	0.06934	R,s		170	3.04	0.007551	S
	146	17.17	0.14344	R,S		171	14.28	0.03547	R,s
	148	5.74	0.04795	R		172	21.83	0.05423	R,S
	150	5.62	0.04695	R		173	16.13	0.04007	R,s
		100	0.8355			174	31.83	0.07907	S,R
62 Sm	144	3.0734	0.00781	P		176	12.76	0.03170	R
	147	14.9934	0.03811	R,s			100	0.2484	
	147*		*0.03926*		71 Lu	175	97.416	0.03480	R,s
	148	11.2406	0.0286	S		176	2.584	0.000923	S
	149	13.8189	0.0351	R,S		176*		*0.001008*	
	150	7.3796	0.0188	S			100	0.03572	
	152	26.7421	0.0680	R,S	72 Hf	174	0.1620	0.000275	P
	154	22.752	0.0578	R		176	5.2502	0.0089201	S

Table 4.2 (cont.)

Element	A	Atom %	Abundance	Process	Element	A	Atom %	Abundance	Process
	176*		*0.0088353*			195	33.83156	0.45909	R
	177	18.5973	0.0315968	R,s		196	25.24166	0.34253	R
	178	27.2840	0.046356	R,S		198	7.16349	0.09721	R
	179	13.6225	0.023145	R,s			100	1.357	
	180	35.0840	0.059608	S,R	79 Au	197	100	0.1955	R
		100	0.1699		80 Hg	196	0.15344	0.00063	P
73 Ta	180	0.0123	0.00000258	p,s,r		198	9.968	0.0411	S
	181	99.9877	0.020987	R,S		199	16.873	0.0697	R,S
		100	0.02099			200	23.096	0.0953	S,r
74 W	180	0.1198	0.000153	P		201	13.181	0.0544	S,r
	182	26.4985	0.03384	R,s		202	29.863	0.1233	S,r
	183	14.3136	0.01828	R,s		204	6.865	0.0283	R
	184	30.6422	0.03913	R,s			100	0.4128	
	186	28.4259	0.03630	R	81 Tl	203	29.524	0.0545	R,S
		100	0.1277			205	70.476	0.1300	S,R
75 Re	185	37.398	0.01965	R,s			100	0.1845	
	187	62.602	0.03289	R	82 Pb	204	1.9820	0.064573	S
	187*		*0.03544*			206	18.7351	0.61039	R,S
		100	0.05254			206*		*0.60091*	
76 Os	184	0.0198	0.000133	P		207	22.5900	0.67082	R,S
	186	1.5922	0.010728	S		207*		*0.66497*	
	187	1.644	0.011080	S		208	58.6929	1.91222	R,s
	187*		*0.008532*			208*		*1.90335*	
	188	13.2865	0.089524	R,s			100	3.2580	
	189	16.1992	0.10915	R	83 Bi	209	100	0.1388	R,s
	190	26.3438	0.17750	R	90 Th	232	100	0.03512	RA
	192	40.9142	0.27568			232*		*0.04399*	
		100	0.6738		92 U	235	0.7200	0.000067	RA
77 Ir	191	37.272	0.2403	R		235*		*0.005918*	
	193	62.728	0.4045	R		238	99.2745	0.009238	RA
		100	0.6448			238*		*0.018713*	
78 Pt	190	0.013634	0.000185	P			100	0.009306	
	192	0.78266	0.01062	S					
	194	32.967	0.44736	R					

Abundances from Lodders (2003).

Nucleosynthetic processes from Anders and Grevesse (1989). Processes are listed in order of importance, with minor processes (10–30%) shown in lower case.

U = cosmological nucleosynthesis; H = hydrogen burning; N = hot or explosive hydrogen burning; He = helium burning; C = carbon burning; O = oxygen burning; Ne = neon burning; Ex = explosive nucleosynthesis; E = nuclear statistical equilibrium; S = s-process; R = r-process; RA = r-process producing actinides; P = p-process; X = cosmic-ray spallation.

*Radioactive and radiogenic isotopes used in radiochronology.

Italicized values refer to abundances 4.55×10^9 years ago.

due to decay of radioactive isotopes, as discussed in Chapter 2). At the same time, models for the formation of the solar system envisioned that it passed through a hot gaseous state where all pre-existing solids were evaporated. Had such a state existed, it would have isotopically homogenized the solar system. So observations and experiments pointed to a single, well-defined composition that could be measured, and the idea of a single homogenized solar system composition became a cornerstone of cosmochemistry. The "fly in the ointment" was the noble gases, which exhibited a range of isotopic compositions in different materials, well outside the range to be expected from known processes in the solar system.

Starting in 1973, evidence began to accumulate from elements other than noble gases that the isotopic composition of the solar system was not homogeneous. As you will see in later chapters, isotopic variations, though typically small, are ubiquitous in solar system materials. These isotopic "anomalies" appear in the most primitive solar system materials, the components of chondritic meteorites. With the exception of oxygen, the anomalies either disappear or are much smaller in objects with more complicated histories involving processes that mix isotopes, such as evaporation and condensation, melting and crystallization, and aqueous processes. Products of these processes typically have the same isotopic compositions, suggesting that each has formed from an isotopically representative sample of the bulk solar system material. Thus, although the solar system was not homogenized isotopically by passing through a hot gas phase, the mixture of gas and dust that made up the solar system was apparently well mixed, and the processes that acted on that material served to homogenize it at the atomic scale. The result is a specific isotopic composition for each element, found in a wide variety of materials that can be considered representative of the bulk solar system. These are the compositions that we present in Table 4.2.

Along with the abundances of the isotopes, Table 4.2 also provides information on the processes that synthesized the isotopes. The processes are listed in order of importance, with minor processes shown in lower case. Note that most isotopes are produced by more than one process, and that isotopes of elements heavier than iron are produced predominantly by the *s*- and *r*-processes. *P*-process isotopes invariably have quite low abundances.

The isotopic compositions of several elements have changed since the formation of the solar system. Radioactive isotopes have decayed, and the abundances of their daughter isotopes have increased over time. For long-lived isotopes of particular importance to radiochronology (flagged with an asterisk), Table 4.2 gives both the present abundance and the abundance at the time the solar system formed (italicized values).

Table 4.2 and similar tables should *not* be used as the source of isotopic compositions of terrestrial standards for high-precision isotopic measurements. While Table 4.2 gives a good overview of the abundances of the isotopes, the values in the table do not always represent state-of-the-art isotopic measurements. Nor do they attempt to take into account the isotopic fractionations that occur in terrestrial materials. Typically, an isotope system that has been measured for many years has a convention about how isotopic ratios are reported. For example, oxygen isotopic compositions are typically reported relative to the Vienna determination of Standard Mean Ocean Water

(VSMOW). Secondary standards are developed with precisely determined compositions that have a known relationship to this benchmark standard. Measurements are made using secondary standards and final data are calculated relative to the VSMOW ratios. Other isotope systems have similar conventions and official standard compositions. Those who develop measurement techniques for a new isotope system must address the standard problem before they can publish any of their data.

How did solar system abundances arise?

As discussed in Chapter 3, the abundances inherited by the solar system are the result of a long history of nucleosynthesis in the galaxy. By the time the solar system formed, many generations of massive stars and several generations of intermediate-mass stars had contributed material to the galaxy over the billions of years leading up to the formation of the solar system. Low-mass stars were just beginning to return newly synthesized material to the galaxy when the solar system formed. The elements produced by all these different sources were mixed through the galaxy by turbulence and thermal mixing driven primarily by stellar explosions. The same types of stars live and die throughout the galaxy, but there are more of them in the galactic center than on the edges. Over time scales of a few hundred million years, rough chemical and isotopic homogeneity can be attained over an annulus of the galactic disk, although radial gradients remain (see below). Therefore, it is no accident that the first measurements of the compositions of the Sun, the stars, galaxies, comets, and other celestial objects gave compositions that are to first order rather similar.

On a local scale, gas and dust are regularly forced together by expanding gas from supernova explosions into molecular clouds, where material cools and densities increase until especially dense regions collapse to initiate star formation. Most stars form in giant molecular clouds out of which hundreds or thousands of stars may form in what is often called “cluster star formation.” The solar system probably formed in such a region. The solar system primarily incorporated material inherited by the molecular cloud, but depending on the timing of solar system formation, it may also have incorporated newly synthesized material ejected by the earliest-formed massive stars in the cloud. There is good evidence from short-lived radionuclides that this happened in the solar system, as we will discuss in Chapters 9 and 14. An active area of research is trying to infer the details of the environment in which and the materials from which the solar system formed.

The solar system abundances of the elements are the result of the Big Bang, which produced hydrogen and helium, ~7.5 billion years of stellar nucleosynthesis, which produced most of the rest of the elements, and the physical processes that mixed the materials together to form the Sun’s parent molecular cloud. The unique features of the solar system composition may also reflect the stochastic events that occurred in the region where the Sun formed just prior to solar system formation.

Differences between solar system and cosmic abundances

As mentioned in the introduction to this chapter, the terms "solar system abundances" and "cosmic abundances" have been used interchangeably over the last century. This was justified because the available evidence suggested that other stars had essentially the same composition as the Sun. However, with the new observational capability provided by state-of-the-art telescopes and instrumentation, we are learning that the composition of the solar system is not the same as that of most of the rest of the galaxy. There is really no reason to expect that the compositions should be the same. The chemical and isotopic composition of the galaxy has been evolving continuously since it formed. Stellar nucleosynthesis has added elements heavier than helium to the mix, and the galaxy has been growing through accretion of metal-poor gas and assimilation of smaller galaxies. When the Sun formed ~4.57 billion years ago, it captured a snapshot of this evolution in the region where it formed. But the galaxy has continued to evolve. It is also likely that the Sun no longer resides in the same region of the galaxy where it formed due to dynamical scattering caused by close passages with other stars and the mass of the galactic arms. To further complicate matters, self-enrichment of the cloud from which the solar system formed by massive stars that formed and died in the same star-forming region, or mechanical separation of gas from dust in the Sun's parent molecular cloud could have caused the Sun to acquire a composition different from that of the galaxy in the solar neighborhood.

It is not straightforward to determine the current chemical composition of the galaxy in the neighborhood of the Sun. Although characteristic absorption lines are generated by cold matter in interstellar space, their strengths are not necessarily proportional to the amounts of elements present. Elements in the gas phase absorb efficiently, while those in dust do not. So absorption lines cannot be used directly to provide details of elemental abundances. Stars produce emission lines in their photospheres, but low-mass stars live billions of years and the surrounding galaxy can evolve considerably during that time. Low- and intermediate-mass stars provide a way to look back at the chemical composition of the galaxy billions of years ago. The best way to estimate the current composition of the galaxy in the solar neighborhood is to look at the photospheres of B stars. These massive stars are short-lived, and thus formed recently, within the last ~10 million years, and there has not been time for the composition of the galaxy to evolve. Nor has there been time for the stars to migrate from where they formed.

Systematic observations of B stars show that their heavy-element abundances relative to hydrogen are only 50–70% of those in the Sun (the new lower abundances derived from 3D solar models do not eliminate this difference). Theory predicts that the metallicity of the galaxy has been increasing with time, and a systematic study of stars formed over most of the history of the galaxy shows this to be true. In addition, there can be a spread of almost an order of magnitude in the Fe/H ratios of stars that formed at roughly the same time. Relative to nearby solar-type stars of similar age, the Sun has a ~50% higher Fe/H ratio than average.

Table 4.3 Isotopic ratios of C, N, and O in molecular clouds relative to solar ratios

Material	$^{13}C/^{12}C$	$^{15}N/^{14}N$	$^{18}O/^{16}O$	$^{17}O/^{18}O$
Solar system	0.01124	0.003676	0.00204	0.1861
Outer galaxy	0.0157±0.0034	0.00291±0.00034	0.00204±0.00041	0.275±0.009
Galactic center	0.0360±0.0090	0.00147±0.00034	0.0041±0.0016	0.296±0.19

Data from Wannier (1989)

The Sun might have acquired a higher Fe/H ratio than many stars of similar age because of where the solar system formed. If the Sun formed closer to the galactic center, where star formation and galactic evolution proceed more rapidly, it would have acquired a higher abundance of heavy elements from the average material in that location. After formation, the Sun could then have been gravitationally scattered outward to where it now resides. On the other hand, the galaxy is not a closed system, and new heavy-element-poor gas has been falling onto the galaxy from surrounding intergalactic space. If enough metal-poor gas fell into the solar neighborhood, more-recently formed stars might have lower metallicity than the Sun.

The solar system is different than the rest of the galaxy in other ways as well. Although one cannot use spectral observations of cold matter to reliably determine elemental abundances, it is possible to measure isotopic abundances using absorption lines. This is because the different isotopes of most elements do not partition significantly between gas and solid phases in the interstellar medium. However, because absorption lines can become saturated if the column density between the source and the observer is too high (no light gets through so, for example, doubling the amount of material makes no measurable difference), it is often easier to measure ratios of isotopes that have similar abundances. For example, $^{16}O/^{17}O$ in solar system material is ~2630, whereas $^{16}O/^{18}O$ is ~490. The ^{16}O line often saturates, resulting in spurious results. However, $^{17}O/^{18}O$ is ~0.19 and thus is relatively easy to measure. Table 4.3 shows isotopic data for carbon, nitrogen, and oxygen for molecular clouds in the galactic center and the outer galaxy compared to the solar system ratios.

The $^{13}C/^{12}C$ ratios for molecular clouds throughout the galaxy are higher than in the solar system, with ratios increasing toward the galactic center. The $^{15}N/^{14}N$ ratios in molecular clouds throughout the galaxy are lower than in the solar system and the ratios decrease toward the galactic center. The carbon and nitrogen ratios apparently reflect the addition of the products of CNO-catalyzed hydrogen burning to the interstellar medium. The oxygen ratios are harder to understand. CNO cycling should produce higher $^{17}O/^{16}O$ ratios and lower $^{18}O/^{16}O$ ratios. Yet $^{18}O/^{16}O$ increases toward the galactic center, while $^{17}O/^{18}O$ ratios, which are everywhere higher than in the solar system, are nearly the same across the galaxy. An additional source of ^{18}O is required, one that produces enough ^{18}O to balance its destruction by CNO burning in the outer galaxy but which is operating much more efficiently in the galactic core.

Another possible way to reconcile some of the chemical and isotopic differences between the solar system and the solar neighborhood is to postulate that the solar system formed in a

region of active star formation, where the abundances of material from massive stars was enhanced over the galactic average due to supernova explosions just before the solar system formed. These models are currently poorly constrained and to date have not been very successful, but the concept behind them may well be true, as indicated by the presence of short-lived radionuclides in our solar system (see Chapters 9 and 14).

How are solar system abundances used in cosmochemistry?

We have now considered how the solar system abundances are determined and have discussed the uncertainties in the abundance numbers. Here we briefly discuss how these abundances are used in cosmochemistry. These uses will be discussed further in later chapters.

Solar system abundances help to determine the nature of the materials from which the solar system formed. As discussed above, the solar system abundances arose through a long history of star formation, stellar nucleosynthesis, and ejection of newly formed elements into the interstellar medium. If we know the isotopic compositions of materials formed within the solar system, we can recognize materials that were formed outside of the solar system. These "presolar grains," discussed in Chapter 5, provide ground truth for models of stellar nucleosynthesis. By studying solar system abundances in the context of models of stellar nucleosynthesis, cosmochemists can infer a great deal about the types of stars that contributed to the solar system mixture and the environment in which the solar system formed. Comparison of solar system abundances with the elemental and isotopic compositions of nearby and distant stars and molecular clouds and with the isotopic compositions of presolar grains gives insight into galactic chemical evolution. For this kind of work, the solar system abundances are known with sufficient accuracy and precision to serve as a firm foundation.

As models for the origin of the solar system become more sophisticated, they make increasingly precise predictions about the evolution of the chemical and isotopic composition of solar system materials. For example, oxygen isotopes are used to classify meteorites (discussed in Chapter 6) and to investigate relationships between different bodies in the early solar system. However, the origin of the oxygen isotopic variations is currently not understood. Several models have been proposed, but in order to distinguish between them we need to know the oxygen isotopic composition of the bulk solar system. That is why so much effort is being expended to determine the oxygen isotopic composition of the Sun (see Box 4.4). Determining the origin of the Earth's water is another problem where the bulk composition of the hydrogen in the solar system provides critical input, as discussed in Chapter 14. Various proxies have been identified and measured to infer the solar system composition (e.g. Jupiter's atmosphere, cometary ices), and depending on the composition that is chosen, different models for the origin of the Earth's water can be constructed. For studies like these, it would be very helpful to have a better knowledge about the isotopic compositions of hydrogen, oxygen, and other elements in the solar system.

Box 4.4 The oxygen isotopic composition of the Sun

The oxygen isotopic composition of the solar system is a key constraint for understanding the environment in which the Sun formed, the environment in the early solar system, and the processes that operated in the early solar system. Oxygen isotopic composition is also a key property by which we classify meteorites. Yet until very recently, we have not been able to make any measurement that could unambiguously tell us what the oxygen isotopic composition of the Sun, and by extension the solar system, really is.

Previous measurements

Meteorites show a very large range in oxygen isotopic compositions (see Chapter 6). Unlike the range in oxygen compositions observed on Earth, which can be explained by mass-dependent processes operating on a single terrestrial composition, the meteorite compositions fall well off of the terrestrial mass fractionation line. At one extreme are the calcium-aluminum-rich inclusions (CAIs), which have compositions that are depleted by ~5% in ^{16}O relative to the terrestrial composition. At the other extreme is a chondrule that is enriched in ^{16}O by ~3.5% compared to the terrestrial composition. Although both extremes have been proposed as the true composition of the solar system, most of the mass of the solar system has a composition very close to that of the Earth, so historically the terrestrial composition has been viewed as a reasonable approximation to the solar composition.

Attempts have been made to measure the isotopic composition of the solar photosphere with spectroscopy. Unfortunately, the photosphere is too hot to look at the best lines for this work and the results to date have uncertainties that span the range of compositions determined for meteorites and planetary bodies. Recently, two attempts to measure the oxygen isotopic composition of the Sun were carried out on metal grains (which should be free of intrinsic oxygen) from lunar soils. The results were confusing, however, with one study reporting a solar oxygen composition enriched in ^{16}O relative to terrestrial oxygen by ~4% and the other showing it to be depleted in ^{16}O by ~4% (Hashizumi and Chaussidon, 2005; Ireland *et al.*, 2006). Apparently, the metal in lunar soil is not a good place to look for solar oxygen.

A new attempt

The Genesis Mission, described in Box 4.2, was designed, in large part, to get a precise measurement of the oxygen composition of the solar wind. A special concentrator was designed so that enough atoms could be collected to make a measurement of high precision. A special ion microprobe, called Megasims, was designed with some of the features of an accelerator mass spectrometer in order to measure the solar wind oxygen composition. Although the crash of the Genesis spacecraft into the Utah desert was a setback for the mission, three of the four targets in the concentrator survived the crash intact. As of this writing, the first round of measurements have been completed, and although the definitive results have not yet been published, preliminary results indicate that the Sun is enriched in ^{16}O relative to the Earth by several percent. McKeegan *et al.* (2009) report the oxygen composition of the solar wind as $\delta^{17}O = -65$ permil, $\delta^{18}O = -60$ permil, slightly more ^{16}O-rich than most CAIs.

The processes that produced the planets, their moons, meteorites, and comets from the raw materials from which the solar system formed resulted in changes in the chemical compositions relative to the starting material. We refer to these changes as chemical fractionations, and they will be discussed at length in Chapter 7. In order to have a sensible discussion about how the elements have been fractionated by a given process, it is necessary to know the starting composition. For discussions of processes in the early solar system, the solar system abundances give the starting composition, although in some cases the compositions of the CI carbonaceous chondrites (on which solar system abundances are based) are used for that purpose.

Normalizing to solar system abundances

In the cosmochemistry literature, you will often see data normalized to (that is, divided by) solar system abundances (most commonly those of CI chondrites). An important reason for doing this is illustrated in Figure 4.6. The top panel of this figure shows a plot of the composition of a chondrule with the elements arranged in order of their volatility from most

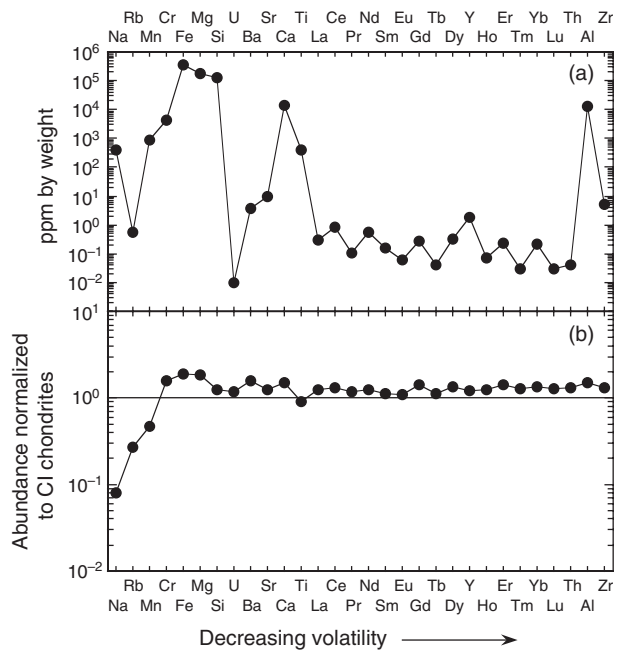

Fig. 4.6 (a) Composition of a chondrule from a CR chondrite, plotted as ppm by weight. Elements are arranged in order of decreasing volatility. (b) The same data shown normalized to the abundances in CI chondrites (Table 4.1). A composition that is the same as CI will plot on the horizontal line at a value of 1 ($=10^0$). In the normalized plot, depletions of the most volatile elements in this chondrule relative to solar system abundances are now evident. Elements more refractory than chromium have the same relative abundances as CI chondrites, although the absolute abundances are higher due to depletion of volatile elements.

volatile on the left to most refractory on the right. This plot reveals little about the extent to which the chondrule differs from the composition of the bulk solar system. However, if the composition is normalized to the solar system abundances, as in the bottom panel of Figure 4.6, the pattern of chemical fractionation is immediately evident. This chondrule is depleted in volatile elements relative to solar system abundances and is enriched in elements more refractory than chromium. (Note that in a chemical plot such as this, which plots either the weight percent or the atom percent of each constituent, if the volatile elements are depleted, the remaining elements in the solid must have higher concentrations because they must total to 100%. Some of it plus the rest of it must equal all of it!)

In geochemical as well as cosmochemical literature, you will often see compositions normalized to carbonaceous chondrites, meaning CI chondrites. In many cases, this normalization is chosen because it is "conventional," not because the normalization is particularly instructive for the problem being investigated. It is not necessary to normalize data in this way. You can normalize trace-element compositions of minerals to the bulk composition of the system to illustrate fractionation processes during formation of the minerals, or you can normalize everything, including the bulk composition, to CI chondrites. When reading the literature, make sure you understand how data have been normalized, and when you report your data, make sure that you clearly explain any normalizations. Normalizing data is a powerful tool, but if the wrong normalizations are used, they can generate artifacts in the data that can result in spurious interpretations.

Summary

In this chapter, we have introduced solar system abundances and cosmic abundances of the elements and isotopes and briefly discussed their importance in cosmochemistry. The idea of cosmic abundances has been around for over a century and is rooted in measurements of many different celestial objects. Only in the last 20–30 years has our knowledge of the compositions of the solar system, of stars and molecular clouds in our galaxy, and of other galaxies grown sufficiently that we can now detect clear compositional differences between our solar system and other objects in the galaxy and the universe.

Solar system abundances are determined by a combination of spectroscopy of the solar photosphere, detailed chemical measurements of CI chondrites, and in the case of elements not amenable to direct measurement, theoretical considerations. The solar system and galactic abundances arose through a combination of Big Bang nucleosynthesis, nucleosynthesis in stars over the history of the universe, and cosmic-ray induced spallation reactions that fragment pre-existing nuclei. Solar system abundances differ from the abundances in other parts of the galaxy and the universe because the details of the processes and rates of nucleosynthesis vary from place to place. Thus, it is no longer appropriate to use the terms "cosmic abundances" and "solar system abundances" interchangeably.

Solar system abundances are a cornerstone of our understanding of the origin and evolution of the solar system and the elements from which it formed. To understand

how physical and chemical processes produced the current planets, asteroids, comets, and other solar system bodies, it is necessary to know what the original composition of the material was that those processes operated on. Knowledge of the chemical and isotopic composition of the solar system is required to recognize objects that formed outside of the solar system. To decipher the role of recent stellar nucleosynthesis in the solar system and in the solar neighborhood, it is necessary to know what the chemical and isotopic composition of the material was before the nucleosynthesis began to operate.

In the next few chapters, we will investigate these topics further. For example, in Chapter 5, we will introduce presolar grains and show how they can be used to investigate stellar nucleosynthesis and processes operating in interstellar space and in the early solar system, and in Chapter 7, we will discuss chemical and isotopic fractionation processes that operate in the solar system.

Questions

1. What are the three main ways of obtaining information about solar system abundances?
2. What are the advantages and limitations of spectroscopic measurements of the solar photosphere for determining solar system abundances?
3. Why are CI chondrites so important to cosmochemistry?
4. What are some of the differences between the composition of the solar system and the composition of the galaxy? How might these differences have arisen?
5. Why would you want to normalize chemical data obtained for a chondrule or a meteorite? What would you normalize the data to and why?

Suggestions for further reading

Asplund, M. (2005) New light on stellar abundance analyses: departures from LTE and homogeneity. *Annual Reviews of Astronomy and Astrophysics*, **43**, 481–530. A review of the determination of stellar abundances using the new three-dimensional modeling of the solar photophere.

Christensen-Dalsgaard, J. (2002) Helioseismology. *Reviews of Modern Physics*, **74**, 1073–1129. A comprehensive introduction to helioseismology.

Grevesse, N., Asplund, M. and Sauval, A. J. (2007) The solar chemical composition. *Space Science Reviews*, **130**, 105–114. A discussion of solar system abundances from the perspective of astrophysics.

Lodders, K. (2003) Solar system abundances and condensation temperatures of the elements. *Astrophysical Journal*, **591**, 1220–1247. A comprehensive discussion of the solar system abundances of the elements from the perspective of a cosmochemist.

References

Anders, E. and Grevesse, N. (1989) Abundances of the elements: meteoritic and solar. *Geochimica et Cosmochimica Acta*, **53**, 197–214.

Basu, S. and Antia, H. M. (2004) Constraining solar abundances using helioseismology. *Astrophysical Journal*, **606**, L85–L88.

Bonanno, A., Schlattl, H. and Paternò, L. (2002) The age of the Sun and the relativistic corrections in the EOS. *Astronomy and Astrophysics*, **390**, 1115–1118.

Castro, M., Vauclair, S. and Richard, O. (2007) Low abundances of heavy elements in the solar outer layers: comparisons of solar models with helioseismic inversions. *Astronomy and Astrophysics*, **463**, 755–758.

Christensen-Dalsgaard, J. (1998) The 'standard Sun'. Modelling and helioseismology. *Space Science Reviews*, **85**, 19–36.

Clarke, F. W. (1889) The relative abundances of the chemical elements. *Bulletin of the Philosophical Society of Washington*, **11**, 131–142.

Gabriel, M. (1997) Influence of heavy element and rotationally induced diffusions on solar models. *Astronomy and Astrophyics*, **327**, 771–778.

Goldschmidt, V. M. (1937) Geochemische Verteilungsgesetze der Elemente, IX, Skrifter Norske Videnskaps-Akad. Oslo. I. Mat. Natur. Kl. No. 4.

Grevesse, N. and Sauval, A. J. (1998) Standard solar composition. *Space Science Reviews*, **85**, 161–174.

Harkins, W. D. (1917) The structure of atoms and the evolution of the elements as related to the composition of the nuclei of atoms II. *Science*, **46**, 443–448.

Hashizume, K. and Chaussidon, M. (2005) A non-terrestrial ^{16}O-rich isotopic composition for the protosolar nebula. *Nature*, **434**, 619–622.

Hill, V. (2001) From stellar spectra to abundances. *Astrophysics and Space Science*, **277** (Supplement), 137–146.

Ireland, T. R., Holden, P., Norman, M. D. and Clark, J. (2006) The oxygen-isotope composition of the Sun. *Nature*, **440**, 776–778.

Jarosewich, E. (1990) Chemical analyses of meteorites: A compilation of stony and iron meteorite analyses. *Meteoritics*, **25**, 323–337.

Kallemeyn, G. W. and Wasson, J. T. (1981) The compositional classification of chondrites. 1. The carbonaceous chondrite groups. *Geochimica et Cosmochimica Acta*, **45**, 1217–1230.

Lockyer, J. N. (1890) *The Meteoritic Hypothesis*. New York: MacMillan and Co., 560 pp.

McKeegan, K. D., Kallio, A. P., Heber, V. *et al*. (2009) Oxygen isotopes in a GENESIS concentrator sample (abstr.). *Lunar and Planetary Science XL*, CD# 2494.

Payne, C. H. (1925) *Stellar Atmospheres: A Contribution to the Obervational Study of High Temperature in the Reversing Layers of Stars*. Harvard Observatory Monograph No. 1, Cambridge, MA.

Russell, H. N. (1929) On the composition of the Sun's atmosphere. *Astrophysical Journal*, **70**, 11–82.

Suess, H. E. and Urey, H. C. (1956) Abundances of the elements. *Reviews of Modern Physics*, **28**, 53–74.

Vauclair, S. (1998) Elemental settling in the solar interior. *Space Science Reviews*, **85**, 71–78.

Wannier, P. G. (1989) Abundances in the galactic center. In *The Center of the Galaxy*, Morris, M., ed., IAU Symposium #136, pp. 107–119.

5 Presolar grains: a record of stellar nucleosynthesis and processes in interstellar space

Overview

Presolar grains give us a direct window into stellar nucleosynthesis and provide probes of processes in interstellar space and in the solar nebula. Known types of presolar grains originated in the winds or ejecta of stars that lived and died before the solar system formed. After presenting a short history of how presolar grains came to be recognized, we describe how to identify presolar grains, the techniques used to study them, and the various types of grains currently available for study. We then review what presolar grains can tell us about stellar nucleosynthesis, the environments around evolved stars and in the interstellar medium, and how they can be used as probes of conditions in the early solar system.

Grains that predate the solar system

In recent years, a new source of information about stellar nucleosynthesis and the history of the elements between their ejection from stars and their incorporation into the solar system has become available. This source is the tiny dust grains that condensed from gas ejected from stars at the end of their lives and that survived unaltered to be incorporated into solar system materials. These *presolar grains* (Fig. 5.1) originated before the solar system formed and were part of the raw materials for the Sun, the planets, and other solar-system objects. They survived the collapse of the Sun's parent molecular cloud and the formation of the accretion disk and were incorporated essentially unchanged into the parent bodies of the chondritic meteorites. They are found in the fine-grained matrix of the least metamorphosed chondrites and in interplanetary dust particles (IDPs), materials that were not processed by high-temperature events in the solar system.

There are two types of presolar grains. *Circumstellar condensates* condensed from hot gas ejected from dying stars in the immediate vicinity of their parent stars. They are also sometimes called *stardust*. Circumstellar condensates give snapshots of the life histories of the stars from which they formed. Although the stars themselves no longer exist, the

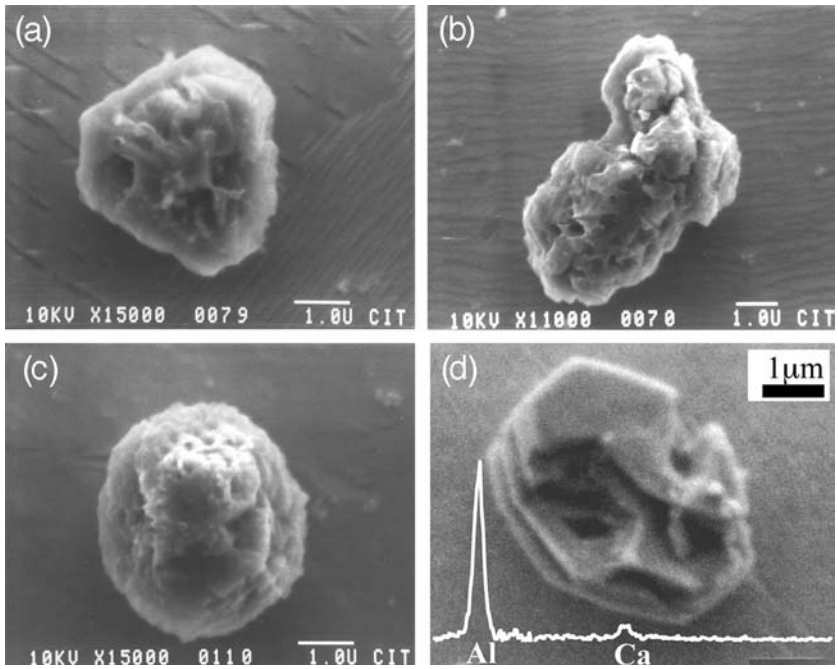

Fig. 5.1 Examples of presolar silicon carbide from the Orgueil meteorite (a, b, c) and hibonite from the Semarkona meteorite (d). These are relatively large for presolar grains. Note the geometric outlines of crystal faces in images (a) and (d). Image (d) is reproduced by permission of the AAS.

grains can tell us the mass and metallicity of the stars and the stages of their evolution when the grains formed. Most of the known types of presolar grains are circumstellar condensates.

Interstellar grains are those that formed in interstellar space. These grains have no direct association with a specific stellar source. Their constituents started out in stars, just as those that make up circumstellar condensates, but either they did not condense into grains immediately after being ejected from stars, or the grains into which they were originally incorporated were vaporized in interstellar space by supernova shocks or by intense radiation. The atoms subsequently recondensed into grains in dense molecular clouds. Interstellar grains probably have poorly defined compositions and structures. They are unstable and are easily transformed to crystalline grains in high-energy environments such as the solar nebula. Most of the material that was to become the solar system likely resided in interstellar dust grains, but these are hard to recognize and only a handful of candidates are currently known.

The potential of presolar grains to provide information about nucleosynthesis, stellar evolution, galactic chemical evolution, interstellar processes, and nebular processes is only beginning to be tapped. But as new instrumentation is developed, more and more of the information that they carry will be extracted.

A cosmochemical detective story

By the 1960s, mass spectrometers were evolving from specialty tools to investigate fundamental physics questions to more general analytical tools that could be used by geochemists and cosmochemists. After some false starts, where reported isotopic anomalies in meteorites turned out to be experimental artifacts, most workers came to the conclusion that the isotopic compositions of the elements in the solar system were consistent with a single homogeneous mixture. The only known isotopic variations could be explained either as the result of radioactive decay or of processes that resulted in mass-dependent fractionation of isotopes. At about the same time, Alastair Cameron published a theoretical model that indicated that the solar system must have passed through a stage where temperatures were so high that all solids had evaporated (Cameron, 1962). The solar system would have been completely homogenized isotopically in passing through this stage, so the apparent absence of isotopic anomalies was consistent with theory. But even at this time, there was an exception to this picture, although it was not recognized as such. In 1964, John Reynolds and Grenville Turner, working at the University of California at Berkeley, reported two types of isotopic anomalies in the noble gas, xenon, from the Renazzo chondrite. There were clear excesses of ^{129}Xe, which were attributed to the decay of extinct radioactive ^{129}I (discussed more fully in Chapter 8). But there was also a general anomaly in the form of excesses of the heavy isotopes of xenon (^{134}Xe, ^{136}Xe) relative to the underlying meteoritic composition. The authors did not make much of these excesses, but attributed them to some form of nuclear fission. This was the first evidence of presolar grains in meteorites.

The story of how the xenon anomalies led to the discovery of presolar grains is full of twists, turns, dead ends, and luck. During the 1960s, excesses of heavy xenon isotopes were found in a number of carbonaceous chondrites. The pattern of the excesses is similar to that expected from fission, but it does not match the pattern produced by uranium fission. This xenon component became known as *CCFXe*, for Carbonaceous Chondrite Fission Xenon. In 1972, Oliver Manuel and colleagues at the University of Missouri at Rolla showed that the supposed fission xenon is accompanied by excesses of the lightest xenon isotopes (Fig. 5.2). They proposed that the excesses resulted from the release of an "isotopically anomalous xenon" component, which they called *Xe-X*, that contained excesses of both heavy and light isotopes. This interpretation was not immediately accepted, however. A more popular explanation of the Xe-X pattern was that it was due to severe mass-dependent fractionation favoring the light isotopes plus fission xenon.

Meanwhile, work was being carried out to determine the parent of the supposed fission xenon component. In 1971, Calvin Alexander, working at Berkeley, measured the isotopic composition of a sample of plutonium that had been produced by a nuclear reactor. The sample was heated to release all trapped gases and then left on a shelf for 23 months to allow pure plutonium fission xenon to accumulate. The resulting precise composition of plutonium fission xenon eliminated plutonium as the parent of CCFXe. Another hypothesis, championed by Edward Anders of the University of Chicago, was that the CCFXe had been produced by fission of a super-heavy element. Nuclear physicists had presented theoretical

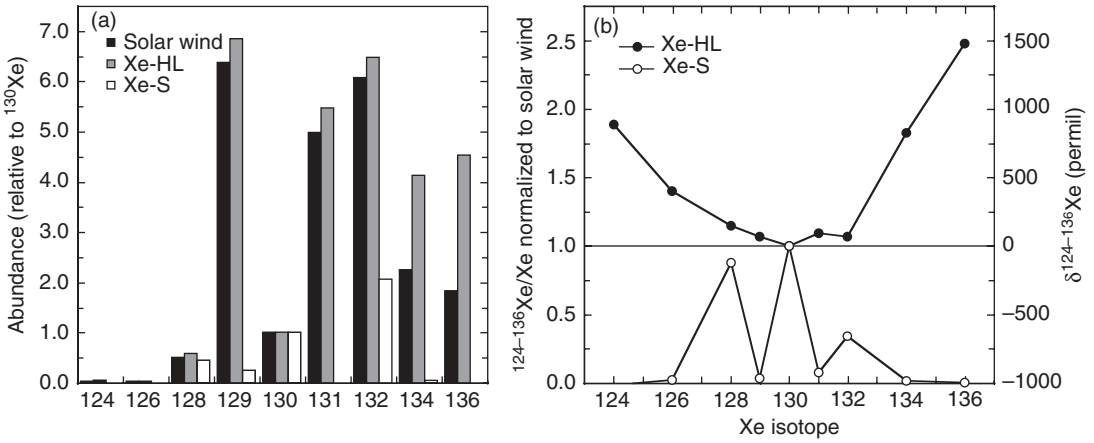

Fig. 5.2 Isotopic compositions of Xe-HL and Xe-S compared to the isotopic composition of solar-wind xenon. In (a), the isotopic abundances of all three compositions are shown as histograms, normalized so that ^{130}Xe has the same abundance in all of them. In (b), the Xe-HL and Xe-S compositions have been normalized to the composition of solar xenon, which now plots as a flat line at Y=1 (0 in delta notation). This plot highlights the deviations from the solar-wind composition. Xe-HL has large excesses of the heaviest (H) and lightest (L) isotopes. Xe-S consists of only the middle five xenon isotopes. Delta notation, shown on the right axis, is given by $\delta^{xxx}Xe/^{130}Xe = [((^{xxx}Xe/^{130}Xe)_{HL}/(^{xxx}Xe/^{130}Xe)_{solar})\text{-}1] \times 1000$. This notation was devised to facilitate discussions of isotopic shifts relative to a standard composition and works well for shifts of a few parts in 10^2 to 10^3. However, with large shifts it becomes very asymmetrical, with the maximum positive value of infinity and a maximum negative value of −1000.

arguments that nuclei near proton number 114 and neutron number 184, heavier than any known natural nuclide, might form an "island of stability" and might be stable enough to survive for some time in nature.

In 1975, during a search for the supposed carrier phase of the super-heavy element, Roy Lewis, B. Srinivasan, and Anders made a remarkable discovery. To isolate the carrier of CCFXe, these workers dissolved a sample of the Allende carbonaceous chondrite in a caustic acid mixture. They found that a residue containing <1% of the starting mass contained most of the noble gases in the bulk meteorite. They further discovered that when they treated this residue with oxidizing nitric acid, the major noble gas component in the meteorite was removed, leaving behind the CCFXe in almost pure form. The mass loss involved in this "etching" was very small. Based on this work, these authors named the carrier of the major noble gas component in carbonaceous chondrites Q, for quintessence. The remaining residue that carried the CCFXe was dominated by chromite, which they assumed to be the carrier.

For the next decade, the Berkeley group under John Reynolds and the University of Chicago group under Edward Anders struggled to identify the carrier of CCFXe. The Berkeley group focused on carbonaceous material, while the Chicago group designed their work around finding the mineral that would have carried the supposed super-heavy element postulated to be the parent for CCFXe.

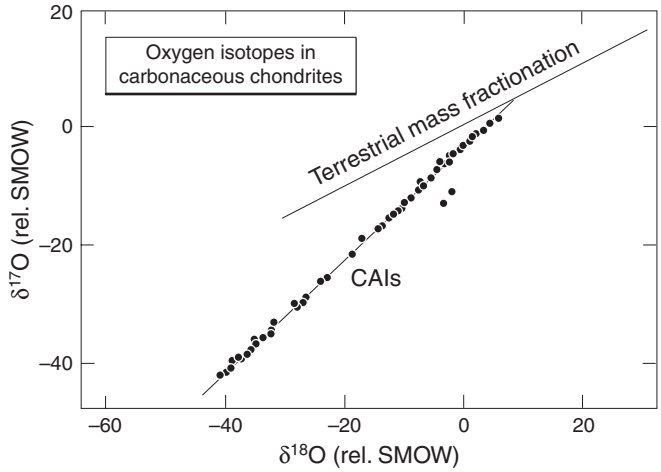

Fig. 5.3 **Oxygen 3-isotope plot showing excesses of ^{16}O in minerals from calcium-aluminum inclusions (CAIs). All samples from Earth rocks plot along the terrestrial fractionation line. Mass-dependent fractionation processes cannot move a composition off of this line, so the excesses of ^{16}O were clearly isotopic anomalies. After Clayton *et al.* (1977).**

As the search for the carrier of CCFXe was going on, several important related discoveries were made. In 1969, David Black and Robert Pepin, working at the University of Minnesota, reported extreme isotopic variations in neon from the Orgueil carbonaceous chondrite. They defined five neon components, which they labeled A through E. Neon-E was inferred to be almost pure ^{22}Ne. The only plausible source that these authors could come up with for pure ^{22}Ne was the decay of very short-lived ^{22}Na (half-life = 2.6 years). These authors stated that the carrier of the Ne-E was likely to be presolar material, having survived from a stellar source where ^{22}Na was produced. This interpretation did not attract much attention at the time.

In 1973, Robert Clayton, Larry Grossman, and Toshiko Mayeda, of the University of Chicago, reported the discovery of isotopic anomalies in oxygen that could not be explained by known processes operating in the solar system. Analyzing calcium-aluminum-rich inclusions, these authors found an array of oxygen compositions that varied in the amount of ^{16}O present and that plotted along a slope ~1 line on an oxygen three-isotope plot (Fig. 5.3). These anomalies were interpreted as reflecting addition of material from a supernova that exploded shortly before the solar system formed.

In 1978, Srinivasan and Anders reported that a highly processed acid residue from the Murchison meteorite had a xenon composition enriched in ^{128}Xe and ^{130}Xe and depleted in ^{129}Xe, ^{131}Xe, ^{134}Xe, and ^{136}Xe. When they calculated the pure end-member composition, they found a component that almost exactly matched predictions for *s*-process nucleosynthesis (Fig. 5.2). Again, the authors had to postulate that presolar dust grains were the carrier of this new component that they called Xe-S.

By the end of the 1970s, support for the fission hypothesis for the origin of CCFXe was waning, and over the next few years the component's name was changed to Xe-HL, which describes the enrichments in Heavy and Light xenon isotopes without ascribing a mode of

origin. Searches continued for the carriers of Xe-HL, Xe-S, and Ne-E at Berkeley and Chicago, and in Bern, Switzerland, under the direction of Peter Eberhardt.

Starting with the discovery of oxygen isotopic anomalies in Allende refractory inclusions and continuing at an increasing pace throughout the early 1980s, a stream of isotopic anomalies in many elements (strontium, neodymium, titanium, calcium, etc.) were reported (summarized by Clayton *et al*., 1988). These discoveries posed a serious challenge to the idea that the solar system was isotopically homogeneous. In addition, by the late 1980s, many theoretical models were also showing that the accretion disks around newly forming stars are not hot enough to vaporize pre-existing dust except very close to the star. These observations and models implied that the solar nebula did not pass through a hot gaseous stage where all dust was evaporated. Thus, by the late 1980s, the stage was set for the discovery of surviving presolar grains.

The discovery happened by accident. Lewis and Anders were frustrated by their failure to find the carrier of anomalous xenon in carbonaceous chondrites. They decided to try an extreme treatment to see if they could dissolve the carrier. They treated a sample of the colloidal fraction of an Allende residue with the harshest chemical oxidant known, hot perchloric acid. The black residue turned white, and to their surprise, when they measured it, the anomalous xenon was still there! The residue consisted entirely of carbon, and when they performed electron diffraction measurements on it, they found that it consisted of tiny (nanometer sized) diamonds. After a detailed characterization that included chemical, structural, and isotopic studies, they reported the discovery of presolar diamond in early 1987 (Lewis *et al*., 1987). The 23-year search for the carrier of CCFXe (Xe-HL) was over, and the study of presolar grains had begun.

The carriers of anomalous Ne-E (two forms of which were now known) and Xe-S were quickly identified. Neon-E(H), which is released at temperatures above ~1200 °C in stepped heating experiments, and Xe-S were found to be carried in presolar silicon carbide (Tang and Anders, 1988). Neon-E(L), which is released below ~900 °C, was found to be carried by presolar graphite (Amari *et al*., 1990). Once these presolar compounds were shown to be present in meteorites, studies were carried out to identify all of the different types of meteorites that carry presolar grains. Concentrated searches for other presolar phases were also initiated, and many new types of presolar grains have been found. This work is just beginning, however, and we cannot yet account for the majority of the presolar components that must have been present in the Sun's parent molecular cloud.

Recognizing presolar grains in meteorites

At the present time, the only way to definitively identify a grain as presolar is by its exotic isotopic composition. The logic is based on the old idea that the solar system passed through a hot gaseous stage during which all pre-existing solids evaporated, producing a single homogeneous isotopic composition. Any grain that has an isotopic composition that cannot be explained in terms of known processes (radioactive decay, mass-dependent fractionation) acting on this solar-system composition must have originated elsewhere. Although few

believe any longer that the solar system was homogenized in this way, this reasoning is still basically valid. Most processes acting in the solar system and on planetary bodies (evaporation, melting, dissolution by a fluid, etc.) tend to homogenize the isotopic composition of the starting materials. So an object with an anomalous isotopic composition must have survived homogenizing processes. A stronger case for a presolar origin can be made if the observed isotopic composition can be explained by a process operating elsewhere, such as nucleosynthesis in stars. We will present examples of such compositions later in this chapter.

In practice, it is not sufficient for an object to have an isotopic composition that cannot be explained by radioactive decay or mass-dependent fractionation effects. The object must also have *physical and chemical* characteristics making it unlikely to be a product of solar system processes. For example, millimeter- to centimeter-sized refractory inclusions from primitive chondrites have been shown to contain small (parts in 10^3 to 10^4) isotopic anomalies in many elements. However, based on the size, composition, physical characteristics, and abundance of the inclusions, it is generally believed that these objects formed within the solar system. They preserve small isotopic anomalies because they did not form from a representative sample of the bulk solar system (see Chapters 7 and 14). So, isotopic anomalies can indicate either that an object is itself presolar or that it formed in the solar system from precursor material that was not fully homogenized in the solar system. As mass spectrometry has become more precise, small isotopic anomalies of the second type have shown up in a wide variety of chondritic materials. As we discuss below and in Chapter 7, these anomalies and bona fide presolar grains can be used as probes of processes in the early solar system.

As noted previously, most of the presolar grains so far identified are circumstellar condensates (stardust), but some grains formed in interstellar space. The interstellar grains are not likely to contain large isotopic anomalies. So how can we recognize these interstellar grains in meteorites?

Although we have not found other characteristics that are as definitive as anomalous isotopic composition, there are a number of ways to potentially recognize interstellar grains. A general idea of the nature of most interstellar dust comes from astronomical observations, which give information on the size, shape, composition, and structure of dust particles. These observations indicate that interstellar dust has a power-law size distribution that peaks at around 0.1 microns. Polarization studies indicate that interstellar grains tend to be elongate rather than equant. The abundances of elements in the gas phase in the diffuse interstellar medium are inversely proportional to their condensation temperature. Volatile elements tend to remain in the gas phase, whereas the moderately volatile and refractory elements are located mostly in the dust. Structurally, most of the dust appears to be amorphous. Upper limits on the crystalline fraction are in the order of a few percent. This is consistent with formation via condensation in a cold environment where kinetics inhibit the formation of well-crystallized mineral phases. Based on these observations, much of the dust that went into making the solar system consisted of <1-micron grains of amorphous material containing moderately volatile and refractory elements in approximately bulk solar system abundances. Unfortunately, material like this is very susceptible to being altered or destroyed by processes in the accretion disk or within meteorite parent bodies, where temperatures are higher and liquid water may have been present. However, material like

that expected from astronomical observations does occur in a handful of the least altered chondrites.

Some of the common processes that operate in interstellar space should leave recognizable effects in grains. For example, high-energy galactic cosmic rays, atomic nuclei traveling near the speed of light, permeate the galaxy. These cosmic rays are strongly attenuated in the inner solar system by the Sun's magnetic field, but dust grains in interstellar space are subject to a constant bombardment. This bombardment disrupts the structure of silicate grains and can turn crystals into amorphous grains. Atoms can be ejected from the grains and atomic nuclei can break into smaller pieces (a process known as spallation). The internal structure of a silicate subject to tens of millions of years of cosmic ray bombardment should have been almost completely destroyed and its composition modified. In the mid 1990s, John Bradley found a large number of tiny amorphous grains within interplanetary dust particles (IDPs, discussed in Chapter 9). He named these Glassy particles with Embedded Metal and Sulfide, *GEMS*, and proposed that they might be presolar grains (Bradley, 2004). But without isotopic data to back up his proposal, this idea has remained controversial. With the invention of a new generation of ion microprobes in the early 2000s, particularly the NanoSIMS, it has become possible to measure the isotopic compositions of the GEMS in IDPs. Most have isotopic compositions indistinguishable from solar-system values (although the uncertainties are large), but a few have exhibited isotopic anomalies that label them as true presolar grains. Now the debate centers on the isotopically "normal" GEMS. Are they presolar as well?

Cold molecular clouds exhibit deuterium/hydrogen ratios up to ~125 times the value for the average interstellar medium. It is believed that high D/H ratios in molecular clouds result from ion-molecule reactions involving organic molecules on grain surfaces. Given enough time, extreme enrichments are possible. Meteorites and IDPs also contain organic material with high deuterium/hydrogen (D/H) ratios, up to ~25 times the value in the local interstellar medium. The molecules that carry these isotopic anomalies may be derived from the Sun's parent molecular cloud and thus may be presolar components. The isotopic compositions of organic matter in meteorites are discussed in Chapter 10.

Known types of presolar grains

Approximately 20 different types of material have been identified as presolar (Table 5.1). The carbon-rich types were the first to be recognized. These were the phases that survived chemical treatments and either had anomalous noble gases to serve as beacons to guide the search or were found inside presolar graphite or silicon carbide grains. These materials have chemical compositions that are alien to the solar system (oxides are typically more stable in our system, due to the abundance of oxygen). Presolar oxides and nitrides were the next types to be found. They survived the harsh chemical treatments and were found primarily by measuring their oxygen isotopic compositions by ion microprobe. Silicates were not identified until later because they are destroyed by the chemical treatments used to separate carbon-rich grains and oxides. *In situ* measurements of thin sections using isotope-ratio

Table 5.1 Known types of presolar grains

Name	Composition	Size	Matrix-normalized abundance
Diamond	C	1–2 nm	1500 ppm
Silicon carbide	SiC	0.1–10 μm	10–15 ppm
Graphite	C	0.1–20 μm	5–10 ppm
TiC, MoC, ZrC, RuC, FeC, Fe–Ni	Inside other materials	1–25 nm	n.d.
Spinel	$MgAl_2O_4$	0.1–20 μm	1.2 ppm
Corundum	Al_2O_3	0.2–3 μm	100 ppb
Hibonite	$CaAl_{12}O_{19}$	1–5 μm	20 ppb
TiO_2	TiO_2	n.d.	<10 ppb
Si_3N_4	Si_3N_4	1–5 μm	1–20 ppb
Forsterite	Mg_2SiO_4	0.2–0.5 μm	10–1800 ppm
Enstatite	$MgSiO_3$	0.2–0.5 μm	10–1800 ppm
Amorphous silicate	variable	0.2–0.5 μm	20–3600 ppm
D-rich organics	HCNO	n.d.	n.d.
Carrier of P1 (=Q) noble gases	Probably organic compounds	n.d.	n.d.

mapping have located these phases. Deuterium-rich organic matter probably contains a presolar component, but the organic fraction consists of many different compounds with a variety of different histories. Techniques are not yet available to identify individual presolar organic compounds. The carrier of the dominant heavy-noble-gas component in chondrites has not been identified, but it is likely to be some kind of organic material. An origin in cold interstellar molecular clouds has been proposed to explain the high abundance of the heavy noble gases, the low abundances of helium and neon, and the close association of the carrier with presolar diamond, silicon carbide, and graphite. The list of presolar compounds is likely to grow rapidly in the next decade as we better characterize the material that makes up the most primitive chondrites, IDPs, and comet samples.

Identification and characterization of presolar grains

Locating and identifying presolar grains

There are two basic approaches to locating and identifying presolar grains for further study. One approach – the one used to find the first presolar grains – can be likened to burning down the haystack to find the needle. Meteorite samples are dissolved in a series of strong acids, leaving behind only the most acid resistant phases (spinel ($MgAl_2O_4$), corundum (Al_2O_3), hibonite ($CaAl_{12}O_{19}$), silicon carbide (SiC), diamond, graphite, etc.), many of which are presolar. Details of this chemistry can be found in Amari *et al*. (1994) and Huss and Lewis (1995). This method is used now primarily to generate large collections of presolar grains for survey work or to investigate in detail a particular aspect of stellar nucleosynthesis (see below).

We now know that the haystack is important as well. Therefore, searches are now carried out on material that has been either minimally processed or not processed at all. The secondary ion mass spectrometer (SIMS), also known as the ion probe, is the instrument used for this work. The ion probe uses a focused beam of high-energy ions to sputter and ionize atoms from the sample. These secondary ions are analyzed using a high-performance mass spectrometer. Modern ion microprobes such as the NanoSIMS or Cameca ims 1270 or 1280 equipped with a solid state imaging detector called SCAPS (see Appendix) have spatial resolutions of 100–500 nm, similar to or smaller than the sizes of most presolar grains, so these instruments can be used to identify presolar grains *in situ* in meteorite matrix or in interplanetary dust particles (IDPs). To search for presolar grains, the ion microprobe is used in ion-imaging mode to make isotope ratio maps. Presolar grains show up as "hot spots" on these maps. The isotopes of oxygen, a major element in many types of grains, are commonly used in this work. The technique can also be applied to separates from meteorites that are enriched in presolar grains relative to the bulk meteorite. Isotope-ratio mapping by ion probe resulted in identification of the first presolar silicates (forsterite, enstatite, amorphous silicate) in meteorites and IDPs (Messenger *et al*., 2003; Nguyen and Zinner, 2004; Nagashima *et al*., 2004).

Characterization of presolar grains

Once the grains are identified, the next task is to characterize them. Properties of interest include size, shape, crystal structure, major-, minor-, and trace-element composition, and isotopic composition. When presolar grains were first discovered, scientists were only able to determine the basic mineralogy and show that the grain was presolar by measuring the isotopic compositions of one or two elements. However, it soon became clear that more information on each grain was needed to fully understand their sources and their history. Major progress has been made in this direction, and it is now possible to gather detailed structural and chemical information and to measure isotopic compositions of five or six elements in the same 2–3 μm grain. Some techniques are destructive, while others are not. To get the most information from a grain, it makes sense to use the non-destructive techniques first. Non-destructive techniques can provide chemical and, occasionally, structural data on a presolar grain, but unfortunately they cannot unequivocally identify a grain as presolar. Therefore, as described above, the ion microprobe is commonly used to identify the grains, particularly silicates, and then a combination of destructive and non-destructive techniques can be applied to characterize them.

Grains found *in situ* pose a special problem. Because other grains surround them in a close-packed arrangement, clean measurements of their chemical and isotopic compositions are difficult to make. The grains can be removed from the surrounding material using a focused ion beam (FIB) lift-out technique (see Appendix), but this is currently very time consuming. The most detailed information comes from grains that have been separated by physical and chemical means from the surrounding material.

Nondestructive characterization

Morphological information and major-element compositions can be obtained using a scanning electron microscope (SEM). The SEM uses a focused electron beam to scan the sample and creates an image from either secondary electrons or backscattered electrons. Features as small as several tens of nanometers can be resolved on the surfaces of presolar grains with field emission SEMs (see Appendix). The chemical composition can be determined with an energy dispersive X-ray spectrometer (EDS), which measures characteristic X-rays excited in the sample by the electron beam of the SEM. The spatial resolution of the SEM-EDS combination is ~1 μm. The auger microprobe, which studies electrons emitted at characteristic energies, can analyze the composition of a thin layer on the surface of a grain and has a spatial resolution of $\leq$20 nm. This instrument is thus very useful in gathering chemical information on small presolar grains *in situ* in a meteorite matrix or in an IDP. Raman spectroscopy, which measures the inelastic (Raman) scattering of laser light, can identify the mineralogy of grains and can provide basic structural information for some materials. It is particularly useful to study the structural characteristics of organic materials. Modern micro-Raman systems have spatial resolutions approaching 1 μm. Electron backscatter diffraction (EBSD) examines the diffraction patterns of electrons scattered at low angles from the surface layers of a sample. The diffraction patterns are characteristic of the internal structure of a mineral grain. This technique is normally applied to carefully prepared polished sections, but in some instances it can produce a pattern from an isolated presolar grain. All of these techniques are non-destructive; the sample remains for further analysis.

The transmission electron microscope (TEM) is a powerful tool to study the internal structure and composition of a presolar grain. The TEM can obtain images and chemical compositions on objects as small as a few tens of nanometers across (Fig. 5.4) and can resolve the atomic structure of a grain from lattice fringe effects. The TEM requires a very thin (tens of nanometers thick) sample to get good electron diffraction and electron-energy-loss spectral (EELS) data. TEM measurements require careful sample preparation, which is, in part, destructive. Presolar grains are typically sliced in a microtome and the slices are mounted on porous grids for analysis. Exquisitely detailed information can be obtained from these sections, but one has little control over which section will be in the right place on the sample mount to be studied. The FIB technique can also prepare samples for TEM work. This technique uses the ion beam to remove all of the material of no interest, leaving behind a well-characterized sample for TEM analysis. These techniques are discussed in more detail in the Appendix.

Even more elaborate instruments are now used to determine the chemical composition of interplanetary dust particles and comet grains. Some day these techniques might also find applications in the study of presolar grains. There are several techniques based on synchrotron radiation that can only be performed at synchrotron facilities such as the Advanced Light Source at Lawrence Berkeley Laboratory, the Advanced Photon Source at Argonne National Laboratory, or the National Synchrotron Light Source at Brookhaven National Laboratory, among others. These facilities are supported by large facility grants and users apply for beam time, which is generally provided at no cost to the user. An important synchrotron technique is X-ray absorption near-edge spectroscopy (XANES), which uses

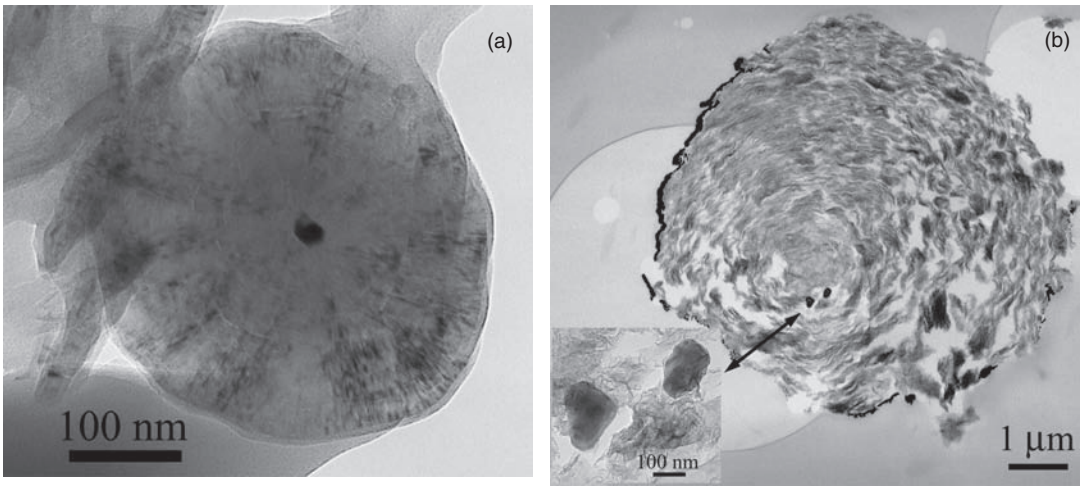

Fig. 5.4 TEM images of presolar graphite. (a) An "onion type" presolar graphite grain containing a central titanium-vanadium carbide grain. This grain apparently served as a nucleation site for the graphite. (b) A "cauliflower type" graphite showing concentric layers of graphite and two (Ti,Zr,Mo)C crystals, indicated by the arrows. Images from Kevin Croat.

hard X-rays to investigate the electronic structure of target materials and can investigate the element composition, oxidation state, and symmetry of a material. Spot sizes as small as 50–100 nm are possible. Scanning transmission X-ray spectroscopy allows a map of a target to be generated by scanning the X-ray beam over the sample. Synchrotron techniques are nominally non-destructive, although X-ray beams carry a lot of energy and can disrupt the structures of some materials. To date, they have not been used specifically for presolar-grains work.

Destructive techniques

In order to get isotopic information about a grain it is necessary to count the atoms, which means that the grains must be at least partially destroyed. The ion probe can measure the major-, minor-, and trace-element abundances and isotopic compositions of presolar grains. Several types of ion probes are used (see Appendix). With the earlier generation of ion probes, it was possible to measure the isotopic compositions of silicon, carbon, nitrogen, magnesium, and titanium in individual 4 to 8 μm-sized grains (e.g. Fig. 5.1). With the newer, more sensitive instruments, multiple elements can be measured in considerably smaller grains. But even the most sensitive ion probes put only about one atom in 10^3 to 10^4 into the detector to be counted.

Resonance ionization mass spectrometry (RIMS) is much more efficient at getting ions into the detectors. First, atoms are removed from the sample surface with a pulsed laser, which can release the atoms thermally without ionizing them. Then, by using carefully tuned lasers, the element of interest in the resulting gas plume can be ionized at almost 100% efficiency, while other elements are not ionized at all. The ions are extracted into a time-of-flight

mass spectrometer and measured. A RIMS instrument is thus ~10^3 times more sensitive than an ion microprobe. The CHARISMA instrument, located at Argonne National Laboratory, has measured the isotopic compositions of trace elements such as strontium, zirconium, molybdenum, ruthenium, and barium in individual presolar silicon grains (Nicolussi *et al*., 1998). In some cases, two elements were measured in the same grain.

Bulk techniques such as noble-gas mass spectrometry, thermal-ionization mass spectrometry (TIMS), and inductively coupled plasma mass spectrometry (ICPMS) can be used to measure trace elements in presolar grains. These techniques give the most precise isotopic results of any technique, but to utilize this capability, one must have enough atoms. For some elements, there are not enough atoms in a single grain to provide a meaningful isotopic composition. Consider xenon, which has nine isotopes that vary in abundance by a factor of ~200. In order to get a meaningful isotopic composition, ~30 000 atoms must be measured. But only about one in a million presolar diamonds has a xenon atom in it, and a single 1-μm presolar SiC grain only has ~1000 xenon atoms. Thus, large collections of grains must be measured at one time, and the resulting compositions are averages from many stellar sources. Such compositions still provide important information, and bulk measurements of noble gases led to the discovery of presolar grains in the first place.

Bulk techniques still have a place in the search for presolar components. Although they cannot identify the presolar grain directly, they can measure anomalous isotopic compositions, which can then be used as a tracer for separation procedures to identify the carrier. There are several isotopically anomalous components whose carriers have not been identified. For example, an anomalous chromium component enriched in ^{54}Cr appears in acid residues of the most primitive chondrites. The carrier is soluble in hydrochloric acid and goes with the colloidal fraction of the residue, which means it is likely to be submicron in size (Podosek *et al*., 1997). Measurements of molybdenum and ruthenium in bulk primitive meteorites and leachates from primitive chondrites show isotopic anomalies that can be attributed to the *s*-process on the one hand and to the *r*- and *p*-processes on the other. The *s*-process anomalies in molybdenum and ruthenium correlate with one another, while the *r*- and *p*-process anomalies do not. The amounts of *s*-process molybdenum and ruthenium are consistent with their being carried in presolar silicon carbide, but they are released from bulk samples with treatments that should not dissolve that mineral. Thus, additional carriers of *s*-, *r*-, and *p*-process elements are suggested (Dauphas *et al*., 2002).

Identification of stellar sources

Grains from AGB stars

Most presolar silicon carbide and oxide grains and a significant fraction of presolar silicate grains found in meteorites come from low- to intermediate-mass stars in the asymptotic giant branch (AGB) phase (see Chapter 3). Evidence for this conclusion derives from two sources: (1) spectroscopic observations of the envelopes of these stars; and (2) comparison

of the measured compositions of presolar grains with theoretical models of stellar nucleosynthesis.

Spectroscopic observations have provided important information about nucleosynthesis in low- and intermediate-mass stars. AGB stars of low to intermediate mass often show high abundances of *s*-process elements in their envelopes. These elements are brought to the surface during third dredge-up mixing events (Chapter 3). Although these observations do not tell us anything about the isotopic compositions of the *s*-process elements, their high abundances in stellar envelopes show that *s*-process synthesis is going on. One of the first indications that presolar grains were present in meteorites was the discovery of Xe-S in an acid residue of the Murchison meteorite (Fig. 5.2). Presolar silicon carbide grains carry *s*-process signatures in krypton, xenon, barium, strontium, neodymium, samarium, and other elements.

Spectroscopic observations have also identified a class of AGB stars in which carbon is more abundant than oxygen. These are known as carbon stars. Before the discovery of presolar grains, theoretical modeling had shown that the envelopes of low-mass stars could become carbon-rich through the dredge-up of ^{12}C from the helium shell during the AGB phase (Iben and Renzini, 1983). Carbon and oxygen combine to form CO before either combines in significant amounts with other elements. When oxygen is more abundant than carbon, oxide minerals will form using the leftover oxygen. When carbon is more abundant than oxygen, carbon-rich compounds will form from the excess carbon. Carbon stars provide an ideal environment for the formation of carbon-rich presolar grains such as silicon carbide. A strong case that presolar silicon carbide comes from carbon stars can be made from the observations of spectral features of silicon carbide in the outflows of some carbon-rich AGB stars. The case is strengthened further by the close similarity between the $^{12}C/^{13}C$ ratios measured in SiC grains and $^{12}C/^{13}C$ ratios measured spectroscopically in carbon stars (Fig. 5.5). This similarity not only indicates that presolar silicon carbide came from carbon stars, but also that a population of stars much like those in the galaxy today contributed silicon carbide grains to the early solar system, rather than a single carbon star.

Spectroscopic observations show that red giant stars typically have higher $^{17}O/^{16}O$ ratios than the solar system and near solar or slightly lower than solar $^{18}O/^{16}O$ ratios. This is the basic pattern expected in the envelopes of stars where the products of partial hydrogen burning have been mixed into the envelope. Most of the measured red giant stars are in the mass range where they should evolve into AGB stars. Measurements from presolar oxide grains match the stellar observations fairly well (Fig. 5.6), in spite of rather large errors in the stellar measurements. But as the number of measurements of presolar oxide grains increased, and as biases in the screening methods to locate the grains were recognized and accounted for, new groups of oxide grains were recognized that were not obvious in the stellar data.

Theoretical modeling provides strong evidence that most presolar silicon carbide grains come from 1.5 to 3 $M_\odot$ stars. As discussed in Chapter 3, stellar modeling of the evolution of the CNO isotopes in the envelopes of these stars makes clear predictions about the $^{12}C/^{13}C$, $^{14}N/^{15}N$, $^{17}O/^{16}O$, $^{18}O/^{16}O$ ratios as a star evolves. For example, in the envelopes of low- to intermediate-mass stars of solar composition, the $^{12}C/^{13}C$ ratio drops to ~40 (from a starting value of 89), and $^{14}N/^{15}N$ increases by a factor of six as carbon and nitrogen processed by

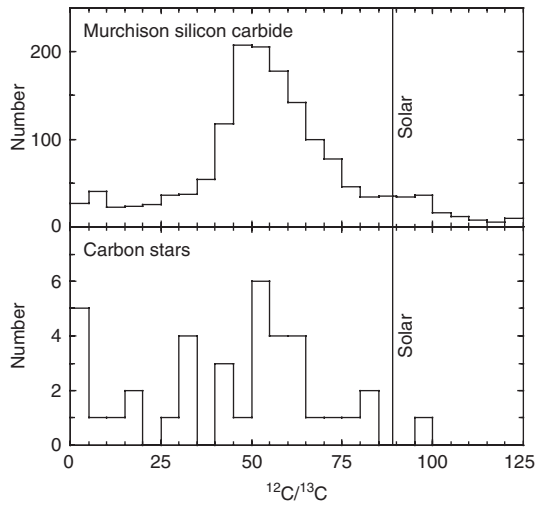

Fig. 5.5 Carbon isotopic compositions of silicon carbide grains from the Murchison meteorite compared with the carbon isotopic compositions of carbon stars (low- to intermediate-mass AGB stars). The composition of carbon in the solar system is indicated by the vertical line. Note the similarity in the distributions of compositions in the two plots. These data indicate that the silicon carbide in the Orgueil meteorite came from a population of carbon stars very similar to that in the galaxy today.

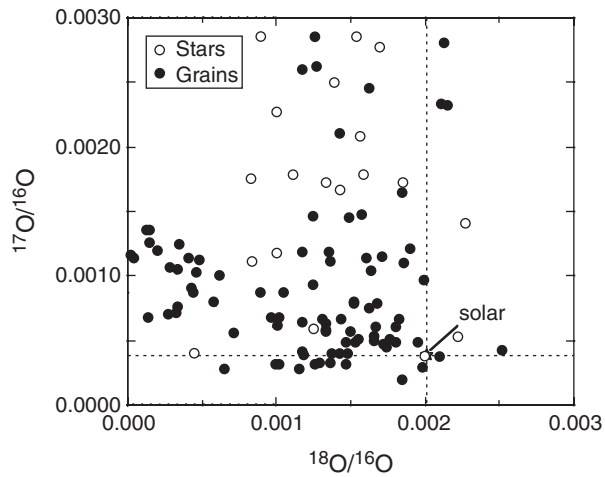

Fig. 5.6 Oxygen isotopic compositions of presolar oxide grains compared with those of red giant stars. Stellar data are shown without error bars, which are large on this scale. Both data sets are characterized by higher $^{17}O/^{16}O$ ratios and lower $^{18}O/^{16}O$ ratios compared to solar oxygen. Stellar data from Smith and Lambert (1990).

hydrogen burning via the CNO cycle during the main sequence are mixed into the envelope by first dredge-up. When the third dredge-up thermal pulses start, newly synthesized ^{12}C from the helium shell is added to the envelope and the $^{12}C/^{13}C$ ratio rises, while nitrogen is unaffected. After several pulses, the actual number of which depends on the stellar mass, the

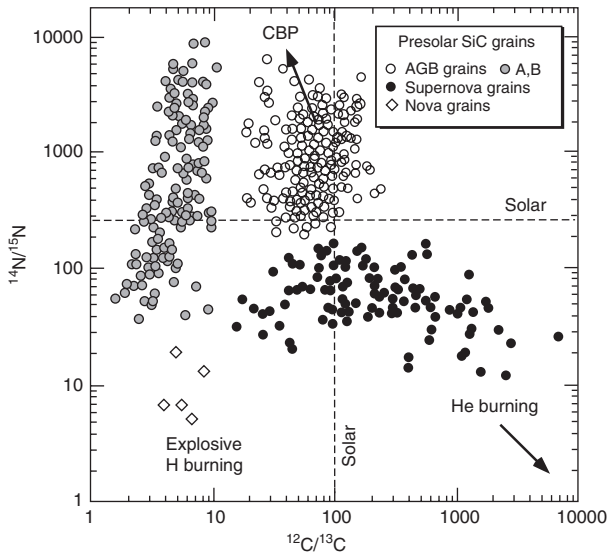

Fig. 5.7 Carbon and nitrogen isotopic ratios for presolar silicon carbide grains. The vast majority of grains (AGB grains) plot above and to the left of the solar composition (indicated by the dashed lines). Grains with $^{14}N/^{15}N$ ratios >2000 and $^{12}C/^{13}C$ ratios <40 are not predicted by standard AGB models. But if extra mixing (cool-bottom processing, CBP) is put into the models, compositions move in the direction of the arrow. Supernova grains, which are rich in ^{12}C from helium burning, plot in the lower right quadrant. Rare grains thought to come from novae, which are powered by explosive hydrogen burning, plot in the lower left quadrant. The sources for the A and B grains are not currently known, but some may be AGB grains. Modified from Zinner (2004).

envelope becomes carbon-rich and SiC grains can form from the star's ejecta. Without extra hydrogen burning in the envelope, the $^{12}C/^{13}C$ ratios can rise to >150. But in stars greater than ~4 $M_\odot$, hot-bottom burning at the base of the envelope processes the new ^{12}C to ^{13}C and on to ^{14}N. The $^{12}C/^{13}C$ ratio continues to drop, approaching the CNO equilibrium value of ~2.5. Such stars probably do not become carbon stars because carbon is converted to nitrogen more quickly than oxygen is and does not accumulate in the envelope. The distributions of $^{12}C/^{13}C$ and $^{14}N/^{15}N$ ratios predicted from models of carbon-rich AGB stars of less than ~4 $M_\odot$ are similar to the distribution exhibited by silicon carbide grains (Fig. 5.7). This similarity supports the idea that silicon carbide grains come from carbon stars. Figure 5.7 also shows silicon carbide grains with $^{12}C/^{13}C$ ratios below ~40 and/or $^{14}N/^{15}N$ ratios above 2000. These grains are not accounted for by standard models, but as we discuss below, the existence of these grains has led to new insight into the structure of low-mass stars.

Oxide grains can form in the winds ejected from red giant stars or from AGB stars before they become carbon-rich (Chapter 3). Theoretical modeling predicts that the stellar envelopes at the time these oxide grains might form should be depleted in ^{18}O and enriched in ^{17}O relative to the starting material, with ^{16}O largely unaffected. The results of such models are summarized on an oxygen 3-isotope plot in Figure 5.8a, along with measured compositions of presolar oxides. For a given initial composition, the envelopes of stars of different

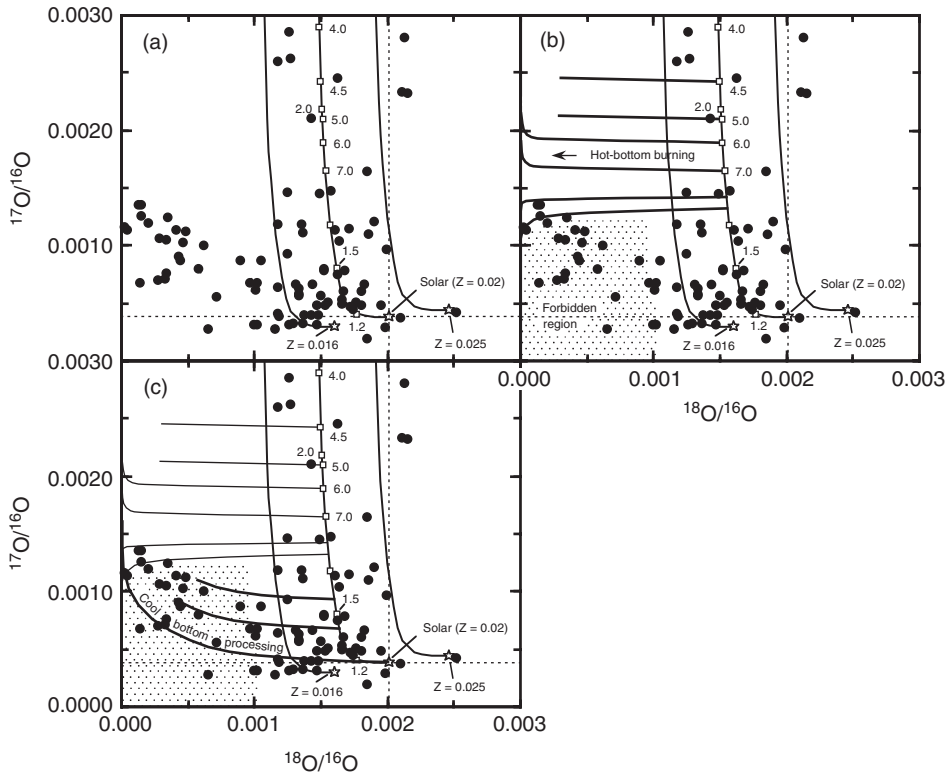

Fig. 5.8 Oxygen 3-isotope plots comparing predictions of stellar models with measurements of presolar oxide grains (solid circles). (a) Solid curves are arrays of final compositions of the stellar atmospheres of stars of masses 1.2 to 7 $M_\odot$ (small open squares). The three curves represent stars of different metallicity; the middle line is solar metallicity, the one on the left is for metallicity 25% less than solar, and the one on the right is for metallicity 25% higher than solar. Oxygen compositions of many grains fall within the area covered by these curves, so the models can successfully explain these grains. But many grains fall to the left of these curves. (b) If hot-bottom burning at the base of the stellar envelope is permitted in the models, the envelopes of stars of mass $\geq$4.5 $M_\odot$ evolve to the left from their positions on the curves in the top panel. Stars that experienced hot-bottom burning can explain grains in the upper left quadrant of the plot, but this quadrant has almost no grains. Grains in the lower left quadrant cannot be explained by this process. (c) Models of low-mass stars that include a parameterized prescription for rotational mixing at the base of the envelope (known as cool-bottom processing) can produce compositions at the lower left of the plot. The match between the grain compositions and these models strongly indicates that three-dimensional models that correctly describe the mixing in a rotating star are required to adequately model the compositions of low-mass stars.

mass at the end of the First Dredge-up define an array of compositions. For all but the least-massive stars, the $^{18}O/^{16}O$ ratio achieves a near-constant value controlled primarily by dilution of processed material by unprocessed material. In contrast, the $^{17}O/^{16}O$ ratio increases with mass to a maximum value for stars near ~4 $M_\odot$, and declines again in stars of higher mass. Different initial compositions produce different arrays. The initial compositions are thought to generally reflect the metallicity of the star, with $^{18}O/^{16}O$ and $^{17}O/^{16}O$

increasing with increasing metallicity. Standard models can explain approximately 75% of the oxide grains that have been measured (Fig. 5.8a), indicating that the grains come primarily from low- to intermediate-mass stars. We will return to the other grains later in this chapter.

Theoretical modeling of the *s*-process is well developed and makes specific predictions that can be tested against the compositions of presolar grains. Noble gas data for presolar silicon carbide show clear *s*-process compositions that agree well with detailed theoretical models. Data for different size fractions show clear evidence for a predicted branching in the krypton *s*-process chain. Unstable ^{85}Kr has a half-life that is long enough for it to capture another neutron before it can decay and become stable ^{86}Kr, if the neutron density is high enough. The abundance of ^{86}Kr varies dramatically among silicon carbide size separates (Fig. 5.9), demonstrating that, on average, larger silicon carbide grains contain krypton processed at higher neutron densities than smaller grains. Isotopic measurements of barium, strontium, neodymium, and samarium in bulk samples of silicon carbide by thermal ionization mass spectrometry match general expectations for the *s*-process. Barium and strontium isotope ratios in bulk samples show a grain-size effect similar to that in krypton, but the relationship between neutron exposure and grain size is opposite to that in krypton. The data described above were obtained from samples containing many silicon-carbide grains, and thus give only a general picture of the *s*-process. Measurements of individual silicon carbide grains by laser resonance ionization mass spectrometry allow direct comparisons of the

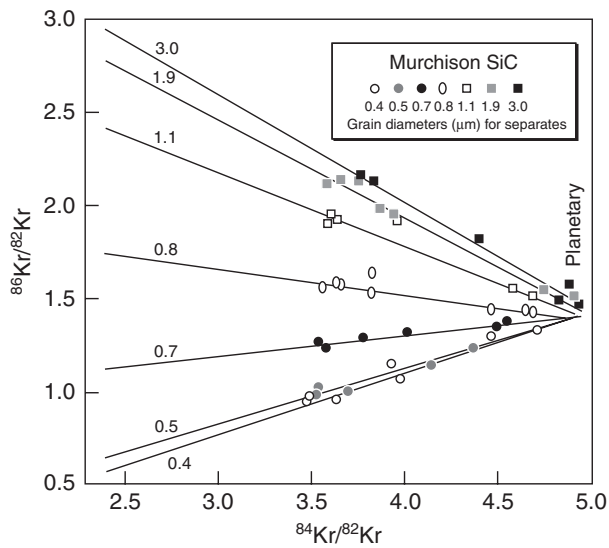

Fig. 5.9 Krypton 3-isotope plot of silicon carbide from the Murchison meteorite, showing that ^{86}Kr/^{82}Kr varies with grain size while ^{84}Kr/^{82}Kr is essentially unchanged. The labeled lines are mixing lines between the *s*-process end-member estimated by Gallino *et al.* (1990) on the left, and normal solar system krypton on the right. The variation in ^{86}Kr/^{82}Kr is due to a branch point in the krypton *s*-process chain that permits the production of ^{86}Kr if the neutron density is high enough. Because neutron density correlates with stellar mass, these data indicate that many stars contributed to the silicon carbide found in the Murchison meteorite. After Lewis *et al.* (1994).

Box 5.1 Can presolar grains constrain the age of the galaxy?

Do presolar grains provide a constraint on the age of the galaxy? Nittler and Cowsik (1997) proposed that they do. Their logic was as follows.

The solar system formed at ~4.57 Ga. In order for a star to contribute grains to the early solar system, it must have completed its life cycle by 4.57 Ga. The lifetimes of stars are a strong function of the stellar mass (see Fig. 3.2), with lifetimes of low-mass stars exceeding 10 Gyr. Silicon carbide grains apparently come mostly from AGB stars of 1.5 to 3 $M_{\odot}$. The lifetimes of such stars range from a few hundred million years to ~1.5 Gyr. Oxide grains apparently come from stars that range from 1.1–1.3 $M_{\odot}$ up to several solar masses. The low-mass end of this range corresponds to stars that live 3–9 Gyr. If the longest-lived star that contributed material to the solar system lived ~9 Gyr, then it must have formed at 9 + 4.57 = 13.57 Ga. This calculation provides a lower limit on the age of the galaxy.

The stars that provided oxide grains to the solar system apparently had metallicities between half of solar and somewhat greater than solar (similar to the case for silicon carbide grains). According to models of galactic chemical evolution, it took a billion years or longer for the average metallicity to reach half the Sun's value. This time must be added to the minimum age estimated above. Nittler and Cowsik (1997) used theoretical curves such as those in Figure 5.8 to estimate the mass and metallicity of the parent stars for a number of grains. This gave them the lifetimes of the parent stars. They then used a galactic chemical evolution model to estimate the time it took for the galaxy to achieve the estimated metallicity. They added this time to the lifetime of the parent star and to the age of the solar system to get an estimate for the galactic age from each grain. They then took an average of the eight oldest determinations to get an estimate for the age of the galaxy of 14.4±1.3 Ga.

Nittler and Cowsik (1997) recognized that their estimate of the galactic age has large systematic uncertainties. The greatest uncertainty comes from the mass estimate for the parent star. For example, increasing the mass from 1.1 to 1.15 $M_{\odot}$ can decrease its lifetime by a billion years. The masses and metallicities of the parent stars are inferred from models of stellar nucleosynthesis, and these models still have significant uncertainties. The theoretical estimates of stellar lifetimes as a function of mass also have uncertainties. Errors can be introduced from the estimate of metallicity, which depends on the accuracy of stellar models. There are also large uncertainties in the galactic chemical evolution models, which means that the time estimated for the galaxy to reach the metallicities inferred for the parent stars of the grains is quite uncertain. In fact, the only number in this calculation that does not have a large uncertainty is the age of the solar system.

In spite of these uncertainties, the resulting estimate of galactic age seems reasonable. The age of the universe is estimated at 13.7±0.2 Ga, and the galaxy must be younger than the universe. Ballpark estimates for the time necessary for galaxies to form are roughly a billion years. So from these considerations, the galaxy should have formed at 12.7 Ga. This is just outside of the quoted uncertainty in the Nittler and Cowsik (1997) estimate. This is reasonable agreement and suggests that as we continue to improve stellar models and our understanding of galactic chemical evolution, presolar grains might provide an independent constraint on the age of the galaxy.

compositions of molybdenum, zirconium, strontium, and barium from discrete times in the lives of individual stars with predictions of theoretical models. Not only are the agreements remarkable, confirming that 1.5 to 3 $M_{\odot}$ stars are the source of the silicon carbide grains, but these data also provide specific tests of nucleosynthetic models (see below).

Supernova grains

Not all presolar grains are derived from AGB stars. Some come from type II supernovae. Massive stars that have exhausted their nuclear fuel experience core collapse, which in turn results in a supernova explosion (Chapter 3). The nucleosynthetic products of a type II supernova are the result of the regular sequence of shell burning in the pre-supernova massive star overprinted by explosive nucleosynthesis. Detailed predictions of the compositions of supernova grains are difficult to make because mixing and the details of the mass cut below which material cannot escape from the star are not understood. However, in general, supernova ejecta should be enriched in ^{12}C, ^{16}O, ^{20}Ne, ^{24}Mg, ^{28}Si, etc., isotopes that are produced from helium, carbon, and oxygen burning. About 1% of the silicon carbide grains in meteorites are highly enriched in ^{12}C and ^{28}Si compared to the AGB grains (Figs. 5.7 and 5.10; such grains are overabundant in these figures because special efforts have been made to find and study these unusual grains). Immediately upon their discovery, these so-called "X" grains were proposed to have come from supernovae. The case was dramatically strengthened when large excesses of ^{44}Ca, the decay product of ^{44}Ti ($t_{1/2}$ = 59 years), were found in the X grains. One grain had 138 times more ^{44}Ca than it should have based on the other isotopic abundances; the calcium was almost pure ^{44}Ca! Other isotopic signatures attributed to type II supernovae include excesses of ^{15}N and ^{18}O relative to solar system nitrogen and oxygen, very high inferred initial abundances of the short-lived radionuclides ^{26}Al ($t_{1/2}$ = 730 000 years) and ^{41}Ca ($t_{1/2}$ = 350 000 years), and excesses of ^{42}Ca, ^{43}Ca, and ^{49}Ti. Supernova grains make up a small percentage of presolar graphite, silicon carbide, and oxide grains and are the dominant source of Si_3N_4 grains.

Nova grains

A few silicon carbide and graphite grains appear to have come from novae (Chapter 3). These grains carry the signatures of explosive hydrogen burning, although the magnitudes of the isotopic effects are not as extreme as models predict. The silicon carbide grains have low $^{12}C/^{13}C$ ratios and very low $^{14}N/^{15}N$ ratios, large ^{30}Si excesses and high $^{26}Al/^{27}Al$ ratios. A nova origin for some graphite grains is indicated by low $^{12}C/^{13}C$ ratios and $^{20}Ne/^{22}Ne$ ratios lower than predicted from models of AGB stars. Very low $^{20}Ne/^{22}Ne$ ratios imply that the ^{22}Ne came from the decay of ^{22}Na ($t_{1/2}$ = 2.5 years). Very low ^{4}He abundances accompanying the low $^{20}Ne/^{22}Ne$ ratios imply that the grains are almost devoid of implanted noble gases.

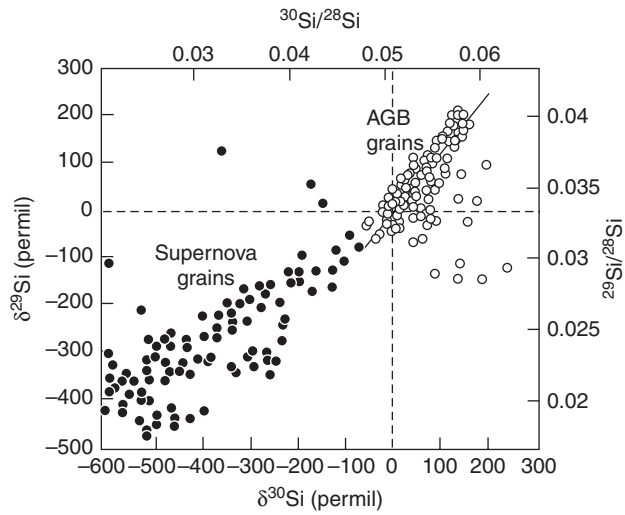

Fig. 5.10 **Silicon isotopic compositions for presolar silicon carbide grains. The top and right axes give the isotope ratios and the left and bottom axes give the ratios in terms of delta notation. Grains from AGB stars tend to fall in the upper right quadrant, with most grains falling along a steep array that passes slightly to the right of the solar composition (dashed lines). This "mainstream" array primarily reflects galactic chemical evolution, although the slight shift to the right of the solar and AGB points significantly to the right of the array probably reflect *s*-process nucleosynthesis in the AGB stars. Grains from supernovae are typically strongly enriched in ^{28}Si and ^{12}C relative to the starting compositions of the parent stars. Modified from Zinner (2004).**

Other stellar sources

The stellar sources of a relatively small fraction of presolar grains, such as the A and B SiC grains (Fig. 5.7) remain unknown. The isotopic compositions of these grains do not match expectations for grains from the sources discussed above. Possible sources include massive Wolf-Rayet stars and J-type carbon stars and other stars whose origin and/or compositions are not well understood. Better modeling, better stellar observations, and more grain data will be required to sort out the sources of these unusual grains.

Presolar grains as probes of stellar nucleosynthesis

Presolar grains provide precise isotopic compositions that give snapshots of the envelope compositions of stars at fixed points in their evolution. But we will never be able to study those stars directly because they no longer exist. In contrast, observational astronomy provides relatively low-precision isotopic measurements of the envelopes of specific stars, which can be studied for many different characteristics. The two data sets complement each other, with the presolar grains providing the detailed information and the astronomical observations providing the context. Data from presolar grains have resulted in a resurgence

of the study of stellar nucleosynthesis. The detailed information from presolar grains points out problems with theoretical models or their input data. The new constraints also permit modelers to investigate processes for which there were previously no observational constraints.

Input data for stellar models

Nuclear reaction rates and neutron-capture cross-sections are key inputs to stellar models. Numerical values for these rates and cross-sections come from laboratory experiments or from theoretical estimates. Some are well determined, while others have large uncertainties. The isotopic compositions of presolar grains have pointed out cases where reaction rates or cross-sections were significantly in error. One spectacular example concerns barium. Early attempts to model the isotopic composition of *s*-process barium in silicon carbide grains produced relatively poor agreement. However, good agreement could be achieved if the neutron-capture cross-sections were adjusted by factors of 30% to more than a factor of two. Gallino *et al*. (1993) proposed that the experimental values were incorrect and made specific predictions for what the correct values should be. A few years later, these predictions were fully confirmed by new experimental determinations (e.g. Beer *et al*., 1997). Similar predictions by Gallino *et al*. (1993) regarding the neutron-capture cross-sections for ^{142}Nd and ^{144}Nd were also confirmed. Other suggestions for reactions and cross-sections that need re-evaluation have been made and are being tested. As models become better and measurements of presolar grains become more precise, additional predictions for improvements in reaction-rate determinations will undoubtedly result.

Internal stellar structure

Presolar grains have also provided examples of where theoretical models are not adequate to describe the internal structure of real stars. Oxygen isotopic data for presolar oxide grains are broadly consistent with low- and intermediate-mass stars as their sources. As already discussed, most grains are significantly enriched in ^{17}O and slightly depleted in ^{18}O relative to the starting compositions of the stars. However, the data for some grains are not consistent with the model predictions. Figure 5.8a shows data for presolar oxide grains compared to the arrays of envelope compositions as a function of mass and initial composition predicted by standard stellar models. Many grains plot well away from the region predicted by the standard models. In intermediate-mass stars, hydrogen burning via the CNO cycle takes place at the base of the convecting envelope after the first dredge-up, destroying ^{18}O and producing ^{17}O, while leaving ^{16}O largely unchanged. This hot-bottom burning shifts the predicted oxygen compositions as shown in Figure 5.8b. However, the region explained by hot-bottom burning has essentially no oxide grains, and most of the oxide grains fall in a "forbidden region" that was not explained by any of the models.

A significant problem with stellar nucleosynthesis models is that they do not adequately describe the *physical* state of the star. To decrease the amount of computer time required to

run the models to a manageable level, most models have been one-dimensional, meaning that the star was assumed to be spherically symmetrical. Convective mixing can be modeled based on density considerations, but effects of mixing generated by stellar rotation cannot. Even before the data for presolar oxides were available, there were observations of low-mass red giant stars that showed lower $^{12}C/^{13}C$ and higher $^{14}N/^{15}N$ ratios in the envelopes than predicted by the models. Extra mixing of envelope material into nuclear burning zones was postulated as an explanation. When extra mixing was put into the models in a parameterized way, it was found that it can explain not only the oxygen isotopic compositions of the presolar grains (Fig. 5.8c), but also the nitrogen isotopic compositions of silicon carbide grains, the ^{26}Al abundances observed in presolar grains, and the ^{3}He budget of low-mass stars. Although it is not yet possible to model this extra mixing from first principles in three-dimensional models, it is clear what the nature of the mixing must be and the extent to which it modifies the envelope compositions of RGB and AGB stars.

The neutron source(s) for the *s*-process

Silicon carbide grains provide a means to study the details of the *s*-process in low-mass stars. The structures of these grains accommodate a wide variety of minor and trace elements. The neutrons that drive the *s*-process come from two sources. One source is the reaction $^{13}C(\alpha,n)^{16}O$, which occurs in the intershell region between the hydrogen shell and helium shell while the hydrogen shell is burning and the helium shell is quiescent. This reaction is most likely the dominant source of neutrons in low-mass stars. Unfortunately, it is not yet possible to determine the strength of this neutron source from first principles in stellar models. The other neutron source is the $^{22}Ne(\alpha,n)^{25}Mg$ reaction, which occurs at higher temperatures in the helium shell when it ignites (see Chapter 3). This short-duration source can be modeled from first principles. The relative strengths of these two sources can be evaluated by looking at the details of the isotopic compositions of *s*-process elements such as strontium, zirconium, molybdenum, ruthenium, and barium. There are a number of branch points where, at low neutron density, a nucleus decays by β-decay to the element with a higher Z, but if the neutron density is high enough, the nucleus can capture a neutron before it decays to form a neutron-rich isotope. Because of these branch points, the isotopic compositions of the *s*-process elements vary as a function of neutron density. The neutron density is a function of the temperature and the neutron source.

Comparisons of the calculated compositions from models of stellar nucleosynthesis and the measured compositions of strontium, zirconium, molybdenum, ruthenium, and barium in the most common type of AGB silicon carbide grains SiC (Fig. 5.11) indicate that the ^{13}C source is the most important and that the parent stars of these grains were mostly 1.5–2 $M_\odot$ stars, with a few 3 $M_\odot$ stars also contributing. A similar analysis done with silicon and titanium isotopes seems to indicate stars of slightly higher mass, 2–3 $M_\odot$. The discrepancy between the results of these two studies may indicate either that the grains that were measured come from different populations of stars, or that the models or their input data need to be improved. As discrepancies like this are resolved, our understanding of stellar nucleosynthesis will continue to improve.

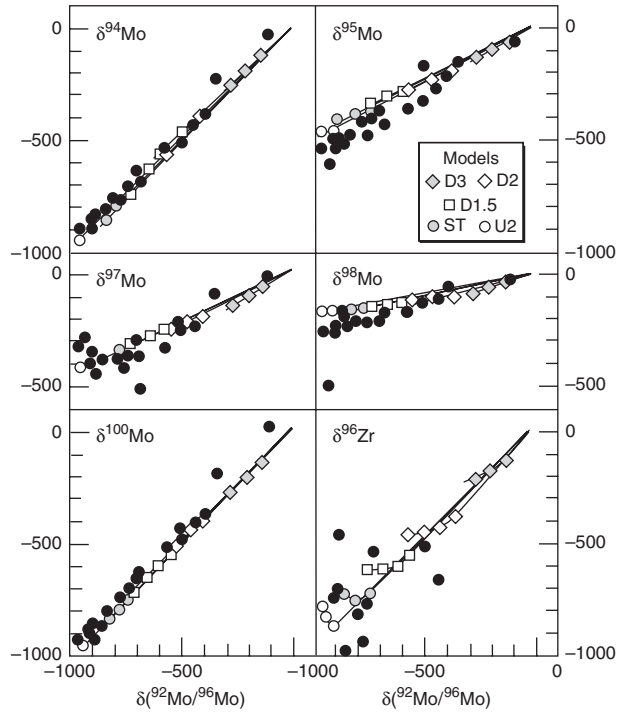

Fig. 5.11 **Isotopic compositions of molybdenum in presolar silicon carbide grains compared with model predictions for a 2 $M_\odot$ AGB star with initial solar metallicity. The models shown differ in the strength of the ^{13}C neutron source. The models match the grain compositions well except that the grains tend to lie below the predictions of $\delta^{95}Mo$ vs. $\delta^{92}Mo$, suggesting that the neutron-capture cross-section for ^{95}Mo may need to be re-measured. Data from Nicolussi *et al.* (1998).**

Constraining supernova models

It is important to understand the nucleosynthesis and dynamics of core-collapse supernovae for many reasons. These stars produce the majority of the heavy elements in the universe. Because of their power and the short-lifetimes of the pre-supernova stars, they play a significant role in the formation, evolution, and destruction of star-forming regions. A supernova may have been responsible for triggering the gravitational collapse of the solar system and probably provided the short-lived radionuclides that are the major tools of early solar system chronology (see Chapters 8, 9, and 14). Prior to the discovery of presolar grains, supernova models generally started with an onion-shell structure of the pre-supernova star (see Chapter 3) and then propagated a shock wave through this spherically symmetrical (one-dimensional) model. Such a model does a reasonable job of describing nucleosynthesis in the supernova. However, when presolar grains from supernovae were identified and studied, some interesting problems appeared. Many of the grains contained newly synthesized matter from several different zones in the supernova. According to the models, these materials should not have come into contact with one another, but clearly they

did. High-resolution observations of recent supernova remnants also show clear evidence of mixing in the ejecta. But until the grains were studied, the extent and spatial scale of the mixing were unknown. It will be a huge task to generate models that accurately describe the mixing that takes place during supernova explosions. But with the grains providing "ground truth," such modeling may eventually be possible.

Galactic chemical evolution

Presolar grains from low- and intermediate-mass stars also carry a record of the initial compositions of the parent stars, before any stellar nucleosynthesis took place. Elements such as silicon and titanium are only slightly affected by nuclear burning in the hydrogen and helium shells. For example, the most common kind of AGB silicon carbide grains fall along a rather steep array on a silicon three-isotope plot (Fig. 5.10). Grains that fall along this array are often called "mainstream" grains in the literature. Theoretical modeling shows that stellar nucleosynthesis in low- and intermediate-mass stars cannot produce this array. Instead, silicon compositions evolve along much shallower lines. Thus, the array defined by the grains must dominantly represent the compositions of the parent stars, with only a small overprint of *s*-process nucleosynthesis. Nucleosynthesis within the parent stars is probably responsible for shifting the array to the right of the solar composition. Similar plots show that titanium isotopes in silicon carbide generally track the silicon isotopes (Fig. 5.12). The *s*-process has the greatest effect on ^{50}Ti, but the data arrays for silicon carbide show large spreads for ^{46}Ti that are almost as great as those observed for ^{50}Ti. This indicates that the titanium isotope variations among the grains were also probably inherited in large part from the parent stars.

The general expectation is that secondary isotopes, such as ^{17}O, ^{18}O, ^{29}Si, ^{30}Si, and ^{46}Ti, ^{47}Ti, ^{49}Ti, and ^{50}Ti increase in relative abundance compared to primary isotopes, such as ^{16}O, ^{28}Si, and ^{48}Ti, with time and overall metallicity in the universe (Chapter 3). The first relatively simplistic attempts to model galactic chemical evolution based on nucleosynthetic yields for massive stars confirm this expectation. But the models are not able to reproduce in detail the data arrays derived from the presolar grains.

From the basic trend of galactic chemical evolution, we would expect the grains at the lower left of the silicon-isotope mainstream array to be from stars of lower metallicity than those at the upper right (Fig. 5.10). Thus, the Sun appears to lie at the low-metallicity end of the trend. This implies that the parent stars of the silicon carbide grains, especially the larger ones, had metallicities higher than that of the Sun even though the stars lived and died before the solar system formed. There have been several attempts to explain this apparent contradiction. One idea is that the Sun formed closer to the galactic center than it is now and was scattered outward through gravitational interactions with other stars. There is a gradient of increasing metallicity from the edge to the center of the galaxy due to the higher star formation rate near the center, where the density of matter is higher. On the other hand, metallicity need not closely track isotopic composition. Stochastic variation in the metallicity of the gas going into new stars can result in a spread of metallicities and a spread in isotopic compositions in

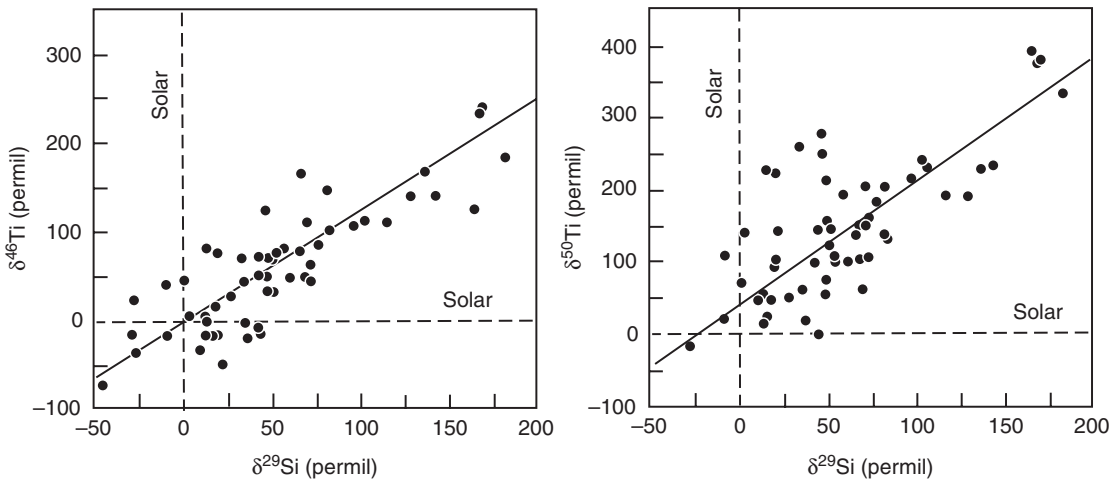

Fig. 5.12 **Titanium isotopic data for mainstream silicon carbide grains versus δ^{29}Si. The correlation between excesses of minor titanium isotopes and minor silicon isotopes most likely reflects galactic chemical evolution. The offset of the δ^{50}Ti trend to pass above the solar composition probably reflects *s*-process nucleosynthesis in the parent stars, which most strongly affects ^{50}Ti. Data from Huss and Smith (2007) and references therein.**

a relatively limited region of the galaxy. But there is something else to consider. Isotopic measurements of presolar grains are easiest on larger grains, where there are more atoms to measure. During the 1990s, essentially all measurements were made on grains making up the high-mass tail of the distribution of presolar grains. NanoSIMS and the large-geometry ion probes that have come into service in the last decade open up more of the mass distribution to measurement. Measurements have shown that smaller grains tend to have isotopic compositions with lower abundances of secondary isotopes, consistent with lower-metallicity parent stars. It may be that the silicon and titanium arrays for silicon carbide shown in Figures 5.10 and 5.12 are biased toward higher metallicity because larger grains form more easily when the constituent elements are more abundant, as they would be in high-metallicity stars. In this case, the Sun would only *appear* to be at the low-metallicity end of the array of stars that supplied silicon carbide to the solar system because data are biased against the silicon carbide from the stars of solar or lower-than-solar metallicity.

Variations in the oxygen isotopic compositions of presolar oxides also reflect galactic chemical evolution overprinted by stellar nucleosynthesis (Nittler *et al*., 1997). While the range in $^{17}O/^{16}O$ is governed mostly by stellar nucleosynthesis, the range in $^{18}O/^{16}O$ can only partially be explained by stellar processing. The data clearly point to a range of initial compositions for the parent stars of the measured grains, but with oxygen, it is less clear where the solar system fits relative to this range than in the cases of silicon and titanium.

The discussions above show that presolar grains can give considerable information on galactic chemical evolution. However, the theoretical framework within which to interpret that information is not as mature at that for stellar nucleosynthesis. This is an area with great promise for future work.

Presolar grains as tracers of circumstellar and interstellar environments

Circumstellar condensates carry information about the environments in which they formed and about the environments through which they passed on the way to being incorporated into meteorites and IDPs. To date, studies to extract this information have been done primarily on presolar silicon carbide and graphite (Bernatowicz *et al*., 2006).

Silicon carbide

The structure of presolar silicon carbide grains can provide information about the conditions of formation. Crystalline silicon carbide is known to form about 100 different polytypes, including cubic, hexagonal, and rhombohedral structures. Presolar silicon carbide exists in only two of these, a cubic (β-SiC) polytype and a hexagonal (α-SiC) polytype (Daulton *et al*., 2003). These two types are the lowest-temperature forms of silicon carbide. The temperatures of formation are broadly consistent with expectations for conditions in circumstellar outflows.

Silicon carbide grains are known to contain subgrains of titanium carbide. Equilibrium thermodynamics predicts that titanium carbide will condense before silicon carbide (Fig. 5.13). The titanium carbide grains were apparently accreted by the growing silicon carbide grains and were enclosed as the silicon carbide grains continued to grow.

The external morphology of presolar silicon carbide grains also provides useful information. Comparing grains that have experienced chemical treatments required to produce silicon carbide separates with grains that have been identified *in situ* ("pristine grains") helps to identify the features that reflect their formation and their journey through the interstellar medium and the solar nebula. Most pristine grains are bounded by one or more crystal faces, and more than half of these crystal faces exhibit polygonal depressions with symmetries consistent with the internal crystal structure. On chemically processed grains, the polygonal depressions are accompanied by numerous surface pits, probably etched defects in the crystal structure. These observations indicate that the polygonal depressions are primary features. Together, the polygonal depressions and high density of defects indicate that the growth of the grains was initially very rapid and was quenched when the gas pressure dropped.

Graphite grains from AGB stars

Presolar graphite grains are inviting targets for study because of their larger sizes (up to 20 μm in diameter) and because they are relatively soft and easier to slice for study. Graphite grains from AGB stars and from supernovae (identified by their isotopic compositions) have been extensively studied. AGB graphite grains exhibit two morphologies that have been labeled "onion-type" and "cauliflower-type". The outer portions of the onion-type grains consist of well-crystallized layers that form concentric shells (Fig. 5.4a). The cores of many of these grains

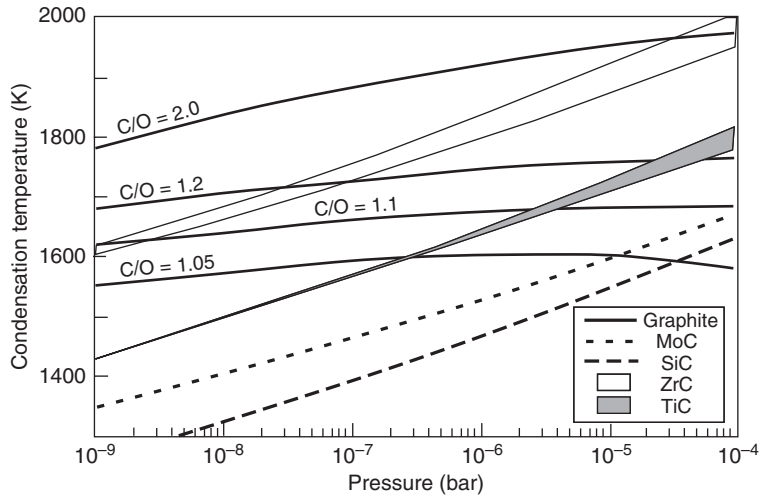

Fig. 5.13 **Condensation curves for graphite, silicon carbide, titanium carbide, molybdenum carbide, and zirconium carbide as a function of temperature, gas pressure, and C/O ratio. The curves represent the conditions at which the phases condense from a gas of solar composition, except for the C/O ratio. The carbide condensation curves are roughly parallel and all crosscut the graphite condensation curve. At low pressures, graphite condenses before most of the carbides, particularly at high C/O ratios. At higher pressures, the carbides condense before graphite. Zirconium carbide would have been the easiest to incorporate into presolar graphite because it condenses at higher temperatures than graphite over most of the pressure range illustrated and under C/O ratios up to almost 2. Presolar graphite grains that contain subgrains of titanium carbide would have condensed at pressures between ~3× 10^{-7} and 10^{-4} bars, depending on the C/O ratio. Silicon carbide is not observed in graphite grains and it is difficult to incorporate into graphite because it condenses after graphite under most conditions. After Bernatowicz *et al.* (1996).**

consist of nanocrystalline carbon comprised of randomly oriented graphene sheets. (Graphene sheets are one-atom-thick planar sheets of carbon rings densely packed into a honeycomb lattice. Graphite consists of many graphene sheets stacked together in a regular pattern.) As much as one-quarter of the core material may be in the form of polycyclic aromatic hydrocarbons (PAHs). Some of the grains contain a central grain of refractory carbide, such as the (Ti,V)C grain in the center of the graphite in Figure 5.4a, while others have no discernable central grain. Onion-type graphite grains apparently grew rapidly from supersaturated gas during the initial stages, producing the nanocrystalline cores. Subsequently, heterogeneous nucleation on these cores produced the concentric graphite sheets. Cauliflower-type graphites consist of turbostratic graphite sheets that are wavy and contorted. Some show roughly concentric structures with short-range coherency (<50 nm thickness). The structures tend to be loose-packed with visible gaps in cross-section (Fig. 5.4b). Many contain tiny carbide crystals. It is not clear whether or not the onion-type and cauliflower-type graphite formed in the same astrophysical environments.

Both types of AGB graphite contain small inclusions of refractory carbides. Some grains have cores of refractory carbide (usually titanium carbide) that served as nucleation sites for the graphite. Titanium carbide is the most abundant type, and many carbides have substantial

enrichments in *s*-process elements (zirconium, molybdenum, ruthenium). In some cases the *s*-process elements can dominate the carbides, with only minor amounts of titanium. The presence of these carbides places relatively strong constraints on the environment of formation of the graphites. Carbides of molybdenum, zirconium, and titanium always condense before silicon carbide over a wide range of temperature and pressure conditions (Fig. 5.13). Unlike for the carbides, whose appearance depends on both nebular pressure and temperature, the appearance of graphite depends little on pressure, but depends strongly on the C/O ratio. This means that the lines of first appearance for graphite cross those for the carbides. Observations indicate that the carbides formed before graphite. Figure 5.13 indicates that titanium carbide will condense before graphite, at $P \geq 3 \times 10^{-7}$ atmospheres for C/O = 1.05 and at $P \geq 3 \times 10^{-5}$ atmospheres for C/O = 1.2; low C/O ratios and relatively high pressures were the rule where graphite condensed. Astronomical observations show that carbon stars have a mean C/O ratio of 1.15±0.16. This compares favorably to the conditions indicated in Figure 5.13 for condensation of graphite grains with inclusions of refractory carbides.

Graphite grains from supernovae

Graphite grains from supernovae are identified by isotopic excesses of ^{18}O and ^{28}Si. The grains that have been studied in detail are 4–10 μm in diameter. Structurally, they consist of concentric turbostratic layers with a degree of graphitization intermediate between the onion and cauliflower types from AGB stars. Supernova graphite grains have high abundances of tiny internal crystals of titanium carbide. These crystals differ from those in AGB graphite grains in that they do not have significant amounts of *s*-process elements such as molybdenum, zirconium, and ruthenium. Supernova graphite grains often contain metallic iron-nickel, either as discrete grains or epitaxially grown onto crystal faces of the titanium carbide crystals. The sequence of condensation indicated by these grains is titanium carbide first, followed by iron-nickel metal, followed in turn by graphite.

Both the number and composition of the internal titanium carbide grains can vary as a function of distance from the center of the graphite grains. The vanadium/titanium ratio in the titanium-carbide grains tends to increase from the core to the rim of the graphite grains, while the abundance of the titanium carbide grains per volume of graphite typically decreases significantly. Vanadium carbide condenses at a substantially lower temperature than titanium carbide, and thus serves as a monitor of gas-phase temperature during the growth of the graphite grains. The abundance differences from core to rim could either reflect a changing growth rate of the graphite grains or a decrease with time in the abundance of titanium carbide grains (Croat *et al*., 2003).

The morphologies of the titanium carbide grains in supernova graphites show evidence of "weathering" in the supernova outflows. Most grains show some erosion of the crystal faces, but the faces are still clearly defined. Some titanium carbides and some metal grains have rims of amorphous or nearly amorphous material 3–15 nm thick (Croat *et al*., 2003). These rims resemble the ~50 nm amorphous rims observed on grains in lunar soils. The lunar rims were caused by irradiation with solar-wind protons and helium ions, which hit the grains at several hundred kilometers per hour. The rims on the inclusions in supernova graphites are likely due

to the grains traveling at high speed and impacting slower-moving parcels of gas. It is unlikely that the rims are due to chemical reactions because the rims appear on two different mineral phases, and gas that is condensing these phases and graphite is unlikely to be corrosive to them.

The observations summarized above provide some basic information about the supernova ejecta in which the graphite grains formed. The high abundances of titanium carbide grains imply a very dusty environment. Gas pressures necessary to supply the titanium necessary to produce the high abundance of titanium carbide grains are in the range of a few $\times 10^{-7}$ to a few $\times 10^{-6}$ atmospheres. As we learn more about supernova graphite grains, it may be possible to make detailed models of the conditions in supernova ejecta based on the grains produced there.

Interstellar grains

For the most part, the work that has been done on presolar grains has focused on circumstellar condensates because they are the grains with large isotopic anomalies that make them easy to identify. As we discussed earlier in this chapter, much of the material in interstellar space has probably been evaporated and recondensed many times because of the passage of shocks generated by strong stellar winds or stellar explosions. The resulting interstellar dust may consist of chemically unstable material that was easily converted to more stable compounds in the solar nebula. But grains from the more-stable tail of this material may have survived somewhere in the solar system, in primitive meteorites or in comets. If we can find and recognize this material, we will have a means of probing the details of the environment in interstellar space. GEMS, found in interplanetary dust particles, may be some of this material. They have experienced extreme radiation damage and perhaps chemical fractionation. The site of this processing is not clear. Some GEMS have anomalous isotopic compositions suggesting that they either started out as circumstellar condensates or incorporated such material at some point in their history.

Presolar grains as probes of the early solar system

The solar system inherited a complex mixture of different types of presolar grains. The known types of presolar grains (Table 5.1) exhibit a wide range of thermal and chemical stabilities. There are highly refractory components, such as diamond, Al_2O_3, and hibonite. There are components that are outgassed or destroyed at relatively low temperature, such as graphite and the low-temperature P3 noble-gas component in diamond. There are components that are stable in a gas with C/O > 1 and components that are stable in a gas with C/O < 1. Because of this range of thermal and chemical stability, the relative abundances of the different types of presolar grains in a meteorite give direct information about the processes and environments that affected the meteorite and its precursor material.

Almost immediately after the discovery of presolar grains, it was clear that they could only be found in the most primitive chondrites, those that had suffered the least amount of thermal metamorphism. Further work showed that the abundances of presolar grains, when normalized to the content of fine-grained matrix where the grains reside, correlated strongly

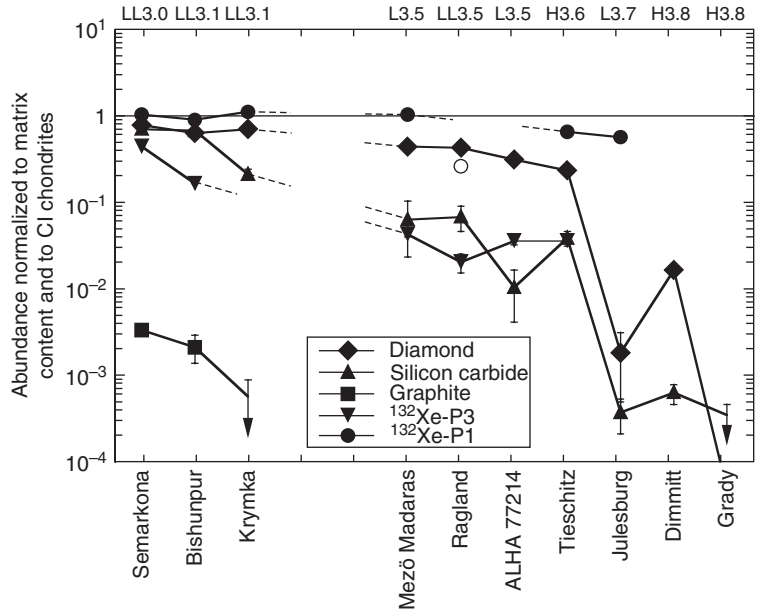

Fig. 5.14 **Abundances of presolar diamond, silicon carbide, graphite, and two noble gas components, P3 sited in diamonds, and P1 sited in the elusive phase Q, are plotted as a function of metamorphic grade for type 3 ordinary chondrites. The abundances are normalized to the matrix content of the host meteorite and to the abundances in the essentially unheated CI chondrites in order to illustrate the differences in abundance as a function of metamorphic grade. The line at unity represents abundances equal to those in CI chondrites. The abundances vary with metamorphic grade, reflecting the thermal and chemical stability of the grains (metamorphism in type 3 chondrites is discussed in Chapter 6). For example, meteorites of grades 3.0–3.5 retain their full complement of ^{132}Xe-P1. However, only types 3.0–3.1 show any evidence of presolar graphite. Types 3.7 and higher have less than half of the ^{132}Xe-P1 and only traces of other presolar components. Adapted from Huss *et al.* (2006).**

with the metamorphic grade of the host meteorite (Huss and Lewis, 1995). Abundances drop with increasing metamorphic grade. Figure 5.14 shows this correlation for ordinary chondrites, but similar patterns are seen in all classes in which enough meteorites have been studied to evaluate the trend. Note that the *relative* abundances of the different types of presolar components also change with metamorphic grade. Thermally resistant components survive best, while thermally labile components are destroyed at low grade. The survival rate changes with the chemical environment. Diamond and silicon carbide survive to higher metamorphic grades in the highly reduced enstatite chondrites, relative to the more oxidized ordinary and carbonaceous chondrites.

The characteristics of the presolar diamonds also change with the metamorphic grade of the host meteorite. Figure 5.15 shows the typical bimodal release of heavy noble gases (here illustrated by xenon) in Orgueil, an unheated chondrite. This pattern is compared to the xenon-release patterns of two ordinary chondrites that have experienced different degrees of mild metamorphism. The amount of low-temperature gas, labeled P3 for historical reasons, is a sensitive function of temperature. Its abundance correlates well with other indicators of

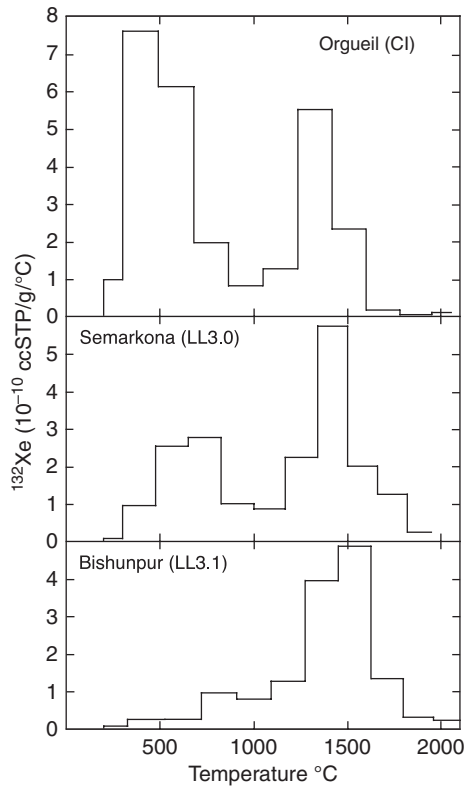

Fig. 5.15 Release curves for ^{132}Xe in presolar diamonds as a function of temperature during stepped heating experiments. Data are normalized to °C so that the areas under the histograms accurately represent gas amounts. Orgueil, which can be considered unheated, has the largest release of low-temperature P3 xenon. The low-temperature peak decreases systematically with increasing metamorphic grade from the unheated Orgueil to slightly more heated Semarkona to Bishunpur. Higher petrologic types show even smaller low-temperature gas releases. Data from Huss and Lewis (1994).

metamorphism (Chapter 6). A very rough temperature scale can be derived for the metamorphism in primitive chondrites from these different features.

In addition to the metamorphic effects in the host meteorite, the abundances of presolar grains in unmetamorphosed chondrites seem to reflect thermal processing in the nebula prior to accretion (Huss *et al*., 2003). The differences in thermal and chemical resistance among grain types mean that mixtures of grains exposed to different conditions in the nebula have been modified in different ways. Chondritic material exposed to high temperatures in the nebula loses volatile elements through evaporation. If one looks at the least metamorphosed members of each chondrite class, those that have been only very slightly heated on their parent bodies, the abundances of presolar grains show patterns that correlate with the abundances of the chemical elements (Fig. 5.16). The presolar components that are easiest to destroy are depleted most in the meteorites that have low abundances of volatile elements. The correlations suggest that the same thermal processing was responsible for both sets of depletions. These depletions and their possible causes will be discussed in more detail in Chapter 7.

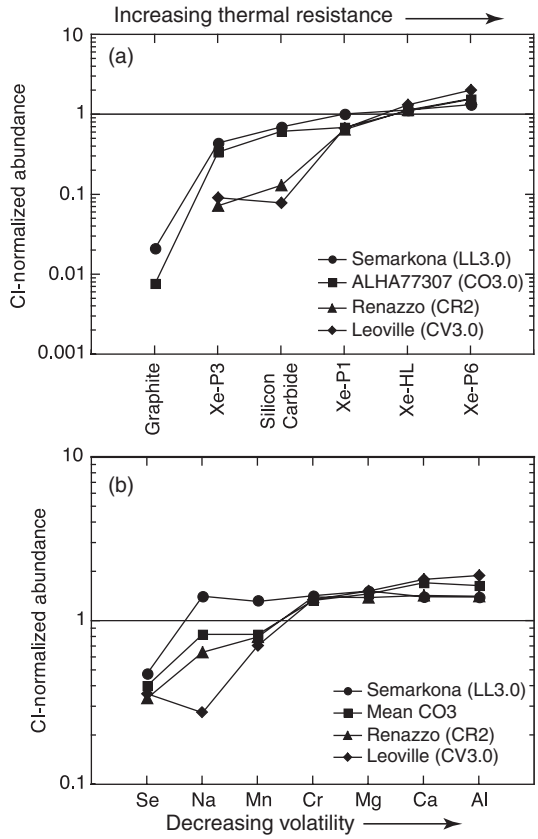

Fig. 5.16 (a) Abundances of six presolar components with different thermal stability, normalized to the abundances in CI chondrites, for the least metamorphosed members of the LL, CO, CR, and CV chondrites. The components are arranged in order of increasing thermal resistance. Peak metamorphic temperatures for these meteorites are constrained to be less than 200 °C. (b) Abundances of seven chemical elements with volatilities ranging from volatile to refractory are plotted as a function of their volatility for the same meteorites, normalized to the abundances in CI chondrites. Note that the LL chondrite, Semarkona, which has the smallest depletions of easy-to-destroy presolar grains, is depleted only in the most volatile element plotted, selenium. The other elements are present in CI relative abundances, although their absolute abundances are higher than in CI due to depletion of the most volatile elements. Depletions in fragile presolar grains and volatile and moderately volatile elements increase from LL to CO to CR to CV chondrites. These correlated depletions indicate that the same process was responsible for the loss of easy-to-destroy presolar grains and the volatile elements.

Summary

As we write this book, it has been just over 20 years since the discovery of the first presolar grains. These grains are unambiguous, though at present highly biased, samples of the material that made up the Sun's parent molecular cloud. Presolar grains have revitalized the study of stellar nucleosynthesis by providing "ground truth" against which to check models of stellar nucleosynthesis. They provide the first direct look at some of the types of dust present

in interstellar space. They also provide a means to investigate the environments around dying stars, conditions in interstellar space, and conditions in the early solar system. In addition, they have fundamentally changed the way we think about the formation of the solar system. The widespread existence of presolar grains in primitive materials shows that the solar system did not pass through a hot nebular stage in which all pre-existing solids were vaporized. All of this has occurred in spite of not yet having a complete census of the types of presolar material and without having fully characterized the presolar materials that we currently recognize. Studying presolar grains will be a rich area for research for many years to come.

Presolar grains are very difficult to study because of their small size. The technical requirements for studying presolar grains have led to the development of a new generation of analytical equipment that has made analysis of particles of a few tenths of a micron in diameter and larger feasible. Further improvements in analytical capability can be expected in the near future. We may even reach the point where the precision of our measurements is limited by the number of atoms present in a grain, a limit that cannot be overcome by any analytical technique.

We have so far discussed the origin of the elements and their abundances and isotopic compositions in the solar system and in the galaxy. We have investigated the grains that carry the elements from their stellar sources to the solar system. In the next chapter, we examine the largest suite of cosmochemical samples available for study, the meteorites. Most meteorites survive from the earliest epochs of solar system history and thus contain a direct record of that history. A few meteorites come from the Moon and Mars, providing the only direct samples of Mars available for study and greatly expanding the set of lunar samples returned by Russian and American spacecraft.

Questions

1. What are presolar grains and why are they important?
2. How are presolar grains recognized?
3. What are the important differences between circumstellar condensates and interstellar grains?
4. How can presolar grains tell us about stellar nucleosynthesis?
5. What can presolar grains tell us about the environment of their formation?
6. What can presolar grains tell us about the environment and processes in interstellar space and in the early solar system?

Suggestions for further reading

Bernatowicz, T. J. and Zinner, E. (1997) *Astrophysical Implications of the Laboratory Study of Presolar Materials*. AIP Conference Proceedings 402. American Institute of Physics, Woodbury, New York, 750 pp. An important volume describing the first decade of research on presolar grains.

Lewis, R. S., Tang, M., Wacker, J. F., Anders, E. and Steel, E. (1987) Interstellar diamonds in meteorites. *Nature*, **326**, 160–162. The paper describing the discovery of the first presolar grains.

Nittler, L. R. (2003) Presolar stardust in meteorites: recent advances and scientific frontiers. *Earth and Planetary Science Letters*, **209**, 259–273. A good accessible review of presolar grains in meteorites.

Zinner, E. (2004) Presolar grains. In *Treatise on Geochemistry, Volume 1: Meteorites, Comets, and Planets*, ed. Davis, A. M. Oxford: Elsevier, pp. 17–39. A recent review of the state of knowledge about presolar grains. The on-line version is updated periodically.

References

Alexander, E. C., Jr., Lewis, R. S., Reynolds, J. H. and Michel, M. C. (1971) Plutonium-244: Confirmation as an extinct radioactivity. *Science*, **172**, 837–840.

Amari, S., Anders, E., Virag, A. and Zinner, E. (1990) Interstellar graphite in meteorites. *Nature*, **345**, 238–240.

Amari, S., Lewis, R. S. and Anders, E. (1994) Interstellar grains in meteorites. I. Isolation of SiC, graphite, and diamond; size distributions of graphite and SiC. *Geochimica et Cosmochimica Acta*, **58**, 459–470.

Beer, H., Corvi, F. and Mutti, P. (1997) Neutron capture of the bottleneck isotopes ^{138}Ba and ^{208}Pb, *s*-process studies, and the *r*-process abundance distribution. *Astrophysical Journal*, **474**, 843–861.

Bernatowicz, T. J., Cowsik, R., Gibbons, P. E. *et al*. (1996) Constraints on stellar grain formation from presolar graphite in the Murchison meteorite. *Astrophysical Journal*, **472**, 760–782.

Bernatowicz, T. J., Croat, T. K. and Daulton, T. L. (2006) Origin and evolution of carbonaceous presolar grains in stellar environments. In *Meteorites and the Early Solar System II*, eds. Lauretta, D. S. and McSween, H. Y., Jr. Tucson: University of Arizona Press, pp. 109–126.

Black, D. C. and Pepin, R. O. (1969) Trapped neon in meteorites II. *Earth and Planetary Science Letters*, **6**, 395–405.

Bradley, J. P. (2004). Interplanetary dust particles. In *Treatise on Geochemistry, Vol. 1. Meteorites, Comets, and Planets*, ed. Davis, A. M. Oxford: Elsevier, pp. 689–711.

Cameron, A. G. W. (1962) The formation of the Sun and planets. *Icarus*, **1**, 13–69.

Clayton, R. N., Grossman, L. and Mayeda, T. K. (1973) A component of primitive nuclear composition in carbonaceous meteorites. *Science*, **182**, 485–487.

Clayton, R. N., Onuma, N., Grossman, L. and Mayeda, T. K. (1977) Distribution of the presolar component in Allende and other carbonaceous chondrites. *Earth and Planetary Science Letters*, **34**, 209–224.

Clayton, R. N., Hinton, R. W. and Davis, A. M. (1988) Isotopic variations in the rock-forming elements in meteorites. *Philosophical Transactions of the Royal Society of London*, **A325**, 483–501.

Croat, T. K., Bernatowicz, T., Amari, S., Messenger, S. and Stadermann, F. J. (2003) Structural, chemical, and isotopic microanalytical investigations of graphite from supernova. *Geochimica et Cosmochimica Acta*, **67**, 4705–4725.

Daulton, T. L., Bernatowicz, T. J., Lewis, R. S. *et al*. (2003) Polytype distribution in circumstellar silicon carbide: Microstructural characterization by transmission electron microscopy. *Geochimica et Cosmochimica Acta*, **67**, 4743–4767.

Dauphas, N., Marty, B. and Reisberg, L. (2002) Molybdenum nucleosynthetic dichotomy revealed in primitive meteorites. *Astrophysical Journal Letters*, **569**, L139–L142.

Galllino, R., Busso, M., Picchio, G. and Raiteri, C. M. (1990) On the astrophysical interpretation of isotope anomalies in meteoritic SiC grains. *Nature*, **348**, 298–302.

Gallino, R., Raiteri, C. M. and Busso, M. (1993) Carbon stars and isotopic Ba anomalies in meteoritic SiC grains. *Astrophysical Journal*, **410**, 400–411.

Huss, G. R. and Lewis, R. S. (1994) Noble gases in presolar diamonds II: Component abundances reflect thermal processing. *Meteoritics*, **28**, 811–829.

Huss, G. R. and Lewis, R. S. (1995) Presolar diamond, SiC, and graphite in primitive chondrites: Abundances as a function of meteorite class and petrologic type. *Geochimica et Cosmochimica Acta*, **59**, 115–160.

Huss, G. R. and Smith, J. A. (2007) Titanium isotopes in isotopically characterized silicon carbide grains from the Orgueil CI chondrite. *Meteoritics and Planetary Science*, **42**, 1055–1075.

Huss, G. R., Meshik, A. P., Smith, J. B. and Hohenberg, C. M. (2003) Presolar diamond, silicon carbide, and graphite in carbonaceous chondrites: Implications for thermal processing in the solar nebula. *Geochimica et Cosmochimica Acta*, **67**, 4823–4848.

Huss, G. R., Rubin, A. E. and Grossman, J. N. (2006) Thermal metamorphism in chondrites. In *Meteorites and the Early Solar System II*, eds. Lauretta, D. S. and McSween, H. Y., Jr. Tucson: University of Arizona Press, pp. 567–586.

Iben, I., Jr. and Renzini, A. (1983) Asymptotic giant branch evolution and beyond. *Annual Reviews of Astronomy and Astrophysics*, **21**, 271–342.

Lewis, R. S., Srinivasan, B. and Anders, E. (1975) Host phase of a strange xenon component in Allende. *Science*, **190**, 1251–1262.

Lewis, R. S., Amari, S. and Anders, E. (1994) Interstellar grains in meteorites. II. SiC and its noble gases. *Geochimica et Cosmochimica Acta*, **58**, 471–494.

Manuel, O. K., Hennecke, E. W. and Sabu, D. D. (1972) Xenon in carbonaceous chondrites. *Nature*, **240**, 99–101.

Messenger, S., Keller, L. P., Stadermann, F. J., Walker, R. M. and Zinner, E. (2003) Samples of stars beyond the solar system: silicate grains in interplanetary dust. *Science*, **300**, 105–108.

Nagashima, K., Krot, A. N. and Yurimoto, H. (2004) Stardust silicates from primitive meteorites. *Nature*, **428**, 921–924.

Nguyen, A. N. and Zinner, E. (2004) Discovery of ancient silicate stardust in a meteorite. *Science*, **303**, 1496–1499.

Nicolussi, G. K., Pellin, M. J., Lewis, R. S. *et al.* (1998) Molybdenum isotopic compositions of individual presolar silicon carbide grains from the Murchison meteorite. *Geochimica et Cosmochimica Acta*, **62**, 1093–1104.

Nittler, L. R. and Cowsik, R. (1997) Galactic age estimates from O-rich stardust in meteorites. *Physical Review Letters*, **78**, 175–178.

Nittler, L. R., Alexander, C. M. O'D., Gao, X., Walker, R. M. and Zinner, E. (1997) Stellar sapphires: the properties and origins of presolar Al_2O_3 in meteorites. *Astrophysical Journal*, **483**, 475–495.

Podosek, F. A., Brannon, J. C., Neal, C. R. *et al*. (1997) Thoroughly anomalous chromium in Orgueil. *Meteoritics and Planetary Science*, **32**, 617–627.

Reynolds, J. H. and Turner, G. (1964) Rare gases in the chondrite Renazzo. *Journal of Geophysical Research*, **49**, 3263–3281.

Smith, V. V. and Lambert, D. L. (1990) The chemical composition of red giants. III. Further CNO isotopic and *s*-process abundances in thermally pulsing asymptotic giant branch stars. *Astrophysical Journal Supplement*, **72**, 387–416.

Srinivasan, B. and Anders, E. (1978) Noble gases in the Murchison meteorite: possible relics of *s*-process nucleosynthesis. *Science*, **201**, 51–56.

Tang, M. and Anders, E. (1988) Isotopic anomalies of Ne, Xe, and C in meteorites. II. Interstellar diamond and SiC: carriers of exotic noble gases. *Geochimica et Cosmochimica Acta*, **52**, 1235–1244.

6 Meteorites: a record of nebular and planetary processes

Overview

Most meteorites (~86%) are chondrites, which are primitive rocks that have elemental compositions similar to that of the Sun. They are named for the millimeter-sized droplets of quenched silicate melt, called chondrules, that are particularly abundant in these meteorites. Chondrites come from the asteroid belt. They are physical mixtures of accreted components (chondrules, refractory inclusions, metal and sulfide, dust) whose characteristics and mineralogy we will describe. The classification of chondrites utilizes a combination of primary features (bulk chemical composition, oxygen isotopes) and secondary features (thermal metamorphism or aqueous alteration). About 14% of meteorites arriving on Earth consist of differentiated materials. Their compositions have been affected by melting and crystallization, and they include various kinds of achondritic meteorites, irons, and stony irons from the asteroid belt, along with lunar samples and Martian meteorites. Achondrites, so-named because they do not contain chondrules, are divided into two types. Primitive achondrites are the solid residues left behind after extraction of partial melts from chondritic material. Magmatic achondrites crystallized from the extracted melts or from completely melted and differentiated chondritic material. Irons and stony irons formed by separation of molten metal/sulfide from silicates. Lunar rocks include cumulates from the ancient highlands and mare basalts that flooded huge craters. Martian meteorites include basalts and cumulates formed from basaltic magmas.

Primitive versus differentiated

Cosmochemistry is the study of the chemical compositions of various solar system materials. Chondrites are the most abundant primitive samples. They are essentially sedimentary rocks composed of mechanical mixtures of materials with different origins (chondrules, refractory inclusions, metal, sulfide, matrix), which we will call "components." Chondrites formed by the accretion of solid particles within the solar nebula or onto the surfaces of growing planetesimals. They are very old (>4.5 billion years, as measured by radioactive chronometers) and contain some of the earliest formed objects in the solar system. Chondrites have bulk chemical compositions very similar to the solar photosphere, except

that they lack the gaseous elements and are often depleted in volatile and moderately volatile elements. CI chondrites are not depleted in volatile and moderately volatile elements and are representative of the bulk solar system composition (see Chapter 4).

Chondrites have never been melted, although some of their components melted and solidified before being accreted. Where melting occurs in nature, it is commonly incomplete. Partial melting selectively affects minerals that liquefy at lower temperatures, so the melt fraction and the solid residue have complementary chemical compositions. Melts ("magmas" in geologic parlance) tend to be mobile, and segregation of a melt from its residue occurs readily once a critical amount of melt is present. Consequently, the solid residue and the rocks formed by crystallization of the magma have different chemical compositions, a result described as *differentiation*. Other changes in chemical composition can occur during crystallization of the magma. Early-formed crystals may segregate because of density differences between crystals and magma or because they become concentrated in certain regions by convecting melt. Separation of crystals from the melt ("residual liquid") is called *fractional crystallization*. Because the early crystals and the melt have different compositions, this process also leads to differentiation.

Some meteorites, and all planetary samples, have undergone melting and differentiation at some stage. Hence, the compositions of differentiated materials do not resemble solar system abundances. These samples can, however, tell us about various geochemical processes within asteroids and planets.

We will now describe each of the various kinds of meteoritic samples available for cosmochemical investigation, progressing from primitive materials to samples from differentiated bodies. Presolar grains extracted from meteorites have already been described in Chapter 5, and interplanetary dust particles (IDPs) and returned comet samples will be described in Chapter 12.

Components of chondrites

Chondrites are physical aggregates of various components, most of which formed in the nebula. Before describing the chondrites themselves, let's take a look at these components.

Chondrules

Chondrules, the dominant constituent of most chondrites, were first named by the German mineralogist Gustav Rose in 1864, although references in the literature to "curious globules" in meteorites appeared as early as 1802. These droplets were formed by flash melting at temperatures of 1770–2120 K, and subsequently experienced rapid cooling and solidification in minutes to hours. The heating mechanisms for chondrules remain a contentious subject, and we will discuss various hypotheses in a later chapter. Chondrule cooling rates are fairly well constrained by laboratory experiments that reproduce the distinctive igneous textures of chondrules. Not all chondrules were completely melted, and relict grains of

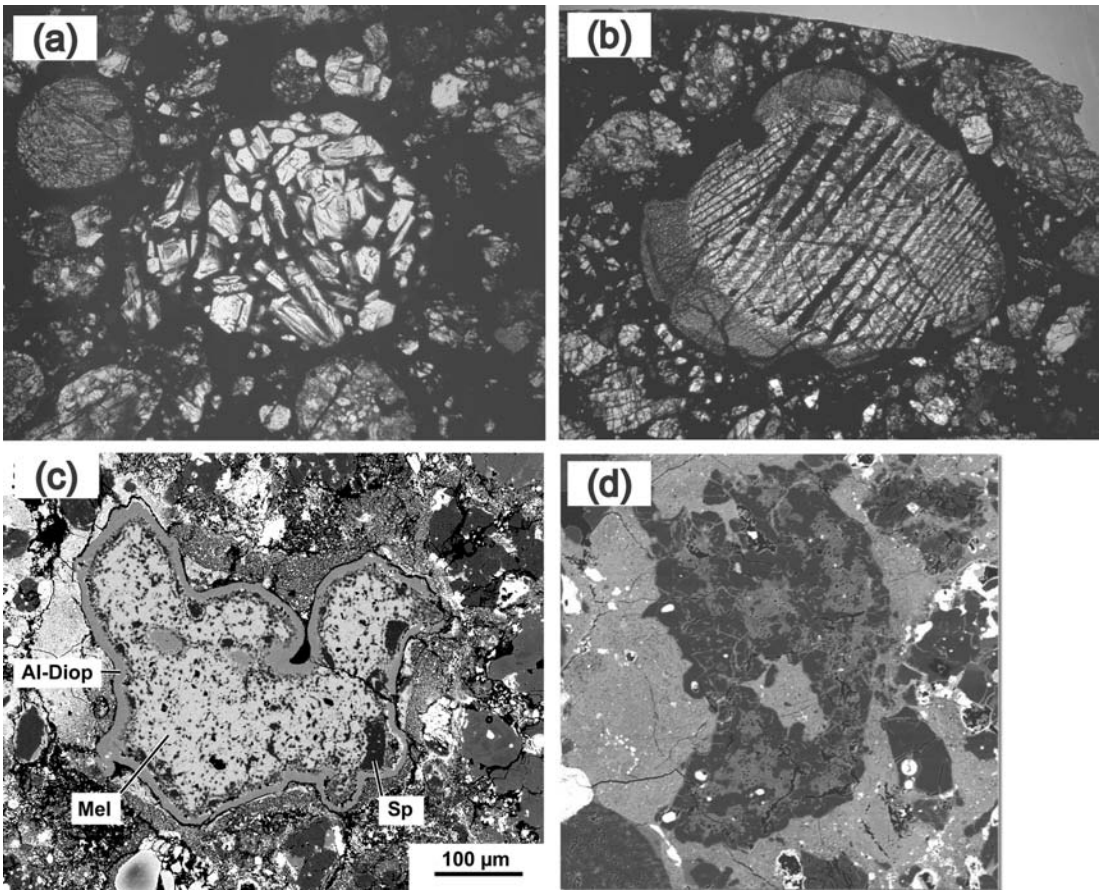

Fig. 6.1 Components of chondrites. (a) Photomicrograph of porphyritic chondrule showing olivine crystals in glassy mesostasis (dark), in the Clovis ordinary chondrite, field of view (FOV) ~1.8 mm. (b) Photomicrograph of barred chondrule, containing oriented plates of olivine in glass (dark), in the Bushunpur ordinary chondrite, FOV ~2.7 mm. (c) Backscattered electron image of CAI in the MAC 87300 carbonaceous chondrite; mineral abbreviations are Mel (melilite), Sp (spinel), and Al-Diop (aluminum-rich diopside). (d) Backscattered electron image of AOA in the Y-81020 carbonaceous chondrite, containing olivine (dark gray) and clots of spinel-anorthite-diopside (lighter gray), FOV = 300 μm. (a) and (b) reprinted from Lauretta *et al.* (2006), with permission; (c) reprinted from Russell *et al.* (2000), with permission; (d) figure courtesy of L. Chizmadia.

olivine can sometimes be recognized in them. The relict grains appear to be igneous crystals themselves, suggesting that chondrules may have been repeatedly cycled through the chondrule furnace. Many chondrules have abraded surfaces and some have rims of melted material.

Chondrules exhibit a bewildering variety of compositions and textures (Fig. 6.1a,b). Most are composed primarily of olivine and/or pyroxene, commonly with some glass. (For a crash course in mineral names and compositions, see Box 6.1.) If melt solidifies so quickly that its atoms cannot organize into crystalline minerals, it quenches into glass. Iron-nickel metal and iron sulfide occur in many chondrules, often clustered near the peripheries. The textures of

Box 6.1 A crash course in mineralogy

The documented mineralogy of meteorites is quite varied; more than 300 different meteoritic minerals have been reported (tabulated by Lodders and Fegley, 1998). In the list below we focus only on those minerals that are especially important, either because they are volumetrically abundant or provide important constraints on meteorite formation.

By definition, a *mineral* must possess a unique crystal structure (regular internal arrangement of atoms or ions) and a specific chemical composition or limited range of composition. Minerals having a range of composition are called "solid solutions," and allowed chemical substitutions are shown in chemical formulae by elements in parentheses. For example, olivine [$(Mg,Fe)_2SiO_4$] represents solid solution compositions between the end members forsterite [Mg_2SiO_4] and fayalite [Fe_2SiO_4]. Different minerals having the same chemical composition but distinct crystal structures are called "polymorphs."

Although the crystallography of minerals is an inherent part of their definition, here the focus will be on the chemistry of minerals, given the subject of this book. Readers interested in crystallography are referred to any number of texts in mineralogy. Materials without ordered crystal structures are either glasses (quenched from high temperatures so quickly that crystals did not form), amorphous (poorly crystalline phases usually formed at low temperatures where crystallization is sluggish), metamict (formerly crystalline minerals whose atomic structures have been destroyed by irradiation), or diaplectic (formerly crystalline minerals whose atomic structures have been randomized by impact shock).

Minerals can be subdivided into the following groups:

- *Native elements* – elements not combined with any other elements.
- *Silicates* – SiO_2, or compounds of various cations with various complex ions of silicon and oxygen. Cations can combine with individual SiO_4^{4-} tetrahedra, chains of SiO_3^{2-}, and sheets of $Si_4O_{10}^{4-}$. Silicates are the most abundant minerals in chondrites, IDPs, and most types of differentiated materials.
- *Oxides and hydroxides* – compounds of cations (most commonly Fe) with O^{2-} or OH^-.
- *Sulfides and phosphides* – compounds of cations (usually Fe) with S^{2-} or P^{6-}, respectively.
- *Carbonates* – compounds of cations (usually Ca, Mg, or Fe) with CO_3^{2-}.
- *Sulfates* – compounds of cations (usually Ca or Mg) with SO_4^{2-}.
- *Phosphates* – compounds of cations (usually Ca) with PO_4^{3-}.
- *Halides* – compounds of cations (usually Na or K) with Cl^-, Br^-, or F^-.

The following minerals are important in meteorites and other extraterrestrial samples. Some important classes of minerals in terrestrial rocks are not observed or are extremely rare in meteorites or planetary samples (e.g. micas, amphiboles) and will not be considered.

Native elements

- Kamacite – Fe alloy with minor Ni.
- Taenite – Fe alloy with 77–24% Ni.
- Platinum group alloy – various alloys of Pt, Ir, Os, Ru, Rh with Fe.
- Graphite, diamond – C polymorphs.

Silicates

- SiO_2 – tridymite is the most common polymorph in meteorites. Quartz is most common on Earth.
- Zircon – $ZrSiO_4$.
- Olivine – solid solution of Mg_2SiO_4 (forsterite) and Fe_2SiO_4 (fayalite).
- Pyroxenes – can be divided into low-calcium pyroxenes and high-calcium pyroxenes. Low-calcium pyroxenes make up a solid solution between $Mg_2Si_2O_6$ (enstatite) and $Fe_2Si_2O_6$ (ferrosilite) and include minerals such as bronzite and hypersthene. Low-calcium pyroxenes can be orthorhombic or monoclinic. Low-calcium pyroxene in type 3 chondrites is predominantly monoclinic, but becomes orthorhombic in higher petrologic types. High-calcium pyroxenes are monoclinic and make up a solid solution between $CaMgSi_2O_6$ (diopside) and $CaFeSi_2O_6$ (hedenbergite), including $Ca(Mg,Fe)Si_2O_6$ (augite). Extensive substitution of aluminum and titanium into high-calcium pyroxenes produces aluminous-diopside and a titanium-rich pyroxene commonly known as fassaite. Pigeonite is intermediate in composition between clinoenstatite and diopside and is monoclinic.
- Melilite – solid solution between $Ca_2Al_2SiO_7$ (gehlenite) and $Ca_2MgSi_2O_7$ (åkermanite).
- Plagioclase – feldspar solid solution between $CaAl_2Si_2O_8$ (anorthite) and $NaAlSi_3O_8$ (albite). Maskelynite is a diaplectic glass of plagioclase composition.
- Orthoclase – $KAlSi_3O_8$ feldspar.
- Nepheline – $NaAlSiO_4$ feldspathoid.
- Serpentine – $(Mg,Fe)_6Si_4O_{10}(OH)_8$ phyllosilicate. Although Fe-rich varieties are uncommon on Earth, they are abundant in some meteorites.
- Phyllosilicates (clay minerals) – layered silicates such as $Al_4Si_4O_{10}(OH)_8$ (kaolinite) and $(Ca,Na)_{0.7}(Al,Mg,Fe)_4(Si,Al)_8O_{20}(OH)_4.nH_2O$ (montmorillonite, also called smectite).

Oxides

- Magnetite – Fe_3O_4
- Spinel – $MgAl_2O_4$
- Chromite – $(Mg,Fe)Cr_2O_4$
- Ilmenite – $FeTiO_3$
- Hematite – Fe_2O_3
- Perovskite – $CaTiO_3$
- Corundum – Al_2O_3
- Grossite – $CaAl_4O_7$
- Hibonite – $CaAl_{12}O_{19}$

Sulfides, phosphides, carbides

- Troilite – FeS (stoichiometric)
- Pyrrhotite – $Fe_{1-x}S$ (non-stoichiometric)
- Pyrite – FeS_2
- Pentlandite – $(Fe,Ni)_9S_8$
- Oldhamite – CaS

- Alabandite – (Mn,Fe)S
- Niningerite – MgS
- Schreibersite – $(Fe,Ni)_3P$
- Cohenite – Fe_3C
- Moisanite – SiC (artificial SiC is called carborundum)

Carbonates, sulfates, phosphates, halides

- Calcite – $CaCO_3$
- Magnesite – $MgCO_3$
- Dolomite – $CaMg(CO_3)_2$
- Siderite – $FeCO_3$
- Gypsum – $CaSO_4 \cdot 2H_2O$
- Anhydrite – $CaSO_4$
- Kieserite – $MgSO_4 \cdot H_2O$ (one of many magnesium sulfates with varying H_2O)
- Jarosite – $KFe_3(SO_4)_2(OH)_6$
- Merrillite (whitlockite) – $Ca_3(PO_4)_2$
- Apatite – $Ca_5(PO_4)_3(F,Cl,OH)$
- Halite – NaCl
- Sylvite – KCl

most chondrules are porphyritic, meaning that they contain large crystals set in a finer-grained or glassy background ("mesostasis"). Porphyritic chondrules are sometimes subdivided into type I chondrules, which contain MgO-rich olivine and pyroxene, and type II chondrules, which have FeO-rich silicates. Barred olivine chondrules consist of parallel plates of olivine with interstitial glass, sometimes armored by a surface layer of olivine. Excentroradial chondrules contain thin pyroxene blades that radiate from a point of nucleation. Other chondrules are aluminum-rich and contain plagioclase, spinel, and sometimes silica.

The chemical compositions of individual chondrules have been determined by neutron activation of extracted samples or by electron microprobe analyses of chondrules *in situ*. Some, but not all chondrules are depleted in moderately volatile elements. There is a compositional continuum between the olivine-rich and aluminum-rich chondrules. Original concentrations of the short-lived radionuclide ^{26}Al in chondrules suggest they formed very early, before all of this isotope decayed, but as much as 2–5 million years after the formation of CAIs (see Refractory Inclusions, below).

Chondrules are volumetrically abundant in most chondrites, comprising up to 70% of some chondrite groups. However, chondrule abundance varies among different groups, and one kind of chondrite (CI, see Chondrite Classification, below) contains no chondrules at all. Occasionally, compound chondrules consisting of several objects stuck together are observed. The chondrules must have been hot when they touched, implying that the densities of melt droplets in the nebula formation region were high enough that molten droplets encountered each other.

Refractory inclusions

Two types of refractory-element-rich inclusions are found in chondrites, *calcium-aluminum-rich inclusions* ("CAIs," Fig. 6.1c) and *amoeboid olivine aggregates* ("AOAs," Fig. 6.1d). CAIs were first described in the newly fallen Allende chondrite in 1970, and AOAs were first described in 1976, also in Allende. CAIs elicited considerable excitement because the minerals that comprise them were the very phases predicted to condense from a cooling gas of solar composition. In the early 1970s, the paradigm for the early solar system was that all solids evaporated during the gravitational collapse of the Sun's parent molecular cloud and that the solids we now observe condensed from the cooling gas. Although the "hot nebula" paradigm has changed, the refractory mineralogy of CAIs makes them unique among cosmochemical samples.

CAIs are composed of a variety of minerals, primarily hibonite, perovskite, melilite, spinel, aluminum- and titanium-rich diopside, anorthite, forsterite, and occasionally corundum or grossite. They also show significant enrichments in refractory trace elements. CAIs exhibit a host of isotopic anomalies inherited from incorporated presolar grains or from the early nebula itself.

Evidence for the former existence of the short-lived radionuclide ^{26}Al was first documented by analyzing CAIs. The high abundance of ^{26}Al, as well as ages determined from long-lived isotope chronometers, reveal that CAIs are the most ancient components of chondrites (excluding presolar grains). In fact, they appear to be the oldest surviving objects that formed within the solar system.

Some, about a third, of CAIs are thought to have condensed directly from the gas phase. These have irregular shapes, fine-grained fluffy textures, and mineralogies that match condensation calculations, as discussed in Chapter 7. Other CAIs are coarser grained and more compact, and their textures show that they crystallized from melts. Many melted CAIs show evidence of evaporation of more-volatile elements during the melting event. The melted CAIs are probably refractory residues formed by heating and partial evaporation of clumps of refractory dust. Many CAIs are surrounded by delicate rims composed of forsterite and other minerals that probably condensed in the nebula. CAIs can be subdivided into various types, based on their mineralogy.

CAIs are especially abundant in carbonaceous chondrites, but they occur in lesser abundance in other chondrite groups as well. Most types of refractory inclusions occur in all groups, but their relative proportions and sizes vary.

The "amoeboid" descriptor for amoeboid olivine aggregates refers to their irregular shapes. AOAs tend to be fine-grained and porous, and have comparable sizes to CAIs in the same meteorite. They consist mostly of forsterite and lesser amounts of iron-nickel metal, with a refractory component composed of anorthite, spinel, aluminum-rich diopside, and rarely melilite. The refractory component is sometimes recognizable as a CAI embedded within the AOA. The AOAs show no evidence of having been melted, but some contain CAIs that have melted.

AOAs, like CAIs, are depleted in volatile and moderately volatile elements, but to a lesser degree. AOAs are generally interpreted as aggregates of grains that condensed from nebula

gas. Forsterite and metal are predicted to have condensed after the minerals that comprise CAIs, and lower abundances of ^{26}Al suggest that AOAs formed after CAIs (typically by a few hundred thousand years). Mineralogical similarities between AOAs and the forsterite-rich rims on some CAIs may suggest that they formed contemporaneously.

Metals and sulfide

Two different kinds of *metals* are found in chondrites. Small nuggets composed of highly refractory siderophile elements (iridium, osmium, ruthenium, molybdenum, tungsten, rhenium) occur within CAIs. These refractory alloys are predicted to condense at temperatures above 1600 K from a gas of solar composition. Except for tungsten, they are also the expected residues of CAI oxidation.

More commonly, larger and much more abundant grains of metallic iron, or more properly iron-nickel-cobalt, occur within and as rims on chondrules. Metal grains of similar composition outside chondrules may have originally formed within chondrules and been expelled. On slow cooling, the solidified metal separates into low-nickel (kamacite) and high-nickel (taenite) phases. Most metal compositions have been modified by later heating events, so it is difficult to find metal grains that retain their original compositions. However, primitive iron-nickel-cobalt grains found in one chondrite group (CH) have compositions consistent with condensation at about 1400 K.

Calculations predict that metallic iron should react with sulfur in nebular gas when temperatures drop below 650 K to produce iron sulfide FeS (*troilite*). Indeed, brassy troilite grains are commonly observed in association with metal in chondrites. However, sulfur is so readily mobilized during later heating so that it is doubtful that troilite grains formed by nebular reactions have been preserved in their original form.

Matrix

Another chondrite component is an optically opaque (in thin section) assortment of very fine-grained minerals that fills the spaces between the larger chondrules, refractory inclusions, and metal grains. This material is called *matrix*. Characterization of matrix minerals is hampered by their tiny particle sizes (as small as 50–100 nm). Moreover, the fine grain sizes, high porosity, and permeability of matrix make it especially susceptible to alteration during later heating or exposure to aqueous fluids.

Matrix minerals are complex mixtures of silicates (especially olivine and pyroxene), oxides, sulfides, metal, phyllosilicates, and carbonates. The bulk chemical composition of matrix is broadly chondritic, and richer in volatile elements than the other chondrite components. Some chondrules have rims of adhering matrix that appear to have been accreted onto them prior to final assembly of the meteorite. Small lumps of matrix also occur in many chondrites. Presolar grains, described in Chapter 5, occur in the matrix.

The origin of matrix materials is uncertain. Matrices are probably complex mixtures of presolar grains, nebular condensates formed at various temperatures, and disaggregated

chondrules and refractory inclusions. Matrix material has almost always been altered to varying degrees after accretion of the meteorite parent bodies. In chondrites of type 4 and above (see below), the original matrix has been altered beyond recognition.

Chondrite classification

Chondrules, refractory inclusions, metal, troilite, and matrix have been assembled in varying proportions to form chondrites. Some microscopic images of chondrite thin sections are illustrated in Figure 6.2.

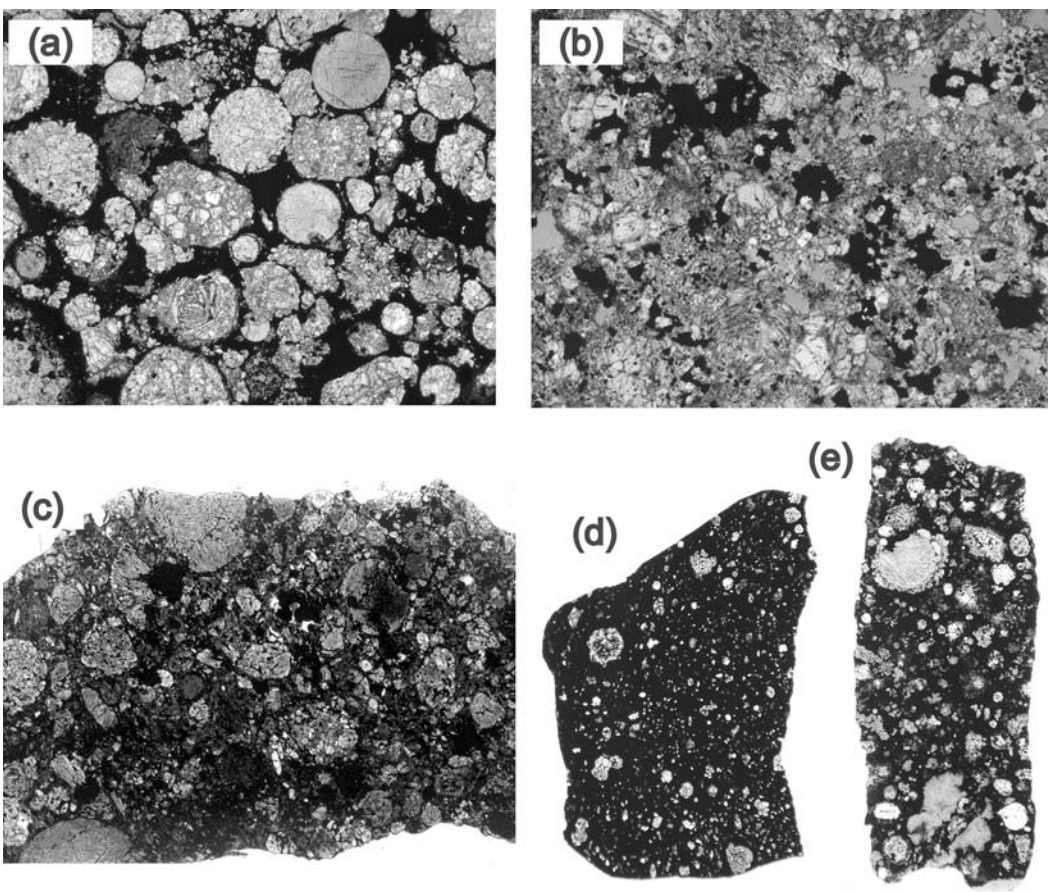

Fig. 6.2 Photomicrographs of chondrites, all in plane polarized light. (a) Unmetamorphosed Semarkona LL3 chondrite, containing abundant chondrules and dark matrix, FOV = 5.4 mm. (b) Metamorphosed Mt. Tazerzait L5 chondrite, with original chondrule outlines unrecognizable because of recrystallization, FOV = 5.4 mm. (c) KLE 98300 EH3 chondrite, showing chondrules in dark matrix, FOV = 5.4 mm. (d) Murchison CM2 chondrite, in which dark matrix is particularly abundant, FOV = 1 cm. (e) Allende CV3 chondrite, with CAIs (large white objects) and chondrules in dark matrix, FOV = 1 cm. All images from Lauretta and Killgore (2005), with permission.

A serviceable classification scheme for chondrites has taken many decades to develop, because earlier schemes confused primary and secondary properties. A primary property is one resulting from the chondrite's original formation as an accreted rock, and a secondary property is one acquired at some later time by another process. The bulk chemical composition of a chondrite is a primary property, as are the relative abundances of chondrules, CAIs, metal, and matrix. Most chondrites have suffered some kind of alteration after accretion, either thermal metamorphism (changes brought on by heating) or aqueous alteration (changes resulting from interaction with fluids, probably produced by melting of ice that was accreted along with rock). Recrystallization occurs during metamorphism, blurring original chondrite textures (compare Figs. 6.2a and 6.2b) and equilibrating the mineral compositions. Aqueous alteration produces pervasive changes in mineralogy, forming hydrated minerals (phyllosilicates) from olivine and pyroxene, and precipitating salts (carbonates, sulfates, and halides). Many chondrites have also experienced shock metamorphism (changes wrought by the high pressures achieved during impacts). Shock produces new minerals and causes fracturing or melting of target rocks. Thermal metamorphism, aqueous alteration, and shock metamorphism are examples of secondary processes. The current chondrite classification scheme utilizes both primary and secondary properties and is based on a taxonomy formulated by Van Schmus and Wood (1967).

Primary characteristics: chemical compositions

Using bulk chemical compositions, chondrites are divided into clans and subdivided into groups, identified by a letter or combination of letters. The *ordinary* (O) chondrite clan, so called because these chondrites are the most abundant types of meteorites, is separated into the H, L, and LL groups. H chondrites have the highest concentration of iron, occurring mostly as metal (hence the "H"), and L chondrites have lower iron. The LL group was subsequently recognized to have an even lower abundance of iron, occurring mostly as ferrous iron in silicates. Since the group name L was already taken, an extra L was added. Ordinary chondrites are shown in Figures 6.2a and 6.2b.

Another clan, the *enstatite* (E) chondrites, are strongly reduced, with virtually all the iron in them occurring as metal. Unusual sulfide minerals result from changes in the behavior of some elements, like calcium and manganese, from lithophile to siderophile, at these low oxidation states. Two groups, called EH and EL, are distinguished based on their high (H) and low (L) iron metal contents. An EH3 chondrite is shown in Figure 6.2c.

The *carbonaceous* (C) chondrites are traditionally considered to be a large clan with many chemical groups: CI, CM, CR, CB, CO, CV, CK, and CH. The second letter refers to a type specimen for each meteorite group: Ivuna (I), Mighei (M), Renazzo (R), Bencubbin (B), Ornans (O), Vigarano (V), Karoonda (K), and ALHA 85085 (H – this last one violates that convention; the H refers to high iron concentration and metal abundance). These groups reflect a wide variety of compositions, oxidation states, and petrography. In fact, the carbonaceous chondrites encompass a group with essentially unfractionated elemental abundances, a high proportion of presolar grains, and no chondrules (CI chondrites), and other groups with

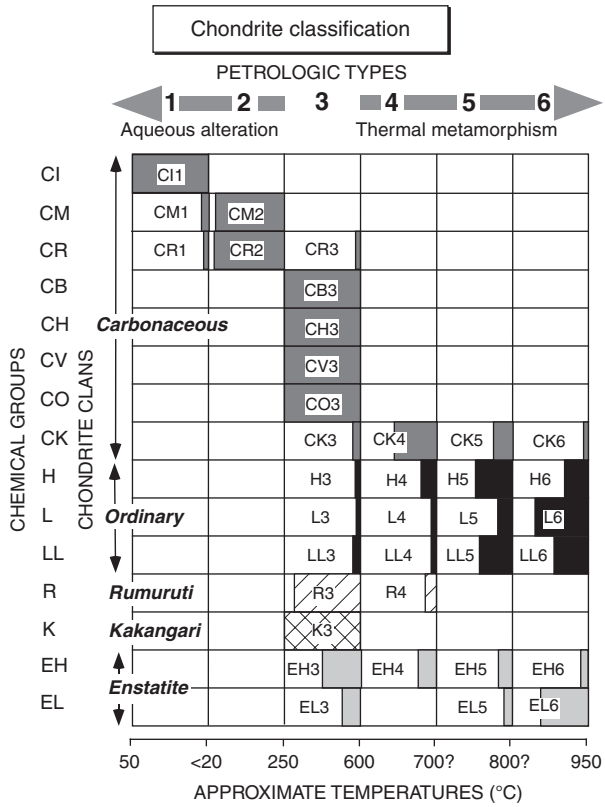

Fig. 6.3 Classification system for chondrites, adapted from Van Schmus and Wood (1967). A meteorite is classified by identifying its chemical group and petrologic type. Approximate temperatures for metamorphism or alteration are shown at the bottom. The relative abundances of meteorites assigned to various petrologic types are indicated by the shaded proportion of each box (data from Scott and Krot, 2004).

compositions highly depleted in volatile elements and enriched in refractory elements, with moderate numbers of chondrules and low proportions of presolar grains (CV and CO chondrites). Unlike ordinary and enstatite chondrites, the carbonaceous chondrites cannot be thought of as a clan consisting of closely related meteorites. In the following discussions, we will refer to individual chondrite groups rather than the carbonaceous chondrite clan as a whole. A CM and a CV chondrite are shown in Figures 6.2d and 6.2e, respectively.

The *Rumaruti* (R) group is highly oxidized and has a high abundance of matrix (~50%), but is otherwise similar in many respects to ordinary chondrites. The *Kakangari* (K) group does not fall into any of the previous chondrite classes, although it is most similar to some of the carbonaceous chondrites. Its composition is sufficiently distinct to designate these few meteorites as a separate group.

These chemical groups constitute one (vertical) axis of a diagram defining the Van Schmus-Wood classification system, as illustrated in Figure 6.3. The other (horizontal) axis is based on secondary characteristics.

Secondary characteristics: petrologic types

Chondrites are divided into various "petrologic types" based on the degree to which they have been thermally metamorphosed or altered. In the original Van Schmus-Wood (1967) classification, CI chondrites were considered to be the most primitive meteorites, because their compositions provide the best match to solar elemental abundances. They were classified as petrologic type 1, some other carbonaceous chondrites were type 2, relatively unmetamorphosed ordinary and enstatite chondrites were type 3, and petrologic types 4, 5, and 6 indicated progressively higher degrees of thermal metamorphism. Type 7 is sometimes recognized, although it is unclear whether this type reflects the effects of shock as well as thermal metamorphism. Van Schmus and Wood (1967) provided mineralogical and textural criteria to recognize each petrologic type.

Although this serviceable chondrite taxonomy remains in use, its original interpretation was flawed. As currently used, petrologic types 2 and 1 are reinterpreted to reflect increasing degrees of aqueous alteration (McSween, 1979), while types 3–6 continue to be interpreted as increasing degrees of thermal metamorphism (arrows in Figure 6.3). Thus, the most primitive chondrites are actually petrologic type 3, at least from the perspective of secondary characteristics. Carbonaceous chondrites of types 1 and 2 have altered matrix material composed primarily of serpentine, a clear indication of aqueous alteration. Many of these meteorites also contain veins of sulfate and carbonate that precipitated from aqueous solutions. The iron in most type 1 and 2 chondrites is completely oxidized; much of it is present as magnetite. CR2 chondrites, which contain abundant metal, are an exception. Much of the oxidation in carbonaceous chondrites may also result from aqueous alteration processes that converted metal to magnetite. The CI chondrites, although type 1 and highly aqueously altered, remain the most primitive meteorites in terms of solar system abundances, so the alteration that affected them is inferred to have occurred without chemical change.

Sears *et al*. (1980) subdivided type 3 chondrites into types 3.0 to 3.9, based on their thermoluminescence (TL) characteristics. TL sensitivity is controlled by the degree of crystallization of chondrule mesostasis (the very fine-grained minerals or quenched glass between the larger crystals). Chondrules in type 3.0 chondrites have a glassy mesostasis, which progressively crystallizes into feldspar during mild metamorphism. Subtypes 3.0–3.9 can also be distinguished from a plot of CaO versus FeO concentrations in olivine chondrules (Scott *et al*., 1994). Detailed studies have revealed subtle changes in the compositions of minerals (Grossman and Brearley, 2005) and the structure of organic matter in types 3.0–3.9 chondrites (Bonal *et al*., 2006). These studies have resulted in further subdivision of the type 3.0–3.2 chondrites. The subdivision of type 3 chondrites has proven very useful in identifying the most primitive chondritic materials (sometimes called "unequilibrated chondrites" because their minerals have not been heated sufficiently for equilibration to occur). A recent compilation of the diagnostic characteristics is summarized in Table 6.1.

The CV3 chondrites show a diversity of secondary characteristics that have resulted in their subdivision into two subgroups, the oxidized CV3s ($CV3_{ox}$) and the reduced CV3s ($CV3_{red}$), primarily on the basis of metal content (McSween, 1977). The oxidized subgroup

Table 6.1 Criteria for classifying chondrites according to petrologic type (Weisberg *et al.*, 2006)

Criterion	1	2	3	4	5	6	7
Homogeneity of olivine compositions	–	> 5% mean deviations		≤5%	Homogeneous		
Structural state of low-Ca pyroxene	–	Predominantly monoclinic		>20% monoclinic	≤20% monoclinic	Orthorhombic	
Feldspar	–	Minor primary grains		Secondary <2 μm grains	Secondary 2–50 μm grains	Secondary >50 μm grains	
Chondrule glass	Altered or absent	Mostly altered, some preserved	Clear, isotropic	Devitrified	Absent		
Metal: maximum Ni (Wt. %)	–	<20 taenite minor or absent	>20 kamacite and taenite in exsolution relationship				
Sulfides: Mean Ni (Wt. %)	–	>0.5	<0.5				
Matrix	Fine grained opaque	Mostly fine-grained opaque	Opaque to transparent	Transparent, recrystallized			
Chondrule-matrix integration	No chondrules	Sharp chondrule boundaries		Some chondrules can be discerned, fewer sharp edges	Chondrules poorly delineated	Primary textures destroyed	
Carbon (wt. %)	3–5	0.8–2.6	0.2–1	<0.2			
Water (wt. %)	18–22	2–16	0.3–3	<1.5			

has been subsequently divided into the Allende-like (CV_{oxA}) and Bali-like (CV_{oxB}) subgroups (Krot *et al*., 1998). The CV_{oxB} chondrites experienced aqueous alteration and contain abundant phyllosilicates, magnetite, fayalite, and other alteration products. The matrices of CV_{oxA} chondrites consist largely of lath-shaped Fe-rich olivine, Ca, Fe pyroxene, and nepheline. These meteorites may have been reheated and dehydrated after experiencing aqueous alteration. The reduced CV3 chondrites experienced only very little aqueous alteration. Sub-typing of CV3 chondrites based on thermal metamorphism has been provided by Raman spectroscopy (Bonal *et al*., 2006).

Chondrite taxonomy

As seen in Figure 6.3, the taxonomy used for chondrites is a combination of chemical group and petrologic type, as in H4 or CM2. This system avoids the problems of previous chondrite classifications, by cleanly separating primary and secondary characteristics.

This is also a very useful scheme for recognizing whether other characteristics are primary or secondary. For example, noble gases and carbon were driven out of ordinary chondrites during thermal metamorphism, as revealed by an inverse correlation of noble gas and carbon abundances with increasing petrologic type. In fact, a characteristic that historically defined carbonaceous chondrites was the relatively high carbon contents, along with opaque matrix. The vast majority of ordinary chondrites are metamorphosed and so do not contain significant carbon. However, type 3.0–3.5 ordinary chondrites are as carbon-rich as many carbonaceous chondrites. Thus, the historical distinction between carbonaceous and ordinary chondrites is in part a reflection of metamorphism, a secondary property.

Temperatures corresponding to the various petrologic types are difficult to determine. At high temperatures, they can be roughly constrained using "geothermometers" – coexisting mineral pairs that exchange chemical components by reactions that are dependent on temperature. At lower temperatures, estimates come from non-reversible transitions in the structure of compounds or from the destruction of certain phases. Estimates of the temperatures corresponding to the various petrologic types are shown at the bottom of Figure 6.3. Also illustrated in this figure are the relative proportions of meteorites in each group that fall into the various petrologic types (indicated by the proportion of each box that is shaded). From this diagram and the relative abundances of the different classes of chondrites, it should be obvious that most chondrites have suffered high degrees of thermal metamorphism or aqueous alteration. This makes the least altered (types 3.0–3.1) chondrites especially important for cosmochemistry, although as noted earlier, CI chondrites (we typically do not write CI1 because all CI chondrites are type 1) provide the best match to solar composition.

Other classification parameters: shock and weathering

Another important secondary process affecting many chondrites is shock metamorphism. Stöffler *et al*. (1991) quantified the shock effects observed in olivine and plagioclase, and

used these for a shock classification of ordinary chondrites. Scott *et al*. (1992) extended this shock classification to carbonaceous chondrites, and Rubin *et al*. (1997) developed a scheme for enstatite chondrites by including shock effects in orthopyroxene. The classification recognizes shock stages S1 to S6, representing increasing degrees of shock pressure, finally culminating in completely melted rocks.

Many shocked chondrites are *breccias*, formed from fragments of rocks that have been cemented together to form new rocks. A chondritic breccia in which all the fragments are of the same chemical group (but usually different petrologic types) is called *genomict*. A breccia containing fragments of different meteorite groups is called *polymict*.

Terrestrial weathering has significantly altered the chemistry of some meteorites. Weathering leaches out certain mobile elements and introduces others, as well as oxidizes metals to form rust. Meteorites that are recovered after having been on Earth for some time ("finds") are commonly weathered, with effects ranging from mild to severe enough to make the meteorite hard to recognize. Terrestrial weathering completely destroys meteorites on timescales of a few thousand to tens of thousands of years (barring extreme circumstances of preservation). Even "falls," however, can experience some alteration during long and sometimes unclean storage in museums. A weathering classification scheme has been proposed by Wlotzka (1993) for ordinary chondrites from temperate climates. A different weathering classification is used for Antarctic meteorites.

Oxygen isotopes in chondrites

Because of the isotopic variability and the high cosmic abundance of oxygen, oxygen isotopes are very useful for meteorite classification. Below the condensation temperature of silicates and above the condensation temperature of ices, approximately 25% of the oxygen in the solar nebula is predicted to have occurred in condensed solids, with the remainder in gaseous molecules. Chondrites provide samples of the condensed oxygen in the early solar system.

Each meteorite class has a unique oxygen composition. The origin of these unique compositions is not fully understood, but is known to reflect two types of isotopic variations. Mass-dependent isotope variations, introduced in Chapter 2, result from physical and chemical processes that slightly favor one isotope over another due to the difference in mass. Mass-independent variations probably reflect mixing of components with isotopic compositions that originated either through nucleosynthesis or through processes that do not depend on mass. We will discuss these processes in more detail in Chapter 7.

Figure 6.4 shows the measured whole-rock isotopic compositions for various chondrite groups on a three-isotope plot (Clayton, 2004). This figure uses the delta (δ) notation, where measured isotopic ratios to ^{16}O are reported as deviations from a terrestrial standard. Terrestrial samples all lie along a single line with a slope of approximately one-half on a three-isotope plot. This reflects the larger shift of $\delta^{18}O$ relative to $\delta^{17}O$ due to the twice larger mass difference between ^{18}O-^{16}O compared to ^{17}O-^{16}O. Except for the enstatite chondrites, the different groups of chondrites plot in various positions off of

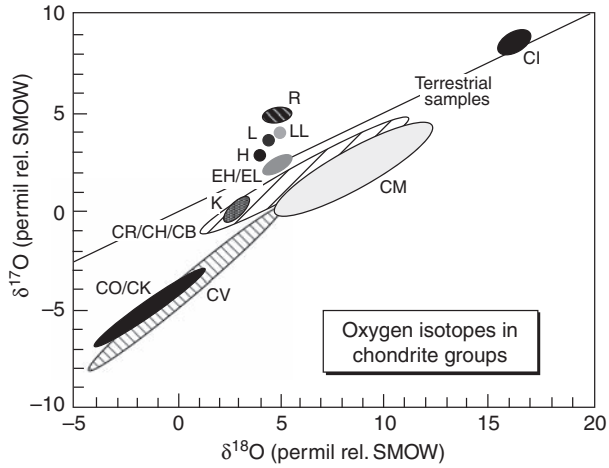

Fig. 6.4 **Oxygen isotopic compositions for bulk chondrites, after Clayton (2004). By convention, $^{17}O/^{16}O$ and $^{18}O/^{16}O$ ratios are plotted as deviations from the composition of standard mean ocean water (SMOW) in units of parts per thousand (permil). The δ values are calculated as follows: $\delta^{17}O = [((^{17}O/^{16}O)_{sample}/(^{17}O/^{16}O)_{SMOW})\text{-}1] \times 1000$, and similarly for $\delta^{18}O$.**

the terrestrial mass-fractionation line, which indicates that they formed from different mixtures of oxygen components. The carbonaceous chondrites are arrayed along a mass-independent mixing line with a slope of approximately unity in Figure 6.4, and the ranges for individual carbonaceous chondrite groups tend to be significantly greater than for other chondrite groups. The large variation among CV chondrites has been shown to result from varying amounts of ^{16}O-rich refractory inclusions. Ordinary chondrite groups (H, L, LL) and Rumaruti (R) chondrites have small but clearly resolvable differences in oxygen isotopes.

The systematic variations in oxygen isotopes provide an independent means of classifying chondrites that generates the same groups as the chemical compositions. The oxygen isotopes also work for classifying non-chondritic meteorites. Oxygen isotopic compositions are somewhat easier to obtain than detailed chemical data and so are often used to nail down a classification.

Because chondrites formed from components with diverse origins and histories, these components may have different oxygen isotopic compositions (unless they have been equilibrated during metamorphism). Figure 6.5 shows the compositions of individual chondrules from various chondrite groups (Clayton, 2004). These chondrules show mass-independent variations. Interestingly, the ranges of isotopic compositions of chondrules from H, L, and LL chondrites are indistinguishable, even though the bulk-meteorite compositions are distinct. The various minerals in some individual CAI may also have different oxygen isotopic compositions, all aligned on the three-isotope plot. The sequence, in terms of decreasing ^{16}O enrichment, is typically spinel, pyroxene, olivine, melilite, and anorthite. The linearity suggests mixing of two components, one possibly a ^{16}O-poor nebular gas.

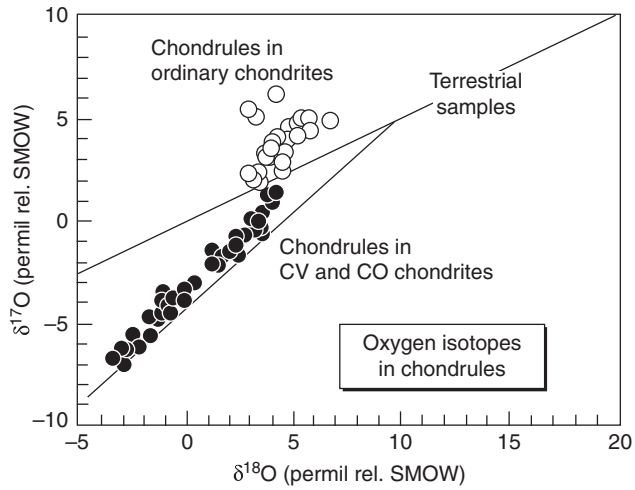

Fig. 6.5 Oxygen isotopic compositions of individual chondrules in various chondrite groups, after Clayton (2004).

Classification of nonchondritic meteorites

Differentiated meteorites do not have chondritic compositions. *Achondrites* are stony meteorites that have undergone melting and differentiation. Their precursors are commonly assumed to have had chondritic compositions, although no chondrules survived the melting process. Transitional meteorites that share some characteristics with both chondrites and achondrites are called *primitive achondrites* (an unfortunately confusing term, but widely used in the meteoritics literature). Primitive achondrites are the solid residues left when partial melts of rocks have been extracted. If only a small amount of melting occurred, the composition of the residue may be difficult to distinguish from the precursor chondrite. Magmatic achondrites (usually just called "achondrites") are igneous rocks, formed directly from melts – they are either solidified magmas or "cumulates" formed when crystals accumulate in magma chambers. Cumulate rocks no longer have the compositions of their parent melts.

Stony irons are nonchondritic meteorites that contain roughly equal proportions of silicate minerals and metal. Two types of stony irons – pallasites and mesosiderites – are distinguished. Pallasites consist of approximately equal amounts of metal and olivine (one small group contains pyroxene as well). Mesosiderates also have approximately equal proportions of metal and silicate, but the silicate fraction is basalt.

Irons are non-chondritic meteorites that are predominantly metal. Iron meteorites formed by melting of, most likely, chondritic material and segregation of metal melt from silicate. Many apparently represent asteroidal cores, although some may have formed as dispersed metal pockets in the parent asteroids.

Partial melting of chondritic materials can produce a variety of melt compositions. With increasing temperature, the first melt to form is a eutectic metal-sulfide liquid. Eutectic melts are those that form at the lowest temperatures. Segregation of dense metallic liquids

produced iron and stony-iron meteorites. With further heating, the silicate minerals begin to melt, producing silicate magmas rich in magnesium, calcium, and aluminum. These magmas are termed "basaltic," as they are similar in composition to the common basalts produced by partial melting of the Earth's mantle rock.

The behavior of elements during partial melting and crystallization of the resulting magma can vary greatly, depending on how the elements are partitioned between crystals and coexisting liquid. The size and charge of an ion determine whether it will fit easily into sites in common mineral structures. For example, Ni^{2+} is similar in size and has the same charge as Mg^{2+}, so it substitutes readily into magnesium-rich olivine. Nickel is said to be "compatible." On the other hand, U^{3+} is a large ion with high charge, and most common minerals exclude it. Only minerals containing other large, high-charge cations as major elements can easily incorporate "incompatible" uranium. Such minerals usually crystallize late after most of the liquid has solidified, causing incompatible element concentrations to increase in the residual liquid during fractionation. Compatibility also determines how elements partition during partial melting, as incompatible elements prefer the melt phase and thus are concentrated in magmas. Partitioning of elements between crystals and magma is important for understanding differentiated meteorites; it will be described more rigorously in Chapter 7.

Possible heat sources for melting in meteorite parent bodies are discussed in Chapter 11. Differentiated meteorites generally have old radiometric ages (Chapter 9), which indicate igneous activity began and ended soon after their parent bodies accreted.

A classification of nonchondritic meteorites is shown in Table 6.2. These meteorites will be described in the following sections, and their chemistry will be considered in Chapter 11.

Primitive achondrites

Primitive achondrites exhibit metamorphic textures, as appropriate for the solid residues from which melts were extracted. In effect, these meteorites represent an extension of the highly metamorphosed type 6 chondrites, which show no eutectic melting of metal and sulfide. In a few cases, some primitive achondrites have recognizable chondritic textures, but often they are so thoroughly recrystallized that chondrules are not identifiable.

Goodrich and Delaney (2000) noticed that primitive achondrites could be readily distinguished from magmatic achondrites using a diagram of molar Fe/Mn versus Fe/Mg (Fig. 6.6). The primitive achondrites plot within the wedge of chondritic Mn/Mg values, whereas achondrites crystallized from magmas have higher Mn/Mg ratios. Partial melts of chondrites have higher Mn/Mg ratios than the original chondrite source (manganese is more compatible than magnesium) and the corresponding solid residues have lower Mn/Mg, as shown by the arrows in Figure 6.6. The Mn/Mg ratio of a magma itself can change, if it accumulates or loses crystals. The residue composition moves to the left on this diagram as the degree of partial melting increases. Primitive achondrites have nearly chondritic abundances of iron, manganese, and magnesium, because they commonly represent residues from very low degrees of partial melting, so Figure 6.6 serves to distinguish them from magmatic achondrites.

Table 6.2 Classification of differentiated meteorites

Primitive achondrites – residues from partial melting
Acapulcoites – lodranites
Brachinites
Ureilites
Winonaites
Magmatic achondrites – crystallized from silicate magma
Aubrites
Howardites – Eucrites – Diogenites (HED)
Angrites
Stony irons
Mesosiderites
Pallasites – main-group, Eagle Station-group, pyroxene-group
Irons
IAB
IC
IIAB
IIC
IID
IIE
IIIAB
IIICD
IIIE
IIIF
IVA
IVB
Martian meteorites (SNCs)
Shergottites – basaltic, olivine-phyric, lherzolitic
Nakhlites
Chassignites
Orthopyroxenite (ALH 84001)
Lunar Meteorites
Highlands breccias
Mare basalts

Here we describe three important groups of primitive achondrites, omitting other less important primitive achondrites identified in Table 6.2.

Acapulcoites and lodranites

The acapulcoites (Fig. 6.7a) have recrystallized textures, but a few relict chondrules have been reported (McCoy *et al*., 1997a). The relative proportions of the minerals (olivine, orthopyroxene, diopside, plagioclase, metal) in acapulcoites are similar to those in ordinary chondrites, and the abundances of the major elements are nearly chondritic. However,

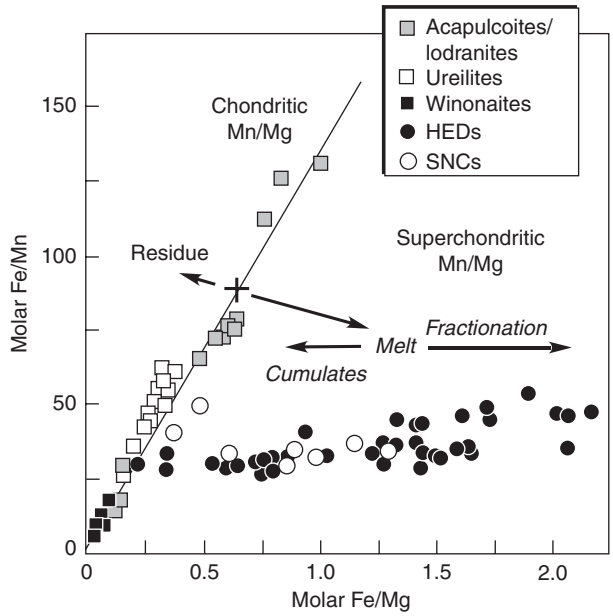

Fig. 6.6 Diagram used to distinguish achondrites that crystallized from melts and primitive achondrites that represent the solid residue once melt has been extracted. Primitive achondrites plot on or to the left of the chondritic Mn/Mg ratio, whereas igneous achondrites have higher Mn/Mg. These differences occur because a chondrite (symbolized schematically by the cross; most chondrites actually plot closer to the origin, but this is offset for clarity) and the partial melts formed from it have different Mn/Mg values, as shown by arrows. The arrowhead for residue compositions represents extraction of 30% melt, and residues from less complete melt extraction lie along that arrow. The arrow pointing to melt represents 2% melting, and melts formed by higher degrees of melting lie along the arrow joining the 2% melt to its chondritic source. The magma composition can be modified by fractional crystallization, forming cumulates and fractionated liquids, as shown by horizontal arrows. After Goodrich and Delaney (2000).

elements that have siderophile or chalcophile affinities are depleted, reflecting extraction of a eutectic metal-sulfide melt. Some acapulcoites exhibit tiny metal-troilite veins that represent pathways for melts migrating out of the rocks.

The closely related lodranites (Fig. 6.7b) are more thoroughly recrystallized and show no vestige of chondrite textures (McCoy *et al*., 1997b). Their bulk chemical compositions are no longer chondritic, because a greater degree of partial melting produced a silicate liquid of basaltic composition which migrated out of the rocks. The compositions of lodranites are depleted in the incompatible trace elements that were concentrated in basaltic melt. Siderophile and chalcophile elements are also depleted, as in acapulcoites.

Ureilites

The ureilites (Fig. 6.7c) constitute the second largest group of non-chondritic meteorites (Takeda, 1987). They are composed primarily of olivine and pyroxene, with interstitial

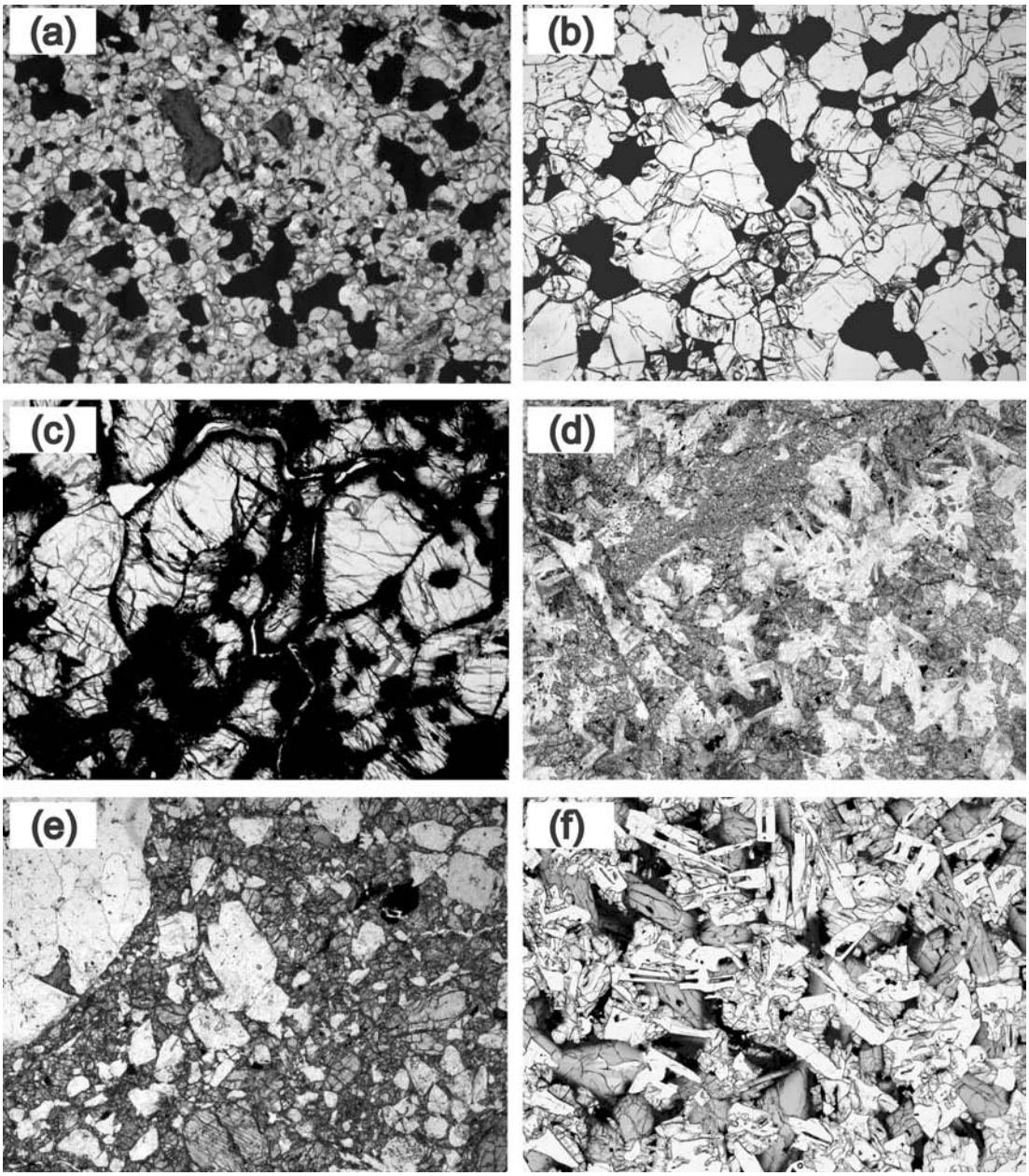

Fig. 6.7 Photomicrographs of primitive and magmatic achondrites, all in plane polarized light with FOV = 5.4 mm. (a) Acapulco and (b) Lodran, the type specimens for acapulcoite and lodranite; light grains are olivine and pyroxene, and black grains are metal. (c) NWA 942 ureililte, showing olivine crystals (white) in dark, carbonaceous mesostasis. (d) Millbillillie eucrite, consisting of pyroxene (gray) and plagioclase and nepheline (white), and (e) NWA 1401 diogenite, consisting of brecciated pyroxene – both members of the HED class. (f) D'Orbigny angrite, consisting of pyroxene and olivine (gray), plagioclase (white), and mesostasis (black). All images from Lauretta and Killgore (2005), with permission.

material that is rich in elemental carbon (mostly graphite). The textures of silicate minerals are variable but highly recrystallized – so much so that they resemble igneous rocks, which has led to past controversy about whether ureilites are magmatic rocks or residues. Graphite was apparently the original carbon mineral in ureilites, but intense shock pressures have converted some of it into its dense polymorph, diamond, in some meteorites. The chemical compositions of ureilites indicate depletion in many lithophile elements, reflecting loss of a basaltic melt. Their high carbon contents and oxygen isotopic compositions (discussed later) suggest that ureilites formed as residues from melting carbonaceous chondrite.

Winonaites and IAB silicate inclusions

The winonaites are compositionally similar to silicate inclusions in some IAB irons (described below). They have chondritic compositions, and relict chondrules have been found in some meteorites. They consist of olivine, pyroxenes, plagioclase, metal, troilite, and other minor minerals (Benedix *et al*., 1998), and most have been recrystallized. Like the acapulcoites, they have experienced only small degrees of melting.

Magmatic achondrites

The various groups of magmatic achondrites either formed as solidified melts or cumulates from a crystallizing magma, as noted earlier. Although they are thought to have formed by melting of chondritic sources, their elemental abundances are far from chondritic, owing to the differentiation resulting from partial melting and fractional crystallization. Partial melts of chondritic material are always basaltic, so the achondrites are either basalts or cumulates derived from basaltic magmas. However, they exhibit surprising variability in composition and oxidation state, reflecting differences in their chondrite precursors. Here we describe several of the more prominent achondrite groups.

Aubrites

The aubrites are the most reduced achondrites (Keil *et al*., 1989). Their silicates are essentially free of iron, and they contain minor metallic iron. A variety of unusual sulfides of calcium, chromium, manganese, titanium, and sodium – all usually lithophile elements – occur in aubrites. These unusual sulfides also characterize the highly reduced enstatite chondrites, which may have been precursors for these rocks.

The most abundant mineral in aubrites is coarse-grained orthopyroxene (as it is in enstatite chondrites), and only a small amount of plagioclase is present. Aubrites are commonly brecciated, and several clasts of related basalt have been observed. The aubrites are depleted in siderophile and chalcophile elements relative to chondritic abundances,

indicating fractionation of metal and sulfide, and their concentrations of incompatible elements are variable (McCoy *et al*., 1999).

Howardites–eucrites–diogenites

The howardite–eucrite–diogenite group, commonly abbreviated as HED, is the largest suite of differentiated meteorites, represented by more than a hundred meteorites (Mittlefehldt *et al*., 1998). This group consists of the following rock types: lavas (basaltic eucrites); coarse-grained basalts, called gabbros, that contain some accumulated crystals (cumulate eucrites); cumulates of orthopyroxene (diogenites); and mechanical mixtures of eucrite and diogenite clasts (howardites). Most of these meteorites are breccias, and many have been thermally metamorphosed.

The basaltic eucrites (Fig. 6.7d) are fine-grained rocks with textures formed by rapid cooling of magmas on or near the surface of their parent asteroid. However, the igneous textures of many eucrites are obscured by brecciation and metamorphism. They are composed of pigeonite and plagioclase, with minor tridymite, ilmenite, chromite, and other accessory minerals. The mineralogy of cumulate eucrites is similar, but their coarse grain sizes attest to slower cooling in intrusions at depth. Diogenites (Fig. 6.7e) consist mostly of orthopyroxene, with small but variable amounts of olivine and minor chromite. These rocks are cumulates related to eucrite magmas. Howardites were formed from eucrites and diogenites that were pulverized and mixed by impacts on the parent-body surface.

The geochemistry of HED meteorites reflects pervasive melting and differentiation of the parent asteroid. They are depleted in siderophile elements, lost when a metallic core segregated during differentiation. Partial melting and fractional crystallization induced changes in incompatible lithophile elements in the HED magmas. This igneous activity occurred very early in solar system history (ending by about 4.4 billion years ago), as judged from radiometric dating.

Angrites

The angrites (Fig. 6.7f) are basaltic rocks with unusual mineralogy (Mittlefehldt and Lindstrom, 1990). They contain aluminum- and titanium-rich diopside (a variety called fassaite), calcium-rich olivine (kirschsteinite), plagioclase, and nepheline, as well as accessory spinel, troilite, whitlockite, magnetite, and other minerals. Their textures vary – some have quenched textures indicating rapid solidification from a melt, some are porphyritic suggesting slower crystal growth, and one (Angra dos Reis) contains coarse crystals that join at triple junctions indicating metamorphic textural equilibration.

The geochemistry of angrites is characterized by strong silica undersaturation, by which we mean that there is not enough SiO_2 to combine with various cations to form common silicate minerals. The result is the formation of silica-poor minerals like kirschsteinite and nepheline. These meteorites also show strong depletions in moderately volatile elements. They are thought to have formed as partial melts of a chondritic source under oxidizing conditions.

Irons and stony irons

Iron meteorites offer the unique opportunity to examine metallic cores from deep within differentiated bodies. Most of these samples were exposed and dislodged when asteroids collided and fragmented. Although irons constitute only about 6% of meteorite falls, they are well represented in museum collections. Most iron meteorites show wide variations in siderophile-element abundances, which can be explained by processes like fractional crystallization in cores that mimic those in achondrites. However, some show perplexing chemical trends that may be inconsistent with their formation as asteroid cores.

Classification and composition of iron meteorites

Iron meteorites consist primarily of iron-nickel metal that commonly occurs as intergrowths of kamacite and taenite (Haack and McCoy, 2004). Historically, irons were classified according to the geometries of their metallic structures into hexahedrites, octahedrites, and ataxites. Octahedrites exhibit a Widmanstätten pattern (Fig. 6.8), developed as an intergrowth of kamacite and taenite during slow cooling. Hexahedrites have lower nickel contents and consist entirely of kamacite. Common accessory minerals include troilite, schreibersite, graphite, chromite, and cohenite. Sulfur- and phosphorus-rich minerals, such as troilite and schreibersite, vary in abundance among groups of irons. Also, differences in oxidation state are reflected in accessory minerals, as typified by the presence of graphite and cohenite in more reduced irons and phosphates in more oxidized irons.

Once the chemical compositions of enough irons had been measured, it became clear that, although the various structural classes were reflected in chemical differences, chemical

Fig. 6.8 **Widmanstätten pattern composed of intergrown plates of kamacite and taenite, in the Tres Castillos iron meteorite. The black phase is graphite, surrounded by troilite (dark gray), and the lighter gray phase is schreibersite.**

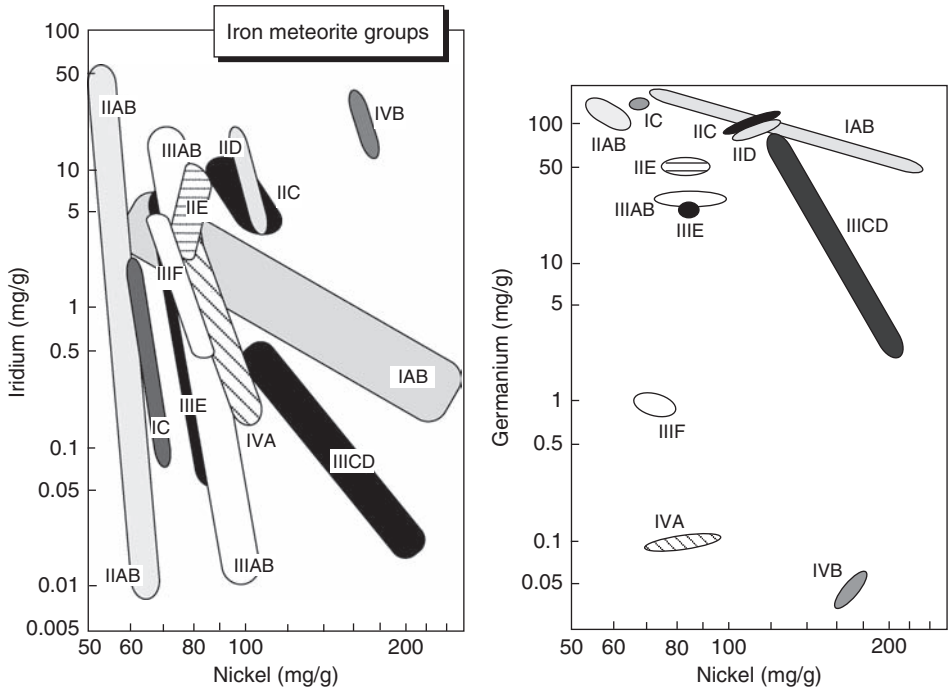

Fig. 6.9 **Siderophile element diagrams used to classify iron meteorites. Modified from Scott and Wasson (1975).**

composition cannot be deduced reliably from structure. Using instrumental neutron activation analysis, John Wasson and his colleagues have analyzed hundreds of iron meteorites for siderophile elements over the past three decades. Compositional clusters (Fig. 6.9) based on the abundances of nickel, cobalt, germanium, gallium, iridium, gold, tungsten, and other elements define samples from different asteroid cores.

The taxonomy for irons is complicated, reflecting the tortured historical evolution of their classification. Originally, groups I to IV were defined by their gallium and germanium concentrations. As more data became available, some groups were subdivided (e.g. group III was separated into IIIA and IIIB and then recombined (IIIAB) as meteorites with intervening compositions were found). Thirteen major groups are now recognized, as shown in Table 6.2. Numerous ungrouped irons, representing as many as 50 distinct classes, are also known.

Many of the compositional trends seen in irons can be explained by fractional crystallization within metallic liquid cores. Various iron groups have different concentrations of these elements, but their inter-element trends are parallel, suggesting common magmatic processes (Fig. 6.9). These meteorites are called the "magmatic irons." A few iron groups, however, do not show the large fractionations in siderophile elements seen in the other groups, but exhibit extreme variations in nickel, gallium, and germanium. These iron groups (IAB, IIICD, and IIE) also contain abundant silicate inclusions, often having chondritic compositions. They are commonly labeled "silicate-bearing" or "nonmagmatic" irons (the

latter term is unfortunate, because all irons were once molten; however, they apparently formed by different processes, perhaps within dispersed metal pools rather than large, central cores).

Pallasites and mesosiderites

The ~50 known pallasites can be divided into "main group" pallasites, the Eagle Station grouplet (currently with three members), and the pyroxene pallasite grouplet (with four members) (Haack and McCoy, 2004). Main group pallasites contain magnesium-rich olivine and iron-nickel metal. The green olivine is sometimes dispersed and sometimes clustered, and grains are either rounded or angular. In fact, there are large areas of the Brenham pallasite that contain no olivine at all. As a pallasite weathers, the green olivine turns brown. The metal composition in pallasites is similar to that in IIIAB irons, suggesting a possible relationship. The Eagle Station trio, in addition to olivine and metal, contains pyroxenes, chromite, and phosphates. Olivines are more iron-rich than in main group pallasites, and metal has higher iridium and nickel contents. The pyroxene pallasites differ in mineralogy and appear to represent a distinct group.

Olivine and metal are expected to be in contact at the boundary between a core and its overlying silicate mantle. That is the traditionally favored location for the formation of pallasites, although there are numerous problems with that explanation.

Mesosiderites are a highly enigmatic group of differentiated meteorites. They are breccias composed of iron-nickel metal and silicate in roughly equal proportions. The metal represents molten material from the deep interior of an asteroid, whereas the silicate fraction consists of basalts and pyroxene cumulates similar to HED meteorites that formed near the surface. It is difficult to construct models that allow mixing of such diverse materials, but these disparate materials are generally thought to have been violently mixed by impact.

Lunar samples

The Apollo astronauts returned 382 kg of lunar sample to Earth, and this collection was supplemented by 326 g of soil samples collected by the Soviet Luna landers. The first lunar meteorite was found in 1982 in Antarctica. Since that time, over 120 lunar meteorites representing about 60 different fall events have been collected. The total mass of these meteorites is ~48 kg. About one-third of these meteorites were recovered in Antarctica by American and Japanese teams, and most of the rest were recovered in the deserts of North Africa and Oman. The lunar meteorites have significantly expanded the areas of the Moon from which we have samples.

Lunar rocks (Fig. 6.10) represent samples from the ancient highlands and the younger maria (Papike *et al*., 1998; Warren, 2004). Highlands rocks are readily distinguished by having high Al/Si ratios (reflecting their high abundance of aluminum-rich plagioclase) and

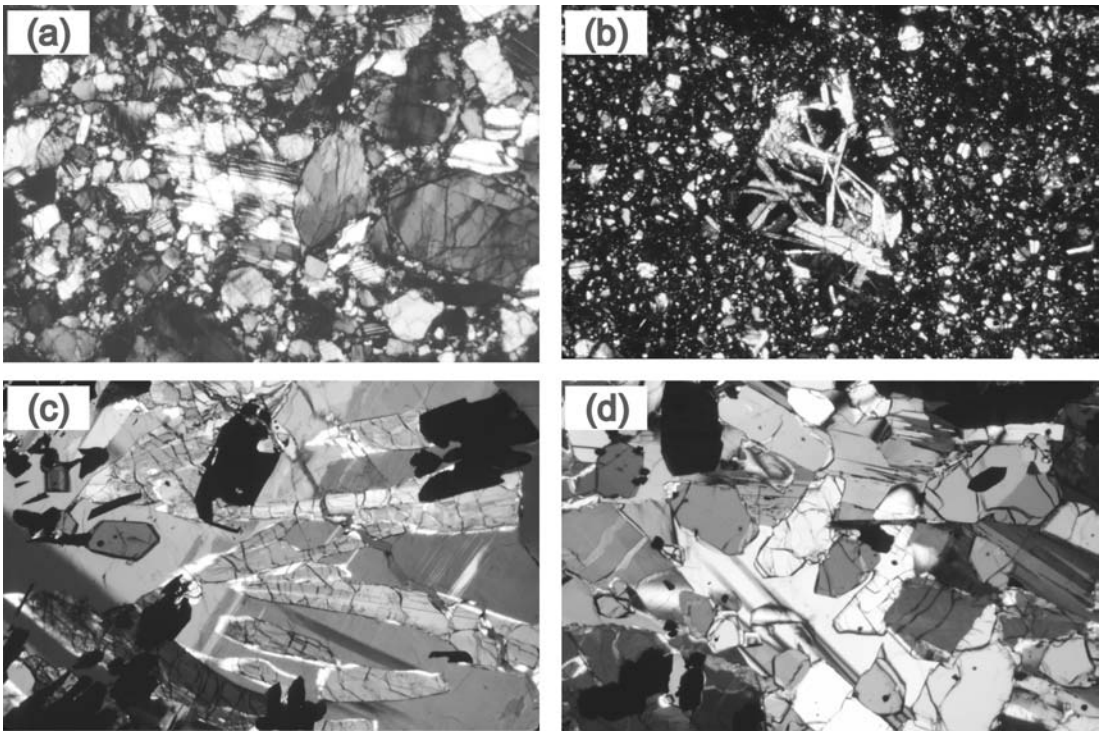

Fig. 6.10 **Microscopic images of lunar rocks, all viewed under crossed nicols with FOV = 5.4 mm. (a) Ferroan anorthosite 60025, composed almost entirely of plagioclase. (b) KREEP-rich breccia 70126, exhibiting mineral and basaltic rock clasts. (c) High-Ti mare basalt 70017, composed of pyroxene, plagioclase, and opaque minerals (elonged grains are ilmenite). (d) Low-Ti mare basalt 12005, composed of pyroxene, plagioclase, and opaque oxides. Images courtesy of David Kring.**

lower TiO_2 contents (which are higher in ilmenite-rich mare basalts). Lunar samples also include volcanic glasses and soils.

Almost all highlands rocks are breccias composed of clasts fragmented by impacts. "Pristine" highlands rocks (Warren and Wasson, 1977) have chemical compositions corresponding to igneous rocks, despite the fact that many are brecciated samples of a single rock type (monomict). Non-pristine rocks are breccias composed of multiple rocks (polymict), and their compositions reflect their mixed parentage and/or contamination by the impacting meteor. Pristine highlands samples fall into three categories: ferroan anorthosites, magnesium-rich rocks, and alkali rocks. The anorthosites are coarse-grained cumulates of plagioclase with only minor amounts of pyroxenes and olivine. These rocks represent the most ancient lunar crust, formed at ~4.5 billion years ago. The magnesium-rich suite is slightly younger and consists of coarse-grained rocks composed of olivine, pyroxenes, and plagioclase. The alkali suite includes basalts, anorthosites and gabbros with higher sodium contents, and "granites" containing K-feldspar. Non-pristine breccias exhibit a wide variety of textures, reflecting the complex processes that produced them. These polymict breccias typically contain highly variable amounts of KREEP (potassium, rare earth elements, phosphorus), an incompatible-element-rich component.

Mare basalts are composed of pyroxenes, plagioclase, sometimes with olivine or silica, and a variety of minor minerals. The most prominent accessory mineral is ilmenite, which is commonly present in higher abundances than in terrestrial basalts. Ilmenite concentration, which controls TiO_2 abundance, is used to subdivide mare basalts into high-titanium (>6 wt. %), low-titanium (1.5–6%), and very low-titanium (<1.5%) varieties. (These are relative terms; it is somewhat of a misnomer to call a rock with 5% TiO_2 "low-titanium.") A secondary classification is based on abundances of K_2O and Al_2O_3. Mare basalts are younger than highlands rocks, with radiometric ages varying between approximately 3.9 and 2.0 billion years.

Several kinds of volcanic glass beads were collected by Apollo astronauts. Numerous chemical classifications have been devised. The best known are the Apollo 15 green glasses and the Apollo 17 orange glasses. Each of these glasses is compositionally uniform in terms of major elements but coatings on beads are enriched in highly volatile elements formed during fire-fountain eruptions.

Lunar soil (more properly called "regolith") is a collection of highlands and mare rocks pulverized by impacts. These soils consist of recognizable mineral grains and rock fragments, often bonded by impact-melted glass into small aggregates ("agglutinates"). Because of impact gardening over long periods of time, the soils were repeatedly exposed on the lunar surface and provide chemical evidence of irradiation by the solar wind. Soils that have been lithified into coherent rocks are regolith breccias.

The chemistry of lunar materials will be considered in much greater detail in Chapter 13.

Martian meteorites

Martian meteorites ("SNC" for shergottite, nakhlite, chassignite) comprise a diverse suite of igneous rocks (McSween, 2004). With only one exception, they are geologically young. Presently, 34 of these meteorites are recognized, most recovered from Antarctica and North African deserts.

Basaltic shergottites (Fig. 6.11a) are lavas composed of pyroxenes (pigeonite and augite), plagioclase (converted to maskleynite by shock), and a variety of accessory minerals including iron-titanium oxides, sulfides, and whitlockite. Olivine-phyric shergottites are texturally and mineralogically similar, except that they also contain olivine. Most of the large olivine crystals ("phenocrysts") in them crystallized from the shergottite liquid, although some grains may be foreign crystals incorporated into the magma ("xenocrysts"). Lherzolitic shergottites are cumulate rocks (gabbros), composed of olivine, pyroxenes, and lesser amounts of maskelynite, and formed by slow cooling of shergottite-like magmas at depth. The shergottites range in age from 575–165 million years.

Nakhlites (Fig. 6.11b) are augite-rich basaltic rocks. They are cumulates formed by concentration of augite and minor olivine. They formed on or close to the surface, as indicated by the fine grain size of their groundmass, which consists of needles of feldspars, delicate spinel crystals, and glass. All the nakhlites are ~1.3 billion years old, and compositional similarities indicate that they are related.

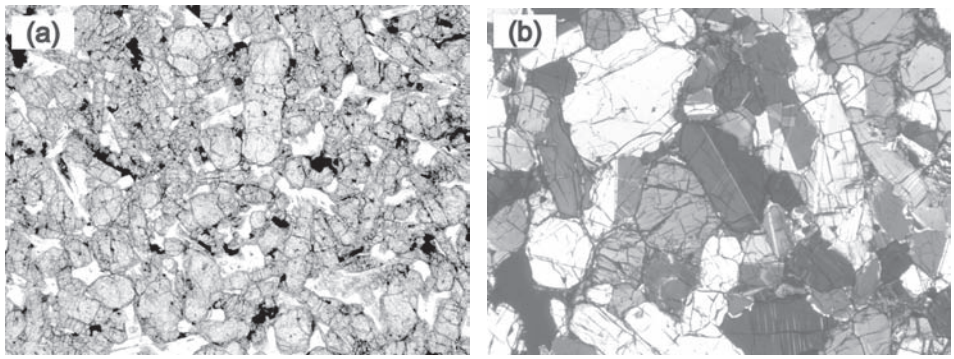

Fig. 6.11 **Martian meteorites, viewed in plane polarized light with FOV = 5.4 mm. (a) Zagami basaltic shergottite, composed of pyroxene and plagioclase (white), which has been converted to maskelynite by shock. (b) Lafayette nakhlite, composed mostly of high-calcium pyroxene. (a) from Lauretta and Killgore (2005), with permission.**

The two known chassignites are olivine cumulates with minor pyroxene. They are also 1.3 billion years old and appear to be related to nakhlites, although the exact connection is unclear.

ALHA 84001 is a unique Martian meteorite with an ancient age of ~4.5 billion years. It consists mostly of orthopyroxene crystals that accumulated in basaltic magma. Its most distinctive feature, however, is the occurrence of small globules of carbonates with unusual compositions and textures. The controversial (now largely discredited) hypothesis that the carbonates contain evidence of extraterrestrial life (McKay *et al*., 1996) made this the most famous meteorite on Earth. ALHA 84001 has also experienced intense shock metamorphism.

We will return to a more detailed consideration of the chemistry of Martian meteorites in Chapter 13 and of their chronology in Chapter 9.

Oxygen isotopes in differentiated meteorites

Many achondrites, lunar meteorites, and Martian (SNC) meteorites can be distinguished by their oxygen isotopic compositions. The data for various groups (Clayton, 2004) are illustrated in the upper part of Figure 6.12. Lunar rocks plot squarely on the terrestrial fractionation line, as do aubrites, but SNCs and HEDs are displaced along parallel mass fractionation lines. The Moon is thought to have formed from a massive impact onto the Earth, and the identical oxygen isotopic compositions of both bodies suggest that the Earth and impactor were compositionally similar or that their materials were thoroughly mixed during the collision. The aubrites plot on the terrestrial fractionation line, as do the enstatite chondrites from which they were probably derived. The similarity between the oxygen isotopic concentrations of these meteorites and the Earth support the idea based on chemical arguments that the Earth may have accreted from enstatite chondrite-like material.

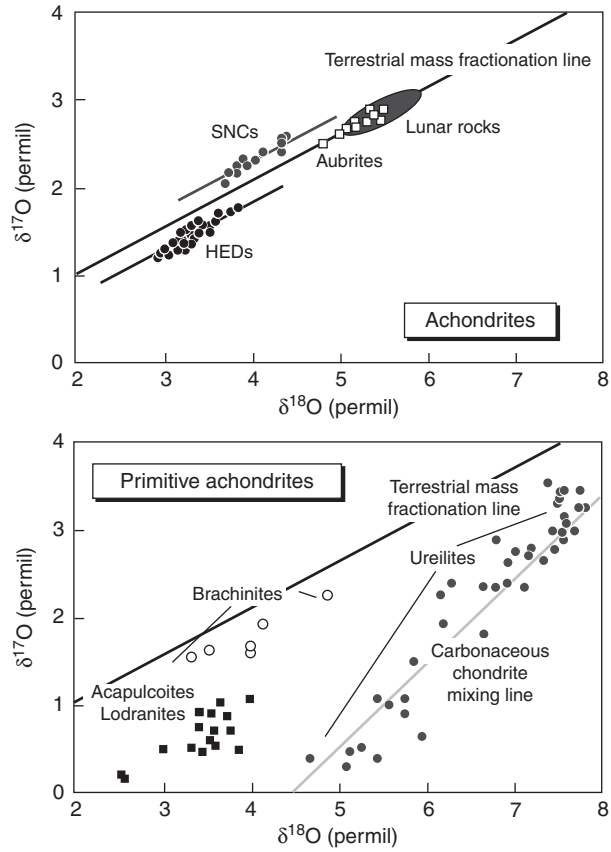

Fig. 6.12 **Oxygen isotopes in achondrites (above) and primitive achondrites (below). The δ notation and units are explained in the caption for Figure 6.4. Most achondrites define mass fractionation lines parallel to, but slightly offset from the terrestrial line. Aubrites and lunar samples plot squarely on the terrestrial line. Primitive achondrites generally do not define oxygen mass fractionation lines, but are scattered and resemble their chondrite precursors.**

Unlike chondrites, the achondrites define mass-dependent fractionation lines with slope $+^1/_2$, parallel to the terrestrial fractionation line. Melting homogenizes oxygen isotopes in the parent body, and differentiation of those magmas smears them along a mass-dependent fractionation line. Primitive achondrites, however, do not always define mass fractionation lines. The partial melts extracted from those meteorites presumably had homogenized oxygen isotopes, but the solid residues could have remained heterogeneous unless metamorphism and melting were extensive. For example, limited melting in the acapulcoite–lodranite parent body did not erase its chondritic isotopic signature (lower part of Fig. 6.12). The ureilites are arrayed along the mixing line seen in carbonaceous chondrites (Fig. 6.12), consistent with their formation as residues from partial melting of carbonaceous chondrites.

Iron meteorites commonly contain oxygen-bearing minerals, such as chromite, phosphates, and sometimes silicates. Oxygen isotopes in such inclusions provide information on

possible connections between irons and other meteorite groups. For example, the isotopic fingerprint of inclusions in IIIAB irons is similar to that of the olivines in main group pallasites, suggesting that these meteorites might be samples of the same core and core-mantle boundary.

Box 6.2 Meteorite data sources

New meteorites are constantly added to the world's collections, and keeping track of them is a difficult task. The British Museum's *Catalogue of Meteorites* (Grady, 2000, referenced at the end of the chapter) serves as an authoritative resource, although it is not constantly updated. It is available in printed and electronic form. This reference not only provides classification, mass, and information on circumstances of recovery, but also lists publications on each meteorite. The Meteoritical Society, an international organization devoted to meteorite research, periodically publishes the *Meteoritical Bulletin*, listing newly classified meteorites and approved meteorite names. This database can be accessed online at meteoriticalsociety.org. Also, MetBase, a commercially produced computer database for meteorites, is available for purchase online at www.metbase.de. It includes meteorite descriptions, analyses, and a bibliography of relevant scientific literature.

Summary

Primitive chondrites provide a record of nebular processes and conditions. In this chapter we have described the components (chondrules, refractory inclusions, metal and sulfide, and matrix) that formed in the nebular setting and were collected together to produce chondrites. Each of these components, in turn, consists of phases whose compositions, mineral associations, and textures constrain their origin. Proper interpretations of cosmochemical analyses of bulk chondrites, their components, and their constituent minerals also require an understanding of their geologic histories after accretion into planetesimals. Chondrite parent bodies experienced a variety of secondary processes including thermal metamorphism, aqueous alteration, and shock metamorphism. A serviceable classification scheme for chondrites is based on a primary characteristic (differences in their bulk chemical compositions) and several secondary characteristics (the intensity of metamorphism or alteration). Oxygen isotopes provide a convenient way to distinguish most chondrite groups.

Differentiated meteorites record geologic processes on or within bodies that were heated to the point of melting. Melting of primitive chondritic materials was partial rather than complete, producing a metal-sulfide eutectic liquid and, as melting advances, a silicate magma having the composition of basalt. Partial melting and fractional crystallization of the resulting liquids produce changes in the chemical composition of the resulting rocks (differentiation). Magmatic achondrites (usually just called achondrites) formed by crystallization of magmas, and irons and stony irons formed by solidification of metallic liquids and their commingling with silicates. Samples of the solid residues left behind after extraction of

partial melts are primitive achondrites. Lunar rocks and all planetary samples, such as Martian meteorites, are differentiated rocks as well. These rocks formed in most cases by more protracted planetary evolution, encompassing multiple periods of melting and differentiation, so that the mantles that partially melted to produce magmas may no longer have had chondritic compositions. Oxygen isotopes in differentiated rocks show mass-dependent fractionations, but their compositions can sometimes be used to recognize differentiated samples from a common parent body.

Now that we have gained some appreciation of the value and limitations of the various kinds of samples available for cosmochemical analysis, we will begin to consider what these materials really tell us. In Chapter 4, we saw how solar system abundances of elements and isotopes are determined using the most primitive chondrites. In subsequent chapters, we will see how elements are fractionated in space, planetesimals, and planets.

Questions

1. Describe the components of chondritic meteorites.
2. Explain the classification system used for chondrites.
3. What is differentiation, and how does it cause chemical changes?
4. Distinguish between the origins of magmatic achondrites, primitive achondrites, and irons.
5. How are oxygen isotopes in chondrites and achondrites illustrated graphically, and how are the isotopic compositions useful in classifying meteorites and recognizing relationships between them?

Suggestions for further reading

There are a number of excellent (but rather technical) chapters in recent books that describe the classification of meteorites in greater detail than presented here. The following are highly recommended. All have excellent photographs, but some of these resources probably offer more information than most readers can use.

Heiken, G. H., Vaniman, D. T. and French, B. M., eds. (1991) *Lunar Sourcebook: A User's Guide to the Moon*. Cambridge: Cambridge University Press, 736 pp.

Grady, M. M. (2000) *Catalogue of Meteorites*. Cambridge: Cambridge University Press, 689 pp. plus disk.

Krot, A. N., Keil, K., Goodrich, C. A., Scott, E. R. D. and Weisberg, M. K. (2004) Classification of meteorites. In *Treatise on Geochemistry, Volume 1: Meteorites, Comets, and Planets*, ed. Davis, A. M. Oxford: Elsevier, pp. 83–128.

McSween, H. Y. and Treiman, A. H. (1998) Martian meteorites. In *Planetary Materials, Reviews in Mineralogy* **36**, ed. Papike, J. J. Washington, D.C.: Mineralogical Society of America, pp. 6–1 to 6–53.

Scott, E. R. D. and Krot, A. N. (2004) Chondrites and their components. In *Treatise on Geochemistry, Volume 1: Meteorites, Comets, and Planets*, ed. Davis, A. M. Oxford: Elsevier, pp. 143–200.

Weisberg, M. K., McCoy, T. J. and Krot, A. N. (2006) Systematics and evaluation of meteorite classification. In *Meteorites and the Early Solar System II*, eds. Lauretta, D. S. and McSween, H. Y., Jr. Tucson: University of Arizona Press, pp. 19–52.

Brearley, A. J. and Jones, R. H. (1998) Chondritic meteorites. In *Planetary Materials, Reviews in Mineralogy* **36**, ed. Papike, J. J. Washington, D.C.: Mineralogical Society of America, pp. 3–1 to 3–398.

References

Benedix, G. K., McCoy, T. J., Keil, K., Bogard, D. D. and Garrison, D. H. (1998) A petrologic and isotopic study of winnonaites: evidence for early partial melting, brecciation, and metamorphism. *Geochimica et Cosmochimica Acta*, **62**, 2535–2554.

Bonal, L., Quirico, E., Bourot-Denise, M. and Montagnac, G. (2006) Determination of the petrologic type of CV3 chondrites by Raman spectroscopy of included organic matter. *Geochimica et Cosmochimica Acta*, **70**, 1849–1863.

Clayton, R. N. (2004) Oxygen isotopes in meteorites. In *Treatise on Geochemistry, Volume 1: Meteorites, Comets, and Planets*, ed. Davis, A. M. Oxford: Elsevier, pp. 129–142.

Goodrich, C. A. and Delaney, J. S. (2000) Fe/Mg-Fe/Mn relations of meteorites and primary heterogeneity of primitive achondrite parent bodies. *Geochimica et Cosmochimica Acta*, **64**, 149–160.

Grossman, J. N. and Brearley, A. J. (2005) The onset of metamorphism in ordinary and carbonaceous chondrites. *Meteoritics and Planetary Science*, **40**, 87–122.

Haack, H. and McCoy, T. J. (2004) Iron and stony-iron meteorites. In *Treatise on Geochemistry, Volume 1: Meteorites, Comets, and Planets*, ed. Davis, A. M. Oxford: Elsevier, pp. 325–345.

Keil, K., Ntaflos, Th., Taylor, G. J., Brearley, A. J., Newsom, H. E. and Roming, A. D. (1989) The Shallowater aubrite: evidence for origin by planetesimal impact. *Geochimica et Cosmochimica Acta*, **53**, 3291–3307.

Krot, A. N., Petaev, M. I., Scott, E. R. D. *et al*. (1998) Progressive alteration in CV3 chondrites: More evidence for asteroidal alteration. *Meteoritics and Planetary Science*, **33**, 1065–1085.

Lauretta, D. S. and Killgore, M. (2005) *A Color Atlas of Meteorites in Thin Section*. Tuscon: Golden Retriever Press, 301 pp.

Lauretta, D. S., Nagahara, H. and Alexander, C. M. O' D. (2006) Petrology and origin of ferromagnesian silicate chondrules. In *Meteorites and the Early Solar System II*, eds. Lauretta, D. S. and McSween, H. Y., Jr. Tucson: University of Arizona Press, pp. 431–462.

Lodders, K. and Fegley, B., Jr. (1998) *The Planetary Scientist's Companion*. New York: Oxford University Press, 371 pp.

McCoy, T. J., Keil, K., Muenow, D. W. and Wilson, L. (1997a) Partial melting and melt migration in the acapulcoite-lodranite parent body. *Geochimica et Cosmochimica Acta*, **61**, 639–650.

McCoy, T. J., Keil, K. Clayton, R. N. *et al*. (1997b) A petrologic and isotopic study of lodaranites: evidence for early formation as partial melt residues from heterogeneous precursors. *Geochimica et Cosmochimica Acta*, **61**, 623–637.

McCoy, T. J., Dickinson, T. L. and Lofgren, G. E. (1999) Partial melting of the Indarch (EH4) meteorite: a textural, chemical, and phase relations view of melting and melt migration. *Meteoritics and Planetary Science*, **34**, 735–746.

McKay, D. S., Gibson, E. K., Thomas-Keprta, K. L. *et al*. (1996) Search for past life on Mars: possible relic biogenic activity in Martian meteorite ALH84001. *Science*, **273**, 924–930.

McSween, H. Y. (1977) Petrographic variations among carbonaceous chondrites of the Vigarano type. *Geochimica et Cosmochimica Acta*, **41**, 1777–1790.

McSween, H. Y. (1979) Are carbonaceous chondrites primitive or processed? A review. *Reviews of Geophysics and Space Physics*, **17**, 1059–1078.

McSween, H. Y. (2004) Mars. In *Treatise on Geochemistry, Volume 1: Meteorites, Comets, and Planets*, ed. Davis, A. M. Oxford: Elsevier, pp. 601–621.

Mittlefehldt, D. W. and Lindstrom, M. M. (1990) Geochemistry and genesis of the angrites. *Geochimica et Cosmochimica Acta*, **54**, 3209–3218.

Mittlefehldt, D. W., McCoy, T. J., Goodrich, C. A. and Kracher, A. (1998) Non-chondritic meteorites from asteroidal bodies. In *Planetary Materials, Reviews in Mineralogy* **36**, ed. Papike, J. J. Washington, D.C.: Mineralogical Society of America, pp. 4–1 to 4–195.

Papike, J. J., Ryder, G. and Shearer, C. K. (1998) Lunar samples. In *Planetary Materials, Reviews in Mineralogy* **36**, ed. Papike, J. J. Washington, D.C.: Mineralogical Society of America, pp. 5–1 to 5–234.

Rubin, A. E., Scott, E. R. D. and Keil, K. (1997) Shock metamorphism of enstatite chondrites. *Geochimica et Cosmochimica Acta*, **61**, 847–858.

Russell, S. S., Davis, A. M., MacPherson, G. J., Guan, Y. and Huss, G. R. (2000) Refractory inclusions from the ungrouped carbonaceous chondrites MacAlpine Hills 87300 and 88107. *Meteoritics and Planetary Science*, **35**, 1051–1066.

Scott, E. R. D. and Wasson, J. T. (1975). Classification and properties of iron meteorites. *Reviews of Geophysics and Space Physics*, **13**, 527–546.

Scott, E. R. D., Jones, R. H. and Rubin, A. E. (1994) Classification, metamorphic history, and pre-metamorphic composition of chondrules. *Geochimica et Cosmochimica Acta*, **58**, 1203–1209.

Scott, E. R. D., Keil, K. and Stöffler, D. (1992) Shock metamorphism of carbonaceous chondrites. *Geochimica et Cosmochimica Acta*, **56**, 4281–4293.

Sears, D. W. G., Grossman, J. N., Melcher, C. L., Ross, L. M. and Mills, A. A. (1980) Measuring the metamorphic history of unequilibrated ordinary chondrites. *Nature*, **287**, 791–795.

Stöffler, D., Keil, K. and Scott, E. R. D. (1991) Shock metamorphism of ordinary chondrites. *Geochimica et Cosmochimica Acta*, **55**, 3845–3867.

Takeda, H. (1987) Mineralogy of Antarctic ureilites and a working hypothesis for their origin and evolution. *Earth and Planetary Science Letters*, **81**, 358–370.

Van Schmus, W. R. and Wood, J. A. (1967) A chemical-petrologic classification for the chondritic meteorites. *Geochimica et Cosmochimica Acta*, **31**, 747–765.

Warren, P. H. (2004) The Moon. In *Treatise on Geochemistry, Volume 1: Meteorites, Comets, and Planets*, ed. Davis, A. M. Oxford: Elsevier, pp. 559–599.

Warren, P. H. and Wasson, J. T. (1977) Pristine nonmare rocks and the nature of the lunar crust. *Proceedings of the 8th Lunar and Planetary Science Conference*, 2215–2235.

Wlotzka, F. (1993) A weathering scale for the ordinary chondrites. *Meteoritics*, **28**, 460.

7 Cosmochemical and geochemical fractionations

Overview

Various processes that lead to the separation of elements from each other, or isotopes of the same element from each other, are considered. Examples of such processes are evaporation and condensation (which separate elements based on volatility), melting and crystallization, physical mixing and unmixing of components, and changes in redox conditions. We explain the basics of equilibrium condensation and how condensation sequences are calculated, and discuss the applicability of the condensation theory to the early solar nebula. We explore whether processes that separated elements as a function of their volatility occurred under equilibrium conditions, or were kinetically controlled. Isotopic fractionations may accompany volatility-controlled fractionations under specific conditions and can be diagnostic to inferring the formation conditions for various objects. The roles of other types of elemental fractionations in the solar system are also discussed, including the physical sorting and segregation of chondrite components and the element fractionations resulting from melting, crystallization, and planetary differentiation. Finally, we explore how light stable isotopes have been fractionated in the nebula, in the interstellar medium, and in planetesimals and planets, and show why elemental fractionations are critical for using radioactive isotopes as chronometers.

What are chemical fractionations and why are they important?

The solar system formed from a well-mixed collection of gas and dust inherited from its parent molecular cloud. The bulk composition of this material, as best we can know it, is given by the solar system abundances of elements and isotopes (Tables 4.1 and 4.2). From this bulk material, the planets, asteroids, and comets formed, each with its own unique composition. The processes that produced these compositions separated, or *fractionated*, elements and isotopes from one another. By studying these elemental and isotopic fractionations, we can potentially identify the processes that separated the elements and can learn about the physical conditions involved. This is particularly important for understanding the early solar system, because its processes and conditions are not directly observable.

Quantifying the chemical and isotopic fractionations in planetary samples and in meteorites, the closest analogues to the materials that formed planets, is a necessary first step. This involves careful measurement of chemical and isotopic compositions of the various bodies and an understanding of the composition of the material from which they formed. Once these fractionations have been identified, experiments (and theory, when the relevant experiments cannot be performed) that yield similar fractionations can point to the processes and conditions that produced them.

A great deal is known about chemical and isotopic fractionations on or within the Earth; these are the business of geochemistry. It is important to remember, though, that our planet is a grand experiment carried out under a particular, and possibly unique, set of conditions. Meteorites, and the few samples available from the Moon and Mars, allow us to see how similar grand experiments proceeded under different conditions. Based on measured element and isotopic fractionations in meteorites, a rich variety of fractionation processes is indicated.

Vapor–solid and vapor–liquid transformations (condensation of a gas, or its reverse, evaporation) can fractionate elements and sometimes isotopes. Each element condenses over a very limited temperature range, so one would expect the composition of the condensed phase and vapor phase to change as a function of the ambient temperature. Many of the chemical fractionations that took place in the early solar system are due, in one way or another, to this phenomenon. It is convenient to quantify volatility by use of the *50% condensation temperature*, that is, the temperature by which 50% of the mass of a particular element has condensed from a gas of solar composition. Table 7.1 lists the 50% condensation temperatures for the solid elements in a gas of solar composition at a pressure of 10^{-4} atmospheres, thought to be a typical pressure for the solar nebula. Based on 50% condensation temperatures, the elements can be placed into several groups. For example, the *moderately volatile elements* condense at temperatures between ~1300 K and ~640 K. Elements having higher 50% condensation temperatures than chromium are considered *refractory elements*, while those with condensation temperatures below that of sulfur, which condenses as FeS, are considered *highly volatile elements*. Fractionation of volatile elements has been comprehensively reviewed by Davis (2006).

Other processes can also cause elemental fractionation. During crystallization of a melt, minerals form that have compositions different from the melt from which they are crystallizing. Thus, their crystallization changes the composition of the melt, and if the crystals are segregated from the melt, the composition of the final products will differ significantly from that of the starting melt. Physical sorting and segregation of solids can also lead to elemental fractionations in the nebula or during the aggregation of particles into planetesimals. A few elements can sometimes be segregated by redox state, typically in combination with either a volatility fractionation or in an aqueous setting. Finally, gross planetary differentiation into crust, mantle, and core obviously leads to marked segregations of elements.

Some of these processes also cause measurable isotopic effects. Evaporation into empty space can cause the residual liquid or solid to become enriched in heavy isotopes. Processes that do not necessarily produce chemical fractionations can also produce isotopic effects. Diffusion is an example of such a process. Also, if the various constituents that go into making asteroids and planets have different isotopic compositions, the formation of these bodies can result in bulk compositions that are isotopically fractionated. Oxygen isotopes

Table 7.1 Equilibrium 50% condensation temperatures for a gas of solar composition at 10^{-4} atm

Element	T_{cond} (K)	Initial condensate	Cosmochemical classification	Element	T_{cond} (K)	Initial condensate	Cosmochemical classification
Li	1225	Li_2SiO_3 in $MgSiO_3$	mod. volatile	Ag	993	dissolved in Fe alloy	mod. volatile
Be	1490	$BeAl_2O_4$ in mel. and sp.	refr. lithophile	Cd	430*	CdS in FeS	highly volatile
B	964	$CaB_2Si_2O_8$ in feldspar	mod. volatile	In	470	InS in FeS	highly volatile
F	736	$Ca_5(PO_4)F$	mod. volatile	Sn	720	dissolved in Fe alloy	mod. volatile
Na	970	$NaAlSi_3O_8$ in feldspar	mod. volatile	Sb	912	dissolved in Fe alloy	mod. volatile
Mg	1340	Mg_2SiO_4	major element	Te	680	FeTe dissolved in FeS	mod. volatile
Al	1650	Al_2O_3	refr. lithophile	I			highly/mod. vol.?
Si	1340	$Ca_2Al_2SiO_7$	major element	Cs			highly/mod. vol.?
P	1151	Fe_3P	mod. volatile	Ba	1162	dissolved in $CaTiO_3$	refr. lithophile
S	648	FeS	mod. volatile	La	1544	dissolved in $CaTiO_3$	refr. lithophile
Cl	863	$Na[AlSiO_4]_3Cl$	mod. volatile	Ce	1440	dissolved in $CaTiO_3$	refr. lithophile
K	1000	$KAlSi_3O_8$ in feldspar	mod. volatile	Pr	1557	dissolved in $CaTiO_3$	refr. lithophile
Ca	1518	$CaAl_{12}O_{19}$	refr. lithophile	Nd	1563	dissolved in $CaTiO_3$	refr. lithophile
Sc	1652	Sc_2O_3	refr. lithophile	Sm	1560	dissolved in $CaTiO_3$	refr. lithophile
Ti	1549	$CaTiO_3$	refr. lithophile	Eu	1338	dissolved in $CaTiO_3$	refr. lithophile
V	1455	dissolved in $CaTiO_3$	refr. lithophile	Gd	1597	dissolved in $CaTiO_3$	refr. lithophile
Cr	1301	dissolved in Fe alloy	mod. volatile	Tb	1598	dissolved in $CaTiO_3$	refr. lithophile
Mn	1190	Mn_2SiO_4 in olivine	mod. volatile	Dy	1598	dissolved in $CaTiO_3$	refr. lithophile
Fe	1337	Fe alloy	major element	Ho	1598	dissolved in $CaTiO_3$	refr. lithophile
Co	1356	dissolved in Fe alloy	refr. siderophile	Er	1598	dissolved in $CaTiO_3$	refr. lithophile
Ni	1354	dissolved in Fe alloy	refr. siderophile	Tm	1598	dissolved in $CaTiO_3$	refr. lithophile
Cu	1170	dissolved in Fe alloy	mod. volatile	Yb	1493	dissolved in $CaTiO_3$	refr. lithophile

Table 7.1 (cont.)

Element	T_{cond} (K)	Initial condensate	Cosmochemical classification	Element	T_{cond} (K)	Initial condensate	Cosmochemical classification
Zn	684	ZnS dissolved in FeS	mod. volatile	Lu	1598	dissolved in $CaTiO_3$	refr. lithophile
Ga	918	dissolved in Fe alloy	mod. volatile	Hf	1690	HfO_2	refr. lithophile
Ge	825	dissolved in Fe alloy	mod. volatile	Ta	1543	dissolved in $CaTiO_3$	refr. lithophile
As	1012	dissolved in Fe alloy	mod. volatile	W	1794	refractory metal alloy	refr. siderophile
Se	684	FeSe dissolved in FeS	mod. volatile	Re	1818	refractory metal alloy	refr. siderophile
Br	~350	$Ca_5(PO_4)_3Br$	highly volatile	Os	1812	refractory metal alloy	refr. siderophile
Rb	~1080	dissolved in feldspar	mod. volatile	Ir	1603	refractory metal alloy	refr. siderophile
Sr	1217	dissolved in $CaTiO_3$	refr. lithophile	Pt	1411	refractory metal alloy	refr. siderophile
Y	1622	Y_2O_3	refr. lithophile	Au	1284	refractory metal alloy	refr. siderophile
Zr	1717	ZrO_2	refr. lithophile	Hg			highly/mod. vol.?
Nb	1517	dissolved in $CaTiO_3$	refr. lithophile	Tl	448	dissolved in Fe alloy	highly volatile
Mo	1595	refractory metal alloy	refr. siderophile	Pb	520	dissolved in Fe alloy	highly volatile
Ru	1565	refractory metal alloy	refr. siderophile	Bi	472	dissolved in Fe alloy	highly volatile
Rh	1392	refractory metal alloy	refr. siderophile	Th	1598	dissolved in $CaTiO_3$	refr. lithophile
Pd	1320	dissolved in Fe alloy	mod. volatile	U	1580	dissolved in $CaTiO_3$	refr. lithophile

* Temperature for 10^{-5} bar.

Data from Wasson (1985), Lodders and Fegley (1998).

are the most important example of this type of isotopic fractionation, although it is also seen to a much smaller degree in other elements.

Condensation as a fractionation process

Some of the materials comprising the solar system have apparently been processed through a high-temperature stage, where solids were vaporized. As the system cooled, new solids and

perhaps liquids condensed. If the condensates were removed from contact with the remaining gas, compositions that are fractionated relative to the solar system composition would occur. Evaporation is essentially the opposite of condensation, if both occur under equilibrium conditions. Thus, partial evaporation might also explain the composition of some nebular materials.

Condensation sequences

In Chapter 1 and again above, we introduced the cosmochemical classification of elements based on their relative volatilities in a system of cosmic (solar) composition. In a cooling solar gas, elements condense in a certain order, depending on their volatility (Table 7.1). Condensation and evaporation partition elements between coexisting gas and solid (or liquid) phases, and the removal of one or the other of these phases can fractionate element abundances of the system as a whole from their original cosmic relative proportions.

Condensation under the conditions obtained in the solar nebula is not really amenable to direct experiment. However, experiments have provided thermodynamic data with which the condensation process can be modeled theoretically.

Condensation calculations were done long before digital computers made complex calculations possible. In the 1950s and 1960s, Harold Urey and other investigators performed relatively simple calculations to model the condensation behavior of elements in astrophysical settings. Grossman (1972) improved these calculations by taking into account the compositional changes in the gas as condensed materials were removed. Complex calculations now normally consider the behavior of the 23 elements with the highest cosmic abundance: H, He, C, N, O, F, Ne, Na, Mg, Al, Si, P, S, Cl, Ar, K, Ca, Ti, Cr, Mn, Fe, Co, and Ni. These calculations also consider thousands of compounds that can potentially form from these elements. Quite a number of especially good reviews of condensation calculations are available (e.g. Grossman and Larimer, 1974; Fegley, 1999; Davis and Richter, 2004; Ebel, 2006).

Condensation theory is based on thermodynamic equilibrium. More than a century's worth of experiments have yielded thermodynamic data (entropy and enthalpy of formation, plus heat capacity) for elements and compounds. Equations of state describing the stabilities of different compounds under various conditions can be calculated from these data, as briefly described in Box 7.1. Because liquids are not normally stable at the low pressures appropriate for space, the compounds in condensation calculations are generally solid minerals, but liquids can exist at higher pressures (achievable if areas of the nebula with enhanced dust concentrations relative to gas were vaporized).

The temperatures of appearance of various solid phases as a cooling solar gas condenses are illustrated in Figure 7.1. This particular condensation calculation was performed at a pressure of 10^{-4} atm (thought to be appropriate for parts of the nebula). It is important to note that not every mineral in the sequence actually condenses directly from the vapor. Instead, some minerals form by reaction of previously condensed solids with the vapor. For example, FeS forms by reaction of already condensed Fe metal with sulfur in the gas phase, and olivine first condenses as the magnesium end member forsterite and then becomes progressively more iron-rich by reaction with vapor as temperature decreases.

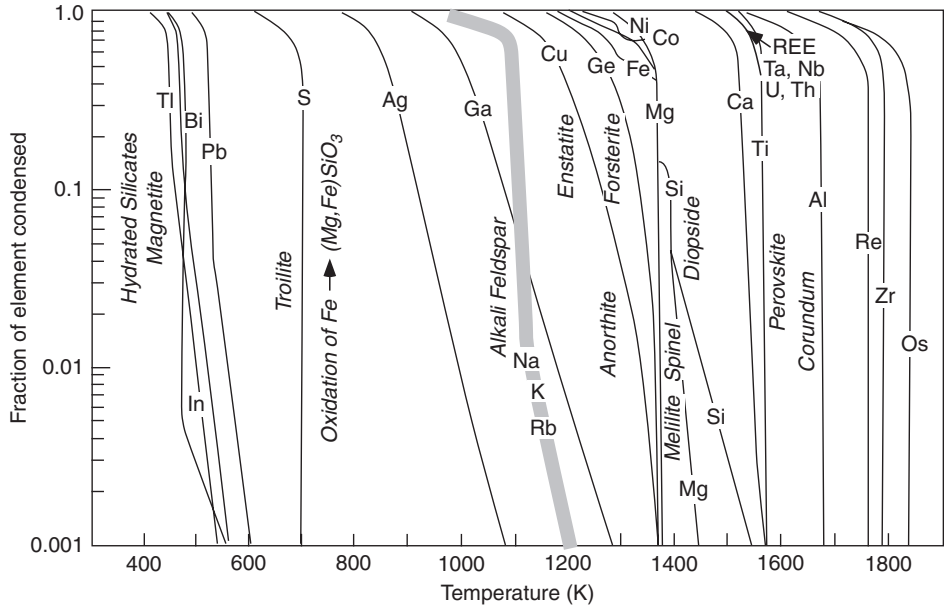

Fig. 7.1 Calculated condensation sequence for a gas of solar composition at 10^{-4} atm. Condensed minerals are labeled in italics and curves show the fraction of each element condensed as a function of temperature. Modified from Grossman and Larimer (1974).

Box 7.1 **Gibbs free energy and condensation calculations**

Gibbs free energy (G) is a convenient way to describe the energy of a system. More easily measured thermodynamic quantities are enthalpy (H) and entropy (S), which describe the heat exchanged during a reaction and the subsequent loss of capacity to do work. The change in free energy ΔG during a reaction (such as condensation of a solid phase from gaseous species) is related to changes in enthalpy and entropy by:

$$\Delta G = \Delta H - T\Delta S$$

where T is the absolute temperature in Kelvins, and ΔH and ΔS refer to values calculated for reactants minus products. Energy is available to produce a spontaneous change in the system as long as ΔG is negative. Once free energy is minimized ($\Delta G = 0$), the system has attained equilibrium.

Experimentally determined ΔH and ΔS values for the formation of various compounds from their constituent elements are tabulated under standard conditions (normally 298 K and 1 bar). These values are temperature-sensitive, and can be extrapolated to the temperature of interest using the measured heat capacity ΔC_P by integrating the following equation between 298 K and the temperature of interest:

$$\Delta G_T = \Delta H^0 + \int_{298}^{T} \Delta C_P dT - T\left(\Delta S^0 + \int_{298}^{T} (\Delta C_P/T) dT\right)$$

where the superscript 0 denotes enthalpy and entropy values in their standard states.

To illustrate how a (simple) condensation calculation works, let's consider the condensation of corundum (Al_2O_3), one of the earliest phases predicted to condense from a solar gas. The partial pressures of aluminum (P_{Al}) and oxygen (P_O) in the gas phase must first be determined, based on their solar abundances, over a range of temperatures. The equilibrium between solid (s) corundum and gas (g) can be represented by this equation:

$$2Al(g) + 3O(g) = Al_2O_3(s).$$

The equilibrium constant (K_{eq}) for this reaction takes the form:

$$K_{eq} = \frac{a_{Al_2O_3}}{(P_{Al}{}^2) \times (P_O{}^3)}$$

where $a_{Al_2O_3}$ is the activity of corundum (equal to 1 for a pure phase). Because

$$\Delta G = -RT \ln K_{eq},$$

we can calculate the temperature at which corundum is in equilibrium with the gas (that is, where $\Delta G = 0$), which is the condensation temperature at 1 bar (1758 K) for this mineral.

In practice, laborious modern calculations find the optimum distribution of elements between vapor and solid (or liquid) phases by minimizing the Gibbs free energy of the entire system. This calculation is accomplished in the following steps (Ebel, 2006):

(1) At a particular temperature and pressure, the thermodynamic stability of all potential condensates is calculated from their equations of state.
(2) A small mass increment of each stable solid condensate is added to the system, with complementary subtraction of that mass from the gas composition.
(3) Matter is then redistributed between all the coexisting condensed phases and gas, until the calculated free energy of the system achieves its lowest value.
(4) Thermodynamic stability of each condensate phase is then checked again.
Iteration of this process at successively lower temperatures gives a condensation sequence. These calculations would be extremely tedious, except for the advent of modern computer systems.

Four condensation sequences for a gas of solar composition (all at the same pressure, in this case 10^{-3} atm) calculated by various investigators are compared in Figure 7.2. The differences in these sequences result primarily from the choice of thermodynamic data. These diagrams illustrate the temperatures of appearance (and, for some cases, disappearance) of phases, but not the fraction of each element condensed. There is remarkable agreement, considering that some calculations did not take titanium or noble gases into account. The absence of titanium prevents condensation of perovskite, which, in turn, affects the stabilities of other minerals, and the presence of noble gases changes total gas pressure in the calculation.

In condensation calculations, internally consistent thermodynamic datasets are preferred (but not always used) over data haphazardly collected from disparate sources. Another

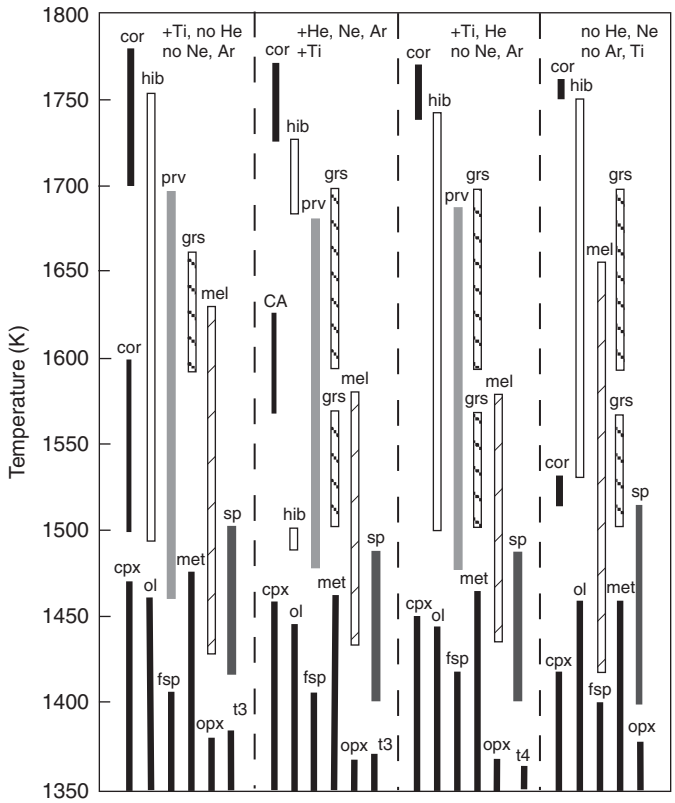

Fig. 7.2 Comparison of four condensation sequences, all at 10^{-3} atm but using different models. These calculations are from (left to right) Petaev and Wood (1998), Ebel and Grossman (2000), Yoneda and Grossman (1995), and Wood and Hashimoto (1993). Mineral abbreviations and formulae are given in Table 7.2. Modified from Ebel (2006).

problem is determining how solid–solution minerals are modeled. Many of the condensate minerals, such as melilite and pyroxene, are not pure phases, but chemical mixtures of several end member components. Various mixing models for solid solutions have been devised, which may give different results.

Variations in gas pressure also affect the condensation sequence, as illustrated in Figure 7.3. Except for differing pressures (10^{-3} to 10^{-5} atm), the parameters for these two calculations are identical. The temperatures and orders of appearance of condensed minerals clearly vary with pressure.

So far, we have been discussing the condensation of elements with high cosmic abundances. Generally, thermodynamic data for trace elements are lacking, or are only available for pure elements or simple compounds. Chemical analysis of high-temperature minerals in meteorites guides our understanding of the condensation of elements in trace abundances. The analyses indicate that most elements in trace quantities tend to substitute into various host minerals, rather than forming pure phases of their own (see Table 7.1). In calculations, they are allowed to condense as simple metals, oxides, or sulfides, which are then assumed

Table 7.2 Mineral names, abbreviations, and formulae commonly found in condensation sequences

Mineral	Abbreviation	Chemical Formula
corundum	cor	Al_2O_3
hibonite	hib	$CaAl_{12}O_{19}$
grossite	grs	$CaAl_4O_7$
Ca-monoaluminate	CA	$CaAl_2O_4$
perovskite	prv	$CaTiO_3$
melilite	mel	$Ca_2(Al_2,MgSi)SiO_7$
spinel	sp	Al-rich $(Fe,Mg,Cr,Al,Ti)_3O_4$
olivine	ol	$(Mg,Fe)_2SiO_4$
clinopyroxene	cpx	$Ca(Mg,Fe)Si_2O_6$
orthopyroxene	opx	$(Mg,Fe)_2Si_2O_6$
feldspar	fsp	$(CaAl,NaSi)AlSi_2O_8$
metal	met	Fe,Ni,Co
	t3	Ti_3O_5
	t4	Ti_4O_7

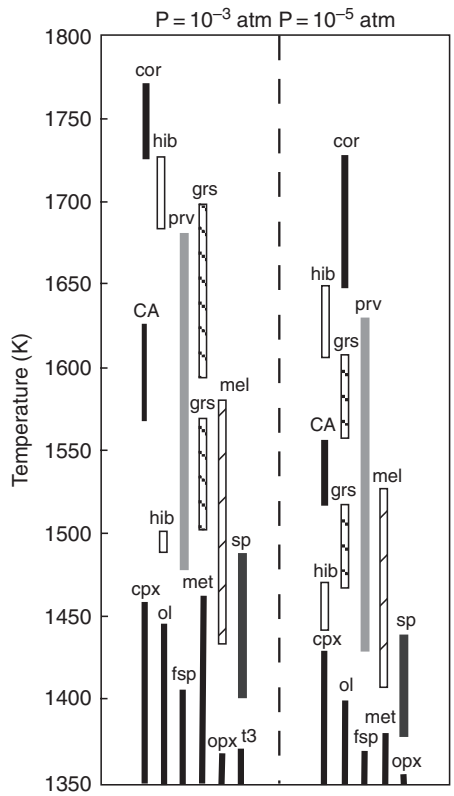

Fig. 7.3 Comparison of two condensation sequences calculated at different pressures. Abbreviations and formulae are given in Table 7.2. Modified from Ebel (2006).

to dissolve into appropriate major phases that are stable under corresponding conditions. For example, rare earth elements condense as oxides and substitute into perovskite or hibonite, and cadmium condenses as CdS and substitutes into FeS. Platinum-group elements (Ru, Rh, Pd, Re, Os, Ir, Pt) condense as metals at very high temperatures (Fig. 7.1) before Fe metal, so they form a separate refractory metal phase – actually found as tiny nuggets in refractory inclusions.

Condensation calculations have also been performed using non-solar starting compositions. The solar composition has more oxygen than carbon, so it is oxidizing. Compositions where carbon is more abundant than oxygen tie up oxygen as CO, so they are reducing. Condensation of a carbon-rich gas, which occurs in gases expelled from red giant stars, produces graphite (C) and carbides (SiC and TiC), as found in presolar grains. Parts of the solar nebula may also have been enriched in carbon, yielding the reduced minerals found in enstatite chondrites. Local vaporization of dust-enriched areas may also have produced non-solar gas compositions, possibly allowing silicate liquids (chondrules?) to condense.

Applicability of condensation calculations to the early solar system

During the 1970s and 1980s, equilibrium condensation calculations were thought to be generally applicable to the formation of meteorites, their constituents, and even to planetary bodies. This idea fit well with the hot solar nebula model introduced by Cameron (1962), which was supported by observations that all materials available for study had apparently sampled the same uniform isotopic reservoir. The calcium-aluminum inclusions (CAIs) found in chondrites were identified in the early 1970s as initial condensates from the solar nebula (Grossman and Larimer, 1974). The bulk compositions of meteorites were interpreted in terms of condensation (Larimer and Anders, 1967, 1970; Wai and Wasson, 1977). Differences in abundances of moderately volatile elements between chondrites were ascribed to differences in their accretion temperatures. Metal was thought to have condensed from the nebula and was accreted in different proportions relative to silicates in the different meteorite classes. CI chondrites were considered to be complete condensates from the solar nebula, with even their mineralogy resulting from gas–solid equilibrium reactions (Larimer and Anders, 1970). However, since that time, improved techniques for measuring isotopic compositions have shown that isotopic variation among samples is the norm, not the exception, and many different examples of preserved presolar material have been found in chondrites, as discussed in Chapter 5. None of these isotope anomalies or presolar grains could have survived complete evaporation of the nebular solids. In addition, we have learned a great deal more about chondrites and their components. So we must ask the question, did equilibrium gas–solid exchange, either condensation or evaporation, actually take place in the early solar system?

Consider first the CAIs. In general, their bulk compositions are consistent with those calculated for the first 5% of condensable matter (Davis and Richter, 2004). Moreover, many of the minerals that comprise CAIs (hibonite, perovskite, spinel, melilite, diopside, anorthite) are predicted to have been the earliest condensed phases. However, not all CAIs are

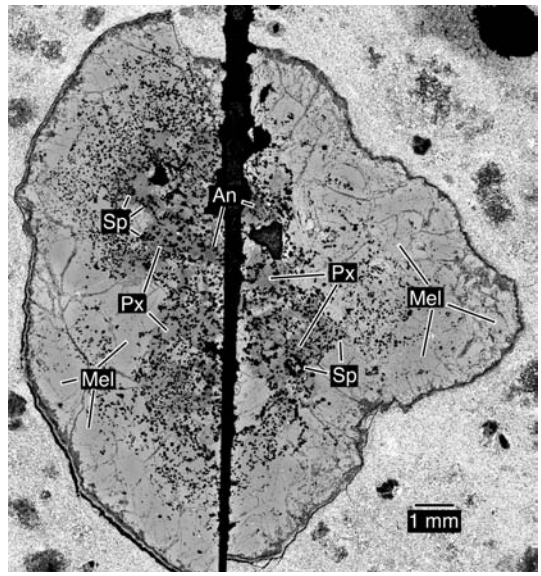

Fig. 7.4 **Backscattered electron image of a Type B CAI in the Allende CV3 chondrite. This object crystallized from a melt and has an outer mantle of melilite (Mel) surrounding an inner zone of pyroxene (Px) and anorthite (An). Tiny grains of spinel (Sp) are abundant in the inner portion of the inclusion. Image courtesy of A. Krot.**

alike. For example, Type B CAIs are coarse-grained igneous objects whose mineralogy and mineral chemistry are controlled by igneous processes (Fig. 7.4). Crystallization of a refractory liquid with the compositions of CAIs produces many of the same minerals as equilibrium condensation would, but the details of the partitioning of elements between phases and the textural relationships are quite different. Thus, type B CAIs are not condensates, although the bulk compositions of these objects permit their precursors to have been condensates. The isotopic systematics of type B CAIs imply that the precursors were not composed entirely of condensates either. Type B CAIs are characterized by isotopic anomalies relative to both the bulk solar system composition and to each other in calcium, titanium, and other elements (Niederer *et al*., 1981; Jungck *et al*., 1984; Rotaru *et al*., 1992). Such anomalies could not survive a general evaporation and condensation because the isotopes would have been thoroughly mixed in the gas phase. Local evaporation and condensation in the immediate region where each CAI formed might be permitted. But another possibility is that the immediate precursors to the type B CAIs were collections of refractory grains from a wide variety of sources, some or most of them presolar, that were concentrated by evaporation of more volatile material, then melted in the solar nebula, and subsequently crystallized to form the objects that we see.

On the other hand, fine-grained CAIs consist of aggregates of nodules with a concentric structure consisting of spinel cores surrounded by melilite, anorthite, and diopside, or melilite cores surrounded by anorthite and diopside (Fig. 7.5). The sequence of minerals in the nodules is consistent with a condensation sequence. However, the textures of the overall objects are complicated and often indicate extended and multistage histories. For

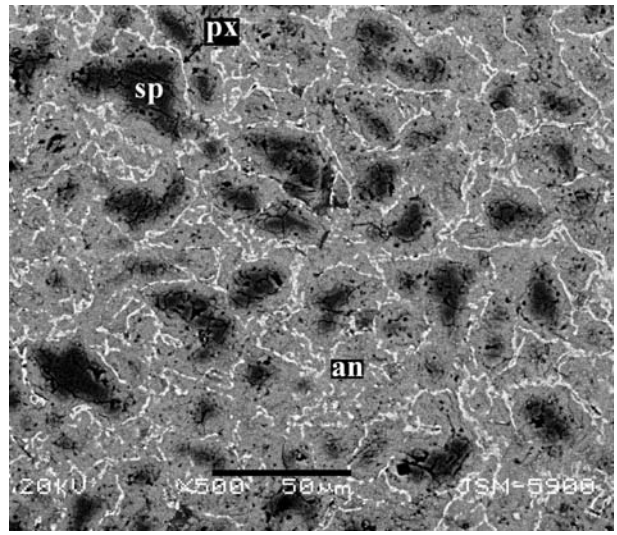

Fig. 7.5 **Backscattered electron image of a portion of a fine-grained Type A CAI in the Efremovka CV3 chondrite. This inclusion consists of nodules of spinel (sp) surrounded by anorthite (an) and thin rims of pyroxene (px). This CAI may be an aggregate of condensates.**

these objects, nebular condensation clearly played a major role in their formation, but even in these objects the story is more complicated than envisioned decades ago when they were first described.

Metal, too, has diverse origins. Much of the metal that we currently observe in ordinary chondrites no longer retains its original features, but instead reflects diffusion and grain growth in meteorite parent bodies. In the least metamorphosed chondrites, we get some glimpses of the origin of the metal. Fine-grained matrices of the most primitive chondrites contain tiny micron-sized grains of metal and sulfide. The origin of these grains is not clear. They could be inherited from the interstellar medium or they could be the result of condensation in the nebula. These grains are quickly destroyed by parent-body metamorphism, with their constituent atoms combining into larger metal grains (Huss *et al*., 2006). Careful study of the trace-element patterns in metal grains inside and outside of chondrules from CR chondrites shows that much of the metal in these meteorites was produced by reduction during chondrule formation and was expelled from the molten chondrules before they solidified (e.g. Connolly *et al*., 2001). Other metal grains in these meteorites, particularly those coating the surfaces of chondrules, show evidence of recondensation of elements that evaporated during the chondrule-heating event. The metal grains in CH chondrites have unusual zoning patterns in siderophile elements consistent with condensation calculations from a gas of solar composition (Campbell *et al*., 2001). These grains, and some of the chondrules found in CB and CH chondrites, are considered to be equilibrium condensates from a local gas plume produced by a collision between two large asteroids.

The volatile element depletions among the various classes of chondrites were once considered to be the result of equilibrium condensation, with accretion of the different classes of meteorites taking place at different temperatures before the missing volatiles could

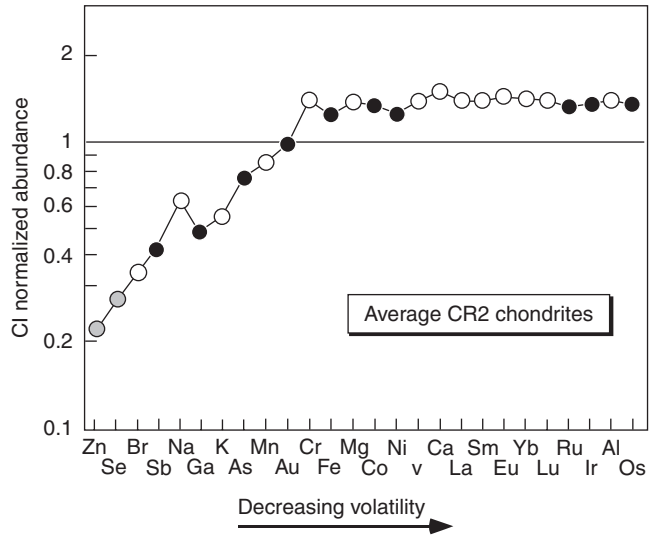

Fig. 7.6 **Elemental abundances in CR2 chondrites normalized to the CI composition and plotted in order of decreasing volatility from left to right. Lithophile elements are shown with open circles, siderophile elements with black circles, and chalcophile elements with gray circles. CR2 data from Kallemeyn *et al.* (1994).**

condense. However, evaporation and condensation can both produce solids depleted in volatile elements. Equilibrium evaporation or condensation should produce sharp steps on an abundance versus condensation temperature plot because once the condensate becomes stable, the elements will quickly and quantitatively condense, and once it becomes unstable, it will quickly and quantitatively evaporate. But this is not what is observed. Figure 7.6 shows the average bulk composition of CR2 chondrites, normalized to CI chondrites. The elements are arranged in order of decreasing volatility from left to right. Elements more volatile than chromium are depleted, but the depletions increase steadily with increasing volatility over a range in condensation temperatures of 600 K. The easiest way to understand this is if the loss of the volatile elements took place through destruction of various mineral phases formed at different places and times and under different conditions. Evaporation then is a function of the stability of the mineral in which the element is sited, not of the element itself, so the removal of the volatiles from the solid occurs over an extended temperature interval. In Chapter 5, we observed that the depletions of fragile types of presolar grains vary in concert with the volatile element depletions of the host meteorite (see Fig. 5.16). It seems fairly clear, then, that equilibrium condensation did not control the bulk compositions of the chondrites.

We should also address the question of whether CI chondrites represent the complete, low-temperature condensate from the solar nebula. Their bulk composition is consistent with such a model. However, CI chondrites contain among the highest abundances of presolar grains that are not destroyed by aqueous alteration (the mineralogy of CI chondrites is almost entirely due to such alteration). This suggests that it is more likely that CI chondrites formed from representative samples of the dust inherited from the Sun's parent

molecular cloud, heavily processed, but neither fractionated nor vaporized in the solar system.

In summary, equilibrium condensation represents one end member of a continuum of gas–solid interactions that took place in the early solar system. Some samples appear to have formed under conditions that closely match those of equilibrium condensation. But the volatility-based fractionations that are widely observed in solar system materials are due to much more complicated processes that involve evaporation (the opposite of condensation) or mixing of materials produced under different conditions, as well as a variety of processes in which kinetic effects played an important role.

Volatile element depletions

In most classes of chondrites, highly volatile and moderately volatile elements are depleted relative to refractory elements when compared to CI chondrites. A plot of elemental abundances in CV chondrites, normalized to CI chondrites and silicon, versus their 50% condensation temperatures is shown in Figure 7.7. Figure 7.6 shows the same trend for CR chondrites in a different format. Like most other chondrite groups, the CV and CR chondrites show a smooth drop-off in the abundances of elements with higher volatility. Different symbols distinguish siderophile, lithophile, and chalcophile elements, illustrating that this pattern is unrelated to geochemical affinity. As discussed above, these depletions were traditionally interpreted in terms of equilibrium condensation from a gas of solar composition. However, there are other ways in which such depletions might arise.

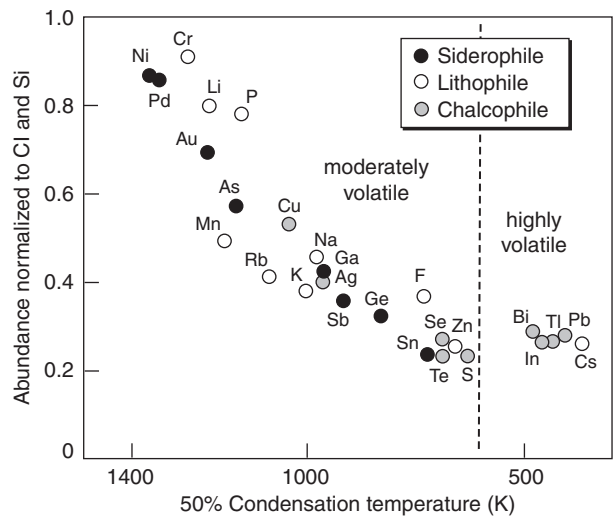

Fig. 7.7 Volatile element abundances in CV chondrites (normalized to CI chondrites and silicon) lie along a linear array on semi-log plots versus their 50% condensation temperatures. This depletion pattern persists, whether the elements are siderophile, lithophile, or chalcophile.

Gas–solid interactions

Consider the dust that made up the Sun's parent molecular cloud. It contained mineral grains that condensed in the atmospheres of dying stars (Chapter 5). Stellar atmospheres also likely produced amorphous grains as the temperature and density dropped during expansion of the ejected gas, and some atoms may have reached interstellar space without condensing into grains at all. The journey from the site of nucleosynthesis to the molecular cloud that gave rise to the solar system was a treacherous one. Supernova explosions send shock waves driven by extremely hot gas through the interstellar medium, evaporating all dust for large distances in all directions. Massive stars emit a tremendous flux of UV light that can also evaporate dust. The atoms from these vaporized dust grains were part of a tenuous gas consisting of elements of all volatilities, from the most volatile to the most refractory. When gas and dust came together to form the Sun's parent molecular cloud, the particle density increased and the temperature dropped to as low as 10 K. Condensable elements in the gas condensed onto dust nuclei. But this was not equilibrium condensation because the temperatures were too low. Atoms of different volatilities were mixed together without long-range structure. The grains were amorphous and perhaps icy and had a lot of chemical potential energy. So solar system formation began in a cloud consisting of gas composed mostly of hydrogen, helium, and perhaps neon and carbon monoxide, and dust composed mostly of amorphous material plus some mineral grains that condensed in the atmospheres of dying stars.

As a portion of the molecular cloud collapsed to form the proto-Sun and its accretion disk, the temperature rose and things began to happen in the dust. Ices evaporated, taking included atoms of refractory elements into the gas phase with them. The refractory elements typically condensed out again on the first grain they encountered. The ice coatings evaporated, leaving behind amorphous silicate grains. As temperatures rose still further, the kinetic barriers that kept the amorphous grains from crystallizing were overcome and minerals began to crystallize from the amorphous grains. At the same time, volatile elements were lost from the grains. This general process provides a way for volatile elements in the dust to have been fractionated without the system ever achieving chemical equilibrium.

Two types of models have been proposed that use this general picture as the basis for understanding volatile depletions in chondrites. Yin (2005) proposed that the volatile element depletions in the chondrites reflect the extent to which these elements were sited in refractory dust in the interstellar medium. Observations show that in the warm interstellar medium, the most refractory elements are almost entirely in the dust, while volatile elements are almost entirely in the gas phase. Moderately volatile elements are partitioned between the two phases. The pattern for the dust is similar to that observed in bulk chondrites. In the Sun's parent molecular cloud, the volatile and moderately volatile elements condensed onto the dust grains in ices. Within the solar system, the ices evaporated putting the volatile elements back into the gas phase, which was separated from the dust. Thus, in Yin's model, the chondrites inherited their compositions from the interstellar medium. A slightly different model proposes that the fractionated compositions were produced in the solar nebula by

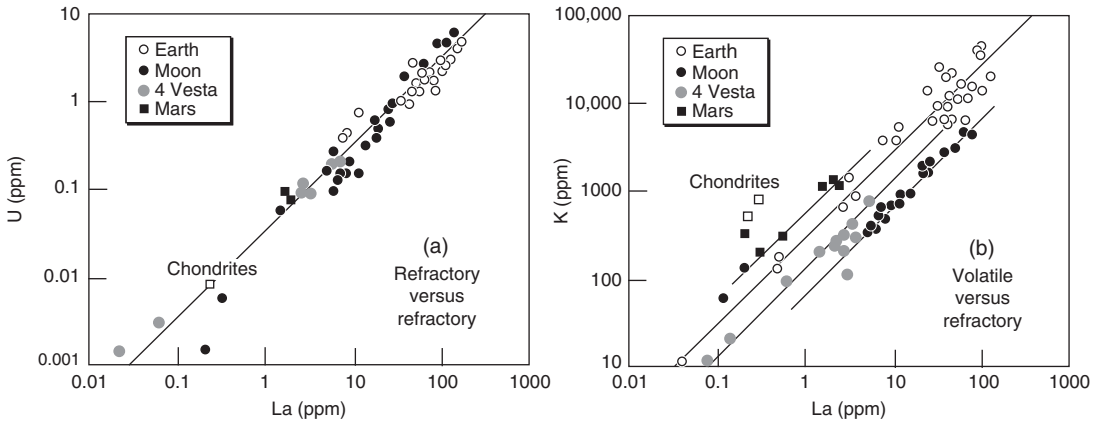

Fig. 7.8 **Plots of uranium versus lanthanum (two refractory elements), and potassium versus lanthanum (a volatile element and a refractory element) for terrestrial and lunar basalts, HED achondrites (Vesta), and Martian meteorites. All three elements are incompatible elements and thus fractionate together, so their ratios remain constant. However, ratios of incompatible elements with different volatilities (K/La) reveal different degrees of volatile element depletion in differentiated bodies. After Wänke and Dreibus (1988).**

thermal processing of gas and dust inherited from the molecular cloud (Huss *et al*., 2003; Huss, 2004). As the temperature rose in the accretion disk, ices evaporated releasing trapped refractory elements, as in Yin's model. However, rather than simply being lost from the system, these elements were refluxed back into the dust with an efficiency proportional to their volatility. In this model, the different chondrite groups formed at nebular locations where the ambient temperatures were slightly different. Those with the most volatile-depleted compositions formed at the highest temperatures. In support of this model is a general correlation between the depletion of volatile elements in a chondrite group and the relative abundances of presolar grains in the least metamorphosed meteorites of that group. As shown earlier in Figure 5.16, as the depletions of moderately volatile elements increase from LL to CO to CR to CV, the abundances of the more fragile presolar components decrease.

The depletion of volatile elements in achondrites, and in planets, is even more extreme than in chondrites. To see this effect, it is necessary to remove effects of magmatic fractionations from the data, as all these samples are igneous rocks. This subject is treated in some detail in a later section of this chapter. For our present purposes, it is sufficient to note that some elements behave similarly during melting and crystallization. Examples are potassium, lanthanum, and uranium, as illustrated in Figure 7.8. In the plot of uranium versus lanthanum (both refractory elements), samples from all the bodies plot along the same line, which is the chondritic ratio of these elements. However, in the plot of potassium versus lanthanum (potassium is volatile), samples from different planets or meteorite parent bodies are arrayed along different lines, all defining volatile-to-refractory element ratios lower than in chondrites. Thus the various planets and differentiated asteroids show different degrees of volatile element depletion. It is likely that these fractionations reflect similar processes to those that fractionated the compositions of chondrites.

Gas–liquid interactions

In general, silicate melts are unstable under the conditions that prevailed in the solar nebula. However, chondrules and some CAIs crystallized from partially molten to completely molten droplets. The melting events that produced chondrules and CAIs thus present an ideal situation for chemical and isotopic fractionations to occur.

Chondrules

Chondrules formed in the nebula by crystallization of molten droplets produced by some sort of flash heating event(s). Heating times are estimated to have been from several seconds to a few minutes to reach peak temperatures between 1770 and 2120 K, followed by rapid, but not instantaneous cooling over a few minutes to a few hours. Chondrule melts are unstable in a gas of solar composition and so should have been rapidly losing sulfur, alkalis, iron, and even magnesium. However, evidence that volatile elements were lost from chondrules while they were molten is equivocal. Measurements of the sodium content in crystals from chondrules show no apparent change during crystallization, implying that sodium was not lost from the melt (Alexander *et al*., 2008). Chondrules generally do not show evidence of isotopic mass fractionation in major elements. On the other hand, the bulk compositions of chondrites could be interpreted in terms of minor volatile element loss during chondrule formation overprinting the volatility fractionation already in the precursors. One possible explanation for the apparently minor loss of volatiles from chondrules is that many chondrules formed at the same time in close proximity, so that evaporation created a dense atmosphere of evaporated chondrule material that back-reacted with the molten chondrules, minimizing volatile loss and isotopic mass fractionation.

CAIs

Let's consider the Type B CAIs (Fig. 7.4), which formed via crystallization from a melt during relatively rapid (hours to days) cooling in the solar nebula. Because CAI liquids are unstable under most nebula conditions, it is likely that they were evaporating as they cooled. Isotopic measurements show that silicon and magnesium in most Type B CAIs are isotopically fractionated, favoring the heavy isotopes (Fig. 7.9a). As mentioned in Chapter 2, evaporation typically results in the gas being enriched in the light isotopes of evaporating materials. Equilibrium fractionation between liquid and gas, where liquid and gas exchange molecules, is quite small at high temperature. However, if the gas is removed from contact with the liquid, then a kinetic fractionation known as Rayleigh distillation can occur (see Box 7.2). Figure 7.9b compares the chemical compositions of Type A and B CAIs with the compositions expected for condensates from a gas of solar composition. The Type A CAIs plot close to the condensates trend, but the Type B CAIs plot to the left of it. Using the measured isotopic compositions of silicon and magnesium to infer the amounts of silicon and magnesium that were lost from the molten CAIs, one finds that the bulk compositions have moved down and to the left in the direction of the arrow and have lost from 10–40% of

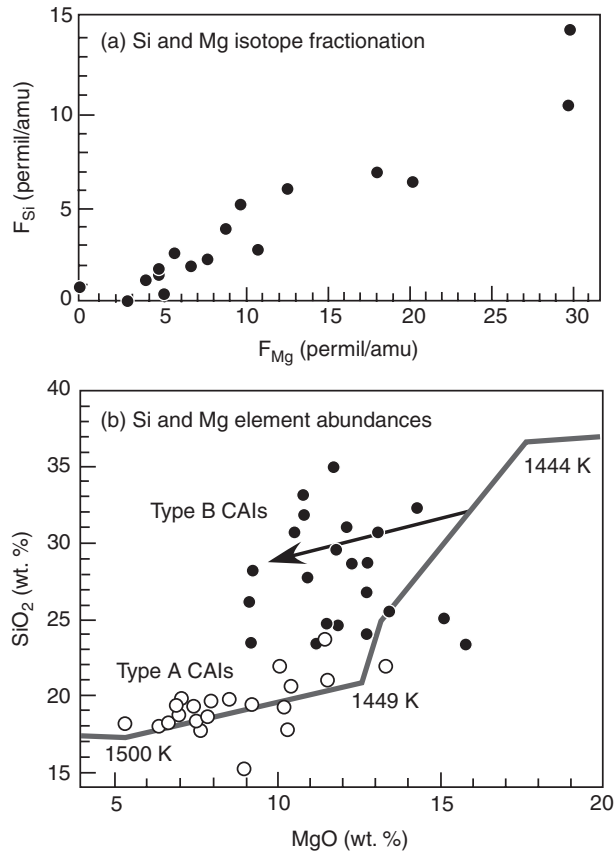

Fig. 7.9 **Element and isotopic abundances of Si and Mg in CAIs suggest evaporation. (a) Correlated isotopic fractionations in Type B CAIs. (b) SiO_2 versus MgO for CAIs, relative to the calculated condensation sequence abundances (heavy line). Unmelted Type A inclusions (open circles) follow the condensation path, whereas partly melted Type B inclusions (filled circles) deviate, because of loss of both Mg and Si, as illustrated by the arrow. Modified from Davis and Richter (2004).**

Box 7.2 **Isotopic fractionations by Rayleigh distillation**

In a closed system consisting of a liquid and gas at equilibrium, molecules move across the boundary from liquid to gas and back again. The vapor pressure, the pressure of gas above the liquid at equilibrium, is a function of temperature. The vapor pressures of isotopically lighter molecules are always higher than those of heavier molecules of the same chemical compound. The reason is straightforward. Isotopically lighter forms have higher translational velocities at a given temperature and thus can more easily escape from the surface of the liquid into the vapor phases.

In an open system, where the gas is removed and not permitted to back-react with the liquid, the tendency for the light isotope to preferentially go into the gas phase results in an isotopically light gas and the liquid composition becomes increasingly isotopically heavy. This

phenomenon is known as Rayleigh distillation. A familiar system that approaches the conditions of Rayleigh distillation is the evaporation of ocean water to make clouds. The solar nebula is another place where Rayleigh distillation could have occurred, because the pressure in the nebula was so low. At standard nebular pressure, molecules and atoms that evaporate from molten chondrules and CAIs are effectively lost forever, so we might expect both chemical and isotopic fractionations to increase the longer a chondrule or CAI remains molten.

In a system undergoing Rayleigh distillation, an isotopic ratio in the liquid will evolve according to

$$\frac{R^{res}_{2,1}}{R^{0}_{2,1}} = f_1^{(\alpha-1)} \tag{7.2.1}$$

where $R^{res}_{2,1}$ is the isotopic composition of the residual liquid, $R^{0}_{2,1}$ is the initial isotopic composition of the liquid, f_1 is the fraction of isotope 1 remaining, and α is the isotopic fractionation factor given by

$$\alpha = \left(\frac{\gamma_{i,2}}{\gamma_{i,1}}\right) \times \sqrt{\frac{m_{i,1}}{m_{i,2}}} \tag{7.2.2}$$

In this equation, $m_{i,1}$ and $m_{i,2}$ are the masses of the two isotopes making up $R_{2,1}$, and the γ terms are condensation coefficients for the two isotopes, which are determined experimentally and are typically close to 1. Equation (7.2.1) is valid if α is independent of the evolving composition of the evaporating liquid, and the diffusive transport rate is fast enough to keep the liquid homogeneous. The last condition is violated in solids, where diffusion is very slow relative to the evaporation rate, so solids do not undergo Rayleigh distillation.

Type B CAIs apparently formed under conditions approaching those of Rayleigh distillation (Fig. 7.9). We can do a back-of-the-envelope calculation to show that this is true. We will ignore the γ terms for the moment and assume that α is equal to the square-root of the masses. Thus, for $^{25}Mg/^{24}Mg$, $\alpha \approx 0.9798$. Isotopic fractionation for magnesium observed in Type B CAIs is typically around 4–6 ‰, but can be lower or higher in some cases (Fig. 7.9a). Using these values, we can solve Equation (7.2.1) for f_1, the amount of magnesium lost, and we find values of 18–26%, consistent with observations (Fig. 7.9b).

their original magnesium. This puts their starting compositions close to the condensation trend, which indicates that the bulk compositions of the precursors were controlled by gas-solid interactions in an environment of near-solar composition.

Igneous fractionations

Magmatic processes that lead to fractionation

Melting and crystallization can both produce large chemical fractionations. Any situation in which a melt is separated from the residual solid, or in which crystals forming from a melt are separated from the melt, will produce melt and crystal segregations that differ in

composition from the starting material. Igneous fractionation processes are important in the histories of achondrites, iron and stony-iron meteorites, and the terrestrial planets. Igneous fractionations are less important in chondrites because these meteorites did not melt and their constituent chondrules melted and crystallized without fractionating crystals from melt. This subject is traditionally considered to be within the realm of geochemistry, but we include it in this chapter because the partitioning of elements in differentiated meteorites has often involved compositions and conditions outside the range of terrestrial experience.

Partial melting

When a rock is heated and begins to melt, it does not melt all at once. Components with the lowest melting temperature melt first, and the initial melt typically has a different composition from that of the original rock. Peridotite, composed of olivine + pyroxenes + garnet or spinel, is a product of planetary differentiation of chondritic material and is found in the mantles of terrestrial planets and differentiated asteroids. Partial melting of peridotite generates basaltic magmas, which are richer in silicon, titanium, calcium, aluminum, sodium, and some other elements than the starting peridotite. These magmas are buoyant in a gravitational field and move toward the surface of the body. Basalt is the most abundant rock type on the surfaces of the terrestrial planets and differentiated asteroids like 4 Vesta.

Low-degree partial melts of undifferentiated chondritic material generate a range of different compositions. The first melt from a chondritic precursor appears at ~950 °C and forms by melting of FeS, Fe-Ni metal, and phosphates. Melts of this composition are observed in primitive achondrites (acapulcoites and lodranites). As the temperature increases, silicates begin to melt. At 5 to 10% partial melting, the melt is basaltic in composition (McCoy *et al*., 1997).

Basaltic magmas tend to be buoyant in a gravitational field. Once some critical amount of melt is generated, the magma ascends towards the surface of the body, providing a means of separating liquid from residual solids and thus causing element fractionation.

Fractional crystallization

Crystallization of melts provides another way to fractionate chemical elements. Most crystals are denser than the melt from which they form, so crystal settling can separate the phases. Convection currents in hot magma can also entrain crystals and carry them to the bottom of a magma chamber. Accumulations of crystals are a common occurrence on the floors of terrestrial plutons, and many achondrites are “cumulates” formed in an analogous way in asteroids. Cumulates and the complementary melt have different elemental compositions.

Element partitioning

A magnesium-rich silicate such as forsterite (magnesium olivine, Mg_2SiO_4) is commonly the first crystallizing mineral at high temperature from a cooling basaltic magma. For this reason, magnesium progressively decreases in residual melt as forsterite crystallizes. Even

though forsterite is a silicate, its silica content is actually lower than that of basaltic magma, so silica commonly increases in the liquid during crystallization. If the forsterite is removed from the system as it crystallizes, the remaining melt will be depleted in magnesium and enriched in silica and in other elements relative to the original basaltic composition. As cooling proceeds, different minerals will crystallize and the melt composition will evolve further, becoming more fractionated from the starting composition. The combination of partial melting to produce a basaltic melt followed by fractional crystallization can generate the wide range of compositions seen in many solar system materials.

Elements present in only minor or trace concentrations are partitioned in quite different ways. These elements are not abundant enough to form their own minerals, so they must be incorporated into minerals composed of the major elements. Because they must fit into crystalline sites whose sizes and coordination are already fixed, the ease with which they can be included depends on ionic size and charge. Trace ions that fit nicely into sites otherwise occupied by major ions having similar sizes and charges are said to be "compatible." Conversely, large ions with high charge, referred to as "incompatible" elements, tend to be excluded from most crystal sites.

Element partitioning is expressed in terms of a distribution coefficient D, defined as

$$D = C_{crystal}/C_{melt}$$

where $C_{crystal}$ is the concentration of that element in a particular mineral and C_{melt} is that element's concentration in a coexisting melt. For compatible elements, D is greater than or equal to one, whereas for incompatible elements D is less than one (often far less).

Some trace elements actually are preferentially incorporated into certain sites in crystal structures. For example, Ni^{2+} is partitioned into olivine more strongly than the Mg^{2+} it displaces. Thus, fractional crystallization of olivine produces residual liquids that are increasingly depleted in nickel. This preferential partitioning is a result of crystal field stabilization, whereby certain transition metal ions are bonded more strongly in certain sites than others. An explanation of crystal field theory is beyond the scope of this book, but it can be found in various geochemistry texts; understanding this theory is also important for spectroscopy.

Another example of the utility of trace element partitioning is provided by the rare earth elements (REE). These occur in trace amounts because their cosmic abundances are so low. Almost all REE are incompatible in common rock-forming minerals, because they have ionic radii that are large and charges that are high (trivalent). However, under reducing conditions europium (Eu) can exist as a divalent cation, and in this form it is compatible, substituting comfortably for Ca^{2+} in plagioclase. When REE concentrations are plotted versus atomic number, they exhibit a zigzag pattern because elements with even atomic numbers have higher cosmic abundances than those with odd atomic numbers (Chapter 4). Therefore, the REE abundances are usually plotted normalized to CI abundances, which removes this effect and produces a smoothly varying pattern, as shown in Figure 7.10. In this figure europium is clearly enriched relative to the other REE (a "positive europium anomaly"), indicating that plagioclase has been added as cumulus crystals to the magma that formed this rock. Some rocks also show negative europium anomalies, indicating removal of plagioclase during fractional crystallization.

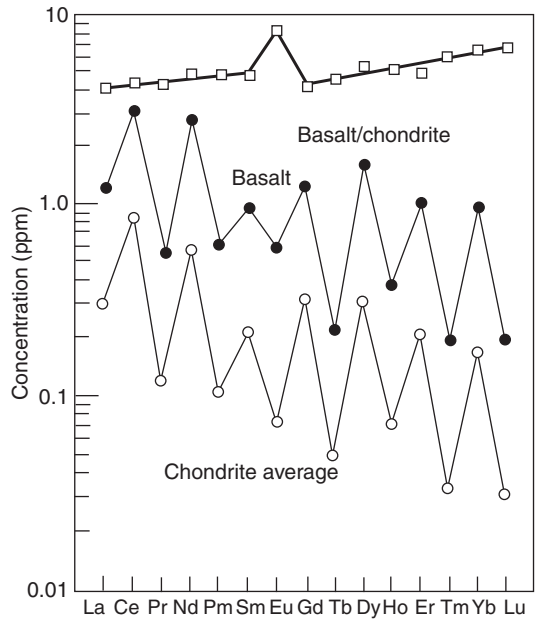

Fig. 7.10 **Rare earth element patterns for basalt and chondrite, and the chondrite-normalized basalt REE pattern. Normalization removes the zigzag pattern due to differences in odd and even atomic number abundances. The europium (Eu) anomaly in the normalized pattern is due to incorporation of extra plagioclase.**

Metallic liquids can also experience fractional crystallization. The abundances of trace elements such as gold, gallium, germanium, and iridium and the major element nickel in various classes of iron meteorites vary because of the separation of crystalline metal phases (kamacite or taenite).

These examples involve partitioning of elements as liquids cooled and crystallized. Partial melting of a solid rock also results in partitioning of incompatible elements into the liquid phase, which contains no rigid crystalline sites. Separation of the melt then fractionates incompatible elements from the compatible elements left behind in the solid residue.

Although it is beyond the scope of this book, we will note that trace element partitioning can be modeled if partitioning coefficients between a magma and specific minerals have been measured. These models (described numerically in most geochemistry texts) provide quantitative constraints on melting or crystallization processes.

Physical fractionations

Sorting of chondrite components

Physical processes that separate one type of material from another can also produce chemical and isotopic fractionations. Several important chemical properties of chondrites probably reflect some sort of physical fractionation process.

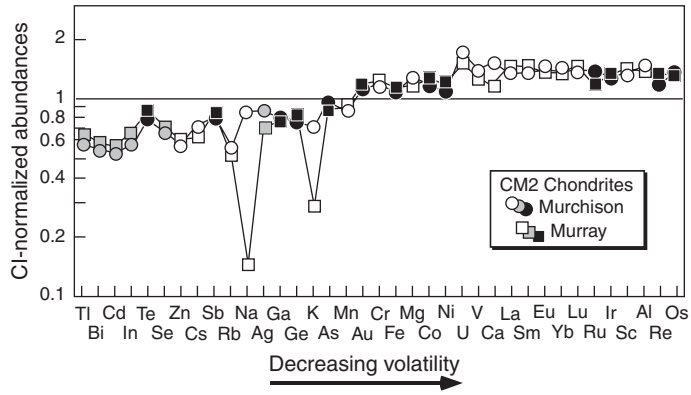

Fig. 7.11 **Bulk compositions of two CM chondrites normalized to CI abundances. Elements are plotted in order of decreasing volatility from left to right. Lithophile elements are shown with open symbols, siderophile elements with black symbols, and chalcophile elements with gray symbols. The elements form two relatively flat plateaus at ~1.25 × CI and ~0.6 × CI. Note that there is no fractionation between lithophile, siderophile, and chalcophile elements. CM data from Kallemeyn and Wasson (1981) and Krähenbühl *et al.* (1973).**

One example is the mixing of high-temperature components and matrix. CM chondrites provide the clearest example of this. These meteorites consist of chondrules and CAIs, which are highly depleted in volatile and moderately volatile elements, and matrix material very similar to CI chondrites, both in chemical composition and in abundances of presolar grains. The bulk compositions of two CM chondrites are shown in Figure 7.11. The elements more refractory than gold form a relatively flat plateau at ~1.25 × CI, reflecting the chondrule-CAI component, while the volatile elements form another plateau at ~0.6 × CI, reflecting the matrix. A third component, carried in the refractory CAIs that makes up several percent of CM chondrites, can be seen in slightly higher abundances of elements more refractory than uranium. The observation of two plateaus on diagrams such as Figure 7.11 was critical to the interpretation given by Larimer and Anders (1970) that chondrites are mixtures of high-temperature and low-temperature condensates. Although we no longer believe that the two components resulted from different degrees of nebular condensation, the observation that two components were mixed to make the meteorites is valid. In most chondrites, the matrix, which varies in abundance from ~60% in CM chondrites to ~15% in ordinary and enstatite chondrites, is the component that carries the majority of volatile elements, although in most chondrites the matrix has also experienced volatility fractionation relative to CI.

There are also more-subtle examples of physical mixing of components. Figure 7.12 shows the bulk Si/Al and Mg/Al ratios in the various chondrite classes. The CI, ordinary (H, L, LL), K, R, and enstatite (EH, EL) chondrite classes are arrayed along a roughly linear trend that suggests loss of an olivine-rich component, perhaps chondrules. In the same diagram, the carbonaceous (CV, CM, CO, CI) chondrite classes fall along a line pointing toward the origin. Because aluminum is a refractory element, this suggests that CV, CM, and CO chondrites are related to CI by addition of a refractory component. Petrographically, CI

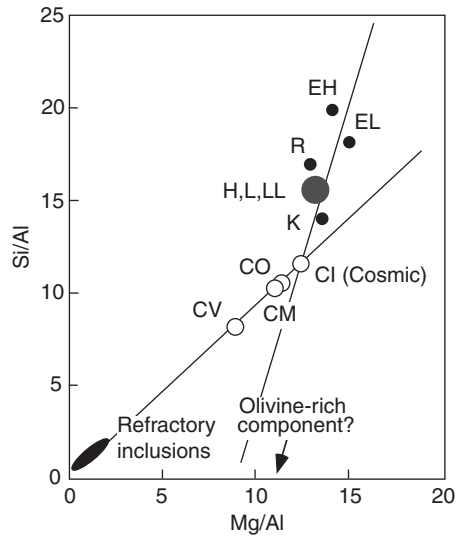

Fig. 7.12 **Physical fractionation of silicate components (refractory CAIs and an olivine-rich component, perhaps chondrules) are suggested by trends in Si/Al and Mg/Al in bulk chondrites.**

chondrites do not appear to contain CAIs, and the abundance of CAIs increases from CO to CM to CV. This strongly indicates that the refractory component reflected in Figure 7.12 is CAIs. Mass balance calculations based on the modal abundances of CAIs are broadly consistent with this interpretation and with the slight hump in the plateau for the most refractory elements in Figure 7.11.

Another example of fractionation that apparently involved a physical process is the metal-silicate fractionation exhibited by chondrites. Figure 7.13 shows the bulk compositions for the ordinary (H, L, and LL) chondrites with the elements arranged in order of increasing volatility and normalized to the composition of CI chondrites. Lithophile elements are shown as open circles, and siderophile elements are black circles. The lithophile and siderophile elements behave as coherent groups, but the proportions of the two groups differ among the three chondrite classes, with the abundance of the siderophile component increasing from LL to L to H. Petrographically, the abundance of metal follows the same sequence, with LL chondrites having the lowest metal abundance and H chondrites having the highest. Together, these observations suggest that a physical process has fractionated the metal from the silicates and produced different mixtures in these meteorites. The process that produced the metal-silicate fractionation is not known. Sorting by mass in a quiescent nebula or aerodynamic size sorting in turbulent nebular eddies have been suggested (Kuebler *et al.*, 1999).

Fractionations by impacts or pyroclastic activity

Several kinds of physical processes have been hypothesized to have affected planetesimals prior to their accretion into planets. These processes could conceivably explain some chemical fractionations observed among asteroids and planets.

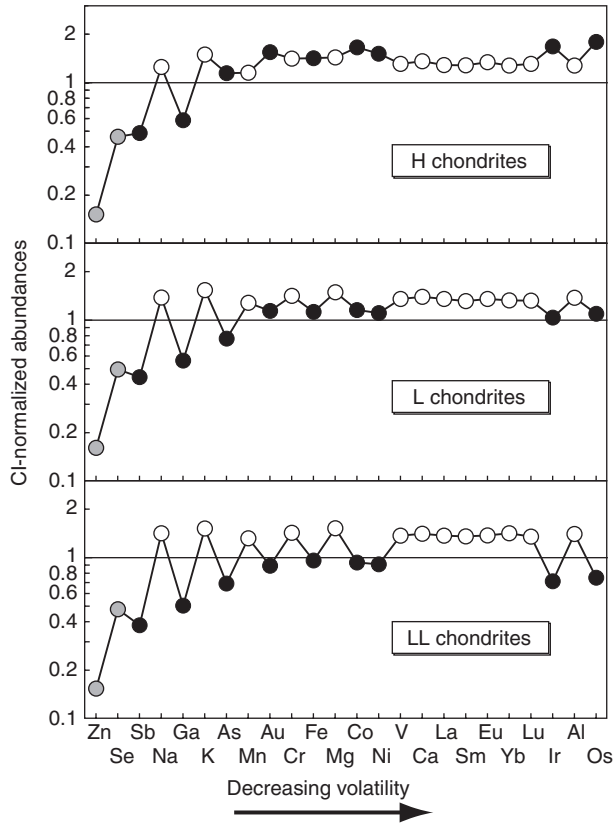

Fig. 7.13 **Bulk compositions of H, L, and LL chondrites normalized to CI abundances. Elements are plotted in order of decreasing volatility from left to right. Lithophile, siderophile, and chalcophile elements are designated with open, black, and gray symbols, respectively. These diagrams reveal fractionation of these element groups among different ordinary chondrite classes. Data from Kallemeyn *et al.* (1989).**

Collisions between bodies of comparable size are more likely to have been glancing ("hit and run") impacts than direct hits (Asphaug *et al.*, 2006). A differentiated, or actively differentiating body might lose a significant portion of its crust and mantle in such a collision, with a resulting major change in the bulk composition of the body. Yang *et al.* (2007) appealed to this process to explain the extremely rapid cooling rates measured for some iron meteorites. In their model, glancing collisions could produce naked iron cores, which would cool much faster than those with silicate mantles. On a much larger scale, Mercury's massive core might reflect impact stripping of some of its silicate crust and mantle. If this were a common process among planetesimals, it might explain the metal-silicate fractionations seen in asteroids and subsequently accreted planets.

The production of volatile-charged magmas in planetesimals with high H_2O or CO_2 contents might result in explosive eruptions, producing pyroclastic melt droplets (Wilson and Keil, 1991) that could escape the objects' gravitational grasp (Warren, 2008). Such a process might explain the lack of basaltic meteorites corresponding to achondrite residues

from partial melting (e.g. ureilites and aubrites). Dispersal and loss of the basaltic fraction, which would otherwise have comprised the crusts of those asteroids, would result in chemical fractionation of the remaining bodies. Their subsequent accretion into planets would then carry a non-chondritic chemical signature of lost elements that melted at low temperatures or were volatile (Warren, 2008).

Element fractionation resulting from oxidation/reduction

Although some kind of physical fractionation of metal and silicate among chondrites is clearly indicated, it is not the entire explanation for the compositions of chondrites. It has been known for a century that, in ordinary chondrites, the abundance of oxidized iron anticorrelates with the abundance of metal. The observations, also known as Prior's rules, are that H chondrites have the most metal, the metal has low nickel, and the silicates have low FeO contents, whereas LL chondrites have the least metal, the metal has the highest nickel content, and the silicates have the highest FeO contents. L chondrites are intermediate in all three properties. In a plot of metallic Fe versus oxidized Fe, both normalized to silicon, loss of metal from material having the cosmic Fe/Si ratio will move compositions directly downward from the solar-composition line (Fig. 7.14). All chondrite classes have lower Fe/Si ratios than CI, suggesting metal loss. However, the various chondrite classes also exhibit varying oxidation states, reflected in different ratios of oxidized Fe/Si, that are independent of the degrees of metal loss, i.e. the vertical distance to the cosmic Fe/Si ratio line. Thus the cosmochemical behavior of iron is dependent not only on the physical fractionation of metal from silicate, but also its oxidation or reduction in different parts of the nebula.

Changes in oxidation state can have a significant effect on the volatility of some elements, including cerium, ytterbium, tungsten, and molybdenum, all of which are refractory in reducing conditions but become increasingly volatile as conditions become more oxidizing.

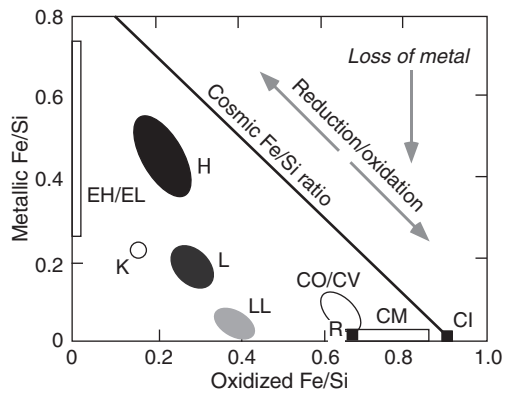

Fig. 7.14 Concentrations of metallic iron and oxidized iron, normalized to silicon, indicate that both oxidation/reduction and loss of metal are required to explain the compositions of various chondrite classes.

Aluminum and calcium can become volatile if they form hydroxides. Depletions of these elements compared to others with similar volatility in a gas of solar composition can help us to investigate the redox conditions under which certain objects formed.

Element fractionation resulting from planetary differentiation

Planetary differentiation is a fractionation event of the first order, and it involves both chemical fractionation and physical fractionation processes. Planetary crusts are enriched in elements that occur in silicate minerals that melt at relatively low temperatures. Recall from Chapter 4 that the high solar system abundances of magnesium, silicon, and iron mean that the silicate portions of planetesimals and planets will be dominated by olivine and pyroxenes. Partial melting of sources dominated by olivine and pyroxene ("ultramafic rocks") produces basaltic liquids that ascend buoyantly and erupt on the surface. It is thus no surprise that most crusts are made of basalts. Remelting of basaltic crust produces magmas richer in silica, eventually resulting in granites, as on the Earth.

The formation of the Moon's crust, composed primarily of feldspar (the rock is called anorthosite) illustrates how physical fractionation can occur during differentiation. Early in its history, a significant portion of the Moon was melted to form a magma ocean. The first minerals to crystallize, olivine and pyroxene, sank because of their high densities and formed an ultramafic mantle. Once feldspar began to crystallize, it floated and accumulated near the surface to produce the crust.

The Earth's crust and, indeed, the crusts of all differentiated bodies, are enriched in incompatible elements relative to their mantles. This reflects the partial melting of mantle material and extraction and transport of the basaltic melt to the surface. On Earth, further partial melting of the basaltic crust in the presence of water produces magma compositions even richer in silica (andesite and granite), which form the bulk of the continental crust. Because other differentiated bodies are effectively dry, this second level of differentiation did not occur.

The formation of cores, whether in planets or asteroids, is the most spectacular display of physical fractionation, in this case segregation of metallic liquids from silicate material. The composition of the metallic liquid depends on the degree of melting. Very limited partial melting produces liquids that have the metal-sulfide eutectic composition, which is sulfur-rich (~85 wt. % FeS). The eutectic melt is the first melt to form in the Fe-Ni-S system as temperature increases, at ~950 °C. As the degree of melting increases, the metallic melt will become progressively richer in iron and nickel. No iron meteorites, nor any planetary cores, have the eutectic composition, although veins of eutectic metal-sulfide occur in acapulcoites-lodranites formed by low degrees of melting.

In experimental studies, metal-sulfide liquids form rounded globules that will sink through a silicate matrix that is itself partly molten (e.g. Walker and Agee, 1988). The density difference is sufficient that segregation of a metallic core though a mush of liquid and crystals should be rapid. However, sinking of metallic liquid through a solid or mostly

solid silicate matrix is greatly inhibited. FeNi-rich melts "wet" silicate grains, forming isolated pockets of liquid, and segregation is sluggish or does not occur at all (Taylor, 1992). Only anion-rich (sulfur or perhaps oxygen) metallic melts form interconnected networks and thus can be separated from solid silicate (Haack and McCoy, 2004). However, dynamic experiments indicate that metal-sulfide segregation may be possible at high pressures and strain rates, even in the absence of silicate melting (Rushmer *et al*., 2000).

Box 7.3 Pioneers in understanding the Earth's core

The discovery that the Earth has as its core a sphere of metal as large as a small planet has a long and interesting history, with some brilliant players. The first hint of a core was found in 1798, when Lord Cavendish devised a scheme to weigh the whole Earth. Drawing on Newton's understanding of gravitational attraction, Cavendish used the balance period of a pendulum to calculate the Earth's mass. When divided by its volume (deduced centuries earlier by Egyptian scholars), this estimate yielded the planet's mean density. Cavendish's estimated value, 5.45 g cm^{-3}, is nearly identical to the presently accepted density of 5.25 g cm^{-3}. This surprising high value is nearly twice the density of surface rocks on the Earth. Clearly, the heart of our planet must contain some very dense material to account for its high mean density.

In 1900, Richard Oldham of the Geological Survey of India showed that earthquake vibrations – seismic waves – actually travel through the body of the Earth. Then, in a landmark 1906 paper, he carefully analyzed the travel times of these seismic waves to demonstrate the existence of the core. Following closely on the heels of Oldham's pioneering discovery, Beno Gutenberg, working in Germany, analyzed seismic waves reflected from the top of the core and fixed its depth rather accurately at 2900 km. This achievement was memorialized in the name of this reflective boundary: the Gutenberg discontinuity. Some seismic waves reaching this boundary are reflected back to the surface, as noted by Gutenberg, whereas others are strongly bent, or refracted, on entering the dense core. The result is a loss of signal on the other side of the Earth. This seismic shadow zone is, in fact, the ghostly image of the Earth's core.

Oldham discovered that there are actually two kinds of seismic vibrations, one called P (or "primary," because it travels faster and arrives first) and the other called S (or "secondary," because of its later arrival at the same station). The compressional motion of the P waves can be transmitted through most substances, although the speed at which the wave moves decreases as the stiffness of the medium decreases. In contrast, the transverse motion of S waves cannot be transmitted through a liquid, because the loosely bonded molecules in a liquid slip past each other too easily. S waves are observed to disappear at the top of the core. Then, at a depth of approximately 5100 km, the P wave velocity abruptly increases and there is a hint of the reappearance of an S wave. From such observations, Danish geophysicist Inge Lehman hypothesized in 1936 that the core was stratified, with an outer liquid portion and an inner solid portion. The existence of molten metal at core pressures requires some light element to act as antifreeze.

The velocities deduced for seismic waves emanating from the core revealed that it must consist of very dense material, but its composition remained a mystery. However, cosmochemical reasoning provided important constraints. The core comprises approximately

a third of the mass of the Earth, and iron is the only heavy element with a high enough cosmic abundance to compose it. The rocks of the crust and mantle contain only a small fraction of the iron predicted to occur in an Earth with roughly chondritic bulk composition. If that were not logic enough, the existence of iron meteorites demonstrates that this element formed cores in other differentiated bodies.

Harvard professor Francis Birch, an ingenious experimentalist, spent his career devising ways to measure seismic velocities in various materials at elevated pressures and temperatures. Such laboratory experiments are difficult and dangerous, but Birch's successful measurements bridged the gap between seismology and geochemistry. He showed that the velocities of seismic waves traveling through metallic iron provide an acceptable match to those measured for the core, especially when the iron is held at high pressure. His experiments also demonstrated that an alloy of iron with nickel provides a closer match than iron alone. The identity of the light element in the outer core, however, remains undefined, although sulfur, oxygen, and hydrogen are plausible candidates.

Fractionation of isotopes

Mass-dependent fractionation

Mass-dependent fractionation among isotopes occurs because some thermodynamic properties of minerals depend on the masses of the atoms of which they are composed. In Chapter 2, we discussed two types of mass-dependent isotope fractionation. Equilibrium fractionation depends on the zero-point energy of a molecule, with heavier isotopes having lower zero-point energies and lower vibrational frequencies. Kinetic fractionation depends on the velocity of the isotope, which is faster for lighter isotopes in order to maintain constant kinetic energy. Isotope mass fractionation effects are most pronounced for light elements, in which the relative difference in mass is larger.

Earlier in this chapter, we discussed isotopic fractionation during evaporation. Under appropriate conditions, where the condensed phase remains isotopically well mixed and the gas phase is removed from the system to prevent back reaction, Rayleigh distillation will occur (Box 7.2), resulting in a condensed phase that is isotopically heavy relative to the starting composition (Fig. 7.9). Isotopic fractionation can occur during both condensation and evaporation, as demonstrated by experiments (Richter *et al.*, 2002). But it is not necessary that isotopes fractionate during evaporation or condensation. It depends on the details of the process. If evaporation occurs into a gas phase that is sufficiently dense, back reactions between gas and liquid can reduce the isotopic fractionation to near the equilibrium value, which is very small. For example, sulfur in chondrules does not show the isotopic fractionation (Tachibana and Huss, 2005) expected during evaporation from a liquid. Also, evaporation from a solid does not produce isotopic fractionation in the solid because diffusion is much too slow to equilibrate the few layers of surface atoms that are fractionated with the bulk of the material.

The degree of equilibrium isotopic fractionation among phases depends on temperature, so the isotopic compositions of co-existing phases can be used for thermometry. Oxygen is widely used in this way. For example, Clayton and Mayeda (1984) found that the oxygen isotopic compositions of calcite and phyllosilicates from Murchison lie on a mass-dependent fractionation line and differ in $\delta^{18}O$ by ~22‰. This difference requires a temperature of around 0 °C, which is interpreted to be the temperature of aqueous alteration on the Murchison parent asteroid. Similar measurements for CI chondrites indicate that aqueous alteration for these meteorites occurred at higher temperature, 50–150 °C (Clayton and Mayeda, 1999).

Oxygen isotopes can also be used to provide constraints on the water-to-rock ratio during aqueous alteration. CM chondrites show clear disequilibrium between trapped water and carbonates produced *in situ* from the fluid phase on the one hand and the bulk matrix of the meteorites. Mass-dependent isotope exchange coupled with mixing of reservoirs that differ in compositions in a mass-independent way (see below and Chapter 6), can be modeled as both closed and open systems, although lack of depletion of water-soluble elements argues against an open-flow system. A model by Clayton and Mayeda (1999) indicates that CM chondrites were altered under conditions of relatively low water content, with water/rock ratios of 0.35–0.6, whereas CI chondrites were altered at higher water/rock ratios of ~2.5.

Fractionations produced by ion–molecule reactions

The relative mass difference between deuterium and hydrogen is the greatest of any common isotope pair, so it should come as no surprise that these isotopes are readily fractionated. Organic matter in meteorites and interplanetary dust particles, in particular, exhibit extreme enrichments in deuterium, reflected in *D*/*H* ratios up to 25 times higher than those seen on Earth. Other isotopic pairs, such as $^{13}C/^{12}C$, $^{15}N/^{14}N$, and $^{34}S/^{32}S$, in meteoritic organic compounds also show distinctive fractionations, as described in Chapter 10. These extreme isotopic fractionations cannot be attributed to equilibrium partitioning of atoms having different masses. Instead, they are due to kinetic effects that occurred during reactions between ions and molecules at very low temperatures such as those found in interstellar space (Herbst, 2003). The temperatures in molecular clouds are so low that chemical reactions between molecules frozen out onto grain surfaces effectively cannot proceed. The activation energy is well beyond the internal energy available in the molecules. However, the kinetic barriers can be overcome by high-energy ions striking the molecules. The incoming ion supplies energy to the molecule, increasing its vibrational frequency enough to cause it to eject an atom. The lost atom is preferentially the light isotope. The molecule will then combine with another atom to restore charge balance, but this process is not isotopically selective. Over time, as the molecule repeatedly loses the light isotope, it becomes isotopically heavy. Scientists have recently realized that this process is not limited to interstellar space, but could also have occurred in the cold regions of the nebula.

Planetary mass-dependent fractionations

During most geologic processes, including melting and crystallization, light stable isotopes can be fractionated according to their masses. The distinct bulk oxygen isotope compositions for achondrite parent bodies that were originally established in the nebula were smeared along mass fractionation lines with slopes of approximately $+^1/_2$ in the $\delta^{17}O$ versus $\delta^{18}O$ diagram. The slope of t reflects the mass differences between ^{17}O-^{16}O on the one hand, and ^{18}O-^{16}O on the other. Similar fractionations occurred in planets during melting and differentiation.

Hydrogen isotopes have also been fractionated during planetary geologic processes. Compared to the Earth, Venus and Mars have significantly elevated *D*/*H* ratios ($\delta D = 125\,000$ permil and 4000 permil, respectively). These fractionations are thought to result from preferential loss of H relative to D from the atmospheres of these planets (Robert *et al*., 2000); atmospheric escape of hydrogen from the Earth was apparently not important.

Ion microprobe analyses of hydrous minerals in Martian meteorites reveal two different sources of hydrogen. One is interpreted as magmatic water, with $\delta D = 900$ permil, and thought to reflect the mantle composition; the other is thought to reflect the atmospheric composition, with $\delta D = 4000$ permil (Leshin, 2000). The incorporation of atmospheric water into these meteorites suggests some kind of cycling of water between the atmosphere and lithosphere on Mars.

Mass-independent fractionation

Isotopic differences that do not depend upon mass are observed in a handful of elements, including oxygen and sulfur. The first mass-independent effects were observed in oxygen. In Chapter 6, we have seen how oxygen isotopes are used for meteorite classification (see Figs. 6.4 and 6.12). Different parts of the solar nebula apparently had different proportions of ^{16}O, ^{17}O, and ^{18}O. The individual components of chondrites, such as chondrules and CAIs, have different oxygen isotopic values. CAIs, chondrules, and other nebula solids accreted to form planetesimals and, eventually, planets with different oxygen isotopic compositions. The use of oxygen isotopes for classification works well even though we do not yet know how the isotopic variations arise.

Once differences in oxygen isotope composition for different bodies were established, the compositions of individual samples were smeared along slope +1/2 lines by mass-dependent fractionation. The mass difference between ^{16}O and ^{18}O is twice that between ^{17}O and ^{18}O, so the fractionation effect for ^{16}O-^{18}O is twice as large. This leads to the slope +1/2 distribution in a plot of $^{16}O/^{18}O$ versus $^{17}O/^{18}O$ (the δ notation in Fig. 7.15 refers to those ratios, relative to a standard). Examples of these lines are the terrestrial fractionation line in Figure 7.15 and the various lines for achondrite groups in Figure 6.12.

When differences in the oxygen isotopic composition of CAIs were first measured in 1973, Robert Clayton and his coworkers attributed these mass-independent variations to mixing of normal solar system gas (plotting on or above the terrestrial mass-fractionation

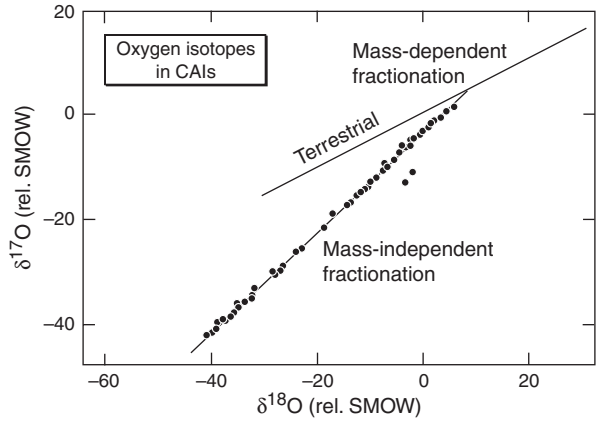

Fig. 7.15 **Oxygen isotopic compositions of minerals in CAIs on an oxygen three-isotope diagram. Axes are given in delta notation: $\delta^{18}O = [(({}^{18}O/{}^{16}O)_{sample}/({}^{18}O/{}^{16}O)_{standard})-1] \times 1000$, and similarly for $\delta^{17}O$. After Clayton *et al.* (1977).**

line in Fig. 7.15) with exotic solids containing pure ^{16}O (plotting on an extension of the diagonal line in Fig. 7.15). In this model, the isotopic compositions result from mixing of different proportions of distinct components produced in different locations, not from a process operating on the solar system oxygen. Subsequently, Thiemens and Heidenreich (1983) showed that mass-independent oxygen fractionations with a similar trend to that observed in meteorites could be produced in the laboratory in reactions involving ozone (O_3). It is now well established that mass-independent fractionations are generated during the production of ozone in the terrestrial stratosphere by photochemical reactions, and that the isotope effects are transferred to other molecular species, most notably sulfate, nitrate, and CO_2 (Thiemens, 2006). Although a complete understanding of the process for this mass-independent fractionation is not yet in hand, it depends on molecular symmetry, with symmetrical molecules such as $^{16}O_3$ being more stable than $^{16}O_2{}^{17}O$, $^{16}O_2{}^{18}O$, or other configurations. However, it is not clear that the processes operating in the stratosphere are relevant to the solar nebula.

Recently Clayton (2002) and others have argued that this isotopic variation arose from self-shielding during photodissociation of CO, a major nebular gas. Because ^{16}O is so abundant, there were large differences in the amounts of $C^{16}O$, on the one hand, and $C^{17}O$ and $C^{18}O$ on the other. The abundant $C^{16}O$ became optically thick near the outside of the nebula (closer to the source of radiation – other stars), whereas $C^{17}O$ and $C^{18}O$ remained optically thin and dissociated to a greater extent in the interior of the nebula. This produced an inner zone enriched in ^{17}O and ^{18}O, which reacted with H_2 to make H_2O. This ^{16}O-depleted water then reacted with ^{16}O-rich dust or condensates to form nebular solids. In this model, the Sun and CAIs are ^{16}O-rich and represent normal solar system oxygen isotope compositions, and the ^{16}O-depleted meteorites and planets are the exotic compositions – this is the opposite of the original interpretation of CAI oxygen isotopes. A preliminary measurement of the solar wind composition (McKeegan *et al.*, 2009) is consistent with this model (see Box 4.4). However, the agreement between the measurement

and the expectation of the self-shielding model does not guarantee that the model is correct. This problem will be the topic of intense study for some time to come.

CAIs, chondrules, and other nebula solids exhibiting a range of oxygen isotopic compositions accreted to form planetesimals and, eventually, planets. Different mixtures of these components produce different bulk isotopic compositions, as described in Chaper 6. Once differences in oxygen isotope composition for different bodies were established, the compositions of individual samples were smeared along slope $+1/2$ lines (like the terrestrial fractionation line in Fig. 7.15 and the various lines for achondrite groups in Fig. 6.12) by mass-dependent fractionation. The combination of mixing of materials with different compositions and mass-dependent fractionations resulting from any of a number of processes together explain the oxygen isotopic variations among solar system materials.

Sulfur isotopes also show mass-independent effects that are probably produced by the same photochemical mechanism as oxygen effects in the Earth's upper atmosphere. Mass independent variations in sulfur from Martian meteorites have been interpreted to result from volcanic injections of SO_2 and H_2S into the Martian atmosphere followed by photolysis, which fractionates the sulfur isotopes. There is also evidence from ancient terrestrial sediments that the same photolytic process was operating on sulfur in the Earth's atmosphere prior to ~2.4 Ga, before oxygen began to accumulate in the atmosphere (see review by Thiemens, 2006).

Radiogenic isotope fractionation and planetary differentiation

Finally, chemical fractionations of elements between minerals, between lavas and their parent reservoirs, and between cores, mantles, and crusts of planetary bodies can segregate radioactive elements from their daughter elements, changing the rate at which the daughter isotopes accumulate. The differences in the isotopic compositions of the radiogenic isotopes that result from these fractionations are the basis for radiochronology (see Chapter 8). As one example, let's consider the element rubidium, which is more incompatible than strontium. When the Earth's crust and mantle segregated, the crust incorporated greater proportions of the incompatible elements, including rubidium. Rubidium has a radioactive isotope (^{87}Rb), which, over geologic time, has partly decayed to form ^{87}Sr. As a consequence, the amount of ^{87}Sr and the ratio of ^{87}Sr to non-radiogenic ^{86}Sr in the crust have increased more rapidly in the crust than in the mantle. By knowing the decay rate of ^{87}Rb and the degree to which rubidium has been enriched relative to strontium, and by measuring the isotopic composition of the strontium in the crust, we can infer the time when the segregation of crust from mantle occurred.

Another example is provided by the chemical fractionation of tungsten into planetary cores. Tungsten has a short-lived radioactive isotope, ^{182}W, which decays into ^{182}Hf. Tungsten is siderophile and hafnium is lithophile. Consequently, the daughter isotope, ^{182}Hf, will be found either in the core or the mantle depending on how quickly metal fractionation (core formation) occurred relative to the rate of decay. The ^{182}Hf-^{182}W system is used to date core formation on planetary bodies. We will discuss the details of using radioactive isotopes as chronometers in Chapters 8 and 9.

Summary

All of the bodies in the solar system formed from the same mixture of gas and dust inherited from the Sun's parent molecular cloud. The composition of the dust is best approximated by CI chondrites. The current compositions of the bodies in our solar system came about because various chemical and physical processes fractionated the elements and isotopes in that initial composition. Understanding how and why elements and isotopes fractionate is a central theme of cosmochemistry. It is easy to visualize fractionations using certain kinds of diagrams that compare elements and isotopes with different chemical characteristics.

We have seen that elements can be separated based on their volatility, either through gas–solid or gas–liquid reactions. There are many types of reactions that form a continuum between equilibrium condensation (or its inverse, evaporation) on the one hand and purely kinetically controlled reactions, such as Rayleigh distillation, on the other. In some cases, isotopic fractionation can assist in identifying the processes involved.

Common igneous processes (partial melting and fractional crystallization) lead to element fractionations. Incompatible elements tend to be concentrated in melts and compatible elements in solids. Separation of partial melts from residual crystals as the melts ascend to higher levels, or accumulation of early-formed crystals from melts, ultimately produces rocks with compositions different from the starting materials. These processes account for the fractionations seen in differentiated meteorites and planetary samples.

Fractionation of elements can also occur when solid components are physically sorted and segregated. The components of chondrites – metal grains, CAIs, chondrules, and matrix – occur in varying proportions among chondrite groups, accounting for some of their bulk chemical properties. Other physical processes that might lead to chemical fractionations are glancing collisions between planetesimals, which strip silicate mantles from cores, and explosive eruptions, which disperse basaltic magma that would otherwise have formed crusts. The subsequent accretion of such planetesimals could yield non-chondritic planets.

Planetary differentiation allows for segregation of elements according to their geochemical affinities on a gross scale. Incompatible lithophile elements are concentrated in basaltic liquids during partial melting, and thus are especially abundant in planetary crusts. Siderophile and sometimes chalcophile elements are segregated into planetary cores because of their high densities.

Mass-dependent isotope fractionation arises from variations in bond strengths and translational velocities resulting from mass differences. Mass-independent oxygen isotopic fractionations in meteorites can be explained by nebular photodissociation of carbon monoxide molecules having different isotopic compositions. Extreme fractionations in hydrogen and other light elements in the organic compounds of chondrites result from kinetic reactions between ions and molecules in interstellar space. Planetary geologic processes can cause mass-dependent fractionations, as seen in hydrogen and oxygen isotopes in achondrites and planetary atmospheres. Physical and chemical processes can fractionate parent radioactive elements from their daughter elements, facilitating isotope chronology, the subject of Chapter 8.

Next we will examine unstable isotopes in some detail. The chronologic information they provide, coupled with knowledge of cosmochemical and geochemical fractionations, are powerful tools in understanding nebular and planetary processes.

Questions

1. What are the major processes that produce chemical fractionations of importance in cosmochemistry?
2. Describe the important minerals in the condensation sequence, and their order of appearance from a cooling gas of solar composition.
3. What are the main processes involved in volatility-based chemical fractionations in cosmochemical samples? Why is volatility-based chemical fractionation important?
4. What chemical fractionations are produced during planetary differentiation?
5. Explain how stable isotopes might be fractionated in the solar nebula and in cold molecular clouds.
6. Explain how mass-dependent and mass-independent isotopic fractionation of oxygen isotopes interact to produce the range of compositions that we observe in cosmochemical materials.

Suggestions for further reading

Davis, A. M. and Richter, F. M. (2004) Condensation and evaporation of solar system materials. In *Treatise on Geochemistry, Vol. 1: Meteorites, Comets and Planets*, ed. Davis, A. M. Oxford: Elsevier, pp. 407–430. A good recent discussion of the processes of condensation and evaporation and associated isotopic effects and their applications to solar system materials.

Ebel, D. S. (2006) Condensation of rocky material in astrophysical environments. In *Meteorites and the Early Solar System, II*, eds. Lauretta, D. S. and McSween, H. Y., Jr. Tucson: University of Arizona Press, Tucson, pp. 253–277. A good summary of the modern condensation calculations and modeling of solar system processes.

Grossman, L. (1972) Condensation in the primitive solar nebula. *Geochimica et Cosmochimica Acta*, **36**, 597–619. This paper describes the first comprehensive calculations of equilibrium condensation under nebula conditions.

Robert, F., Gautier, D. and Dubrulle, B. (2000) The solar system *D*/*H* ratio: observations and theories. *Space Science Reviews*, **92**, 201–224. This paper reviews what is known about hydrogen isotopes and what they can tell us about the history of the solar system.

Sharp, Z. (2007) *Principles of Stable Isotope Geochemistry*. Upper Saddle River, New Jersey: Pearson Prentice Hall, 344 pp. A good recent textbook covering the basics of isotope fractionation and its application to geochemistry and cosmochemistry.

Wänke, H. and Dreibus, G. (1988) Chemical composition and accretion history of terrestrial planets. *Philosophical Transactions of the Royal Society of London*, **A325**, 545–557. This paper describes how chemical fractionations resulted from accretion of different materials to form the terrestrial planets.

References

Alexander, C. M. O'. D., Grossman, J. N., Ebel, D. S. and Ciesla, F. J. (2008) The formation conditions of chondrules and chondrites. *Science*, **320**, 1617–1619.

Asphaug, E., Agnor, C. B. and Williams, Q. (2006) Hit-and-run planetary collisions. *Nature*, **439**, 155–160.

Cameron, A. G. W. (1962) The formation of the Sun and planets. *Icarus* **1**, 13–69.

Campbell, A. J., Humayun, M., Meibom, A., Krot, A. N. and Keil, K. (2001) Origin of zoned metal grains in the QUE94411 chondrite. *Geochimica et Cosmochimica Acta*, **65**, 163–180.

Clayton, R. N. (2002) Self-shielding in the solar nebula. *Nature*, **415**, 860–861.

Clayton, R. N. and Mayeda, T. K. (1984) The oxygen isotope record in Murchison and other carbonaceous chondrites. *Earth and Planetary Science Letters*, **67**, 151–166.

Clayton, R. N. and Mayeda, T. K. (1999) Oxygen isotope studies of carbonaceous chondrites. *Geochimica et Cosmochimica Acta*, **63**, 2089–2104.

Clayton, R. N., Grossman, L. and Mayeda, T. K. (1973) A component of primitive nuclear composition in carbonaceous chondrites. *Science*, **182**, 485–488.

Connolly, H. C., Jr., Huss, G. R. and Wasserburg, G. J. (2001) On the formation of Fe-Ni metal in CR2 meteorites. *Geochimica et Cosmochimica Acta*, **65**, 4567–4588.

Davis, A. M. (2006) Volatile element evolution and loss. In *Meteorites and the Early Solar System, II*, eds. Lauretta, D. S. and McSween, H. Y., Jr. Tucson: University of Arizona Press, pp. 295–307.

Ebel, D. S. and Grossman, L. (2000) Condensation in dust-enriched systems. *Geochimica et Cosmochimica Acta*, **65**, 469–477.

Fegley, B., Jr. (1999) Chemical and physical processing of presolar materials in the solar nebula and the implications for preservation of presolar materials in comets. *Space Science Reviews*, **72**, 311–326.

Grossman, L. and Larimer, J. W. (1974) Early chemical history of the solar system. *Reviews of Geophysics and Space Physics*, **12**, 71–101.

Haack, H. and McCoy, T. J. (2004) Iron and stony-iron meteorites. In *Treatise on Geochemistry, Vol. 1: Meteorites, Comets and Planets*, ed. Davis, A M. Oxford: Elsevier, pp. 325–345.

Herbst, E. (2003) Isotopic fractionation by ion-molecule reactions. *Space Science Reviews*, **106**, 293–304.

Huss, G. R. (2004) Implications of isotopic anomalies and presolar grains for the formation of the solar system. *Antarctic Meteorite Research*, **17**, 132–152.

Huss, G. R., Meshik, A. P., Smith, J. B. and Hohenberg, C. M. (2003) Presolar diamond, silicon carbide, and graphite in carbonaceous chondrites: Implications for thermal processing in the solar nebula. *Geochimica et Cosmochimica Acta*, **67**, 4823–4848.

Huss, G. R., Rubin, A. E. and Grossman, J. N. (2006) Thermal metamorphism in chondrites. In *Meteorites and the Early Solar System, II*, eds. Lauretta, D. S. and McSween, H. Y., Jr. Tucson: University of Arizona Press, pp. 295–307.

Jungck, M. H. A., Shimamura, T. and Lugmair, G. W. (1984) Ca isotope variations in Allende. *Geochimica et Cosmochimica Acta*, **48**, 2651–2658.

Kallemeyn, G. W. and Wasson, J. T. (1981) The compositional classification of chondrites-I. The carbonaceous chondrite groups. *Geochimica et Cosmochimica Acta*, **45**, 1217–1230.

Kallemeyn, G. W., Rubin, A. E., Wang, D. and Wasson, J. T. (1989) Ordinary chondrites: bulk composition, classification, lithophile-element fractionations, and composition-petrographic type relationships. *Geochimica et Cosmochimica Acta*, **53**, 2747–2767.

Kallemeyn, G. W., Rubin, A. E. and Wasson, J. T. (1994) The compositional classification of chondrites: VI. The CR carbonaceous chondrite group. *Geochimica et Cosmochimica Acta*, **58**, 2873–2888.

Krähenbühl, U., Morgan, J. W., Ganapathy, R. and Anders, E. (1973) Abundances of 17 trace elements in carbonaceous chondrites. *Geochimica et Cosmochimica Acta*, **37**, 1353–1370.

Kuebler, K. E., McSween, H. Y., Carlson, W. D. and Hirsch, D. (1999) Sizes and masses of chondrules and metal-troilite grains in ordinary chondrites: possible implications for nebular sorting. *Icarus*, **141**, 96–106.

Larimer, J. W. and Anders, E. (1967) Chemical fractionations in meteorites-II. Abundance patterns and their interpretation. *Geochimica et Cosmochimica Acta*, **31**, 1239–1270.

Larimer, J. W. and Anders, E. (1970) Chemical fractionations in meteorites-III. Major element fractionations in chondrites. *Geochimica et Cosmochimica Acta*, **34**, 367–387.

Leshin, L. A. (2000) Insights into Martian water reservoirs from analyses of Martian meteorite QUE 94201. *Geophysical Research Letters*, **27**, 2017–2020.

Lodders, K. and Fegley, B. (1998) *The Planetary Scientist's Companion*. New York: Oxford University Press, 371 pp.

McCoy, T. J., Keil, K., Muenow, D. W. and Wilson, L. (1997a) Partial melting and melt migration in the acapulcoite-lodranite parent body. *Geochimica et Cosmochimica Acta*, **61**, 639–650.

McKeegan, K. D., Jarzebinski, G. J. *et al*. (2008) A first look at oxygen in a Genesis concentrator sample (abstr.). *Lunar and Planetary Science XXXIX*, CD #2020.

Niederer, F. R., Papanastassiou, D. A. and Wasserburg, G. J. (1981) The isotopic composition of titanium in the Allende and Leoville meteorites. *Geochimica et Cosmochimica Acta*, **45**, 1017–1031.

Petaev, M. I. and Wood, J. A. (1998) The condensation with partial isolation (CWPI) model of condensation in the solar nebula. *Meteoritics and Planetary Science*, **33**, 1123–1137.

Richter, F. M., Davis, A. M., Ebel, D. S. and Hashimoto, A. (2002) Elemental and isotopic fractionation of Type B CAIs: Experiments, theoretical considerations, and constraints on their thermal evolution. *Geochimica et Cosmochimica Acta*, **66**, 521–540.

Rotaru, M., Birck, J. L. and Allegre, C. J. (1992) Clues to early solar-system history from chromium isotopic in carbonaceous chondrites. *Nature*, **358**, 465–470.

Rushmer, T., Minarik, W. G. and Taylor, G. J. (2000) Physical processes of core formation. In *Origin of the Earth and Moon*, eds. Canup, R. M. and Righter, K. Tucson: University of Arizona Press, pp. 227–243.

Tachibana, S. and Huss, G. R. (2005) Sulfur isotope composition of putative primary troilite in chondrules from Bishunpur and Semarkona. *Geochimica et Cosmochimica Acta*, **69**, 3075–3097.

Taylor, G. J. (1992) Core formation in asteroids. *Journal of Geophysical Research*, **97**, 14717–14726.

Thiemens, M. H. (2006) History and applications of mass-independent isotope effects. *Annual Reviews of Earth and Planetary Sciences*, **34**, 217–262.

Thiemens, M. H. and Heidenreich, J. E. III (1983) The mass-independent fractionation of oxygen: a novel isotope effect and its possible cosmochemical implications. *Science*, **219**, 1073–1075.

Wai, C. M. and Wasson, J. T. (1977) Nebular condensation of moderately volatile elements and their abundances in ordinary chondrites. *Earth and Planetary Science Letters*, **36**, 1–13.

Walker, D. and Agee, C. B. (1988) Ureilite compaction. *Meteoritics*, **23**, 81–91.

Warren, P. H. (2008) A depleted, not ideally chondritic bulk Earth: The explosive-volcanic basalt loss hypothesis. *Geochimica et Cosmochimica Acta*, **72**, 2217–2235.

Wasson, J. T. (1985) *Meteorites*. New York: W. H. Freeman and Company, 267 pp.

Wilson, L. and Keil, K. (1991) Consequences of explosive eruptions on small solar-system bodies: the case of the missing basalts on the aubrite parent body. *Earth and Planetary Science Letters*, **104**, 505–512.

Wood, J. A. and Hashimoto, A. (1993) Mineral equilibrium in fractionated nebular systems. *Geochimica et Cosmochimica Acta*, **57**, 2377–2388.

Yang, J., Goldstein, J. F. and Scott, E. R. D. (2007) Iron meteorite evidence for early catastrophic disruption of protoplanets. *Nature*, **446**, 888–891.

Yin, Q.-Z. (2005) From dust to planets: the tale told by moderately volatile elements. In *Chondrites and the Protoplanetary Disk, ASP Conference Series 341*, eds. Krot, A. N., Scott, E. R. D. and Reipurth, B. San Francisco: Astronomical Society of the Pacific, pp. 632–644.

Yoneda, S. and Grossman, L. (1995) Condensation of CaO-MgO-Al_2O_3-SiO_2 liquids from cosmic gases. *Geochimica et Cosmochimica Acta*, **59**, 3413–3444.

8 Radioisotopes as chronometers

Overview

So far we have discussed the materials that make up the solar system and the processes that caused those materials to be in their current state. We will now investigate the chronology of the events that led to the current state of the solar system. There are several different approaches to determine the timing of events. The sequence of events can often be established from spatial relationships among objects (e.g. younger things rest on older things). Absolute ages are provided by long-lived radioactive nuclides. Time intervals can be determined using short-lived radionuclides. Production of nuclides through irradiation by cosmic rays can also be used for age determinations. For a complete chronological picture, it is often necessary to use more than one method of age determination. In this chapter, we focus on the basic principles of radiometric dating. We review individual isotopic clocks, the types of materials that each can date, and the measurements that are made to determine the ages of different objects. In Chapter 9, we discuss the chronology of the solar system derived from these clocks.

Methods of age determination

Placing events in chronological order and attaching an absolute time scale to that order constitute one of the major areas of research in cosmochemistry. There is no single clock that works for everything, so the chronology of the solar system has been built on a wide variety of observations and measurements. The methods of age determination can be divided into two main types. Some methods give *relative ages*. In other words, they tell us that one object is older than another or that one event occurred before another. But they cannot tell us exactly when the object formed or the event occurred. Relative age determination has a long history and is particularly important in geology. For example, consider a sandstone, a rock made up of grains of sand cemented together. The sand grains are older than the sandstone itself, because the sand had to exist before it was incorporated into the rock. In a geologic setting consisting of several layers of rock, the layer of the bottom of the pile must be the oldest because it had to be there before the others could be laid down on top of it. This type of relative age dating can be applied to extraterrestrial materials as well. For example,

a chondritic meteorite consists of chondrules, refractory inclusions, metal, sulfide, and matrix, each of which formed independently. Like the sandstone, the chondrite is younger than the constituents that comprise it. We cannot tell how much younger, but the chondrite could not have formed before the constituents came to exist. Occasionally, we find a chondrule that contains an embedded refractory inclusion. There are currently no clear cases of a chondrule inside a refractory inclusion. This suggests that refractory inclusions are older than chondrules, and as we will see, radiometric dating techniques show this to be true. As we mentioned in Chapter 1 and discuss in detail later, short-lived radionuclides provide a quantitative relative chronology. But to get ages in years before present, the relative ages must be tied to a chronometer that gives *absolute ages*. Absolute ages are provided by long-lived radionuclides, which are still present today in the solar system. Although typically the absolute ages provided by long-lived radionuclides are less precise than the relative ages provided by short-lived radionuclides, the combination of the two can provide a detailed chronology of the early solar system.

Cosmic-ray interactions provide the basis for another type of chronometer. Cosmic rays are high-energy protons and other atomic nuclei that originate either in the Sun or in interstellar space. They are ubiquitous in interstellar space and in the solar system. When a cosmic ray encounters an atomic nucleus, it may break the nucleus into two or more pieces. The resulting stable and radioactive nuclei accumulate over time in objects exposed to cosmic rays. The abundances of these *cosmogenic nuclides* provide information about how long an object was exposed to cosmic rays. Cosmic-ray exposure ages will be considered in the following chapter.

Discussing radiometric ages and time

You will see several different ways of describing units of time in the literature and in this book. There are subtle differences in the meanings of these units that you should be aware of. For example, if we want to say that the formation of a river valley took 1 million years, we could write that it took 1 Myr. On the other hand, if we want to say that the mountains through which the river flows formed 100 million years ago, we could write that it formed at 1 Ma, meaning one million years before present. In this book, when we discuss the period of time over which something happened, we will use the symbols Kyr, Myr, and Gyr (kiloyears, megayears, and gigayears). When we discuss a formation age relative to the present, we will use Ka, Ma, and Ga.

Basic principles of radiometric age dating

Radiometric age dating is a powerful chronological tool. It is based on the accumulation of the daughter nuclide produced by the decay of the parent isotope. If the decay rate is known, and if one can measure the amounts of parent element and daughter isotope, then it is

straightforward to calculate the time necessary for the daughter element to accumulate to its measured abundance. In this section, we present the basic principles of radiometric dating. Details of the pathways of radioactive decay were discussed in Chapter 2.

A good way to think about radioactive decay is to envision a bag of coins, perhaps gold coins. You want to take the coins to someone in a city far away. To get there you must travel through a series of toll gates, one every ten miles. At each gate, a gatekeeper demands that you pay 1% of your coins in order to pass. At the first gate, when you have 1000 coins, you must pay 10 coins to pass. At the next gate, when you have 990 coins, you must pay 9.9 coins (the gatekeeper gives change). At the next gate, the toll is 9.8 coins. At each gate, the number of coins you have decreases by 1%, and as the number of coins gets smaller, the 1% that you pay gets smaller too. The toll is proportional to the number of coins you have, and your bag of coins gets depleted by the same percentage every ten miles. Radioactive decay works the same way. The number of decays in a given period of time is proportional to the number of atoms present:

$$-\frac{dN}{dt} \propto N \tag{8.1}$$

This relationship is transformed into an equality by introduction of a proportionality constant, λ, which represents the probability that an atom will decay within a stated period of time. The numerical value of λ is unique for each radionuclide and is expressed in units of reciprocal time. Thus, the equation describing the rate of decay of a radionuclide is

$$-\frac{dN}{dt} = \lambda N \tag{8.2}$$

where λN gives the rate of decay at time t. To determine the total number of atoms of a radioactive isotope, N, after a particular time t has elapsed, we integrate Equation (8.2):

$$-\int_{N_0}^{N} \frac{dN}{N} = \lambda \int_0^t dt$$

$$\ln N - \ln N_0 = -\lambda t - \lambda 0$$

Rearrange the terms (remembering that $\lambda 0 = 0$):

$$\ln \frac{N}{N_0} = -\lambda t$$

$$\frac{N}{N_0} = e^{-\lambda t}$$

$$N = N_0 e^{-\lambda t} \tag{8.3}$$

Equation (8.3) is the basic equation that describes all radioactive decay processes. It gives the number of atoms (N) of a radioactive parent isotope remaining at any time t from a starting number N_0 at time $t = 0$.

What about the daughter isotope? If the original number of atoms of the stable daughter isotope is taken to be zero at $t = 0$, and no daughter atoms are added to or lost from the system

except by radioactive decay, then the number of daughter atoms (D*) produced by the decay of the parent isotope at any given time is

$$D^* = N_0 - N \tag{8.4}$$

$$D^* = N_0 - N_0 e^{-\lambda t}$$

$$D^* = N_0\left(1 - e^{-\lambda t}\right) \tag{8.5}$$

Equation (8.5) gives the number of stable radiogenic daughter atoms (D^*) at any time t formed by decay of a radioactive parent whose initial abundance at $t = 0$ was N_0.

When dating rocks and minerals, it is often more convenient to relate the number of daughter nuclei (D^*) to the number of parent atoms remaining (N), the quantity that can be measured, rather than to N_0. Starting from Equation (8.4)

$$D^* = N_0 - N$$

and replacing N_0 by $Ne^{\lambda t}$ (from Equation (8.3)) gives

$$D^* = Ne^{\lambda t} - N = N\left(e^{\lambda t} - 1\right) \tag{8.6}$$

In most natural systems, the number of atoms of the daughter nuclide (D) consists of initial atoms already present in the system (D_0) plus those resulting from *in situ* radioactive decay (D*):

$$D = D_0 + D^* \tag{8.7}$$

Substituting Equation (8.6) into (8.7) gives the basic equation that is used to calculate a date for a rock or mineral from the decay of a radioactive parent to a stable daughter:

$$D = D_0 + N(e^{\lambda t} - 1) \tag{8.8}$$

Both D and N are measurable quantities and D_0 is a constant whose value can either be assumed or calculated from the data (see below). Solving this equation for t gives the date:

$$\frac{D - D_0}{N} = e^{\lambda t} - 1$$

$$t = \frac{1}{\lambda}\ln\left[\frac{D - D_0}{N} + 1\right] \tag{8.9}$$

The rate of decay of a radionuclide is often discussed in terms of its half-life. The half-life ($T_{1/2}$) is the time required for one-half of a given number of atoms of a radionuclide to decay. Mathematically, when $t = T_{1/2}$, $N = 0.5 \times N_0$. Substituting these values into Equation (8.3), we find

$$\frac{1}{2}N_0 = N_0 e^{-\lambda T_{1/2}}$$

$$\ln\left(\frac{1}{2}\right) = -\lambda T_{1/2}$$

$$\ln 2 = \lambda T_{1/2}$$

$$T_{1/2} = \frac{ln2}{\lambda} = \frac{0.693}{\lambda} \tag{8.10}$$

Equation (8.10) gives the relationship between the half-life and the decay constant, λ.

Another parameter that is used to describe the decay of a radioactive species is the mean life (τ), which is the average life expectancy of a radioactive atom. The mean life is defined as

$$\tau = -\frac{1}{N_0}\int_{t=0}^{t=\infty} t \cdot dN \tag{8.11}$$

From Equation (8.2),

$$-dN = \lambda N \cdot dt$$

Therefore,

$$\tau = \frac{1}{N_0}\int_{t=0}^{t=\infty} \lambda N t \cdot dt$$

because

$$N = N_0 e^{-\lambda t}$$

$$\tau = \lambda \int_{t=0}^{t=\infty} te^{-\lambda t} \cdot dt = -\left[\frac{\lambda t + 1}{\lambda} e^{-\lambda t}\right]_0^{\infty}$$

$$\tau = \frac{1}{\lambda} \tag{8.12}$$

Thus, the mean life τ is equal to the reciprocal of the decay constant and is longer than the half-life by a factor of $^1/_{0.693}$. The activity of a radionuclide is reduced by a factor of $^1/_e$ during each mean life. The decay of a radioactive nuclide can be discussed in terms of half-life or mean life, and you will see both in the cosmochemistry literature. We will use the half-life in this chapter because this formulation is used more often in chronology applications. Discussions of galactic chemical evolution and the age of the elements (Chapter 9) are often done in terms of mean life.

Figure 8.1 shows graphically the decay of the radionuclide, ^{87}Rb, to its stable radiogenic daughter, ^{87}Sr, as a function of time given in units of half-life. In this example, there are initially many atoms of the ^{87}Rb and no atoms of the daughter ^{87}Sr. In natural systems there is always some ^{87}Sr present initially; these atoms would shift the zero point on the y-axis of Figure 8.1 to a finite value. After one half-life, half of the atoms of the ^{87}Rb have decayed to ^{87}Sr. After two half-lives, half of the atoms of the ^{87}Rb remaining at the end of the first half-life have decayed and three-quarters of the original ^{87}Rb now exist as ^{87}Sr. In general, the initial number of radionuclide atoms is reduced over time by 2^{-n}, where n is the number of half-lives, and the number of daughter nuclides approaches the initial abundance of ^{87}Rb

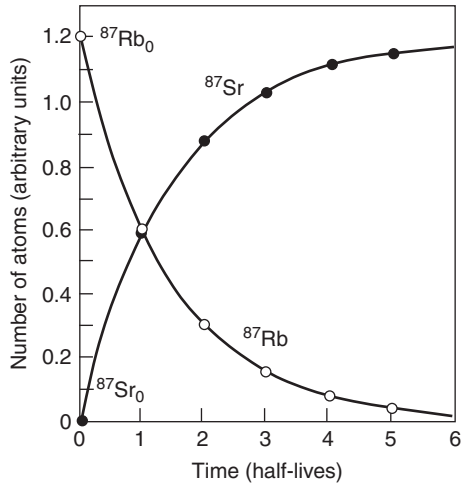

Fig. 8.1 **Number of atoms of radioactive ^{87}Rb and daughter ^{87}Sr as a function of time in units of half-life. For each half-life the number of radioactive ^{87}Rb atoms drops by a factor of two as the ^{87}Rb atoms decay to ^{87}Sr. After 10 half-lives, the parent isotope is effectively gone.**

asymptotically as $t \rightarrow \infty$. For most purposes, a radionuclide can be considered to have decayed away after ~10 half-lives, when N_0 has been reduced by 2^{-10} ($^1/_{1024}$). Note that the number of decays of a radionuclide per unit time is not constant, but decreases exponentially with time. What is constant is the proportion of the radionuclides that decay during one half-life. This is counter to our normal experience because the decay of an atom does not become more likely as the atom becomes older. Radioactive decay is a quantum-mechanical phenomenon, and the probability of decay of a radioactive nuclide can be accurately described from its basic quantum-mechanical properties.

In order for a radiometric date to provide a valid age, the following criteria must be met: (1) There must have been a specific event that homogenized the isotopic compositions of the parent and daughter element. The homogeneous composition of the parent element assures that additions to the amount of daughter isotope reflect only the amount of parent element and the time that has passed. This homogeneous composition of the daughter element is the background above which the accumulation of a radiogenic daughter isotope can be recognized and measured. (2) The isotopic system (e.g. a rock or mineral) must have remained closed, with no loss or gain of parent or daughter element, since the event being dated. (3) The value of the decay constant (λ) must have remained constant over the age of the solar system and the galaxy, and it must be accurately known. As we discussed in Chapter 2, this third assumption is well founded for conditions relevant to cosmochemistry. The concordance of dates given by systems using a variety of decay paths and astronomical observations of decay rates of newly synthesized elements over billions of years provides strong evidence that the decay rates have remained constant. In addition, detailed experiments and theoretical models have identified the extreme conditions (e.g. centers of stars) under which this assumption breaks down for certain isotopes, thereby identifying the "exceptions that prove the rule." (4) It must be possible to assign a realistic value to the initial abundance of the

daughter element, D_0. If these criteria are met, an isotope system can provide an age for the dated material. In practice an additional criterion is also desirable for many isotope systems. The event being dated should somehow generate minerals or other components with different ratios of parent/daughter element. This helps us to recognize the portion of the daughter isotope that resulted from radioactive decay. The importance of this criterion will become clear below.

One can apply the formalism discussed above to a wide variety of systems to produce a radiometric date. In this book, we will use the word "date" to mean the time calculated from the ratio of a radioactive isotope and its daughter isotope using the equation for radioactive decay. An "age" is the time between a natural event and the present. A "date" becomes a valid "age" when the conditions described in the previous paragraph are met. This terminology, suggested by Faure (1986), is not always used in the literature, where "age" and "date" are often used interchangeably. But there is value to the distinction because it helps a reader understand which numbers are significant.

Radiometric age dating is a powerful tool, but it cannot date everything. The clock must be started by a discrete event, the duration of which is short compared to the time elapsed since the event. Crystallization of a melt is an ideal event for dating. Melting will homogenize the parent and daughter elements, and crystallization will typically produce minerals with a variety of parent/daughter element ratios. Crystallization usually occurs relatively quickly. Precipitation of minerals from a fluid phase may also be datable if the dissolution and re-precipitation of the minerals is complete (i.e. the precipitates do not nucleate on pre-existing mineral phases). In contrast, metamorphic episodes are hard to date by radiometric methods. This is because the time scale for metamorphism, both on Earth and in extra-terrestrial bodies, is typically long, and cooling from peak temperatures takes place slowly. Diffusion occurs at high temperatures, which could potentially homogenize the isotopic compositions of parent and daughter elements, but because elements stop diffusing in different minerals at different temperatures (the blocking temperatures), the clock in one mineral may start at a different time than that in another mineral. Under special conditions, even these mineral clocks can be useful, but for the most part metamorphic events cannot be directly dated. Cold accumulation of objects, such as the accumulation of sediments to form sedimentary rocks or the accretion of chondrules and CAIs to form a chondrite, cannot be dated by radiometric means because there is no discrete event that homogenizes the system and starts the clock. However, in the case where one body impacts another at hypervelocity, the resulting explosion may melt and homogenize material, providing an event that can be dated.

One of the criteria for obtaining a valid age is that the decay constant must be known. It turns out that decay constants can be very hard to measure accurately, and different measurements may not agree. If different labs use different decay constants, the dates they produce for the same object will be different. To get around this problem, a subcommission on chronology has established recommended values for decay constants of radionuclides used in chronology. The results of the subcommission's work were published by Steiger and Jäger (1977). This article does not claim to establish the true value of the decay constants of the various nuclides, but it does provide a single number for each nuclide that all laboratories can use to calculate ages. With the passage of time, better values for some decay constants

have been determined, and some decay schemes now use values of the decay constants different to those proposed by Steiger and Jäger (1977). But in general everyone uses the same decay constants and thus the published ages for a single isotope system can be directly compared. Comparing older dates with newer ones can be problematic, however. It should be noted that an agreement on which decay constants to use does not guarantee that ages determined by different chronometers will agree. This is because there are still significant uncertainties in the absolute values of the decay constants, and these uncertainties can result in systematic offsets between chronometers. This issue is seldom discussed in cosmochemistry papers, but users of these ages should be aware of it.

Long-lived radionuclides

Long-lived radionuclides are those with half-lives long enough that a significant fraction of the original atoms incorporated into the solar system when it formed are still present today. Long-lived radionuclides can give absolute ages for events all the way back to the formation of the solar system. If we can figure out how to apply them, they also have the potential of dating events prior to solar system formation. Table 8.1 summarizes the properties of several long-lived radionuclides. Those given in bold type are commonly used as chronometers. In this section, we briefly review each of these chronometers. We will not be able to cover all of the subtleties of each system, but the suggestions for further reading and the cited references provide a wealth of additional details.

Table 8.1 Long-lived radionuclides used in cosmochemistry

Nuclide	Half-life (years)	Daughter isotope	Decay mode*
^{40}K	**1.27×10^{9}**	**^{40}Ar (11%)**	**E.C.**
		^{40}Ca (89%)	β^-
^{87}Rb	**4.88×10^{10}**	**^{87}Sr**	**β^-**
^{138}La	1.05×10^{11}	^{138}Ba (34%)	E.C.
		^{138}Ce (66%)	β^-
^{147}Sm	**1.06×10^{11}**	**^{143}Nd**	**α**
^{176}Lu	**3.75×10^{10}**	**^{176}Hf**	**β^-**
^{187}Re	**4.12×10^{10}**	**^{187}Os**	**β^-**
^{190}Pt	4.50×10^{11}	^{186}Os	α
^{238}U	**4.47×10^{9}**	**^{206}Pb**	α, **(S.F.)**
^{235}U	**7.04×10^{8}**	**^{207}Pb**	α, **(S.F.)**
^{232}Th	**1.40×10^{10}**	**^{208}Pb**	αt, **(S.F.)**

* Decay modes: E.C. = electron capture, β^- = beta decay, α = alpha decay, S.F. = spontaneous fission.

The ^{40}K–^{40}Ar system

Potassium-40 decays to ^{40}Ar by electron capture (11%) and to ^{40}Ca by β^- decay (89%) with a combined half-life of 1.250×10^9 years. Although ^{40}Ca is the more-abundant daughter isotope, ^{40}Ca is the major isotope of calcium, and, because calcium is equally or more abundant than potassium in most materials, the fractional addition of radiogenic ^{40}Ca is typically very hard to detect. Thus, the ^{40}K–^{40}Ca system is only useful in systems with very high K/Ca ratios. In contrast, because argon is a gas and is effectively absent from solids when they crystallize from melts or condense from a gas phase, the addition of radiogenic ^{40}Ar to the sample is easy to recognize. Thus, the ^{40}K–^{40}Ar system is the one primarily used for age dating. One problem with the ^{40}K–^{40}Ar system is that argon is relatively easily released from the crystal structure of minerals. If this happens, then the measured date will be too young. Argon-40 from the atmosphere can also be adsorbed onto or trapped in the structure of the rock or mineral to be dated. This ^{40}Ar can typically be recognized because atmospheric argon has two other isotopes, ^{36}Ar and ^{38}Ar.

History

The minor isotope ^{40}K was discovered by Nier (1935) and was shown to be radioactive by Smythe and Hemmendinger (1937). Aldrich and Nier (1948) found that the isotopic ratio $^{40}Ar/^{36}Ar$ was several times higher in argon extracted from potassium-bearing minerals than in the atmosphere, clear evidence that ^{40}Ar was a radiogenic daughter of ^{40}K. Determining the decay constant for ^{40}K–^{40}Ar decay was a significant challenge. Direct experimental measurements gave a relatively high decay rate and a branching ratio between the ^{40}K–^{40}Ar and ^{40}K–^{40}Ca channels of 0.13, but measurements on minerals of known age suggested a lower value. Wasserburg and Hayden (1955) used the newly developed isotope dilution technique to make precise measurements of potassium feldspars and concluded that the branching ratio should be 0.085±0.005. But Wetherill *et al.* (1955) noted that feldspar gave lower $^{40}Ar/^{40}K$ ratios than coexisting micas, which implied that some of the ^{40}Ar had diffused out of the feldspars, making the branching ratio suggested by Wasserburg and Hayden (1955) too low. Further work confirmed this observation. The currently accepted values of the decay constants for the two channels shown in Table 8.2 give a branching ratio of 0.117.

Technical details

As with all radiometric dating systems, the ^{40}K–^{40}Ar system will only produce a valid age if the basic assumptions of radiometric dating are satisfied. In particular, a valid age can only be obtained if the samples remained closed to diffusion of argon either into or out of the system. Two different approaches can be taken to date an object with the ^{40}K–^{40}Ar system.

^{40}K–^{40}Ar dating

In conventional ^{40}K–^{40}Ar dating, the abundance of potassium is measured on one aliquot of the sample and the argon abundance and isotopic composition are measured on another. The

Table 8.2 Decay constants for ^{40}K[1] and isotopic abundances of potassium[2] and argon[3]

Pathway	Half-life	Decay constant
β-decay	1.397×10^9 yr	$\lambda_\beta = 4.962 \times 10^{-10}$ yr^{-1}
Electron capture	1.193×10^{10} yr	$\lambda_\varepsilon = 0.581 \times 10^{-10}$ yr^{-1}
Combined	1.250×10^9 yr	$\lambda_C = 5.543 \times 10^{-10}$ yr^{-1}

Isotopic abundances (%)			(% in air)
^{39}K	93.2581	^{36}Ar	0.337
^{40}K	0.01167	^{38}Ar	0.063
^{41}K	6.7302	^{40}Ar	99.600

[1] Steiger and Jäger (1977).
[2] Garner *et al*. (1975).
[3] Nier (1950).

current abundance of ^{40}K is calculated using the measured content of potassium in the sample and the isotopic abundance of ^{40}K given in Table 8.2. The $^{40}Ar^*$ is calculated from the argon data by first correcting the raw data for instrumental fractionation effects through comparison with standards, and then subtracting the non-radiogenic ^{40}Ar from atmospheric argon or other components. The radiometric age can be calculated as follows (Equations (8.6) and (8.9)):

$$^{40}Ar^* = \frac{\lambda_{EC}}{\lambda_{total}} {}^{40}K\left(e^{\lambda_{total} t} - 1\right) \tag{8.13}$$

Solving for t gives:

$$t = \frac{1}{\lambda_{total}} \ln\left(\frac{\lambda_{total}}{\lambda_{EC}} \frac{^{40}Ar^*}{^{40}K} + 1\right) \tag{8.14}$$

Inserting the values for the constants from Table 8.2 gives:

$$t = 1.804 \times 10^{-9} \ln\left(9.540 \frac{^{40}Ar^*}{^{40}K} + 1\right) \tag{8.15}$$

^{40}Ar–^{39}Ar dating

The ^{40}Ar–^{39}Ar method, first developed by Merrihue and Turner (1966), has several advantages over the conventional ^{40}K–^{40}Ar method. In this method, the sample is irradiated with fast neutrons and a portion of stable ^{39}K is converted to ^{39}Ar. The argon in the sample is then measured by stepped heating and the ^{39}Ar is released with the radiogenic ^{40}Ar. Provided that the proportion of ^{39}K that was converted to ^{39}Ar is known, dates can be calculated from the argon released in each temperature step. The ^{40}Ar–^{39}Ar method eliminates the need for a separate measurement of the potassium content. But more importantly, it provides a way to

directly associate ^{40}Ar* with the potassium from which it decayed in specific sites in a rock or mineral. Because argon is first released in the experiments from the less retentive mineral sites, the effect of argon loss can be detected.

Each temperature step of the stepped heating procedure of the ^{40}Ar–^{39}Ar method yields a date. To calculate this date, one must determine how many ^{39}K atoms in the sample are represented by the measured number of ^{39}Ar atoms. To determine this number, a sample of known age is included as a monitor of the neutron flux. From measurements of this monitor, a parameter J can be calculated (see Appendix). The date for each step of the ^{40}Ar–^{39}Ar measurement can then be calculated from

$$t = \frac{1}{\lambda}\ln\left(\frac{^{40}\mathrm{Ar}^*}{^{39}\mathrm{Ar}}J + 1\right) \tag{8.16}$$

In a sample that conforms perfectly to the assumptions listed above for the K–Ar dating method, the dates for the temperature steps will be equivalent and will correspond to the age of the sample. However, in natural samples this is not typically found. In order to make sense out of the measurements, the "age-spectrum diagram" was developed, in which the

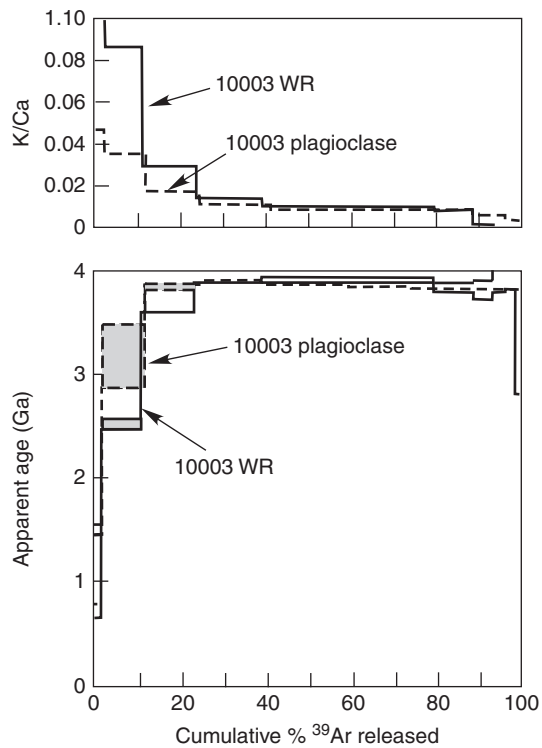

Fig. 8.2 Age-spectrum diagram and K/Ca plots for lunar basalt sample 10003. The first few (low-temperature) steps give dates that are too young, but for steps between 12–30% release and ~90% release, the dates form "plateaus". The plateaus begin at slightly different temperatures for each mineral. The individual temperature steps release gas from sites of different retentivity within the samples. The K/Ca plot provides information about the mineralogy of the sites. After McDougall and Harrison (1988).

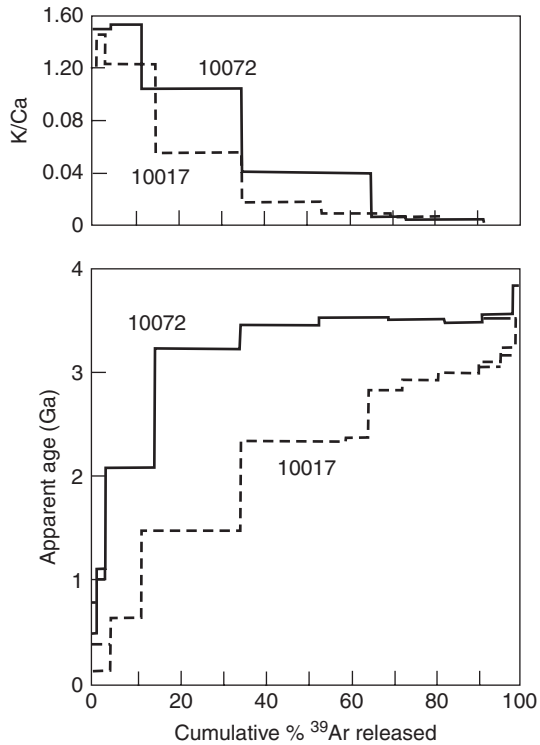

Fig. 8.3 **Age-spectrum diagram and K/Ca plot for two lunar basalt samples showing disturbance of the ^{40}Ar–^{39}Ar system. The basalt 10072 has experienced modest argon loss of ~14% but shows a plateau for steps between 60% and 90% release and gives an age of ~3.5 Ga. In contrast, sample 10017 has experienced ~45% argon loss. Its age spectrum has no plateau and gives only a minimum age of ~3.2 Ga. After McDougall and Harrison (1988).**

calculated date of each temperature step is plotted against the cumulative percentage of the ^{39}Ar (=^{39}K) released. Examples of such diagrams are shown in Figures 8.2 and 8.3.

Typically the low-temperature steps give younger dates than the high-temperature steps. This is due to loss of $^{40}Ar^*$ from the least retentive sites over time. Interpretation of an age-spectrum diagram involves identifying the gas-release from sites that have quantitatively retained their $^{40}Ar^*$ and calculating the age from these steps. Results are often discussed in terms of a "plateau" on the age spectrum diagram. For example, in Figure 8.2, the plateau for plagioclase consists of the steps from ~12% to ~90% of the cumulative ^{39}Ar release. For the whole rock, and for ilmenite and clinopyroxene, the plateau starts at a higher cumulative release. The definition of what constitutes a plateau is somewhat arbitrary, but generally a plateau must consist of at least three contiguous steps that give the same age within errors and these steps must contain a substantial fraction of the ^{39}Ar release. In unusual cases it may be possible to identify two plateaus, representing either the formation age and a major metamorphic event or two metamorphic events, but more often a multistage history results in age-spectrum diagrams with no plateau (sample 10017 in Fig. 8.3).

The irradiation of the sample that is done to convert ^{39}K to ^{39}Ar also converts calcium to various isotopes of argon. A small correction for this effect must be made to the calculated potassium abundance. This correction is done using ^{37}Ar, which is produced exclusively from calcium. In addition to providing a correction to better determine the potassium concentration, the ^{37}Ar also provides a means of estimating the calcium concentration. Plotting the K/Ca ratio versus cumulative ^{37}Ar release (Figs. 8.2 and 8.3) can provide information on the mineralogy of the site(s) that release the $^{40}Ar^*$ in each temperature step.

Applications

Because potassium is relatively abundant in many materials, the ^{40}K–^{40}Ar chronometer has been widely used in geochemistry and cosmochemistry. It can often be used where other dating methods cannot. The half-life of ^{40}K is sufficiently long that the ^{40}K–^{40}Ar system can date objects that formed during the earliest epochs of solar system history, and is short enough to permit dating of objects that formed as recently as a few million years ago. The ^{40}K–^{40}Ar system is ideal for dating objects that crystallized from a melt or condensed from a gas phase because $^{40}Ar^*$ from the decay of ^{40}K in the precursor material is typically completely degassed from the sample. The ^{40}K–^{40}Ar system has been used to date meteorites and samples from the Moon and Mars (SNC meteorites). Today, most ^{40}K–^{40}Ar dating in cosmochemistry is done with the ^{40}Ar–^{39}Ar method.

The ^{40}Ar–^{39}Ar method has been particularly useful in unraveling the history of the Moon. For example, Figure 8.2 shows the age-spectrum diagram for the whole rock and three mineral separates from Apollo 11 basalt 10003. This is a well-behaved rock that gives a clear plateau consisting of >50% of the cumulative ^{39}Ar release for all four sub-samples. The age of eruption and crystallization on the lunar surface inferred for this basalt is 3.86±0.02 (2σ) Ga ($\lambda = 5.543 \times 10^{-10}$ yr^{-1}). Other basalts are not so well behaved. For Apollo 11 basalt 10072, the plateau for 50–98% cumulative release gives an age of 3.5 Ga (Fig. 8.3), which is consistent with the ^{87}Rb–^{87}Sr age (3.57±0.05 Ga) and the ^{147}Sm–^{143}Nd age (3.57±0.03 Ga). The close agreement between the dates obtained by three independent techniques shows that ^{40}Ar–^{39}Ar ages are reliable when the system has remained closed and a good plateau is obtained on the age- spectrum diagram. On the other hand, Apollo 11 basalt 10017 does not give a plateau (Fig. 8.3) and only a minimum age of 3.2 Ga can be inferred.

The ^{87}Rb–^{87}Sr system

Rubidium-87 β-decays to ^{87}Sr with a half-life of ~4.88×10^{10} years ($\lambda_\beta = 1.42 \times 10^{-11}$ yr^{-1}). Rubidium has two naturally occurring isotopes, ^{85}Rb and ^{87}Rb (Table 4.2). Rubidium is an alkali metal and belongs to Group 1A of the periodic table (Fig. 2.4). Other alkali metals are lithium, sodium, potassium, cesium, and francium. The ionic radius of rubidium (1.48 Å) is similar enough to that of potassium (1.33 Å) to permit it to substitute for potassium in all potassium-bearing minerals. As a consequence, rubidium does not form minerals of its own, but instead occurs in easily detectable amounts in many minerals.

Strontium has four naturally occurring isotopes (Table 4.2). It is a member of the alkaline earths (Group 2A) along with beryllium, magnesium, calcium, barium, and radium (Fig. 2.4). Strontium substitutes for calcium and is abundant in minerals such as plagioclase, apatite, and calcium carbonate.

History

The natural radioactivity of rubidium was demonstrated by Campbell and Wood (1906), and ^{87}Rb was identified as the radioactive isotope by Hemmendinger and Smythe (1937). Mattauch (1937) determined the isotopic composition of strontium separated from a rubidium-rich mica and found that it was nearly pure ^{87}Sr. This led Hahn and Walling (1938) to discuss using the ^{87}Rb–^{87}Sr system to determine ages of rocks. They envisioned determining abundances of rubidium and strontium by chemical means, which meant that their method was limited to minerals such as mica and potassium feldspar that form with high rubidium concentrations and essentially no common strontium. Although the chemical strontium method was used for several years, it was clear that isotopic analyses were desirable to permit detection of and correction for common strontium. After World War II, with the improved mass spectrometers and the newly developed isotope dilution technique for measuring very low elemental abundances (Inghram, 1954), the isotopic ^{87}Rb–^{87}Sr method replaced the chemical strontium method.

The ^{87}Rb–^{87}Sr technique was first applied to meteorites in 1956. However, the decay constant for rubidium was then poorly known. Measurements of one chondrite and one achondrite by Schumacher (1956) gave very old ages, 5.46 and 5.80 Ga, using the then-recommended half-life of 58 Gyr. Schumacher proposed a "geological value" for the half-life that gave ^{87}Rb–^{87}Sr ages for the meteorites of 4.7±0.4 Ga, in reasonable agreement with the Pb–Pb ages determined by Patterson (1956). ^{87}Rb–^{87}Sr chronology was plagued by the uncertainty in the half-life of ^{87}Rb throughout the 1950s and 1960s. Values ranged from 47 Ga as determined by direct counting to a geological value of 50 Ga. The current uncertainty in the half-life is still on the order of 2%. Steiger and Jäger (1977) recommended a value of 48.8 billion years, but cosmochemists often use values of 49.4 to 50 Ga. One can easily recalculate ages to a different decay constant using the following equation:

$$t_{1.42} = \frac{date \times 1.39 \times 10^{-11}}{1.42 \times 10^{-11}} \tag{8.17}$$

In this equation, $t_{1.42}$ is the date based on $\lambda = 1.42 \times 10^{-11}$ yr^{-1} and the original date was calculated using $\lambda = 1.39 \times 10^{-11}$ yr^{-1}.

The ^{87}Rb–^{87}Sr method reached its modern level of maturity during the mid to late 1960s as scientists prepared for the return of lunar samples. The technology that enabled this work was a new generation of automated mass spectrometers with digital data acquisition. Leaders in developing this new technology were the Australian National University group headed by W. Compston and the Caltech group headed by G. J. Wasserburg. The other development was the application of the mineral or "internal" isochron technique to meteorites (see below). The ^{87}Rb–^{87}Sr system played an important role in unraveling the history

of the Moon and in establishing the antiquity of meteorites. It is often used in conjunction with other techniques to evaluate the evolution of differentiated bodies.

Technical details

There are two basic ways to apply the ^{87}Rb–^{87}Sr technique to natural samples. The original method is to simply measure the isotopic composition of strontium and the abundance of rubidium in a rock and then calculate a date. If the rock contains no common strontium, a date can be calculated from:

$$t = \frac{1}{\lambda}\ln\left(\frac{^{87}Sr^{*}}{^{87}Rb} + 1\right) \tag{8.18}$$

Here, $^{87}Sr^{*}$ denotes radiogenic ^{87}Sr from *in situ* decay. However, most rocks do contain common strontium, which must be subtracted from the measured ^{87}Sr to determine $^{87}Sr^{*}$:

$$t = \frac{1}{\lambda}\ln\left(\frac{^{87}Sr_{total} - ^{87}Sr_{0}}{^{87}Rb} + 1\right) \tag{8.19}$$

It is difficult from a single measurement to determine the amount of common Sr ($^{87}Sr_0$), so in practice, measurements are generally made on several cogenetic rocks or minerals, and the results are plotted on a ^{87}Rb–^{87}Sr evolution diagram.

Let us assume that a geological event caused the strontium isotopes to be homogenized within a rock. This means that at time zero, all of the minerals in the rock had the same initial $^{87}Sr/^{86}Sr$ ratio [$(^{87}Sr/^{86}Sr)_0$]. The Rb/Sr ratio differs among the minerals of a rock, so with the passage of time, the $^{87}Sr/^{86}Sr$ ratio in each mineral changes at a rate that is proportional to the Rb/Sr ratio (Fig. 8.4). Although Figure 8.4 illustrates what happens to the $^{87}Sr/^{86}Sr$ ratio with time in the various minerals in a rock, it is not particularly useful in dating the rock. Returning to Equation (8.18) above, we can write:

$$^{87}Sr = {}^{87}Sr_0 + {}^{87}Rb\left(e^{\lambda t} - 1\right) \tag{8.20}$$

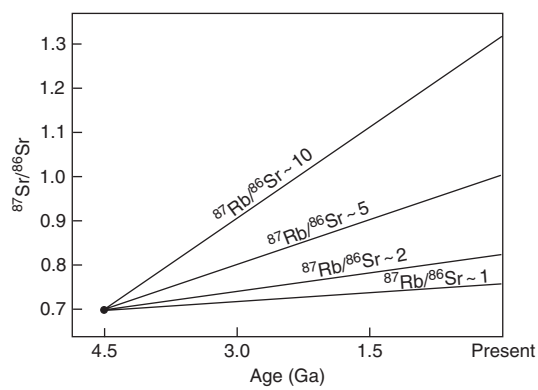

Fig. 8.4 Compston–Jeffery diagram showing the growth of radiogenic ^{87}Sr as a function of time in minerals with different $^{87}Rb/^{86}Sr$ ratios.

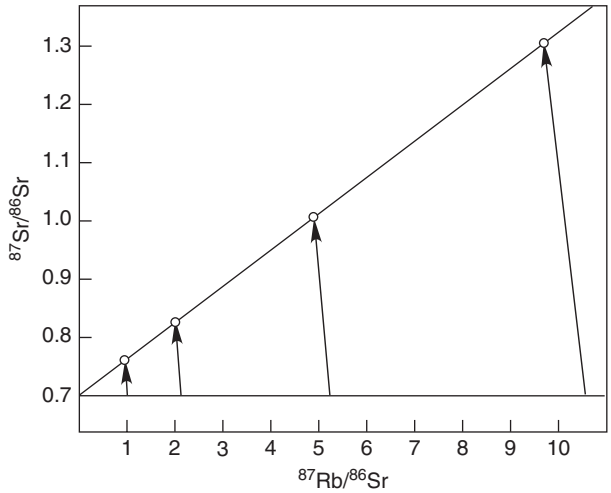

Fig. 8.5 **Rubidium–strontium evolution diagram showing the isochron generated by the minerals in Figure 8.4. Note that the $^{87}Rb/^{87}Sr$ ratio decreases slightly as ^{87}Rb decays to ^{87}Sr.**

Dividing through by ^{86}Sr, which is stable and is not involved in radioactive decay, the following equation is obtained:

$$\frac{^{87}Sr}{^{86}Sr} = \left(\frac{^{87}Sr}{^{86}Sr}\right)_0 + \frac{^{87}Rb}{^{86}Sr}\left(e^{\lambda t} - 1\right) \tag{8.21}$$

This is the equation for a straight line on a diagram of $^{87}Sr/^{86}Sr$ vs. $^{87}Rb/^{86}Sr$, also known as a ^{87}Rb–^{87}Sr evolution diagram. The line is an "isochron", with the slope and intercept given by

$$slope = e^{\lambda t} - 1 \qquad intercept = \left(\frac{^{87}Sr}{^{86}Sr}\right)_0$$

Figure 8.5 shows schematically the data from Figure 8.4 plotted on a ^{87}Rb–^{87}Sr evolution diagram, also known as an isochron diagram. At time zero, the event that we hope to date homogenized the strontium isotopes throughout the system, so each of the minerals started with the same $^{87}Sr/^{86}Sr$ ratio, $[(^{87}Sr/^{86}Sr)_0]$. With the passage of time, some of the ^{87}Rb decays to ^{87}Sr, and the minerals each move up and to the left on the diagram. Because the position of each mineral at any given time is described by Equation (8.21), the minerals always fall on a linear array, the slope of which is proportional to the amount of time that has passed. The date is thus given by solving the equation for the slope for time t:

$$t = \frac{1}{\lambda}\ln[slope + 1] \tag{8.22}$$

To apply this method, the scientist measures the $^{87}Sr/^{86}Sr$ and $^{87}Rb/^{86}Sr$ ratios in several samples and plots the results on a ^{87}Rb–^{87}Sr evolution diagram. Each data point has a measurement uncertainty associated with it, so the points will not fall exactly on a straight line even in the

best-behaved system. An error-weighted linear regression of the data provides the equation for the isochron. Regression methods that take into account the uncertainties in both $^{87}Sr/^{86}Sr$ and $^{87}Rb/^{86}Sr$ and provide as output the slope and intercept of the isochron along with their uncertainties and a measure of the goodness of fit to the data are available in the literature (York, 1966, 1969; Williamson, 1968; Ludwig, 2003) and are used by most laboratories.

An isochron that is built from measurements of several mineral phases provides an internal check on whether or not the system has remained closed, one of the requirements for a valid age. If the system has not remained closed and has been affected by subsequent events, the isochron will be "disturbed." On the ^{87}Rb–^{87}Sr evolution diagram, the data will plot farther from the isochron than expected based on measurement errors. Such a line is known as an "errorchron." Figure 8.6 shows schematically what might happen to the isochron in Figure 8.5 if the rubidium and strontium are partially or totally redistributed. "Disturbed" isochrons may also result if the minerals being measured are not cogenetic, i.e. they did not form together from the same isotopic reservoir. If the isochron is highly disturbed, the problem is easy to recognize, but if it is only slightly disturbed, the fit to the data may look pretty good, but the errorchron will not give an accurate age.

Ideally one would like to construct the isochron based on distinct mineral phases. In practice, it is not always possible to get clean mineral separates for analysis. However, if the

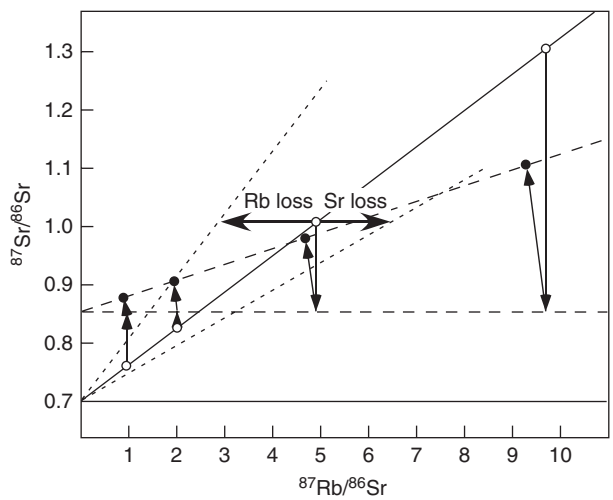

Fig. 8.6 Rubidium–strontium evolution diagram illustrating what happens when an isochron is disturbed, perhaps by a later thermal event. If the thermal event happens in a closed system, the strontium isotopes simply re-equilibrate. Minerals with high $^{87}Sr/^{86}Sr$ ratios exchange with minerals with low $^{87}Sr/^{86}Sr$ ratios and, if the process goes to completion, a new equilibrium composition shown by the dashed horizontal line results. When the system cools, radiogenic ^{87}Sr begins to accumulate again and a new, sloped isochron is generated (dashed line with solid points). If rubidium is lost or gained while the strontium isotopes remain undisturbed, the points on the original isochron (open symbols) move either left or right on the diagram and the correlation line becomes steeper or shallower. Unless the gain or loss is directly proportional to the amount of rubidium present, the correlation will be destroyed. Both kinds of disturbance can happen simultaneously. The result, if the system is not completely reset, is a general correlation that cannot be interpreted as an isochron.

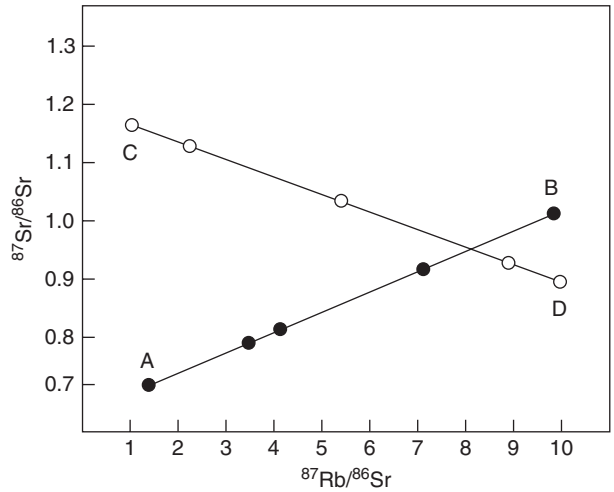

Fig. 8.7 **Two mixing lines on a rubidium–strontium evolution diagram. On any three-isotope diagram with a common denominator (or numerator), mixtures of two components will fall on straight lines connecting the two components. Different mixtures of components A and B produce a line with a positive slope that could be mistaken for an isochron. Different mixtures of C and D produce a line with a negative slope that is easy to recognize as a mixing line. If supposed internal isochrons are based only on different whole-rock samples, one must be aware of the possibility that a correlation on the evolution diagram could be a mixing line.**

rock meets the conditions necessary for a valid age, an isochron can be generated from impure mineral separates or even different fragments of the rock that have different proportions of the constituent minerals. The different mixtures of minerals produce different $^{87}Rb/^{86}Sr$ ratios and provide the spread to generate the isochron. There is a danger in using this type of sample. Suppose a rock consists of two phases that did not form in a single event, such as plagioclase rich in strontium cut by a vein of a rubidium-rich orthoclase. Several samples of this rock containing different mixtures of the two phases could be measured, resulting in a series of $^{87}Rb/^{86}Sr$ and $^{87}Sr/^{86}Sr$ ratios that form a linear array on a ^{87}Rb–^{87}Sr evolution diagram. However, in this case, the array is not an isochron, but is a mixing line between the two phases. Figure 8.7 shows two examples of such arrays, along with the hypothetical mineral phases (end members of the mixing lines) from which they were generated. The data fall solidly on the linear arrays, so there is no way to determine from the fit of the data to the line that these are not isochrons. If the slope or intercept of the array were unreasonable, such as in the case of array C–D on Figure 8.7, one could tell, but array A–B could easily be mistaken for an isochron. Although such cases are rare, one must be aware of this possibility.

Applications

A wide variety of rock types can be dated by the ^{87}Rb–^{87}Sr system, provided that the samples satisfy the assumptions that the system was initially isotopically homogeneous (had a uniform $^{87}Sr/^{86}Sr$ ratio) and did not gain or lose rubidium or strontium after if formed. Both

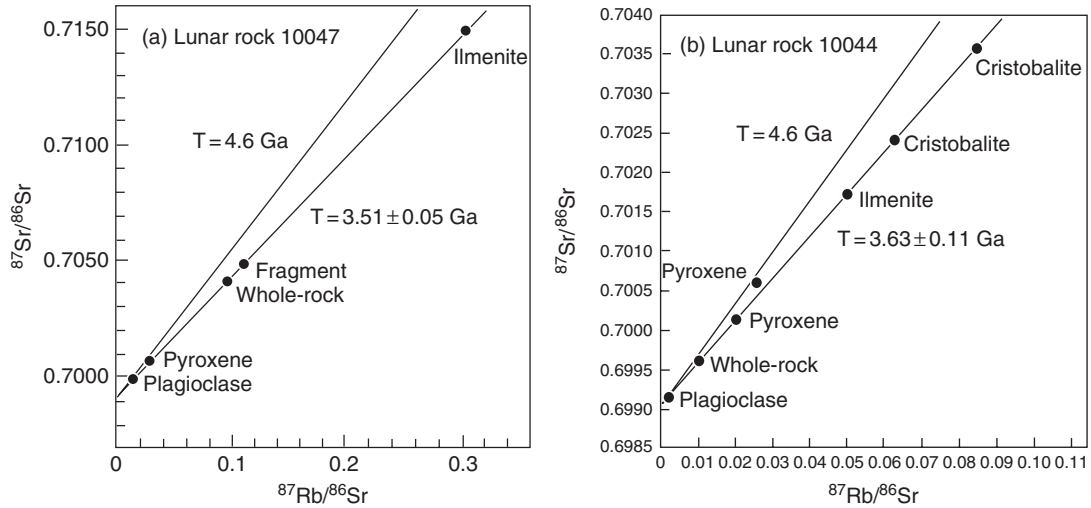

Fig. 8.8 **Rubidium–strontium evolution diagrams for two different Apollo 11 rocks. Rock 10047 has high potassium and rubidium and the measured $^{87}Sr/^{86}Sr$ ratios of the rubidium-rich phases, pyroxene and ilmenite, are quite high, with the result that the isochron produced from plagioclase, pyroxene, ilmenite, and two whole-rock fragments has a precisely determined slope. Rock 10044 is a low-potassium rock with lower rubidium content. The $^{87}Rb/^{86}Sr$ ratios are lower as are the measured $^{87}Sr/^{86}Sr$ ratios. However, because the data are very precise, the isochron is still well determined. After Papanastassiou *et al.* (1970).**

the slope and the intercept of the ^{87}Rb–^{87}Sr isochron give chronological information. If the conditions for radiometric dating are met, the slope of the array gives the age before present when an object formed. Differences in the intercept values among objects that formed from the same material reservoir also provide information about relative time differences.

Chronology with slope of an isochron

Two types of isochrons can be constructed. An internal isochron is one constructed from measurements of different cogenetic minerals in the same rock. The internal isochron gives information about the formation time of that rock. An isochron can also be constructed from bulk samples of different rocks thought to have formed from the same source material at the same time. Such isochrons are known as "whole-rock" isochrons. Early attempts to date chondrites by the ^{87}Rb–^{87}Sr method were carried out by constructing whole-rock isochrons, first for meteorites of all classes, and later for meteorites from single classes. These isochrons demonstrated that chondrites are ~4.5 Ga old (e.g. Minster and Allègre, 1981).

Internal ^{87}Rb–^{87}Sr isochrons were particularly useful in unraveling the history of the Moon and Mars. As an example, consider mare basalts from the Sea of Tranquility collected by Apollo 11. These lunar basalts consist primarily of calcium-rich (anorthitic) plagioclase and low-calcium pyroxene, along with ilmenite, crystobalite, and other minor phases. Strontium is concentrated in the calcium sites in plagioclase and is excluded from most other phases, resulting in a variation of a factor of several hundred in the strontium

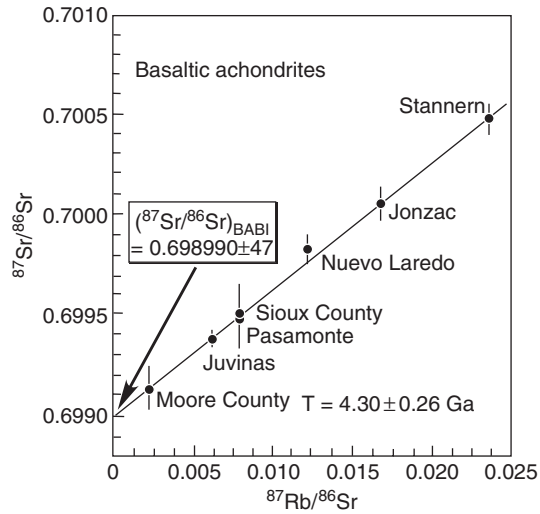

Fig. 8.9 **Rubidium–strontium evolution diagram for basaltic achondrites. A least-squares regression through the data gives an isochron age. The intercept of the isochron gives the $(^{87}Sr/^{86}Sr)_0$ ratio at the time the parent planet of the basaltic achondrites differentiated. After Papanastassiou and Wasserburg (1969).**

abundance among minerals. On the other hand, rubidium is present in most minerals and the abundance varies by only a factor of about ten. As a result, the $^{87}Rb/^{86}Sr$ ratio in the samples varies by a factor of several hundred among the mineral phases. This large spread and the high-precision measurements of the $^{87}Sr/^{86}Sr$ ratio using thermal ionization mass spectrometry (TIMS) permit precise age determinations. Figure 8.8 shows internal isochrons for two different Apollo 11 rocks, one with high total potassium content and one with low total potassium. Mineral separates were obtained by a combination of hand picking, density separation, and magnetic separation. Note how small the measurement errors are compared to the spread in the isotope ratios among the samples and the precision of the resulting dates.

Chronology using the initial $^{87}Sr/^{86}Sr$ ratio

The intercept of a ^{87}Rb–^{87}Sr isochron gives the initial $^{87}Sr/^{86}Sr$ ratio of the sample when it crystallized. The intercepts of isochrons will be different in objects that formed from the same reservoir at different times due to the continuing decay of ^{87}Rb to ^{87}Sr within the reservoir. As time passes, each new object to form will have a slightly higher initial $^{87}Sr/^{86}Sr$ ratio $[(^{87}Sr/^{86}Sr)_0]$. In order to use the initial value for chronology, it is necessary to determine it very precisely. The best samples for this work are those with very low Rb/Sr ratios, so that the $^{87}Sr/^{86}Sr$ ratio has not evolved very much since the object formed. As an example, let us consider the $(^{87}Sr/^{86}Sr)_0$ ratio for eucrites, basaltic achondrites that we think come from the asteroid 4 Vesta. Eucrites have low Rb/Sr ratios and the resulting $^{87}Sr/^{86}Sr$ ratios have a total spread of only ~0.2%. Papanastassiou and Wasserburg (1969) measured the $^{87}Rb/^{86}Sr$ ratios and made high precision measurements of the $^{87}Sr/^{86}Sr$ ratios

in several of these meteorites. Their data are plotted on a ^{87}Rb–^{87}Sr evolution diagram (Fig. 8.9). The best-fit line through the data has a slope corresponding to an age of $(4.30\pm0.26) \times 10^9$ years (recalculated to $\lambda = 1.42 \times 10^{-11}$ yr^{-1}). The initial ratio indicated by the isochron is 0.698990±0.000047. The isochron age has an uncertainty of ~6%, but the initial ratio is determined to better than 0.01%. Papanastassiou and Wasserburg (1969) also calculated the initial ratios for each individual eucrite from the measured $^{87}Rb/^{86}Sr$ and $^{87}Sr/^{86}Sr$ ratios by assuming that the formation age for all meteorites was 4.5 Ga. If the $^{87}Rb/^{86}Sr$ ratios are low enough, the $^{87}Sr/^{86}Sr$ ratio evolved so little over 4.5 Ga that the estimated initial ratio is not sensitive to the exact choice of the formation age of the meteorites. The two precisely measured meteorites with the lowest $^{87}Rb/^{86}Sr$ ratios (Juvinas and Sioux County), and therefore the ones with the least radiogenic ^{87}Sr, had the smallest uncertainties. The average of the initial ratios for these two meteorites gave $(^{87}Sr/^{86}Sr)_0 = 0.698976\pm0.000055$, which is essentially identical to the intercept of the isochron. Papanastassiou and Wasserburg (1969) defined the Basaltic Achondrite Best Initial value (BABI, Table 8.3) as an estimate of the $(^{87}Sr/^{86}Sr)_0$ ratio in the early solar system.

It was soon discovered that there were other solar system objects that were older and had more primitive strontium than the basaltic achondrites. Table 8.3 compares the $(^{87}Sr/^{86}Sr)_0$ value determined for BABI with those from some other important samples from the early solar system. If Allende, Angra dos Reis, and the basaltic achondrites formed directly from the solar nebula, then the time intervals shown in the right-hand column of Table 8.3 are valid. Note that the uncertainties on these time intervals, a few million years, are much smaller than the uncertainty in the eucrite isochron shown in Figure 8.9 (~260 Myr). However, the validity of the time intervals determined from the initial ratios depends completely on the validity of the idea that they all formed directly from the bulk material of the solar nebula.

The $(^{87}Sr/^{86}Sr)_0$ ratio of a system depends not only on time but also on the details of the history of the system from which the final object formed. Figure 8.10 illustrates this

Table 8.3 Initial strontium $[(^{87}Sr/^{86}Sr)_0]$ ratios for solar-system samples

Sample	$(^{87}Sr/^{86}Sr)_0$	$(^{87}Sr/^{86}Sr)_0$ adjust to NBS 987[1]	ΔT if formed from chondritic reservoir
Allende (ALL)[2]	0.69877±0.00002	0.69888±0.00002	0
Angra dos Reis (ADOR)[3]	0.69884±0.00004	0.69895±0.00004	$(4.5\pm2.8) \times 10^{-6}$ yrs
Basaltic achondrites (BABI)[4]	0.69898±0.00003	0.69909±0.00003	$(13.5\pm2.3) \times 10^{-6}$ yrs

[1] The numerical value of the NBS 987 standard was increased, so all numbers reported relative to that standard must also be increased to compare with modern values.
[2] Gray *et al*. (1973).
[3] Papanastassiou *et al*. (1970).
[4] Papanastassiou and Wasserburg (1969).

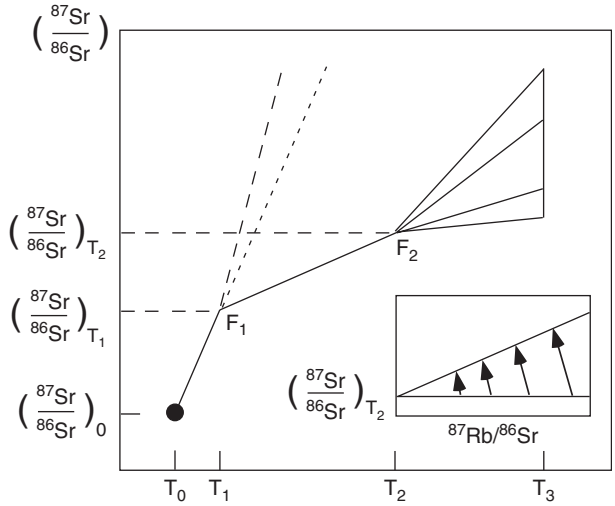

Fig. 8.10 Schematic diagram showing a hypothetical multi-stage fractionation of rubidium and strontium and the subsequent isotopic evolution of strontium. At T_0, a system with fixed $^{87}Rb/^{86}Sr$ and $^{87}Sr/^{86}Sr$ ratios (black circle) begins to evolve. At time T_1, when the system has reached F_1, a fractionation event occurs which extracts material with a lower $^{87}Rb/^{86}Sr$ ratio. This new material evolves toward point F_2, while the original reservoir, which now has a slightly higher $^{87}Rb/^{87}Sr$ ratio, evolves along the dashed line. The dotted line shows the evolution of the body as a whole. When the material reaches F_2 at time T_2, a second fractionation event occurs that generates four new materials (minerals perhaps) with different $^{87}Rb/^{86}Sr$ ratios. Each mineral evolves along its own trend, and if the system remains closed, the four new minerals will generate an isochron (inset).

point. Suppose that a batch of material evolves as a closed system for some period of time, but then experiences a fractionation event that produces a new material. An example might be differentiation of an asteroid or planet into a core, mantle, and crust. In our example, we will assume that the mantle has a lower $^{87}Rb/^{86}Sr$ ratio than the material from which it formed, so the $^{87}Sr/^{86}Sr$ ratio evolves more slowly, along a line with a shallower slope in Figure 8.10. The $(^{87}Sr/^{86}Sr)_{T1}$ ratio of the mantle reflects the time (T_1) that it separated from the original material. Now suppose that at a later time (T_2), the mantle generates a magma that crystallizes into several minerals. Each of the minerals has a different $^{87}Rb/^{86}Sr$ ratio and thus evolves along a line with its own slope. If the system remains closed until today, an isochron can be generated from these several minerals (inset in Fig. 8.10), and the time of crystallization can be determined from the isochron. The initial ratio obtained from this isochron reflects the evolution of the ^{87}Rb–^{87}Sr system in the mantle of the original body, but not the original body as a whole. The original body as a whole continued to evolve along the original trajectory, shown in Figure 8.10 as a dotted line. With appropriate knowledge of the $^{87}Rb/^{86}Sr$ ratio of the original body, a two-stage model can be constructed that accurately reflects the history of the system. However, if interpreted with a single-stage model, the history inferred from the initial ratio of the isochron will not be correct. A more complicated history that produces a magma with the $(^{87}Sr/^{86}Sr)_0$ shown schematically by $(^{87}Sr/^{86}Sr)_{T2}$ in Figure 8.10 could

also be constructed. Reservoir evolution models typically are not unique and additional information is often required to choose the correct model. We will discuss reservoir evolution in more detail below.

The ^{147}Sm–^{143}Nd system

Samarium has seven naturally occurring isotopes, two of which, ^{147}Sm and ^{148}Sm are radioactive (Table 4.2). The α-decay of long-lived ^{147}Sm to ^{143}Nd ($t_{1/2} = 1.06 \times 10^{11}$ years; $\lambda_\alpha = 6.54 \times 10^{-12}$ yr^{-1}) is a widely used chronometer. In contrast, the half-life of ^{148}Sm, which α-decays to ^{144}Nd with a half-life ~7×10^{15} years, is too long for it to be useful for chronology. The now-extinct nuclide ^{146}Sm, which has a half-life of 1.03×10^8 years ($\lambda_\alpha = 6.71 \times 10^{-9}$ yr^{-1}), is potentially useful as a chronometer for the first few hundred million years of solar system history (see below). It also is the daughter of short-lived ^{150}Gd, which α-decays to ^{146}Sm with a half-life of 1.8×10^6 years.

All three of the radioactive samarium isotopes decay to isotopes of neodymium. Neodymium has seven isotopes, one of which, ^{144}Nd, is slightly radioactive with a half-life of 2.4×10^{15} years, too long to be of use for chronology. Both samarium and neodymium are rare earth elements (REE) and are not fractionated from each other very much by melting and crystallization. They are both also refractory lithophile elements, and so are not fractionated much by evaporation and condensation processes or metal-silicate fractionation in the solar system. In igneous systems, neodymium is preferentially concentrated in the melt during partial melting because the slightly larger ionic radius of Nd^{3+} makes it more incompatible than Sm^{3+}. Thus, basaltic magmas have lower Sm/Nd ratios than the source rocks from which they form, and on Earth, crustal rocks such as granite have lower Sm/Nd ratios than basalts. But overall, the range in Sm/Nd ratios in igneous systems is only a factor of a few.

The ^{147}Sm–^{143}Nd decay scheme has been useful in both cosmochemistry and geochemistry in two different ways. The ^{147}Sm–^{143}Nd system can give an isochron, from which both a date and the initial ^{143}Nd/^{144}Nd ratio can be obtained. Because most of the materials of interest to cosmochemistry are old, the slow decay rate and relatively minimal fractionation of samarium from neodymium are overcome by long decay times. Very precise isotopic measurements also facilitate dating by the ^{147}Sm–^{143}Nd method. The ^{147}Sm–^{143}Nd system is also good for dating major fractionation events, such as formation of the crust and mantle. In this application, the ^{143}Nd/^{144}Nd ratio of the bulk system can be used to extract the time of differentiation. The geochemical behavior of the ^{147}Sm–^{143}Nd system is opposite that of the ^{87}Rb/^{87}Sr system during partial melting. In the ^{147}Sm–^{143}Nd system, the radioactive isotope is left behind in the residual solids, whereas in the ^{87}Rb/^{87}Sr system, the radioactive isotope is concentrated in the melt phase. This difference means that the combination of the ^{147}Sm–^{143}Nd system and the ^{87}Rb/^{87}Sr systems is very powerful in investigating the petrogenesis of igneous rocks. Because it is difficult to fractionate samarium from neodymium under a variety of conditions, the ^{147}Sm–^{143}Nd system can provide chronological information in situations where the ^{87}Rb–^{87}Sr or U–Th–Pb systems have been compromised by later events.

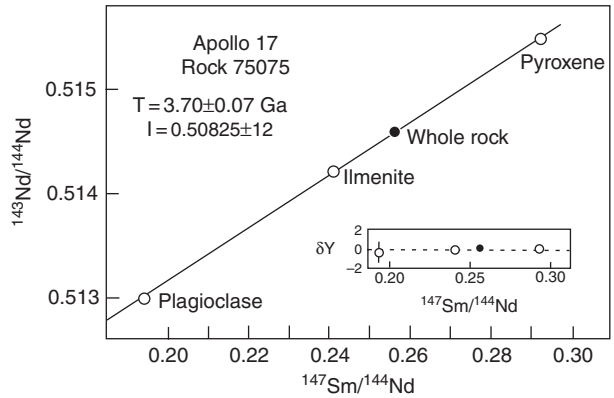

Fig. 8.11 **Samarium–neodymium evolution diagram for lunar mare basalt 75075. Data points for the total rock, plagioclase, ilmenite, and pyroxene form a precise linear array, the slope of which gives a crystallization age of 3.70±0.07 Ga for this rock ($\lambda = 6.54 \times 10^{-12}$ yr^{-1}). The insert shows the deviations from the best-fit line in parts in 10^4. After Lugmair *et al.* (1975a).**

History

The ^{147}Sm–^{143}Nd system was first used in cosmochemistry by Lugmair *et al.* (1975a), who published a precise isochron age for an Apollo 17 basalt (Fig. 8.11). The system developed rapidly thereafter. Note that the spread in $^{147}Sm/^{144}Nd$ in the mineral phases of this basalt is less than 50%, not factors of ten, several hundred, or even a few thousand, as can be seen in other systems. The fact that precise isochron ages can still be obtained is a testament to the care taken in chemical separation of samarium and neodymium and the precision of modern mass spectrometric analysis.

Lugmair *et al.* (1975a) also showed that the initial $^{143}Nd/^{144}Nd$ ratio inferred from their isochron was measurably different from that expected from the closed-system evolution of a "chondritic" composition. DePaolo and Wasserburg (1976a, 1976b) expanded on this observation to create a methodology and reporting notation in which the timing of events that fractionated samarium from neodymium can be estimated from differences between the measured $^{143}Nd/^{144}Nd$ ratios and the ratio expected from the evolution of a "chondritic uniform reservoir," or CHUR. Using this system, the ratios measured at the present time are compared to the inferred composition of the CHUR today, in contrast to the ^{87}Rb–^{87}Sr system, where the initial ratio from the isochron is compared with an initial ratio inferred for the early solar system (e.g. BABI or ALL).

Technical details

Several samarium and neodymium isotopes are isobars (Table 4.2) and cannot be separated by mass spectrometry. Thus, samarium and neodymium must be completely separated by chemical procedures prior to measuring them in a mass spectrometer. The ion-exchange chemistry necessary to separate these elements is now well developed (see Appendix). Isotope measurements can be done either by TIMS or ICPMS (inductively

coupled plasma mass spectrometry). The elemental ratios can be determined by isotope dilution using either TIMS or ICPMS (see Appendix).

Isochrons

In suitable systems, it is possible to obtain relatively precise internal isochrons from the ^{147}Sm–^{143}Nd system. In an igneous system, the REE partition differently among the crystallizing minerals. In olivine and orthopyroxene, the light REE are depleted relative to the heavy REE, resulting in an enrichment of the parent samarium over the daughter neodymium. In plagioclase, the light REE are enriched. This partitioning provides the fractionation of parent and daughter necessary to produce an isochron (Fig. 8.11). As with other isochron systems, the date is calculated from the slope of the isochron.

Reservoir evolution

Figure 8.12 is a schematic diagram of the evolution of the $^{143}Nd/^{144}Nd$ ratio in the bulk solar system and in two planetary objects. The $^{143}Nd/^{144}Nd$ ratio of the solar system increases with time due to the decay of ^{147}Sm, and the increase can be numerically modeled if one knows the $^{147}Sm/^{144}Nd$ ratio in the solar system. In the original theoretical framework, the first solids began to condense from the hot solar nebula at 4.57 Ga. But the starting time can also represent melting or local evaporation and condensation of the mixed gas and dust inherited from the molecular cloud. The exact time of formation of the first solids in the solar system is assumed because it cannot be determined from the ^{147}Sm–^{143}Nd system. Due to variations in the relative abundances of samarium and neodymium caused by thermal processing of nebular material, planetary bodies could accrete with different Sm/Nd ratios. The evolution of two such bodies is illustrated in Figure 8.12a. Planet "A" formed at time T_A with a lower Sm/Nd ratio than the bulk solar system, so its bulk $^{143}Nd/^{144}Nd$ ratio evolved more slowly with time than the bulk solar system. Planet "B" formed at time T_B with a higher Sm/Nd ratio, and thus its $^{143}Nd/^{144}Nd$ ratio evolved more quickly.

In the early solar system, most planetary bodies may have formed in only a few million years. The ^{147}Sm–^{143}Nd system is not particularly sensitive to short time intervals at 4.6 Ga because of the slow decay ratio of ^{147}Sm. In addition, because the fractionation of samarium from neodymium tends to be relatively small, the slopes of the lines on plots like Figure 8.12 tend to be similar. As a result, the precision required to resolve differences in formation time based on the intercepts of the isochrons is beyond current experimental capabilities. Also, in contrast to the situations for the $^{87}Rb/^{87}Sr$ and U–Th–Pb systems, for which large fractionations of parent and daughter elements have provided samples of strontium and lead with essentially primordial compositions, there are no examples of objects without significant samarium that can give a "direct" measurement of the $(^{143}Nd/^{144}Nd)_0$.

DePaulo and Wasserburg (1976a, 1976b) showed how to get around these problems. Rather than attempting to determine the intercept of an isochron at extremely high precision and to compare it to a poorly known initial value for the solar system, they instead chose to

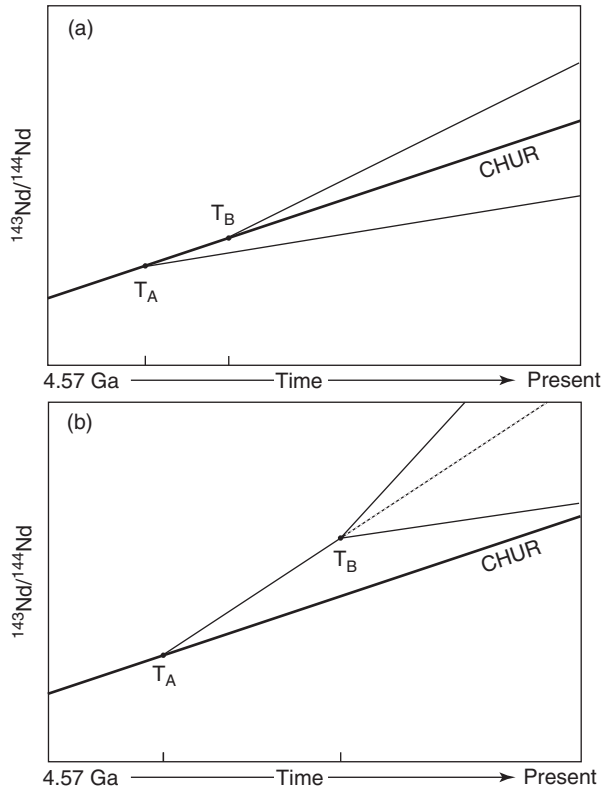

Fig. 8.12 (a) Schematic diagram of $^{143}Nd/^{144}Nd$ versus time for the bulk solar system (CHUR, dark heavy line) and for two hypothetical planets formed from solar system material. When planet "A" formed at time T_A, it acquired a lower $^{147}Sm/^{144}Nd$ ratio than the parent reservoir, so from that point onward, the $^{143}Nd/^{144}Nd$ ratio evolved more slowly than the bulk solar system. Planet "B" formed slightly later with a higher $^{147}Sm/^{144}Nd$ ratio and its $^{143}Nd/^{144}Nd$ ratio evolved faster than the bulk solar system. (b) Schematic diagram of $^{143}Nd/^{144}Nd$ versus time for two-stage evolution of material separated from the CHUR reservoir. At time T_A, a planet forms with a higher $^{147}Sm/^{144}Nd$ ratio than the bulk solar system and subsequently evolves along a steeper trend. Some time later, at time T_B, the planet differentiates into two layers with different $^{147}Sm/^{144}Nd$ ratios. Each layer evolves from that point on with a different trend. It is generally not possible to determine from the samarium–neodymium data alone whether a sample is the result of a single or multi-stage history. But in the example in panel (b), the planetary layer with the lowest $^{147}Nd/^{144}Nd$ ratio cannot be the result of a single-state evolution because the evolution line intersects the CHUR line in the future.

compare the *present* bulk $^{143}Nd/^{144}Nd$ ratio with that expected for a uniform reservoir of chondritic composition (the "chondritic uniform reservoir" or CHUR). In other words, they worked with the values that plot on the right axis of Figure 8.12, where the differences are the greatest. With sufficiently precise measurements of $^{143}Nd/^{144}Nd$ and $^{147}Sm/^{144}Nd$ for the sample, and well-known parameters for CHUR, one can calculate the evolution of the $^{143}Nd/^{144}Nd$ ratio as a function of time for both and find out when the sample and CHUR had the same composition. With current levels of analytical precision, the $^{143}Nd/^{144}Nd$ ratio can be measured with an accuracy of ~50 ppm and the $^{147}Sm/^{144}Nd$ ratio can be measured to ~0.05%. This translates into an uncertainty of ~10 ppm in the $^{143}Nd/^{144}Nd$ ratio at 4.6 Ga.

Table 8.4 Accepted values for CHUR

	Present	4.56 Ga
$^{143}Nd/^{144}Nd$	0.512638	0.5066866
$^{147}Sm/^{144}Nd$	0.1966	0.20255

Jacobsen and Wasserburg (1980), Bouvier *et al*. (2008).

In contrast, the uncertainty in the intercept of an isochron obtained with data of similar precision is on the order of 200 ppm.

A critical input value necessary to use the bulk $^{143}Nd/^{144}Nd$ ratio to determine the time of Sm/Nd fractionation is the present day composition of the CHUR. Samarium and neodymium are both refractory and are not expected to have fractionated very much in the accretion disk, so bulk chondrites are expected to give similar $^{147}Sm/^{144}Nd$ and $^{143}Nd/^{144}Nd$ ratios. Jacobsen and Wasserburg (1980) found that the $^{147}Sm/^{144}Nd$ ratios had a range of ~4% and the $^{143}Nd/^{144}Nd$ ratios exhibited a range of 5.3 parts in 10^4 among chondrites. The CHUR values (Table 8.4) have been refined only slightly since the original set of values proposed by Jacobsen and Wasserburg (1980).

The $^{143}Nd/^{144}Nd$ ratio of a sample is typically reported as:

$$\varepsilon_j^0 = \left[\frac{\left({}^{143}\mathrm{Nd} \Big/ {}^{144}\mathrm{Nd} \right)^0_{meas}}{\left({}^{143}\mathrm{Nd} \Big/ {}^{144}\mathrm{Nd} \right)^0_{CHUR}} - 1 \right] \times 10^4 \tag{8.23}$$

This "epsilon notation" gives the difference between the measured ratio in the sample and the CHUR value for the present time in parts per 10 000. The difference in the $^{147}Sm/^{144}Nd$ ratio relative to the CHUR (the elemental fractionation) is given by:

$$f_j^{\mathrm{Sm/Nd}} = \frac{\left({}^{147}\mathrm{Sm} \Big/ {}^{144}\mathrm{Nd} \right)_j}{\left({}^{147}\mathrm{Sm} \Big/ {}^{144}\mathrm{Nd} \right)^0_{CHUR}} - 1 \tag{8.24}$$

To interpret these numbers, consider again the line for the bulk solar system (CHUR) in Figure 8.12. The $^{143}Nd/^{144}Nd$ ratio at any time, T, in the past can be calculated as follows:

$$\left(\frac{^{143}\mathrm{Nd}}{^{144}\mathrm{Nd}} \right)^T_{CHUR} = \left(\frac{^{143}\mathrm{Nd}}{^{144}\mathrm{Nd}} \right)^0_{CHUR} - \left(\frac{^{147}\mathrm{Sm}}{^{144}\mathrm{Nd}} \right)^0_{CHUR} [exp(\lambda T) - 1] \tag{8.25}$$

where the time, 0, refers to the present time. The ratio for 4.56 Ga is shown in Table 8.4. The same equation is used to calculate the evolution of a sample, with the values $^{143}Nd/^{144}Nd$ and $^{147}Sm/^{144}Nd$ obtained from the sample inserted in place of the CHUR values. The value of epsilon can be calculated for any specified time from Equation (8.23) by inserting the ratios for the sample and CHUR calculated for that time using Equation (8.25), although care must be taken to specify the time if it is other than the present.

One can determine the time at which the parent reservoir for a sample was separated from the CHUR by setting Equation (8.25) for the CHUR equal to Equation (8.25) for the sample and solving for T:

$$T_{model} = \frac{1}{\lambda}\left[1 + \frac{\left(\frac{^{143}Nd}{^{144}Nd}\right)^{0}_{Sample} - \left(\frac{^{143}Nd}{^{144}Nd}\right)^{0}_{CHUR}}{\left(\frac{^{147}Sm}{^{144}Nd}\right)^{0}_{Sample} - \left(\frac{^{147}Sm}{^{144}Nd}\right)^{0}_{CHUR}}\right] \quad (8.26)$$

The time, T_{model}, is a model age that assumes a single-state evolution of the sample once it was separated from the CHUR. On Figure 8.12a, the time T_{model} is the time, T_A, for planet "A" and the time T_B for planet "B".

More-complicated histories can be envisioned and modeled. Figure 8.12b shows a two-stage history. In this example, a planet separates from the CHUR at time T_A and its composition evolves along a steeper trend. Some time later, this body differentiates into a mantle and a crust, with the crust having a lower Sm/Nd ratio and the mantle a higher Sm/Nd ratio than the bulk planet. The crust and the mantle then each evolve along their own trends. Using the present day $^{147}Sm/^{144}Nd$ and $^{143}Nd/^{144}Nd$ ratios for crust and mantle, one can calculate the time when all layers had the same $^{143}Nd/^{144}Nd$ ratio. This is the time of the differentiation. If the bulk $^{147}Sm/^{144}Nd$ ratio of the planet can be reconstructed from the data on crust and mantle, the evolution of the bulk planet (the first stage of the two-stage evolution) can be calculated. But if a single-stage model is used to evaluate measurements of either the crust or the mantle, the model time of separation from the CHUR will be incorrect. Multi-stage models are not unique and are often difficult to constrain with ^{147}Sm–^{143}Nd data alone. However, in combination with other information, the ^{147}Sm–^{143}Nd system is a powerful tool for unraveling the differentiation history of a planetary body.

Applications

The ^{147}Sm–^{143}Nd system is particularly well suited for dating basaltic and ultramafic igneous rocks, which cannot be dated with the $^{87}Rb/^{87}Sr$ or U–Th–Pb systems. In general, the more mafic the rock, the lower the REE concentration and the higher the $^{147}Sm/^{144}Nd$ ratio. The REEs are not easily affected by weathering or by metamorphism, so crystallization ages can be obtained even from rocks that have been metamorphosed. These features make the ^{147}Sm–^{143}Nd system particularly well suited to date terrestrial Archean rocks.

Chronology with ^{147}Sm–^{143}Nd isochrons

The ^{147}Sm–^{143}Nd system has been widely used to date samples of differentiated bodies. The initial application of the ^{147}Sm–^{143}Nd system in cosmochemistry was to produce an isochron age for a lunar mare basalt (Fig. 8.11). The ^{147}Sm–^{143}Nd system is still used for lunar samples, although care must be taken to avoid the effects of secondary, impact-produced melting. Precision has improved over the years, as shown in Figure 8.13 for a magnesium-suite lunar norite. The internal isochron gives an age of 4.334±0.037 Ga (Edmunson *et al.*, 2009). The same authors also determined a concordant ^{207}Pb–^{206}Pb age

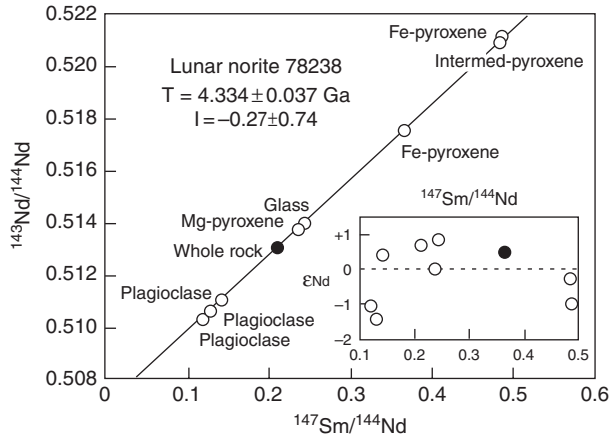

Fig. 8.13 **^{147}Sm–^{143}Nd evolution diagram for nine mineral fractions and a whole-rock sample of lunar norite 78238. The inset shows the deviations from the best-fit line in parts in 10^4. In spite of a small amount of scatter attributed to the inclusion of tiny fragments of other rock types into the measured sample, the isochron is very well defined. After Edmunson *et al.* (2009).**

of 4.333±0.059 Ga for this rock, confirming that the ^{147}Sm–^{143}Nd system can produce precise and accurate ages for undisturbed rocks. This system has also played a major role in dating of Martian meteorites. Reliable ^{147}Sm–^{143}Nd ages of ~1.3 Ga have been obtained for the nakhlites and for Chassigny. These dates are concordant with dates obtained from ^{40}Ar–^{39}Ar, ^{87}Rb–^{87}Sr, and U–Th–Pb systems (Nyquist *et al.*, 2001b; Misawa *et al.*, 2006). Dates for the Martian shergottites are more controversial (see Chapter 9).

Reservoir evolution inferred from the ^{147}Sm–^{143}Nd system

The ^{147}Sm–^{143}Nd system is actively used to investigate the differentiation and magmatic history of the Moon, Mars, and the Earth. This system is used together with the ^{87}Rb–^{87}Sr, ^{176}Lu–^{176}Hf, U–Th–Pb, and ^{187}Re–^{187}Os systems to extract information on the timing and nature of melting and differentiation in planetary bodies. These results will be discussed in Chapters 9 and 13.

The U–Th–Pb system

Uranium has two long-lived isotopes, ^{235}U and ^{238}U, that decay to ^{207}Pb and ^{206}Pb, respectively. Thorium has one long-lived isotope, ^{232}Th, that decays to ^{208}Pb. The isotopic abundances of uranium and thorium are summarized in Table 8.5. The isotopic abundances of terrestrial lead are given in Table 4.2.

The principal decay mode of ^{238}U is α-decay, but a small fraction of the decays are by spontaneous fission. The emission of an α-particle initiates a series of decays known as the *uranium series* (Fig. 8.14), which ends at ^{206}Pb. The uranium series can be summarized as

$$^{238}\mathrm{U} \rightarrow {}^{206}\mathrm{Pb} + 8\,{}^{4}\mathrm{He} + 6\,\beta^{-} \qquad (8.27)$$

Table 8.5 Decay constants and isotopic abundances of uranium and thorium

Isotope	Abundance	Decay mode	Half-life	Decay constant
^{232}Th	100	alpha	14.010×10^9 years	$\lambda_\alpha = 4.9475 \times 10^{-11}$ yr^{-1}
^{235}U	0.7200	alpha	0.7038×10^9 years	$\lambda_\alpha = 9.8485 \times 10^{-10}$ yr^{-1}
^{238}U	99.2743	alpha	4.468×10^9 years	$\lambda_\alpha = 1.55125 \times 10^{-10}$ yr^{-1}

Steiger and Jäger (1977).

The decay path splits at several points where decay can be either by α- or β-decay, but all paths end at ^{206}Pb (Fig. 8.14).

The decay of ^{235}U is also primarily by α-decay through the *actinium series* (Fig. 8.15). The actinium series can be summarized as

$$^{235}\mathrm{U} \rightarrow {}^{207}\mathrm{Pb} + 7\,{}^{4}\mathrm{He} + 4\,\beta^- \tag{8.28}$$

Similarly, the decay series initiated by the α-decay of ^{232}Th (Fig. 8.16) can be summarized as

$$^{232}\mathrm{Th} \rightarrow {}^{208}\mathrm{Pb} + 6\,{}^{4}\mathrm{He} + 4\,\beta^- \tag{8.29}$$

Although these decay series consist of 43 isotopes of 12 elements, none is a member of more than one series, so each decay chain always leads to a specific isotope of lead:

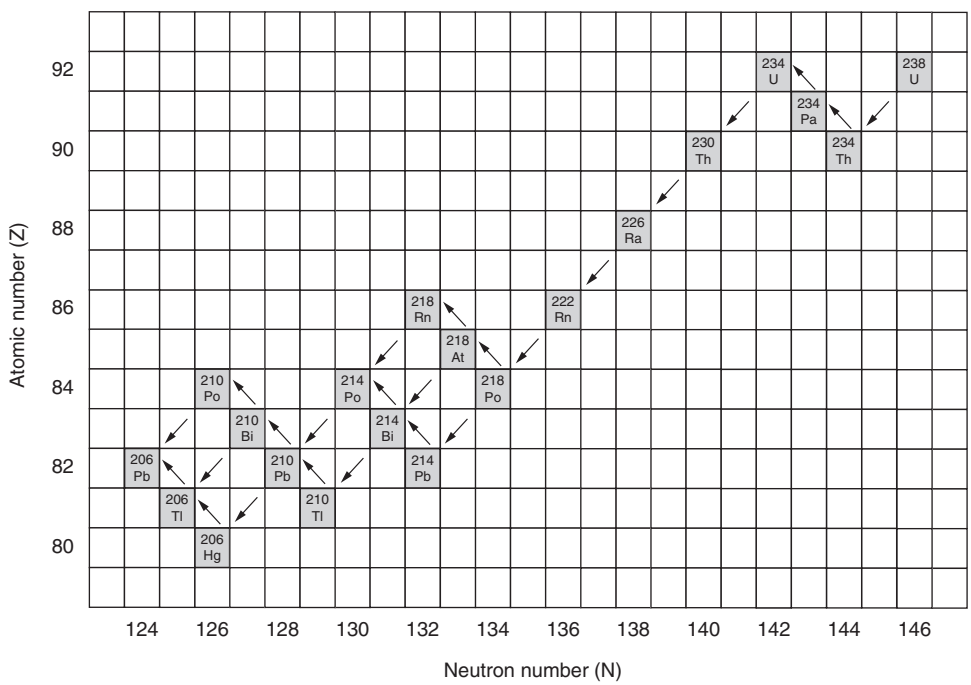

Fig. 8.14 Portion of the chart of the nuclides illustrating the decay of ^{238}U to ^{206}Pb. The decay occurs by a series of α-decays, which cause the nuclide to move down and to the left, and β-decays, which cause the nuclide to move up and to the right.

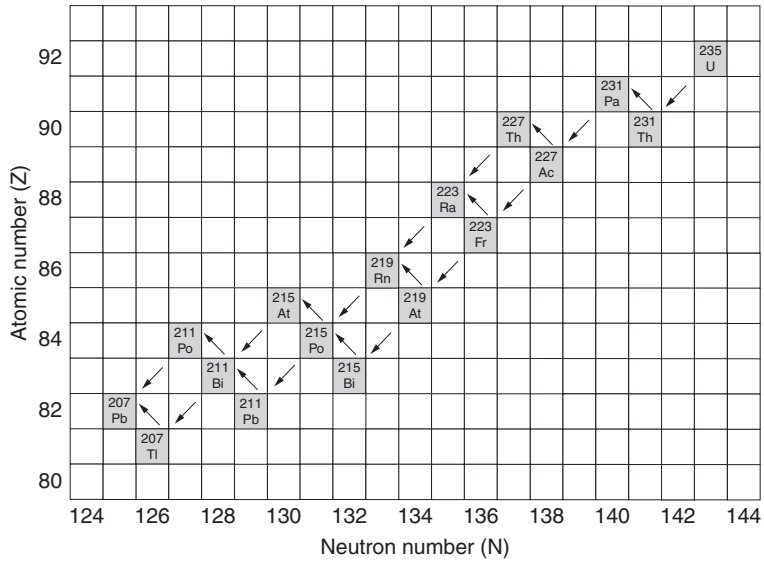

Fig. 8.15 Portion of the chart of the nuclides illustrating the decay of ^{235}U to ^{207}Pb. This decay series is often called the actinium series.

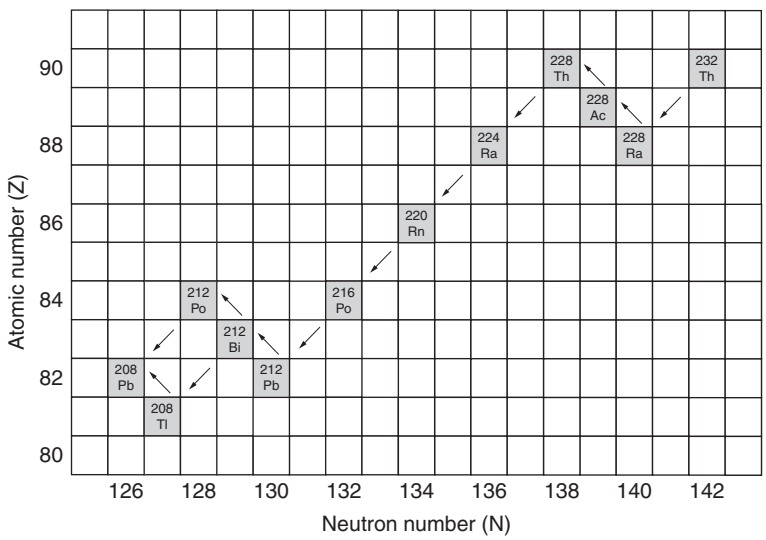

Fig. 8.16 Portion of the chart of the nuclides illustrating the decay of ^{232}Th to ^{208}Pb.

$$^{238}\text{U} \rightarrow {}^{206}\text{Pb} \qquad ^{235}\text{U} \rightarrow {}^{207}\text{Pb} \qquad ^{232}\text{Th} \rightarrow {}^{208}\text{Pb}$$

The half-lives of ^{238}U, ^{235}U, and ^{232}Th are all very much longer than those of the radioactive daughter isotopes in their decay chains. Therefore, a condition known as secular equilibrium is quickly established in which the decay rates of the daughter isotopes in the decay chain equal that of the parent isotope. In a closed system, once secular equilibrium is

established, the rate of production of the stable daughter at the end of the chain equals the rate of decay of the parent isotope at the head of the chain.

Uranium and thorium are actinide elements. Their chemical behavior is similar under most conditions. Both are refractory elements, both occur in nature in the +4 oxidation state, and their ionic radii are very similar (U^{+4} = 1.05 Å, Th^{+4} = 1.10Å). However, uranium can also exist in the +6 state as the uranyl ion (UO_2^{+2}), which forms compounds that are soluble in water. Thus, under oxidizing conditions, uranium can be separated from thorium through the action of water.

In contrast to refractory uranium and thorium, lead is a moderately volatile element. Uranium and thorium are lithophile, while lead can exhibit lithophile, siderophile, or chalcophile behavior. This means that in many cosmochemical situations, it is possible to strongly fractionate the daughter lead from parent uranium and thorium, a favorable situation for radiochronology. On the other hand, lead tends to be mobile at relatively low temperatures and can be either lost from a system or introduced at a later time. As already mentioned, uranium can also become mobile under oxidizing conditions. This means that the U–Th–Pb system is more susceptible to open-system behavior than several other commonly used dating techniques. However, as we discuss below, there are ways to recognize and account for the open-system behavior in many cases.

History

The first attempts to determine ages of natural samples using uranium were chemical methods, because the nature of isotopes was not yet understood. Two methods based on uranium were initially used, the "chemical lead method" and the "helium method." Both methods assumed that the daughter element was initially absent from the rock or mineral analyzed and that the contribution of thorium to the daughter elements could be neglected. Thus, initially, these methods were applied only to uranium-rich, nearly lead-free materials. It was soon determined that most rocks and minerals slowly leak helium, so that dates determined by measuring the uranium content and the helium content of a rock were typically too young. It also turned out that the contribution from thorium was not negligible in many cases.

By the late 1920s, isotopic measurements had shown that uranium and thorium decayed to different isotopes of lead. A third lead isotope, ^{207}Pb, was also identified and was shown to be radiogenic. It appeared to be the product of the decay of actinium, but it was postulated that the ultimate source might be another isotope of uranium, ^{235}U. In a pair of classic papers, Nier (1939a, 1939b) placed the uranium–lead system on a much more solid footing. He determined that ^{235}U was indeed the parent of ^{207}Pb, measured the isotopic composition of lead extracted from uranium-rich minerals, and determined the decay constants for ^{235}U and ^{238}U to within 2% of their currently accepted values.

In 1946, Arthur Holmes and Fredrich Houtermans built on previous work to independently develop a general model for isotopic evolution of lead in the Earth. The Holmes–Houtermans "common-lead" method enabled determination of the ages of common leads that have had single-stage histories and was used by Clair Patterson in the mid-1950s to determine the age of the Earth.

A significant problem in using the uranium–lead system for age dating is that the system is relatively easily disturbed. However, George Wetherill showed that by using both the

^{238}U–^{206}Pb and ^{235}U–^{207}Pb systems together, isotopic disturbance can be recognized (Wetherill, 1956). Wetherill's concordia curve permits one to determine the formation age and the timing of an episode of lead loss in a rock (see below).

Uranium–thorium–lead methods

Uranium, thorium, and lead comprise three independent chronometers that are described by the following equations (cf. Equation (8.21)):

$$\frac{^{206}Pb}{^{204}Pb} = \left(\frac{^{206}Pb}{^{204}Pb}\right)_0 + \frac{^{238}U}{^{204}Pb}\left(e^{\lambda_{238}t} - 1\right) \tag{8.30}$$

$$\frac{^{207}Pb}{^{204}Pb} = \left(\frac{^{207}Pb}{^{204}Pb}\right)_0 + \frac{^{235}U}{^{204}Pb}\left(e^{\lambda_{235}t} - 1\right) \tag{8.31}$$

$$\frac{^{208}Pb}{^{204}Pb} = \left(\frac{^{208}Pb}{^{204}Pb}\right)_0 + \frac{^{232}Th}{^{204}Pb}\left(e^{\lambda_{232}t} - 1\right) \tag{8.32}$$

Under ideal conditions, all three chronometers should give the same age. However, lead loss is common in natural samples and can be difficult or impossible to recognize using just one of the above chronometers.

The uranium–lead concordia diagram

If a rock or mineral being dated has remained a closed system since it formed, and if an appropriate correction can be made for the lead that was incorporated into the rock or mineral at the time of its formation, the two independent chronometers described by Equations (8.30) and (8.31) should give the same date. The dates are said to be concordant. The amounts of radiogenic ^{206}Pb and ^{207}Pb at any time (see Equation (8.8)) are given by:

$$\frac{^{206}Pb^*}{^{238}U} = e^{\lambda_{238}t} - 1 \tag{8.33}$$

$$\frac{^{207}Pb^*}{^{235}U} = e^{\lambda_{235}t} - 1 \tag{8.34}$$

The $^{235}U/^{238}U$ ratio at the present time is the same for the vast majority of samples from the Earth, the Moon, Mars, and meteorites and has a numerical value of 1/137.88 (Table 8.5). Therefore, in a system that remains closed, Equations (8.33) and (8.34) describe a pair of unique values for $^{206}Pb^*/^{238}U$ and $^{207}Pb^*/^{235}U$ for every time t. The set of values for a system that has remained closed, and for which the two ages are concordant, is known as *concordia* (Wetherill, 1956) and is shown in Figure 8.17. Any rock or mineral that has remained a closed system, after an appropriate correction for any inherited lead, will plot somewhere on the concordia curve. When the rock or mineral first forms (time t_0), it contains no radiogenic lead and will plot at the origin of Figure 8.17. As time passes the rock will move up and to the right along the concordia curve.

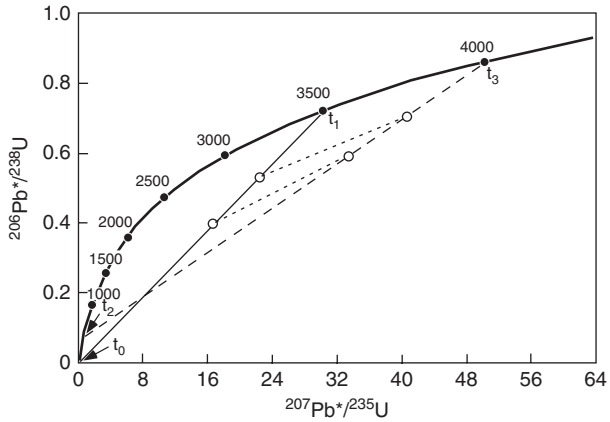

Fig. 8.17 **Wetherill's concordia diagram for interpreting discordant U–Pb dates caused by episodic loss of radiogenic lead.**

Suppose at a later time t_1, the system suffers the loss of some of its lead. The loss will lower both $^{206}Pb^*/^{238}U$ and $^{207}Pb^*/^{235}U$. Because it is almost impossible to fractionate the isotopes of an element as heavy as lead, the $^{206}Pb/^{207}Pb$ ratio of the lead that is lost will equal that of the lead that is retained. Lead loss moves the system in a straight line toward the origin on Figure 8.17. This line is known as *discordia*. A group of rocks that formed together and suffered varying degrees of lead loss at the same time will spread out along the discordia line. If, following the lead-loss event, the system becomes closed again, each rock or mineral will evolve along a new line with a similar shape to concordia but displaced on the diagram. The points that mark the intersections of discordia with concordia will also evolve along the concordia line (e.g. dashed line on Fig. 8.17). For example, the point at the origin (labeled t_0) will move along concordia to point t_2, while the point labeled t_1 will move to point t_3. So in principle, we can determine both the original age of the rock or mineral, given by t_3, and the time of the event that resulted in lead loss, given by t_2. However, in order to do this, a suite of samples that experienced different degrees of lead loss at the same time must be measured so that the discordia line can be experimentally defined.

Although widely used and generally very successful in dating geologic events, the concordia approach makes some explicit assumptions about the history of the rocks being dated that may not always be true. For example, the concordia treatment assumes that the event that disturbed the uranium–lead system was discrete and of short duration. This need not be the case. Lead loss might occur by continuous diffusion over long periods of time if temperatures are high enough, or by loss due to the radiation damage that crystals incur through the alpha-decay of uranium, thorium, and their daughter isotopes. Models have been generated that can describe these two types of behavior. The geologic history of the sample may involve different formation episodes that did not fully reset the system. Zircons are a prime example, often consisting of cores having one age with one or more overgrowths of different ages. The ion microprobe provides a means of dating each of the overgrowths independently, helping to sort out such complex systems.

Tera and Wasserburg (1972) introduced a second kind of concordia diagram to handle another complication. The U–Th–Pb ages determined for many lunar rocks by standard methods appear to be significantly older than the ^{87}Rb–^{87}Sr and ^{40}Ar–^{39}Ar ages. The reason for the discrepancy is that many lunar rocks contain excess radiogenic lead that was not produced *in situ*. The Tera–Wasserburg concordia diagram does not require prior knowledge of the initial $^{206}Pb/^{204}Pb$ and $^{207}Pb/^{204}Pb$ ratios.

The number of atoms of ^{206}Pb and ^{207}Pb can be described as the number of atoms of each isotope present initially plus the number created *in situ* by radioactive decay. Tera and Wasserburg (1972, 1974) defined a concordia in parametric form where the x-coordinate is given by

$$\frac{^{238}U}{^{206}Pb^*} = \frac{1}{e^{\lambda_{238}t} - 1} \tag{8.35}$$

and the y-coordinate is given by

$$\left(\frac{^{207}Pb}{^{206}Pb}\right)^* = \frac{1}{137.88}\left(\frac{e^{\lambda_{235}t} - 1}{e^{\lambda_{238}t} - 1}\right) \tag{8.36}$$

The Tera–Wasserburg concordia is constructed by solving Equations (8.35) and (8.36) for various values of t. As with the Wetherill concordia (Fig. 8.17), the Tera–Wasserburg concordia curve (Fig. 8.18) is the locus of all concordant U–Th–Pb ages, based on the decay constants in Table 8.5 and assuming that $^{235}U/^{238}U = 1/137.88$. Figure 8.18 shows a discordia line intersecting concordia at $t_1 = 3.2$ Ga and $t_2 = 0.2$ Ga. The system described by this discordia line formed originally at 3.2 Ga and contained no radiogenic lead. It then accumulated radiogenic lead in a closed system until 0.2 Ga, when the system was reset. The radiogenic lead that had accumulated in the system between time t_1 and t_2 would have an

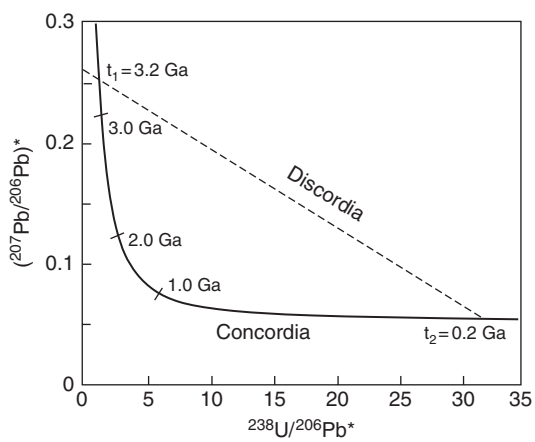

Fig. 8.18 **Tera–Wasserburg concordia diagram. This diagram does not require prior knowledge of the initial $^{206}Pb/^{204}Pb$ and $^{207}Pb/^{204}Pb$ ratios and permits determination of ages for samples that have inherited radiogenic lead.**

isotopic composition given by the intersection of the discordia line with the y-axis, and the numerical value is given by

$$I_0 = \frac{1}{137.88}\frac{e^{\lambda_{235}t_1} - e^{\lambda_{235}t_2}}{e^{\lambda_{238}t_1} - e^{\lambda_{238}t_2}} \tag{8.37}$$

If a uranium-free mineral formed during the resetting event at t_2, then it would contain lead with a $^{207}Pb/^{206}Pb$ ratio given by Equation (8.37), and that lead would represent the history of the system from t_1 to t_2. If a lead-free mineral formed during the resetting event represented by t_2, then all of the lead measured in this mineral would have accumulated by uranium decay after time t_2. In this case, both t_1 and t_2 give valid dates for events in the history of the system. Alternatively, the radiogenic $^{207}Pb/^{206}Pb$ given by I_0 could be the result of processes unrelated to the event at time t_2. In that case, the discordia line represents a mixing line between the inherited lead with $^{207}Pb/^{206}Pb = I_0$ and the uranium–lead system given by point t_2. In this case, point t_1 has no chronological significance.

As an example of the application of the Tera–Wasserburg methodology, Figure 8.19 shows a Tera–Wasserburg concordia diagram for lunar basalt 14053. This rock gave a ^{87}Rb–^{87}Sr age of 3.88±0.04 Ga ($\lambda = 1.42 \times 10^{-11}$ yr^{-1}) (Papanastassiou and Wasserburg, 1971) and ^{40}Ar–^{39}Ar ages of 3.81–3.83 Ga ($\lambda = 4.962 \times 10^{-10}$ yr^{-1}, $^{40}K/K = 1.167 \times 10^{-4}$) (Turner *et al.*, 1971). The slope, m, of the discordia is related to the initial $(^{207}Pb/^{206}Pb)^*$ ratio and to the age of the uranium–lead system by

$$m = \frac{e^{\lambda_{235}t} - 1}{137.88} - \left(\frac{^{207}Pb}{^{206}Pb}\right)_i \left(e^{\lambda_{238}t} - 1\right) \tag{8.38}$$

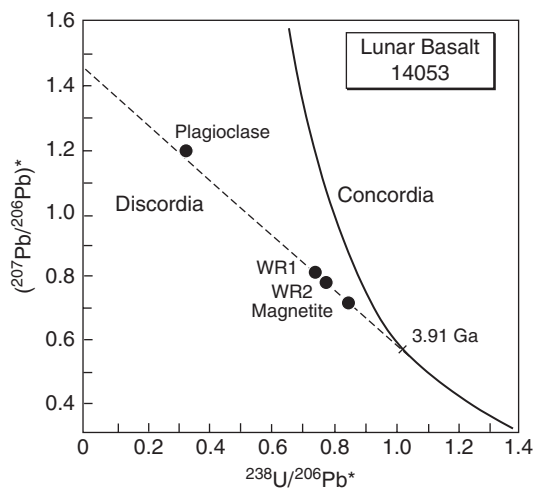

Fig. 8.19 **Tera–Wasserburg diagram for lunar basalt 14053. The measured data define a discordia line that intersects the y-axis at $(^{207}Pb/^{206}Pb)_i = 1.46$. The slope of the line, based on two whole-rock samples and a magnetite separate, is −0.88366. The intersection of the discordia line with the concordia curve gives the age of the sample. After Faure and Mensing (2005).**

The equation is solved by iteration to find the value that gives the same t in Equations (8.36) and (8.38). The time t can also be determined graphically from a plot of the slope of the concordia curve versus time. As shown in Figure 8.19, the intersection of discordia and the Tera–Wasserburg concordia gives an age of 3.91 Ga, quite consistent with the ^{87}Rb–^{87}Sr and ^{40}Ar–^{39}Ar ages. Using standard methods, this sample gave highly discordant U–Th–Pb dates in excess of 5 Ga.

The Wetherill concordia and Tera–Wasserburg concordia can both be extended to include ^{232}Th. The ^{232}Th system simply takes the place of either ^{235}U or ^{238}U in the calculation of concordia. In general, this just introduces a potential additional complication because uranium can be fractionated from thorium. Fractionation of uranium from thorium would mean that the ratio of the two parent isotopes has changed and must be properly accounted for. Thus U–Th concordia treatments are rarely employed in cosmochemistry.

^{207}Pb–^{206}Pb dating

An alternative way to utilize the dual decay scheme, ^{235}U–^{207}Pb, ^{238}U–^{206}Pb, is to calculate the date from the ratio of radiogenic isotopes, $^{207}Pb^*$ and $^{206}Pb^*$ alone, without using the U/Pb ratio. The $^{207}Pb^*/^{206}Pb^*$ ratio is insensitive to recent fractionation between parent and daughter elements caused either by natural processes or by laboratory treatments such as chemical etching. Uranium-235 decays six times faster than ^{238}U, and only a little over 1% of the original abundance of ^{235}U in the solar system is still present. This means that the $^{207}Pb^*/^{206}Pb^*$ ratio evolved rapidly during the early history of the solar system. Thus the precision of the date obtained for a given uncertainty in the measured $^{207}Pb^*/^{206}Pb^*$ ratio increases with the age of the sample. The current experimental uncertainties result in a precision in an absolute age determination of an early solar system object approaching those of short-lived nuclides.

The Pb–Pb system can be applied in two ways. If the sample is sufficiently large and diverse that mineral separates with different U/Pb ratios can be produced, an internal isochron can be generated. The equation for the $^{207}Pb^*$–$^{206}Pb^*$ isochron can be obtained by combining Equations (8.30) and (8.31):

$$\frac{\frac{^{207}Pb}{^{204}Pb} - \left(\frac{^{207}Pb}{^{204}Pb}\right)_0}{\frac{^{206}Pb}{^{204}Pb} - \left(\frac{^{206}Pb}{^{204}Pb}\right)_0} = \frac{^{235}U}{^{238}U}\left[\frac{e^{\lambda_{235}t} - 1}{e^{\lambda_{238}t} - 1}\right] \tag{8.39}$$

where $^{235}U/^{238}U = 1/137.88$ (Table 8.5). If the ^{238}U–^{206}Pb and ^{235}U–^{207}Pb dates are concordant, this equation represents a family of straight lines (isochrons) with slopes of

$$m = \frac{1}{137.88}\left[\frac{\left(e^{\lambda_{235}t} - 1\right)}{\left(e^{\lambda_{238}t} - 1\right)}\right] = \left(\frac{^{207}Pb}{^{206}Pb}\right)^* \tag{8.40}$$

that pass through the point

$$\left(\frac{^{207}Pb}{^{204}Pb}\right)_0, \left(\frac{^{206}Pb}{^{204}Pb}\right)_0$$

The determination of an age using the Pb–Pb isochron method relies on the assumption that all samples that define the isochron had the same initial lead isotopic composition, formed at the same time, and remained closed to uranium and lead until the very recent past.

If an internal isochron cannot be generated, a model age can be determined from the measured $^{207}Pb^*/^{206}Pb^*$ of the sample and the assumed initial lead isotopic ratios. For studies of the early solar system, this initial lead composition is assumed to be that measured in troilite (FeS) from the Canyon Diablo meteorite. Troilite is a uranium-free mineral and its host meteorite formed very early in the history of the solar system. Because the U/Pb ratio of the solar system is low, the lead incorporated into the troilite should not have evolved significantly from the initial composition in the solar system.

The most accurate Pb–Pb dates on early solar system materials come from objects with very low abundances of common lead (= high U/Pb ratios). The smaller the correction for common lead, the less susceptible the calculated age is to variations in the composition of the common lead. In addition to the primordial lead, lead may also be introduced by later events in the history of the rock, including, in the case of meteorites, terrestrial weathering. Because the Pb–Pb system is not affected by recent lead loss, samples are typically leached with acids to remove common lead. This leaching can also remove a significant fraction of the radiogenic lead, but this does not affect the measurement so long as the leaching does not fractionate the radiogenic lead isotopes and there is enough lead left to get an accurate measurement. In most cases, etching also disturbs the U/Pb ratio, eliminating the possibility of using U–Pb systematics to recognize a disturbed or multistage system.

One drawback of the Pb–Pb system is that two-stage or three-stage evolution of the U–Pb isotopic system can produce linear arrays on a Pb–Pb isochron plot (Gale and Mussett, 1973). If these arrays are interpreted as single-stage isochrons, incorrect dates may be obtained. In some cases, measurements of the U/Pb ratio can help identify multistage samples. But if several events occurred sufficiently early in solar system history, even a concordia approach may not be able to identify a multistage system (Tera and Carlson, 1999). Thus, to the extent possible, workers attempt to identify objects with simple histories, so that a single-stage evolution can be assumed.

There are several important assumptions that are made when using any of the methods based on the U–Th–Pb systems. As the precision of the $^{207}Pb^*/^{206}Pb^*$ measurements improves, these assumptions should be re-evaluated. One assumption is that the $^{235}U/^{238}U$ ratio is constant in solar system materials. One place where this has been demonstrated not to be true is at Oklo, Gabon, in West Africa. At Oklo, the uranium is severely depleted in ^{235}U, apparently because at 2 Ga ago, when the ^{235}U abundance was much higher, conditions were right to produce a natural fission reactor that burned out the ^{235}U. Fortunately, such situations are extremely rare.

One implication of the discovery that all pre-existing solids were not vaporized and recondensed in the early solar system is the possibility that variations in the $^{235}U/^{238}U$ ratio could have been inherited from the Sun's parent molecular cloud. In addition, the short-lived nuclide ^{247}Cm, which decays to ^{235}U, might have been present. Recent studies have begun to re-investigate the assumption of constant $^{235}U/^{238}U$ in early solar system materials. A search for uranium isotopic anomalies in relatively large samples of a wide range of chondrites, achondrites, and terrestrial rocks found the $^{235}U/^{238}U$ ratio to be constant to

within ±0.02% (Stirling *et al*., 2005). This level of uncertainty in the $^{235}U/^{238}U$ ratio would correspond to an uncertainty in a $^{207}Pb^*/^{206}Pb^*$ date of ~0.3 Myr, smaller than the current best precision for these measurements. More recently, measurements of bulk samples of the Murchison (CM2) and Allende (CV3) chondrites and several Allende CAIs showed small shifts to a lower $^{235}U/^{238}U$ ratio in some samples. The measured shifts of −3.5 permil would correspond to age shifts of up to 5 Myr (Brennecka *et al*., 2009). If these results hold up under further study, modifications will have to be made in the determination of $^{207}Pb^*/^{206}Pb^*$ ages in primitive chondritic materials.

A second assumption implicit in most U−Th−Pb chronology is that the composition of primordial lead is the same as that currently measured in Canyon Diablo troilite. As measurements become more precise, more accurate corrections for the lead inherited from precursor materials must be made. The Canyon Diablo meteorite formed several million years after the earliest solar system solids. During that time, the lead isotopic composition evolved to some degree, even though the uranium–lead ratio in the solar system is low. Tera and Carlson (1999) reanalyzed data for CAIs, chondrules, and matrix from the Allende meteorite and concluded that there is evidence for a more primitive composition than that found in Canyon Diablo troilite. If so, then high-precision $^{207}Pb^*/^{206}Pb^*$ dates that use Canyon Diablo troilite to correct for non-radiogenic lead would be slightly in error. As in the case of uranium, it is also possible that some samples may have inherited lead of a different composition than that inferred for the bulk solar system. Currently, the CAIs being dated have sufficiently small corrections that this effect is not significant, but at some point it may limit the ultimate accuracy of $^{207}Pb^*/^{206}Pb^*$ dates. A bigger problem today is that the non-radiogenic lead in most samples is a mixture of primordial lead and terrestrial lead acquired either from weathering on the Earth's surface or in the laboratory. The main method for dealing with this issue in $^{207}Pb^*/^{206}Pb^*$ dating is to measure samples with very radiogenic lead and to leach the sample to remove the majority of the non-radiogenic lead prior to measurement.

The absolute accuracy of $^{207}Pb^*/^{206}Pb^*$ dates also depends on knowing the decay constants of ^{235}U and ^{238}U very precisely. The current level of uncertainty in the decay constants puts a systematic error of ~9.3 million years on a date for an object formed 4.57 Ga ago. This is important primarily when comparing with dates determined by other long-lived chronometers. When comparing $^{207}Pb^*/^{206}Pb^*$ ages for early solar system objects, this uncertainty effectively cancels out.

The common-lead method

The common-lead method looks at the isotopic evolution of lead in systems with U/Pb and Th/Pb ratios similar to or less than the ratios in bulk solar system materials. The original formulation, by Holmes and Houtermans, is a single stage model that accounts for the isotopic composition of any sample of common lead in terms of primordial lead plus radiogenic lead produced in the source up to the time that lead was separated from uranium and thorium. Multistage models that more accurately describe the evolution of natural systems have been developed. The common-lead method is used in cosmochemistry primarily to study the time of differentiation and reservoir evolution in differentiated bodies

such as the Earth, Moon, Mars, and some asteroids. This method complements similar approaches used for the ^{147}Sm–^{143}Nd and ^{176}Lu–^{176}Hf systems.

The $^{206}Pb/^{204}Pb$ ratio of a uranium-bearing system of age T that has remained closed is (cf. Equation (8.30)):

$$\frac{^{206}Pb}{^{204}Pb} = \left(\frac{^{206}Pb}{^{204}Pb}\right)_0 + \frac{^{238}U}{^{204}Pb}\left(e^{\lambda_{238}T} - 1\right) \tag{8.41}$$

If lead was removed from such a system without isotope fractionation t years ago, the $^{206}Pb/^{204}Pb$ ratio of that lead is

$$\left(\frac{^{206}Pb}{^{204}Pb}\right)_t = \left(\frac{^{206}Pb}{^{204}Pb}\right)_0 + \frac{^{238}U}{^{204}Pb}\left(e^{\lambda_{238}T} - 1\right) - \frac{^{238}U}{^{204}Pb}\left(e^{\lambda_{238}t} - 1\right) \tag{8.42}$$

which can be simplified to

$$\left(\frac{^{206}Pb}{^{204}Pb}\right)_t = \left(\frac{^{206}Pb}{^{204}Pb}\right)_0 + \frac{^{238}U}{^{204}Pb}\left(e^{\lambda_{238}T} - e^{\lambda_{238}t}\right) \tag{8.43}$$

Analogous equations can be written for $(^{207}Pb/^{204}Pb)_t$ and $(^{208}Pb/^{204}Pb)_t$. It is useful at this point to introduce some new symbols to simplify the equations:

$$\frac{^{238}U}{^{204}Pb} = \mu \qquad \frac{^{235}U}{^{204}Pb} = \frac{\mu}{137.88} \qquad \frac{^{232}Th}{^{204}Pb} = \mu\kappa$$

where $\kappa = {}^{232}Th/^{238}U$.

The resulting set of equations is:

$$\left(\frac{^{206}Pb}{^{204}Pb}\right)_t = \left(\frac{^{206}Pb}{^{204}Pb}\right)_0 + \mu\left(e^{\lambda_{238}T} - e^{\lambda_{238}t}\right) \tag{8.44}$$

$$\left(\frac{^{207}Pb}{^{204}Pb}\right)_t = \left(\frac{^{207}Pb}{^{204}Pb}\right)_0 + \frac{\mu}{137.88}\left(e^{\lambda_{235}T} - e^{\lambda_{235}t}\right) \tag{8.45}$$

$$\left(\frac{^{208}Pb}{^{204}Pb}\right)_t = \left(\frac{^{208}Pb}{^{204}Pb}\right)_0 + \mu\kappa\left(e^{\lambda_{232}T} - e^{\lambda_{232}t}\right) \tag{8.46}$$

As can be seen, the isotopic shift observed in lead removed from a system at time t depends on the value of μ. Discussions of reservoir evolution are often cast in terms of the μ of the system. By combining Equations (8.44) and (8.45), μ can be eliminated to give

$$\frac{\frac{^{207}Pb}{^{204}Pb} - \left(\frac{^{207}Pb}{^{204}Pb}\right)_0}{\frac{^{206}Pb}{^{204}Pb} - \left(\frac{^{206}Pb}{^{204}Pb}\right)_0} = \frac{1}{137.88}\left[\frac{e^{\lambda_{235}T} - e^{\lambda_{235}t}}{e^{\lambda_{238}T} - e^{\lambda_{238}t}}\right] \tag{8.47}$$

This equation gives the time, for a single-stage model, when lead was removed from the uranium-rich source.

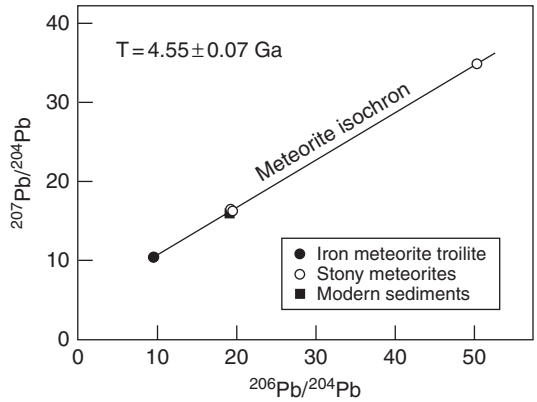

Fig. 8.20 **The Pb–Pb isochron used by Patterson (1956) to determine the age of the Earth. The isochron was constructed from troilite (FeS) from two iron meteorites and three bulk chondrites. Because troilite contains essentially no uranium, the lead in troilite is almost unchanged from the time the meteorite formed – it is "primordial" lead. Modern terrestrial sediments fall on the same isochron, indicating that the Earth and the meteorites are of essentially the same age. The slope of the isochron gives an age of T = 4.55±0.07 Ga using the decay constants used by Patterson (1956).**

Equation (8.47), with $t = 0$ and the composition of lead from meteoritic troilite used for the initial isotopic ratio of lead, was used by Clair Patterson (1955, 1956) to determine the age of the Earth. In the 1950s, the largest uncertainty in determining the age of the Earth was the composition of primordial lead. In 1953, Patterson solved this problem by using state-of-the-art analytical techniques to measure the composition of lead from troilite (FeS) in iron meteorites. Troilite has an extremely low U/Pb ratio because uranium was separated from the lead in troilite at near the time of solar-system formation. Patterson (1955) then measured the composition of lead from stony meteorites. In 1956, he demonstrated that the data from stony meteorites, iron meteorites, and terrestrial oceanic sediments all fell on the same isochron (Fig. 8.20). He interpreted the isochron age (4.55±0.07 Ga) as the age of the Earth and of the meteorites. The value for the age of the Earth has remained essentially unchanged since Patterson's determination, although the age of the solar system has been pushed back by ~20 Myr.

The ^{187}Re–^{187}Os system

Rhenium has two naturally occurring isotopes (Table 4.2), one of which, ^{187}Re, β-decays to ^{187}Os with a half-life of 4.16×10^{10} years ($\lambda_\beta = 1.666 \times 10^{-11}$ yr^{-1}). Rhenium is a member of Group 7B of the periodic table and has chemical properties similar to molybdenum. Osmium has seven naturally occurring isotopes (Table 4.2), one of which, ^{186}Os, is slightly radioactive, decaying by α-decay to ^{182}W with a half-life of 2×10^{15} years. Two isotopes are daughters of radioactive isotopes. Osmium-187 is the daughter of ^{187}Re, and ^{186}Os is produced by α-decay of ^{190}Pt with a half-life of 4.5×10^{11} years. The ^{190}Pt–^{186}Os system is also potentially useful in geochronology and cosmochronology

(see below). Osmium is a platinum group element. Rhenium and osmium are both highly siderophile and refractory, and in chondrites and iron meteorites, their abundances are highly correlated. They are extracted almost completely from planetary mantles into the metallic cores.

A direct experimental determination of the half-life of ^{187}Re was carried out by Lindner *et al*. (1989), giving a half-life of (4.23±0.13) × 10^{10} years, which gives a decay constant of 1.64 × 10^{-11} yr^{-1}. The half-life and decay constant have been refined based on high-precision whole-rock ^{187}Re–^{187}Os isochrons for iron meteorite groups. The current best estimate of the decay constant is (1.666±0.017) × 10^{-11} yr^{-1}, which has an uncertainty of about ±1% (Shirey and Walker, 1998).

History and technical details

The ^{187}Re–^{187}Os method was first applied to extraterrestrial samples in the early 1960s when Hirt *et al*. (1963) reported a whole-rock isochron for 14 iron meteorites that gave an age of ~4 Ga. Further development of this system was hindered by several technical difficulties. Rhenium and osmium each exist in multiple oxidation states and can form a variety of chemical species, so complete digestion of the samples, which is required to chemically separate rhenium and osmium for mass spectrometry, is difficult. In addition, accurate determination of rhenium abundance and osmium isotopic composition requires spiking the samples with isotopically labeled rhenium and osmium, and equilibration of spikes and samples is challenging. A third problem is that osmium and, particularly, rhenium are very difficult to ionize as positive ions for mass spectrometry. These problems were only gradually overcome.

Following the work by Hirt *et al*. (1963), the next significant step in applying the ^{187}Re–^{187}Os method came when Shimizu *et al*. (1978) and Luck *et al*. (1980) used the ion microprobe to measure rhenium and osmium separated from iron meteorites and metal grains from chondrites. Luck and Allegre (1983) showed that iron meteorites and metal grains fit the same isochron and therefore must have been separated from a homogeneous solar nebula within a short interval of ~90 Myr. But the poor ionization of rhenium and osmium was still a major problem. This problem was solved first when the Caltech group demonstrated a negative-thermal-ionization technique (NTIMS) for rhenium and osmium for which they obtained ionization efficiencies of 2–6% for osmium and >20% for rhenium (Creaser *et al*., 1991). Shortly thereafter, high-precision ICPMS also removed ionization efficiency as an issue. Reliable procedures for chemical dissolution and spike equilibration were first developed for iron meteorites and other metal phases (Shirey and Walker, 1995; Shen *et al*., 1996). Chondrites, which are mixtures of silicates, metal, and sulfides, proved to be more difficult, but by the late 1990s, a reliable chemical procedure had been developed for them as well (Chen *et al*., 1998).

Applications

The ^{187}Re–^{187}Os system in cosmochemistry has been primarily used to investigate the crystallization paths and ages of asteroidal cores through measurements of magmatic iron

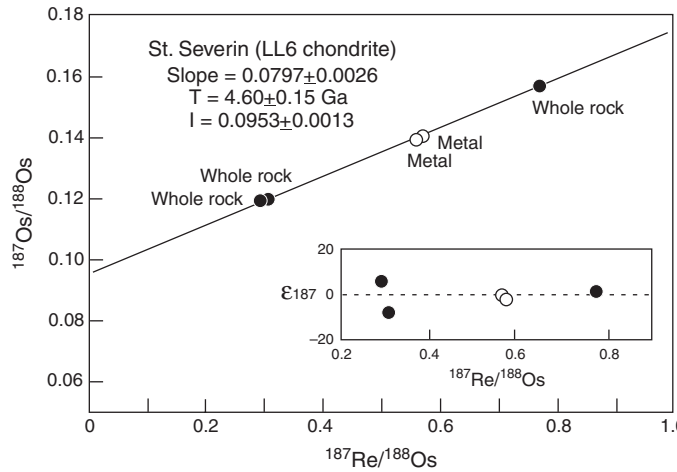

Fig. 8.21 **^{187}Re–^{187}Os evolution diagram for the St. Severin LL6 chondrite. The isochron is generated from three whole-rock fragments and two metal separates. Deviations from the best-fit line are shown in part in 10^3 in the inset. Modified from Chen *et al.* (1998) using $\lambda = 1.666 \times 10^{-11}$ yr^{-1}.**

meteorites (e.g. Shen *et al.*, 1996; Smoliar *et al.*, 1996) and to characterize the budget of highly siderophile elements added to the terrestrial planets via late accretion (e.g. Meisel *et al.*, 1996). This system also has some potential for investigating age relationships among different classes of metal-bearing chondrites.

Chronology with Re–Os isochrons

The ^{187}Re–^{187}Os system does not lend itself to the determination of internal isochrons for most meteorites. Chen *et al.* (1998) produced an internal isochron for the St. Severin (LL6) chondrite using metal separates and whole-rock samples (Fig. 8.21). The slope of the isochron gives a date of 4.60±0.15 Ga ($\lambda = 1.666 \times 10^{-11}$ yr^{-1}), consistent with expectations based on other chronometers, but not precise enough to improve upon other techniques.

Most of the work with the ^{187}Re–^{187}Os system in cosmochemistry has been done using "whole-rock" isochrons. For example, Shen *et al.* (1996) measured 16 iron meteorites from Groups IIAB, IVA, IVB, IIIAB, and IAB. They found that all measured samples fell on a single isochron. Smoliar *et al.* (1996) were able to resolve small differences in the isochrons of various iron meteorite groups. When only the genetically related magmatic IIA and IIB irons are considered, both groups formed the same isochron, within errors (Fig. 8.22).

Attempts to generate whole-rock isochrons for chondrites have proved less successful, primarily because of difficulties with the chemistry. As chemical procedures improved, the spread around isochrons determined for H chondrites decreased significantly (Meisel *et al.*, 1996; Chen *et al.*, 1998). The most recent data exhibit relatively little variation in ^{187}Re/^{188}Os ratios and the data cluster closely around the IIAB isochron.

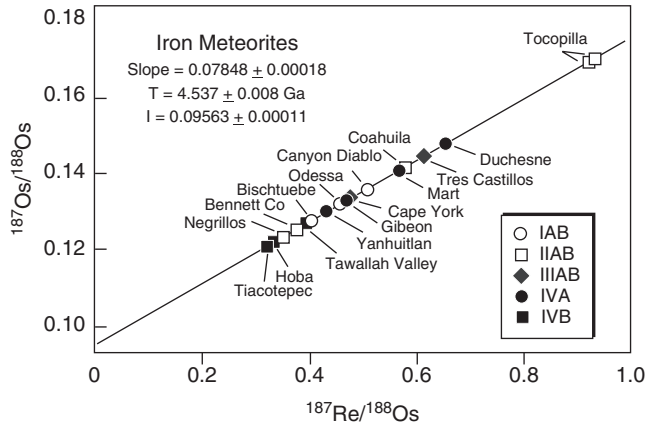

Fig. 8.22 **^{187}Re–^{187}Os evolution diagram for 16 iron meteorites from diverse chemical groups. The line is the best-fit correlation for the IIA and IIB irons. Modified from Shen *et al.* (1996) using $\lambda = 1.666 \times 10^{-11}$ yr^{-1}.**

Reservoir evolution inferred from the ^{187}Re–^{187}Os system

As with the ^{87}Rb–^{87}Sr, ^{147}Sm/^{143}Nd, U–Th–Pb, and ^{176}Lu–^{176}Hf systems, the ^{187}Re–^{187}Os system can be used to investigate reservoir evolution in differentiated bodies. Most of this work has been carried out to investigate differentiation of the Earth and the degree to which a late addition of chondritic material may have been involved in Earth's accretion. Parameters for a chondritic uniform reservoir (CHUR) have been established for the ^{187}Re–^{187}Os system (Table 8.6).

Differences between the current ^{187}Os/^{188}Os of a sample and the CHUR are expressed as:

$$\gamma(\mathrm{Os})_j^0 = \left[\frac{\left({}^{187}\mathrm{Os} \Big/ {}^{188}\mathrm{Os} \right)_{meas}^{0}}{\left({}^{187}\mathrm{Os} \Big/ {}^{188}\mathrm{Os} \right)_{CHUR}^{0}} - 1 \right] \times 10^2 \qquad (8.48)$$

Note that $\gamma(\mathrm{Os})$ is expressed in percent, not parts in 10^4, as in the case of epsilon neodymium, primarily because the variations can be large and the measurement precision is typically somewhat lower than for the ^{147}Sm/^{143}Nd system. Occasionally you will see osmium data presented as ε(Os) in units of parts in 10^4. Although most work has been done on terrestrial systems, there is potential for applications to the Moon and Mars.

Table 8.6 Accepted values for Re-Os CHUR

	Present	4.56 Ga
^{187}Re/^{188}Os	0.423±0.007	0.4564
^{187}Os/^{188}Os	0.12863±0.00046	0.095243

Chen *et al.* (1998).

The ^{176}Lu–^{176}Hf system

Lutetium has two naturally occurring isotopes (Table 4.2), one of which, ^{176}Lu, is radioactive with a branched decay. The β-decay channel (~97% of the decays), which produces ^{176}Hf, is relevant for chronology. The half-life for β-decay is 3.73×10^{10} years ($\lambda_\beta = 1.86 \times 10^{-11}$ yr^{-1}). Hafnium has six naturally occurring isotopes (Table 4.2). Of these, ^{174}Hf is radioactive and α-decays to ^{170}Yb with a half-life of ~2×10^{15} years, too long to be useful for chronology. Both lutetium and hafnium are refractory lithophile elements that should not have been fractionated by either condensation/evaporation processes or metal silicate fractionation.

History

The ^{176}Lu–^{176}Hf system attracted the attention of chronologists around 1980 due to the work of Patchet and Tatsumoto (1980). However, it turned out to be a very difficult system to use because of the very poor ionization efficiency of hafnium by TIMS. In addition, the ^{176}Hf/^{177}Hf and ^{143}Nd/^{144}Nd ratios in most terrestrial basalts are strongly correlated, which implied that in these rocks ^{176}Lu–^{176}Hf is redundant to the easier to use and more precise ^{147}Sm–^{143}Nd system. The technical limitations were largely removed with the introduction of high-precision ICPMS. Recent work has shown that phosphates in meteorites strongly fractionate lutetium and hafnium, which suggests applications for the ^{176}Lu–^{176}Hf system in situations where the ^{147}Sm–^{143}Nd system is not suitable (Fig. 8.23). However, for the most part ^{176}Lu–^{176}Hf is used in conjunction with ^{147}Sm–^{143}Nd to evaluate reservoir evolution in differentiated bodies. Much of the effort in recent years has gone into establishing the parameters for the CHUR in this system (Table 8.7).

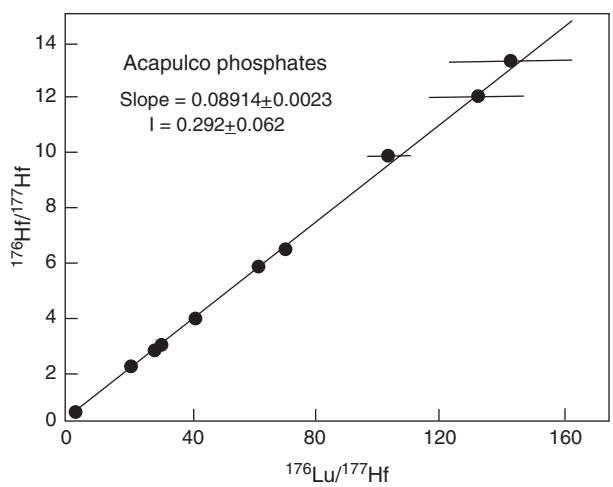

Fig. 8.23 **^{176}Lu–^{176}Hf evolution diagram for phosphates from the Richardton (H5) chondrite. The data form a tight isochron, but the isochron does not give an independent age estimate because the half-life of ^{176}Lu is poorly known. After Amelin (2005).**

Table 8.7 Proposed values for Lu-Hf CHUR

	Present	4.56 Ga
$^{176}Hf/^{177}Hf$	0.282785 (11)	0.279810
$^{176}Lu/^{177}Hf$	0.0336 (1)	0.03657

Bouvier *et al*. (2008).

Another area of significant effort has been to determine the decay constant for ^{176}Lu. The half-life has not been precisely measured in the laboratory; recent determinations range from ~3.69×10^{10} years to 4.08×10^{10} years (e.g. Grinyer *et al*., 2003). The preferred value ($t_{1/2} = 3.73 \times 10^{10}$ years) is derived from measurements of terrestrial and extraterrestrial samples with known ages determined by U–Th–Pb chronology.

Technical details

As with the ^{147}Sm–^{143}Nd and ^{187}Re–^{187}Os systems, careful chemistry is required to cleanly separate the parent and daughter elements because mass spectrometry cannot resolve ^{176}Lu from ^{176}Hf. The ion-exchange chemistry is similar to that for samarium–neodymium. In fact, fractions of samarium, neodymium, lutetium and hafnium are often produced in a single procedure. Mass spectrometry is done by ICPMS because this is the only method that effectively ionizes hafnium.

As with $^{147}Sm/^{144}Nd$, the $^{176}Lu/^{177}Hf$ ratio does not vary much in chondrites, making it very difficult to extract information about the initial $^{176}Hf/^{177}Hf$ of the solar system from isochron diagrams. Thus, the methodology developed for ^{147}Sm–^{143}Nd of comparing the current $^{143}Nd/^{144}Nd$ with the value for the CHUR has been adapted to the ^{176}Lu–^{176}Hf system. Table 8.7 shows recently proposed values for the ^{176}Lu–^{176}Hf CHUR. The evolution of the CHUR is calculated in the same way as for the ^{147}Sm–^{144}Nd system, and differences between the current $^{176}Hf/^{177}Hf$ of a sample and CHUR are expressed as ε(Hf), which is defined in an analogous manner to ε(Nd):

$$\varepsilon(\mathrm{Hf})_j^0 = \left[\frac{\left({}^{176}\mathrm{Hf} \Big/ {}^{177}\mathrm{Hf} \right)_{meas}^{0}}{\left({}^{176}\mathrm{Hf} \Big/ {}^{177}\mathrm{Hf} \right)_{CHUR}^{0}} - 1 \right] \times 10^4 \tag{8.49}$$

As with ε(Nd), ε(Hf) values are reported as parts in 10^4.

Applications

As with $^{147}Sm/^{143}Nd$, the ^{176}Lu–^{177}Hf system can potentially be used to date an object using the isochron method or to study differentiation processes. Figure 8.23 shows an isochron generated from phosphates in the Richardton chondrite. The isochron is precisely determined, but in this case, the isochron was used to estimate the decay constant of ^{176}Lu by

applying an age determined from the U–Th–Pb system. Until the decay constant is known, using ^{176}Lu–^{176}Hf to directly date planetary materials will be problematic.

The ^{176}Lu–^{176}Hf system is often used together with the ^{147}Sm–^{143}Nd system to investigate planetary differentiation. The two systems are often highly correlated. All four elements are incompatible, so their relative abundances do not change much until the degree of fractional crystallization becomes extreme. A few minerals, such as ilmenite and garnet, can separate hafnium from the REEs. Garnet has been implicated to explain the isotopic relationships between the ^{147}Sm–^{143}Nd and ^{176}Lu–^{176}Hf systems in the source regions of terrestrial, lunar and Martian lavas. The eucrites require a different explanation because pressures on the eucrite parent body are not high enough for the source regions to be in the garnet stability field. This suggests that ilmenite is the cause of lutetium–samarium fractionation in eucrites and raises the possibility that ilmenite might also play a role in the evolution of larger bodies (Blichert-Toft *et al*., 2002). As with the ^{147}Sm–^{143}Nd system, multistage evolutionary models can be created for the ^{176}Lu–^{176}Hf system.

Other long-lived nuclides of potential cosmochemical significance

There are several other potential chronometers available. Some preliminary work has been done on some systems, but they are either not widely applicable or have yet to reach mainstream status. Here we briefly review some of them.

^{40}K–^{40}Ca

The branched decay of ^{40}K results in 89% of the daughter atoms ending up as ^{40}Ca. However, the ^{40}K–^{40}Ca system is less useful than the ^{40}K–^{40}Ar system because the doubly magic ^{40}Ca is by far the most abundant isotope of calcium (~97%) and calcium is widely distributed in natural samples. In a few samples, most notably granites, the K/Ca ratio is high enough to make this technique viable. An advantage of the ^{40}K–^{40}Ca system is that ^{40}Ca is less mobile than ^{40}Ar. This system has been used to date two lunar granites, giving results consistent with other techniques (Shih *et al*., 1994).

U–Th–He

Because the decay of uranium to lead generates seven or eight helium atoms, this was one of the first systems applied to dating rocks. However, it was quickly realized that helium is not quantitatively retained in most minerals, so the measured ages are typically lower limits on the true age. For this reason, uranium–helium dating is almost never used in cosmochemistry. A minor revival of this method has occurred in terrestrial geological applications. Apatite thermochronometry using U–Th–He has been used to investigate the cooling history of crystal rocks as they are exposed by erosion (e.g. Ehlers and Farley, 2003). An attempt has been made to apply this technique to the low-temperature cooling history of the Acapulco meteorite, a primitive achondrite that was partially melted and

annealed to a metamorphic texture in the early solar system (Min *et al*., 2003). Their results were consistent with early rapid cooling of Acapulco, as indicated for cooling through higher temperatures, but were somewhat discordant with results from other radiochronometers.

^{190}Pt–^{186}Os

Platinum-190 decays to ^{186}Os by emission of an α-particle. Both are platinum-group elements and thus the system has potential use for iron meteorites and PGE-bearing mineral deposits. Walker *et al*. (1997) determined the decay constant of ^{190}Pt ($\lambda = (1.542 \pm 0.015) \times 10^{-12}$ yr^{-1}; half-life $= 4.5 \times 10^{11}$ years) and established parameters for ^{190}Pt–^{186}Os CHUR:

$$\left(^{186}Os/^{188}Os\right)^{0}_{CHUR} = 0.119834 \pm 0.000002 \qquad \left(^{186}Os/^{188}Os\right)^{4.56Ga}_{CHUR} = 0.119820$$

$$\left(^{190}Pt/^{188}Os\right)^{0}_{CHUR} = 0.001659 \pm 0.000075$$

This system has seen only very limited application to natural samples.

^{138}La–^{138}Ba and ^{138}La–^{138}Ce

Lanthanum-138 decays to ^{138}Ba by electron capture (66%) and to ^{138}Ce by β-decay (34%). Lanthanum and cerium are REEs, whereas barium is an alkaline-earth element like calcium and strontium. Both systems have been studied as potential chronometers but are not in current use.

The ^{138}La/^{138}Ba system has been investigated by Nakai and coworkers (1988). Lanthanum has two naturally occurring isotopes, ^{178}La (0.09%) and ^{139}La (99.91%). Barium has four isotopes with ^{138}Ba being the most abundant at 71.7%. This means that very large La/Be elemental fractionations are required for the system to be useful. The best value for the half-life of decay by electron capture is $(1.57 \pm 0.05) \times 10^{11}$ years ($\lambda = (4.42 \pm 0.14) \times 10^{-12}$ yr^{-1}; Faure and Mensing, 2005). A proof of principle study was carried out by Nakai *et al*. (1988), who dated a bastnaesite (a carbonate-fluoride mineral enriched in light REEs) deposit in Burundi. The resulting age of 586.8±3.7 Ma shows that in suitable samples, high precision dates are possible. However, samples enriched in light REEs to the level of bastnaesite are very rare in nature.

The ^{138}La/^{138}Ce system has been investigated by several groups (e.g. Tanaka and Masuda, 1982). The half-life of ^{138}La by β-decay is relatively uncertain, with a best value of $(2.97 \pm 0.28) \times 10^{11}$ years ($\lambda = (2.33 \pm 0.24) \times 10^{-12}$ yr^{-1}; Faure and Mensing, 2005). Cerium has four isotopes, with ^{138}Ce the second smallest at 0.251%. However, because lanthanum is an odd-Z element, the elemental ratio is not favorable. This system has been studied in several types of terrestrial igneous systems, but the isochrons that are produced typically have large uncertainties. Makishima and Masuda (1993) calculated ^{138}La–^{138}Ce CHUR parameters:

$$\left(\frac{^{138}Ce}{^{142}Ce}\right)^{0}_{CHUR} = 0.0225652 \qquad \left(\frac{^{138}Ce}{^{142}Ce}\right)^{4.56Ga}_{CHUR} = 0.0225321$$

$$\left(\frac{^{138}La}{^{142}Ce}\right)^{0}_{CHUR} = 0.003069$$

This system has not produced useful results for cosmochemistry.

Short-lived radionuclides

The short-lived radionuclides that were originally present in the early solar system have effectively decayed away. They are sometimes called *extinct* radionuclides. Short-lived radionuclides potentially provide high-resolution chronometers for early solar system events. The faster a nuclide decays, the shorter the time scale over which it provides time information, but the higher the time resolution that it can provide. Table 8.8 lists some short-lived radionuclides of interest in cosmochemistry. Those shown in bold have been developed as early solar system chronometers to varying degrees. These and others, such as ^{41}Ca, ^{60}Fe, and ^{107}Pd, are also of interest in determining the environment in which the solar system formed (see Chapter 9). Isotopes such as ^{10}Be, ^{14}C, ^{26}Al, and ^{36}Cl are produced continuously by cosmic ray interactions and are useful in determining cosmic ray exposure ages (Chapter 9). They were also present in the early solar system. The nuclides ^{22}Na and ^{44}Ti have half-lives that are much too short to have been incorporated live into the solar system after their synthesis in stars. However, the decay products of these nuclides have been valuable in establishing the stellar sources of some presolar grains (see Chapter 5).

Because the short-lived nuclides are extinct, a different approach must be taken to use them as chronometers. Equation (8.9) cannot be used to calculate a date because the number of parent nuclides, N, is zero and the equation is undefined. However, if a short-lived nuclide was homogeneously distributed throughout a system, then one can determine the order in which objects formed within that system based on the amount of radionuclide that was present when each object formed. The oldest object would form with the highest amount of the radionuclide relative to a stable isotope of the same element, and the youngest will have the lowest amount. Obviously, no chronological information can be obtained about objects that formed after the radionuclide has reached a level too small to detect the radiogenic daughter isotope.

Consider a hypothetical system that has an initial abundance of a short-lived radionuclide N_R. This nuclide is present as a fixed fraction of the parent element and its abundance can be written as the ratio of the radionuclide to a stable reference isotope of the same element, N_S. When the short-lived nuclide has completely decayed to its daughter nuclide, D^*, we have:

$$\left(\frac{N_R}{N_S}\right)_0 = \frac{D^*}{N_S} \tag{8.50}$$

Table 8.8 Short-lived radionuclides used in cosmochemistry

Nuclide N_R	Half-life (years)	Daughter isotope(s)	Decay mode*	Stable nuclide N_S	$(N_R/N_S)_0$
^{7}Be	53 days	^{7}Li	E.C.	^{9}Be	
^{10}Be	1.5×10^{6}	^{10}B	β^-	^{9}Be	1×10^{-3}
^{14}C	5715	^{14}N	β^-	^{12}C	
^{22}Na	2.604	^{22}Ne	β^+	^{23}Na	
^{26}Al	**7.3×10^{5}**	**^{26}Mg**	**β^+, E.C.**	**^{27}Al**	**5×10^{-5}**
^{36}Cl	3.01×10^{5}	^{36}Ar (98.1%)	β^-	^{35}Cl	5×10^{-6}
		^{36}S (1.9%)	E.C., β^+		
^{41}Ca	1.03×10^{5}	^{41}K	E.C.	^{40}Ca	1.5×10^{-8}
^{44}Ti	59.9	^{44}Ca (via ^{44}Sc)	E.C., E.C.		
^{53}Mn	**3.7×10^{6}**	**^{53}Cr**	**E.C.**	**^{55}Mn**	**9.1×10^{-6}**
^{60}Fe	1.5×10^{6}	^{60}Ni (via ^{60}Co)	β^-	^{56}Fe	$(5–10) \times 10^{-7}$
^{92}Nb	36×10^{6}	^{92}Zr	E.C.		
^{107}Pd	6.5×10^{6}	^{107}Ag	β^-	^{108}Pd	2×10^{-5}
^{129}I	**1.7×10^{7}**	**^{129}Xe**	**β^-**	**^{127}I**	**1×10^{-4}**
^{146}Sm	**1.03×10^{8}**	**^{142}Nd**	**α**	**^{144}Sm**	**8×10^{-3}**
^{182}Hf	**8.9×10^{6}**	**^{182}W**	**β^-**	**^{180}Hf**	**$\tilde{9}7 \times 10^{-5}$**
^{244}Pu	8.2×10^{7}	^{208}Pb, Xe isotopes	α, S.F.	^{232}Th	3×10^{-3}

* E.C. = electron capture, β^- = beta decay, β^+ = positron decay, α = alpha decay, S.F. = spontaneous fission.

The initial ratio, $(N_R/N_S)_0$, is what we hope to determine. We can measure two quantities to extract this information. One is the ratio of the daughter isotope to a stable isotope of the same element. The abundance of the daughter isotope is the sum of the initial abundance, D_0, and the radiogenic component D^*:

$$\frac{D_0 + D^*}{D_{ref}} \tag{8.51}$$

The other is the ratio of the abundance of the reference isotope of the parent element to the abundance of the reference isotope of the daughter element:

$$\frac{N_S}{D_{ref}} \tag{8.52}$$

If we know the initial ratio of the daughter isotope (D_0/D_{ref}), we can calculate the ratio of the radiogenic daughter isotope to the reference isotope:

$$\frac{D_m}{D_{ref}} - \frac{D_0}{D_{ref}} = \frac{D_0 + D^*}{D_{ref}} - \frac{D_0}{D_{ref}} = \frac{D^*}{D_{ref}} \tag{8.53}$$

The initial ratio can then be calculated by dividing Equation (8.53) by Equation (8.52):

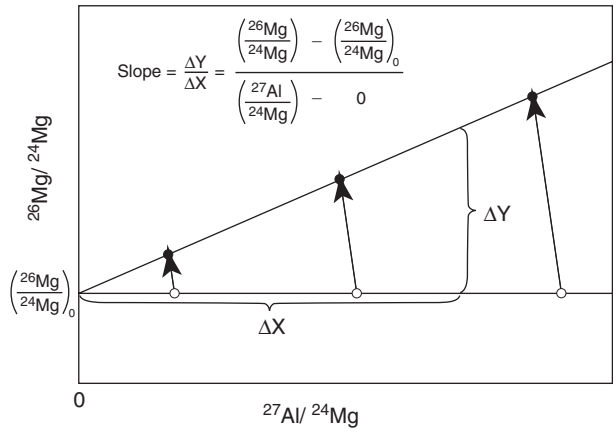

Fig. 8.24 Schematic drawing of an ^{26}Al–^{26}Mg evolution diagram (isochron diagram). The slope of such a diagram gives the $(^{26}Al/^{27}Al)_0$ ratio and the intercept gives the $(^{26}Mg/^{24}Mg)_0$ ratio for the system.

$$\frac{D*}{D_{ref}} \Big/ \frac{N_S}{D_{ref}} = \frac{D*}{N_S} = \left(\frac{N_R}{N_S}\right)_0 \tag{8.54}$$

If the ratio (N_s/D_{ref}) is very high, the initial ratio of the parent isotope to a stable isotope of the same element can be calculated very precisely by this method because the correction for the initial abundance of the daughter isotope is small.

In many cases, however, the elemental ratio is not very high and the contribution of the radiogenic component to the overall abundance of an isotope is small. An isochron diagram, analogous to those used for long-lived radionuclides, provides a powerful way to determine the initial abundance of the parent isotope. But in this case, the x-axis plots the ratio of a stable isotope of the parent element to a stable isotope of the daughter element. Figure 8.24 shows a schematic isochron diagram for the ^{26}Al–^{26}Mg system. As in any other isochron diagram, the ratio of the daughter isotope to a stable isotope of the same element ($^{26}Mg/^{24}Mg$ in Figure 8.24) increases as the radioactive isotope decays. The extinct radionuclide has now completely decayed away, so the isochron is frozen. The slope of the isochron gives the ratio of the radioactive isotope to a stable isotope of the same element at the time the object formed [$(^{26}Al/^{27}Al)_0$]:

$$Slope = \frac{\Delta Y}{\Delta X} = \frac{\left(\frac{^{26}Mg}{^{24}Mg}\right)_{meas} - \left(\frac{^{26}Mg}{^{24}Mg}\right)_0}{\left(\frac{^{27}Al}{^{24}Mg}\right)_{meas} - 0}$$

The ^{24}Mg in this equation represents the indigenous magnesium in the sample and so is the same in numerator and denominator and can be eliminated. The radiogenic $^{26}Mg*$ equals the measured ^{26}Mg minus the original ^{26}Mg in the sample, so the above equation becomes:

$$Slope = \frac{^{26}Mg_{meas} - {}^{26}Mg_0}{^{27}Al_{meas}} = \frac{^{26}Mg*}{^{27}Al} = \left(\frac{^{26}Al}{^{27}Al}\right)_0 \tag{8.55}$$

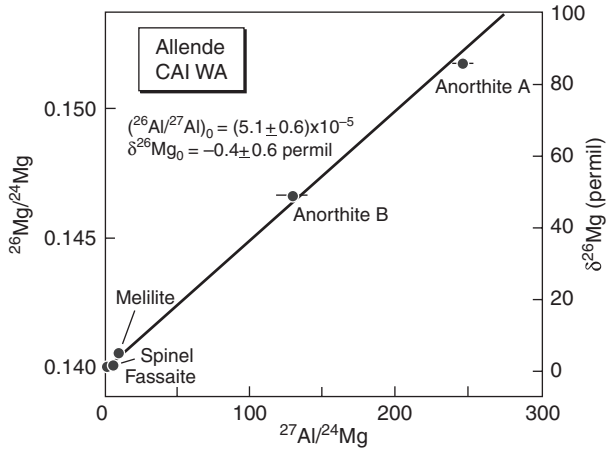

Fig. 8.25 **^{26}Al–^{26}Mg evolution diagram of CAI WA from Allende, the first sample to show clear evidence of live ^{26}Al in the solar system. $^{26}Mg/^{24}Mg$ ratios are given on the left vertical axis and delta values calculated relative to terrestrial magnesium are given on the right. After Lee *et al.* (1977).**

Three types of isochron diagrams are used in discussions of short-lived radionuclides. An *internal isochron* is one based entirely on measurements from the object being dated. By measuring several minerals with different parent/daughter elemental ratios, one can obtain an array of data that gives both the initial ratio $[(N_R/N_S)_0]$ and the initial isotopic ratio of the daughter element (D_0/D_{ref}). Figure 8.25 shows an example of an internal isochron for an Allende CAI. In this figure, the initial $^{26}Mg/^{24}Mg$ ratio is given as $\delta^{26}Mg$ relative to the terrestrial standard (right axis); it is within uncertainties of normal terrestrial magnesium.

Often, however, the sample does not lend itself to measurements of multiple phases. In these cases, one can create a *model isochron* in which the initial isotopic ratio of the daughter element (D_0/D_{ref}) is assumed and is used to anchor the y-intercept. With this assumption, a single measurement can provide the initial ratio $[(N_R/N_S)_0]$ of an object. A third type of isochron diagram makes the assumption that a group of bodies all formed from the same homogeneous isotopic reservoir at the same time. This *whole-rock* isochron is constructed from bulk measurements of each sample, and the resulting slope and initial ratio describe the reservoir from which all of the samples formed.

As with long-lived radiochronometers, some basic conditions must be satisfied for a short-lived nuclide to provide chronological information: (1) The object to be dated must have been isotopically homogeneous at the time that it formed in order for the contribution of the radiogenic isotope to be recognized in the daughter element. (2) In order to generate an internal isochron, a chemical fractionation creating phases with different parent–daughter ratios must have occurred. (3) And, as with all radiometric dating systems, the system must have remained closed and undisturbed since the event being dated. A precise internal isochron provides a test of whether or not the system has remained closed. Because a model isochron can be generated with a single measurement, a chemically homogeneous object can be dated. In addition, even if an object has had its isotopes redistributed after formation, if the system has remained closed, a bulk measurement can still provide a valid

model isochron. But an open system, in which the parent or daughter element has exchanged with the outside, cannot provide valid chronological information. Unfortunately, a model isochron provides no test of whether or not the bulk system has remained closed.

If the above conditions are satisfied and differences in $(N_R/N_S)_0$ are due to time of formation only, the time interval between the formation of two objects, 1 and 2, can be calculated as follows:

$$\Delta t = \frac{1}{\lambda} \ln \left\{ (N_{R1}/N_{S1})_0 \Big/ (N_{R2}/N_{S2})_0 \right\} \tag{8.56}$$

However, to determine the absolute time of formation of the objects, one or both of them must also be dated with a long-lived chronometer.

The ^{129}I–^{129}Xe system

Iodine-129 decays to ^{129}Xe by β-decay. The literature contains several values for the half-life of ^{129}I, ranging from 15.6 Myr to 19.7 Myr. The latest recommended value is 17 Myr ($\lambda = 4.077 \times 10^{-8}$ yr^{-1}) (Holden, 1990), which seems to give relative ages consistent with other techniques. The half-life is long enough that the ^{129}I–^{129}Xe system can potentially date events during the first 100 Myr of solar system history. Because the excesses of ^{129}Xe are often very large, the system has a high intrinsic precision and can resolve time differences as small as 100 000 years. Both iodine and xenon are volatile and mobile elements. These properties mean that the ^{129}I–^{129}Xe system is well suited for dating parent-body events using minerals with low isotopic closure temperatures. An excellent review of the ^{129}I–^{129}Xe system as a chronometer is given by Hohenberg and Pravdivtseva (2008).

History

Iodine-129 was the first short-lived nuclide shown to have been present in the early solar system. Brown (1947) proposed that the age of the elements might be determined if the decay product of an extinct radionuclide could be found in meteorites. Although the proposal itself was flawed, it led to a very important discovery. Initial searchers for ^{129}Xe from the decay of ^{129}I in the Beardsley H5 chondrite and in the Nuevo Laredo eucrite came up empty, but in 1960, John Reynolds found a large excess of ^{129}Xe in the Richardson H4 chondrite and an even larger excess in the Indarch enstatite chondrite (Reynolds, 1960a, 1960b). He argued that the excess was due to decay of ^{129}I primarily on the basis of the improbability of the other options, but proof of an origin from ^{129}I came by irradiating samples with neutrons, which converts some ^{127}I to ^{128}Xe, and showing that the excess ^{129}Xe was associated with the neutron-produced ^{128}Xe (Jeffery and Reynolds, 1961).

Over the next few decades, much effort was devoted to using the ^{129}I–^{129}Xe system as an early solar system chronometer. However, because many of the results did not agree with the relative chronology indicated by the petrography of the samples and with ages determined by long-lived chronometers, and because people did not understand how the iodine was sited in the meteorites and the extent to which metamorphic heating and aqueous alteration

could remobilize iodine and xenon, the ^{129}I–^{129}Xe chronometer fell into disrepute, with most workers concluding that it could not be used for age dating. Research since the mid 1990s has begun to redeem the reputation of the ^{129}I–^{129}Xe chronometer. Detailed work on phosphates, first from Acapulco and then from ordinary chondrites, showed that ^{129}I–^{129}Xe ages and Pb–Pb ages give the same time differences relative to the Shallowater aubrite (Nichols *et al*., 1994; Brazzle *et al*., 1999). This work also resulted in determination of a precise Pb–Pb age for Shallowater, which put the ^{129}I–^{129}Xe ages on an absolute scale. When care is taken to produce clean mineral separates and to interpret the results in the context of the petrography of the materials, results that are consistent with other chronometers can be obtained.

Technical details

If the iodine in a system is isotopically homogeneous, then a suite of objects forming at the same time from that system will have the same ^{129}I/^{127}I ratio. If the system remains closed, then ^{129}Xe* from the decay of ^{129}I will remain in association with ^{127}I. Because it is difficult to measure the abundance of iodine in a sample by chemical means, the ^{129}I–^{129}Xe system is typically measured by irradiating a sample with thermal neutrons, turning a portion of the ^{127}I to ^{128}Xe*. The xenon isotopes are then measured and the ratio of radiogenic ^{129}Xe* from the decay of ^{129}I to the ^{128}Xe* produced in the irradiation is determined. The method is directly analogous to the ^{40}Ar–^{39}Ar method discussed above for the ^{40}K–^{40}Ar system.

The treatment of the data is different than in the ^{40}Ar–^{39}Ar system, however. In an iodine-bearing phase, the measured ^{129}Xe consists of radiogenic ^{129}Xe* from the decay of ^{129}I and the ^{129}Xe that was originally trapped in the sample (^{129}Xe$_t$). In the same way, the measured ^{128}Xe consists of ^{128}Xe* produced by irradiation from the ^{127}I and the ^{128}Xe$_t$ originally trapped in the sample. Thus, both ^{129}Xe and ^{128}Xe will be two-component mixtures between a trapped component and an iodine-derived component, and, if the assumptions of radiometric dating have been met, measured samples of the same age will plot on a single line. In the case where the xenon isotopes are normalized to ^{132}Xe, the equation of the line, the isochron, on a ^{129}Xe/^{132}Xe vs. ^{128}Xe/^{132}Xe plot such as Figure 8.26 is:

$$\frac{^{129}\mathrm{Xe}}{^{132}\mathrm{Xe}} = \mathrm{M} \times \frac{^{128}\mathrm{Xe}}{^{132}\mathrm{Xe}} + \left[\left(\frac{^{129}\mathrm{Xe}}{^{132}\mathrm{Xe}}\right)_t - \mathrm{M} \times \left(\frac{^{128}\mathrm{Xe}}{^{132}\mathrm{Xe}}\right)_t\right] \tag{8.57}$$

where M is the slope (^{129}Xe*/^{128}Xe*) and the term in brackets is the trapped component represented by the end point of the line at the lower left on Figure 8.26 (analogous plots and equations can be created if ^{130}Xe is used for normalization). The trapped component is typically the dominant noble-gas component in chondrites, known as Xe-P1 or Q-Xe (see Chapter 10). Although the measurements must be corrected for the blank in the mass spectrometer and for adsorbed air, these corrections are usually very small and the composition of atmospheric xenon has similar isotopic ratios to the trapped component, so uncertainties in the corrections do not affect the slope of the isochron.

A piece of the Shallowater aubrite is typically included in every irradiation as a flux monitor, and the inferred initial ^{129}I/^{127}I ratios of the samples are determined relative to the

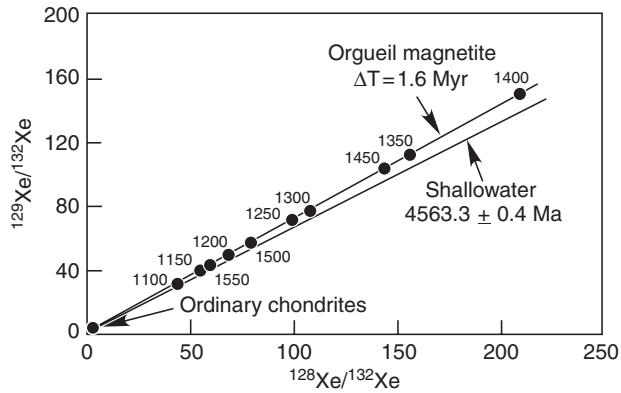

Fig. 8.26 **^{129}I–^{129}Xe isochrons for magnetite separated from the Orgueil CI chondrites and for the Shallowater meteorite (the irradiation standard). The difference in the slopes of the two correlation lines corresponds to the difference in closure times of the ^{129}I–^{129}Xe systems. After Hohenberg and Pravdivtseva (2008).**

ratio for Shallowater (Fig. 8.26). Over the last few years, the absolute age of the Shallowater meteorite (4563.3±0.4 Ma) has been determined through use of several isotope chronometers. This has placed the ^{129}I–^{129}Xe ages determined relative to Shallowater on an absolute scale.

Applications

The greatest asset of the ^{129}I–^{129}Xe technique is its ability to investigate the post-formational evolution of early solar system materials. The ^{129}I–^{129}Xe chronometer has been successfully used to investigate the secondary alteration of a suite of CV3 chondrites. It has also been applied to chondrules, which often show two isochrons, a primary one reflecting formation and a secondary one reflecting later alteration. Attempts have also been made to use the ^{129}I–^{129}Xe system to evaluate the cooling history of IAB iron meteorites. The ^{129}I–^{129}Xe system is probably the best tool for investigating secondary processes.

The ^{26}Al–^{26}Mg system

Aluminum-26 decays to ^{26}Mg by positron emission and electron capture with a half-life of ~730 000 years ($\lambda = 9.50 \times 10^{-7}$ yr^{-1}). Magnesium is the sixth most abundant element in the solar system; aluminum is a factor of ~13 less abundant. Thus, relatively large elemental fractionations favoring aluminum are required for the detection of ^{26}Al effects. Aluminum is a refractory element with a condensation temperature of ~1650 K, while magnesium condenses at ~1340 K (Table 7.1). Thus, both elements tend to resist vaporization, and thermal processing tends to increase the Al/Mg ratio. In minerals where magnesium is a major structural element, magnesium tends to be resistant to thermal metamorphism. But in minerals such as feldspar, where magnesium does not fit into the structure, mild heating will cause any magnesium present to migrate out of the crystal.

Overall, the ^{26}Al–^{26}Mg system is relatively sensitive to thermal resetting. The half-life of 730 000 years means that the ^{26}Al–^{26}Mg system is suitable for dating events during the first 5 Myr of solar system history.

Aluminum-26 is produced by stellar nucleosynthesis in a wide variety of stellar sites. Its abundance relative to other short-lived nuclides provides information about the stellar source(s) for short-lived nuclides and the environment in which the Sun formed. Aluminum-26 is also produced by interactions between heavier nuclei such as silicon atoms and cosmic rays. Aluminum-26 is one of several nuclides used to estimate the cosmic-ray exposure ages of meteorites as they traveled from their parent asteroids to the solar system.

History

The idea that ^{26}Al might have been present in the early solar system and might have provided a heat source for melting and differentiation in early solar system bodies was first presented by Urey (1955). With the development of high-precision thermal-ionization mass spectrometers in the late 1960s, it became possible to search for evidence of ^{26}Al in early solar system materials. The initial searches were unsuccessful, in part because the wrong samples were being measured. However, as scientists prepared to study the lunar samples due to arrive in 1969, the newly fallen Allende meteorite provided ideal samples to renew the search. CAIs from Allende, then interpreted as primitive nebular condensates, were ideal candidates to measure for ^{26}Al. In 1974, isotopic anomalies were found in magnesium (Gray and Compston, 1974; Lee and Papanastassou, 1974), but they could not be directly attributed to decay of ^{26}Al. Clear proof that excesses of ^{26}Mg were due to decay of ^{26}Al came when Lee *et al*. (1977) measured large, clean plagioclase crystals and mineral separates of spinel, melilite, and fassaite from an Allende CAI. The plagioclase crystals showed large excesses of ^{26}Mg and the excesses correlated with the Al/Mg ratio (Fig. 8.25). The initial ^{26}Al/^{27}Al ratio inferred from this inclusion was $(5.1\pm0.6) \times 10^{-5}$. A good summary of the early development of the ^{26}Al–^{26}Mg system as a chronometer is given by Wasserburg and Papanastassiou (1982).

Over the years, numerous studies of CAIs have been carried out by a variety of techniques. MacPherson *et al*. (1995) compiled all available data and found that the ^{26}Al/^{27}Al ratios for CAIs have a bi-modal distribution (Fig. 8.27). Many have ratios near 5×10^{-5}, which they interpreted as the initial ratio for the solar system (the "canonical" ratio). Many others have initial ratios near zero. Resetting or isotopic disturbance by secondary processes is responsible for the low ratios in most cases. But a few CAIs formed with little or no ^{26}Al. These so-called FUN CAIs (Fig. 8.27) also exhibit large isotopic mass fractionations and isotopic anomalies reflecting different mixtures of nucleosynthetic components. In 1995, evidence for ^{26}Al in objects other than CAIs was rare.

By the late 1980s ion microprobe techniques had become sufficiently refined to search for ^{26}Al in chondrules, the dominant component of chondrites. A few studies showed positive results, such as a feldspar-bearing clast chondrule from Semarkona that gave an initial ratio of 7.7×10^{-6} (Hutcheon and Hutchison, 1989). However many did not. Eventually, it was shown that feldspar and glass in chondrules are easily affected by parent body

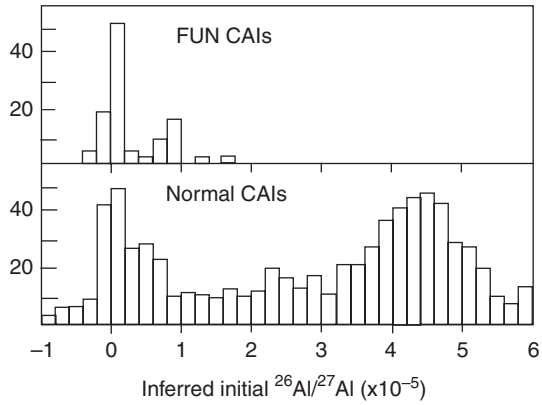

Fig. 8.27 **Histograms of inferred initial ratios for a large number of CAIs measured by a variety of techniques. Normal CAIs show two peaks, one near the canonical ratio of 5×10^{-5} and one at zero. Most of the normal CAIs with initial ratios less than the canonical ratio have been partially or completely reset by secondary processes. However, the FUN inclusions appear to have formed with little or no ^{26}Al. After MacPherson *et al.* (1995).**

metamorphism, and that reliable data for chondrules was limited to type 3.0–3.1 ordinary chondrites and the most primitive members of the other chondrite classes (e.g. Kita *et al.*, 2005).

The development of high-precision multicollector ICPMS (MC-ICPMS) has permitted measurements of ^{26}Al–^{26}Mg systematics in materials with low Al/Mg ratios, including differentiated meteorites. Using high-precision multicollector ICPMS, Thrane *et al.* (2006) directly tested the degree of homogeneity of ^{26}Al in the early solar system. In a material with a solar system Al/Mg ratio, the decay of ^{26}Al present at an initial ratio of 5×10^{-5} would produce a shift in the $^{26}Mg/^{24}Mg$ ratio of ~36 ppm. Measurements of bulk meteorites of various types showed that ^{26}Al was homogeneously distributed throughout the inner solar system to a level of ~15%.

Applications

Because its half-life is ideally suited to investigations of the first 5 Myr of solar system history, and because aluminum-rich minerals are available to measure, the ^{26}Al–^{26}Mg system has been used extensively to study the formation and history of CAIs and chondrules from carbonaceous, ordinary, and enstatite chondrites. The ^{26}Al–^{26}Mg system has also given some information about the metamorphic history of chondritic bodies, although the timescale for metamorphism is a bit too long. There is now also evidence that ^{26}Al was present in the eucrites when they crystallized.

There is clear evidence that live ^{26}Al was incorporated into presolar silicon carbide and aluminum oxide grains (see Chapter 5). These grains acquired their ^{26}Al in the atmospheres of the dying stars in which they formed. It had almost certainly decayed away long before the grains reached the solar system. In presolar grains, ^{26}Al serves as a probe of nucleosynthesis in the parent stars.

Aluminum-26 is an important nuclide for investigating the cosmic-ray exposure history of meteorites on their way to Earth from the asteroid belt. It can also be used to estimate the terrestrial age of a meteorite. In both of these applications, the ^{26}Al is alive in the samples, having been produced by cosmic-ray interactions with elements heavier than aluminum, primarily silicon. Cosmic-ray-exposure dating will be discussed in Chapter 9.

The ^{41}Ca–^{41}K system

Calcium-41 decays to ^{41}K with a half-life of 1.03×10^5 yr ($\lambda = 6.73 \times 10^{-6}$ yr^{-1}). Calcium is a refractory alkaline earth element, while potassium is a moderately volatile alkaline element. Thus, calcium and potassium can be separated by both chemical and thermal processes. The short half-life of ^{41}Ca means that the abundance in the early solar system was very low. Therefore, minerals with very high Ca/K ratios are required in order for the radiogenic ^{41}K to be detected.

History

Hutcheon *et al*. (1984) found strong hints of radiogenic ^{41}K* in pyroxene from two Allende CAIs, but they were unable to completely exclude the possibility that the effects were due to an interference. The first clear evidence of ^{41}Ca was found in pyroxene and perovskite from two CAIs from the Efremovka CV3 chondrite (Srinivasan *et al*., 1994). The initial ^{41}Ca/^{40}Ca ratio inferred for these inclusions was $(1.5\pm0.3) \times 10^{-8}$. These results were confirmed by subsequent measurements of CAIs and refractory mineral grains from Murchison, Allende, and Efremovka (Srinivasan *et al*., 1996; Sahijpal *et al*., 1998).

Technical details

In general, it is not possible to obtain enough suitable material to do a chemical separation of calcium and potassium. This limits measurements of the ^{41}Ca–^{41}K system to the ion microprobe. But the ^{41}Ca–^{41}K system presents an additional, very tough, experimental problem because ^{40}Ca^{42}Ca^{++} has a mass/charge ratio that is so close to that of ^{41}K^{+} that it cannot be separated by mass spectrometry. This means that there is an unresolvable interference that correlates with the Ca/K ratio in exactly the same way that radiogenic ^{41}K* should correlate with the Ca/K ratio. Even worse, the interference tends to be large compared to the amount of radiogenic ^{41}K*. To get around this problem, careful monitoring of the ^{40}Ca^{43}Ca^{++}/^{43}Ca^{+} ratio is required to provide a means to accurately correct for the ^{40}Ca^{42}Ca^{++} interference on ^{41}K^{+}.

Applications

To date, the ^{41}Ca–^{41}K system has not been used for chronology of the early solar system. The short half-life and the experimental challenges mean that measurements are confined to demonstrating that ^{41}Ca was present in an object. While this constrains the object to have

formed well within the first million years of solar system history, the presence of ^{41}Ca is more useful as a means of constraining the time of nucleosynthesis of the short-lived nuclides and the formation environment of the solar system (see Chapter 9).

The ^{53}Mn–^{53}Cr system

Manganese-53 decays by electron capture to ^{53}Cr with a half-life of 3.7 Myr ($\lambda = 1.87 \times 10^{-7}$ yr^{-1}). Manganese and chromium are both relatively abundant and are thus present in most materials. Both are moderately volatile elements, with manganese somewhat more volatile than chromium. They undergo fractionation in evaporation/condensation processes, in magmatic processes, and during aqueous alteration. The half-life of ^{53}Mn is long enough that the ^{53}Mn–^{53}Cr system can be used to date events over the first ~20 Myr of solar system history. Its half-life is also long enough that a significant fraction of the initial solar system inventory could have been inherited from the ambient interstellar medium.

History

The first suggestion that ^{53}Mn might have been present in the early solar system came from ^{53}Cr deficits in the low Mn/Cr fractions of some Allende CAIs. These deficits were interpreted to reflect formation of the manganese-poor CAIs before ^{53}Mn had decayed (Birck and Allègre, 1985). Birck and Allègre (1988) found the first clear evidence that ^{53}Mn was alive in the early solar system in the form of excesses of ^{53}Cr that correlated with the Mn/Cr ratio in mineral separates of an Allende inclusion. Lugmair and Shukolyukov (1998) presented an extensive data set on a wide variety of meteorites, mostly differentiated meteorites, and constructed a relative chronology for their formation. To get absolute ages, they tied this chronology to the angrite LEW 86010, a meteorite with a simple igneous history and a precisely determined Pb–Pb age of 4557.8±0.5 Ma (Lugmair and Galer, 1992). The ^{53}Mn–^{53}Cr system has also been applied to bulk chondrites, chondrules from a variety of chondrite classes (e.g. Nyquist *et al*., 2001c), sulfides from enstatite chondrites (e.g. Wadhwa *et al*., 1997), and secondary minerals from a variety of carbonaceous chondrites (e.g. Endress *et al*., 1996; Hutcheon *et al*., 1998). There has been some inconsistency between the ^{53}Mn–^{53}Cr system and other chronometers, particularly with respect to the time interval between CAI formation and LEW 86010. However, Nyquist *et al*. (2009) have derived a new, significantly lower ^{53}Mn/^{55}Mn initial ratio for CAIs based on comparisons of several chronometers that may have resolved this problem (see Chapter 9).

Lugmair and Shukolyukov (1998) also presented data on initial ^{53}Cr/^{52}Cr ratios that they interpreted to show a radial gradient in initial ^{53}Mn/^{55}Mn in the early solar system. The proposed gradient was too subtle to have affected the ^{53}Mn–^{53}Cr chronometer in the asteroid belt. Later authors have argued that the data can be explained by fractionation of manganese from chromium due to their relative volatilities and that the isotopic composition of manganese was isotopically homogeneous (e.g. Birck *et al*., 1999).

Technical details

The ^{53}Mn–^{53}Cr system can be studied by TIMS, ICPMS, and SIMS techniques. For TIMS and ICPMS work, bulk samples or mineral separates are dissolved and the solutions are passed through ion-exchange columns to produce clean solutions of manganese and chromium. For minerals with high Mn/Cr ratios SIMS can obtain isotopic data while retaining the petrographic context of the measurements. The chromium isotopic compositions may have to be corrected for small additions of chromium from spallation reactions induced by cosmic rays. This is particularly important in iron-rich meteorites.

Direct measurements of the initial abundance of ^{53}Mn in the early solar system have proven unreliable. CAIs, the first solids to form in the early solar system, are highly depleted in both manganese and chromium, both of which are moderately volatile. Operationally, the relative ^{53}Mn–^{53}Cr timescale has been anchored to an angrite, LEW 86010 (see above). Age differences have been calculated relative to LEW 86010 from

$$\Delta t = \frac{1}{\lambda_{53}} \ln \left[\left(\frac{^{53}\mathrm{Mn}}{^{55}\mathrm{Mn}} \right)_{LEW} \Big/ \left(\frac{^{53}\mathrm{Mn}}{^{55}\mathrm{Mn}} \right)_{Sample} \right] \tag{8.58}$$

where λ_{53} is the decay constant of ^{53}Mn. However, the new solar system initial ratio derived by Nyquist *et al*. (2009) can be used in this equation instead of the LEW 86010 ratio.

Applications

The ^{53}Mn–^{53}Cr system is widely used to investigate early solar system chronology. Because of its relatively long half-life, the ^{53}Mn–^{53}Cr chronometer is well suited to provide precise relative ages of differentiated meteorites. It is also well suited for dating aqueous alteration. Fayalite, hedenbergite, and carbonates that precipitated from aqueous fluids typically have very high Mn/Cr ratios. The ^{53}Mn–^{53}Cr system can also be used to date chondrule formation, but because the half-life is relatively long, because manganese is more volatile the chromium leading to relatively low Mn/Cr ratios, and because manganese and chromium are easily mobilized in thermal metamorphism, the results have not been as precise as those from other chronometers.

The ^{60}Fe–^{60}Ni system

Iron-60 β-decays to ^{60}Ni by way of ^{60}Co with a half-life of 1.5 Myr. Thus ^{60}Fe is suitable for dating events in the first 10 Myr of solar system history. Iron is the ninth most abundant element in the solar system (by number); its abundance is similar to those of magnesium and silicon. Nickel is the fifteenth most abundant element. Both exist as oxides, sulfides, and metal. They are constituents of many minerals. This raises the possibility that the ^{60}Fe–^{60}Ni system might be widely applicable to dating early solar system materials. However, unfavorable nickel isotopic abundances (Table 4.2), the mobility of iron and nickel during mild metamorphism, and limited elemental fractionations in many materials significantly

degrade its usefulness. Iron and nickel are both moderately volatile elements, so little fractionation occurs by evaporation/condensation. Iron can be fractionated from nickel by melting and crystallization and by aqueous processes.

History

The first hints that ^{60}Fe was present in the early solar system came from isotopic measurements of Allende CAIs, which showed excesses of ^{60}Ni (Birck and Lugmair, 1988). However, these excesses were accompanied by excesses of ^{62}Ni, and could not be shown to correlate with the Fe/Ni ratio. The first clear evidence of live ^{60}Fe in early solar system materials was found through TIMS measurements of three eucrites, Chervony Kut, Juvinas, and Caldera (Shukolyukov and Lugmair, 1993a, 1993b). The $(^{60}Fe/^{56}Fe)_0$ ratio inferred for these three meteorites differed by an order of magnitude (from ~4×10^{-10} to ~4×10^{-9}), but the $(^{53}Mn/^{55}Mn)_0$ ratios in the same meteorites are quite similar. This indicates that the Fe–Ni system was disturbed in at least some of these eucrites.

The first clear evidence for ^{60}Fe in chondritic material came from ion microprobe measurements of troilite in type 3.0–3.1 ordinary chondrites (Tachibana and Huss, 2003; Moustefaoui *et al*., 2005). An example of data from the Krymka meteorite is shown in Figure 8.28. The $(^{60}Fe/^{56}Fe)_0$ ratio inferred from the sulfides in Bishunpur and Krymka was in the range of (1–2) $\times 10^{-7}$ (Tachibana and Huss, 2003), but Semarkona sulfides gave a higher value (~1.6×10^{-6}) (Moustefaoui *et al*., 2005). Later studies of type 3 enstatite chondrites showed that the ^{60}Fe–^{60}Ni system in sulfides is easily disturbed (Guan *et al*., 2007). Work shifted to silicate minerals in chondrules, particularly Fe-rich pyroxene, because the Fe–Ni system in silicates is less susceptible to secondary thermal disturbance. Inferred $(^{60}Fe/^{56}Fe)_0$ ratios obtained from pyroxene-rich chondrules were in the range of (2–4) $\times 10^{-7}$, somewhat higher than in the Bishunpur and Krymka sulfides (Tachibana *et al*., 2006). Based on ^{26}Al/^{27}Al ages from chondrules in the same meteorites (1.5–2 Myr after CAIs), Tachibana *et al*. (2006) inferred an initial ^{60}Fe/^{56}Fe ratio for the early solar system of (0.5–1.0) $\times 10^{-6}$.

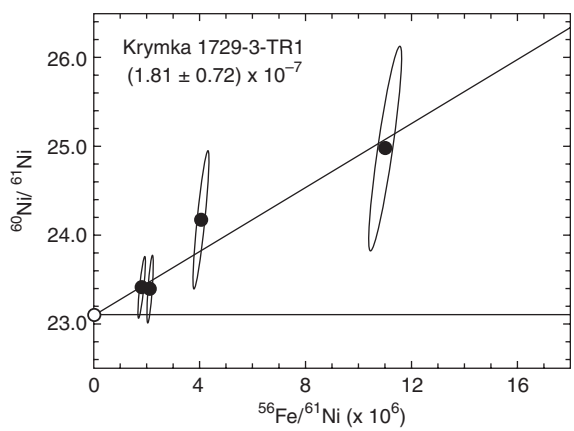

Fig. 8.28 **^{60}Fe–^{60}Ni evolution diagram for a troilite grain from the Krymka LL3.1 chondrite. Errors are shown as ellipses because the large counting-statistical uncertainty for ^{61}Ni results in a correlated component in the errors. The open symbol marking the intercept of the isochron is from an adjacent metal grain. After Tachibana and Huss (2003).**

The demonstration that ^{60}Fe was present at such high levels in chondritic components led to new bulk measurements using MC-ICPMS and the newest generation of TIMS machines. These high-precision techniques can measure the nickel isotope ratios in nickel-rich materials, looking for deficits of ^{60}Ni in materials that formed early and evaluating the distribution of ^{60}Fe in the early solar system. Initial results indicate the ^{60}Fe was homogeneously distributed, with residual variations limited to <10% (Dauphas *et al*., 2008).

Technical details

Nickel-60 is the second most abundant nickel isotope (26.2%), so either very high Fe/Ni ratios or very-high-precision measurements are required to detect radiogenic ^{60}Ni*. For an ion microprobe, Fe/Ni ratios approaching 10^4 are required to detect ^{60}Fe at the abundance it has been found in chondritic materials. For MC-ICPMS and TIMS, both of which can achieve precisions of order 10 ppm, samples with elemental ratios of less than 100 can give resolvable excesses of ^{60}Ni. For these studies, the iron and nickel must be separated from bulk samples and purified on ion exchange columns.

Applications

The ^{60}Fe–^{60}Ni system has the potential to be a useful chronometer for early solar system events, but it is far from mature. Measurements made over the past few years have yielded confusing and conflicting results. These problems should resolve themselves as we learn how better to measure the samples and learn how to choose samples that meet the requirements for successful age dating.

Early work indicates that the ^{60}Fe–^{60}Ni system may be useful for dating chondrule formation. Fe-rich olivine and pyroxene exclude nickel when they crystallize and both are stable against the degrees of metamorphism found in type 3.0–3.1 chondrites. The ^{60}Fe–^{60}Ni system also seems suitable to date aqueous alteration. Fayalite and hedenbergite formed by precipitation from aqueous fluids exclude nickel and have very high Fe/Ni ratios. High-precision measurements have the potential to date the formation of objects by differences in the ^{60}Ni abundance in high-nickel samples.

Iron-60 could have been a significant heat source in the early solar system. In a body of solar composition, assuming initial ^{26}Al/^{27}Al and ^{60}Fe/^{56}Fe ratios of 5×10^{-5} and 0.75×10^{-6}, respectively (see Chapter 9), ^{60}Fe would provide ~14% of the heat provided by ^{26}Al. Because ^{60}Fe can only be synthesized in stars, it will likely also play an important role in understanding the environment in which the solar system formed and the source of the latest contribution of newly synthesized elements to the early solar system (see Chapter 9).

The ^{107}Pd–^{107}Ag system

Palladium-107 β-decays to ^{107}Ag with a half-life of 6.5 Myr and is suitable for dating events during the first ~40 Myr of solar system history. Both elements are siderophile, but silver will also partition into sulfide. Melting and segregation of metal and troilite produces

segregation of palladium from silver, but major chemical fractionation of palladium from silver primarily reflects volatility control. Palladium condenses at ~1320 K, while silver condenses at ~993 K (Table 7.1), so palladium is expected to be highly enriched relative to silver in metal that is depleted in volatile elements.

History

Following the discovery that ^{129}I was present in the early solar system, searches were carried out for evidence of other short-lived nuclides. In the early 1960s, there were reports of excess ^{107}Ag in iron meteorites, but these reports turned out to be in error, and the search for evidence of ^{107}Pd was suspended for over a decade. The discovery that ^{26}Al was present in the early solar system renewed the interest in searching for evidence of ^{107}Pd. Kelly and Larimer (1977) suggested that IVB irons, which are strongly depleted in volatile siderophile elements and have high Pd/Ag ratios, might be a good place to look for evidence of ^{107}Pd. Based on this suggestion, Kelly and Wasserburg (1978), using new chemical procedures and careful mass spectrometry, found clear excesses of ^{107}Ag that correlated with Pd/Ag in the Santa Clara (IVB) meteorite. Kaiser and Wasserburg (1983) confirmed this initial work and extended the observations to include several other IVB meteorites as well as meteorites from other classes. However, this work also showed that silver can be mobile in iron meteorites, making age determinations problematic (Chen and Wasserburg, 1990). Development of MC-ICPMS improved the measurement sensitivity of these elements by more than an order of magnitude (Carlson and Hauri, 2001). The higher sensitivity has permitted isotopic measurements of chondrites and has led to a new determination for the initial ^{107}Pd/^{108}Pd ratio in the early solar system that appears to produce a chronology for iron meteorites that is consistent with those of other isotopic systems (Schönbächler *et al*., 2008).

Technical details

Measurement of the ^{107}Pd–^{107}Ag system requires careful chemistry to remove terrestrial silver and palladium and to eliminate interferences in the mass spectrometer. Because silver has only two isotopes, great care must be taken to account for mass-dependent fractionation, both in the mass spectrometer and in the samples. Interpretation of the ^{107}Pd–^{107}Ag system in iron meteorites is not straightforward. In many iron meteorites, fractionation of palladium from silver took place early, followed by an extended period of slow cooling during which time the radiogenic silver could migrate throughout the body. Shock metamorphism may affect the ^{107}Pd–^{107}Ag systematics, and cosmic-ray spallation can produce palladium and silver isotopes both during and after the decay of the original inventory of ^{107}Pd.

Applications

The ^{107}Pd–^{107}Ag system has been applied most effectively to dating iron meteorites and pallasites. The best examples are the internal isochron for the Gibeon IVA iron (Chen and Wasserburg, 1990) and for the Brenham pallasite (Carlson and Hauri, 2001). New measurements of carbonaceous chondrites (Schönbächler *et al*., 2008) have provided a reasonably

precise estimate of the $(^{107}Pd/^{108}Pd)_0$ ratio in the early solar system, which provides a key parameter for using the ^{107}Pd–^{107}Ag system as a chronometer.

The ^{146}Sm–^{142}Nd system

Samarium-146 α-decays to ^{142}Nd with a half-life of 103 Myr ($\lambda_\alpha = 6.71 \times 10^{-9}$ yr^{-1}). Its half-life is too long to provide a high-resolution chronometer of the first few million years of solar system history, but it can provide time information about the first several hundred million years. As with the long-lived ^{147}Sm–^{143}Nd system, both parent and daughter are REE that are not fractionated very much by melting and crystallization or evaporation and condensation. When used together with the ^{147}Sm–^{143}Nd system, the ^{146}Sm–^{142}Nd system can help identify objects that are isotopically disturbed in spite of apparently precise isochrons.

History

The possible importance of ^{146}Sm in the early solar system was first suggested by Kohman (1954), although he cautioned that it might have only limited usefulness due to the small degree of chemical fractionation between parent and daughter in natural systems. Audouze and Schramm (1972) suggested that it might be used as a chronometer for the synthesis of *p*-process elements. The first search for evidence of ^{146}Sm in early solar system materials was carried out by Lugmair *et al*. (1975b) in the Juvinas eucrite. Although they only found a hint of its presence, their work prompted Jacobsen and Wasserburg (1984) to extend the search to several other achondrites. But again, only hints of ^{146}Sm were found. Prinzhofer *et al*. (1992) and Stewart *et al*. (1994) found clear evidence of live ^{146}Sm in several meteorites and were able to establish an initial $^{146}Sm/^{144}Sm$ ratio for the early solar system of 0.008–0.009. Subsequent work has concentrated on using the ^{146}Sm–^{142}Nd system, along with the long-lived ^{147}Sm–^{143}Nd system, to investigate planetary accretion and differentiation.

Technical details

The chemistry and mass spectrometry for the ^{146}Sm–^{142}Nd system are basically the same as for the long-lived ^{147}Sm–^{143}Nd system. The low abundance of the *p*-process isotopes and the small degree of elemental fractionation of parent and daughter in natural systems result in relatively large uncertainties on the isochrons and initial ratios determined from meteorites. In studies of planetary accretion and differentiation, the isotopic shifts in $^{142}Nd/^{144}Nd$ are reported in parts in 10 000 relative to the terrestrial standard:

$$\varepsilon^{142}Nd = \left[\frac{\left({}^{142}Nd \Big/ {}^{144}Nd \right)_{sample}}{\left({}^{142}Nd \Big/ {}^{144}Nd \right)_{std}} - 1 \right] \times 10^4 \qquad (8.59)$$

Applications

The ^{146}Sm–^{142}Nd system is used primarily to investigate the nature and timing of accretion of planetary bodies, such as the Earth, Moon, Mars, and Vesta. Current work is aimed at unraveling the roles of nebular and planetary processes in the isotopic systematics of these bodies.

The ^{182}Hf–^{182}W system

Hafnium-182 β-decays to ^{182}W with a half-life of 8.9 Myr ($\lambda = 7.79 \times 10^{-8}$ yr^{-1}). (Osmium-186 also α-decays to ^{182}W, but its half-life is so long (2×10^{15} yr) that additions to ^{182}W from this source are insignificant.) The ^{182}Hf–^{182}W system is thus useful for events occurring in the first ~60 Myr of solar system history. Both hafnium and tungsten are highly refractory elements and therefore are expected to occur in chondritic proportions in most solar system objects. Hafnium is strongly lithophile and tungsten is moderately siderophile. Thus, core formation and metal-silicate fractionation are events well suited to ^{182}Hf–^{182}W dating. Within silicates, fractionation of hafnium from tungsten can occur because of the higher incompatibility of tungsten with respect to hafnium. Tungsten is one of the most incompatible elements, while hafnium can be incorporated into high-calcium pyroxene and ilmenite.

History

The ^{182}Hf–^{182}W system was slow to develop because it is extremely difficult to measure tungsten by TIMS. The development of NTIMS allowed some early measurements to be made (e.g. Völkening *et al.*, 1991; Harper and Jacobsen, 1996), but it took the development of MC-ICPMS to make this system truly accessible to study (e.g. Halliday *et al.*, 1996). Since that time, high-precision measurements have been obtained for all types of chondrites, achondrites, iron meteorites, and for the Earth, Moon, and Mars (reviewed by Halliday and Lee, 1999). Recently, high-precision measurements of CAIs have generated a well-defined isochron (Fig. 8.29) that defines the initial ε_W and ^{182}Hf/^{180}Hf at the time of solar system formation (Burkhardt *et al.*, 2008). The chronology resulting from these new values is consistent with those provided by Pb–Pb, ^{26}Al–^{26}Mg, and other chronometers (Chapter 9).

Technical details

The most reliable measurements of the ^{182}Hf–^{182}W system are made by MC-ICPMS, although NTIMS is sometimes used as well. Excesses of ^{182}W are typically reported relative to ^{184}W, the most abundant isotope, and are expressed as deviations in parts per 10 000 from the ratio in the bulk silicate Earth (BSE):

$$\varepsilon_W = \left[\frac{\left({}^{182}W \Big/ {}^{184}W \right)_{sample}}{\left({}^{182}W \Big/ {}^{184}W \right)_{BSE}} - 1 \right] \times 10^4 \qquad (8.60)$$

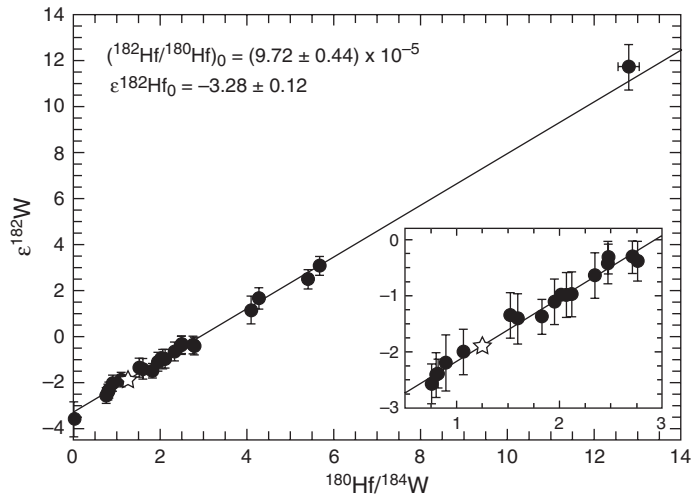

Fig. 8.29 Combined data for ten CAIs fall within errors of a single isochron, the slope of which gives the best estimate for the $(^{182}Hf/^{180}Hf)_0$ of the solar system and the intercept of which gives the best estimate for the initial $\varepsilon^{182}Hf$. The data points represent both bulk samples and mineral separates. Inset shows a magnification of the fit to the isochron for fractions with low $^{180}Hf/^{184}W$. The star is the value for average carbonaceous chondrites. After Burkhardt *et al.* (2008).

Applications

The ^{182}Hf–^{182}W system is particularly powerful for constraining the time scales of accretion and metal-silicate fractionation (e.g. core formation). Because no fractionation of hafnium and tungsten is expected based on volatility, most solar system objects are expected to have a chondritic hafnium/tungsten ratio. If a body remains unfractionated while ^{182}Hf is alive, all parts of the body will have the same tungsten isotopic composition. Carbonaceous chondrites, which have not experienced metal-silicate fractionation, fit this criterion. If metal-silicate fractionation does occur while ^{182}Hf is alive, the hafnium will partition preferentially into the silicate phase and the tungsten will go into the metal phase. As a result, the silicate material will end up with tungsten enriched in ^{182}W, whereas the metal will have a deficit of ^{182}W relative to bulk chondrites.

The ^{10}Be–^{10}B system

Beryllium-10 β-decays to ^{10}B with a half-life of 1.5 Myr. Beryllium and boron (along with lithium) are several orders of magnitude less abundant than the other light elements in the solar system because, except for ^{7}Li, they are not produced in stars. They are produced when high-energy cosmic rays, mostly protons, fragment atomic nuclei into small pieces in a process called spallation. Beryllium-10 is constantly being produced at low levels by spallation in the solar system, and its abundance in bulk meteorites is used to estimate the amount of time that they were exposed to cosmic rays as small bodies (their cosmic-ray

exposure age) as they traveled to Earth from their parent asteroid (see Chapter 9). Beryllium is the lightest alkaline-earth element. It has the same electronic structure as, and commonly substitutes for, magnesium. In contrast, boron is a group 3A element and has the same electronic structure as aluminum. Beryllium is a refractory element that condenses at ~1490 K, whereas boron, a moderately volatile element, condenses at ~964 K (Table 7.1). This strong contrast in volatility leads to high Be/B ratios in refractory materials.

History

The first clear evidence that ^{10}Be was alive in the early solar system was provided by McKeegan *et al*. (2000), who found large excesses of ^{10}B that correlated with the ^{9}Be/^{11}B ratio in an Allende Type B CAI. These results were quickly confirmed in other type B and in type A CAIs, and an initial ratio for the early solar system of ~1×10^{-3} was inferred. This high ratio, coupled with the very low abundance that had at that time been inferred for ^{60}Fe, which can only be produced in stars, led to a model in which all short-lived nuclides were produced by irradiation (e.g. Gounelle *et al*., 2001). The model predicts that the abundances ^{10}Be and ^{26}Al should be correlated, but in some CAIs and in hibonite grains from CM2 chondrites, the abundances are not correlated (Marhas *et al*., 2002; MacPherson *et al*., 2003). These results and further theoretical investigations showing that it is extremely difficult to produce the short-lived nuclides at their observed relative abundances have dampened enthusiasm for irradiation as the source of all short-lived nuclides. But the widespread presence of ^{10}Be in refractory materials shows that irradiation was responsible for at least a portion of them.

Another short-lived isotope of beryllium, ^{7}Be, decays to ^{7}Li by electron capture with a half-life of ~53 days. This half-life is so short that any atoms present in chondrite components must have been produced in the solar system essentially immediately before the host object formed. A hint of the presence of ^{7}Be in the form of large excesses of ^{7}Li in an Allende CAI was presented by Chaussidon *et al*. (2006). However, these authors were not able to demonstrate a tight correlation with the ^{9}Be/^{6}Li ratio.

Applications

To date, the ^{10}Be–^{10}B system has not been shown to be useful as a chronometer for the early solar system. A prerequisite for being able to use a short-lived nuclide as a chronometer is that it was homogeneously distributed, so that differences in initial ^{10}Be/^{9}Be ratios among objects can be interpreted in terms of time. It currently seems unlikely that the ^{10}Be–^{10}B system will ever be very useful as a chronometer because most of the ^{10}Be was probably locally produced and heterogeneously distributed in time and space. However, ^{10}Be may be extremely useful as a measure of the irradiation environment experienced by various objects in the early solar system.

Beryllium-10, like ^{14}C, ^{26}Al, and ^{36}Cl, is used to infer the cosmic-ray exposure history of a meteorite or a planetary surface.

Other short-lived nuclides of potential cosmochemical significance

^{14}C–^{14}N

Carbon-14 β-decays to ^{14}N with a half-life of 5730 years. This system is a mainstay of archeological research. It is useful in cosmochemistry primarily to determine the cosmic-ray exposure history of meteorites as they transit from their parent bodies to Earth.

^{22}Na–^{22}Ne

Sodium-22 decays by positron emission and electron capture to ^{22}Ne with a half-life of 2.6 years. This nuclide is historically significant because it was inferred to be the source of Ne-E, a neon component thought to consist of pure ^{22}Ne, revealed by stepped heating of acid residues of primitive carbonaceous chondrites (Black and Pepin, 1969). This was the first indisputable evidence that presolar grains existed in meteorites, but the significance of this discovery was not fully appreciated for over a decade.

^{36}Cl

Chlorine-36 either β-decays to ^{36}Ar (98.1%) or decays by positron emission or electron capture to ^{36}S (1.9%) with a half-life of 3.01×10^5 years. Attempts to find evidence for ^{36}Cl in the early solar system using the ^{36}Ar channel yielded a strong hint for its presence and an estimated initial $^{36}Cl/^{35}Cl$ ratio of 1.4×10^{-6} (Murty *et al*., 1997). The ^{36}Cl–^{36}S branch has proved more productive, with clear evidence for live ^{36}Cl in secondary sodalite in several CAIs at the time that the sodalite formed. Initial ratios inferred from the sodalite are ~4×10^{-6} (Lin *et al*., 2005; Hsu *et al*., 2006). It is not yet clear whether the ^{36}Cl was produced by a stellar source and incorporated into the solar system or whether it was produced by particle irradiation in the solar system. Chlorine-36 is used in the study of cosmic-ray exposure ages of meteorites.

^{44}Ti–^{44}Ca

Titanium-44 decays by electron capture via ^{44}Sc to ^{44}Ca with a half-life of 60 years. Its half-life is too short for it to have played any role in the solar system. Titanium-44 is produced by explosive nucleosynthesis and it is useful as an indicator of the supernova source for a subset of ^{44}Ca-rich presolar grains.

^{244}Pu–Xenon

Plutonium-244 decays by α-emission and spontaneous fission with a half-life of 82 Ma. The branching ratio, fission/α-emission, is 0.00125. The former existence of ^{244}Pu in the solar system is indicated by the presence of fission tracks in meteorite samples and

by the presence of fission xenon that has an isotopic composition identical to that measured in a sample of man-made ^{244}Pu (Alexander *et al*., 1971). This system has yielded dates for a few solar system objects, including eucrites and Angra dos Reis (Shukolukov and Begamann, 1996; Lugmair and Marti, 1977). However, it is difficult to use, and ^{244}Pu–xenon dating is not likely to ever have the accuracy and precision necessary to improve on the dates obtained by other techniques.

Summary

In this chapter, we have discussed the basic principles of using radioactive isotopes as chronometers. The requirements that a sample must meet in order to provide a valid age were presented. They are: (1) The decay constants must have remained constant over the age of the solar system. We know this to be true from the concordance of chronologies based on radioactive isotopes that decay by very different mechanisms and by the identical time evolution of radioactivity-driven light curves of supernova that exploded 10 billion years ago and a few million years ago. (2) The sample must have experienced an event that homogenized the isotopic compositions of parent and daughter elements. This starts the clock. Ideally, the homogenizing event will also produce a fractionation resulting in two or more phases with different parent-to-daughter elemental ratios, permitting construction of an isochron. (3) The system must have remained closed to exchange with the outside since the event being dated, and in order for an internal isochron to be produced, the system must also have been closed to internal redistribution of the isotopes. One of the most difficult aspects of radiometric dating is finding samples that clearly meet these last two requirements.

We discussed two different types of radiochronometers. Those based on long-lived radionuclides for which a portion of the primordial abundance is still present provide absolute ages relative to the present time on suitable samples. Examples of how these chronometers are used to date individual objects (chondrules, CAIs, achondrites) and fractionation events (planetary differentiation, magma generation) were discussed.

Short-lived radionuclides can provide high-resolution relative chronometers. The shorter the half-life, the higher the time resolution is. Short-lived systems currently in use can resolve time differences of a few hundred thousand years at 4.57 Ga. But in order to get absolute time, the short-lived systems must be tied to a long-lived radionuclide.

The individual isotope systems differ in the objects that they can date, the details of how they are measured, and the specifics of how they are applied. Some systems are best suited to date fractionation events based on volatility. Others are best suited to date igneous processes. Still others are most useful for secondary events. Together they provide the keys to unlocking the time history of the solar system. In Chapter 9, we will summarize the current state of knowledge of the chronology of the solar system obtained from these radiochronometers.

Questions

1. Radiometric dating is one way to get age information. What are some of the other ways of measuring time? How do radiochronometers complement these methods?
2. Why is it necessary for an object to be dated by a radiochronometer to have been isotopically homogeneous when it formed?
3. Which radiochronometer(s) would be best suited to determine the crystallization age of a basaltic meteorite? What are some of the complications that might result in an incorrect age determination?
4. What are the best radiochronometers to use to determine the formation times of CAIs and chondrules? Why?
5. What radiochronometers are best suited for dating aqueous alteration in chondritic meteorites? Why?
6. Which radiochronometers use nuclear reactions as part of the analytical procedure? What are the advantages of this approach?

Suggestions for further reading

Brush, S. G. (1982) Cooling spheres and accumulating lead: The history of attempts to date the Earth's formation. *The Science Teacher*, **54**, 29–34. A very readable history of finding the age of the Earth.

Brush, S. G. (1987) Finding the age of the Earth by physics or by faith. *Journal of Geological Education*, **30**, 34–58. A thoughtful evaluation of the debate between scientists and creationists over the age of the Earth.

Faure, G. and Messing, T. M. (2005) *Isotopes: Principles and Applications*. New Jersey: John Wiley and Sons, 897 pp. A tremendous resource for details about various techniques of radiometric dating.

Hohenberg, C. M. and Pravdivtseva, O. V. (2008) I–Xe dating: from adolescence to maturity. *Chemie der Erde*, **68**, 339–351. A good review of the status of I–Xe dating.

Kleine, T., Touboul, M., Bourdon, B. *et al*. (2009) Hf–W chronology of the accretion and early evolution of asteroids and terrestrial planets. *Geochimica et Cosmochimica Acta*, **73**, 5150–5188. A detailed review of the status of Hf–W dating.

Nyquist, L. E., Bogard, D. D. and Shif, C.-Y. (2001a) Radiometric chronology of the Moon and Mars. In *The Century of Space Science*, eds. Bleeker, A. M., Geiss, J. and Huber, M. C. The Netherlands: Klewer Academic Publishers, pp. 1325–1376. An easy-to-read review of the history of radiometric chronology as it relates to the Moon and Mars.

Wasserburg, G. J. and Papanastassiou, D. A. (1982) Some short-lived nuclides in the early solar system: a connection with the placental ISM. In *Essays in Nuclear Astrophysics*, eds. Barnes, C. A., Clayton, D. D. and Schramm, D. N. Cambridge: Cambridge University Press, pp. 77–140. A good review of the early history of chronology using short-lived radionuclides.

References

Aldrich, L. T. and Nier, A. O. (1948) Argon-40 in potassium minerals. *Physical Review*, **74**, 876–877.

Alexander, E. C., Jr., Lewis, R. S., Reynolds, J. H. and Michel, M. C. (1971) Plutonium-244: confirmation as an extinct radioactivity. *Science*, **172**, 837–840.

Amelin, Y. (2005) Meteorite phosphates show constant ^{176}Lu decay rate since 4557 million years ago. *Science*, **310**, 839–841.

Audouze, J. and Schramm, D. M. (1972) ^{146}Sm: a chronometer for *p*-process nucleosynthesis. *Nature*, **237**, 447–449.

Birck, J. L. and Allègre, C. J. (1985) Evidence for the presence of ^{53}Mn in the early solar system. *Geophysical Research Letters*, **12**, 745–748.

Birck, J. L. and Allègre, C. J. (1988) Manganese chromium isotope systematics and the development of the early solar system. *Nature*, **331**, 579–584.

Birck, J. L. and Lugmair, G. W. (1988) Nickel and chromium isotopes in Allende inclusions. *Earth and Planetary Science Letters*, **90**, 131–143.

Birck, J. L., Rotaru, M. and Allègre, C. J. (1999) ^{53}Mn–^{53}Cr evolution of the early solar system. *Geochimica et Cosmochimica Acta*, **63**, 4111–4117.

Black, D. C. and Pepin, R. O. (1969) Trapped neon in meteorites. *Earth and Planetary Science Letters*, **6**, 395–405.

Blichert-Toft, J., Boyet, M., Télouk, P. and Albarède, F. (2002) ^{147}Sm–^{143}Nd and ^{176}Lu–^{176}Hf in eucrites and the differentiation of the HED parent body. *Earth and Planetary Science Letters*, **204**, 167–181.

Bouvier, A., Vervoort, J. D. and Patchett, P. J. (2008) The Lu–Hf and Sm–Nd isotopic composition of CHUR: constraints from unequilibrated chondrites and implications for the bulk compositions of the terrestrial planets. *Earth and Planetary Science Letters*, **273**, 48–57.

Brazzle, R. H., Pravdivtseva, O. V., Meshik, A. P. and Hohenberg, C. M. (1999) Verification and interpretation of the I–Xe chronometer. *Geochimica et Cosmochimica Acta*, **63**, 739–760.

Brennecka, G. A., Weyer, S., Wadhwa, M. *et al*. (2009) ^{238}U/^{235}U variations in meteoritic materials: Evidence for curium-247 in the early solar system and implications for Pb–Pb dating (abstr.). *Meteoritics and Planetary Science*, **44** Supplement, A40.

Brown, H. (1947) An experimental method for the estimation of the age of the elements. *Physical Review*, **72**, 348.

Burkhardt, C., Kleine, T., Bourdon, B. *et al*. (2008) Hf–W mineral isochron for Ca, Al-rich inclusions: age of the solar system and the timing of core formation in planetesimals. *Geochimica et Cosmochimica Acta*, **72**, 6177–6197.

Campbell, N. R. and Wood, A. (1906) The radioactivity of the alkali metals. *Proceedings of the Cambridge Philosophical Society*, **14**, 15–21.

Carlson, R. W. and Hauri, E. H. (2001) Extending the ^{107}Pd–^{107}Ag chronometer to low Pd/Ag meteorites with multicollector plasma-ionization mass spectrometry. *Geochimica et Cosmochimica Acta*, **65**, 1839–1848.

Chaussidon, M., Robert, F. and McKeegan, K. D. (2006) Li and B isotopic variations in an Allende CAI: evidence for the *in situ* decay of short-lived Be-10 and for the possible presence of the short-lived nuclide Be-7 in the early solar system. *Geochimica et Cosmochimica Acta*, **70**, 224–245.

Chen, J. H., Papanastassiou, D. A. and Wasserburg, G. J. (1998) Re–Os systematics in chondrites and the fractionation of the platinum group elements in the early solar system. *Geochimica et Cosmochimica Acta*, **62**, 3379–3392.

Chen, J. and Wasserburg, G. J. (1990) The isotopic composition of Ag in meteorites and the presence of ^{107}Pd in protoplanets. *Geochimica et Cosmochimica Acta*, **54**, 1729–1743.

Creaser, R. A., Papanastassiou, D. A. and Wasserburg, G. J. (1991) Negative thermal ion mass spectrometry of osmium, rhenium, and iridium. *Geochimica et Cosmochimica Acta*, **55**, 397–401.

Dauphas N., Cook D. L., Sacarabany, A. *et al*. (2008) Iron-60 evidence for early injection and efficient mixing of stellar debris in the protosolar nebula. *Astrophysical Journal*, **686**, 560–569.

DePaolo, D. J. and Wasserburg, G. J. (1976a) Nd isotopic variations and petrogenetic models. *Geophysical Research Letters*, **3**, 249–252.

DePaolo, D. J. and Wasserburg, G. J. (1976b) Inferences about magma sources and mantle structure from variations of ^{143}Nd/^{144}Nd. *Geophysical Research Letters*, **3**, 743–746.

Edmunson, J., Borg, L. E., Nyquist, L. E. and Asmerom, Y. (2009) A combined Sm–Nd, Rb–Sr, and U–Pb isotopic study of Mg-suite norite 78238: further evidence for early differentiation of the Moon. *Geochimica et Cosmochimica Acta*, **73**, 514–527.

Ehlers, T. A. and Farley, K. A. (2003) Apatite (U–Th)/He thermometry: methods and applications to problems in tectonic and surface processes. *Earth and Planetary Science Letters*, **206**, 1–14.

Endress, M., Zinner, E. and Bischoff, A. (1996) Early aqueous activity on primitive meteorite parent bodies. *Nature*, **379**, 701–703.

Faure, G. (1986) *Principles of Isotope Geology*, 2nd edn. New York: Wiley.

Gale, N. H. and Mussett, A. E. (1973) Episodic uranium–lead models and interpretation of variations in isotopic composition of lead in rocks. *Reviews in Geophysics*, **11**, 37–86.

Garner, E. L., Murphy, T. J., Bramlich, J. W., Paulsen, P. J. and Barnes, I. L. (1975) Absolute isotopic abundance ratios and the atomic weight of a reference sample of potassium. *Journal of Research of the National Bureau of Standards A. Physics and Chemistry*, **79A**, 713–725.

Gounelle, M., Shu, F. H., Shang, H. *et al*. (2001) Extinct radioactivities and protosolar cosmic rays: self-shielding and light elements. *Astrophysical Journal*, **548**, 1051–1070.

Gray, C. M. and Compston, W. (1974) Excess ^{26}Mg in the Allende meteorite. *Nature*, **251**, 495–497.

Gray, C. M., Papanastassiou, D. A and Wasserburg, G. J. (1973) The identification of early condensates from the solar nebula. *Icarus*, **20**, 213–239.

Grinyer, G. F., Waddington, J. C., Svensson, C. E. *et al*. (2003) Half-life of ^{176}Lu. *Physical Review C*, **67**, 014302.

Guan, Y., Huss, G. R. and Leshin, L. A. (2007) ^{60}Fe–^{60}Ni and ^{53}Mn–^{53}Cr isotope systems in sulfides from unequilibrated ordinary chondrites. *Geochimica et Cosmochimica Acta*, **71**, 4082–4091.

Hahn, O. and Walling, E. (1938) Über die Möglichkeit geologischer Altersbestimmungen rubidiumhaltiger Mineralen and Gesteine. *Zeitschrift Anorganishen Allgemeine Chemie*, **236**, 78–82.

Halliday, A. N. and Lee, D.-C. (1999) Tungsten isotopes and the early development of the Earth and Moon. *Geochimica et Cosmochimica Acta*, **63**, 4157–4179.

Halliday, A. N., Rehkämper, M., Lee, D.-C. and Yi, W. (1996) Early evolution of the Earth and Moon: new constraints from Hf–W isotope geochemistry. *Earth and Planetary Science Letters*, **142**, 75–89.

Harper, C. L. and Jacobsen, S. B. (1996) Evidence for ^{182}Hf in the early solar system and constraints on the timescale of terrestrial core formation. *Geochimica et Cosmochimica Acta*, **60**, 1131–1153.

Hemmendinger, A. and Smythe, W. R. (1937) The radioactive isotope of rubidium. *Physical Review*, **51**, 1052–1053.

Hirt, B., Tilton, G. R. and Hoffmeister, W. (1963) The half-life of ^{187}Re. In *Earth Science and Meteorites*, eds. Geiss, J. and Goldberg, E. D. North-Holland: Amsterdam, pp. 273–280.

Holden, N. E. (1990) Total half-lives for selected nuclides. *Pure and Applied Chemistry*, **62**, 941–958.

Holmes, A. (1946) An estimate of the age of the earth. *Nature*, **157**, 680–684.

Houtermans, F. G. (1946) Die Isotopenhäufigkeiten im natürlichen Blei und das Alter den Urans. *Naturwissenschaften*, **33**, 186–186, 219.

Hsu, W., Guan, Y., Leshin, L. A., Ushikubo, T. and Wasserburg, G. J. (2006) A late episode of irradiation in the early solar system: evidence from extinct ^{36}Cl and ^{26}Al in meteorites. *Astrophysical Journal*, **640**, 525–529.

Hutcheon, I. D., Armstrong, J. T. and Wasserburg, G. J. (1984) Excess ^{41}K in Allende CAI: A hint re-examined (abstr.). *Meteoritics*, **19**, 243–244.

Hutcheon, I. D. and Hutchison, R. (1989) Evidence from the Semarkona ordinary chondrite for ^{26}Al heating of small planets. *Nature*, **337**, 238–241.

Hutcheon, I. D., Krot, A. N., Keil, K., Phinney, D. L. and Scott, E. R. D. (1998) ^{53}Mn/^{53}Cr dating of fayalite formation in the CV3 chondrite Mokoia: evidence for asteroidal alteration. *Science*, **282**, 1865–1867.

Inghram, M. G. (1954) Stable isotope dilution as an analytical tool. *Annual Review of Nuclear Science*, **4**, 81–92.

Jacobsen, S. B. and Wasserburg, G. J. (1980) Sm–Nd isotopic evolution of chondrites. *Earth and Planetary Science Letters*, **50**, 139–155.

Jacobsen, S. B. and Wasserburg, G. J. (1984) Sm–Nd isotopic evolution of chondrites and achondrites. 2. *Earth and Planetary Science Letters*, **67**, 137–150.

Jeffery, P. M. and Reynolds, J. H. (1961) Origin of excess Xe^{129} in stone meteorites. *Journal of Geophysical Research*, **66**, 3582–3583.

Kaiser, T. and Wasserburg, G. J. (1983) The isotopic composition and concentration of Ag in iron meteorites. *Geochimica et Cosmochimica Acta*, **47**, 43–58.

Kita, N., Huss, G. R., Tachibana, S. *et al*. (2005) Constraints on the origin of chondrules and CAIs from short-lived and long-lived radionuclides. In *Chondrites and the Protoplanetary Disk*, eds. Krot, A. N., Scott, E. R. D. and Reipurth, B. ASP Conference Series, Vol. **341**, pp. 558–587.

Kelly, W. R. and Larimer, J. W. (1977) Chemical fractionations in meteorites, VIII. Iron meteorites and the cosmochemical history of the metal phase. *Geochimica et Cosmochimica Acta*, **41**, 93–111.

Kelly, W. R. and Wasserburg, G. J. (1978) Evidence for the existence of ^{107}Pd in the early solar system. *Geophysical Research Letters*, **5**, 1079–1082.

Khoman, T. P. (1954) Geochronological significance of extinct natural radioactivity. *Science*, **119**, 851–852.

Lee, T. and Papanastassiou, D. A. (1974) Mg isotopic anomalies in the Allende meteorite and correlation with O and Sr effects. *Geophysical Research Letters*, **1**, 225–228.

Lee, T., Papanastassiou, D. A. and Wasserburg, G. J. (1977) Aluminum-26 in the early solar system: fossil or fuel? *Astrophysical Journal Letters*, **211**, L107–L110.

Lin, Y. T., Guan, Y. B., Leshin, L. A., Ouyang, Z. Y. and Wang, D. (2005) Short-lived chlorine-36 in a Ca- and Al-rich inclusion from the Ningqiang carbonaceous chondrite. *Proceedings of the National Academy of Sciences of the United States of America*, **102**, 1306–1311.

Lindner, M., Leich, D. A., Russ, G. P., Bazan, J. M. and Borg, R. J. (1989) Direct determination of the half-life of ^{187}Re. *Geochimica et Cosmochimica Acta*, **53**, 1597–1606.

Luck, J.-M. and Allegre, C. J. (1983) ^{187}Re–^{187}O systematics in meteorites and cosmochemical consequences. *Nature*, **302**, 130–132.

Luck, J.-M., Birck, J. L. and Allegre, C. J. (1980) ^{187}Re–^{187}O systematics in meteorites: early chronology of the solar system and age of the galaxy. *Nature*, **283**, 256–259.

Ludwig, K. R. (2003) Isoplot-3.00, a geochronological toolkit for Microsoft Excel. *Berkeley Geochronology Center Special Publication No. 4*, 70 pp.

Lugmair, G. W. and Galer, S. J. G. (1992) Age and isotopic relationships among the angrites Lewis Cliff 86010 and Angra dos Reis. *Geochimica et Cosmochimica Acta*, **56**, 1673–1694.

Lugmair, G. W. and Marti, K. (1977) Sm–Nd–Pu timepieces in the Angra dos Reis meteorite. *Earth and Planetary Science Letters*, **35**, 273–284.

Lugmair, G. W., Scheinin, N. B. and Marti, K. (1975a) Sm–Nd age and history of Apollo 17 basalt 75075: Evidence for early differentiation of the lunar exterior. *Proceedings of the 6th Lunar Science Conference, Geochimica et Cosmochimica Acta Supplement*, **6**, 1419–1429.

Lugmair, G. W., Sheinin, N. B. and Marti, K. (1975b) Search for extinct ^{146}Sm, 1: the isotopic abundance of ^{142}Nd in the Juvinas meteorite. *Earth and Planetary Science Letters*, **27**, 79–84.

Lugmair, G. W. and Shukolyukov, A. (1998) Early solar system timescales according to the ^{53}Mn–^{53}Cr system. *Geochimica et Cosmochimica Acta*, **62**, 2863–2886.

MacPherson, G. J., Davis, A. M. and Zinner, E. (1995) The distribution of ^{26}Al in the early solar system: a reappraisal. *Meteoritics*, **30**, 365–386.

MacPherson, G. J., Huss, G. R. and Davis, A. M. (2003) Extinct ^{10}Be in type A calcium-aluminum-rich inclusions from CV chondrites. *Geochimica et Cosmochimica Acta*, **67**, 3165–3179.

Makashima, A. and Masuda, A. (1993) Primordial Ce isotopic composition of the solar system. *Chemical Geology*, **106**, 197–205.

Marhas, K. K., Goswami, J. N. and Davis, A. M. (2002) Short-lived nuclides in hibonite grains from Murchison: evidence for solar system evolution. *Science*, **298**, 2182–2185.

Mattauch, J. (1937) Das Paar Rb^{87}–Sr^{87} and die Isobarenregel. *Naturwissenschaften*, **25**, 189–191.

McDougall, I. and Harrison, M. T. (1988) *Geochronology and Thermochronology by the $^{40}Ar/^{39}Ar$ method*. Oxford Monographs on Geology and Geophysics No. 9. Oxford: Oxford University Press, 212 pp.

McKeegan, K. D., Chaussidon, M. and Robert, F. (2000) Incorporation of short-lived ^{10}Be in a calcium-aluminum-rich inclusion from the Allende meteorite. *Science*, **289**, 1334–1337.

Meisel, T., Walker, R. J. and Morgan, J. W. (1996) The osmium isotopic composition of the Earth's primitive upper mantle. *Nature*, **383**, 517–520.

Merrihue, C. M. and Turner, G. (1966) Potassium–argon dating by activation with fast neutrons. *Journal of Geophysical Research*, **71**, 2852–2857.

Min, K., Farley, K. A., Renne, P. R. and Marti, K. (2003) Single-grain (U–Th)/He ages from phosphates in Acapulco meteorite and implications for thermal history. *Earth and Planetary Science Letters*, **209**, 323–336.

Minster, J. F. and Allegre, C. J. (1981) ^{87}Rb–^{87}Sr dating of LL chondrites. *Earth and Planetary Science Letters*, **5**, 361–376.

Misawa, K., Shih, C.-Y., Reese, Y., Bogard, D. D. and Nyquist, L. E. (2006) Rb–Sr, Sm–Nd and Ar–Ar isotopic systematics of Martian dunite Chassigny. *Earth and Planetary Science Letters*, **246**, 90–101.

Mostefaoui, S., Lugmair, G. W. and Hoppe, P. (2005) ^{60}Fe: a heat source for planetary differentiation from a nearby supernova explosion. *Astrophysical Journal*, **625**, 271–277.

Murty, S. V. S., Goswami, J. N. and Shukolyukov, Y. A. (1997) Excess Ar-36 in the Efremovka meteorite: a strong hint for the presence of Cl-36 in the early solar system. *Astrophysical Journal Letters*, **475**, L65–L68.

Nakai, S., Masuda, A., and Lehmann, B. (1988) La–Ba dating of bastnaesite. *American Mineralogist*, **73**, 1111–1113.

Nichols, R. H., Hohenberg, C. M., Kehm, K., Kim, Y. and Marti, K. (1994) I–Xe studies of the Acapulco meteorite: Absolute ages of individual phosphate grains and the Bjurböle standard. *Geochimica et Cosmochimica Acta*, **58**, 2523–2561.

Nier, A. O. (1935) Evidence for the existence of an isotope of potassium of mass 40. *Physical Review*, **48**, 283–284.

Nier, A. O. (1939a) The isotopic composition of uranium and the half-lives of uranium isotopes. *Physical Review*, **55**, 150–153.

Nier, A. O. (1939b) The isotopic constitution of radiogenic leads and the measurement of geological time. II. *Physical Review*, **55**, 153–163.

Nier, A. O. (1950) A redetermination of the relative abundances of the isotopes of carbon, nitrogen, oxygen, argon, and potassium. *Physical Review*, **77**, 793–798.

Nyquist, L. E., Bogard, D. D., Shih, C.-Y. *et al*. (2001b) Ages and geologic histories of Martian meteorites. *Space Science Reviews*, **96**, 105–164.

Nyquist, L. E., Kleine, T., Shih, C.-Y. and Reese, Y. D. (2009) The distribution of short-lived radioisotopes in the early solar system and the chronology of asteroid accretion,

differentiation, and secondary mineralization. *Geochimica et Cosmochimica Acta*, **73**, 5115–5136.

Nyquist, L., Lindstrom, D., Mittlefehldt, D. *et al*. (2001c) Manganese–chromium formation intervals for chondrules from the Bushunpur and Chainpur meteorites. *Meteoritics and Planetary Science*, **36**, 911–938.

Papanastassiou, D. A. and Wasserburg, G. J. (1969) Initial strontium isotopic abundances and the resolution of small time differences in the formation of planetary objects. *Earth and Planetary Science Letters*, **5**, 361–376.

Papanastassiou, D. A. and Wasserburg, G. J. (1971) Rb–Sr ages of igneous rocks from the Apollo 14 mission and the age of the Fra Mauro Formation. *Earth and Planetary Science Letters*, **12**, 36–48.

Papanastassiou, D. A., Wasserburg, G. J., and Burnett, D. S. (1970) Rb–Sr ages of lunar rocks from the Sea of Tranquility. *Earth and Planetary Science Letters*, **8**, 1–19.

Patchett, P. J. and Tatsumoto, M. (1980) Lu–Hf total-rock isochron for eucrite meteorites. *Nature*, **288**, 571–574.

Patterson, C. C. (1955) The Pb^{207}/Pb^{206} ages of some stone meteorites. *Geochimica et Cosmochimica Acta*, **7**, 151–153.

Patterson, C. C. (1956) Age of meteorites and the Earth. *Geochimica et Cosmochimica Acta*, **10**, 230–237.

Prinzhofer, A., Papanastassiou, D. A. and Wasserburg, G. J. (1992) Samarium–neodymium evolution of meteorites. *Geochimica et Cosmochimica Acta*, **56**, 797–815.

Reynolds, J. H. (1960a) Determination of the age of the elements. *Physical Reviews Letters*, **4**, 8–10.

Reynolds, J. H. (1960b) Isotopic composition of xenon from enstatite chondrites. *Zeitschrift für Naturforschung*, **15a**, 1112–1114.

Sahijpal, S., Goswami, J. N., Davis, A. M., Grossman, L. and Lewis, R. S. (1998) A stellar origin for the short-lived nuclides in the early solar system. *Nature*, **391**, 559–561.

Schönbächler, M., Carlson, R. W., Horan, M. F., Mock, T. D. and Hauri, E. H. (2008) Silver isotope variations in chondrites: Volatile depletion and the initial ^{107}Pd abundance of the solar system. *Geochimica et Cosmochimica Acta*, **72**, 5330–5341.

Schumacher, E. (1956) Alterbestimmung von Steinmeteoriten mit der Rubidium–Strontium-Methode. *Zeitschrift für Naturforschung*, **11a**, 206.

Shen, J. J., Papanastassiou, D. A. and Wasserburg, G. J. (1996) Precise Re–Os determinations and systematics of iron meteorites. *Geochimica et Cosmochimica Acta*, **60**, 2887–2900.

Shih, C.-Y., Nyquist, L. E. and Wiesmann, H. (1994) K–Ca and Rb–Sr dating of two lunar granites: relative chronometer resetting. *Geochimica et Cosmochimica Acta*, **58**, 3101–3116.

Shimizu, N., Semet, M. P. and Allegre, C. J. (1978) Geochemical applications of quantitative ion microprobe analysis. *Geochimica et Cosmochimica Acta*, **42**, 1321–1334.

Shirey, S. B and Walker, R. J. (1995) Carius tube digestions for low-blank rhenium–osmium analysis. *Analytical Chemistry*, **67**, 2136–2141.

Shirey, S. B. and Walker, R. J. (1998) The Re–Os isotope system in cosmochemistry and high-temperature geochemistry. *Annual Reviews of Earth and Planetary Science*, **26**, 423–500.

Shukolyukov, A. and Begemann, F. (1996) Pu–Xe dating of eucrites. *Geochimica et Cosmochimica Acta*, **60**, 2454–2471.

Shukolyukov, A. and Lugmair, G. W. (1993a) Live iron-60 in the early solar system. *Science*, **259**, 1138–1142.

Shukolyukov, A. and Lugmair, G. W. (1993b) ^{60}Fe in eucrites. *Earth and Planetary Science Letters*, **119**, 159–166.

Smoliar, M. I., Walker, R. J. and Morgan, J. W. (1996) Re–Os ages of Groups IIA, IIIA, IVA, and IVB iron meteorites. *Science*, **271**, 1099–1102.

Smythe, W. R. and Hemmendinger, A. (1937) The radioactive isotope of potassium. *Physical Review*, **51**, 178–182.

Srinivasan, G., Sahijpal, S., Ulyanov, A. A. and Goswami, J. N. (1996) Ion microprobe studies of Efremovka CAIs: II. Potassium isotope compositions and ^{41}Ca in the early solar system. *Geochimica et Cosmochimica Acta*, **60**, 1823–1835.

Srinivasan, G., Ulyanov, A. A. and Goswami, J. N. (1994) ^{41}Ca in the early solar system. *Astrophysical Journal*, **431**, L67–L70.

Steiger, R. H. and Jäger, E. (1977) Subcommission on geochronology: Convention on the use of decay constants in geo- and cosmochronology. *Earth and Planetary Science Letters*, **36**, 359–362.

Stewart, B. W., Papanastassiou, D. A. and Wasserburg, G. J. (1994) Sm–Nd chronology and petrogenesis of mesosiderites. *Geochimica et Cosmochimica Acta*, **58**, 3487–3509.

Stirling, C. H., Halliday, A. M. and Porcelli, D. (2005) In search of live ^{247}Cm in the early solar system. *Geochimica et Cosmochimica Acta*, **69**, 1059–1071.

Tachibana, S. and Huss, G. R. (2003) The initial abundance of ^{60}Fe in the solar system. *Astrophysical Journal Letters*, **588**, L41–L44.

Tachibana, S., Huss, G. R., Kita, N. T., Shimoda, G. and Morishita, Y. (2006) ^{60}Fe in chondrites: Debris from a nearby supernova in the early solar system? *Astrophysical Journal Letters*, **639**, L87–L90.

Tanaka, T. and Masuda, A. (1982) The La–Ce geochronometer. A new dating method. *Nature*, **300**, 515–517.

Tera, F. and Carlson, R. W. (1999) Assessment of the Pb–Pb and U–Pb chronometry of the early solar system. *Geochimica et Cosmochimica Acta*, **63**, 1877–1889.

Tera, F. and Wasserburg, G. J. (1972) U–Th–Pb systematics in three Apollo 14 basalts and the problem of initial Pb in lunar rocks. *Earth and Planetary Science Letters*, **14**, 281–304.

Tera, F. and Wasserburg, G. J. (1974) U–Th–Pb systematics on lunar rocks and inferences about lunar evolution and the age of the Moon. *Proceedings of the 5th Lunar Science Conference, Geochimica et Cosmochimica Acta Supplement*, **5**, 1571–1599.

Thrane, K., Bizzarro, M. and Baker, J. A. (2006) Extremely brief formation interval for refractory inclusions and uniform distribution of Al-26 in the early solar system. *Astrophysical Journal*, **646**, L159–162.

Turner, G., Huneke, J. C., Podosek, F. A. and Wasserburg, G. J. (1971) ^{40}Ar–^{39}Ar ages and cosmic-ray exposure ages of Apollo 14 samples. *Earth and Planetary Science Letters*, **12**, 19–35.

Urey, H. C. (1955) The cosmic abundances of potassium, uranium and thorium and the heat balances of the Earth, the Moon and Mars. *Proceedings of the National Academy of Sciences of the United States of America*, **41**, 127–144.

Völkening, J., Köppe, M., and Heumann, K. G. (1991) Tungsten isotope ratio determinations by negative thermal ionization mass spectrometry. *International Journal of Mass Spectrometry and Ion Processes*, **107**, 361–368.

Wadhwa, M., Zinner, E. and Crozaz, G. (1997) Mn–Cr systematics in sulfides of unequilibrated enstatite chondrites. *Meteoritics and Planetary Science*, **32**, 281–292.

Walker, R. J., Morgan, J. W., Beary, E. S. *et al*. (1997) Application of the ^{190}Pt–^{186}Os isotope system to geochemistry and cosmochemistry. *Geochimica et Cosmochimica Acta*, **61**, 4799–4807.

Wasserburg, G. J. and Hayden, R. J. (1955) Age of meteorites by the A^{40}–K^{40} method. *Physical Review*, **97**, 86–87.

Wetherill, G. W. (1956) Discordant uranium–lead ages. *Transactions: American Geophysical Union*, **37**, 320–326.

Wetherill, G. W., Aldrich, L. T. and Davis, G. L. (1955) A^{40}/K^{40} ratios of feldspars and micas from the same rock. *Geochimica et Cosmochimica Acta*, **8**, 171–172.

Williamson, J. H. (1968) Least-squares fitting of a straight line. *Canadian Journal of Physics*, **46**, 1845–1847.

York, D. (1966) Least-squares fitting of a straight line. *Canadian Journal of Physics*, **44**, 1079–1086.

York, D. (1969) Least squares fitting of a straight line with correlated errors. *Earth and Planetary Science Letters*, **5**, 320–324.

9 Chronology of the solar system from radioactive isotopes

Overview

In this chapter, we review what is known about the chronology of the solar system, based on the radioisotope systems described in Chapter 8. We start by discussing the age of materials that formed the solar system. Short-lived radionuclides also provide information about the galactic environment in which the solar system formed. We then consider how the age of the solar system is estimated from its oldest surviving materials – the refractory inclusions in chondrites. We discuss constraints on the accretion of chondritic asteroids and their subsequent metamorphism and alteration. Next, we discuss the chronology of differentiated asteroids, and of the Earth, Moon, and Mars. Finally, we consider the impact histories of the solar system bodies, the timescales for the transport of meteorites from their parent bodies to the Earth, and the residence time of meteorites on the Earth's surface before they disintegrate due to weathering.

Age of the elements and environment in which the Sun formed

The presence of radioactive isotopes in meteorites and planets demonstrates that the atoms that make up our solar system are not infinitely old. On the other hand, the abundance ratios for radioactive species, such as $^{235}U/^{238}U$, in the solar system when it formed were much lower than the ratios in which they were produced at the stellar source, as determined from detailed nucleosynthesis models. This indicates that these isotopes were not produced at the time of solar system formation. For example, the production ratio for $^{235}U/^{238}U$ is ~1.79, but the ratio inherited by the solar system was ~0.31. Clearly much of the ^{235}U ($t_{1/2} = 7.04 \times 10^8$ years) originally produced with the ^{238}U ($t_{1/2} = 4.47 \times 10^9$ years) had decayed away before the solar system formed. It is not possible to estimate the age of the elements from ratios like this alone, because nucleosynthesis was not a discrete event in time. We must be able to model stellar nucleosynthesis as a function of time, and this in turn requires knowledge of the physical evolution of the galaxy. Evaluation of the relative abundances of various long-lived radiochronometers indicates that nucleosynthesis began at between 12 and 18 Ga. This is broadly consistent with the age of the galaxy as determined by independent means.

By fixing the age of the galaxy in the models, useful information can be extracted about the radioactive isotopes inherited by our solar system. We now describe a standard model for nucleosynthesis in the galaxy and its implications for the early solar system.

The age of the Milky Way galaxy is ~12 Ga. The elements that make up our solar system were synthesized in stars over ~7.5 Gyr of galactic history prior to the formation of the solar system. Star formation apparently started almost as soon as the galaxy began to form, and once the galactic disk formed, the rate of star formation closely tracked the mass of the gas. The IMF (Chapter 3) shows that in a single episode of star formation, many more low-mass stars form than high-mass stars. Because the lifetime of a star is a strong function of its mass, nucleosynthesis early in galactic history was dominated by massive stars, and the contributions of less massive stars have increased with time. This, along with the increase in overall metallicity with time, resulted in shifts in the isotopic compositions of the elements in the galaxy. Because the ratio of nucleosynthesis tracks the mass of the gas, and because the mass of gas is higher in the center of the galaxy, there are gradients in metallicity and in isotopic compositions with radius in the galaxy. We will therefore construct our model considering an annulus of the galaxy centered on the solar radius.

Many discussions of the galaxy assume that it started out with essentially its current mass. However, a more realistic view is that the galactic mass built up over time through the infall of metal-free gas and assimilation of smaller galaxies. Much of the buildup appears to have occurred relatively early, but the galaxy took some time to reach its current mass. We know this because there are too few low-mass metal-poor stars for the galaxy to have had its present mass at 12 Ga.

The mass of gas at any time in the galaxy is a function of the rate of infall of new gas from the outside, the sequestration of gas into low-mass stars and stellar remnants, and the input of newly synthesized material from dying stars. Figure 9.1 shows a "closed box" model in which infall is set to zero and the galaxy starts with its current mass. The mass of gas declines with time due to sequestration in stars until it reaches the currently observed value of ~10% of the total mass. Figure 9.2 shows a more plausible model in which the galaxy builds up from infalling metal-poor gas. The initial infall rate is high and decreases slowly with time. The mass of gas peaks after a few Gyr and then declines because star formation sequesters gas faster than new gas is added from the outside.

When were the atoms that became our solar system synthesized? The star formation rate in the galaxy was highest early in galactic history and a lot of heavy elements were produced. However, most of this material was subsequently incorporated into stars, and much of that has been "permanently" sequestered. On the other hand, much of the recently synthesized material has not yet been incorporated into a new generation of stars. This balance between synthesis and sequestration means that the birth dates of the elements that became the solar system are roughly evenly distributed over the 7.5 Gyr of galactic history prior to the solar system's birth (Clayton, 1988).

The abundances of radioactive isotopes over time in the galaxy can be modeled based on the above considerations. With an approximately constant production rate, the abundance of a stable nuclide will grow and will be proportional to the time over which it has been produced. In contrast, the abundance of a radionuclide will reach a steady state between production and decay in about eight mean lifetimes. (We will use mean life (τ) instead of

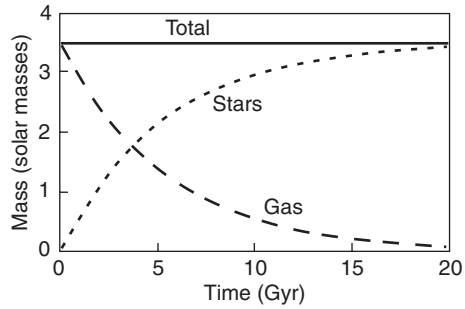

Fig. 9.1 "Closed box" model for the mass of the galaxy and the distribution of mass between stars and gas as a function of time. The mass of gas is constrained to match the currently observed value of ~10%.

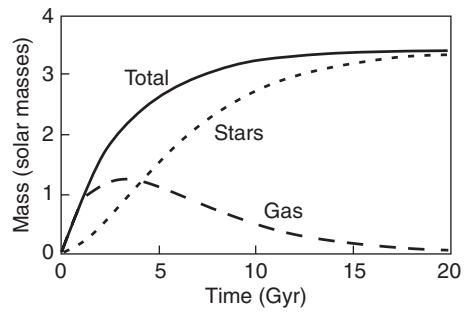

Fig. 9.2 More general model for the mass of the galaxy and the distribution of mass between stars and gas as a function of time. This model includes infall of metal-poor gas onto the galactic disk, sequestration of gas in stellar remnants, and return of newly synthesized elements from stars. The mass of gas is constrained to match the currently observed value of ~10%.

half-life in this discussion because the mathematics is cleaner. Remember that $\tau = t_{1/2}/\ln 2$.) This is because the abundance of the radionuclide is controlled by the amount produced during the last mean life. Figure 9.3 shows these two individual trends with time (in units of mean life) along with the trend for the ratio of the radionuclide to the stable nuclide, which decreases with time. A changing production rate has only a second-order effect on the abundance ratio. Figure 9.4 shows a hypothetical abundance ratio normalized to the production rate for the case of constant production rate (same as Fig. 9.3), an increasing production rate, and a decreasing production rate. Note that except for the special case of a rapidly increasing production rate, the curves all decrease with time.

We can now construct a model that describes the evolution of the abundances of stable and radioactive isotopes in the gas phase of the galaxy as a function of time. Such as model provides an estimate of the abundances of the radioactive nuclides that should have been available in the average interstellar medium at the time the solar system formed. By comparing these predictions with the abundances inferred for the early solar system from meteorites, we can investigate the environment in which the solar system formed.

Figure 9.5 compares the abundance ratios of short-lived radionuclides in the early solar system to the abundance ratios predicted by a standard model for galactic chemical

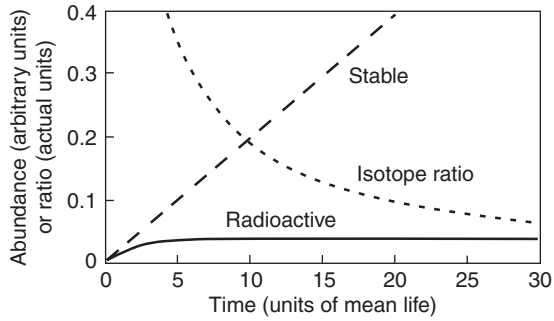

Fig. 9.3 Abundances of hypothetical stable and radioactive nuclides as a function of time when both are produced at the same rate. The abundance of the stable isotope increases continuously, but the abundance of the radioactive isotope reaches a steady state. Thus, the ratio of the radioactive to stable isotope decreases with time from the production ratio (in this case 1).

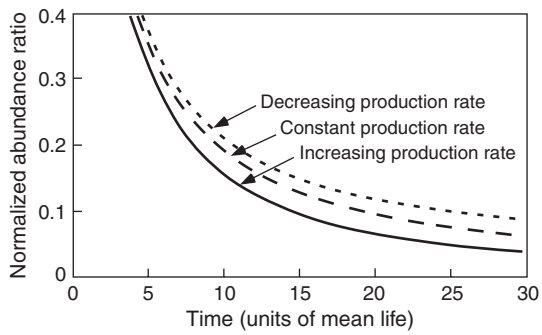

Fig. 9.4 When the abundance ratio in Figure 9.3 is normalized to production rate, the second-order effect of a changing production rate is seen. A constant production rate gives the same curve as in Fig. 9.3. But because the abundance of the radioactive species only reflects production during the last mean life, an increasing production rate results in a lower integrated ratio because more stable nuclide has been produced overall than in the constant-production-rate case. Conversely, a decreasing production rate results in a higher integrated ratio because less stable nuclide has been produced overall than in the constant-production-rate case.

evolution. The x-axis of the plot is the mean life (τ) of the radionuclide. Note that the axis does not extend beyond 10^9 years. The y-axis is the abundance ratio of the radionuclide to a stable nuclide of the same or closely related element (Table 8.8), normalized to the production ratios of the same isotopes. Let's first consider the lines on the diagram – the predictions of the model.

The straight solid line in Figure 9.5 represents the average, steady-state abundances of the radionuclides at a galactic age of 7.5 Ga, when the solar system formed. For times that are much longer than the mean lifetimes of the short-lived radionuclides, the slope of this line is given by the mean life, τ, divided by the galactic age, t. As the mean life approaches t, the steady-state abundance falls below the τ/t line and the trend asymptotically approaches the effective production ratio ($y = 1$ on this plot). The vertical position of this line and the curves derived from it depend on our choice of t.

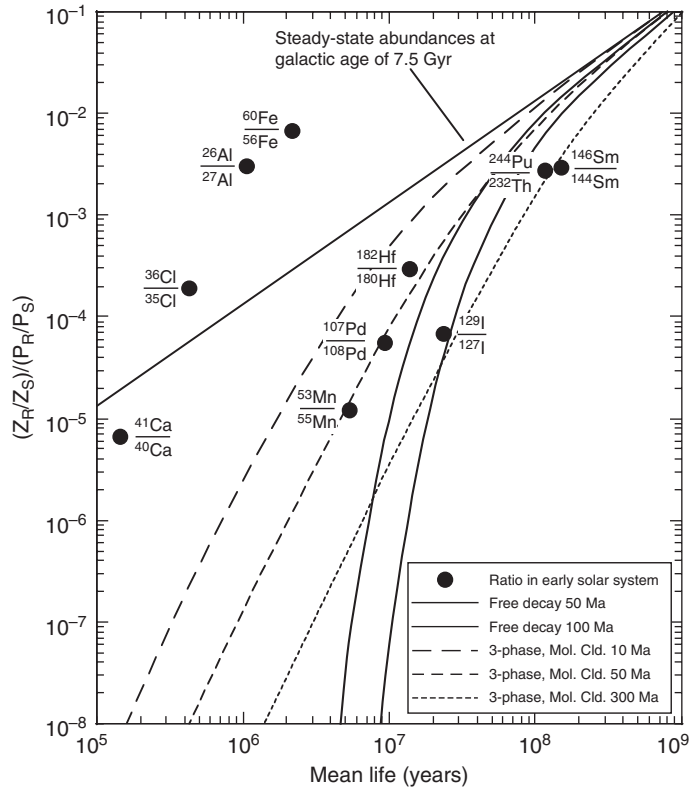

Fig. 9.5 **Abundances of short-lived nuclides in the early solar system compared to abundances predicted by different models for the interstellar medium. The y-axis is the abundance ratio for a short-lived nuclide divided by its effective production ratio. For times long with respect to the mean life (τ), the=abundance ratios normalized to their production ratios plot on a straight line with slope τ/t. This line can be considered to represent the average interstellar medium. For nuclides with longer mean lives, the straight line begins to curve because there has not been enough time to establish a steady state. But these steady-state ratios are not the ratios that would be inherited by a newly forming star. Two models for those ratios are shown by the solid and dashed curves (see text for explanation). The model curves show that nuclides with mean lives <5 Myr can be explained by the galactic background of short-lived nuclides, but those with shorter mean lives (^{41}Ca, ^{36}Cl, ^{26}Al, and ^{60}Fe) require a late addition of newly synthesized material. Adapted from Huss *et al.* (2009).**

When ^{129}I was first shown by John Reynolds to be present in the early solar system (Reynolds, 1960), he quickly realized that the inferred initial ratio for the solar system ($\sim 1 \times 10^{-4}$) was well below that expected from stellar nucleosynthesis (~1). He proposed a period of free decay between the last input of newly synthesized material and the formation of the solar system to explain the low observed ratio and estimated the free decay time at $\sim 3 \times 10^8$ years. As more realistic models of the expected abundances of radionuclides in interstellar space were developed, this interval decreased to $\sim 10^8$ years. The curved solid lines in Figure 9.5 show the effect on the steady-state abundances of short-lived radionuclides of free decay intervals of 5×10^7 and 10^8 years. Nuclides with mean lives of less than ~5 Myr would have completely decayed away. Thus, when Lee *et al.* (1977) discovered ^{26}Al and

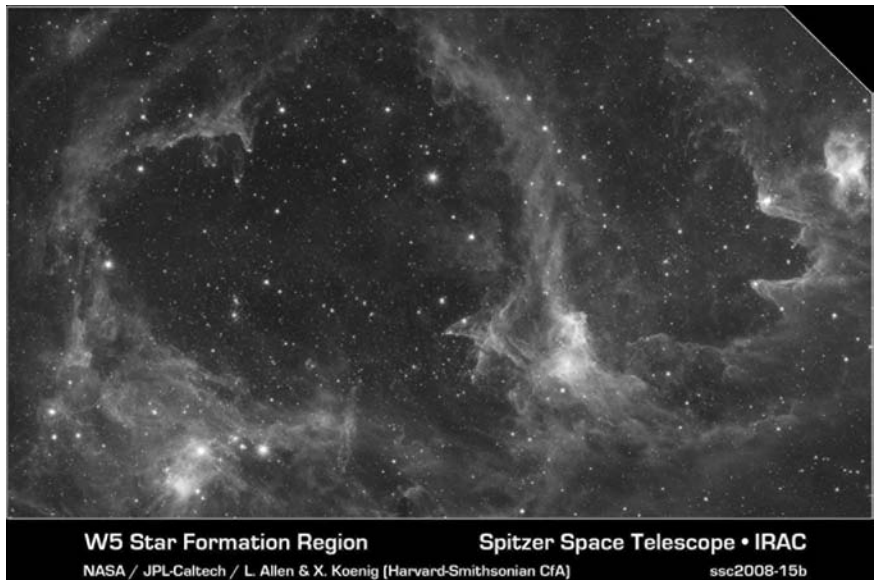

Fig. 9.6 Spitzer space telescope image of a star-forming region in the constellation Cassiopeia. Wispy molecular clouds surround cavities carved out by radiation from the region's most massive stars. The winds push the molecular cloud gas together, potentially triggering star formation. White knotty areas are regions where the youngest stars are forming.

inferred an initial $^{26}Al/^{27}Al$ abundance ratio of 5.1×10^{-5} (see Chapter 8), they were forced to conclude that ^{26}Al had been synthesized immediately before or during the formation of the solar system. Models of stellar nucleosynthesis and of local irradiation in the solar system were investigated to understand how the ^{26}Al was produced, and very quickly a standard model of solar system formation emerged. In this model, the gravitational collapse of the solar system was triggered by a supernova explosion, which also supplied ^{26}Al (and other isotopes) to the early solar system (Cameron and Truran, 1977).

New generations of telescopes have now revealed a tremendous amount about the structure of the interstellar medium (Fig. 9.6). In a classic paper, McKee and Ostriker (1977) described a three-phase interstellar medium regulated by supernova explosions. An adaptation of this model (Clayton, 1988) considers the interstellar medium to consist of three phases: (1) molecular clouds from which stellar systems form; (2) large HI (neutral H) clouds that are too large to be evaporated by supernova shocks; and (3) smaller HI clouds that can be evaporated by supernova shocks along with the surrounding hot medium. Newly synthesized material is injected primarily into the hot medium and mixes into the large neutral clouds and then into the dense molecular clouds on timescales of 10^7 to 10^8 years. In this picture, the so-called free-decay interval is actually the time it takes on average for newly synthesized matter to be distributed through the three phases in the ISM and to become available for incorporation into a stellar system. The dashed lines in Figure 9.5 show the abundances of short-lived radionuclides that would be present in molecular clouds based on a three-phase model. The three lines assume different times for mixing between the phases. The hot medium would plot on a nearly horizontal line near the top of the diagram,

and the large neutral clouds would plot near, but perhaps slightly above, the line for steady-state abundances.

The model abundances for molecular clouds shown in Figure 9.5 are broadly consistent with the early solar system abundances of short-lived radionuclides with mean lives $\geq$5 Myr. For these isotopes, the choice of model plays a critical role in determining whether or how much of a late injection is required. But no version of this model can explain the abundances of ^{41}Ca, ^{36}Cl, ^{26}Al, and ^{60}Fe in the early solar system. A source for these isotopes just before or during solar system formation is required. The large excess of ^{60}Fe, which can only be produced in stars, relative to the models implicates a stellar source, most probably a supernova (discussed more thoroughly in Chapter 14).

The three-phase model for the abundances of short-lived radionuclides in the interstellar medium illustrates the stochastic nature of nucleosynthesis. Stars inject newly synthesized matter into the interstellar medium at discrete times. Between injections, the radionuclides in the interstellar medium decay, and if a longer than average time passes, the abundances can locally drop well below the steady-state line for the galaxy as a whole. When a supernova injects newly synthesized material into the interstellar medium, the local abundances are dramatically higher than the average for the interstellar medium as a whole (the straight solid line on Figure 9.5). But this material is not easily available for incorporation to a newly forming star because of its high temperature (>10^6 K). This hot gas interacts with cold molecular clouds across a shock front. A shock front is characterized by an abrupt, nearly discontinuous change in properties, such as temperature, pressure, and density. Efficient mixing only occurs when the gas cools and the shock front dissipates. This takes a long time for very hot gas because it has no efficient way of radiating thermal energy. On timescales of a few million years, the hot gas can cool and mix with molecular cloud gas, producing material enriched in newly synthesized radionuclides compared to the matter in the cloud prior to mixing. If several supernovae explode relatively close together in time and space, molecular clouds in that region of the galaxy may be enriched relative to the average steady-state abundances in molecular clouds (dashed lines in Figure 9.5). Such "self-enrichment" may be a feature of molecular clouds undergoing star formation. However, the timescale for exchange of matter between phases to form a molecular cloud and for that cloud to generate a new generation of stars means that self-enrichment is unlikely to be the explanation for solar system abundances.

Comparing the relative abundances of short-lived nuclides in the solar system with those predicted by stellar models can provide a constraint on the nature of the stellar source. Based on these considerations, supernovae do the best job of matching solar system abundances, except that they overproduce ^{53}Mn. This problem may be overcome by permitting the ejecta to mix and to have some of it fall back onto the stellar remnant, thereby sequestering much of the ^{53}Mn in the remnant. Supernovae are typically found in star-forming regions because their progenitors are massive stars whose lifetimes are on the order of a few million years, too short for them to drift away from the region where they formed before they explode. In fact, star formation in molecular clouds is typically terminated when the intense stellar winds and radiation of massive stars and their subsequent supernova explosions disperse the cloud. An AGB star of 5–8 $M_\odot$ is a potential source based on matching stellar yields to solar system abundances. But the probability of the newly forming solar system encountering an

AGB star of the right mass in the right stage of its evolution is extremely small. Most researchers currently favor a supernova source for the short-lived nuclides in the early solar system.

What about the environment where the solar system formed? Two types of environments can be envisioned, regions like Taurus, where stars appear to be forming in near isolation, and regions like Orion, where a large number of stars are forming almost simultaneously in what is known as cluster star formation. In such an environment, a burst of star formation can locally disburse a region of a giant molecular cloud while at the same time compressing a nearby region and triggering a new burst of star formation. Lada and Lada (2003) estimated that 70–90% of all stars form in regions of cluster star formation. Thus, based on simple probabilities, it is likely that the Sun formed in a region of cluster star formation. A supernova source for the short-lived radionuclides in the early solar system is quite consistent with this conclusion.

Before closing this section, it is worth mentioning that the γ-rays from the decay of ^{26}Al and ^{60}Fe have been observed in interstellar space using the Compton orbiting observatory and INTEGRAL satellite. These observations can provide ground truth for models of nucleosynthesis in the galaxy. The measurements indicate that there are 2.8±0.8 $M_\odot$ of ^{26}Al in the galaxy. Cosmochemists do not know what to do with solar masses of ^{26}Al; we much prefer to discuss the ^{26}Al/^{27}Al ratio. Converting solar masses of ^{26}Al to a ratio is potentially a problem because we need to know the abundance of ^{27}Al, which is not directly measurable. Published estimates of the ^{26}Al/^{27}Al ratio in the galaxy assume that the galaxy has the metallicity and composition of the solar system. Scaling to the mass of the galaxy gives a mass of ^{27}Al and produces a ^{26}Al/^{27}Al ratio of ~8.4×10^{-6} (Diehl *et al*., 2006). A similar calculation for ^{60}Fe based on the observed flux ratio of 0.148 (Wang *et al*., 2007), equivalent to an ^{60}Fe/^{26}Al abundance ratio of 0.31, gives a ^{60}Fe/^{56}Fe ratio for the galaxy of 2.7×10^{-7}. However, there are two problems with these calculations. First, the galaxy has evolved for ~4.57 Gyr since the solar system formed, and as we have already discussed, the abundance ratios of short-lived nuclides to stable isotopes of the same element decrease with time due to production of the stable nuclides. Thus, the current ^{26}Al/^{27}Al and ^{60}Fe/^{56}Fe ratios must be lower than the published numbers. Huss *et al*. (2009) estimated the effects of 4.57 Gyr of evolution on the ^{27}Al and ^{56}Fe abundances using a galactic chemical evolution model. Using the higher abundances of ^{27}Al and ^{56}Fe, they calculated that the observed abundances imply that the present ratios should be ^{26}Al/^{27}Al $\approx 4 \times 10^{-6}$ and ^{60}Fe/^{56}Fe $\approx 4.4 \times 10^{-8}$, significantly lower than the published numbers. Clearly, galactic chemical evolution must be considered when modeling the abundance ratios for radioactive nuclides.

Age of the solar system

In order to determine the age of the solar system, we must first decide what is really meant by its age. Astronomers and theoreticians tell us that the process of forming a star from a dense core of gas and dust in a molecular cloud takes on the order of a few million years. The process can be divided into four stages that are defined by the characteristics of four classes

of observed stellar objects (Fig. 9.7). *Class 0* objects are young protostars in the early main accretion phase. A hydrostatic core has formed, surrounded by a dense accretion disk, but the core has not yet accreted the majority of its final mass. At this stage the stars are embedded in optically thick dust clouds and are observed in re-radiated energy at sub-millimeter wavelengths. These objects have bipolar outflows and suffer periodic outbursts during which the mass ejection rate in the outflows increases by several orders of magnitude. Each outburst may last only a few years, and they been given the name "FU-Orionis outbursts" after the star in which they were first observed. This stage lasts 10 000 to 30 000 years. *Class I* objects are protostars in the late accretion phase. These objects are embedded in less-dense dust and are observed by re-radiated emission in the infrared.

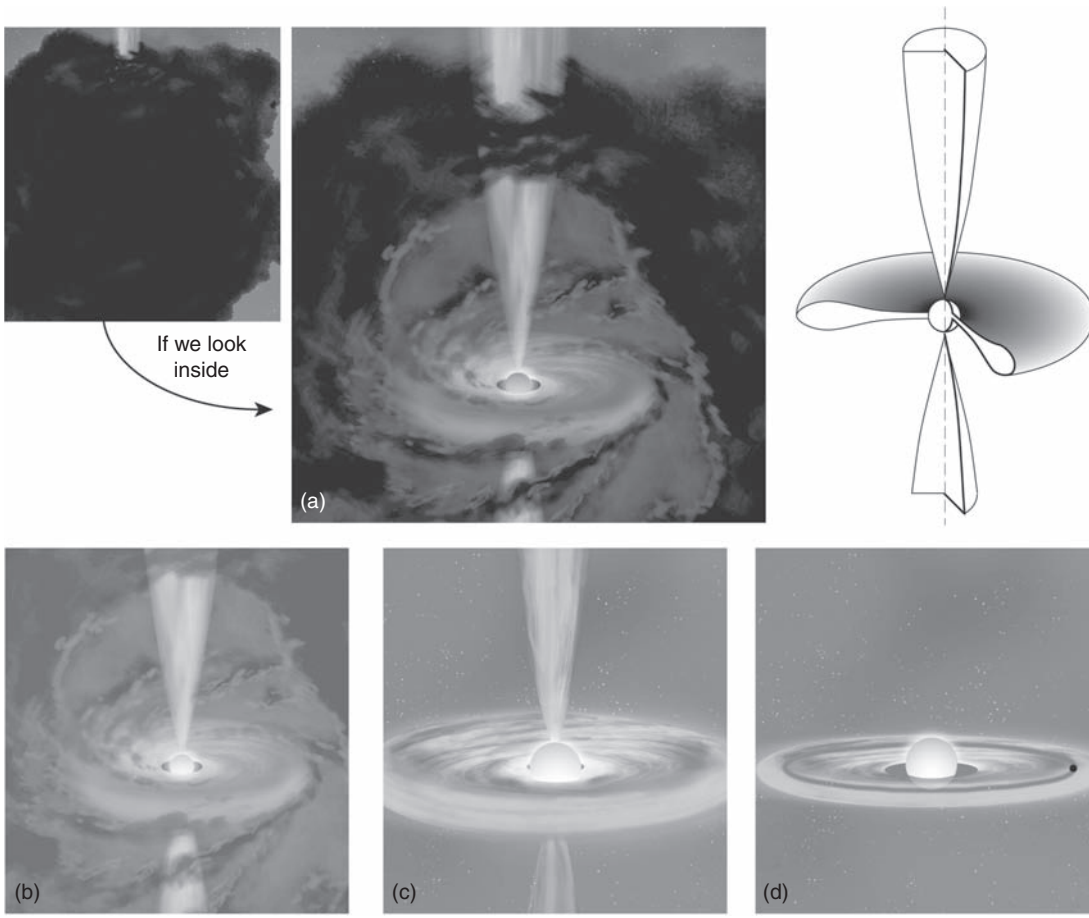

Fig. 9.7 Artistic rendering of four observed stages of star formation. (a) Class 0 object: a deeply embedded hydrostatic core surrounded by a dense accretion disk. Strong bipolar jets remove angular momentum. (b) Class I object: protostar in the later part of the main accretion phase. (c) Class II object or T Tauri star: pre-main-sequence star with optically thick protoplanetary disk. (d) Class III object or naked T Tauri star: star has an optically thin disk and thus can be directly observed. Some may have planets.

Class I objects also have bipolar outflows, but they are less powerful and less well collimated than those of Class 0 objects. This stage lasts 100 000 to 200 000 years. *Class II* objects, also known as classical T Tauri stars, are pre-main-sequence stars with optically thick protoplanetary disks. They are no longer embedded in their parent cloud, and they are observed in optical and infrared wavelengths. They still exhibit bipolar outflows and strong stellar winds. This stage lasts from 1–10 million years. *Class III* objects are the so-called "weak line" or "naked" T-Tauri stars. They have optically thin disks, perhaps debris disks in some cases, and there are no outflows or other evidence of accretion. They are observed in the visible and near infrared and have strong X-ray emission. These stars may have planets around them, although they cannot be observed.

Cosmochemists have access to a variety of samples from the earliest history of our solar system, including CAIs, chondrules, and matrix from primitive chondrites and interplanetary dust from comets. Using a combination of long-lived and short-lived chronometers we can determine which of these is the oldest and can estimate its absolute age. But at the moment, we have no way of connecting the astronomers' stellar stages with the cosmochemical timescale. Gravitational collapse of a portion of a molecular cloud is not a datable event. Did the objects whose ages we measure form when the Sun was a Class 0, Class I, or Class II object? All of these are plausible. In the Class 0 stage, the Sun was very energetic and disk temperatures near the Sun were high, perhaps suitable for making CAIs and chondrules, but the material in the disk at this stage was rapidly accreting onto the star and may not have survived to enter the meteorites. During the Class I stage, the accretion disk was more stable, but the temperatures in the disk, particularly farther out in the disk where the meteorites formed, were probably relatively low. We do not know how CAIs and chondrules formed, but this stage would seem to require transient high-temperature events that have not been directly observed. Stage II is also a plausible time for the formation of the components of chondrites. It is likely that the meteorites represent the end stages of accretion disk evolution. The records of earlier events may have been wiped out by accretion of their products onto the Sun. It is probable that by the time the Sun was a Class III star, asteroids and planets had already formed. For the moment, we must acknowledge that we cannot connect the astronomical and cosmochemical timescales and simply do the best we can to accurately date the materials we have.

The tools that we have to determine the age of the solar system and the chronology of early solar system materials are the long-lived and short-lived radiochronometers discussed in Chapter 8. The long-lived radionuclides tell us that the oldest objects in the solar system formed at ~4.5–4.6 Ga (Fig. 9.8). But the precision of most of these measurements is not sufficient to investigate the details of those early times. In addition, there are uncertainties in the half-lives of the different radionuclides that translate into absolute uncertainties of several million to tens of millions of years. Short-lived radionuclides provide the time resolution necessary to unravel the details of early solar system history.

Several isotope systems indicate that CAIs are the oldest objects to have formed in the solar system. Cosmochemists have adopted their formation age as the age of the solar system. Based on a combination of data from the Pb–Pb and ^{182}H–^{182}W systems (see below), we assign an age for the CAIs of 4568.2±0.5 Ma. To this precise age, we must add an absolute uncertainty of ~0.2% (9 Myr at the age of the solar system) because of

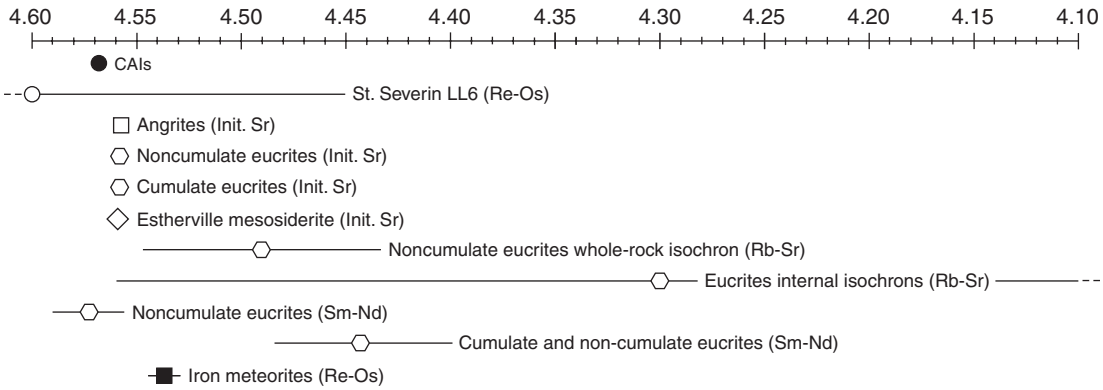

Fig. 9.8 **Formation ages and crystallization ages (given in Ga, at the top of the figure) of various objects as determined by long-lived radiochronometers. The initial strontium isotopic ratio is inherently precise, but a large systematic uncertainty in the half-life gives absolute age determinations relatively large uncertainties. Initial strontium data for eucrites and angrites support the inference from short-lived nuclides that the parent bodies accreted very early. ^{187}Rb–^{187}Sr and ^{147}Sm–^{143}Nd isochron ages indicate that magmatism on the eucrite parent body continued for several hundred Myr. Data from Smoliar (1993), Shen *et al.* (1996), Chen *et al.* (1998), and Wadhwa *et al.* (2006).**

uncertainties in the decay rates of uranium isotopes. This uncertainty is not included in the discussions of early solar system chronology because it applies to the system as a whole, not to the differences in ages between individual objects.

Early solar system chronology

Detailed information about the chronology of the early solar system comes from the short-lived radionuclides (Table 8.8) and the Pb–Pb system. The time resolution of these clocks ranges from a few hundred thousand to a million years. Initial strontium can provide time resolution of approaching a million years in low-Rb/Sr phases, but it is difficult to integrate the information from this system with the Pb–Pb results because of uncertainties in the half-lives. In addition, realization of the inherent precision of initial strontium requires a clear understanding of the strontium evolution of the system from which all objects formed, and at present that understanding is lacking. In order for the short-lived radionuclides to give time information, they must have been homogeneously mixed throughout the region where the objects being dated formed, so that differences in abundances of the daughter isotopes are attributable only to differences in time of formation. For the ^{26}Al–^{26}Mg system and the ^{60}Fe–^{60}Ni system, direct measurements indicate that residual heterogeneity in the distribution of these short-lived nuclides is less than 10–15% (Thrane *et al.*, 2006; Dauphas *et al.*, 2008).

Constructing a self-consistent time line from the various radiochronometers is harder than it may first appear. Each sample providing a date for the time line must meet the criteria for a valid age (see Chapter 8). This is not always easy to demonstrate, in part

because we may not know the closure temperatures for diffusion for each mineral in the system. The dates must be reliable from an experimental point of view. As each new technique is brought on line, there is a period of development during which scientists learn how to make reliable measurements. Eventually bad measurements become obvious as more measurements are made, but in the early stages, it is not always obvious which measurements are reliable. Even if all of the ages are reliable, different systems may not reflect precisely the same time due to differences in the closure temperatures for each system. In fast-cooled systems, this is not an issue, but in slowly cooled systems, such as differentiated asteroids or metamorphosed chondrites, differences in closure temperature can produce large differences in the dates given by different systems. But sometimes, this is an advantage. In spite of these difficulties, we now have a basic outline of the sequence of events in the early solar system. The details of the chronology we present below are still the subject of intense study, and the picture will change as new measurements are made.

Primitive components in chondrites

Figure 9.9 summarizes the chronological results of five different isotopes systems: Pb–Pb, ^{26}Al–^{26}Mg, ^{53}Mn–^{53}Cr, ^{182}Hf–^{182}W, and ^{129}I–^{129}Xe. The Pb–Pb system provides the absolute time anchor for all systems (shown in Ma at the top of the diagram). For the ^{26}Al–^{26}Mg, ^{53}Mn–^{53}Cr, and ^{182}Hf–^{182}W systems, the diagram shows the initial ratios for each of the objects, plotted so that the scales are tied to the absolute time line by the half-life of the nuclide and by an "anchor", an object for which reliable measurements exist both for the Pb–Pb system and for the short-lived nuclide. For the ^{26}Al–^{26}Mg system, the anchor is the CAIs, for which we assign a $(^{26}Al/^{27}Al)_0$ ratio of 5×10^{-5}. This value may be uncertain by as much as 15% due to the possibility that recently reported supracanonical ratios are better estimates of the initial ratio (see below), but the half-life of ^{26}Al is short enough that this uncertainty is not important. The ^{53}Mn–^{53}Cr system has traditionally been anchored to the Pb–Pb system using the LEW 86010 angrite. This achondrite is used because it has a simple igneous history, apparently cooled rapidly, and did not suffer subsequent alteration. However, in detail, there are problems within the angrites with concordancy between the Pb–Pb system and the ^{53}Mn–^{53}Cr system. Nyquist *et al*. (2009a) used a wide variety of materials dated by multiple techniques to derive a $(^{53}Mn/^{55}Mn)_0$ ratio for the CAIs of $(9.1\pm1.7) \times 10^{-6}$. For the purposes of this discussion, we will adopt this ratio for the CAIs as the anchor for the ^{53}Mn–^{53}Cr system. For the ^{182}Hf–^{182}W system, we will use CAIs and the initial ratio determined by Burkhardt *et al*. (2008) of $(^{182}Hf/^{180}Hf)_0 = (9.72\pm0.44) \times 10^{-5}$ as the anchor. For the ^{129}I–^{129}Xe system, we adopt the Shallowater aubrite, which has a Pb–Pb age of 4563.3±0.4 Ma as the anchor. The $(^{129}I/^{127}I)_0$ ratios for objects being dated are determined relative to the Shallowater standard, which is included in every irradiation (see Appendix). The $(^{129}I/^{127}I)_0$ ratio is not directly determined. Instead, the age is calculated as a difference relative to Shallowater and is reported as an absolute age. Thus, the ^{129}I–^{129}Xe system is referenced to the absolute timeline.

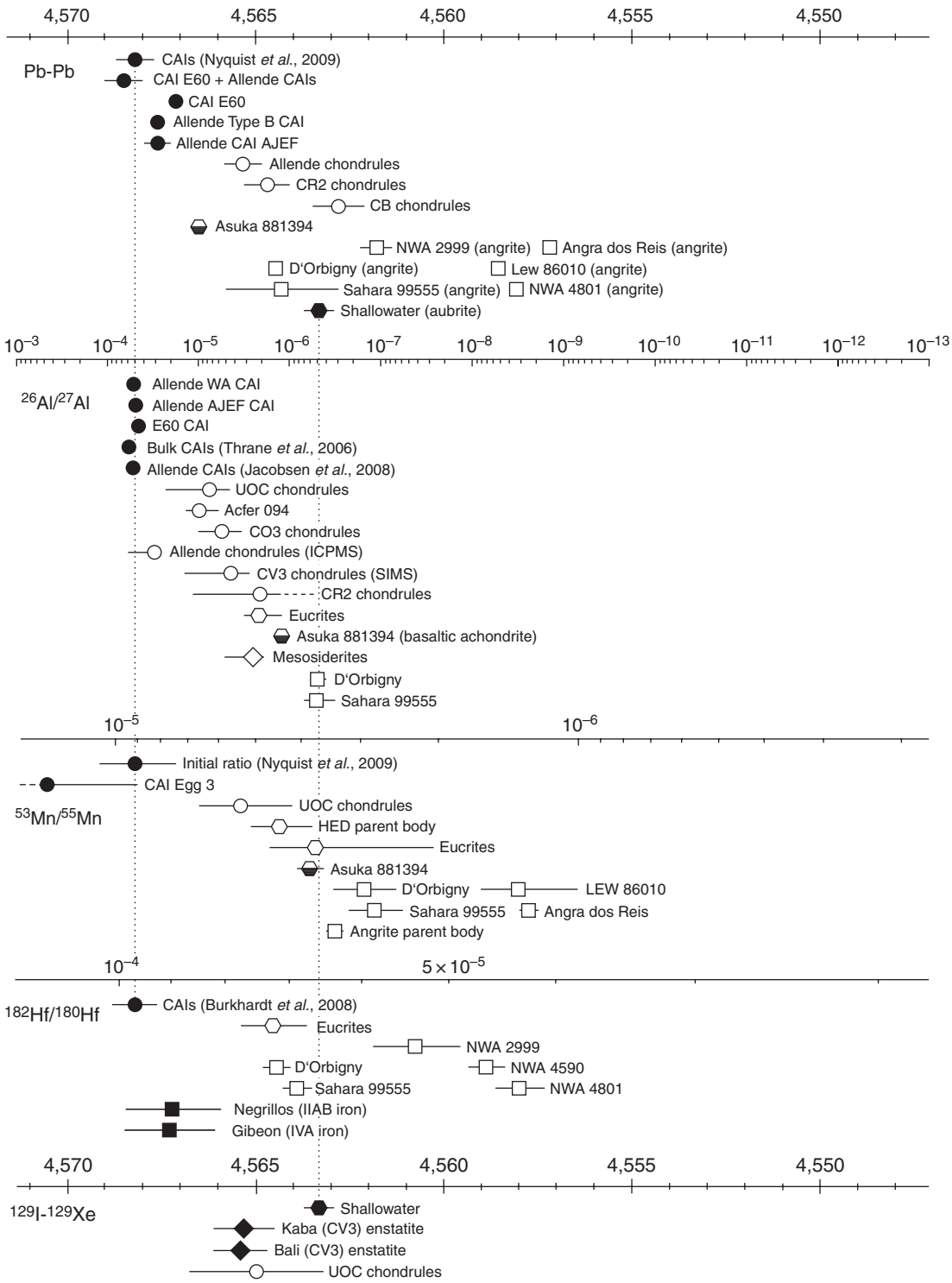
4,570
4,565
4,560
4,555
4,550
Pb-Pb
CAIs (Nyquist et al., 2009)
CAI E60 + Allende CAIs
CAI E60
Allende Type B CAI
Allende CAI AJEF
Allende chondrules
CR2 chondrules
CB chondrules
Asuka 881394
NWA 2999 (angrite)
Angra dos Reis (angrite)
D'Orbigny (angrite)
Lew 86010 (angrite)
Sahara 99555 (angrite)
NWA 4801 (angrite)
Shallowater (aubrite)
10−3 10−4 10−5 10−6 10−7 10−8 10−9 10−10 10−11 10−12 10−13
26Al/27Al
Allende WA CAI
Allende AJEF CAI
E60 CAI
Bulk CAIs (Thrane et al., 2006)
Allende CAIs (Jacobsen et al., 2008)
UOC chondrules
Acfer 094
CO3 chondrules
Allende chondrules (ICPMS)
CV3 chondrules (SIMS)
CR2 chondrules
Eucrites
Asuka 881394 (basaltic achondrite)
Mesosiderites
D'Orbigny
Sahara 99555
10−5
10−6
53Mn/55Mn
Initial ratio (Nyquist et al., 2009)
CAI Egg 3
UOC chondrules
HED parent body
Eucrites
Asuka 881394
D'Orbigny
LEW 86010
Sahara 99555
Angra dos Reis
Angrite parent body
10−4
5 × 10−5
182Hf/180Hf
CAIs (Burkhardt et al., 2008)
Eucrites
NWA 2999
D'Orbigny
NWA 4590
Sahara 99555
NWA 4801
Negrillos (IIAB iron)
Gibeon (IVA iron)
4,570
4,565
4,560
4,555
4,550
129I-129Xe
Shallowater
Kaba (CV3) enstatite
Bali (CV3) enstatite
UOC chondrules

Fig. 9.9

CAIs

The oldest objects so far identified that formed in the solar system are the CAIs. The bulk compositions and mineralogy of the CAIs led many to consider them to be the first condensates from a cooling solar nebula. Later petrographic work showed that many crystallized from melts and their mineralogy is the product of that crystallization. Many exhibit isotopic anomalies in calcium, titanium, strontium, nickel, and other elements that reflect unhomogenized nucleosynthetic components (e.g. Clayton *et al*., 1988). Such inclusions cannot be direct condensates from the solar nebula, because complete evaporation would have resulted in isotopic homogenization. Thus, many, perhaps most, CAIs are not direct nebular condensates. On the other hand, their refractory bulk compositions imply that they formed at high ambient temperatures, which points toward early times, and the isotopic anomalies imply that CAIs are old, because most solar system processes work toward homogenizing the isotopic compositions. By the mid 1990s, Pb–Pb studies had shown that CAIs formed at 4566±2 Ma (Allègre *et al*., 1995), and thus are the oldest reliably dated materials in the solar system. As more-precise Pb–Pb measurements have been made, this value has crept up slightly to a current best estimate of 4568.2±0.5 Ma (Nyquist *et al*., 2009a). There now appear to be real differences in inferred formation times for individual CAIs (Fig. 9.9). These could reflect an extended period of CAI formation, secondary reprocessing in the nebula, or parent-body effects. But several objects and groups of objects support the 4568.2 Ma age.

CAIs also have the highest $(^{26}Al/^{27}Al)_0$ ratios among solar system materials. The first inclusion shown conclusively to have formed with live ^{26}Al, Allende WA, gave an $(^{26}Al/^{27}Al)_0$ ratio of $(5.1\pm0.6) \times 10^{-5}$ (Fig. 8.24). Since then, a ratio of ~5×10^{-5} has been found repeatedly in CAIs of different types and from different classes of meteorites and has become known as the "canonical" ratio.

Recently, high-precision MC-ICPMS techniques have produced a flurry of $(^{26}Al/^{27}Al)_0$ ratios for CAIs higher than the canonical value, so-called "supracanonical" ratios. Some of these results are spurious, but some measurements may be correct. Two types of isochrons have been produced, whole-rock isochrons in which bulk samples of several different CAIs are measured and plotted on a single diagram, and internal isochrons based on minerals from a single CAI. One whole-rock isochron gave an $(^{26}Al/^{27}Al)_0$ ratio of $(5.85\pm0.05) \times 10^{-5}$ (Thrane *et al*., 2006), ~15% higher than the canonical ratio. However, another study of

Fig. 9.9

Caption for Fig. 9.9 Chronology of primitive components in chondrites and of differentiated meteorites in the early solar system as given by five radiochronometers. The Pb–Pb system provides the time anchor (given in Ma, at the top of the figure) for the short-lived nuclides. The anchor points – CAIs for ^{26}Al–^{26}Mg, ^{53}Mn–^{53}Cr, and ^{182}Hf–^{182}W and Shallowater for ^{129}I–^{129}Xe – are shown by dotted vertical lines. The short-lived nuclides are plotted on scales of their initial ratios, except for ^{129}I–^{129}Xe (see text). Data for the Pb–Pb system from Nyquist *et al*. (2009a) and references therein, Connelly and Bizzarro (2009), Amelin *et al*. (2002), Hohenberg and Pravdivtseva (2008); for the ^{26}Al–^{26}Mg system from Nyquist *et al*. (2009a) and references therein, Thrane *et al*. (2006), Jacobsen *et al*. (2008), Bizzarro *et al*. (2005), Wadhwa *et al*. (2009), and references listed for Fig. 9.10; for the ^{53}Mn–^{53}Cr system from Nyquist *et al*. (2009a) and references therein, Wadhwa *et al*. (2009); for ^{182}Hf–^{182}W from Burkhardt *et al*. (2008), Kleine *et al*. (2009); and for ^{129}I–^{129}Xe from Hohenberg and Pravdivtseva (2008).

whole CAIs gave an $(^{26}Al/^{27}Al)_0$ ratio of $(5.23\pm0.15) \times 10^{-5}$ (Jacobsen *et al*., 2008), very similar to the canonical value. The discrepancy between these studies has not been resolved. The tight fits to both of these isochrons indicate that the CAIs formed within ~30 000 years of each other. Whole-rock isochrons need not give the crystallization age of the CAIs, but may instead represent the time the CAIs or their precursors were isolated from the bulk solar nebula.

Internal isochrons obtained by laser-ablation MC-ICPMS and SIMS measurements have also given supracanonical ratios as much as 25% higher than the canonical ratio (e.g. Young *et al*., 2005). These are generally found in minerals with low Al/Mg ratios such as spinel, pyroxene, and melilite. The isochrons of most of these inclusions are disturbed. If the disturbance occurred after ^{26}Al had decayed and radiogenic ^{26}Mg was exchanged among the minerals, then the higher inferred initial ratios would not contain chronological information. If, on the other hand, the spinel and pyroxene remained closed to diffusion, then the higher ratios might reflect the time of initial crystallization of the CAIs. One idea is that the CAIs showing disturbed ^{26}Al–^{26}Mg systematics and supracanonical ratios for spinel and pyroxene were partially remelted while ^{26}Al was still alive. The spinel and pyroxene remained unmelted and their higher ratios reflect the time of the initial crystallization of the CAI, while melilite and anorthite were remelted and their ^{26}Al–^{26}Mg systems were reset. In this interpretation, the "isochrons" were generated over ~10^5 years and the canonical ratio, which comes from high Al/Mg phases, represents the end stage of CAI formation. Although this hypothesis remains to be proven, in rare cases, individual CAIs do show evidence of an extended history. For example, one Allende inclusion gave different Al–Mg isochrons for the main inclusion and for three igneous objects incorporated within it, suggesting that this object formed over a period of ~300 000 years (Hsu *et al*., 2000).

In addition to the possible extended formation history of some CAIs, many CAIs show clear evidence of later heating events, probably in the parent body, that disturbed or reset the Al–Mg systematics. These reset inclusions make up the peak at around zero in the $^{26}Al/^{27}Al$ histogram shown in Figure 8.26. These disturbed inclusions complicate the interpretation of the isotopic record of the early solar system.

A rare group of inclusions give very low $(^{26}Al/^{27}Al)_0$ ratios, show larger-than-normal isotopic anomalies in many elements, and are highly mass fractionated. These so-called FUN inclusions (for *F*ractionation and *U*nidentified *N*uclear effects) pose a problem. The low ratios do not appear to be due to parent-body metamorphism. There are three possible interpretations for their low $(^{26}Al/^{27}Al)_0$ ratios: (1) the inclusions formed or were last remelted late after the ^{26}Al had decayed; (2) they formed early, before ^{26}Al was introduced into the solar system; or (3) they formed at the same time as other CAIs, but from material that did not contain ^{26}Al. The formation time of these "anomalous" CAIs has not been resolved.

In addition to the Pb–Pb and $^{26}Al/^{27}Al$ ratios, CAIs also have the highest $(^{182}Hf/^{180}Hf)_0$ ratios among solar system materials. When anchored to the angrites, the ^{182}Hf–^{182}W system gives an age for the CAIs of 4568.3±0.7 Ma (Burkhardt *et al*., 2008). CAIs also have the lowest initial $(^{87}Sr/^{86}Sr)_0$ values among measured materials (Table 8.3; Fig. 9.8). Thus, various isotope systems consistently indicate that CAIs are the oldest objects to have formed in the solar system.

Chondrules

Chondrules are the most abundant constituent of chondrites. Chronological information on chondrule formation comes from the Pb–Pb, ^{26}Al–^{26}Mg, ^{53}Mn–^{53}Cr, and ^{129}I–^{129}Xe systems (Fig. 9.9). The ^{26}Al–^{26}Mg system provides the most precise information (Fig. 9.10), although only the least metamorphosed chondrites have chondrules with undisturbed ^{26}Al–^{26}Mg systematics. Essentially all of the ^{26}Al–^{26}Mg data on chondrules have been obtained by SIMS.

Ferromagnesian and Al-rich chondrules from type 3.0–3.1 ordinary chondrites typically have $(^{26}Al/^{27}Al)_0$ ratios in the range of (0.5–2.0) $\times$ 10^{-5} (Fig. 9.10). Most of these data are consistent with a single value of (7.5±1.1) $\times$ 10^{-6}, indicating formation ~2 Myr after CAIs. However, a handful of higher values may reflect distinct times of formation. ^{53}Mn–^{53}Cr and ^{129}I–^{129}Xe data indicate a similar, but perhaps slightly later formation time (Fig. 9.9).

Acfer 094 is a very primitive carbonaceous chondrite, perhaps related to CO chondrites. Four chondrules dated from this meteorite are consistent with a single initial value of (9.1±4.2) $\times$ 10^{-6}.

Chondrules from CO3.0 chondrites have a range of $(^{26}Al/^{27}Al)_0$ values similar to that for ordinary chondrite chondrules but displaced slightly to lower values (Fig. 9.10). The uncertainties in the data are not consistent with a single value for CO3.0 chondrules and suggest that formation took place over a ~1 Myr time span, 2–3 Myr after CAIs.

Chondrules from CV3 chondrites give a confusing picture. A high-precision Pb–Pb whole-rock isochron for Allende chondrules gives an age of 4565.32±0.81 Ma, almost 3 Myr after CAIs (Connelly and Bizzarro, 2009). The ^{129}I–^{129}Xe system in enstatite should have closed

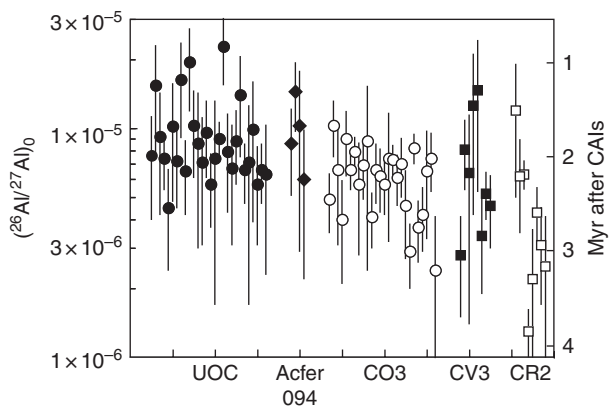

Fig. 9.10 Ion probe (SIMS) measurements of $(^{26}Al/^{27}Al)_0$ for chondrules from several meteorite groups. The right axis shows the formation time relative to CAIs, the oldest solids formed in the solar system. These data indicate that chondrule formation started at least 1 Myr after CAIs formed and continued for 1–2 Myr. For CR chondrites, in addition to the plotted data, a similar number of chondrules show no resolvable evidence for ^{26}Al. Data for unequilibrated ordinary chondrites (UDC) from Kita *et al.* (2000), McKeegan *et al.* (2000), Huss *et al.* (2001, 2007), Mostefaoui *et al.* (2002), and Rudraswami and Goswami (2007); for Acfer 094 from Hutcheon *et al.* (2009), Sugiura and Krot (2007); for CO3 chondrites from Kunihiro *et al.* (2004) and Kurahashi *et al.* (2008); for CV3 chondrites from Sheng *et al.*(1991), Hutcheon *et al.*(2000), Srinivasan *et al.* (2000), Hsu *et al.* (2003), and Kita *et al.* (2004); and for CR chondrites from Hutcheon *et al.* (2009) and Nagashima *et al.* (2007, 2008).

at 1400–1800 °C, during chondrule formation, and should not have been affected by subsequent aqueous alteration or low-temperature metamorphism. Enstatites in Kaba and Bali, CV3 chondrites that experienced lower levels of metamorphism than Allende, Axtell, Efremovka, and Ningqiang, give ages of 4565.3±0.8 and 4565.4±0.7 Ma (Fig. 9.9). SIMS measurements of the ^{26}Al–^{26}Mg system in chondrules from Allende, Axtell, Efremovka, and Ningqiang give $(^{26}Al/^{27}Al)_0$ values between 2.6×10^{-6} and 1.5×10^{-5}. These values are similar to those for chondrules from other classes and indicate formation times of 1.5–3 Myr after CAIs (Fig. 9.10). On the other hand, high-precision ICPMS measurements of the ^{26}Al–^{26}Mg system in Allende chondrules gave initial ratios of $(5.66\pm0.80) \times 10^{-5}$ to $(1.66\pm0.72) \times 10^{-5}$ (Bizzarro *et al.*, 2004). The highest of these ratios are the same as those measured in CAIs, which suggests that chondrule formation was contemporaneous with CAI formation in Allende. It is currently not clear why the ICPMS measurements of the ^{26}Al–^{26}Mg system give older ages for Allende chondrules than other types of measurements.

Chondrules from CR chondrites may have formed later than chondrules from other classes (Fig. 9.10). Pb–Pb data for CR2 chondrules give an age of 4564.7±0.6 Ma, 3.5 Myr after CAIs (Amelin *et al.*, 2002). With only a few exceptions, their $(^{26}Al/^{27}Al)_0$ ratios are below 0.5×10^{-5} (Nagashima *et al.*, 2008). These data imply that most CR2 chondrules formed 1–2 Myr after those in ordinary and CO chondrites (Fig. 9.10).

Chondrules from metal-rich (CH, CB) chondrites formed significantly later than those in other classes (Fig. 9.9), with Pb–Pb measurements giving ages of ~4562.7 Ma, 5.5 Myr after CAIs (Krot *et al.*, 2005). These chondrules likely formed by a different mechanism than the chondrules in other classes. One model of their formation suggests they are products of a collision between two asteroid-sized bodies and that they formed by recondensation of a vapor plume generated in the collision.

Taken together, the data summarized on Figure 9.9 indicate that CAIs were the first solids to form in the solar system, that they formed relatively quickly, and that many were subsequently altered in the nebula and in the host meteorites. Most chondrules probably formed 1–3 Myr after CAIs, although those in metal-rich chondrites formed considerably later.

Accretion and history of chondritic parent bodies

The chondrite parent bodies obviously could not have accreted before their constituent chondrules formed. Based on the formation times of chondrules, accretion of the ordinary chondrite parent bodies began 2.5–3 Myr after CAIs (4565.7–4565.2 Ma). The end of accretion can be inferred from the metamorphic history of the chondrite parent bodies. Isotopic data from metamorphic assemblages, coupled with thermal modeling of the chondrite parent bodies, suggest that the time of peak metamorphism for the H chondrite parent body was at ~4563 Ma. As will be discussed in Chapter 11, it is likely that the source of heat for metamorphism on chondrite parent bodies was the decay of ^{26}Al, perhaps with a contribution from ^{60}Fe. Thermal evolution models indicate that accretion of chondritic asteroids could not have occurred earlier than ~2 Myr after CAI formation, or they would have melted.

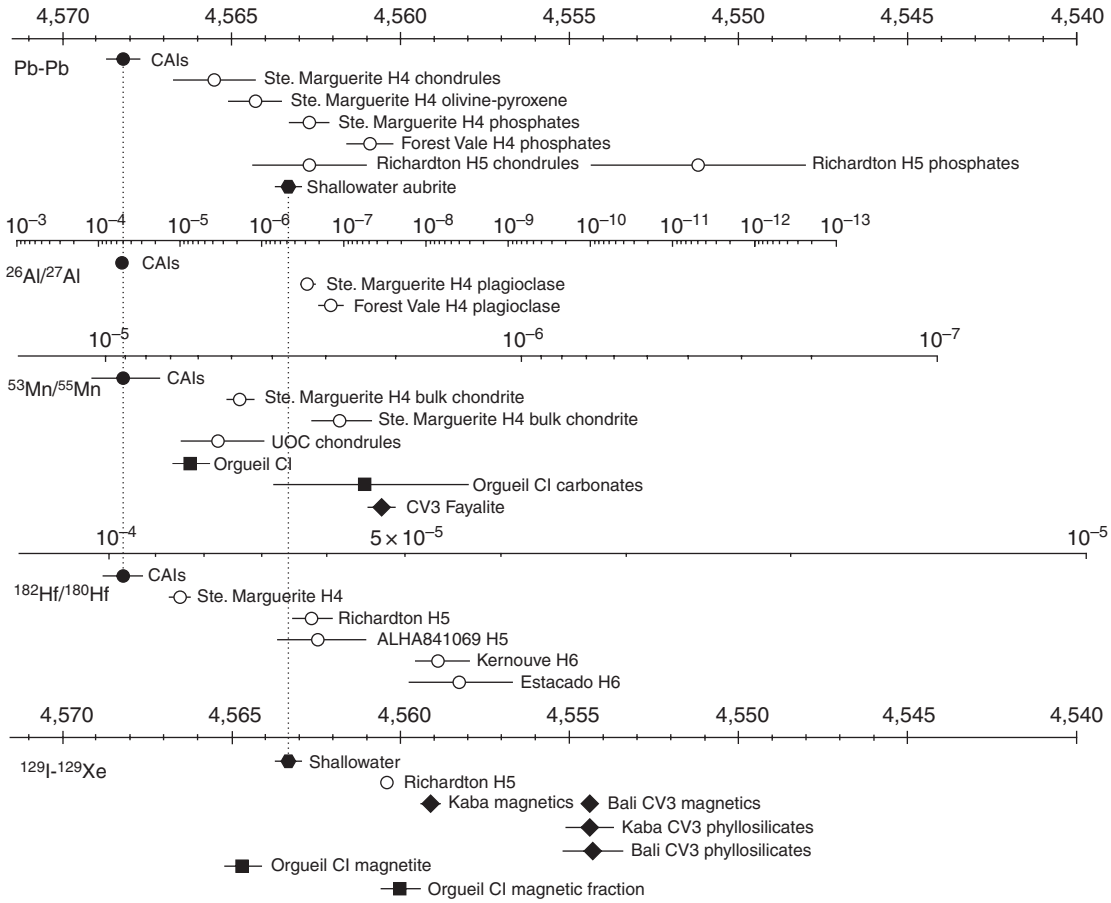

Fig. 9.11 **Chronology of secondary processes in the early solar system. Plot format and anchor points are the same as in Fig. 9.9. Dates related to thermal metamorphism are shown as open symbols, and dates related to aqueous alteration are shown as filled symbols. Both thermal metamorphism and aqueous alteration continued for tens to as much as 100 Myr after CAI formation. Data from Hohenberg and Pravdivtseva (2008), Hutcheon *et al.* (1998), Hua *et al.* (2005), Trinquier *et al.* (2008), Endress *et al.* (1996), Hoppe *et al.* (2004), and Zinner and Göpel (2002).**

Once formed, the chondrite parent bodies experience a variety of processes, including thermal metamorphism, aqueous alteration, shock metamorphism due to impacts, and even disruption from large impacts. Several radiochronometers can provide information on the timing of metamorphism and aqueous alteration. The chronology of this processing is summarized in Figure 9.11.

Ordinary chondrites

Information about the timing of metamorphism in ordinary chondrites is derived from the Pb–Pb, ^{40}Ar–^{39}Ar, ^{53}Mn–^{53}Cr, ^{26}Al–^{26}Mg, and ^{129}I–^{129}Xe systems and by fission-track dating. The dates provided by these chronometers reflect the times when the meteorites

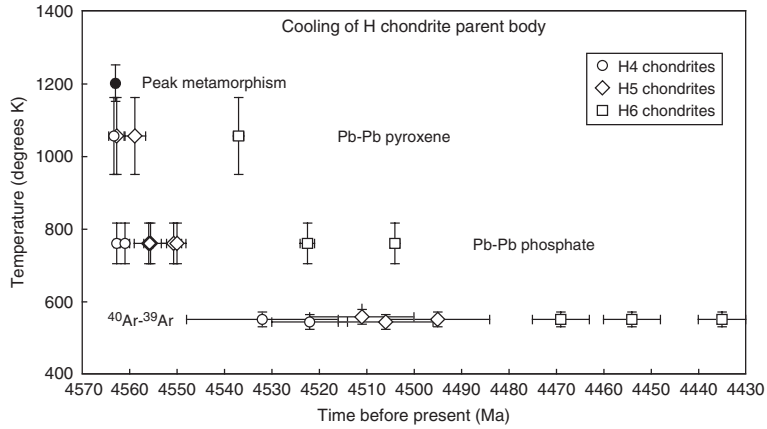

Fig. 9.12 **Cooling history of the H-chondrite parent body summarized using three radiochronometers: Pb–Pb in pyroxene, Pb–Pb in phosphate, and ^{40}Ar–^{39}Ar in bulk H chondrites. The three isotope systems close at different temperatures and thus record different stages of the cooling of the H chondrite parent body. Assuming that the peak temperature of ~925 °C was reached 4563 Ma ago, these data indicate that H4 chondrites cooled to ~475 °C in ~1 Myr and to ~275°C in 30–40 Myr. In contrast, the H6 chondrites reached ~475 °C in 50–60 Myr and ~275 °C in 100–130 Myr. Data from Trieloff *et al.* (2003), Göpel *et al.* (1994), and Bouvier *et al.* (2007).**

cooled sufficiently to become closed to isotopic diffusion. Each isotopic system has a different closure temperature in each mineral. The most detailed information about metamorphic history comes from the H chondrites. Figure 9.12 shows dates from three different isotopic systems for H4, H5, and H6 chondrites. The U–Pb system in pyroxene has the highest closure temperature (~780 °C), followed by the U–Pb system in phosphate (closure at ~475 °C), and followed in turn by the K–Ar system (closure at ~275 °C). For each of the three classes of H chondrites, the dates become younger as the closure temperature decreases. Cooling rates calculated from these data show that H4 chondrites cooled most quickly, followed by H5 chondrites, and then H6 chondrites. This same pattern is observed for fission track dating (Trieloff *et al.*, 2003) and for ^{182}Hf–^{182}W data on metal from several H chondrites (Kleine *et al.*, 2009) (Fig. 9.11).

For L and LL chondrites, the isotopic data do not correlate as well with the petrologic type as they do for H chondrites. This could reflect earlier disruption of the parent asteroids or the subsequent shock history or both. In general, the ages of the L chondrites tend to be younger than for the H group, but the overall timescales are similar for H, L, and LL chondrites.

CV and CO chondrites

As with the ordinary chondrites, the accretion times for CV and CO chondrite parent bodies can be estimated from the times of chondrule formation. The ^{26}Al–^{26}Mg and ^{129}I–^{129}Xe data suggest chondrule formation extended to 4565 Ma, 3.2 Myr after CAIs. This is slightly later than, but within the uncertainties of, the time indicated for the accretion of ordinary chondrite parent bodies.

Some CV chondrites experienced an extended period of aqueous alteration during which primary minerals in chondrules and CAIs were replaced by secondary phyllosilicate, magnetite, Fe, Ni sulfides, fayalite, hedenbergite, and andradite. Several of these phases are amenable to age dating, permitting time constraints to be placed on this alteration. ^{53}Mn–^{53}Cr dating of fayalite in Kaba and in Mokoia gives a relatively tightly constrained $(^{53}Mn/^{55}Mn)_0$ value of (2.2±0.4) × 10^{-6}, implying a formation time of ~7.5 Myr after CAIs (Hutcheon *et al*., 1998; Hua *et al*., 2005). ^{129}I–^{129}Xe measurements of secondary magnetite and phyllosilicates from Kaba and Bali give ages of 9–13 Myr after CAIs (Fig. 9.11).

CI and CM chondrites

Determining the formation time for CI and CM chondrites is not straightforward. We previously learned that CI chondrites have bulk compositions similar to the solar photosphere, and they are used as proxies for the bulk compositions of the solar system. Thus, it would appear that their formation did not produce an elemental fractionation relative to the bulk solar system, making it hard to date their formation. The CI chondrites did experience major aqueous alteration, however, which fractionated elements among the various mineral phases and started some isotopic clocks. The ^{129}I–^{129}Xe and ^{53}Mn–^{53}Cr chronometers are well suited for dating aqueous alteration. An isochron generated from magnetite in Orgueil (Fig. 8.29) gives a date of 1.6 Myr before the Shallowater meteorite, which converts to 4564.9±0.4 Ma. A highly magnetic fraction consisting of magnetite and organic material gives a younger isochron corresponding to 4560.3±0.6 Ma. A ^{53}Mn–^{53}Cr isochron from alteration minerals gave a slope of (6.28±0.66) × 10^{-6} (Trinquier *et al*., 2008), which converts to a formation time of 4566.2±0.6 Ma. ^{53}Mn–^{53}Cr measurements of individual carbonates in Orgueil give $(^{53}Mn/^{55}Mn)_o$ ratios ranging from (1.42±0.16) × 10^{-6} to (3.9 ±0.8) × 10^{-6} (Endress *et al*., 1996; Hoppe *et al*., 2004). These ratios convert to formation times for the carbonates of 4563.6 to 4558.3 Ma. Together, these data indicate that the CI chondrite parent body accreted prior to 4564.9 Ma, ~3.3 Myr after the CAIs formed, and that aqueous alteration continued, perhaps in an episodic manner, until around 4558 Ma, 10 Myr after the solar system formed.

There are fewer data available for CM2 chondrites. Carbonates from several meteorites show large excesses of ^{53}Cr that generally correlate with the Mn/Cr ratio, but none give a tight isochron. Inferred $(^{53}Mn/^{55}Mn)_i$ ratios range from (5.0±1.5) × 10^{-6} to (1.3±0.6) × 10^{-5} (the latter ratio is higher than the adopted initial ratio for the solar system). Leaches from bulk Murchison (CM2) do not fall along any isochron (Trinquier *et al*., 2008). These data suggest relatively early accretion and a period of aqueous alteration extending for several million years.

Accretion and differentiation of achondritic parent bodies

Until recently, it was generally believed that the chondrites, which consist of relatively unaltered nebular material and thus are primitive objects, accreted early, whereas the differentiated meteorites (achondrites, irons, pallasites), which have had a history of melting

and differentiation, formed later from chondritic precursors. This view was supported by data from the long-lived Pb–Pb, ^{87}Rb–^{87}Sr, and ^{147}Sm–^{143}Nd chronometers indicating crystallization ages for a variety of differentiated meteorites extending to ~4.30 Ga (Fig. 9.8). However, these ages typically date the time of magma crystallization on the parent bodies of these meteorites, not the accretion times of their parent bodies, and in many cases later events have disturbed the isotopic systematics. The development of high-precision MC-ICPMS has changed this view by permitting precise measurements of short-lived radiochronometers that can potentially date the accretion and differentiation of the asteroid parent bodies.

HED meteorites

The eucrites, howardites, and diogenites (HEDs) are igneous meteorites that are thought to have originated on the same parent asteroid, 4 Vesta (to be discussed more fully in Chapter 13, Box 13.2). The U–Pb system is disturbed in eucrites and does not give reliable chronological information. Individual internal ^{87}Rb–^{87}Sr isochrons also give a variety of ages, some of which may reflect later disturbance (Fig. 9.8). We are interested in two different types of age information for the HED meteorites. One type concerns the accretion and differentiation of the asteroid. A whole-rock ^{182}Hf–^{182}W isochron indicates that global silicate differentiation on the HED parent body took place ~3.5 Myr after CAIs formed, and a comparison of this whole-rock isochron with a bulk mantle-chondrite isochron suggests that core formation took place ~1 Myr earlier (Kleine *et al*., 2004). A bulk-rock ^{53}Mn–^{53}Cr isochron for the eucrites indicates that global melting and differentiation had occurred by 3.5 Myr after CAIs (Lugmair and Shukolyukov, 1998). High-precision ^{26}Al–^{26}Mg studies of eucrites and diogenites indicate that extensive melting and differentiation occurred 2.6–3.5 Myr after CAIs formed (Bizzarro *et al*., 2005). Taken together, these data imply that differentiation and crust formation began on the HED parent body ~2.5–3 Myr after CAIs formed (Fig. 9.9). This, in turn, implies very rapid accretion, heating, and melting in Vesta, probably within ~1 Myr of the origin of the solar system.

We are also interested in the time of formation of the individual meteorites that make up the HED suite. Initial strontium gives formation intervals relative to Allende CAIs of ~7 Ma for cumulate eucrites and ~11 Ma for non cumulate eucrites (Smoliar, 1993). These ages probably reflect the formation of the parent magmas for these meteorites. Crystallization ages for basaltic eucrites, which erupted and crystallized on the asteroid's surface, tend to be older than those for cumulate eucrites, which crystallized at depth. Five basaltic eucrites give ^{147}Sm–^{143}Nd ages in the range of 4573±17 Ma, slightly older than the accepted age of CAI formation, but with individual measurement uncertainties of ~20 to ~100 Myr (Wadhwa *et al*., 2006). Cumulate and non cumulate eucrites give concordant ^{147}Sm–^{143}Nd ages in the range of 4.40 to 4.48 Ga, between 65 and 170 Myr after CAI formation (Wadhwa *et al*., 2006). A whole-rock ^{87}Rb–^{87}Sr isochron for non cumulate eucrites gives an age of 4490±57 Ma (Smoliar, 1993; $\lambda_\beta = 1.42 \times 10^{-11}$ yr^{-1}). Magmatic activity on Vesta continued for an extended period of time. Not all radiochronometers give reliable dates for the HEDs because of secondary disturbance during an extended period of igneous activity on the parent asteroid and because of later shock overprinting.

Asuka 881394

Asuka 881394 is a basaltic achondrite that appears to be unrelated to the eucrites, implying formation on a different asteroid. High-precision Pb–Pb ages of mineral separates of Asuka 881394 yield a precise and ancient age of 4566.5±0.9 Ma (Wadhwa *et al*., 2009), less than 2 Myr after CAIs. The ^{26}Al–^{26}Mg and ^{53}Mn–^{53}Cr systems give slightly later dates, but still imply that the parent body of Asuka 881394 accreted, melted and differentiated, and erupted the Asuka 881394 basalt all within the first 2–3 Myr of solar system history.

Mesosiderites

These meteorites consist of silicate and metal that were brought together by impact events on the meteorite parent bodies. The silicate portion of the Vaca Muerta mesosiderite gives $(^{26}Al/^{27}Al)_0$ ratios slightly higher than the silicates in eucrites (Bizzarro *et al*., 2005), suggesting that the parent body from which mesosiderites are derived also formed and began to differentiate during the first million years of solar system history.

Angrites

The crystallization ages of angrites, as determined by the Pb–Pb and ^{182}Hf–^{182}W systems, range between 4557.7 and 4564.5 Ma (Fig. 9.9). The oldest of these ages, those for Sahara 99555 and D'Orbigny, are 3.7 Myr after CAIs formed. These ages are in agreement with results from high-precision ^{26}Al–^{26}Mg measurements of the same meteorites, which give ages for the earliest angrite magmatism of 3.2–3.5 Myr after CAIs (Baker *et al*., 2005). Based on the initial ratios from the internal isochrons for these meteorites, the differentiation of the angrite parent body into core and mantle took place <2 Myr after CAIs (Kleine *et al*., 2009). These ages again indicate rapid accretion and melting of the angrite parent body. The spread in crystallization ages indicates that magmatic activity continued for ~7 Myr, but the lack of isotopic disturbance among the angrites implies that magmatic activity ceased on this asteroid shortly after the youngest known angrite formed.

Iron meteorites

In Chapter 6, we learned that iron meteorites are divided into magmatic irons, which apparently formed by fractional crystallization during slow cooling of asteroidal cores, and non-magmatic irons, which formed by a variety of different mechanisms. The most reliable constraints on the timing of core formation in the parent asteroids of the magmatic irons come from ^{182}Hf–^{182}W measurements of the IIAB irons. These meteorites have relatively low cosmic-ray exposure ages (see below) and thus require smaller corrections for cosmogenic effects. The ε^{182}W values for the Gibeon (IVA) and Negrillos (IIAB) magmatic iron meteorites correspond to tungsten model ages for core formation on their parent asteroids of ~1 Myr after CAIs (Fig. 9.9).

The IAB-IIICD irons are non-magmatic irons that often contain silicate inclusions. Tungsten is significantly more radiogenic in these meteorites than in the IIAB irons because

of less efficient separation of metal and silicate. The $\varepsilon^{182}W$ values for these meteorites imply that metal segregation took place on the IAB parent body ~3 Myr after CAIs (Kleine *et al*., 2009).

The early accretion, melting, and differentiation of the parent bodies of the eucrites, mesosiderites, angrites, and IIAB and IAB-IIICD iron meteorites are consistent with ^{26}Al and ^{60}Fe as the heat source for melting. Their short half-lives and relatively high abundances mean that these nuclides were potent heat sources during the first 1–2 Myr of solar system history, but this heat source declined rapidly as the nuclides decayed away. After 3 Myr, the rate of heat generation from ^{26}Al had dropped to ~12% and that from ^{60}Fe had dropped to 25% of the initial rates. By the time the chondrite parent bodies accreted 2–3 Myr after CAIs formed, there was no longer enough energy available to melt them.

Accretion, differentiation, and igneous history of planets and the Moon

Given our focus on cosmochemistry, we will consider only chronology based on radiogenic isotopes. Most planetary chronology is presently based on crater counting (discussed briefly in Box 9.1), and only the Earth, Moon, and Mars have provided samples that can be analyzed in the laboratory for radioisotopes. However, these three bodies illustrate what could be learned from samples of other terrestrial planets.

Age of the Earth

The origin of the Earth is difficult to date, because the geologic record of its first 500 Myr is missing. Most long- and short-lived radionuclides do not appear to provide useful constraints on this event. Only the U–Pb and ^{182}Hf–^{182}W isotopic systems allow valid constraints (reviewed by Halliday, 2004). Both of these systems basically define the timing of the Earth's differentiation, because core formation fractionates the parent/daughter ratios (uranium and hafnium are lithophile, while lead is both siderophile and chalcophile and tungsten is moderately siderophile). In this regard, we caution that these chronometers are not able to distinguish between early accretion with late core formation, and late accretion with concurrent late core formation. Also, if core formation was protracted, then the "age" derived does not define any particular event, but instead a kind of weighted average. That said, there is now a consensus that the Earth's core formation was basically concurrent with accretion, because the conversion of kinetic energy into heat would have allowed silicate and metal melting temperatures to be achieved and because many of the accreting planetesimals would have already been differentiated.

The U–Pb system has been a chronometer of choice for the Earth's age since the pioneering study of Clair Patterson in 1956, as discussed in Chapter 8. Virtually all U–Pb model ages of the Earth (reviewed by Allègre *et al*., 1995) are younger than the ages of chondritic and achondritic meteorites. The oldest Pb–Pb age, based on ancient terrestrial

rocks, is 4.53 Ga (Tera, 1980), and even that postdates the beginning of the solar system by ~30–40 Myr. It is unclear whether this age dates the time of core formation (Galer and Goldstein, 1996) because it may be compromised by an early solar system fractionation of U/Pb, possibly by volatile lead depletion in the nebula (Harper and Jacobsen, 1996).

The ^{182}Hf–^{182}W system unambiguously dates core formation, and thus indirectly constrains accretion timescales. A complication in interpreting these data is that chondrites, and by inference the average solar system, have tungsten isotopic compositions that are clearly distinct from the bulk silicate Earth (Kleine *et al*., 2002; Yin *et al*., 2002). This leads to an uncertainty in the initial ^{182}Hf abundance, which affects ^{182}W and the calculated age. Nevertheless, useful constraints are provided by this system. Yin *et al*. (2002) estimated the mean time for Earth's accretion at ~11 Myr. Halliday (2004), taking into account the uncertainty in initial ^{182}W abundance, estimated mean ages for the Earth's accumulation (with exponentially decreasing accretion rates) of 12–15 Myr. These ^{182}Hf–^{182}W ages are shorter than the time inferred from U–Pb model ages, but may be more accurate.

Age of the Moon

The time of formation of the Moon must also be determined by indirect means. Model ages for various isotope systems can provide brackets on the Moon's age (Halliday, 2004). The initial ^{87}Sr/^{86}Sr ratios in lunar highlands rocks are slightly higher than the solar system initial ratio. The time required to generate this difference is 11±3 Myr. Models of lead isotope evolution suggest lunar formation may have occurred ~45 Myr after the Earth formed. Loss of noble gases as a consequence of the giant impact that formed the Moon, as modeled using the ^{129}I–^{129}Xe and Pu–Xe systems, suggests a period of perhaps 50–80 Myr. A more precise measurement is based on the time of the Moon's differentiation, which would obviously have postdated its formation. That has been determined from ^{182}Hf–^{182}W ages of lunar samples. An early determination of live ^{182}Hf in the Moon was incorrect, because of a failure to recognize that much of the ^{182}W in lunar samples is cosmogenic (this was not a significant factor in applying this system to the Earth, because our atmosphere screens out cosmic rays). Subsequent estimates for the Moon's differentiation vary between ~50 Myr (Halliday, 2000) or $\geq$30 Myr (Kleine *et al*., 2002) after the Earth's formation. The most plausible lunar model age is 40–45 Myr after CAIs. Uncertainty in the ^{182}Hf decay constant limits more precise constraints. Taken together, these data are consistent with an absolute age for the Moon's formation at 4.52–4.53 Ga.

The age of the Moon must obviously be older than its oldest rocks, which formed in a magma ocean. The isotopic characteristics of lunar anorthosites are difficult to unravel, because they have experienced impact events that disturbed their ^{40}Ar–^{39}Ar and ^{87}Rb–^{87}Sr ages. Also, lead isotopes in lunar samples are difficult to interpret, due to lead's volatility and mobility. The ^{147}Sm–^{143}Nd system tends to yield less disturbed dates, but low REE abundances and the nearly monomineralic compositions of these rocks make them hard to date. Ages for three anorthosites range from ~4.5 to 4.3 Ga (Snyder *et al*., 2000 and references therein) (Fig. 9.13a). These ages partly overlap the Moon's formation age.

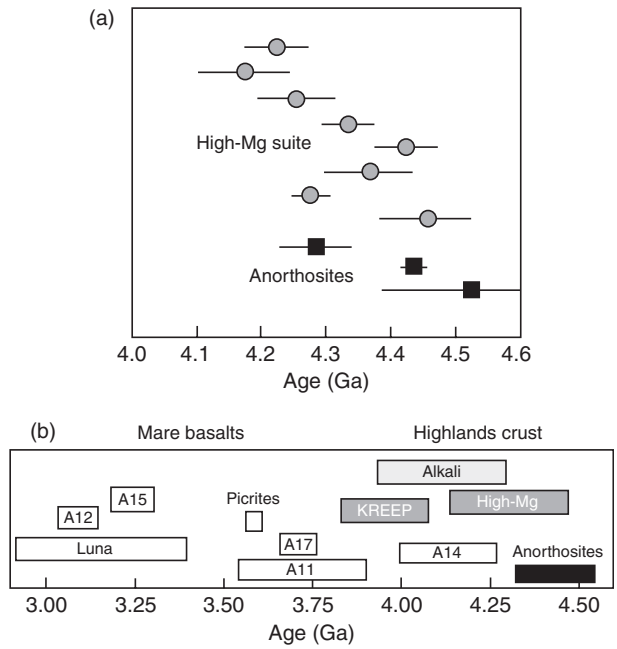

Fig. 9.13 **Summary of radiometric ages for lunar samples, based on a variety of isotope chronometers. (a) Individual highlands crustal rocks (anorthosites and high-Mg suite), and (b) summary of all lunar rock types, including mare basalts. Designations A11, A12, etc. and Luna refer to Apollo and Luna missions. Modified from Snyder *et al.* (2000).**

Other lunar highlands rock types, such as the high-Mg (4.45–4.15 Ga) and KREEP rocks (4.1–3.8 Ga), based on ^{147}Sm–^{143}Nd and ^{87}Rb–^{87}Sr ages, and the alkali suite (~4.3–3.9 Ga), based on ^{147}Sm–^{143}Nd ages and U–Pb ages of zircons, are slightly younger (Fig. 9.13b).

The earliest mare basalts (Apollo 14), which have high-alumina and low-titanium compositions, are 4.3–4.0 Ga (Fig. 9.13b). High-titanium mare basalts from the Apollo 11 and 17 sites have ages ranging from 3.9–3.55 Ga. Low-titanium mare basalts from the Apollo 12 and 15 sites have younger ages of 3.3–3.0 Ga (summarized by Snyder *et al.*, 2000). Mare basalts have usually been dated by the ^{147}Sm–^{143}Nd and ^{87}Rb–^{87}Sr techniques.

Analyzed mare basalts apparently do not bound the full age range for mare volcanism. Crater counting (see Box 9.1) of other maria suggest volcanism may have extended to 2.5±0.6 Ga before surface igneous activity ceased.

Age of Mars

Constraints on the accretion and differentiation of Mars come from the application of four isotopic systems to Martian meteorites: ^{129}I–^{129}Xe, ^{146}Sm–^{142}Nd, ^{182}Hf–^{182}W, and ^{244}Pu–^{136}Xe. Accretion is not directly datable by any of these clocks, so we must rely on dates from early differentiation events to put constraints on the accretion history of Mars.

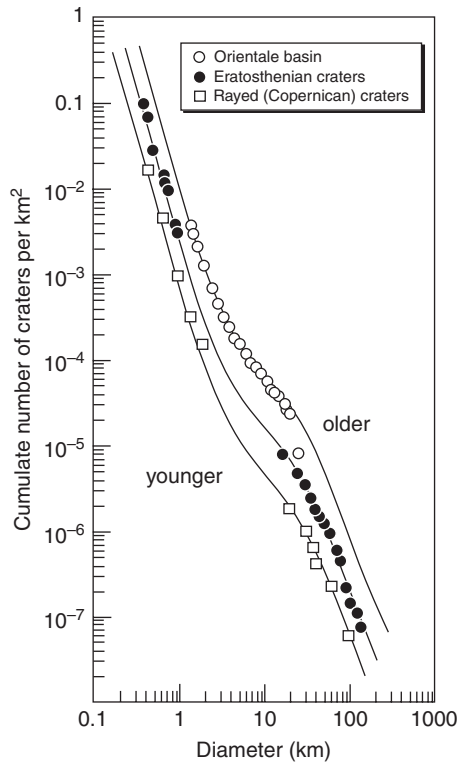

Fig. 9.14 **Plot of the cumulative frequency of craters versus crater diameter, for three geologic units on the Moon. Crater density measurements provide a means of ordering units in relative time. Modified from Neukum *et al.* (2001).**

Box 9.1 **Relative timescales: crater counting and stratigraphy**

Absolute time measurements using radioactive isotopes are presently limited to samples that can be carefully processed and analyzed in the laboratory. Estimates of the *relative* times of formation of various geologic units on other planets can be gained from spacecraft imagery, by crater counting. The older a surface is, the longer it has been exposed to meteorite impacts and thus the higher the density of craters on that surface. However, very old surfaces can become saturated with craters, when every new crater effectively obliterates an older one.

In practice, crater diameters on a particular geologic unit are measured and assigned to various size bins. Then a log-log plot of the cumulative number of craters above some size versus crater diameter is constructed, giving a diagram like that shown in Figure 9.14. The crater distribution has a negative slope, because small craters are always more abundant than large craters. As time passes, the crater distribution curve shifts to the right, so comparison of the crater distributions for several geologic units allows us to determine their relative ages. In Figure 9.14, the higher density of craters within the Orientale basin on the Moon indicates its

antiquity, relative to the age of craters like Eratosthenes and even younger craters with bright rays.

It is beyond the scope of this book to discuss the methodology of crater counting in detail (there are lots of details and caveats). However, we should note that measuring the radiometric age of a rock sample obtained from a mapped geologic unit provides a calibration point for crater counting. If absolute ages are determined for multiple units with different measured crater densities, a crater production curve for that planet can be constructed; then, the absolute ages of other, unsampled geologic units on the same planet can be estimated from their crater densities. Such a crater production curve has been determined for the Moon, based on the radiometric ages of rocks collected from known sites by the Apollo astronauts.

The geologic timescale for the Earth is based mostly on stratigraphy (the depositional succession of layers from bottom to top). Most strata are sedimentary rocks. The relative ages of the sedimentary layers are determined by the sequence of deposition and by the fossils that they contain. It is not possible to use radioactive isotopes to measure the time that a sediment was deposited, because deposition does not reset radiometric clocks. However, the absolute ages of sediment layers and the fossils they contain have been determined by measuring radiometric ages of volcanic ash layers in the sequence or lavas that crosscut sedimentary strata.

The geologic timescale for the Moon is also based on stratigraphy, but in this case the layers are blankets of impact ejecta. Huge craters, occurring mostly during the late heavy bombardment, spread ejecta over much of the lunar surface, producing global stratigraphic units. This serviceable system was first suggested by geologist Eugene Shoemaker, who used it to devise the lunar timescale and to map the Moon's surface. Some limits on the absolute ages of lunar ejecta blankets come from impact ages, determined from isotopic systems like ^{40}Ar–^{39}Ar that are reset by shock. The geologic timescale for Mars presently has only three gross subdivisions, and its only constraints are based on crater counting and an assumed crater production rate. The relative and absolute timescales for geologic units on the Moon and Mars are discussed further in Chapter 13.

Core formation probably began very early, perhaps during the last part of the planet's accretion. The timing of core formation can be investigated using the ^{182}Hf–^{182}W system, as has already been described for the Earth and Moon. Two-stage models of the ^{182}Hf–^{182}W and ^{146}Sm–^{142}Nd systems using the data for shergottites indicate that core formation on Mars occurred at ~4.555 Ga, ~12 Myr after CAIs formed, assuming that core formation was a discrete event. If core extraction was continuous, as seems more likely, it may have been completed somewhat earlier.

There are significant differences in the $\varepsilon^{142}Nd$ and $\varepsilon^{182}W$ values obtained for the different types of Martian meteorites (Fig. 9.15). These variations indicate that the meteorites were derived from distinct mantle reservoirs that were established early in the history of Mars. Modeling based on $\varepsilon^{142}Nd$ and $\varepsilon^{182}W$ indicates that differentiation of the silicate mantle could have taken place contemporaneously with core formation or could have been more extended, taking as long as 60 Myr. Models based on ^{129}I–^{129}Xe and ^{244}Pu–^{136}Xe

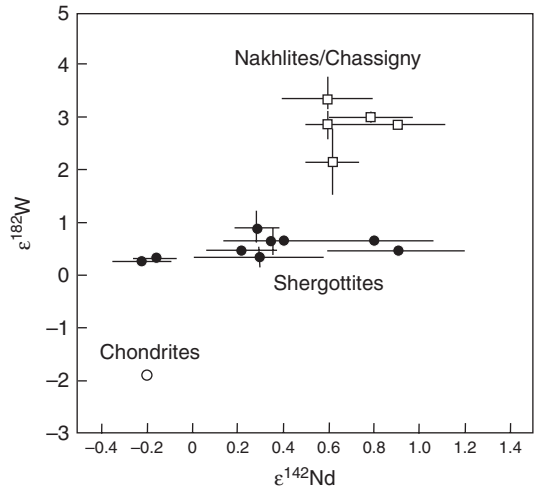

Fig. 9.15 $\varepsilon^{142}Nd$ vs. $\varepsilon^{182}W$ for Martian meteorites. Modified from Lee and Halliday (1997).

systematics indicate that Pu–I fractionation in the Martian mantle occurred $\leq$35 Myr after Mars formed, although degassing of xenon and other volatiles from the mantle may have continued for ~300 Myr. The $\varepsilon^{182}W$ and Hf/W ratios of the Zagami shergottite appear to require extremely rapid separation of metal from silicate in its source region, perhaps in as little as 1 Myr. If so, then the majority of accretion would have been completed by 1 Myr after CAIs. Such rapid accretion is similar to the inferred timescales for differentiated asteroids and is consistent with runaway growth scenarios.

The preservation of distinct mantle reservoirs over time in Mars and the limited degassing experienced by the Martian mantle after the initial period, as indicated by the almost quantitative retention of ^{244}Pu-produced fission xenon, show that Mars has been a static planet with no mantle convection since very early in its history.

Information on the igneous history of Mars is given by the crystallization ages of Martian meteorites (Nyquist *et al*., 2001; Borg and Drake, 2005). The only ancient Martian meteorite is ALH 84001. Its ^{147}Sm–^{143}Nd age is 4.50±0.13 Ga. Different subsamples of this meteorite give ^{87}Rb–^{87}Sr dates ranging from 4.5 to 3.9 Ga, and ^{40}Ar–^{39}Ar ages also cluster around 4.0 Ga; these younger ages have been reset by impact. The ages of nakhlites and chassignites are much younger, ~1.3 Ga (Fig. 9.14). These ages are based on concordant dates from the ^{40}Ar–^{39}Ar, ^{87}Rb–^{87}Sr, ^{147}Sm–^{143}Nd, and U–Pb systems.

The interpretation of radiometric ages for the shergottites has been controversial. Most shergottites give ^{147}Sm–^{143}Nd, ^{87}Rb–^{87}Sr, and ^{176}Lu–^{176}Hf mineral isochrons corresponding to ages of ~175 Ma, although a small number give older ages ranging from 290 to 575 Ma (Fig. 9.16). The ^{40}Ar–^{39}Ar ages appear to be considerably older, but are compromised by the presence of trapped ^{40}Ar from the Martian atmosphere and possibly inherited radiogenic ^{40}Ar as well. In contrast to the mineral (internal) isochrons, whole-rock ^{87}Rb–^{87}Sr and Pb–Pb isochrons for shergottites suggest a much older age of ~4.1 Ga (Bouvier *et al*., 2008). Most workers interpret this age to reflect planetary differentiation that established mantle

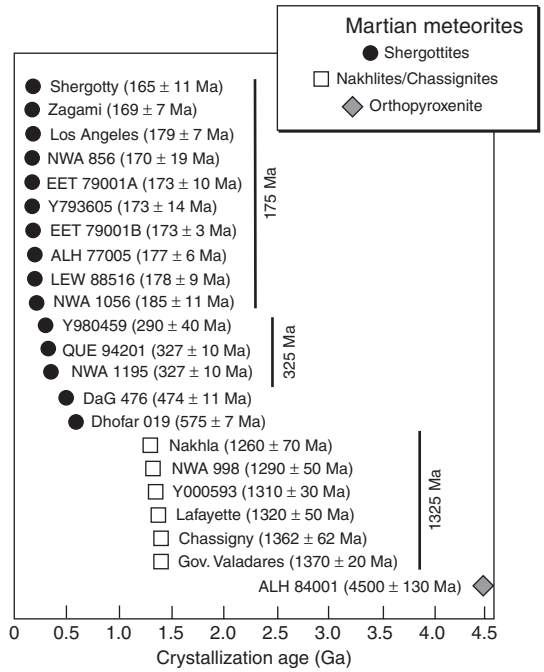

Fig. 9.16 Summary of radiometric ages for Martian meteorites. After Borg and Drake (2005).

reservoirs that then remained closed thereafter (Nyquist *et al*., 2001). However, Bouvier *et al*. (2008) interpreted this age as indicating the time of crystallization of shergottite magmas. In their model, the younger ages from other radiochronometers are biased by phosphate minerals that exchanged isotopes with groundwater, and the young U–Pb age of baddeleyite reflects resetting during shock. This model assumes that ^{40}Ar–^{39}Ar ages, which are older than other mineral isochron ages, represent undegassed argon from an ancient, 4.1 Ga rock; however, the ^{40}Ar–^{39}Ar ages do not anticorrelate with the degree of shock heating, as would be expected if this were correct (Walton *et al*., 2008; Nyquist *et al*., 2009b).

Borg and Drake (2005) have determined the timing of aqueous alteration events in Martian meteorites from the ages of secondary minerals. Carbonates in ALH 84001 formed at ~3.9 Ga, iddingsite in nakhlites formed ~630 Myr ago, and salts in shergottites formed sometime after the crystallization of these rocks, ~170 Myr ago.

Shock ages and impact histories

Shock ages of meteorites

Isotopic chronometers can provide information about the collisional history of the meteorite parent bodies. As discussed in Chapter 8, isotopic chronometers can give the time of

formation of an object provided that specific assumptions are met. One of those conditions is that the system must remain undisturbed since its formation. However, a large impact can partially or completely reset an isotopic clock. Susceptibility to impact resetting varies widely among the various chronometers. Chronometers that involve noble gases are particularly sensitive because a noble gas atom is not incorporated into the structure of a mineral; rather it is interstitial. The U–He and ^{40}Ar–^{39}Ar systems are often used to evaluate shock history. Other systems that can be reset include, in order of decreasing susceptibility to shock, the ^{87}Rb–^{87}Sr, Pb–Pb, and ^{147}Sm–^{143}Nd systems. Because the isotopic clocks have generally not been completely reset, the exact timing of an event is often impossible to determine. The timing is usually inferred by comparing more than one isotopic system or by the clustering of shock ages from many meteorites of the same type. Relatively severe shocks are required to affect these radiometric clocks. In general, the final collision that released a meteorite from its parent body cannot be dated by these clocks, in part because it was so recent, but also because the collision was usually not sufficiently violent. The timing of this last event is inferred from the cosmic-ray exposure ages (see below).

Many chondrites show evidence of having experienced shock from impacts, and a significant fraction show isotopic disturbances that can be interpreted to give shock ages. Data come from the U–He and ^{40}Ar–^{39}Ar systems. A histogram of shock ages for ordinary chondrites is shown in Figure 9.17. There is a small cluster of ages in the range of 3.4–4.1 Ga, but most shock ages are <1 Ga. The inset in Figure 9.17 shows these younger shock ages broken down by chondrite type. The large group of L chondrites with shock ages of ~500 Ma has been associated with a major breakup of the L-chondrite parent body. Because of the nature of shock ages, the precise timing of this breakup is not known. However, a recent discovery that a large number of L chondrites fell to Earth in the early Ordovician period ~480 Myr ago seems to support this conclusion (see Box 9.2).

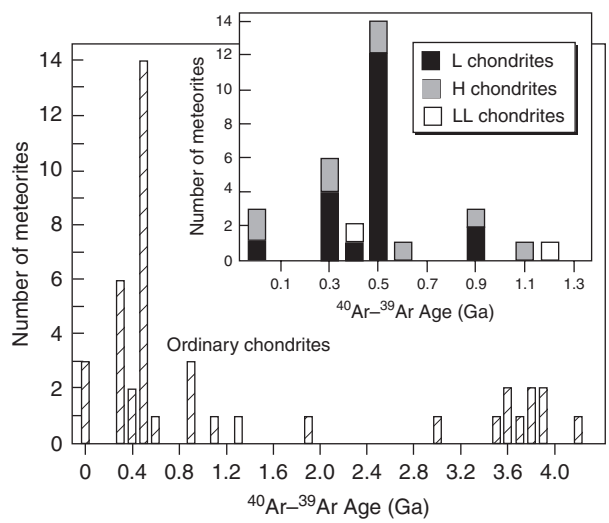

Fig. 9.17 **Shock ages of ordinary chondrites as determined from ^{40}Ar–^{39}Ar measurements. Inset gives an expanded version of the youngest ages separated by compositions group. After Bogard (1995).**

The majority of HED meteorites show evidence of isotopic resetting over a limited period of time between ~3.4 and ~4.1 Ga ago. Most of the evidence comes from the ^{40}Ar–^{39}Ar system, but the ^{87}Rb–^{87}Sr system was also disturbed at this time in some meteorites.

Box 9.2 An Ordovician meteorite rain

In a limestone deposit at Kinnekulle, Sweden, a remarkable collection of more than 40 highly altered meteorites (Fig. 9.18) totaling 7.7 kg have been collected during routine quarrying operations (Schmitz *et al*., 1997, 2001, 2003). The ~3.2-m-thick limestone layer in which they are found was deposited over ~1.75 Myr in the mid-Ordovician. Despite being almost completely replaced by calcite, barite, and phyllosilicates, the meteorites are easily identified by their chondritic texture. Their identification as meteorites is confirmed by measurements of platinum-group elements. The chemical characteristics of relict spinels indicate that they are either L or LL chondrites.

How did so many meteorites become incorporated in this limestone? An obvious possibility is that they represent a single large meteorite that broke in the atmosphere and scattered across the landscape. But this possibility can be ruled out by their positions in the stratigraphic column. The meteorites typically lie on hardgrounds, where they accumulated together with nautiloid shells and other large objects. In many cases the specific horizon at which individual meteorites were deposited can be identified. Based on their stratigraphic positions, at least 12 separate meteorite falls are represented. This is a tremendous number of meteorites to have fallen in a ~2700 m^2 area over $\leq$1.75 Myr. The data imply that the infall rate was ~25 times higher than today.

For many years, we have known that many of the L chondrites experienced a severe shock event at ~500 Ma. One interpretation of these data was that the L-chondrite parent body was disrupted by an impact at that time. Could this catastrophic event have produced the rain of meteorites in the Ordovician? Detailed stratigraphic evaluation places the age of the meteorite-bearing limestone at 467.3±1.6 Ma. Recent ^{40}Ar–^{39}Ar dating of one of the L chondrites that experienced the major shock event gave an age for that event of 470±6 Ma, the same age or slightly older than the limestone layer. Scientists who study orbital dynamics then went to work to identify an asteroid of the correct spectral type that might be in a position to have transferred large numbers of fragments into Earth-crossing orbits quickly after a disrupting impact. Bottke *et al*. (2009) found that the Gefion asteroid family, which consists of ~2200 individual asteroids, is in just the right place, near the 5:2 mean motion resonance with Jupiter. The resonance provides a means of transferring fragments of Gefion-family asteroids into the inner solar system. A dynamical analysis of the Gefion family indicates that its parent asteroid was disrupted ~485 Myr ago (Bottke *et al*., 2009), making it just the right age as well.

So the data indicate that a catastrophic collision 470–480 Myr ago created the Gefion family of asteroids. Fragments from this catastrophic breakup were transferred through a resonance into Earth-crossing orbits. These fragments rained down on Earth at a rate ~25 times the current meteorite influx rate for several million years. Additional support for this model comes from an apparent spike in the cratering rate on Earth at about this time and by a high abundance of dispersed meteoritic chromite of L-chondrite affinity in Ordovician limestone covering an area of ~250 000 km^2 in Sweden.

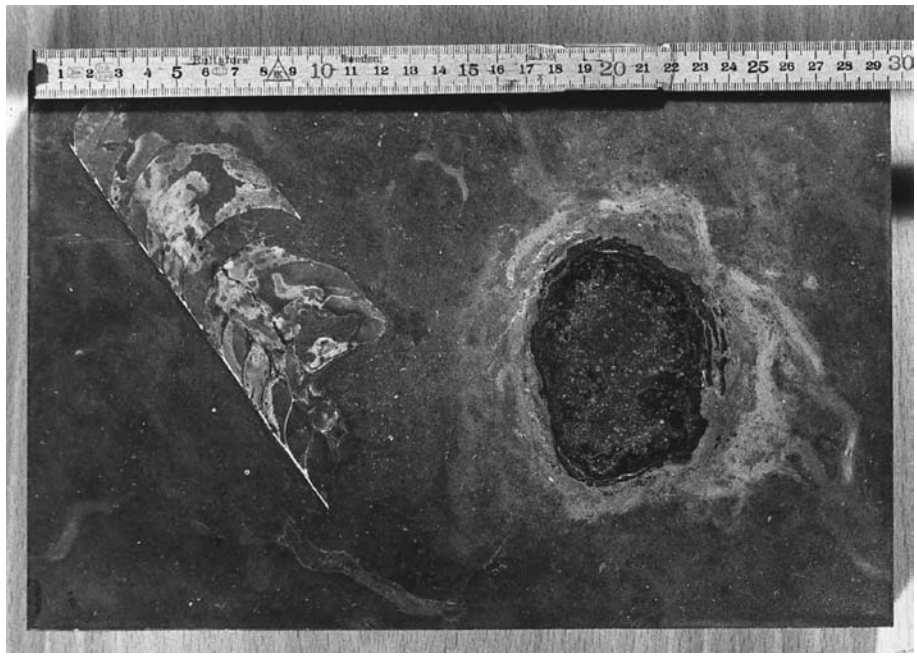

Fig. 9.18 **Fossil meteorite together with a nautiloid shell in a limestone plate sawed parallel to the seafloor surface. Reprinted from Schmitz *et al.* (2001), with permission from Elsevier.**

Shock ages of lunar rocks

The same isotopic techniques that have been used to determine shock ages in meteorites can be applied to lunar samples. Logically, these studies focus on impact melt breccias, which are most likely to have had isotopic ages reset by impact events. ^{87}Rb–^{87}Sr, and to a lesser extent ^{147}Sm–^{143}Nd ages of lunar impact breccias give ages ranging from 4.45 to 3.89 Ga (reviewed by Snyder *et al.*, 2000, and Warren, 2004). Because these breccias are composed of rock clasts, crystal fragments, and impact melt glasses that were likely derived from multiple shock events, their ages represent an average of impact events. Differences in breccia shock ages indicate the scale of sampling of these materials.

The most useful shock ages are based on ^{40}Ar–^{39}Ar data for impact melt breccias. Most lunar breccias yield ^{40}Ar–^{39}Ar plateau ages younger than ~3.85 Ga. By carefully selecting breccias from different Apollo landing sites that are thought to have formed during specific large impact events (that is, that are associated with specific impact basins), the absolute ages of these basins have been defined (Snyder *et al.*, 2000, and references therein). These basins form the basis for the lunar timescale, as noted above. Most lunar basins formed during the period between ~3.9 and 3.75 Ga. For example, Nectaris, Imbrium, and Orientale formed at 3.92, 3.85, and 3.75 Ga, respectively. Serenitatis and Crisium are also thought to have formed during this interval. The youngest lunar basins are the rayed craters Copernicus and Tycho, with inferred ages of ~1.0 and ~0.3 Ga, respectively.

The late heavy bombardment

The pronounced peak in large impact events seen in the ages of lunar impact melt breccias has led to the concept of a lunar cataclysm. Although this is commonly attributed to an enhanced flux, or spike, of large impactors at ~3.85 Ga, some workers have suggested that it represents an inflection in a basically monotonic decline of impacts during the waning stages of planetary accretion (reviewed by Hartmann *et al*., 2000). Skeptics of the spike idea suggest that the clustering of shock ages reflects a "stonewall" effect, where the lunar crust has become so saturated with craters that earlier radiometric clocks were reset in a heated mega-regolith. The term late heavy bombardment could apply to either model. We presume that the Earth must have experienced the same intense bombardment, although the geologic record from that period is largely missing. In Chapter 14, we will consider a dynamical model that might account for a spike in the impact history of the Moon.

A peak in the shock ages for HED meteorites also corresponds to the period of late heavy bombardment on the Moon. This is unlikely to be a coincidence, and provides further support for this important event in solar system history.

Cosmogenic nuclides in meteorites

Cosmic-ray exposure ages

Interplanetary space is permeated by energetic particles called cosmic rays. These particles, mostly protons and α-particles, originate both in the Sun (solar cosmic rays) and in interstellar space (galactic cosmic rays). Solar cosmic rays have a power-law distribution of energies from ~10 to a few hundred MeV. Galactic cosmic rays are more energetic, with energies of 10^2–10^4 MeV, again with a power-law distribution. However, because they are charged particles, they are affected by the Sun's magnetic field. Solar activity thus governs how far the galactic cosmic rays, particularly the low energy ones, penetrate into the inner solar system.

Energetic particles react with solid matter in a variety of ways. Low-energy particles in the solar wind (~1 KeV/nucleon) are implanted into solids to depths of ~50 nm. Energetic heavy particles penetrate more deeply and disrupt the crystal lattice, leaving behind "tracks" that can be imaged by TEM or chemically etched and observed in an optical microscope. Particles with energies of several MeV or more may induce a nuclear reaction. The two main modes of production of cosmogenic nuclides are spallation reactions and neutron capture.

Spallation occurs when a high-energy cosmic ray breaks a target nucleus into two or more pieces. These interactions commonly eject neutrons. The secondary neutrons slow down to thermal energies and eventually react with other nuclei in the target material to generate heavier species. Production of cosmogenic nuclides by secondary neutrons increases with depth to a peak at between 0.5 and 1 m below the surface. Therefore, in order to get an

Table 9.1 Nuclides used for cosmic-ray exposure ages

Nuclide	Half-life	Produced From
^{3}H	12.26	O, Mg, Si, Fe
^{3}He	stable	O, Mg, Si, Fe
^{10}Be	1.5×10^{6}	O, Mg, Si, Fe
^{14}C	5730	O, Mg, Si, Fe
^{21}Ne	stable	Mg, Al, Si, Fe
^{22}Na	2.6	Mg, Al, Si, Fe
^{26}Al	7.17×10^{5}*	Si, Al, Fe
^{38}Ar	stable	Fe, Ca, K
^{36}Cl	3.01×10^{5}	Fe, Ca, K
^{81}Kr	2.29×10^{5}	Rb, Sr, Y, Zr

* Note that the cosmic-ray community uses a different half-life for ^{26}Al than the one used for early solar system studies.

accurate exposure age, it is necessary to estimate the depth in the pre-atmospheric body where the sample was located. This can be done by looking at isotope ratios, which vary with depth.

The fraction of incoming cosmic rays that generate nuclear reactions is quite low. In a meteorite traveling in space, about one in 10^{8} of the target atoms undergoes a nuclear reaction in a 10-Myr period. However, the cosmogenic nuclides that they produce can be measured to estimate the time that an object has been exposed to cosmic rays. Table 9.1 shows some of the nuclides that are used to estimate cosmic-ray exposure ages in meteorites and in materials from planetary surfaces.

Cosmogenic nuclides are measured by a number of techniques. Helium-3, ^{21}Ne, and ^{36}Ar are measured by conventional noble gas mass spectrometry. In many samples concentrations are high enough, especially for helium and neon, that only small corrections for trapped gases are required. They are stable isotopes so their abundances increase proportionally with their cosmic-ray exposure. Krypton-81 is present in lower abundances and is radioactive, and thus requires a more complicated measurement procedure to extract age information. Radioactive isotopes such as ^{3}H, ^{14}C, ^{10}Be, ^{22}Na, ^{26}Al, and ^{36}Cl can be measured by counting the γ-rays emitted by their decay. These isotopes can also be counted directly in an accelerator mass spectrometer. Cosmogenic nuclides can provide information about the travel time between the meteorite parent body and the Earth (its cosmic-ray exposure age), the irradiation environment in interplanetary space, the number of collisions suffered by an object on its way to Earth, whether the object got too close to the Sun, and even the residence time of the meteorite on Earth. In order for a sample to give a cosmic-ray exposure age, several assumptions must be satisfied: (1) the flux of primary cosmic rays was constant in time; (2) the flux of primary cosmic rays was constant in space; (3) the shape of the sample did not change; (4) the chemical composition of the sample did not change; (5) any cosmogenic contributions from previous irradiations are known; (6) all non-cosmogenic contributions to the inventory of the nuclide of interest are known; and

(7) the sample did not lose nuclides of interest except by radioactive decay. Many meteorites appear to fit these requirements. To calculate the age from measured data, the cosmic-ray flux must be known and a model of the shape and size of the pre-atmospheric object and where within it the sample resided is highly desirable (Herzog, 2005; Eugster *et al*., 2006).

Most cosmic-ray exposure ages are calculated from helium, neon, and argon isotopic abundances. Although all isotopes of these noble gases are produced by cosmic rays, the low natural abundance of ^{36}Ar and the extremely low natural abundances of ^{3}He and ^{21}Ne make the cosmogenic component easy to see. In addition, because all three isotopes are stable, the age is easy to determine by dividing the amount of excess ^{3}He, ^{21}Ne, or ^{36}Ar by the rate at which they are produced by cosmic rays. In some cases, the ^{3}He abundance is unusually low relative to ^{21}Ne or ^{36}Ar. This may mean that the sample was heated for an extended period, as would be the case if the orbit passed near the Sun. For meteorites with cosmic-ray exposure ages of <4 Myr, radionuclides such as ^{10}Be, ^{26}Al, and ^{36}Cl are also used, particularly if the meteorites have high abundances of trapped noble gases, as in the cases of CM and CI chondrites. When radionuclides are used, one must take into account the terrestrial age of the meteorite, during which the nuclides decay according to their half-life, to determine the actual time of exposure to cosmic rays.

Figures 9.19, 9.20, and 9.21 summarize the cosmic-ray exposure ages for various classes of meteorites. The CI and CM chondrites have the shortest exposure ages, ranging from a few $\times$ 10^4 to a few $\times$ 10^5 years (Fig. 9.19). Most other chondrites have exposure ages ranging from <1 Myr to nearly 100 Myr (Fig. 9.20). The distributions of exposure ages among chondrites are inconsistent with continuous delivery of meteorites to Earth. The distributions more likely reflect superposition of debris from discrete collisional events in the asteroid belt. Note the strong peak in exposure ages for the H chondrites at 6–7 Ma. This most likely represents a major collision on the H-chondrite parent body at ~7 Ma. An additional large collision at 33 Ma is also indicated. The L chondrites show a different distribution, with collisions occurring at ~28 Ma and ~40 Ma (these ages reflect impact sampling of their immediate parent bodies, rather than the collision that disrupted the original L-chondrite asteroid, as noted in Box 9.2). Like the majority of chondrites, the achondrites have exposure ages of $\leq$1 Myr to nearly 100 Myr. The HED meteorites (Fig. 9.21a) exhibit a

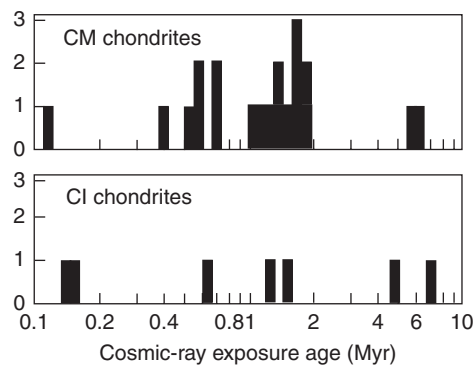

Fig. 9.19 Cosmic-ray exposure ages of CI and CM chondrites. Modified from Eugster *et al*. (2006).

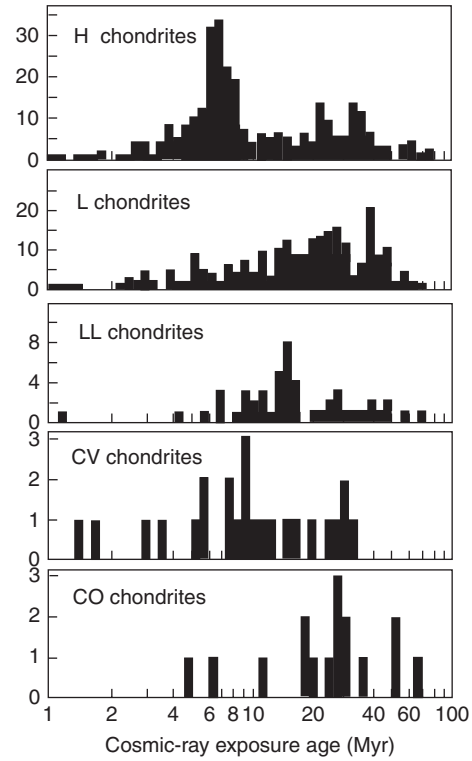

Fig. 9.20 Cosmic-ray exposure ages of ordinary, CV, and CO chondrites. Modified from Eugster *et al.* (2006).

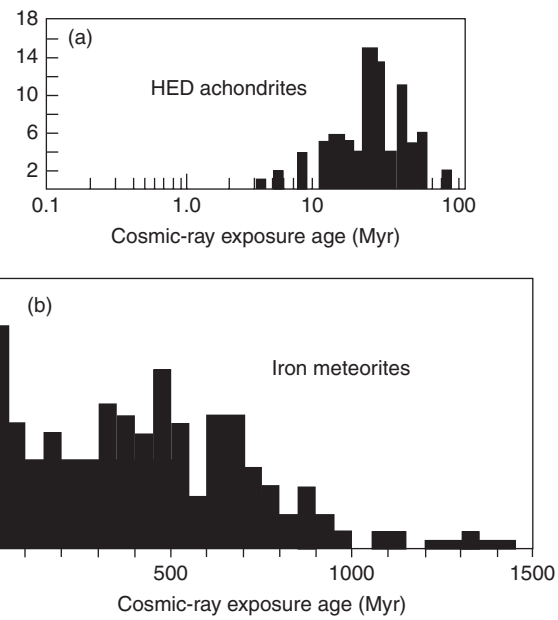

Fig. 9.21 Cosmic-ray exposure ages of differentiated meteorites. (a) HED achondrites, and (b) iron meteorites. Modified from Eugster *et al.* (2006).

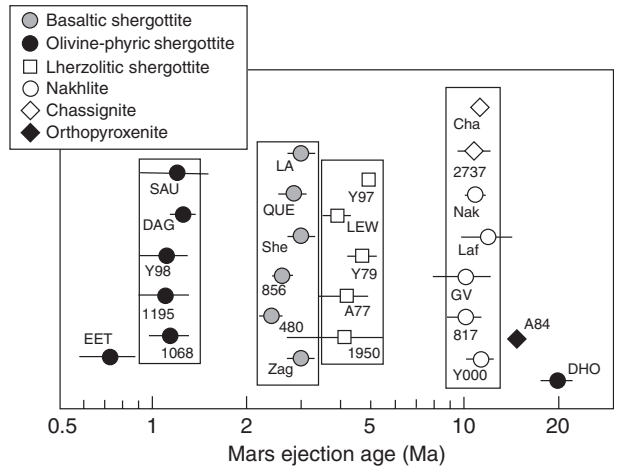

Fig. 9.22 **Ejection ages (sum of cosmic-ray exposure age + terrestrial age) for Martian meteorites. The ages cluster by meteorite type, suggesting that each cluster represents a distinct impact (ejection) event. The only outliers are the EETA 79001 and Dhofar 019 shergottites and ALHA84001. Modified from McSween (2008).**

strong peak at ~22 Ma and a smaller one at ~36 Ma. The eucrites show an additional peak at ~12 Ma.

The iron meteorites generally exhibit much longer cosmic-ray exposure ages than do stony meteorites, with most having exposure ages of several hundred Myr (Fig. 9.21b). The progression of cosmic-ray exposure ages from ~0.1 to <10 Myr for CI and CM chondrites to 1 to 100 Myr for other types of chondrites to several hundred Myr for the irons parallels the sequence of their physical strength. This indicates that collisions and physical abrasion in space are major factors, along with orbital dynamics, in controlling if and when a meteorite reaches the Earth.

Meteorites from Mars comprise ~45 distinct falls. They can be divided into various petrographic types based on their mineralogy (see Chapter 6). The cosmic-ray exposure ages show that these meteorites were ejected in a number of discrete events (Fig. 9.22). Note that there is a tight correlation between ejection time as inferred from the cosmic-ray exposure age and the petrographic classification of the meteorites. For example, all the nakhlites and chassignites have cosmic-ray exposure ages of 10.6±1.0 Myr. All of the lherzolitic shergottites were ejected at 3.8–4.7 Ma, the basaltic shergottites were ejected at 2.4–3.0 Ma, and five of six olivine-phyric shergottites were sent on their way to Earth by an impact at 1.2±0.1 Ma.

We also have over 120 lunar meteorites in our collections. Because the Moon has no atmosphere, the irradiation history of these meteorites can include an extended period in the lunar regolith. The transit times from the Moon to the Earth range from a few $\times 10^4$ years to nearly 10 Myr. Detailed analysis of exposure ages and terrestrial ages indicate that at least three impact events in the lunar highlands and five events in the lunar mare ejected the meteorites that have been recovered to date.

Terrestrial ages

Meteorites are not in chemical equilibrium with the Earth's surface, and thus are quickly degraded and destroyed after they fall. The most striking example of this lack of equilibrium is the presence of Fe–Ni metal in many meteorites, which quickly rusts on Earth. The rate at which meteorites weather and disintegrate can be measured. The time since a meteorite fell is known as its terrestrial age.

When a meteorite falls onto the Earth's surface, it becomes for the most part shielded from the effects of cosmic rays. The cosmic-ray-produced nuclides cease to form so the exposure clock stops. However, because many of the cosmic-ray produced nuclides are radioactive, several new clocks start that can be used to estimate the time that a meteorite has been on the Earth's surface.

The cosmogenic clocks work as follows. In space, while the meteorite is exposed to cosmic rays, the abundances of both radioactive and non-radioactive isotopes increase. However, the radioactive ones also decay and eventually, after about ten half-lives, the abundance of a radioactive species reaches a steady state between production and decay. For a typical stony meteorite, exposure ages are long enough that the abundances of ^{14}C, ^{26}Al, ^{10}Be, and perhaps even ^{36}Cl have reached a steady state. The steady-state level for each nuclide in a meteorite can be inferred from the bulk composition of the meteorite and its exposure history, as measured by stable cosmogenic nuclides. When the meteorite falls to Earth, production of the radioactive isotopes ceases and they begin to decay. By comparing the abundances of one or more of these nuclides in the meteorite now with the expected steady-state abundances, the terrestrial age can be calculated. The ^{14}C clock is useful for terrestrial ages younger than ~30 000 years, while ^{26}Al, ^{10}Be, and ^{36}Cl can provide terrestrial ages for objects that have been on Earth in excess of a million years. The development of the accelerator mass spectrometer, which permits quantitative measurements of isotopes with extremely low abundances (detection limit a few parts in 10^{15}), has greatly facilitated the work on terrestrial ages of meteorites.

A large number of meteorites have been collected from hot desert areas. In these areas, rainfall is low, which helps to preserve the meteorites. In addition, the dry conditions make meteorites easier to find because vegetation is scarce and the wind blows away the fine dust, leaving rocks and meteorites as a lag deposit.

Numerous meteorites have been collected in Western Australia and terrestrial ages have been determined for ~50 of them. Ages range from very young to around 40 000 years. There is a rough exponential decline in the number of meteorites as a function of age. The distribution of ages gives a mean residence time of ~10 000 years at this location.

Thousands of meteorites have also been recovered from the deserts of North Africa. Terrestrial ages of these meteorites extend out to ~50 000 years and again the number of meteorites shows a rough exponential decrease with age. The mean residence time inferred for these meteorites is ~12 000 years.

A third desert site is Eastern New Mexico, where nearly 200 meteorites have been found. Thirty-two of these meteorites have had their terrestrial ages determined. They fall in the range of 10 000 to 50 000 years. They do not show an exponential decrease in abundance

with age. Most of these meteorites were found in blowouts, areas where the topsoil had blown away, exposing an older surface. This suggests that the meteorites were somehow protected from weathering in this area.

A study of 19 larger meteorites from the Great Plains of the United States indicated a shorter mean residence time of ~5200 years. Meteorites that fall in wetter climates typically do not last as long.

Antarctica has turned out to be a wonderful place to collect meteorites. The meteorites are found in areas of blue ice. These areas form when ice is ablated by the wind. The blue ice formed at depths below ~100 m where the pressure of overlying snow forced the air bubbles out of it. Thus, if blue ice is on the surface, then at least 100 m of overlying snow and ice have been removed, and all of the meteorites in that ice that fell over the thousands of years when the snow fell and the ice formed are now concentrated on the surface. Horizontal compression of ice against a barrier, such as a mountain range, can further increase the number of meteorites on the ice. Terrestrial ages of Antarctic meteorites are older than in other parts of the world, with ages ranging from recent to >480 000 years. Different ice fields have meteorites of different ages. Antarctic ice is apparently a very good storage box for meteorites. However, when the meteorites are exposed on the surface of the ice, they begin to weather. There is currently no good way to measure the survival age for a meteorite on the surface of Antarctic ice, but it is probably not longer than a few thousand years.

Summary

We have seen that the age of the elements that now comprise the solar system can be estimated from models of stellar nucleosynthesis in the galaxy. These models are constrained by the abundances of short-lived radionuclides in meteorites. The age of the solar system is estimated to be ~4.568 Ga, determined from CAIs, the oldest materials dated so far. Chondrules, the other important component of chondrites, appear to be several million years younger. The ages of chondrules and the timing of planetesimal accretion and differentiation, relative to CAI formation, can be determined using short-lived radionuclides like ^{26}Al and ^{182}Hf. The absolute ages of these events require that they be anchored to U–Pb ages. Accretion of differentiated asteroids occurred within 2 Myr of CAI formation, as appropriate for their heating by ^{26}Al decay. Accretion of chondritic asteroids occurred slightly later, so that they only experienced thermal metamorphism or aqueous alteration.

The age of the Earth is estimated from U–Pb and ^{182}Hf–^{182}W data. The latter, which may be most accurate, suggest an average accretion time of 11–15 Myr after CAIs. The ^{182}Hf–^{182}W model age for formation of the Moon, after correction for cosmogenic tungsten, is 40–45 Myr after CAIs, corresponding to an absolute age of ~4.52 Ga. ^{182}Hf–^{182}W and ^{147}Sm–^{143}Nd model ages for the formation of Mars are ~12 Ma, similar to the formation time of the Earth.

Impact ages of meteorites and lunar samples can be determined from radioisotope chronometers that are reset by shock. These involve radiogenic nuclides that are gases

(helium, argon), and are thus easily lost. Impact ages for lunar impact melt breccias and for HED meteorites reveal a late heavy bombardment at 3.9–3.75 Ga.

Cosmic-ray exposure ages are determined from spallation-produced radioactive nuclides. Cosmic-ray irradiation normally occurs while a meteoroid is in space, but surface rocks unshielded by an atmosphere may also have cosmogenic nuclides. These measurements provide information on orbital lifetimes of meteorites and constrain orbital calculations. Terrestrial ages can be estimated from the relative abundances of radioactive cosmogenic nuclides with different half-lives as they decay from the equilibrium values established in space. These ages provide information on meteorite survival relative to weathering.

Now that we have an understanding of radioactive isotopes and their utility in constraining the timing and rates of nebular, planetesimal, and planetary processes, we will turn our attention to the most volatile elements and compounds. Stable isotopes in them provide additional constraints on cosmochemical processes.

Questions

1. How accurately do we know the age of the solar system? What is the largest uncertainty in the age? Why can we determine the sequence and timing of events in the early solar system with higher precision than we know the absolute age?
2. Summarize the evidence that chondrules are younger than CAIs. Hint: Several lines of evidence do not involve radionuclides.
3. Give two lines of reasoning to support the idea that differentiated asteroids accreted before chondritic asteroids.
4. Describe cosmic-ray exposure ages of meteorites and summarize what they tell us about the history of meteorites.
5. What is the evidence that Martian meteorites came to Earth as a result of a few discrete impact events on the Martian surface?

Suggestions for further reading

Several papers in a special issue of *Geochimica et Cosmochimica Acta* (Vol. 73, No. 17) are devoted to the chronology of the early solar system, and provide a good entry point into the modern literature.

Huss, G. R., Meyer, G. S., Srinivasan, G., Goswami, J. N. and Sahijpal, S. (2009) Stellar sources of the short-lived radionuclides in the early solar system. *Geochimica et Cosmochimica Acta*, **73**, 4722–4745.

Kleine, T., Touboul, M., Bourdon, B. *et al*. (2009) Hf–W chronology of the accretion and early evolution of asteroids and terrestrial planets. *Geochimica et Cosmochimica Acta*, **73**, 5150–5188.

Nyquist, L. E., Kleine, T., Shih, C.-Y. and Reese, Y. D. (2009a) The distribution of short-lived radioisotopes in the early solar system and the chronology of asteroid accretion, differentiation, and secondary mineralization. *Geochimica et Cosmochimica Acta*, **73**, 5115–5136.

Bogard, D. D. (1995) Impact ages of meteorites: A synthesis. *Meteoritics*, **30**, 244–268. A nice summary of impact ages of meteorites.

Eugster, O., Herzog, G. F., Marti, K. and Caffee, M. W. (2006) Irradiation records, cosmic-ray exposure ages, and transfer time of meteorites. In *Meteorites and the Early Solar System II*, eds. Lauretta, D. S. and McSween, H. Y., Jr. Tucson: University of Arizona Press, pp. 829–851. A good summary of what is known about cosmic-ray exposure ages and the transfer of meteorites from the asteroid belt to Earth.

Jull, A. J. T. (2006) Terrestrial ages of meteorites. In *Meteorites and the Early Solar System II*, eds. Lauretta, D. S. and McSween, H. Y., Jr. Tucson: University of Arizona Press, pp. 889–905. This paper reviews what is known about terrestrial ages of meteorites.

Krot, A. N., Hutcheon, I. D., Brearley, A. J. *et al*. (2006) Timescales and setting for alteration of chondritic meteorites. In *Meteorites and the Early Solar System II*, eds. Lauretta, D. S. and McSween, H. Y., Jr. Tucson: University of Arizona Press, pp. 525–553. A good review of what is known about the timing and nature of secondary processing in chondrites.

References

Allègre, C. J., Manhès, G. and Göpel, C. (1995) The age of the Earth. *Geochimica et Cosmochimica Acta*, **59**, 1445–1456.

Amelin, Y., Krot, A. N., Hutcheon, I. D. and Ulyanov, A. A. (2002) Lead isotopic ages of chondrules and calcium-aluminum-rich inclusions. *Science*, **297**, 1679–1683.

Baker, J., Bizzarro, M., Wittig, N., Connelly, J. and Haack, H. (2005) Early planetesimal melting from an age of 4566.2 Gyr for differentiated meteorites. *Nature*, **436**, 1127–1131.

Bizzarro, M., Baker, J. A. and Haack, H. (2004) Mg isotope evidence for contemporaneous formation of chondrules and refractory inclusions. *Nature*, **431**, 275–278.

Bizzarro, M., Baker, J. A., Haack, H. and Lundgaard, K. L. (2005) Rapid timescales for accretion and melting of differentiated planetesimals inferred from ^{26}Al–^{26}Mg chronometry. *Astrophysical Journal*, **632**, L41–L44.

Borg, L. and Drake, M. J. (2005) A review of meteorite evidence for the timing of magmatism and of surface or near-surface liquid water on Mars. *Journal of Geophysical Research*, **110**, E12S03.

Bottke, W. F., Nesvorny, D., Vokrouhlicky, D. and Borbidelli, A. (2009) The Gefion family as the probable source of the L chondrite meteorites (abstr.). *Lunar and Planetary Science XL*, CD #1445.

Bouvier, A., Blichert-Toft, J., Moynier, F., Vervoort, J. D. and Albarède, F. (2007) Pb–Pb dating constraints on the accretion and cooling history of chondrites. *Geochimica et Cosmochimica Acta*, **71**, 1583–1604.

Bouvier, A., Blichert-Toft, J., Vervoort, J. D., Gillet, P. and Albarede, F. (2008) The case for old basaltic shergottites. *Earth and Planetary Science Letters*, **266**, 105–124.

Burkhardt, C., Kleine, T., Bourdon, B. *et al*. (2008) Hf–W mineral isochron for Ca, Al-rich inclusions: age of the solar system and the timing of core formation in planetesimals. *Geochimica et Cosmochimica Acta*, **72**, 6177–6197.

Chen, J. H., Papanastassiou, D. A. and Wasserburg, G. J. (1998) Re–Os systematics in chondrites and the fractionation of platinum group elements in the early solar system. *Geochimica et Cosmochimica Acta*, **62**, 3379–3392.

Clayton, D. D. (1988) Nuclear cosmochronology with analytic models of the chemical evolution of the solar neighborhood. *Monthly Notices of the Royal Astronomical Society*, **234**, 1–36.

Clayton, R. N., Hinton, R. W. and Davis, A. M. (1988) Isotopic variations in the rock-forming elements in meteorites. *Philosophical Transactions of the Royal Society of London*, A**325**, 483–501.

Cameron, A. G. W. and Truran, J. W. (1977) The supernova trigger for formation of the solar system. *Icarus*, **30**, 447–461.

Connelly, J. N. and Bizzarro, M. (2009) Pb–Pb dating of chondrules from CV chondrites by progressive dissolution. *Chemical Geology*, **259**, 143–151.

Dauphas, N., Cook, D. L., Sacarabany, A. *et al*. (2008) Iron-60 evidence for early injection and efficient mixing of stellar debris in the protosolar nebula. *Astrophysical Journal*, **686**, 560–569.

Diehl, R., Halloin, H., Kretschmer, K. *et al*. (2006) ^{26}Al in the inner galaxy. *Astronomy and Astrophysics*, **449**, 1025–1031.

Endress, M., Ainner, E. and Bischoff, A. (1996) Early aqueous activity on primitive meteorite parent bodies. *Nature*, **379**, 701–703.

Galer, S. J. G. and Goldstein, S. L. (1996) Influence of accretion on lead in the Earth. In *Isotopic Studies of Crust-Mantle Evolution*, eds. Basu, A. R. and Hart, S. R. Washington, D.C.: American Geophysical Union, pp. 75–98.

Göpel, C., Manhès, G. and Allègre, C.-J. (1994) U–Pb systematics of phosphates from unequilibrated ordinary chondrites. *Earth and Planetary Science Letters*, **121**, 153–171.

Halliday, A. N. (2000) Terrestrial accretion rates and the origin of the Moon. *Earth and Planetary Science Letters*, **176**, 17–30.

Halliday, A. N. (2004) The origin and earliest history of the Earth. In *Treatise on Geochemistry, Vol. 1. Meteorites, Comets, and Planets*, ed. Davis, A. M. Oxford: Elsevier, pp. 509–557.

Harper, C. L. and Jacobsen, S. B. (1996) Evidence for ^{142}Hf in the early solar system and constraints on the timescale of terrestrial core formation. *Geochimica et Cosmochimica Acta*, **60**, 1131–1153.

Hartmann, W. K., Ryder, G., Dones, L. and Grinspoon, D. (2000) The time-dependent intense bombardment of the primordial Earth/Moon system. In *Origin of the Earth and Moon*, eds. Canup, R. M. and Righter, K. Tucson: University of Arizona Press, pp. 493–512.

Herzog, G. F. (2005) Cosmic-ray exposure ages of meteorites. In *Treatise on Geochemistry, Vol. 1. Meteorites, Comets, and Planets*, ed. Davis, A. M. Oxford: Elsevier, pp. 347–380.

Hohenberg, C. M. and Pravdivtseva, O. V. (2008) I–Xe dating: from adolescence to maturity. *Chemie der Erde*, **68**, 339–351.

Hoppe, P., Macdougall, D. and Lugmair, G. W. (2004) High spatial resolution ion microprobe measurements refine chronology of Orgueil carbonate formation (abstr.). *Lunar and Planetary Science XXXV*, CD #1313.

Hsu, W., Huss, G. R. and Wasserburg, G. J. (2003) Al–Mg systematics of CAIs, POI, and ferromagnesian chondrules from Ningqiang. *Meteoritics and Planetary Science*, **38**, 35–48.

Hsu, W., Wasserburg, G. J. and Huss, G. R. (2000) High time resolution using ^{26}Al in the multistage formation of a CAI. *Earth and Planetary Science Letters*, **182**, 15–29.

Hua, X., Huss, G. R., Tachibana, S. and Sharp, T. G. (2005) Oxygen, silicon, and Mn–Cr isotopes of fayalite in the oxidized Kaba CV3 chondrite: constraints for its formation history. *Geochimica et Cosmochimica Acta*, **69**, 1333–1348.

Huss, G. R., MacPherson, G. J., Wasserburg, G. J., Russell, S. S. and Srinivasan, G. (2001) Aluminum-26 in calcium-aluminum-rich inclusions and chondrules from unequilibrated ordinary chondrites. *Meteoritics and Planetary Science*, **36**, 975–997.

Huss, G. R., Tachibana, S. and Nagashima, K. (2007) ^{26}Al and ^{60}Fe in chondrules from unequilibrated ordinary chondrites. *Meteoritics and Planetary Science*, **42**, A57.

Hutcheon, I. D., Krot, A. N., Keil, K., Phinney, D. L. and Scott, E. R. D. (1998) ^{53}Mn–^{53}Cr dating of fayalite formation in the CV3 chondrite Mokoia: evidence for asteroidal alteration. *Science*, **282**, 1865–1867.

Hutcheon, I. D., Krot, A. N. and Ulyanov, A. A. (2000) ^{26}Al in anorthite-rich chondrules in primitive carbonaceous chondrites: evidence chondrules postdate CAI (abstr.). *Lunar and Planetary Science XXXI*, CD #1869.

Hutcheon, I. D., Marhas, K. K., Krot, A. N., Goswami, J. N. and Jones, R. H. (2009) ^{26}Al in plagioclase-rich chondrules in carbonaceous chondrites: evidence for extended duration of chondrule formation. *Geochimica et Cosmochimica Acta*, **73**, 5080–5099.

Jacobsen, B., Yin, Q.-Z., Moynier, F. *et al*. (2008) ^{26}Al–^{26}Mg and ^{207}Pb–^{206}Pb systematics of Allende CAIs: canonical solar initial ^{26}Al/^{27}Al ratio reinstated. *Earth and Planetary Science Letters*, **272**, 353–364.

Kita, N. T., Lin, Y., Kimura, M. and Morishita, Y. (2004) The ^{26}Al–^{26}Mg chronology of a type C CAI and POIs in Ningqiang carbonaceous chondrite (abstr.). *Lunar and Planetary Science XXXV*, CD #1471.

Kita, N. T., Nagahara, H., Togashi, S. and Morshita, Y. (2000) A short duration of chondrule formation in the solar nebula: evidence from ^{26}Al in Semarkona ferromagnesian chondrules. *Geochimica et Cosmochimica Acta*, **64**, 3913–3922.

Kleine, T., Mezger, K., Münker, C., Palme, H. and Bischoff, A. (2004) ^{182}Hf–^{182}W isotope systematics of chondrites, eucrites, and Martian meteorites: chronology of core formation and early mantle differentiation in Vesta and Mars. *Geochimica et Cosmochimica Acta*, **68**, 2935–2946.

Kleine, T., Münker, C., Mezger, K. and Palme, H. (2002) Rapid accretion and early core formation on asteroids and the terrestrial planets from Hf–W chronometry. *Nature*, **418**, 952–955.

Krot, A. N., Amelin, Y., Cassen, P. and Meibom, A. (2005) Young chondrules in CB chondrites from a giant impact in the early solar system. *Nature* **436**, 989–992.

Kunihiro, T., Rubin, A. E., McKeegan, K. D. and Wasson, J. T. (2004) Initial $^{26}Al/^{27}Al$ in carbonaceous-chondrite chondrules: too little ^{26}Al to melt asteroids. *Geochimica et Cosmochimica Acta*, **68**, 2947–2957.

Kurahashi, E., Kita, N. T., Nagahara, H. and Morishita, Y. (2008) ^{26}Al–^{26}Mg systematics of chondrules in primitive CO chondrite. *Geochimica et Cosmochimica Acta*, **72**, 3865–3882.

Lada, C. J. and Lada, E. A. (2003) Embedded clusters in molecular clouds. *Annual Reviews of Astronomy and Astrophysics*, **41**, 57–115.

Lee, D. C. and Halliday, A. N. (1997) Core formation on Mars and differentiated asteroids. *Nature*, **388**, 854–857.

Lee, T., Papanastassiou, D. A. and Wasserburg, G. J. (1977) Aluminum-26 in the early solar system: fossil or fuel? *Astrophysical Journal Letters*, **211**, L107–L110.

Lugmair, G. W. and Shukolyukov, A. (1998) Early solar system timescales according to the ^{53}Mn–^{53}Cr system. *Geochimica et Cosmochimica Acta*, **62**, 2863–2886.

McKee, C. F. and Ostriker, J. P. (1977) A theory of the interstellar medium: three components regulated by supernova explosions in an inhomogeneous substrate. *Astrophysical Journal*, **218**, 148–169.

McKeegan, K. D., Greenwood, J. P., Leshin, L. A. and Cosarinsky, M. (2000) Abundance of ^{26}Al in ferromagnesian chondrules of unequilibrated ordinary chondrites (abstr.). *Lunar and Planetary Science XXXI*, CD #2009.

McSween, H. Y. (2008) Martian meteorites as crustal samples. In *The Martian Surface: Composition, Mineralogy, and Physical Properties*, ed. Bell, J. F., III. Cambridge: Cambridge University Press, pp. 383–396.

Mostefaoui, S., Kita, N., Togashi, S. *et al*. (2002) The relative formation ages of ferromagnesian chondrules inferred from their initial aluminum-26/aluminum-27 ratios. *Meteoritics and Planetary Science*, **37**, 421–438.

Nagashima, K., Krot, A. N. and Chaussidon, M. (2007) Aluminum–magnesium isotope systematics of chondrules from CR chondrites (abstr.). *Meteoritics and Planetary Science*, **42**, Supplement, A115.

Nagashima, K., Krot, A. N. and Huss, G. R. (2008) ^{26}Al in chondrules from CR carbonaceous chondrites (abstr.). *Lunar and Planetary Science XXXIX*, CD #2224.

Neukum, G., Ivanov, B. A. and Hartmann, W. K. (2001) Cratering records in the inner solar system in relation to the lunar reference system. *Space Science Reviews*, **96**, 55–86.

Nyquist, L. E., Bogard, D. D., Shih, C.-Y. *et al*. (2001) Ages and geologic histories of Martian meteorites. *Space Science Reviews*, **96**, 105–164.

Nyquist, L. E., Bogard, D. D., Shih, C.-Y. *et al*. (2009b) Concordant Rb–Sr, Sm–Nd, and Ar–Ar ages for Northwest Africa 1460: a 346 Ma old basaltic shergottite related to "lherzolitic" shergottites. *Geochimica et Cosmochimica Acta*, **73**, 4288–4309.

Reynolds, J. H. (1960) Determination of the age of the elements. *Physical Reviews Letters*, **4**, 8–10.

Rudraswami, N. G. and Goswami, J. N. (2007) ^{26}Al in chondrules from unequilibrated L chondrites: onset and duration of chondrule formation in the early solar system. *Earth and Planetary Science Letters*, **257**, 231–244.

Schmitz, B., Peucker-Ehrenbrink, B., Linstrom, M. and Tassinari, M. (1997) Accretion rates of meteorites and cosmic dust in the early Ordovician. *Science*, **278**, 88–90.

Schmitz, B., Tassinari, M. and Peucker-Ehrenbrink, B. (2001) A rain of ordinary chondritic meteorites in the early Ordovician. *Earth and Planetary Science Letters*, **194**, 1–15.

Schmitz, B., Häggström, T. and Tassinari, M. (2003) Sediment-dispersed extraterrestrial chromite traces a major asteroid disruption event. *Science*, **300**, 961–964.

Shen, J. J., Papanastassiou, D. A. and Wasserburg, G. J. (1996) Precise Re–Os determinations and systematics of iron meteorites. *Geochimica et Cosmochimica Acta*, **60**, 2887–2900.

Sheng, Y. J., Hutcheon, I. D. and Wasserburg, G. J. (1991) Origin of plagioclase-olivine inclusions in carbonaceous chondrites. *Geochimica et Cosmochimica Acta*, **55**, 581–599.

Smoliar, M. I. (1993) A survey of Rb–Sr systematics of eucrites. *Meteoritics*, **28**, 105–113.

Snyder, G. A., Borg, L. E., Nyquist, L. E. and Taylor, L. A. (2000) Chronology and isotopic constraints on lunar evolution. In *Origin of the Earth and Moon*, eds. Canup, R. M. and Righter, K. Tucson: University of Arizona Press, pp. 361–393.

Srinivasan, G., Huss, G. R. and Wasserburg, G. J. (2000) A petrographic, chemical and isotopic study of calcium-aluminum inclusions and aluminum-rich chondrules from the Axtell (CV3) chondrite: *Meteoritics and Planetary Science*, **35**, 1333–1354.

Sugiura, N. and Krot, A. N. (2007) ^{26}Al–^{26}Mg systematics of Ca-Al-rich inclusions, amoeboid olivine aggregates and chondrules form the ungrouped carbonaceous chondrite Acfer 094. *Meteoritics and Planetary Science*, **42**, 1183–1195.

Tera, F. (1980) Reassessment of the 'Age of the Earth'. *Carnegie Institution of Washington Year Book*, **79**, 524–531.

Thrane, K., Bizzarro, M. and Baker, J. A. (2006) Extremely brief formation interval for refractory inclusions and uniform distribution of Al-26 in the early solar system. *Astrophysical Journal Letters*, **646**, L159–L162.

Trieloff, M., Jessberger, E. K., Herrwerth, I. *et al*. (2003) Structure and thermal history of the H-chondrite parent asteroid revealed by thermochronometry. *Nature*, **422**, 502–506.

Trinquier, A., Birck, J.-L., Allègre, C. J., Göpel, C. and Ulfbeck, D. (2008) ^{53}Mn–^{53}Cr systematics of early solar system revisited. *Geochimica et Cosmochimica Acta* **72**, 5146–5163.

Wadhwa, M., Srinivasan, G. and Carlson, R. W. (2006) Timescales of planetesimal differentiation in the early solar system. In *Meteorites and the Early Solar System II*, eds. Lauretta, D. S. and McSween, H. Y., Jr. Tucson: University of Arizona Press, pp. 715–731.

Wadhwa, M., Amelin, Y., Bogdanovski, O. *et al*. (2009) Ancient relative and absolute ages for a basaltic meteorite: implications for timescales of planetesimal accretion and differentiation. *Geochimica et Cosmochimica Acta*, **73**, 5189–5201.

Walton, E. L., Kelley, S. P. and Herd, C. R. D. (2008) Isotopic and petrographic evidence for young Martian basalts. *Geochimica et Cosmochimica Acta*, **72**, 5819–5837.

Wang, W., Harris, M. J., Diehl, R. *et al*. (2007) SPI observations of the diffuse ^{60}Fe emission in the galaxy. *Astronomy and Astrophysics*, **469**, 1005–1012.

Warren, P. H. (2004) The Moon. In *Treatise on Geochemistry, Vol. 1. Meteorites, Comets, and Planets*, ed. Davis, A. M. Oxford: Elsevier, pp. 559–599.

Yin, Q. Z., Jacobsen, S. B., Yamashita, K. *et al*. (2002) A short timescale for terrestrial planet formation from Hf–W chronometry of meteorites. *Nature*, **418**, 949–952.

Young, E., Simon, J. I., Galy, A. *et al*. (2005) Supra-canonical $^{26}Al/^{27}Al$ and the residence time of CAIs in the solar protoplanetary disk. *Science*, **308**, 223–227.

Zinner, E. and Göpel, C. (2002) Aluminum-26 in H4 chondrites: implications for its production and its usefulness as a fine-scale chronometer for early solar system events. *Meteoritics and Planetary Science*, **37**, 1001–1013.

10 The most volatile elements and compounds: organic matter, noble gases, and ices

Overview

The most volatile constituents of meteorites, small bodies, and planets are highly depleted in rocky bodies compared to the solar composition. In this chapter we first consider the sometimes bewilderingly complex molecules composed of carbon and hydrogen, often with other elements like oxygen, nitrogen, and sulfur (organic compounds). Following an introduction to terminology and structures, we focus on the organic matter in chondritic meteorites – the only extraterrestrial organic materials currently available for detailed analysis. This material appears to be a mixture of compounds inherited from the interstellar medium and synthesized within solar system bodies. Next, we look at noble gases, which do not condense as solids and thus are strongly depleted in meteorites and planets, relative to solar system abundances. The concentrations and isotopic compositions of noble gases in meteorites and planetary atmospheres provide unique perspectives on processes occurring in the early solar system and during planetary differentiation. Finally, we briefly consider ices, surprisingly abundant phases that dominate the outer solar system. Ices trapped noble gases and provided sites for the formation of simple organic compounds in space.

Volatility

In several previous chapters, we have discussed element volatility. Here we focus on some of the most volatile constituents in meteorites – organic compounds, noble gases, and ices. Each of these actually constitutes a voluminous subject of its own in cosmochemistry, and we can only provide overviews of these interesting components.

This may seem like an eclectic choice of materials to share space in a chapter of this book. However, these components have a number of related characteristics. Ices condensed onto interstellar silicate grains because of the frigid temperatures in the interstellar medium, and they may have remained condensed in the outer reaches of the solar system throughout its history. Noble gases did not condense as ices, at least directly; instead, they were adsorbed onto or trapped within ices of other compounds. The simplest organic compounds are thought to have formed by low-temperature reactions on ice-coated grains in molecular clouds. Although some organic compounds are decidedly not volatile, these

molecules were synthesized from simpler organic precursors that were highly volatile. Organic polymers also serve as hosts for trapped noble gases. Thus the components described in this chapter can be considered fellow travelers in cosmochemical environments.

Organic molecules are composed of carbon and hydrogen, usually combined with other atoms such as oxygen, nitrogen, sulfur, and phosphorus. In modern usage, the term *organic* does not necessarily imply formation by or occurrence in organisms, although that was its original connotation. Abiotic organic compounds are important constituents of chondrites and other solar system objects, and they have been telescopically observed in significant quantities in interstellar space. These molecules are of obvious interest as precursors for life, but organic matter also provides a window into processes in the ISM, the nebula disk, and planetesimals.

Noble gases, occupying the rightmost column of the periodic table, have completely filled electron shells and thus do not easily form chemical compounds. More so than any other elements, they partition into a gas phase. Because the Earth and the rest of the bodies in the inner solar system were made from solids, excluding gases for the most part, noble gases are very scarce in these bodies, accounting for the synonym "rare gases." As we shall see, the important roles that helium, neon, argon, krypton, and xenon play in cosmochemistry are actually related to their miniscule abundances in meteorites and planets.

Ice mantles are important constituents of interstellar grains in molecular clouds, and icy bodies dominate the outer reaches of the solar system. The region of the solar system where ices were stable increased with time as the solar system formed, as accretion rates of materials to the disk waned and the disk cooled. The giant planets and their satellites formed, in part, from these ices, and probably also from the nebular gas itself.

Organic matter: occurrence and complexity

Organic compounds have been observed in interstellar and circumstellar gases using telescopes fitted with infrared and microwave spectrometers. The bonds in organic molecules bend and stretch when absorbing certain wavelengths of energy, and this bending and stretching can be detected by spectroscopic measurements. These absorptions are diagnostic for certain compounds. An updated list of organic molecules telescopically detected in the ISM is maintained by the National Radio Astronomy Observatory web site (www.nrao.edu).

Organic compounds appear to be absent in lunar rocks and soils returned by Apollo astronauts. Similarly, these compounds were not found by life-detection experiments on the Viking landers on Mars, and soil analyzed by APXS on the Mars Pathfinder rover contained no carbon above the detection limit. However, organic compounds have been discovered in Martian meteorites. Some of these compounds are terrestrial contaminants, but others may be indigenous to the meteorites. A recent report presents strong evidence for plumes of methane (CH_4) in the Martian atmosphere (Mumma *et al*., 2009), but whether the methane is geochemical or biological in origin and whether it is ancient or recent has not yet been determined. Methane and several photochemically produced hydrocarbons such as acetylene (C_2H_2) and ethane (C_2H_6) derived from methane have been found in

the atmospheres of Jupiter, Saturn, Uranus, and Neptune. A rich array of organic compounds is prevalent in the hazy atmosphere of Titan, one of Saturn's moons, and there is evidence suggesting that hydrocarbon aerosols may rain onto its surface and persist there as seas of liquefied methane. Dark materials occurring on the surfaces of other icy satellites are thought to contain complex organic molecules, sometimes called "tholins." Organic molecules have also been identified in the dust shed from comets and in interplanetary dust particles (IDPs) that may derive from comets. Organic matter in comets and other ice-bearing planetesimals and satellites is discussed more thoroughly in Chapter 12.

The most important sources of detailed information about extraterrestrial organic compounds are chondritic meteorites. Organic matter in meteorites can be extracted and analyzed using the full panoply of methods available in the laboratory. One major problem, though, is contamination by terrestrial organic matter. Simply holding a meteorite in one's fingers adds enough contaminants to complicate organic analyses, and there are numerous examples of meteorite studies that have been compromised by terrestrial contamination. Developments in understanding the organic components in meteorites have proceeded rapidly, as improvements have been made in analytical capabilities. Organic compounds occurring in trace quantities can now be identified, and the isotopic composition of carbon, hydrogen, nitrogen, and sulfur in specific compounds can be measured. It is also useful to determine *chirality* – chiral compounds that can exist in mirror-image structures (see below). All these properties place constraints on the formation and history of organic compounds.

In this chapter, we will focus on what has been learned from analyses of carbonaceous chondrites, which contain more organic matter than most other chondrites and consequently have been the focus of most research in this area. The organic matter in carbonaceous chondrites can be divided into two very different kinds of material. The most abundant constituents, comprising between 70 and 99% of the total organic matter, are high-molecular-weight compounds ("macromolecules") that cannot be readily extracted from the meteorites with solvents and strong acids. The organic matter in the CO, CV, and CK chondrite classes is almost exclusively macromolecules. The organic matter in the CI, CM, and CR classes also includes up to 30% low-molecular-weight compounds that can be extracted with solvents. These extractable compounds can be much more readily characterized.

Especially large amounts of the uncontaminated CM chondrites Murchison and Tagish Lake have been available since their falls in 1969 and 2000, respectively, and most modern research on extraterrestrial organic matter has focused on these meteorites. Considerable research has also been done on organic matter in the Orgueil CI chondrite, but this meteorite has been contaminated during its nearly 150 years on Earth.

Extractable organic matter in chondrites

Soluble organic compounds in chondrites are highly varied in structure, composition, and size (molecular weight). Table 10.1 lists the groups of extractable organics in Murchison (CM2) and Tagish Lake (another CM-like chondrite). These two falls are the most

Table 10.1 Major groups of soluble organic compounds identified in carbonaceous chondritic meteorites (Pizzarello *et al.*, 2006)

	Tagish Lake		Murchison	
	Conc. (ppm)	Compounds	Conc. (ppm)	Compounds
Aliphatic hydrocarbons	5	12	>35	140
Aromatic hydrocarbons	1	13	15–28	87
Polar hydrocarbons	n.d.	2	<120	10
Carboxylic acids	<0.1	4	60	74
Amino acids	n.d.	0	15	7
Dicarboxylic acids	17.5	18	>30	17
Dicarboximides	5.5	9	>50	2
Pyridine carboxylic acids	7.5	7	>7	7
Sulfonic acids	≥20	1	67	4
Phosphonic acids	n.d.	n.d.	2	4
Amines	<0.1	3	13	20
Amides	<0.1	1	n.d.	27
Sugar derivatives	n.d.	n.d.	30	19

Box 10.1 **A crash course in organic nomenclature**

The basic skeleton of bonded carbon atoms can be arranged in simple straight chains, branched chains, one or more rings, or combinations of these structures. The simplest organic molecules are *hydrocarbons*, which consist solely of carbon and hydrogen atoms. Carbon atoms have four valence electrons that must be satisfied either by single covalent bonds to four separate atoms or some combination of single and double (or rarely triple) bonds. A double bond is one that involves two valence electrons. Hydrocarbons that have only single bonds are said to be *saturated*, whereas those that contain double bonds are *unsaturated*.

Carbon atoms can be linked together to form either straight-chain (*aliphatic*) or cyclical (*aromatic*) structures. A saturated aliphatic hydrocarbon is called an *alkane*, where the suffix *-ane* refers to the lack of any double bonds in the molecule. An unsaturated aliphatic hydrocarbon is called an *alkene*, where the suffix *-ene* denotes the presence of a double bond. Alkanes (and alkenes) are named according to the number of carbon atoms in the chain, as in methane (one), ethane (two), propane (three), butane (four), pentane (five), and so on. Hydrocarbon structures can be represented by a variety of two-dimensional drawings (Fig. 10.1a). All the atoms and bonds can be illustrated (as in the top pentane diagram), all the bonds except those between the carbons in the chain can be omitted (middle pentane diagram), or the chain can be represented by a "sawtooth" drawing (bottom pentane diagram) in which the kink at each line segment represents a carbon atom. Leftover valence electrons (those not involved in bonding the carbon atoms together) attach hydrogen atoms to the molecule at each kink.

Stable configurations of carbon atoms also occur where double (C=C) bonds alternate with single (C-C) bonds to form a pattern like C-C=C-C=C-C. This configuration, referred to as *conjugated*, is common in polyunsaturated compounds. If conjugation occurs in a ring structure with three double and three single bonds (Fig. 10.1a), the configuration is *aromatic*. Aromatic

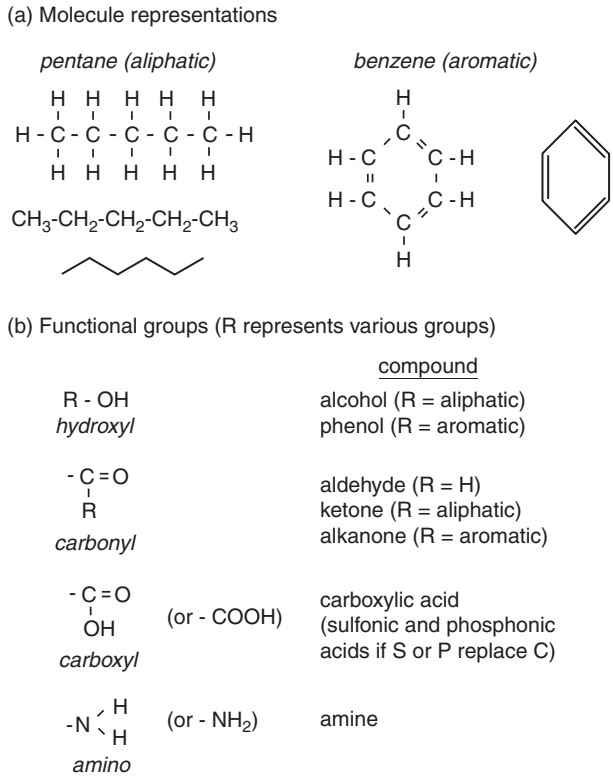

Fig. 10.1 **Molecular representations and functional groups in organic compounds. (a) Different ways to represent the structures of aliphatic and aromatic compounds. (b) Some important functional groups attached to organic skeletons, and the corresponding names of organic compounds.**

compounds are thus unsaturated and typically very stable. Two representations of the simplest aromatic ring (benzene) are shown in Figure 10.1a. In the simple line sketch, carbon atoms are understood to occur at each corner, the single hydrogen atoms attached to each carbon are not shown, and the alternating single and double bonds are indicated.

Groups of elements bonded to the carbon backbone (whether it is a chain or ring) are called *functional groups*, because they are usually reactive and thus control the chemical behavior of the compound. Functional groups (some common ones are illustrated in Fig. 10.1b) involve combinations of hydrogen atoms with one or more atoms of another element, commonly carbon, oxygen, nitrogen, sulfur, or phosphorus. The presence of non-bonding electrons in elements other than carbon in functional groups makes them likely sites for chemical reactions. Organic compounds are often grouped under the name of the functional group they contain. For example, alcohols and phenols are based on combinations of the hydroxyl functional group –OH with aliphatic or aromatic groups, respectively. Carboxylic acids include the carboxyl group, and the carbon atom in a carboxyl can be replaced by sulfur or phosphorus to produce sulfonic or phosphonic acids. Amines are based on the nitrogen-containing amino group. There are other functional groups besides those in Figure 10.1b, but we will ignore them

for now. Massive organic molecules include sugars, which are aliphatic compounds with many hydroxyl groups in place of hydrogen atoms. Polycyclic aromatic hydrocarbons (abbreviated PAHs) involve many aromatic rings hooked together.

Although we typically represent organic compounds with two-dimensional drawings, these molecules are actually three-dimensional structures. Several different spatial configurations of atoms attached to a central carbon atom can exist; these *isomers* have the same chemical formula, but have mirror-image structures (the *chirality* mentioned in an earlier section). Your hands provide an illustration of this phenomenon – each hand has the same structure of four fingers and a thumb, but you cannot superimpose them (palms facing up). Similarly, certain amino acids and sugars have identical compositions but differ by the placement of their functional groups on one side or the other of the central carbon atom. Isomers that are mirror images of each other, called *enantiomers*, rotate polarized light in different directions. Compounds that rotate light clockwise are called dextrorotatory (denoted by the prefix D-), whereas counter-clockwise rotation is referred to as levorotatory (denoted by L-). Abiotic organic compounds usually occur as *racemic mixtures*, which have D- and L-enantiomers in equal proportions. In contrast, biologically produced organic matter strongly favors one enantiomer. However, such compounds tend to racemize in relatively short geologic timescales.

completely analyzed meteorites in terms of organic components, and their differences illustrate the range of compounds so far characterized. Tagish Lake may be especially informative about volatile organics, because it fell in winter onto an ice-covered lake and was recovered in a frozen state. Let's now consider what is known about some specific compounds from this list (Gilmour, 2004; Pizzarello *et al*., 2006).

Aliphatic hydrocarbons in meteorites range in size from methane (which has one carbon and thus really isn't a chain) to long saturated chains (alkanes) with up to 30 carbon atoms. There has been a long debate about whether these hydrocarbons are indigenous meteorite components or terrestrial contaminants. In the 1960s, analyses of alkanes in the Orgueil CI chondrite spawned a heated controversy about extraterrestrial life, but later analyses revealed that these were contaminants (discussed later in Box 10.2). However, analyses of clean samples of the Tagish Lake fall have now demonstrated that some alkanes are indigenous to chondrites. Isotopic analyses of hydrogen and carbon in aliphatic mixtures from Murchison gave average values of $\delta D = 211$ permil and $\delta^{13}C = 9$ permil. (As explained in Chapter 2, the δ notation refers to isotope ratios, in this case D/H or $^{13}C/^{12}C$, referred to some standard and expressed in parts per thousand.) The $\delta^{13}C$ values measured for individual aliphatic compounds tend to be lighter (more ^{12}C-rich). A hypothesis that hydrocarbons formed in the nebula by a Fischer-Tropsch type (FTT) synthesis from CO and H_2 in the presence of iron metal has now been discredited. Catalyzed reactions such as FTT are structurally selective, whereas the aliphatic hydrocarbons in chondrites are structurally diverse, including branched and cyclic molecules.

The literature on *aromatic hydrocarbons* reveals considerable differences in the relative abundances of different compounds, almost certainly a result of different analytical approaches. The most abundant aromatic compounds in Murchison are the PAHs

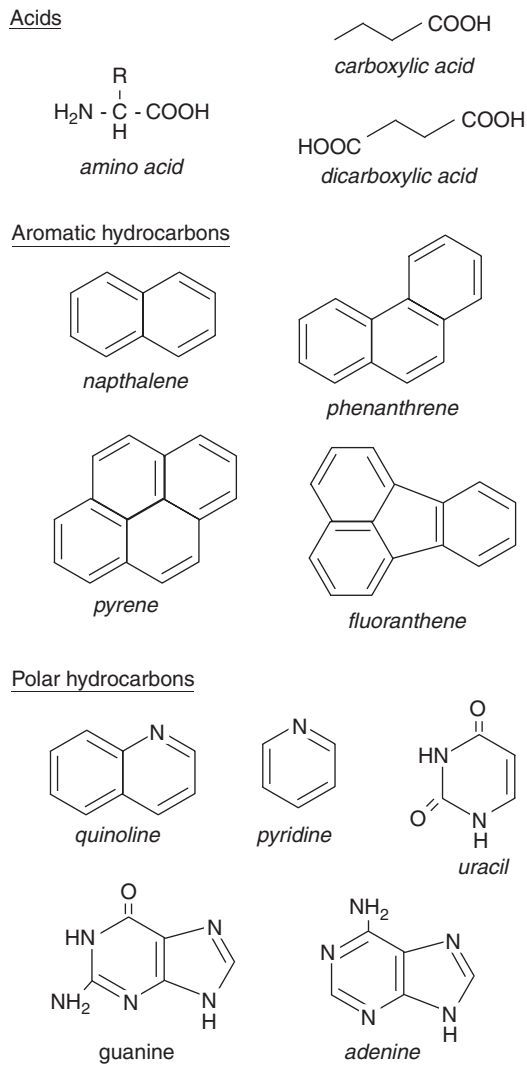

Fig. 10.2 **Structures of some organic compounds found in carbonaceous chondrites.**

fluoranthene and pyrene (Fig. 10.2). The extractable PAHs are quite complex, and include high-molecular-weight compounds with up to 22 carbons. However, low-molecular-weight PAHs such as napthalene (Fig. 10.2) are also fairly abundant. The average isotopic compositions of aromatic hydrocarbons in Murchison are $\delta D = 353$ permil and $\delta^{13}C = 5.5$ permil. As for aliphatic hydrocarbons, all the carbon isotopic compositions measured for individual aromatic compounds are lighter than the average aromatic $\delta^{13}C$.

We did not mention *polar hydrocarbons* in the crash course on organic nomenclature (Box 10.1). This term refers to compounds containing one or more nitrogen, oxygen, or sulfur atoms replacing carbon atoms in ring structures or sometimes attached to them. These

elements are more electronegative than carbon, so C–N, C–O, and C–S bonds are polar, hence the name. A few of the more common examples in carbonaceous chondrites are illustrated in Figure 10.2. In Murchison, these compounds are abundant, comprising nearly two-thirds of the extractable organic matter. However, it is not certain that all these compounds are indigenous to meteorites.

Carboxylic acids are structurally diverse, with equal concentrations of straight-chain and branched compounds. The abundances of carboxylic acids decrease as the number of carbon atoms in the structure increase. Dicarboxylic acids, containing two carboxyl groups (Fig. 10.2), also occur. These acids are abundant in Murchison. The measured $\delta^{13}C$ and δD values are higher for branched than straight-chain acids. This isotopic difference points to synthesis of the branched and linear molecules under different conditions.

Amino acids, which contain both the amino and carboxylic acid functional groups (Fig. 10.2), are essential components of proteins in the Earth's biosphere. Twenty common terrestrial amino acids are almost exclusively L-enantiomers, and this chirality is indispensable for their functioning in living organisms. Amino acids in Murchison and Orgueil show much greater structural diversity, with more than 80 aliphatic species having up to eight carbon atoms (the limit of solubility), and with abundances declining as the number of carbon atoms increases. The molecular complexity of the amino acids and isotopic compositions of individual compounds indicate at least two formation mechanisms. L- and D-enantiomers occur in approximately equal amounts; however, there appears to be a slight excess of L-forms in some amino acids. Terrestrial contamination (pure L-enantiomers) could cause such an excess, but careful analyses of four amino acids not known to occur on Earth also showed these patterns. One hypothesis proffered to explain the chirality in amino acids was photolysis by ultraviolet, circularly polarized light in interstellar space. Another possibility is that L-enantiomers have slightly higher thermodynamic stability than D-forms. A possible correlation with non-racemic amino acids and clay minerals suggests yet another explanation – that formation of organic components on mineral substrates might induce chirality. The last mechanism is consistent with the most popular mechanism for forming amino acids: a Strecker reaction between hydrocarbons (aldehydes and ketones), ammonia and HCN during aqueous alteration on asteroid parent bodies. Curiously, Tagish Lake contains only a few amino acids at low abundance. This implies that a different formation mechanism dominated amino acid production in Tagish Lake.

Sulfonic and *phosphonic acids* contain sulfur and phosphorus in their structures, substituting for carbon in the carboxyl function group. They are fairly abundant, but have not been studied extensively.

Amines are nitrogen-containing compounds found in all meteorites that contain amino acids. Their abundances are comparable to those of amino acids, and abundances decrease with increasing numbers of carbon atoms. Similarities between amines and amino acids in the same meteorite have led to the suggestion that amines formed from the amino acids by decarboxylation (loss of the carboxylic acid functional group). This process commonly occurs on heating.

Alcohols, aldehydes, ketones, and *sugars* occur in small quantities in carbonaceous chondrites.

Insoluble macromolecules in chondrites

The majority of organic carbon in chondrites (70–99% of the total) is present as complex, insoluble macromolecular material. It can be separated from meteorites only by demineralizing the samples with harsh acid treatments. Besides carbon, the insoluble organic fraction contains hydrogen, oxygen, nitrogen, and sulfur, and the proportions of these elements vary from meteorite to meteorite. The average composition of this material, expressed relative to 100 carbon atoms, is $C_{100}H_{70}N_3O_{12}S_2$ for Murchison and $C_{100}H_{46}N_{10}O_{15}S_{4.5}$ for Tagish Lake (Pizzarello *et al*., 2006). Identifying the compounds present in these macromolecules poses a daunting analytical challenge. In the TEM, this material is unstructured and heterogeneous and reveals little about its makeup. Because solvents are not useful in separating the various compounds, macromolecular organic material has mainly been analyzed using harsh heating or chemical degradation techniques that break the huge molecules into smaller fragments that can be studied.

Oxidative degradation together with detailed analysis of the abundance and composition of the fragmentation products have provided a general picture of the insoluble macromolecular material. It consists primarily of aromatic compounds of various types with OH and COOH functional groups. The aromatic compounds are bridged by alkyl chains and ether linkages. Pyrolysis experiments on the insoluble organic matter release aromatic compounds such as benzene, toluene, and napthalene, leaving behind an essentially unmodified residue of PAHs with higher molecular weights. This may suggest two aromatic components are actually present, one more labile and one refractory. The labile compounds tend to be more deuterium rich. It has been suggested that the labile component may have formed in the ISM, and the other during aqueous alteration on asteroid parent bodies. The dominant aromatic structural units in the labile material have one, two, or three rings, highly substituted with alkyl branches and functional groups like –OH and –COOH. Other aromatic molecules such as benzene, carboxylic acids, aromatic ketones, and phenols are also present in pyrolysis products, as are nitrogen-containing compounds like pyridine and quinoline. Aliphatic hydrocarbons occur within and around the aromatic network.

Nuclear magnetic resonance (NMR) spectra of bulk macromolecular material provide information on bonding and the nature of functional groups. The major functional groups identified are illustrated in the NMR spectrum of Figure 10.3, which also shows a prominent peak corresponding to aromatic carbon. NMR spectra confirm the conclusion from decomposition studies that this material is mostly aromatic. The relative abundances of aromatic and aliphatic compounds differ significantly among the chondrite classes (Fig. 10.4). Estimates of the relative proportion of aromatic carbon atoms vary from 61–66% in Murchison to >80% in Tagish Lake (Cody and Alexander, 2005).

In addition to the macromolecular organic compounds, the insoluble organic material also contains graphitic flakes, nanotubes, and spheres, some of which are hollow (Fig. 10.5) (Garvie and Buseck, 2004). These flakes and spheres, which constitute up to 10% of the insoluble material in Tagish Lake, have very low contents of hydrogen, oxygen, and nitrogen compared to the rest of the macromolecular material. Some of the spheres also exhibit large ^{15}N enrichments. It is not clear whether some of the spheres are presolar in origin.

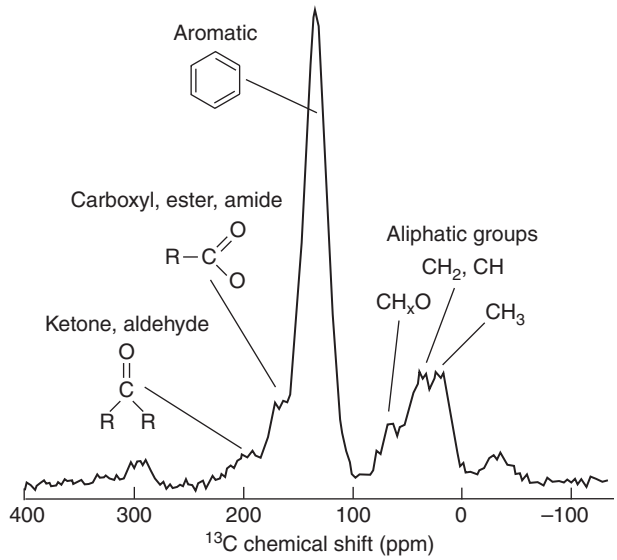

Fig. 10.3 A ^{13}C-NMR spectrum of insoluble organic matter in Murchison showing a prominent peak for aromatic carbon, demonstrating its high abundance. Other, smaller peaks correspond to the various identified functional groups. The small peaks at each end of the spectrum are artifacts of the method. After Cody *et al.* (2002).

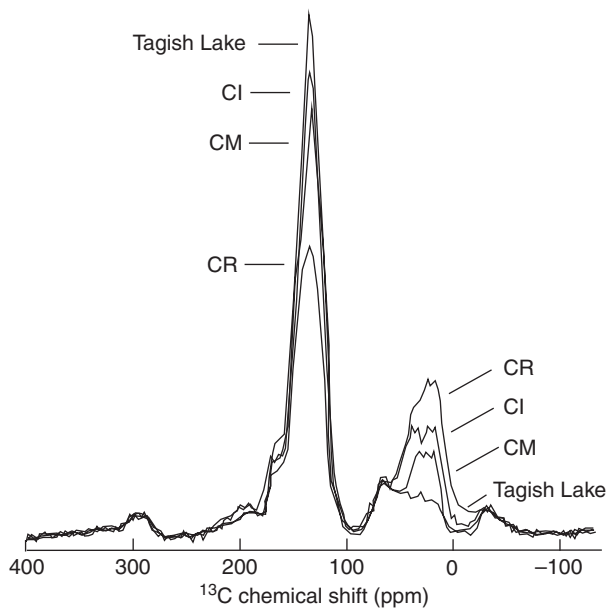

Fig. 10.4 Comparison of ^{13}C-NMR spectra of CR, CI, CM, and Tagish Lake chondrites, illustrating differences in the relative abundances of aromatic and aliphatic compounds in their insoluble organic materials.

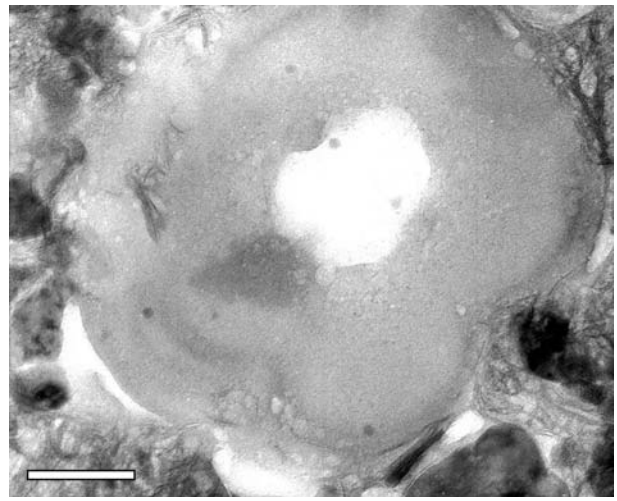

Fig. 10.5 TEM image of a macromolecular particle found in the carbonaceous chondrite Tagish Lake. Up to 10% of the insoluble organic matter in meteorites consists of hollow spheres and flakes. The scale bar is 100 nm. Image courtesy of P. Buseck and K. Nakamura.

Stable isotopes in organic compounds

Traditionally, isotopic compositions of extraterrestrial organic matter have been measured in bulk samples or in assemblages of similar compounds. These measurements provide important constraints on their origins. Isotopic measurements of bulk organic matter extracted from small samples of carbonaceous chondrite matrix reveal huge anomalies and heterogeneities. Values of δD ranging from 1700 to 19 400 permil and $\delta^{15}N$ ranging from 400 to 3200 permil have been reported (Busemann *et al*., 2006).

In the 1990s, developments in instrumentation began to allow direct measurement of the isotopic compositions of individual compounds ("compound-specific isotope analysis"). The approach, relying on gas chromatographic separation, works best for highly volatile compounds with relatively few functional groups. Compound-specific isotope measurements have now been made on aliphatic hydrocarbons, carboxylic and dicarboxylic acids, aromatic compounds, and alkanes (Gilmour, 2004), and ranges of isotopic data for some of these compounds were given in their descriptions above. Polar compounds are less volatile, and they must be chemically modified to increase their volatility and make them amenable to gas chromatographic analysis.

All compounds analyzed have higher δD values than terrestrial samples, confirming the enrichments seen in bulk measurements. Some individual compounds have very high δD values, in one case as high as 3600 permil (4.6 times the solar system ratio). The high δD values seem to correlate with structures that include branching methyl groups.

A major conclusion from analyses of carbon isotopes in organic compounds in chondrites is that $\delta^{13}C$ values decrease as the number of carbon atoms in the molecule

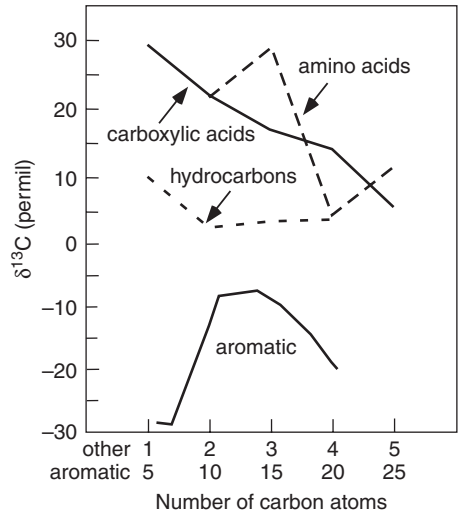

Fig. 10.6 **Changes in carbon isotopic composition as the number of carbon atoms in a molecule increases. These variations occur in aliphatic and aromatic compounds.**

increases. This consistent pattern is seen in aliphatic hydrocarbons, carboxylic acids, α-amino acids, and sulfonic acids in Murchison (Fig. 10.6). This finding is interpreted to indicate that larger molecules formed from smaller ones (this has euphemistically been referred to as the "Lego principle"). The addition of a ring to an aromatic compound likewise increases the ^{12}C content of the resulting compound. Several models have been proposed to explain this trend. One idea is that the ^{13}C-rich compounds formed in interstellar space and the final compounds resulted from transformation of the interstellar organic precursors by aqueous reactions on the meteorite parent bodies (Sephton and Gilmour, 2000). This idea would also explain high δD values. Alternatively, addition of atoms to the carbon skeleton or rings to the aromatic framework under kinetic control could favor ^{12}C. This kinetic isotope effect is not seen in terrestrial PAHs, which mostly form at high temperatures.

The $\delta^{15}N$ values of individual amino acids have been measured, in an attempt to determine whether the reported excess in L-enantiomers is of extraterrestrial origin. The L- and D-isomers of amino acids have higher $\delta^{15}N$ values than their terrestrial counterparts, arguing against terrestrial contamination. Similarities in the nitrogen isotopic compositions of amino acids and amines in the same meteorite support the hypothesis (mentioned above) that heating may transform amino acids into amines.

Compound-specific measurements of hydrogen isotopes have been performed for amino and sulfonic acids in Murchison. Significant enrichments in deuterium suggest interstellar origins for these compounds (more on this below).

Sulfur isotope compositions in sulfonic acids show a mass-independent enrichment in ^{33}S. Determining fractionations that are not controlled by mass is made possible because sulfur has so many stable isotopes. This feature has been attributed to ultraviolet irradiation of carbon disulfide in space, prior to its reaction to make sulfonic acid.

Determining the isotopic compositions of compounds that comprise the insoluble organic matter in meteorites is more difficult. Stepped combustion heating releases fractions of different volatility at different times. Studies have determined that the relatively labile and refractory components of insoluble organic matter differ in their carbon, hydrogen, and nitrogen isotopic compositions (we suggested earlier that these different components might have formed in different environments). By combining pyrolysis followed by compound-specific isotope analysis, it is possible to measure the isotopic compositions of fragments of macromolecular material. However, the results so far are confusing. $\delta^{13}C$ values increase with increasing numbers of carbon atoms in the insoluble material from Murchison, but decrease in Cold Bokkeveld (another CM chondrite) and Orgueil (CI chondrite).

Are organic compounds interstellar or nebular?

Determining the origins of organic molecules is a major goal of cosmochemistry. Some hints are provided by the structures of organic molecules. Structures rich in rings and double or triple bonds linking carbon atoms (in other words, structures with lower ratios of hydrogen to carbon) suggest that reactive hydrogen was uncommon during the assembly of the molecule. Some carbon skeletons can accommodate strain, and survival of strained molecules suggests that they have remained cool since the time they formed. Living organisms are highly specific in the kinds of organic structures they synthesize. Organisms on Earth have a strong preference for L-enantiomers, for example. The identity of functional groups also provides evidence about a molecule's origin. For example, alcohols, aldehydes, and carboxylic acids indicate progressively greater levels of oxidation. The occurrence of functional groups that would react with water indicates that the environments of synthesis and storage were dry. Patterns within mixtures of organic molecules can also be informative about their origins. For example, a preference for molecules with even numbers of carbon atoms would indicate that C_2 reactive units were important in synthesis. Certain catalysts may also provide precise controls on the compositions of organic mixtures. Ratios of the stable isotopes of elements that are used to construct organic molecules can be one of the best indicators of origin.

Let's now turn to the specific question of where organic molecules in chondrites formed. Organics are omnipresent in the interstellar medium and in the solar system. When the solar system formed, it inherited organic material from the parent molecular cloud. Thus, one possibility is that the organic materials were inherited from the interstellar medium. However, we must keep in mind that the collapse of the presolar cloud to form a protostar and accretion disk probably destroyed much of the inherited organic material, at least close to the protostar. Synthesis of new organic compounds then took place in the nebula. Thermal metamorphism and aqueous alteration on the meteorite parent bodies also provided pathways for production and destruction of organic molecules. The organic materials that we observe today in meteorites are the products of this multi-stage history, so it is unlikely that we will find simple direct connections to any specific environment.

We can make some predictions about their structures and isotopic compositions of compounds that might have been inherited from the molecular cloud based on what is known about organic species in the interstellar space. The spectroscopically observed organic molecules in the ISM are not those expected based on conditions of thermodynamic equilibrium. Why is that? Although we sometimes describe molecular clouds as dense, in reality they are highly rarified. This low particle density limits chemical reactions, restricting them to two-body processes, as opposed to three-body reactions that are more common in laboratory experiments. If one body is a positively charged ion and the other is a neutral molecule, reaction is enhanced because they are attracted to each other (that is to say, their reaction has negligible activation energy). Such ion–molecule reactions are fast and are important in ISM chemistry. These reactions occur on dust grains, which develop mantles of condensed ices at the low temperatures (~10 K) of interstellar space. Ultraviolet light photons and cosmic-ray interactions dissociate molecules in the icy mantles into free radicals, which then react with other molecules. The end result of these ion–molecule reactions is the synthesis of a variety of organic molecules, commonly unsaturated. Some of the PAHs in the ISM may have a different origin – formation in carbon-rich stars. The spectra of interstellar dust reveals that PAHs are widespread but contribute only 5–10% of the total carbon. Ion–molecule reactions are also a route by which significant deuterium, ^{15}N, and some ^{13}C enhancement occurs in organic molecules in the ISM. Spectra of interstellar dust show marked D/H enrichment, which might serve as a fingerprint for ISM synthesis of organic molecules. However, we do not yet have the ability to predict from first principles the isotopic fractionations in hydrogen, carbon, and nitrogen produced by ion–molecule reactions on grain surfaces.

Another possibility is that organic matter in meteorites formed within the protoplanetary disk. Synthesis reactions like those in the ISM could occur on the surfaces of nebular grains in distant, cold parts of the disk. As in the interstellar medium, ion–molecule reactions could generate isotopic fractionations, so high δD, $\delta^{15}N$, and $\delta^{13}C$ may not necessarily indicate preservation of interstellar materials. High-energy, ionizing radiation in parts of the disk can result in dehydrogenation of molecules and breaking of aromatic rings.

Chemical reactions on the surfaces of planetesimals are inherently different from those that occur in space. Small bodies with low gravity tend to lose hydrogen preferentially, so that surfaces become oxidizing and organic molecules synthesized there would also be relatively oxidized. Laboratory studies demonstrate that irradiation can produce complex organic molecules (and also break them down) on the surface. Heating by short-lived radionuclides causes ices incorporated into planetesimals to melt, producing aqueous fluids that could also promote organic synthesis and destruction of organics within the interiors of asteroids.

In summary, interstellar chemistry is dominated by ion–molecule reactions on grains at low temperatures, producing radicals and unsaturated organic molecules with high deuterium enrichment and potential enrichments in ^{15}N and ^{13}C. Nebular chemistry could feature similar reactions, but the nebula was also the site of high-energy processes that can destroy molecules or cause loss of hydrogen. Cosmic-ray irradiation of planetesimal surfaces produces more-complex organic molecules, as do reactions with aqueous fluids circulating within planetesimal interiors. The organic matter in carbonaceous chondrites appears to

have formed by random recombination of small free radicals, producing a great variety of structural isomers. Isotopic evidence suggests that ion–molecule reactions in the ISM played an important role. The resulting compounds, when exposed to liquid water in chondrite parent bodies, hydrolyze and otherwise react to form compounds that resemble those in the meteorites. Thus the organic matter in asteroidal materials probably owes its properties to formation and processing in several cosmic environments. The organic matter in comets (discussed in Chapter 12) appears to be more primitive and may be more closely related to the molecules inherited from the ISM. However, even for comets and other ice-bearing bodies, surface irradiation has modified organic molecules.

Box 10.2 Cosmochemical controversies about life in meteorites

At a meeting of the New York Academy of Sciences in 1961, Bartholomew Nagy, Douglas Hennessy, and Warren Meinschein presented a paper comparing the chemistry of organic matter in the Orgueil CI chondrite to that of living tissue. They concluded that life must have existed on the parent body from which the meteorite came. Eight months later Nagy and microbiologist George Claus reported the discovery of tiny clumps of organic matter, which they called "organized elements," in Orgueil. Moreover, they noted that this organic material exhibited chirality, as does organic matter from terrestrial organisms. They suggested that these microscopic clumps were the fossil remains of extraterrestrial organisms. A firestorm of media attention followed, prompting other scientists to search for organized elements in Orgueil. Detailed studies, however, showed that most of these tiny particles were actually oddly shaped mineral grains, not organic matter. A few were demonstrably from living things: pollen grains of ragweed and a few starch particles. The hypothesis crashed on the realization that the organized elements were either abiotic or products of the current denizens of Earth. The meteorites had apparently been contaminated before they were collected or while displayed in less-than-sterile museum cases.

In 1996, a NASA team led by David McKay published a fascinating but controversial report (McKay *et al.*, 1996) describing biochemical markers, biogenic minerals, and possible microfossils in the Mars meteorite ALH 84001. This meteorite, an ancient (~4.5 Ga) achondrite, contains chemically zoned carbonate globules (Fig. 10.7a) that McKay and coworkers suggested were precipitated by organisms. The carbonates contain very small quantities of polycyclic aromatic hydrocarbons (PAHs), which they interpreted as the decayed products of such organisms. However, PAHs commonly form by abiotic processes, as noted earlier, and the PAHs in ALH 84001 comprise all the structural forms ranging from C_{14} to C_{22}, unlike the selected hydrocarbon molecules formed by the decay of terrestrial organisms. Similar PAHs have also been found in EETA 79001, another much younger Martian meteorite found in Antarctica, as well as in Antarctic ice, suggesting that ALH84001 had been contaminated by organic matter on Earth prior to its collection. The presence of optically active amino acids (L-enantiomers, as found in terrestrial proteins) in EETA 79001 supports the hypothesis of organic contamination in the Earth's environment, and the measured carbon isotopic compositions of organic matter in both meteorites ($\delta^{13}C = -22$ to -25 permil) are mostly indistinguishable from terrestrial values. Other evidence cited by McKay and coworkers included very

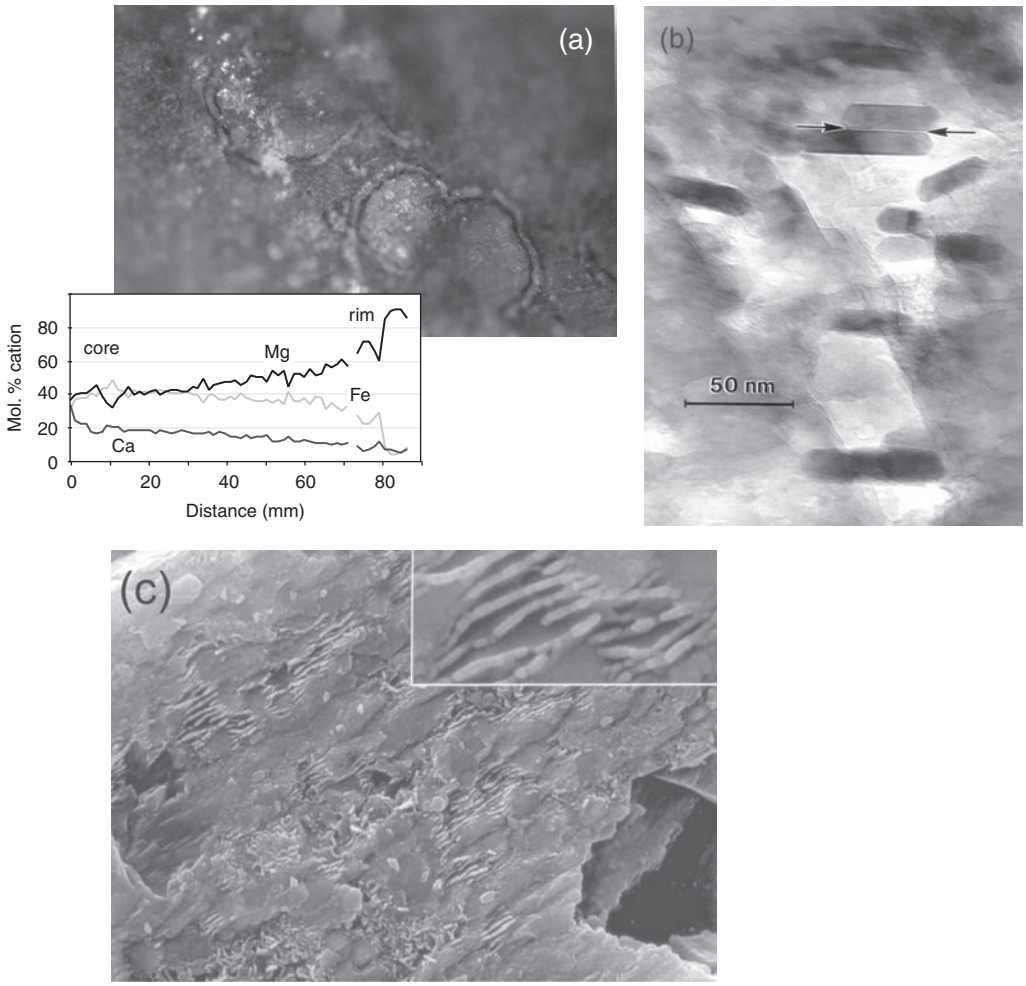

Fig. 10.7 **Images of the ALH 84001 Martian meteorite. (a) Backscattered electron image of a zoned carbonate globule. Compositional profiles for magnesium, iron, and calcium in one carbonate grain, measured by electron microprobe, are shown. (b) TEM image of elongated magnetite grain in ALH84001 carbonate. (c) Electron microscope image of objects in ALH84001 carbonate previously misinterpreted as microfossils. Images in (b) and (c) courtesy of J. Bradley.**

tiny (nanophase) magnetite crystals with unusual morphologies. They proposed that these crystals were formed by bacteria. On Earth, magnetotactic bacteria form chains of tiny magnetite crystals in their cells, used to orient the organisms relative to the magnetic field. The magnetites in ALH 84001 do not occur in chains. Moreover, transmission electron microscope images of them (Fig. 10.7b) actually show a variety of morphologies, including twisted whiskers and platelets – morphologies seen in crystals formed by vapor condensation. The most plausible origin for these magnetites appears to be thermal decomposition of siderite (iron carbonate) in the globules during an impact. Siderite is more readily affected by shock than magnesium or calcium carbonates, and impact could have produced a vapor from which

magnetite condensed. Finally, some intriguing elongated, apparently segmented forms (Fig. 10.7c), described as possible microbial fossils by McKay and coworkers, have been subsequently identified by other workers as either magnetite whiskers or man-made features resulting from gold coating of the sample prior to microscopic examination. In any case, the putative fossils appear to be far too small to represent living forms and could at best be appendages or fragments of organisms. The controversy over life in this Martian meteorite has now largely subsided, with the consensus that abiotic processes provide more compelling explanations for all the observed evidence. However, the interest in ALH 84001 has generated new research into the authenticity of various chemical and physical biomarkers and spawned a reinvigorated Mars exploration program focused on the search for life.

Noble gases and how they are analyzed

Noble gases are most abundant in planetary atmospheres, although even there they are only minor components. They have been measured in the gas envelopes of Venus, Earth (of course), Mars, and Jupiter. We will consider their utility in understanding planetary differentiation and atmospheric evolution shortly, but first we will focus on their rather miniscule abundances in meteorites and other extraterrestrial materials.

Because the chemistry of noble gases is virtually an oxymoron, what is it that makes them so useful in cosmochemistry (and geochemistry)? Noble gas nuclides are produced by a variety of nuclear transformation processes. Although the quantity of newly produced nuclei is typically very small, the even smaller background abundances of noble gases allow these nuclear transformations to be detected, unlike the situation for more common elements. It is understandable, then, that noble gas cosmochemistry mostly deals with isotopes. When applied to measuring noble gas isotopes, mass spectrometry is also much more sensitive than for other elements.

Different nuclear processes produce distinct isotopes or suites of isotopes in specific proportions (usually called "components"). Multiple noble gas components commonly occur within a sample, so the game is to recognize and unmix these components. This can be done by analyzing samples that may contain the components in different proportions, or by stepwise heating or oxidation to release components occurring in various phases (techniques also used in the study of organic compounds). These isotopic components can be visualized by use of a three-isotope diagram, in which two isotope ratios, each with the same reference isotope as its denominator, are plotted against each other. An example using xenon isotopes is illustrated in Figure 10.8. Isotopically distinct components plot at different points on this diagram, and two-component mixtures will define a straight line joining the end members. Mixtures of three components will plot within a triangle defined by the three end members, as in Figure 10.8.

Some noble gas components are referred to as *in situ*, meaning that they were produced within a given meteorite sample by nuclear transmutations. These are the nuclear

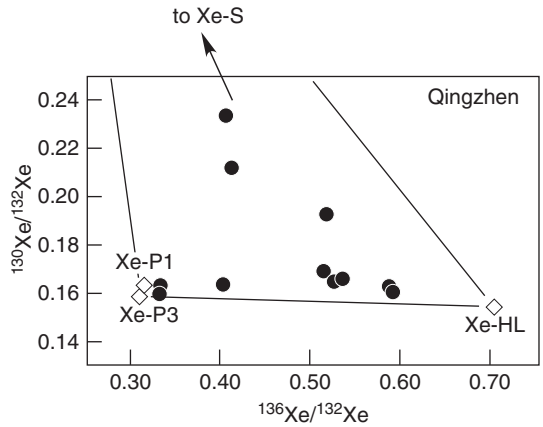

Fig. 10.8 Three-isotope plot of xenon in the Qinghen chondrite, released at different temperatures and illustrating various isotopic components. Modified from Huss and Lewis (1995).

components described in the immediately following section. Other components were *trapped* by the meteorite or its precursor materials. In 1963 cosmochemists Peter Signer and Hans Suess distinguished two kinds of trapped noble gas components in meteorites, "solar" and "planetary." After discussing nuclear components, we will consider solar and planetary noble gases, in turn.

Noble gas components in extraterrestrial samples

Nuclear components

The decay of naturally occurring radionuclides provides one mechanism for producing noble gas isotopes. The best-known examples are ^{4}He, produced by alpha decay of ^{232}Th, ^{238}U, and ^{235}U, and ^{40}Ar, a β-decay product of ^{40}K. The use of ^{40}Ar to determine radiometric ages was discussed in Chapter 8. A few short-lived (now extinct) radionuclides have also yielded noble gas isotopes. Meteorites are so old that they have incorporated these short-lived nuclides when they were alive, and their noble gas decay products can be measured against the low abundance background. The former presence of ^{129}I (with a half-life of only 17 Myr) was documented by measuring its ^{129}Xe decay product.

Spontaneous fission of certain radionuclides (especially ^{238}U) can also produce noble gas isotopes. Rather than produce one specific daughter isotope, the fission of an actinide nucleus produces several isotopes of xenon and krypton (and other elements) in well-defined proportions. For example, the relative proportions of ^{136}Xe, ^{134}Xe, ^{132}Xe, ^{131}Xe, and ^{129}Xe can be used to recognize a noble gas component produced by fission. The prior presence of ^{244}Pu, a short-lived radioisotope with a half-life of 82 Myr, in the early solar system has been inferred from its fission-produced xenon and krypton isotopes.

Noble gas isotopes are also produced through irradiation by cosmic rays. These rays are mostly high-energy protons that produce a cascade of secondary particles when they bombard other target nuclei, in a process called *spallation*. Neon produced by spallation reactions has similar abundances of all three isotopes (Fig. 10.8). Cosmic-ray irradiation occurs on the surfaces of airless bodies like the Moon and asteroids, as well as on small chunks of rock orbiting in space. Using these isotopes, it is possible to calculate cosmic-ray exposure ages, as described in Chapter 9.

The solar components

The original "solar" noble gas component of Signer and Suess (1963) was defined from meteorites based on elemental ratios. The five noble gases occur in relative abundances close to the solar system ratios. Subsequently, the solar noble gas component was determined to be implanted gases from the solar wind. Solar wind has been directly implanted into regoliths on the surfaces of airless bodies like the Moon and asteroids. The depths to which solar wind gases are implanted are very shallow, typically just a few microns. Because noble gases are not depleted in the Sun, as they are in solids in the solar system, solar wind should be less affected by the addition of tiny amounts of nuclear components (described in the previous section). The Sun contains most of the mass of the solar system, and thus is most representative of the bulk composition of the solar system. The one exception is ^{3}He. This is because the deuterium in the protoSun was burned to ^{3}He during the initial nuclear burning, increasing the ^{3}He abundance substantially. Minor production from incomplete hydrogen burning also contributes to the ^{3}He in the solar photosphere. The best estimate for the ^{3}He/^{4}He ratio in the solar nebula comes from the atmosphere of Jupiter.

The solar noble gas component in meteorites is most abundant in regolith breccias, which consist of material that was on the surfaces of asteroids. There is a large database from these so-called gas-rich meteorites. Numerous studies of implanted solar gases in lunar soils returned during the Apollo program have also been carried out. A complication in interpreting the results from lunar and meteorite samples is that spallation by cosmic rays has also added another noble gas component to lunar soils. However, the spallation component is sited more deeply inside soil particles, owing to the higher energies of cosmic rays, so the solar and spallation components can be separated by stepwise heating or etching. The spallation component also has a very different isotopic composition (Fig. 10.8). Some analyses of solar noble gases in lunar soils and the Pesyanoe aubrite are illustrated in Figure 10.9a (plotted relative to solar system abundances). Ideally, solar gas abundances should define a horizontal line on this diagram. The modest slants suggest that some portion of the lighter elements has been lost. Another potential problem in translating these implanted solar wind gases into the composition of the Sun is that some fractionation, both elemental and isotopic, may occur when atoms in the solar atmosphere are accelerated into the solar wind. Determining the magnitude of those effects is a goal of the Genesis spacecraft mission, which collected solar wind to be analyzed in terrestrial laboratories (see Box 4.3 in Chapter 4). Despite the crash of the spacecraft on its return

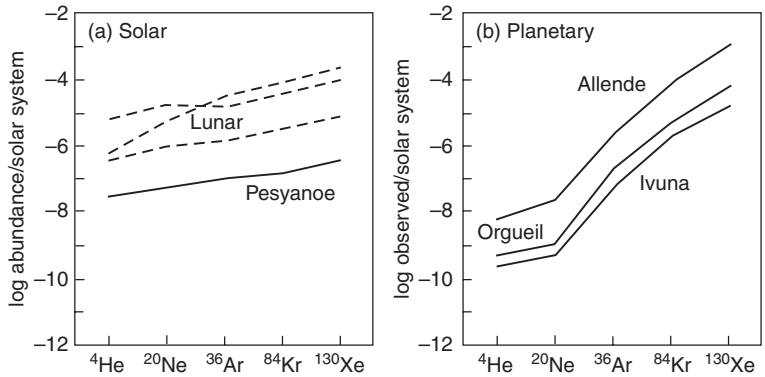

Fig. 10.9 **Noble gas abundances in lunar soils and chondrites. (a) Elemental abundance patterns for trapped solar wind in lunar soils, normalized to solar system abundances. (b) Elemental abundance patterns for planetary trapped noble gases, normalized to solar system abundances. This diagram is intended to illustrate patterns only; vertical positions are arbitrary. Modified from Ozima and Podosek (2002).**

to Earth, reasonable data have been obtained on the noble gases and further refinements are possible. The Genesis samples may soon replace natural samples as the best sample of noble gases in the Sun.

Planetary components

The planetary noble gas component of Signer and Suess (1963) refers to a fractionated elemental abundance pattern highly depleted in the light elements (Fig. 10.9b). This component was designated "planetary" because the elemental ratios mimic those in the Earth's atmosphere. However, trapped planetary gases are much more complex than solar gases and, in fact, the planetary noble gas component is now recognized as being a mixture of several different components. To make matters worse, the noble gases in the terrestrial planets do not have the composition of the meteoritic planetary component and the noble gases in the planets probably originated by a completely different mechanism. Wieler *et al*. (2006) advocated dropping the term, in favor of the term "primordial," whereas Podosek (2004) maintains that "planetary" remains a useful term. In the absence of consensus on an alternate term, we will continue to use "planetary gases" here to describe an ensemble of meteorite components with strongly depleted light elements relative to heavy (Fig. 10.9b).

The terminology used to describe the various admixed components of planetary gases has a long and tortured history. As discussed in Chapter 5, several names have been given to many of the components. Table 10.2 gives the name for the different components that we will use in this book, along with common synonyms, and briefly summarizes their properties. Detailed discussions of these components are given by Ott (2002) and Wieler *et al*. (2006). Each exotic component in Table 10.2 is carried within a specific type of presolar grain: diamond, silicon carbide, or graphite. Each component consists of an

Table 10.2 Trapped planetary noble gas components in meteorites

Component	Synonyms	Carrier	Constituents	Characteristics
P1	Q gases	phase Q (organic?)	all 5 gases	dominates Ar, Kr, Xe
P3		diamond	all 5 gases	similar to but distinct from P1
P6		diamond	all 5 gases	composition poorly defined
HL	Ne-A2*, Xe-X, Xe-HL	diamond	all 5 gases	isotopically anomalous (r-process?)
G	Ne-E(H), Kr-S, Xe-S	SiC and graphite	all 5 gases	isotopically anomalous (s-process)
N		SiC and graphite	all 5 gases	isotopically normal
Ne-E(L)	R	graphite	pure ^{22}Ne	from decay of ^{22}Na

* Ne-A2 is a mixture of Ne-HL and Ne-P6 that is inseparable experimentally.

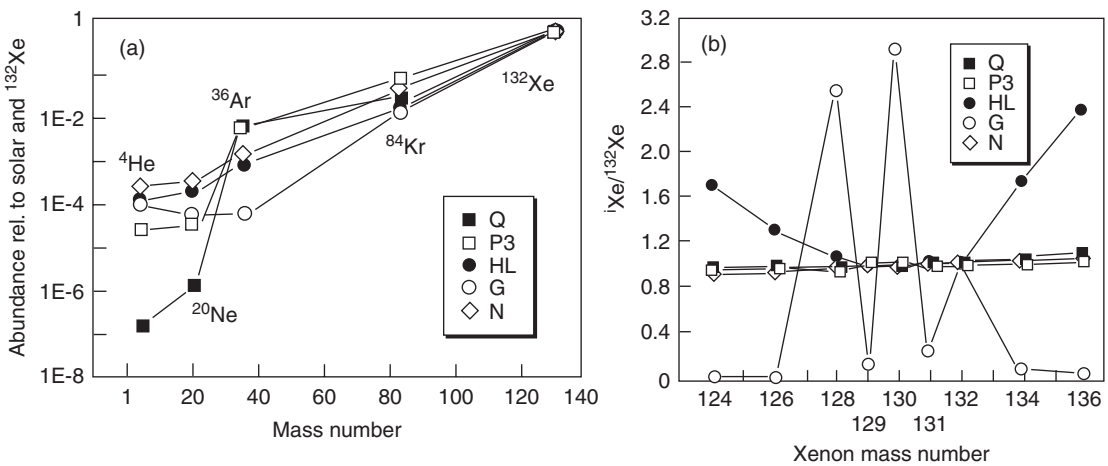

Fig. 10.10 (a) Elemental abundances and (b) xenon isotopic abundances for some exotic noble gas components (defined in Table 8.2) in meteorites. Modified from Wieler *et al.* (2006).

assortment of noble gases having particular elemental and isotopic proportions (Fig. 10.10) and formed by specific nucleosynthetic processes (Table 10.2). This should sound familiar – some of these noble gas components were the tracers used to isolate various presolar grains, as described in Chapter 5. Some of the components differ radically from solar composition, whereas others show only moderate deviations from solar isotopic abundances.

Diamonds are host to the HL component, named because it is enriched in both heavy and light isotopes of xenon (Fig. 10.10b). The high abundances of heavy isotopes suggest *r*-process nucleosynthesis, whereas the abundant light isotopes suggest the *p*-process. Both the *r*- and *p*-processes occur in supernovae. However, it is not obvious why products of the two nucleosynthetic processes would be coupled, and this remains a subject of current research. Diamonds also contain other, less-anomalous noble gas components

(P3 and P6). Rather than being products of specific nucleosynthetic processes in specific stars, these components may represent mixtures of many stellar nucleosynthetic contributions, as might be found in the ISM (and our own solar system). It is worth recalling that presolar diamonds are too small to be analyzed separately, so the assortment of diamonds in a chondrite probably samples multiple stellar sources.

Silicon carbide contains the G component (Fig. 10.10). The xenon and krypton isotope abundances in this component can be understood as arising from *s*-process nucleosynthesis in carbon-rich AGB stars. In fact, the "G" stands for "giant," describing these large, red stars. The G component also includes neon that is especially enriched in ^{22}Ne, consistent with helium burning in AGB stars. The N component in SiC (Fig. 10.10) is thought to represent the outer envelope of the same AGB stars in which helium burning generates the G component.

The origins of presolar graphite grains are diverse. Bulk samples of presolar graphite release large amounts of neon consisting almost entirely of ^{22}Ne at low temperature. This Ne-E(L) is thought to come from the decay of radioactive ^{22}Na (half life = 2.6 years), which is produced by explosive nucleosynthesis, probably in novae. The heavy noble gases, like those in SiC, reflect formation by the s-process in AGB stars. Recall that studies of individual graphite grains identified grains from AGB stars and grains from supernova (Chapter 5). Physical properties and noble-gas components thus indicate at least three production sites for presolar graphite.

Last but not least, the P1 component dominates the planetary argon, krypton, and xenon. It is carried in phase "Q," named for quintessence. This component is easily lost when acid residues of chondrites are oxidized, and its carrier is probably an organic phase. This component actually constitutes everything that remains after separation of all the other exotic components described in Table 10.2. The isotopic composition of Q is normal, perhaps suggesting that it is of local (nebular) origin, but the concentration of the P1 component closely tracks those of the presolar components in meteorites, suggesting that it is also presolar. The extremely low helium and neon abundances relative to heavy noble gases in the P1 component (Fig. 10.10a) suggest that the gases may have been trapped in their carrier at low temperatures, when argon, krypton, and xenon were frozen out into ices and helium and neon were still in the gas phase. It is not resolved whether the P1 component was trapped into its carrier in the Sun's parent molecular cloud, making it a presolar component, or in the solar system.

Planetary atmospheres

Atmospheres are a natural consequence of the origin and evolution of planets. If planets are of sufficient size, they may have captured some nebular gas while they formed. Accretionary and radioactive heating can also release gases that were brought into the planet in solid carriers. The atmospheres of Venus, Earth, and Mars are composed of the same gases (CO_2, N_2, H_2O, O_2), but in markedly different amounts and proportions, reflecting their different evolutionary histories. For example, the rise of life on Earth

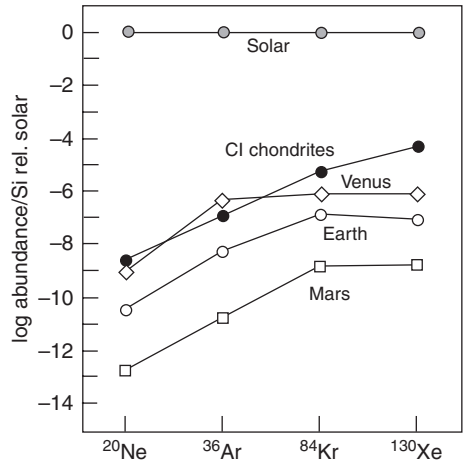

Fig. 10.11 Noble gas abundances in planetary atmospheres and CI carbonaceous chondrites, relative to silicon and solar abundances. After Porcelli and Pepin (2004).

brought about huge changes in the terrestrial atmosphere. Carbon dioxide has been almost completely removed and sequestered in limestone, petroleum, and coal, while O_2 from photosynthesis has accumulated in the atmosphere. The masses of the atmospheres are also very different between the three planets, with surface pressures of 95.6, 1, and 0.0064 bars on Venus, Earth, and Mars, respectively. The noble gases are much less affected by many of the processes that occur in planetary atmospheres and have retained many of the characteristics established early in the histories of the planets.

Atmospheric noble gases are highly depleted in the terrestrial planets relative to their abundances in the Sun and even in CI chondrites (Fig. 10.11). Depletions of the light elements are generally greater than those of the heavy elements (the planetary pattern). Helium is not plotted on Figure 10.11 because it is not gravitationally bound to any of the terrestrial planets. The absolute concentrations of noble gases vary by three orders of magnitude, from gas-rich Venus to gas-poor Mars. The low and varied abundances of noble gases in the terrestrial planets show that their atmospheres cannot be primary (that is, acquired directly from the gaseous nebula without modification). Earth and Venus are massive enough to have captured an atmosphere from the solar nebula if the gas persisted until they grew to approximately their present size. However, if these planets captured such an atmosphere, much of it was subsequently lost and the noble gas abundances were markedly changed. The noble gases in the atmospheres of the terrestrial planets could have been acquired in several ways. They could have been implanted into the precursor material by the solar wind, or carried into the planets by comets or meteorites (Porcelli and Pepin, 2004). Perhaps multiple processes played a role, with the relative importance varying between planets. The Earth and Mars have nearly parallel abundance patterns (Fig. 10.11) that are unlike the Sun, suggesting that noble gases were brought in by accreted planetesimals or comets. Venus gases are more solar-like, suggesting gravitational capture of nebular gases or accretion of particles onto which solar wind had been implanted.

Neon, argon, krypton, and xenon on Earth and Mars and Ne and Ar on Venus are all isotopically heavier than the gases in the Sun. In other words, the light isotopes are preferentially depleted. The depletions are smoothly mass dependent relative to the solar wind ratios, which suggests that the original inventory of noble gases was depleted by loss into space. The implication is that the current inventories of noble gases are remnants of the original inventories. Loss of light gases by thermal escape or sputtering from the top of the exosphere has certainly affected Mars and has probably affected Earth and Venus. But these mechanisms do not work for heavy argon, krypton, and xenon. Hydrodynamic escape, whereby noble gases are entrained by light gases such as hydrogen as it escapes from a hot atmosphere, is a possible mechanism for the loss and mass fractionation of the heavy gases. On Earth, hydrodynamic escape could have been driven by the Moon-forming impact (Pepin, 2006). Noble gases carried by planetesimals could also have been lost during accretion.

In contrast to the terrestrial planets, the giant planets are massive enough to have captured and retained nebular gases directly. However, concentrations of argon, krypton, and xenon measured in Jupiter's atmosphere by the Galileo spacecraft are ~2.5 times solar, which may imply that its atmosphere preferentially lost hydrogen and helium over the age of the solar system.

Some noble gases are also retained in planetary interiors, so a planet's total inventory is the sum of retained and degassed volatiles. We have limited data on noble gases in the mantles of the Earth (from basaltic lavas) and Mars (from Martian meteorites). The compositions of the noble gases in planetary interiors differ from those in the atmosphere due to decay of radioactive isotopes. For example, the ratios of $^{3}He/^{4}He$ in magmas derived from the Earth's mantle vary considerably from the atmospheric ratio, reflecting a mixture of primordial ^{3}He with radiogenic helium produced in the mantle. The ^{40}Ar in the atmospheres of the terrestrial planets results from decay of ^{40}K in the interior and partial outgassing of the daughter ^{40}Ar. The relative contributions of radiogenic and non-radiogenic argon in the atmosphere differ dramatically among the three planets. Radiogenic components produced in planetary interiors and then partially outgassed are also seen in the heavy krypton and xenon isotopes (from fission of U and Pu) and in ^{129}Xe (from decay of ^{129}I). Noble gases sequestered in the interior could have avoided the processing experienced by atmospheric gases. For example, some deep mantle sources on Earth have $^{3}He/^{4}He$ and $^{20}Ne/^{21}Ne$ ratios similar to those in solar wind. For a long time the low Xe/Kr ratios in the atmospheres of Earth and Mars relative to meteoritic gases were thought to reflect sequestration of xenon in the interior or in another reservoir. However, the "missing" xenon has not been found and the low Xe/Kr ratio is now believed to be a property of the planets.

Condensation and accretion of ices

In this chapter, we only briefly consider ices, focusing on their relationship to organic matter and noble gases in the ISM and in the solar nebula. Our understanding of ices is rudimentary because, unlike meteorites, ices have been studied only by remote sensing.

The ISM is predominantly gas, with approximately 1% of its mass in the form of micron-size dust particles. In molecular clouds, some of the gases condense out onto the grains as ices. Water is a major component of the ices. In the frigid environment of molecular clouds, H_2O ice may have an amorphous structure. Other compounds that may condense as ices on grains include CO, CO_2, N_2, CH_4, and H_2CO, with CO being volumetrically most important. All these other ices are more volatile than H_2O. These icy mantles condensed onto grains provide ideal sites for the synthesis of organic compounds and the trapping of noble gases in the interstellar medium.

Interstellar grains with ice mantles probably comprised a significant amount of the material that collapsed to form the solar nebula. Heating of this material caused the icy mantles to sublimate, producing a vapor that subsequently condensed as crystalline ices as the nebula cooled. By mass, H_2O ice rivals rock in terms of potentially condensable matter from a gas of cosmic composition. The amount of water ice depends, of course, on the extent to which oxygen is otherwise tied up with carbon as CO and/or CO_2 (Prinn, 1993). Ice condensation in the solar nebula occurred outboard of the "snowline," defined as the radial distance along the nebular mid-plane beyond which water ice was stable. Calculation of the snowline radius is complicated, and its exact position likely varied with time (Lunine, 2005).

In the region beyond the snowline, condensed ices ultimately accreted along with rocky materials into planetesimals. This is the region where the Oort cloud and Kuiper Belt objects that give rise to comets formed. For at least some of the time, the snowline was apparently located within the asteroid belt, permitting the accretion of ice-bearing asteroids. Alternatively, these bodies formed at greater distance from the Sun and then drifted inward. The nature and importance of ices in these bodies is considered in much greater detail in Chapter 12.

Summary

Admittedly, this chapter is difficult reading. We have considered some of the most complex constituents of meteorites and planets – structurally complicated organic molecules, isotopically diverse noble gases, and ices about which little is really known.

The organic matter in chondritic meteorites consists of compounds that can be extracted using acids and other solvents and thus can be readily characterized, and more abundant, high-molecular-weight material that is insoluble. Moderately abundant extractable compounds include aliphatic and aromatic hydrocarbons, various kinds of organic acids, and amines. All these compounds are structurally diverse, with all possible forms present. The more prevalent macromolecules are mostly aromatic compounds, with some graphite flakes and spheres. The organic material in chondrites has had a complicated history. Isotopic compositions of hydrogen, nitrogen, and carbon indicate that some of the compounds or their precursors originated in interstellar space. Nebular processing destroyed some of the interstellar molecules and new ones were synthesized. Thermal

metamorphism and aqueous processing on meteorite parent bodies further modified the accreted organic compounds.

Noble gases in meteorites comprise an array of components with distinct origins, recognizable by their elemental and isotopic patterns. Nuclear components formed *in situ* by radioactive decay, fission, or spallation by cosmic rays. The solar wind, which has distinctive noble gas isotope abundances, is continuously implanted into meteorites and lunar soil exposed on the surfaces of airless bodies. Planetary noble gases are strongly depleted in light elements, and include an assortment of exotic components found in interstellar grains and produced in other stars. Atmospheric noble gas abundances and isotopic compositions vary considerably from planet to planet, and provide constraints on the origins of planetary volatile inventories and outgassing histories.

Ices formed as mantles on silicate grains in interstellar space, trapping noble gases and providing sites for the synthesis of organic compounds. As the solar system formed, these ices were vaporized, particularly in the warmer regions near the Sun. Water ice recondensed outside the snowline and combined with rocky material and surviving interstellar material to form planetesimals.

We have now set the stage for the next two chapters – anhydrous planetesimals and ice-bearing comets and asteroids. These objects contain the organic matter, noble gases, and sometimes ices that we have just learned about, and they provide us with the best record of primitive materials in the solar system.

Questions

1. Explain the difference between extractable and insoluble organic matter in chondrites, and note why this distinction is significant.
2. What elements are found in organic molecules, and how can isotopes help constrain their origins?
3. What observations or properties of organic molecules suggest that they formed in the interstellar medium or in the solar nebula?
4. What makes noble gases so useful in cosmochemistry?
5. What noble gas components have been identified in meteorites?
6. How much water ice, relative to rocky minerals, is potentially condensable from a solar gas?

Suggestions for further reading

Lunine, J. I. (2005) Origin of water ice in the solar system. In *Meteorites and the Early Solar System II*, eds. Lauretta, D. S. and McSween, H. Y., Jr. Tucson: University of Arizona Press, pp. 309–319. A thoughtful review of the condensation of ices in the nebula and the delivery of ices to the terrestrial planets.

Piazzarello, S., Cooper, G. W. and Flynn, G. J. (2006) The nature and distribution of the organic material in carbonaceous chondrites and interplanetary dust particles. In *Meteorites and the Early Solar System II*, eds. Lauretta, D. S. and McSween, H. Y., Jr. Tucson: University of Arizona Press, pp. 625–651. A comprehensive, up-to-date review of organic matter in carbonaceous chondrites, but not for the faint-hearted.

Podosek, F. A. (2004) Noble gases. In *Treatise on Geochemistry, Vol. 1. Meteorites, Comets, and Planets*, ed. Davis, A. M. Oxford: Elsevier, pp. 381–405. A beautifully crafted, highly informative review of all aspects of noble gas cosmochemistry.

References

Busemann, H., Young, A. F., Alexander, C. M. O'D. *et al*. (2006) Interstellar chemistry recorded in organic matter from primitive meteorites. *Science*, **312**, 727–730.

Cody, G. and Alexander, C. M. O. D. (2005) NMR studies of chemical structural variation of insoluble organic matter from different carbonaceous chondrite groups. *Geochimica et Cosmochimica Acta*, **69**, 1085–1097.

Cody, G., Alexander, C. M. O. D. and Tera, F. (2002) Solid state (^{1}H and ^{13}C) NMR spectroscopy of the insoluble organic residue in the Murchison meteorite: a self-consistent quantitative analysis. *Geochimica et Cosmochimica Acta*, **66**, 1851–1865.

Garvie, L. A. J. and Buseck, P. R. (2004). Nanosized carbon-rich grains in carbonaceous chondrite meteorites. *Earth and Planetary Science Letters*, **184**, 9–21.

Gilmour, I. (2004) Structural and isotopic analysis of organic matter in carbonaceous chondrites. In *Treatise on Geochemistry, Vol. 1. Meteorites, Comets, and Planets*, ed. Davis, A. M. Oxford: Elsevier, pp. 269–290.

Huss, G. R. and Lewis, R. S. (1995) Presolar diamond, SiC, and graphite in primitive chondrites: abundances as a function of meteorite class and petrologic type. *Geochimica et Cosmochimica Acta*, **59**, 115–160.

McKay, D. S., Gibson, E. K., Thomas-Keprta, K. L. *et al*. (1996) Search for past life on Mars: possible relic biogenic activity in Martian meteorite ALH 84001. *Science*, **273**, 924–930.

Mumma, M. J., Villanueva, G. L., Novak, R. E., *et al*. (2009) Strong release of methane on Mars in northern summer 2003. *Science*, **323**, 1041–1045.

Ott, U. (2002) Noble gases in meteorites: trapped components. *Reviews in Mineralogy and Geochemistry*, **47**, 71–100.

Ozima, M. and Podosek, F. (2002) *Noble Gas Geochemistry*, 2nd edition. Cambridge: Cambridge University Press, 286 pp.

Pepin, R. O. (2006) Atmospheres on the terrestrial planets: clues to origin and evolution. *Earth and Planetary Science Letters*, **252**, 1–14.

Porcelli, D. and Pepin, R. O. (2004) The origin of noble gases and major volatiles in the terrestrial planets. In *Treatise on Geochemistry, Vol. 4, The Atmosphere*, ed. Keeling, R. F. Oxford: Elsevier, pp. 319–344.

Prinn, R. G. (1993) Chemistry and evolution of gaseous circumstellar disks. In *Protostars and Planets III*, eds. Levy, E. H. and Lunine, J. I. Tucson: University of Arizona Press, pp. 1005–1028.

Sephton, M. and Gilmour, I. (2000) Aromatic moieties in meteorites: relicts of interstellar grain processes? *Astrophysical Journal*, **540**, 588–591.

Signer, P. and Suess, H. (1963) Rare gases in the Sun, in the atmosphere, and in meteorites. In *Earth Science and Meteorites*, eds. Geiss, J. and Goldberg, E. D. Amsterdam: North Holland Publishing Company, pp. 241–272.

Weiler, R., Busemann, H. and Franchi, I. A. (2006) Trapping and modification processes of noble gases and nitrogen in meteorites and their parent bodies. In *Meteorites and the Early Solar System II*, eds. Lauretta, D. S. and McSween, H. Y., Jr. Tucson: University of Arizona Press, pp. 499–517.

11 Chemistry of anhydrous planetesimals

Overview

Many asteroids are dry, as evidenced by meteorites in which water is virtually absent. These samples include many classes of chondrites, as well as melted chunks of the crusts, mantles, and cores of differentiated objects. Anhydrous bodies were important building blocks of the rocky terrestrial planets, and their chemical compositions reveal details of processes that occurred within our own planet on a larger scale. The distributions of these asteroids within the solar system also provide insights into their formation and evolution.

Dry asteroids and meteorites

Anhydrous planetesimals formed within the inner solar system, unlike the ice-bearing bodies discussed in the next chapter. These objects, composed of rock and metal, were the primary building blocks of the terrestrial planets. Relics of that population may survive today as asteroids that dominate the inner portions of the main belt.

Asteroids have been a focus of spectroscopic studies for decades. Spectra obtained from telescopes on the Earth can identify some of the minerals that make up asteroids, but do not measure asteroid chemistry. Nevertheless, spectroscopic matches can be used to link some meteorite classes to their probable parent bodies, and thus allow indirect assessments of their chemical compositions. A few asteroids have been visited and analyzed by spacecraft. Chemical analyses require long data integrations from orbit or actually landing on the surface, and analyses of only two small near-Earth asteroids have been reported.

Most of the thousands of meteorites in our collections are bits and pieces of rocky or metallic asteroids. Because we can analyze these meteorites in the laboratory, they play a pivotal role in cosmochemistry. In this chapter we will focus on the compositions of meteorites that were anhydrous, or nearly so. The hydrated carbonaceous chondrites, in particular the CI and CM chondrites, which sample bodies that once contained ices and fluids, will be considered in Chapter 12.

Meteoritics involves the laboratory study of rocks without geologic context. Asteroid spectra provide a means to link some asteroid types to specific meteorite classes. Scientists can use the detailed information obtained from meteorites to reconstruct the chemical

compositions and geologic histories of the asteroids from which they were derived. We will show in this chapter how spectral information constrains the compositions of the parent asteroids of the anhydrous meteorites and demonstrates that they reside in the inner portion of the asteroid belt.

One of the primary goals of cosmochemistry is to provide information on processes and events in the early solar nebula. However, most asteroids preserve this record imperfectly, because they have been modified by thermal metamorphism and impacts. Thus, it is important that we understand the consequences of heating and shock. Without taking into account these geologic overprints, any conclusions about the chemistry of nebular materials based on chondrites are likely to be incorrect. We will also consider the ultimate effects of planetesimal heating – melting and differentiation, and see how melted asteroids can inform our understanding of analogous processes in planets.

Asteroids: a geologic context for meteorites

Before considering the chemistry of asteroids, we will briefly review their physical properties, spectral classifications, and distributions in space. This information will provide some context for the chemical data to follow.

Appearance and physical properties

Spacecraft encounters with asteroids offer the most detailed information on their sizes, shapes, surface features, and internal structures. On its way to Jupiter, the Galileo spacecraft zoomed past 951 Gaspra and 243 Ida, imaging their surfaces. Ida was discovered to have a tiny moon, named Dactyl. The NEAR Shoemaker spacecraft flew past and imaged 253 Mathilde, and conducted extensive observations and measurements while orbiting 433 Eros (Sullivan *et al*., 2002). Phobos and Diemos, the tiny satellites of Mars, are thought to be captured asteroids, and both were imaged by Mariner 9. The portraits of all these objects are compared, at approximately correct relative sizes, in Figure 11.1. Another asteroid, 25143 Itokawa (Fig. 11.2), was imaged by the Hayabusa spacecraft (Fujiwara *et al*., 2006). Itokawa is really no more than an asteroid fragment, only ~300 m in diameter (approximately the size of Dactyl in Fig. 11.1).

All of these asteroids are irregular in shape and are marked by craters in various states of degradation. They must be fractured collisional remnants of once-larger asteroids. Only a few of the largest asteroids, such as 1 Ceres and 4 Vesta, are rounded and apparently intact. Itokawa (Fig. 11.2) has a dumbbell shape that suggests it may actually be two asteroidal fragments that have fused together, and its surface is littered with boulders thought to have formed by collisions. Asteroid shapes can also be determined remotely using radar observations, and other dumbbell-shaped objects have been found.

The masses of the smaller asteroids encountered by spacecraft have been estimated from their gravitational effects on the trajectories of passing spacecraft. The generally low

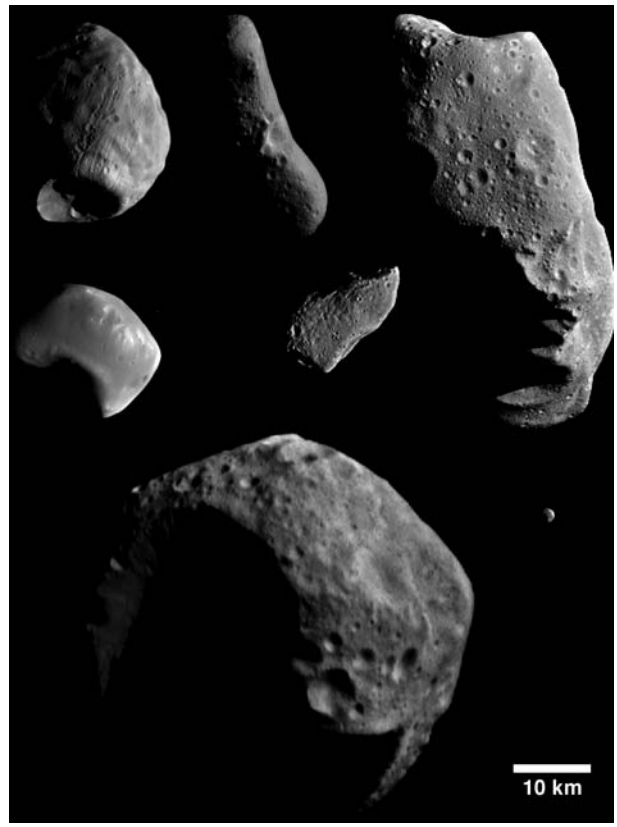

Fig. 11.1 Composite view of asteroids visited by the Galileo and NEAR Shoemaker spacecraft, as well as the asteroid-sized moons of Mars. All are shown approximately at the same scale. Clockwise from upper left are Phobos, Eros, Ida, tiny Dactyl, Mathilde (the largest object), and Deimos, with Gaspra in the center of the figure. After Sullivan *et al.* (2002), with permission.

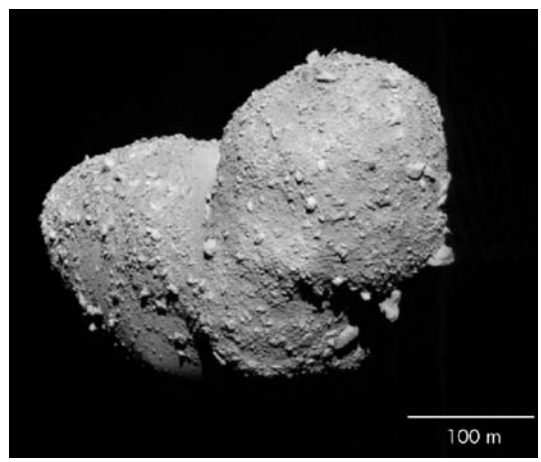

Fig. 11.2 Image of asteroid Itokawa, taken by the Hayabusa spacecraft. The dumbbell shape and abundant boulders suggest this asteroid is a rubble pile, an idea supported by the asteroid's bulk density of ~1.95 g cm^{-3}. Image courtesy of JAXA.

densities of these asteroids (1.3–2.7 g cm^{-3}) suggest high porosities. Measurements of the densities of meteorites invariably show higher values, so the high porosities imply asteroids are fractured internally.

Some asteroids are marked by grooves, and all are pockmarked by impact craters of varying sizes. One crater on Mathilde (Fig. 11.1) is so large that it is difficult to envision how the asteroid survived the impact. The surfaces of all these bodies are covered by fine-grained regoliths and by boulders of various sizes.

Spectroscopy and classification

Incident sunlight is partially absorbed by minerals on an asteroid's surface, and the fraction of light that is reflected can vary as a function of wavelength. Spectrophotometric studies of asteroids have been carried out for decades. Asteroid reflectance spectra have been compared to the spectra of meteorites measured in the laboratory (Fig. 11.3), providing a way to link some kinds of meteorites to possible parent bodies. Most measurements are made at visible wavelengths ranging from ~0.4 to 1.0 μm, because the illuminating solar flux peaks

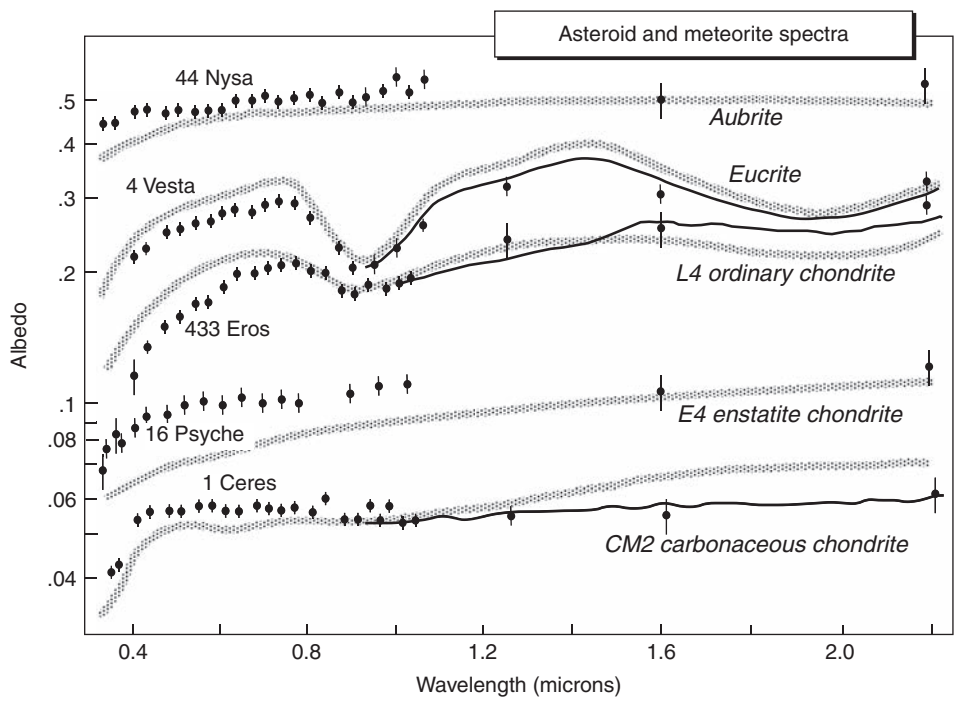

Fig. 11.3 Comparison of telescopic spectra of asteroids (shown by dots and black curves) with meteorite spectra measured in the laboratory (gray curves). Spectral similarities can be used to estimate the compositions of asteroids and infer correlations. Because absolute reflectance (albedo) depends on particle sizes and packing in surface regoliths, it is permissible to translate asteroid spectra up or down in the diagram to obtain a match.

Table 11.1 Asteroid taxonomy based on spectra (Tholen and Barucci, 1989)

Tholen class	Possible phases	Possible meteorite analogs
C	phyllosilicates, organics	CM, CI chondrites
D	phyllosilicates?, organics, ices?	
K	olivine, pyroxene	CV, CO chondrites
P	olivine, organics, ices	
Q	olivine, pyroxene, metal	Ordinary chondrites
B,F,G	phyllosilicates	Carbonaceous chondrites
T	troilite?, metal?	
A,R	olivine, metal?	Pallasites, bracchinites
E	enstatite, metal?	Aubrites
M	metal?	Iron meteorites, enstatite chondrites
S	olivine, pyroxene, metal	Ordinary chondrites, achondrites*, primitive achondrites*
V,J	pyroxene, plagioclase	HED achondrites

* Angrites, acapulcoites-lodranites, winonaites, ureilites

in the visible region and the Earth's atmosphere is relatively transparent at these wavelengths. Near-infrared spectroscopy (~0.9 to 1.7 mm) is also used (some measurements are illustrated in Fig. 11.3). Asteroid spectra may show ultraviolet absorptions due to Fe^{2+} charge transfer in minerals, absorption features centered near 1 and 2 μm due to Fe-bearing silicates, and an increase in slope longward of 0.55 μm ("reddening") due to iron–nickel metal or organic molecules. Measurements in the infrared can reveal the presence of hydrous minerals and ices, as discussed in Chapter 12.

Asteroids are classified based on their visible spectroscopic properties and albedo (reflectivity). At least four different taxonomies have been proposed, each using statistical clustering techniques. The most widely used classification (Tholen, 1984) is based on an eight-color (wavelength) asteroid survey (Table 11.1). A more recent classification (Bus *et al*., 2002), crafted from a much larger spectral dataset, places most asteroids within three large superclasses (the C-, S-, and X-complexes), with small groupings of outlying objects. The superclasses can be divided into smaller ones, producing a total of 26 asteroid classes.

As already noted, spectral similarities between the various asteroid classes and specific types of meteorites provide a way to identify possible meteorite parent bodies. The Tholen and Barucci (1989) asteroid taxonomy has been interpreted as representing the types of meteorites shown in Table 11.1. Using the Bus *et al*. (2002) taxonomy, the C-complex asteroids are probably hydrated carbonaceous chondrites (e.g. CI or CM). These carbonaceous chondrite asteroids probably accreted with ices and will be considered in Chapter 12. Some S-complex asteroids are ordinary chondrite parent bodies, but this superclass is very diverse and includes many other meteorite types as well. The X-complex includes objects with spectra that resemble enstatite chondrites and aubrites, and some irons and stony irons, although other X-complex asteroids are unlike known meteorite types. A few asteroid spectra are unique and provide more definitive connections, such as between 4 Vesta and

HED meteorites. Determining the presence of minerals with specific compositions from asteroid spectra can provide more quantitative correlations with meteorites (Gaffey *et al*., 2002).

In all, there are 13 well-defined groups of chondrites, as well as a comparable number of chondrites that are unique or members of a grouplet that is too small for adequate characterization. There are many more differentiated meteorite groups, including three groups of primitive achondrites, five groups of achondrites, four types of stony-irons, ten well-defined groups of irons, and perhaps 50 ungrouped irons. Thus meteorites represent at least 100 distinct asteroidal parent bodies (Burbine *et al*., 2002). While this may seem like a diverse collection, it represents only a small portion of the approximately 1 million asteroids in the main belt with diameters greater than 1 km. The higher number of anhydrous meteorite groups than hydrated groups may indicate that the inner main belt has been more completely sampled than the outer belt.

Box 11.1 Chemistry of space weathering and regoliths

Many asteroid spectra tend to be "redder" than the spectra of the corresponding meteorites. Reddened spectra have lower reflectivity, weaker absorptions, and spectral slopes that are flatter in the red end. This phenomenon has been attributed to "space weathering," a catchall term referring to any process that modifies the optical properties of surfaces of airless bodies exposed to the space environment.

Space weathering is most prominently displayed in the spectra of lunar soils. As surface soils "mature" over millions of years of exposure to micrometeorites and cosmic rays, they darken noticeably and diagnostic absorption bands weaken. Electron microscope observations demonstrate that the optical changes result from submicroscopic metallic iron grains (Fig. 11.4) that occur in silicate glasses coating the surfaces of fine soil particles (Pieters *et al*., 2000). These tiny iron grains are deposited from vapor produced by micrometeorite impacts or solar wind sputtering. SiO_2 and FeO volatilize before most other components, and the gaseous molecules thermally dissociate into elements. The vapor containing silicon and iron atoms then condenses to form silicate glass and iron particles. In some cases, other combinations of silicon and iron, such as the mineral hapkeite (Fe_2Si), also condense in small amounts. This assemblage represents kinetically controlled condensation, instead of equilibrium condensation.

Although no samples of asteroid surface regoliths have been collected for laboratory analysis, a similar process is thought to have affected the spectra of many asteroid surfaces. An example of possible space weathering is illustrated in Figure 11.5. The spectrum of asteroid 4 Vesta is more subdued than that of eucrites, which are thought to represent Vesta's surface rocks. Space weathering has also been seen in close-up images of asteroids. Ejecta blankets around relatively recent craters on Gaspra and Ida are less spectrally reddened than the surrounding surface materials. Only materials directly exposed to the space environment experience space weathering, and impact excavation exposes unweathered materials from deeper in the regolith.

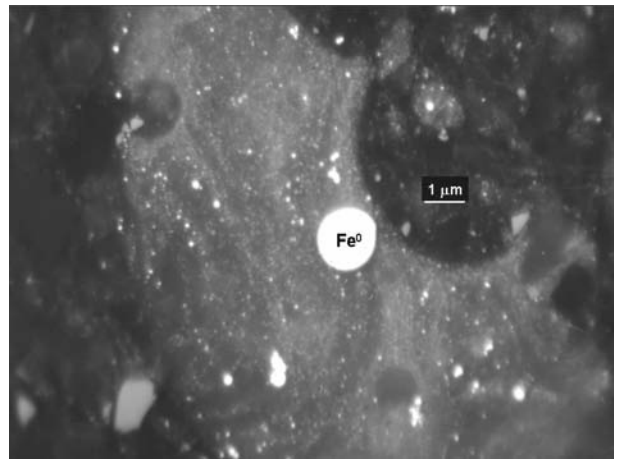

Fig. 11.4 **SEM electron backscatter image of lunar soil particles, showing minute beads of metallic iron (white) in silicate glass coatings. The iron beads modify the spectra, accounting for the phenomenon of space weathering.**

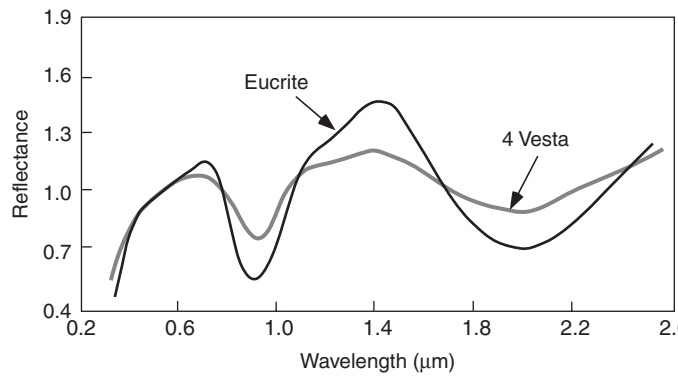

Fig. 11.5 **Comparison of the spectra of asteroid 4 Vesta and the eucrite Jonzac. The subdued and reddened spectra of Vesta suggest space weathering. Modified from Clark *et al.* (2002).**

Meteorite regolith breccias (Fig. 11.6) are mixtures of fine-grained surface materials and coarser subsurface grains. Although they are perceptibly darkened, they do not show the spectral reddening that is characteristic of space weathering.

Although space weathering specifically denotes processes that affect an asteroid's spectra, there are other effects of meteorite bombardment that do not necessarily alter spectra. For example, impact melting produces "agglutinates," small particles of minerals or rocks bonded together by glass. Agglutinates are much more abundant in lunar soils than in meteorite regolith breccias, suggesting that impacts at lower speeds in the asteroid belt may produce less melting than on the Moon. Both lunar regolith and asteroid regolith breccias contain implanted solar wind gases (mostly hydrogen, but also helium and other noble gases, as discussed in Chapter 10).

Fig. 11.6 Millbillillie regolith breccia, in plane-polarized light, 2 cm across. Clasts of basaltic eucrite are visible in a crushed matrix, crosscut by a vein of shock-melted material. Image from Lauretta and Killgore (2005), with permission.

Orbits, distribution, and delivery

It is instructive to compare the orbits of main-belt asteroids with their spectroscopic classification. The distribution of asteroid classes (using the taxonomy of Tholen and Barucci, 1989, presented in Table 11.1) is illustrated in Figure 11.7a, which shows their relative abundances as a function of orbital semi-major axis (heliocentric distance). A decade ago, this pattern was interpreted to indicate that asteroids were stratified according to their thermal histories, with melted (differentiated) bodies near the Sun, metamorphosed bodies farther out, and unaltered bodies at even larger heliocentric distances. A similar exercise, using the newer superclass taxonomy and a large asteroid database (Mothe-Diniz *et al*., 2003), does not indicate such a clear picture. Nevertheless, S-complex asteroids, which include the older E, S, and M groups, dominate the inner and middle belt out to 2.95 AU, C-complex asteroids are most common in the outer belt, and X-complex bodies, which include the P and D classes, are most common at about 3 AU (Fig. 11.7b). Note that this distribution represents only a part of the main asteroid belt shown in Figure 11.7a. Because of uncertainties in the interpretation of S-complex objects as either ordinary chondrites or achondrites, we can no longer say that the innermost asteroids are differentiated but we can infer that S-complex bodies were at least heated (recall from Chapter 6 that ordinary chondrites are mostly metamorphosed). CI and CM2 chondrites have suffered extensive aqueous alteration, suggesting they formed beyond a "snowline" marking the condensation of ice that later melted; that snowline likely marks the transition to C-complex objects at about 3 AU.

The orbits of asteroids in the main belt between Mars and Jupiter show gaps in both heliocentric distance and inclination (degrees from the ecliptic, the plane in which the planets

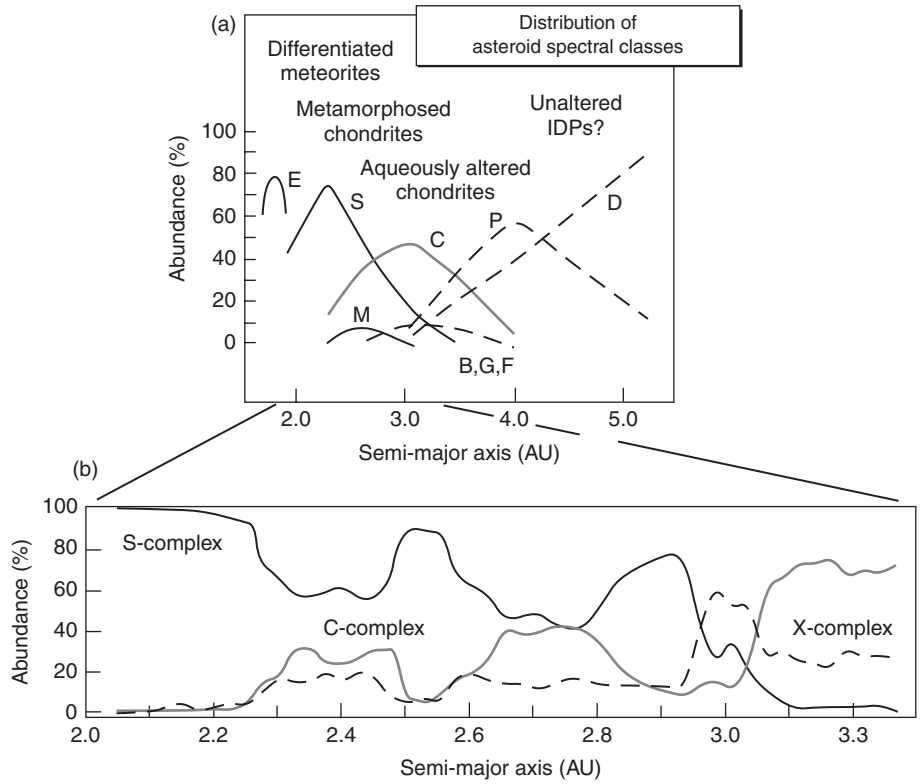

Fig. 11.7 **Heliocentric distribution of asteroid spectral types in the main belt. (a) (modified from Gradie and Tedesco, 1982) and (b) (modified from Mothe-Diniz *et al.*, 2003) show distributions using two different asteroid taxonomies, explained in the text. Petrologic interpretations of the various spectral classes are shown in (a).**

orbit). Several kinds of gravitational resonances act on asteroids at these locations, depopulating the gaps by perturbing the asteroids into different orbits. These "escape hatches" provide a means of scattering materials knocked off asteroids by impact into the inner solar system, where they can be captured as meteorites. Other mechanisms that do not depend on gravity, such as the Yarkovsky effect (resulting from asymmetric heating of small bodies that causes their orbits to drift), can also cause asteroid fragments to enter the inner planet region.

Chemical compositions of anhydrous asteroids and meteorites

Analyses of asteroids by spacecraft remote sensing

Solar X-rays impinge on an asteroid's surface, generating fluorescent spectra that can be measured using an X-ray fluorescence spectrometer. During times when the Sun is

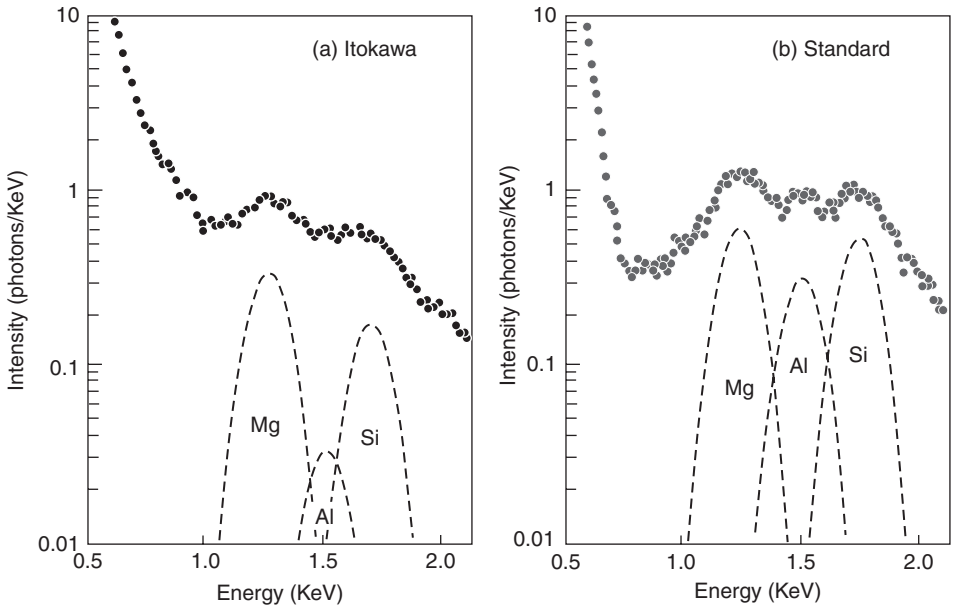

Fig. 11.8 X-ray spectrum of (a) asteroid Itokawa, and (b) a standard, measured by the Hayabusa spacecraft. Locations of the Kα lines for magnesium, aluminum, and silicon are also shown. Modified from Okada *et al.* (2006).

quiet (not producing solar flares), the X-ray flux is fairly low, so that Kα line spectra of only a few low atomic weight rock-forming elements, such as magnesium, aluminum, and silicon, can be measured. An example of such a spectrum for asteroid Itokawa is compared to a standard spectrum in Figure 11.8. During solar flare periods, heavier elements such as calcium, iron, and sulfur may be detectable. Conversion of the observed photon fluxes to element abundances requires a concurrent measurement of the solar spectrum.

Two asteroids have been analyzed using X-ray fluorescene instruments. The NEAR-Shoemaker orbiting spacecraft analyzed 433 Eros (McCoy *et al.*, 2001; Nittler *et al.*, 2001) during a period when the Sun was near the maximum of its 11-year activity cycle. The chemical composition of this asteroid is expressed as element ratios (Table 11.2), because there was no internal calibration for absolute abundances. An analysis of 25143 Itokawa by the Hayabusa spacecraft (Okada *et al.*, 2006) occurred during quiet solar conditions, so only magnesium, aluminum, and silicon data were obtained (Table 11.2). Both asteroids are classified as S-type, and the compositions of both are similar to ordinary chondrites, although anhydrous carbonaceous chondrites (CV, CO, CR) and primitive achondrites cannot be ruled out. Especially interesting is the low measured S/Si ratio for Eros, which might result from impact volatilization or sputtering of sulfur in surface materials or extraction of a FeS-rich partial melt.

NEAR-Shoemaker also carried a gamma-ray spectrometer (Evans *et al.*, 2001). Gamma-ray photons are emitted from the radioactive decay of long-lived radioisotopes and from other elements that are excited by cosmic-ray bombardment. The gamma rays are

Table 11.2 Analyses of asteroids by spacecraft X-ray diffraction and gamma-ray spectroscopy

	433 Eros		25142 Itokawa
Element ratio	XRF	GRS	XRF
Mg/Si	0.85±0.11	0.75	0.78±0.09
Fe/Si	1.65±0.27	0.8	
Al/Si	0.068±0.022		0.07±0.03
S/Si	0.014±0.017		
Ca/Si	0.077±0.006		
Si/O		0.53−0.67	
Fe/O		0.16−0.44	
K		0.07 wt.%	

Eros XRF data from Nittler *et al*. (2001); Eros GRS data from Evans *et al*. (2001); Itokawa XRF data from Okada *et al*. (2006).

detected by a semi-conducting or scintillating material, in this case a NaI crystal. The instrument was designed to collect data from orbit, but a late arrival at Eros and operational considerations did not allow sufficient time at a low enough altitude to provide acceptable measurements. At the end of the mission, the spacecraft made a controlled descent to the asteroid's surface, and the element abundances (again expressed as ratios) obtained over a week-long integration are given in Table 11.2.

Chondritic meteorites

Chondritic meteorites are among the most thoroughly analyzed materials (Brearley and Jones, 1998), and numerous compilations of their chemical compositions are available. Especially notable are analyses by Eugene Jarosewich (e.g. Jarosewich, 1990), who laboriously separated metal and sulfide before performing wet-chemical analyses, so that his data distinguish iron in its various oxidation states. Also, among modern analyses performed by neutron activation, those of Gregory Kallemeyn (e.g. Kallemeyn *et al*., 1989) are especially complete although they do not report silicon abundances or iron oxidation states. The average elemental abundances – encompassing most of the periodic table – for the major chondrite groups that are anhydrous are given in Table 11.3.

As we learned earlier in Chapters 4 and 7, "chondritic" abundances can vary. Figures 11.9a and 11.9c show variations in lithophile elements, and Figures 11.9b and 11.9d illustrate variations in siderophile and chalcophile elements (all normalized to CI chondrite abundances, and plotted in order of increasing volatility from left to right in each diagram) for the major classes of anhydrous meteorites. As is apparent in these

Table 11.3 Average element abundances for anhydrous chondrite groups

Element	H	L	LL	R	K	EH	EL	CV	CO	CR	CH
Li (μg g^{-1})	1.7	1.85	1.8			1.9	0.7	1.7	1.8		
Be (ng g^{-1})	30	40	45			21		50			
B (μg g^{-1})	0.4	0.4	0.7			1		0.3			
C (mg g^{-1})	2.1	2.5	3.1	0.58		3.9	4.3	5.3	4.4	20	7.8
N (μg g^{-1} g^{-1})	48	43	70			420	240	80	90	620	190
O (mg g^{-1})	357	377	400			280	310	370	370		
F (μg g^{-1})	125	100	70			155	140	24	30		
Na (mg g^{-1})	6.11	6.9	6.84	6.63	6.8	6.88	5.77	3.4	4.2	3.3	1.8
Mg (mg g^{-1})	141	149	153	129	154	107	138	143	145	137	113
Al (mg g^{-1})	10.6	11.6	11.8	10.6	13.0	8.2	10.0	16.8	14.0	11.5	10.5
Si (mg g^{-1})	171	186	189	180	169	166	188	157	158	150	135
P (μg g^{-1})	1200	1030	910		1400	2130	1250	1120	1210	1030	
S (mg g^{-1})	20	22	21	40.7	55	56	31	22	22	19	3.5
Cl (μg g^{-1})	140	270	200	<100		570	230	250	280		
K (μg g^{-1})	780	920	880	780	710	840	700	360	360	315	200
Ca (mg g^{-1})	12.2	13.3	13.2	9.14	12.2	8.5	10.2	18.4	15.8	12.9	13.0
Sc (μg g^{-1})	7.8	8.1	8.0	7.75	7.9	6.1	7.7	10.2	9.5	7.8	7.5
Ti (μg g^{-1})	630	670	680	900	700	460	550	870	730	540	650
V (μg g^{-1})	73	75	76	70	73	56	64	97	95	74	63
Cr (μg g^{-1})	3500	3690	3680	3640	3600	3300	3030	3480	3520	3415	3100
Mn (μg g^{-1})	2340	2590	2600	2960	2400	2120	1580	1520	1620	1660	1020
Fe (mg g^{-1})	272	218	198	244	247	305	248	235	250	238	380
Co (μg g^{-1})	830	580	480	610	750	870	720	640	680	640	1100
Ni (mg g^{-1})	17.1	12.4	10.6	14.4	14.6	18.4	14.7	13.2	14.2	13.1	25.7
Cu (μg g^{-1})	94	90	85			215	120	104	130	100	120
Zn (μg g^{-1})	47	57	56	150	145	290	18	110	110	100	40
Ga (μg g^{-1})	6.0	5.4	5.3	8.1	8.2	16.7	11	6.1	7.1	6.0	4.8
Ge (μg g^{-1})	10	10	10			38	30	16	20	18	
As (μg g^{-1})	2.2	1.36	1.3	1.9	2.4	3.5	2.2	1.5	2.0	1.5	2.3
Se (μg g^{-1})	8.0	8.5	9	14.1	20	25	15	8.7	8.0	8.2	3.9
Br (μg g^{-1})	<1	<2	1.0	0.55	0.9	2.7	0.8	1.6	1.4	1.0	1.4
Rb (μg g^{-1})	2.3	2.8	2.2		1.7	3.1	2.3	1.2	1.3	1.1	
Sr (μg g^{-1})	8.8	11	13			7.0	9.4	14.8	13	10	
Y (μg g^{-1})	2.0	1.8	2.0			1.2		2.6	2.4		
Zr (μg g^{-1})	7.3	6.4	7.4			6.6	7.2	8.9	9.0	5.4	
Nb (μg g^{-1})	0.4	0.4						0.5		0.5	
Mo (μg g^{-1})	1.4	1.2	1.1	0.9				1.8	1.7	1.4	2
Ru (ng g^{-1})	1100	750		960	850	930	770	1200	1080	970	1600
Rh (ng g^{-1})	210	155						170			
Pd (ng g^{-1})	845	620	560			820	730	710	710	690	
Ag (ng g^{-1})	45	50	75			280	85	100	100	95	
Cd (ng g^{-1})	<10	30	40		30	705	35	350	8	300	
In (ng g^{-1})	<1.5	<20	<20		3	85	4	32	25	30	

Table 11.3 (cont.)

Element	H	L	LL	R	K	EH	EL	CV	CO	CR	CH
Sn (ng g^{-1})	350	540					1360	680	890	730	
Sb (ng g^{-1})	66	78	75	72	150	190	90	85	110	80	90
Te (ng g^{-1})	520	460	380		2000	2400	930	1000	950	1000	
I (ng g^{-1})	60	70				210	80	200	200		
Cs (ng g^{-1})	<200	<500	150		50	210	125	90	80	84	
Ba (μg g^{-1})	4.4	4.1	4.0			2.4	2.8	4.55	4.3	3.4	3.0
La (ng g^{-1})	301	318	330	310	320	240	196	469	380	310	290
Ce (ng g^{-1})	763	970	880	830		650	580	1190	1140	750	870
Pr (ng g^{-1})	120	140	130			100	70	174	140		
Nd (ng g^{-1})	581	700	650			440	370	919	850	790	
Sm (ng g^{-1})	194	203	205	180	200	140	149	294	250	230	185
Eu (ng g^{-1})	74	80	78	72	80	52	54	105	96	80	76
Gd (ng g^{-1})	275	317	290			210	196	405	390	320	290
Tb (ng g^{-1})	49	59	54			34	32	71	60	50	50
Dy (ng g^{-1})	305	372	360	29		230	245	454	420	280	310
Ho (ng g^{-1})	74	89	82	59		50	51	97	96	100	70
Er (ng g^{-1})	213	252	240			160	160	277	305		
Tm (ng g^{-1})	33	38	35			24	23	48	40		
Yb (ng g^{-1})	203	226	230	216	215	154	157	312	270	220	210
Lu (ng g^{-1})	33	34	34	32	33	25	25	46	39	32	30
Hf (ng g^{-1})	150	170	170	150		140	210	230	220	150	140
Ta (ng g^{-1})	21	21									
W (ng g^{-1})	164	138	115	<180		140	140	160	150	110	150
Re (ng g^{-1})	78	47	32	43		55	57	57	58	50	73
Os (ng g^{-1})	835	530	410	690	550	660	670	800	805	710	1150
Ir (ng g^{-1})	770	490	380	610	550	570	560	730	740	670	1070
Pt (μg g^{-1})	1.58	1.09	0.88	<1.0		1.29	1.25	1.25	1.24	0.98	1.7
Au (ng g^{-1})	220	156	146	183	220	330	240	153	190	160	250
Hg (ng g^{-1})		30	22			60					
Tl (ng g^{-1})	<1	<5	<30		3	100	7	58	40	60	
Pb (ng g^{-1})	240	40				1500	240	1100	2150		
Bi (ng g^{-1})	<10	14	<30		25	90	13	54	35	40	
Th (ng g^{-1})	38	42	47	<50		30	38	58	80	42	
U (ng g^{-1})	13	15	15	<25		9.2	7.0	17	18	13	

Data sources given by Lodders and Fegley (1998).

figures, the greatest disparities occur among volatile elements, which are depleted to different degrees.

Another important chemical difference between chondrite groups is in their oxidation states. In Chapter 7, we learned that differences in chondrite compositions cannot be simply explained by fractionation of metallic iron, but also must involve oxidation or reduction of iron (see Fig. 7.14).

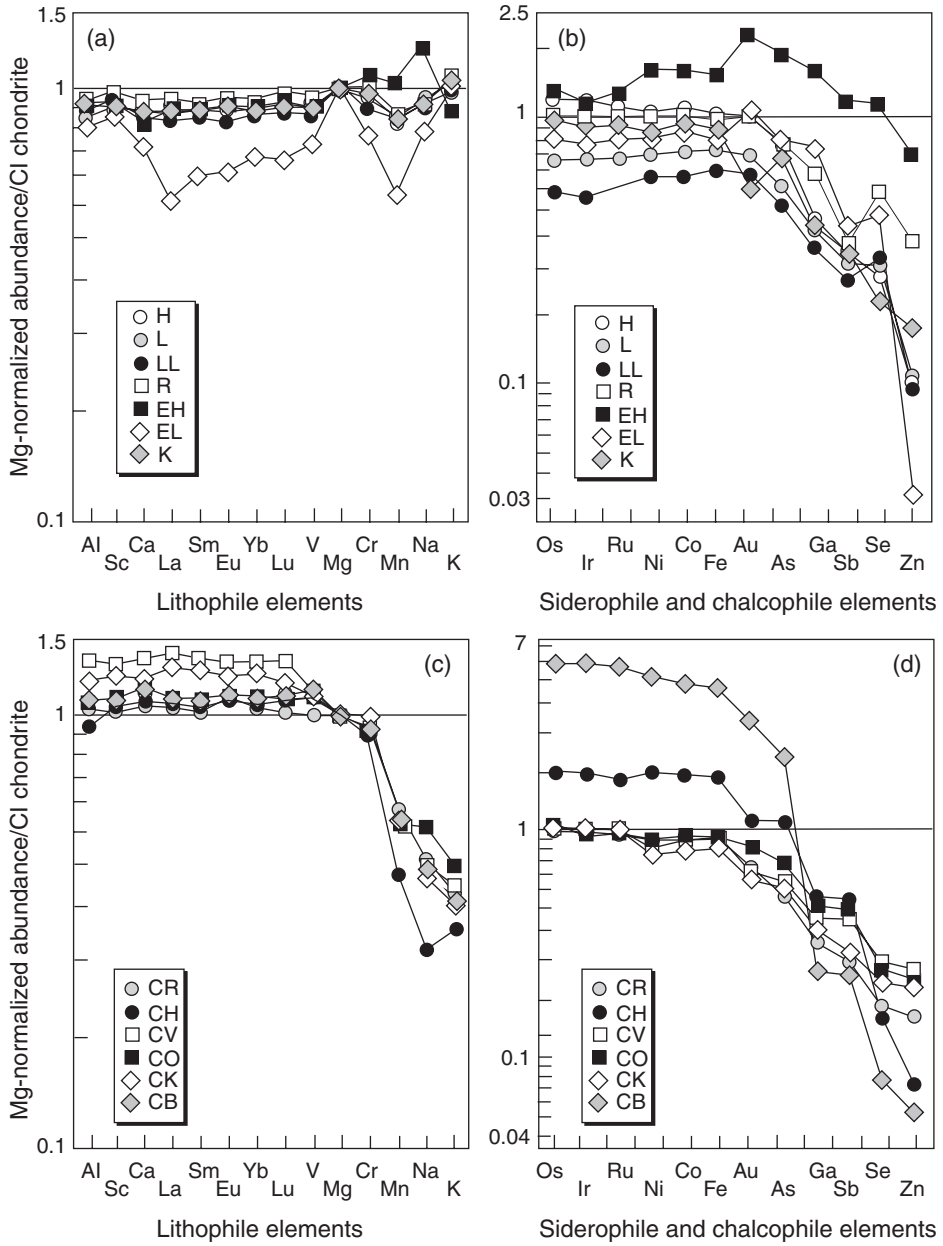

Fig. 11.9 Compositional variations among chondrites. (a) Lithophile and (b) siderophile and chalcophile elements in ordinary (H, L, LL), enstatite (EH, EL), R, and K chondrites. In (c) and (d), the same data are shown for anhydrous carbonaceous chondrite groups. Elements are plotted from left to right in order of increasing volatility. Lithophile elements are normalized to CI chondrites and Mg, siderophile and chalcophile elements are normalized to CI chondrites. Modified from Krot *et al.* (2003).

Differentiated meteorites

Achondrites, irons, and stony-irons are fragments of asteroids that underwent melting and differentiation. In Chapter 6, we learned that achondrites represent crystallized magmas or cumulates from such magmas, and primitive achondrites are the solid residues left when partial melts were extracted. The compositional diversity among achondrites reflects, in part, the compositional differences among their chondritic precursors, but also the geochemical changes that accompany melting and fractional crystallization. Environmental conditions also play a role, as melting of similar chondritic compositions under different oxidation states produces distinct types of achondrites. The reasons that elements are partitioned differently between melts and solids were explained in Chapter 7.

Irons are mostly fragments of asteroid cores. As with achondrites, their compositional variations reflect differences in parent body chemistry as well as changes wrought by crystallization. Pallasites may represent samples of core-mantle boundaries, and mesosiderites indicate poorly understood mixing of crust and core materials, probably by impact.

It is very difficult to reconstruct parent body compositions from differentiated meteorites. In this section, we will describe the chemical characteristics of the meteorites themselves, but the compositions of the bulk asteroids from which they were derived can only be inferred in the broadest terms and are usually assumed to have been chondritic.

Some representative chemical analyses of primitive achondrites (acapulcoites–lodranites, winonaites, and ureilites) are given in Table 11.4 (Lodders and Fegley, 1998). The near-chondritic compositions of acapulcoites, which experienced very limited partial melting, are illustrated in Figure 11.10, where they are compared with ordinary (H group) chondrites. The compositions of lodranites, which are residues from which a greater amount of melt was extracted, are more depleted in those elements that partition into magma. Winonaites are also roughly chondritic in composition (Fig. 11.10) and show similar, though less pronounced depletions. Ureilites apparently represent residues from more extensive melting of a carbonaceous chondrite-like asteroid, and their compositions are highly fractionated from chondritic abundances.

Compositions of some achondrites are given in Table 11.5. Especially useful tabulations are given by Lodders and Fegley (1998), Mittlefehldt *et al*. (1998), and Mittlefehldt (2004). It is challenging to obtain representative samples of many achondrites for chemical analysis, because they can be coarse-grained and heterogeneous. Angrites are basalts that show extreme depletions in silica and in moderately volatile elements such as the alkalis. They formed by melting of a chondritic source, apparently unlike known chondrite classes, under oxidizing conditions. In contrast, the aubrites are the most reduced achondrites, and they share many compositional and mineralogical characteristics with enstatite chondrites. Owing to their abundance, there is a large body of literature on the compositions of HED achondrites. Eucrites are basalts with very limited variations in chemical composition. Diogenites and cumulate eucrites show greater compositional variation, but this may reflect the difficulty in obtaining representative

Table 11.4 Representative chemical analyses of primitive achondrites

	Acapulco	Gibson	Pontlyfni	Udei Station	Havero
Element	acapulcoite	lodranite	winonaite	IAB silicate	ureilite
Na (mg g^{-1})	6.42	2.8	6.42	5.25	0.242
Mg (mg g^{-1})	153.8	188	119.2	197	224
Al (mg g^{-1})	11.2	3.4	13.1	10	1.1
Si (mg g^{-1})	176.5	221	144.8		188
P (mg g^{-1})	1.6		0.48		
S (mg g^{-1})	21.1		70.4		
K (μg g^{-1})		190	700		35
Ca (mg g^{-1})	9.8	9.15	11.8	8.3	
Sc (μg g^{-1})	8.5	10.5	5.79	12.6	4.9
Ti (mg g^{-1})	0.7	0.72	0.6		0.36
V (μg g^{-1})	92			68	
Cr (mg g^{-1})	7.00	2.8	2.09	3.23	4.09
Mn (mg g^{-1})	3.26	4.2	2.02	2.37	2.66
Fe (mg g^{-1})	204.5	159	296	95	150
Co (μg g^{-1})	640	720	883	110	101
Ni (mg g^{-1})	13.3	8.1	23.4	2.75	0.92
Zn (μg g^{-1})	250	62	130	237	235
Ga (μg g^{-1})	7.78	8.1	16.6	5.3	1.13
As (μg g^{-1})	1.57	2.12	3.3	0.33	
Se (μg g^{-1})	10.8	0.51	16	10.4	
Sb (ng g^{-1})	61	150	390	36	
La (ng g^{-1})	742	170	260	158	70
Ce (ng g^{-1})		700	700		
Nd (ng g^{-1})		550			
Sm (ng g^{-1})	250	210	103	92	14
Eu (ng g^{-1})	100	20	100	60	4.1
Tb (ng g^{-1})	62	50			
Yb (ng g^{-1})	300	270	90	147	25
Lu (ng g^{-1})	40	50	13	26	8.5
Hf (ng g^{-1})	120	50			
Ta (ng g^{-1})		14			
W (ng g^{-1})		190			180
Os (ng g^{-1})	670		780	50	
Ir (ng g^{-1})	536	1220	586	37	240
Au (ng g^{-1})	149	90	250	38	24
U (ng g^{-1})	70	50			6

Data sources given by Mittlefehldt (2004).

samples of these coarser grained meteorites. The HED suite is depleted in volatile and siderophile elements, reflecting the composition of the chondritic precursor and the extraction of metallic elements into the core, respectively. Howardite breccias have compositions intermediate between eucrites and diogenites.

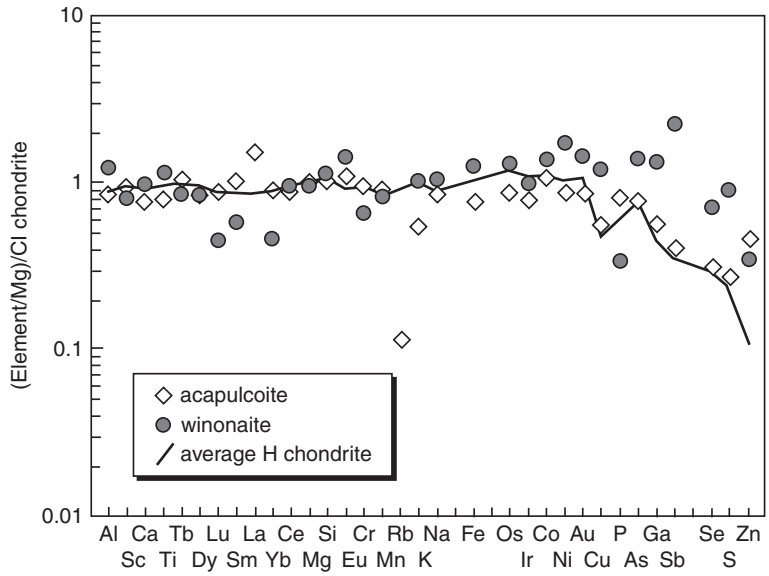

Fig. 11.10 **Elemental abundances, normalized to Mg and CI chondrites, for two groups of primitive achondrites (acapulcoites and winonaites) that experienced low degrees of partial melting. These abundances are similar to chondritic abundances (average H-chondrite composition is illustrated). Modified from Mittlefehldt (2004).**

The compositions of most iron meteorites have been reported by John Wasson and his colleagues in an extensive set of papers published over the past 30 years (reviewed by Haack and McCoy, 2004). These meteorites are highly varied; average compositions for nine siderophile elements in the major iron groups are given in Table 11.6. In part, these differences reflect nebular processes that established siderophile element abundances in chondritic precursors, as discussed in Chapter 7. Group IIAB irons have the lowest nickel concentrations, IIIAB irons have the highest abundance of phosphates, and IVA irons have low volatile element abundances and a distinctive Ir/Au ratio. However, within each group some elements vary along smooth trends that reflect fractional crystallization. Some examples of compositional variations within one core (the IIIAB irons) are illustrated in Figure 11.11.

Thermal evolution of anhydrous asteroids

The heat source for asteroid metamorphism and melting is somewhat controversial. First, let's consider what is probably implausible. The slow decay of long-lived radionuclides (isotopes of potassium, uranium, and thorium), a primary heat source for large planets, is ineffective for asteroids because the time scale for release of energy is long compared to that for conductive heat loss from small bodies. Impacts have been invoked as a heat source for asteroids, and localized melting can certainly occur during cratering events. However, the

Table 11.5 Representative chemical analyses of achondrites

	LEW 87051	Aubres	Sioux Co.	Shalka	Frankfort
Element	angrite	aubrite	eucrite	diogenite	howardite
Na (mg g^{-1})	0.174	0.706	3.3	0.024	1.01
Mg (mg g^{-1})	117	232.7	42.9	155.5	126.3
Al (mg g^{-1})	48.7	2.4	67.97	3.2	22.6
Si (mg g^{-1})	188.9	273.7	229.2	241.1	237.9
P (mg g^{-1})		2	0.39	0.01	0.15
K (μg g^{-1})		517	295	13	81
Ca (mg g^{-1})	77.2	2.77	74.0	5.2	26
Sc (μg g^{-1})	36	6.5	34.5	9.9	20.5
Ti (mg g^{-1})	4.4	0.185	4.08	0.37	1.36
Cr (mg g^{-1})	1.09	0.241	1.98	16.5	7.94
Mn (mg g^{-1})	1.9	1.49	4.34	4.28	4.34
Fe (mg g^{-1})	148	4.1	144.7	126.5	139.1
Co (μg g^{-1})	27.4	6	6.8	18	23.6
Ni (mg g^{-1})	0.044	0.161	0.0017	0.005	0.125
Zn (μg g^{-1})		3.61	5.3		2.17
Ga (μg g^{-1})			1.27		0.51
Se (μg g^{-1})		2.46			0.05
Rb (ng g^{-1})		605	170		230
Sr (μg g^{-1})		130	76		24
Zr (μg g^{-1})	67		41		
La (ng g^{-1})	2320		1820	9	980
Ce (ng g^{-1})	6200	347	5190		2700
Nd (ng g^{-1})		241	4320		1700
Sm (ng g^{-1})	1480		1540	4	560
Eu (ng g^{-1})	536	16.7	415	2	180
Tb (ng g^{-1})	360	25.2	398		150
Yb (ng g^{-1})	1520	101	1940	30	620
Lu (ng g^{-1})	239	14.8	287	6	93
Hf (ng g^{-1})	1170		1160		490
Ta (ng g^{-1})	110		147		40
W (ng g^{-1})			43		126
Os (ng g^{-1})		0.843			
Ir (ng g^{-1})		0.822			4.1
Au (ng g^{-1})		4.27			3.4
Th (ng g^{-1})	220		287		
U (ng g^{-1})		3.17	74		38

Data sources given by Mittlefehldt (2004).

global temperature increase from near-disruptive collisions of asteroids is only a few degrees, because small bodies with low gravity do not produce large amounts of collisional energy. Impacts can be effective heat sources if they involve very large objects, but energy transfer to the interior of the target is inefficient (Keil *et al.*, 1997). Electromagnetic

Table 11.6 Average chemical compositions of major iron meteorite groups

Element	IAB	IIAB	IIIAB	IVA	IVB
Ni (mg g^{-1})	95.0	56.5	83.3	85.1	172
S (mg g^{-1})		(170)	(120)	(30)	(0)
Co (mg g^{-1})	4.9	4.6	5.1	4.0	7.6
Cu (μg g^{-1})	234	133	156	137	<9
Ir (μg g^{-1})	2.0	12.5 (1.3)	3.2 (5.0)	1.8 (1.8)	18.0 (22.0)
Au (μg g^{-1})	1.75	0.71 (1.0)	1.12 (0.7)	1.55 (1.6)	0.14 (0.15)
Ga (μg g^{-1})	63.6	58.6	19.8	2.14	0.23
Ge (μg g^{-1})	247	174	39.1	0.12	0.055
Re (ng g^{-1})	260	1780 (250)	439 (200)	230 (150)	2150 (3500)

Data sources given in Haack and McCoy (2004). Values in parentheses are calculated initial liquid compositions; for elements like Ir and Re with solid/liquid distribution coefficients that are far from unity, meteorite composition may be different from that of the initial liquid core.

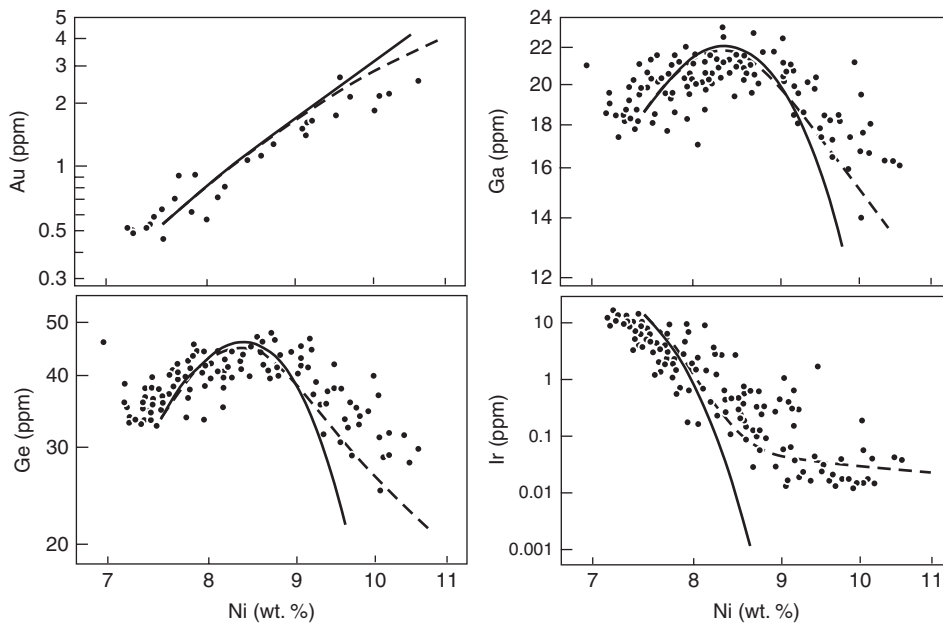

Fig. 11.11 Elemental abundances in group IIIAB iron meteorites (dots) compared to calculated fractional crystallization trends that assume complete separation of crystals and melt (solid curve) and incomplete separation of those phases (dashed curve). Modified from Haack and McCoy (2004).

induction, whereby heat is produced by resistance to the flow of electric currents induced by outflows from the young Sun, has also been promulgated as a cause of asteroid heating (Herbert and Sonnet, 1980). However, outflows from young stars are focused at the stellar poles, avoiding the nebular disk where planetesimals occur. Induction models are also

highly dependent on the choice of parameters, few of which are constrained, so it is difficult to ascertain if these models are reasonable.

The most plausible heat source for heating planetesimals is decay of short-lived radionuclides, such as ^{26}Al and ^{60}Fe. The decay products of these nuclides have been found in both chondrites and achondrites, and their wide distribution and high decay energies make them attractive sources of asteroid heating. In addition, recent evidence that the parent bodies of achondrites formed very early, within 1 Myr of the formation of CAIs (Chapter 9), means that abundances of short-lived radionuclides would have been very high in these bodies, leading to melting. Chondrite parent bodies, which formed >2 Myr after CAIs, may not have inherited enough of the short-lived nuclides to melt.

The peak temperatures that asteroids experienced can be estimated from chemical exchange reactions between minerals – so-called geothermometers. For example, the exchange of calcium between coexisting orthopyroxene and clinopyroxene in highly metamorphosed chondrites has been used to estimate their equilibration temperatures (Slater-Reynolds and McSween, 2005). For ordinary chondrites, these temperatures range up to ~1175 K. The experimental conditions at which achondrites melt provide minimum temperatures for their parent bodies. Melting of achondrites typically requires temperatures of >1200 K.

Metamorphic reactions in anhydrous chondrites mostly involved recrystallization, although a few mineral changes occurred. Of particular interest is an oxidation reaction

$$\underset{\text{metal}}{\text{Fe}} + \text{O}_2 + \underset{\text{pyroxene}}{(\text{Mg},\text{Fe})\text{SiO}_3} = \underset{\text{olivine}}{(\text{Mg},\text{Fe})_2\text{SiO}_4}$$

which may have changed the relative proportions of pyroxene and olivine (McSween and Labotka, 1993). Several studies have observed progressive changes in the olivine/pyroxene ratio and in the proportion of metal with increasing degree of metamorphism. Certain spectral features are sensitive to the olivine/pyroxene ratio, so this change can also be seen in asteroid spectra.

The rates at which parent bodies cooled also provide constraints on thermal models. A method for determining the cooling rates for iron meteorites is described in Box 11.2. A similar method for chondrite cooling rates is also based on the compositions of metal grains. Cooling rates can also be estimated from knowing the blocking temperatures of various radioisotope systems.

The basis for asteroid thermal models is the heat transfer equation:

$$\frac{\partial T}{\partial t} = \frac{1}{R^2}\frac{d}{dR}\left(R^2 \kappa \frac{\partial T}{\partial R}\right) + \frac{Q}{\rho C_v} \tag{11.1}$$

where T is temperature, R is the radius of the asteroid, t is time, κ is thermal diffusivity, Q is the heat generated by radioactive decay, ρ is density, and C_v is the specific heat at constant volume. Let's see how each term in the equation might affect the solution. The term on the left is the rate of change of temperature with time in a layer of infinitesimal thickness at any arbitrary depth in the asteroid. The first term on the right gives the amount of heat gained in (or lost by) the infinitesimal layer by conduction. The amount of heat transmitted by

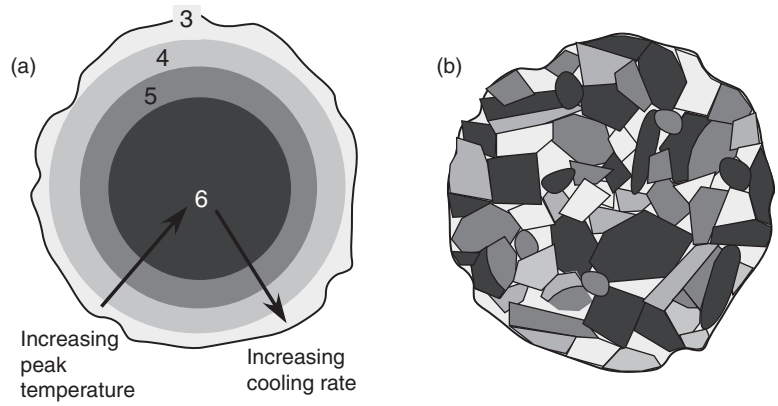

Fig. 11.12 **Sketches of the interiors of chondritic asteroids, illustrating (a) onion shell and (b) rubble pile structures. The numbers and shadings identify petrologic types.**

conduction is proportional to the rate at which the product of thermal gradient ($\partial T/\partial R$) and thermal diffusivity changes. The last term on the right gives the amount of heat generated in the asteroid by radioactive decay.

By necessity, asteroid thermal models must make assumptions about model parameters and initial conditions. However, models based on ^{26}Al heating have been remarkably successful in reproducing asteroid peak temperatures and cooling histories.

Thermal models for anhydrous asteroids that do not melt, such as the parent bodies for ordinary chondrites, are relatively straightforward, because heat migrates through these bodies by conduction. Decay of ^{26}Al results in rapid heating within the few million years after accretion. These models (McSween *et al*., 2003) suggest that asteroid interiors experienced the highest temperatures, producing highly metamorphosed (type 6) chondrites, and that successively less metamorphosed shells occur towards the surface. The resulting thermal structure, called an "onion shell," is illustrated in Figure 11.12a. Cooling rates estimated for chondrites of higher metamorphic grade are slower than those of lower grade (Fig. 11.13), supporting the onion shell model. For asteroids with regoliths, the outer fine-grained layer insulates the interior, preventing efficient heat loss by radiation to space. Consequently, small asteroids with regoliths can produce the same cooling rates as larger asteroids.

Thermal models for differentiated asteroids are much more complex, because radiogenic heat sources move around during the simulation. When partial melting occurs, aluminum (and thus ^{26}Al) partitions into silicate magma, and iron (^{60}Fe) is concentrated into metallic melt. The dense metallic melt drains into the core and the less dense silicate melt ascends towards the surface to form a basaltic crust, as illustrated in Figure 11.14. Such separations are not instantaneous, because melts can "wet" solid residues, so some threshold value of partial melting is usually required to initiate phase separation. Because no individual samples of core, mantle, or crust retain the asteroid's bulk composition, there is considerable uncertainty in estimating the composition of the parent body prior to differentiation. The bulk compositions of differentiated bodies are generally thought to be chondritic but, as we

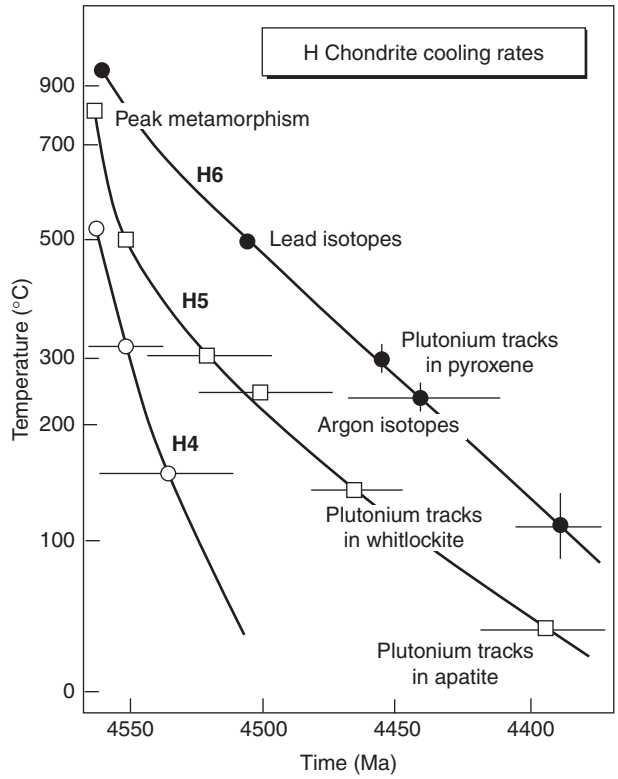

Fig. 11.13 **Cooling rates for H chondrites of different petrologic types can be estimated from the blocking temperatures for diffusion in various radioisotope systems. The age measured by each radioisotope indicates the time the meteorite passed through that blocking temperature. Slower cooling rates for more highly metamorphosed H5 and H6 chondrites are evidence that the parent body had an onion shell structure.**

learned in Chapter 7, they are more depleted in volatile elements than are chondrites. A thermal model for asteroid 4 Vesta (Ghosh and McSween, 1998), thought to be the HED parent body, indicates rapid melting and differentiation, with high temperatures being maintained for perhaps 100 million years. Such models are broadly consistent with radiometric ages for HED meteorites, as discussed in Chapter 9.

Thermal structure of the asteroid belt

The heliocentric pattern of asteroid types, with thermally processed objects closer to the Sun (as inferred from spectra), persists despite subsequent dynamical stirring of asteroid orbits and ejection of bodies from the main belt. Differentiated objects appear to have formed earlier than chondritic bodies, and dynamical modeling suggests they may have accreted

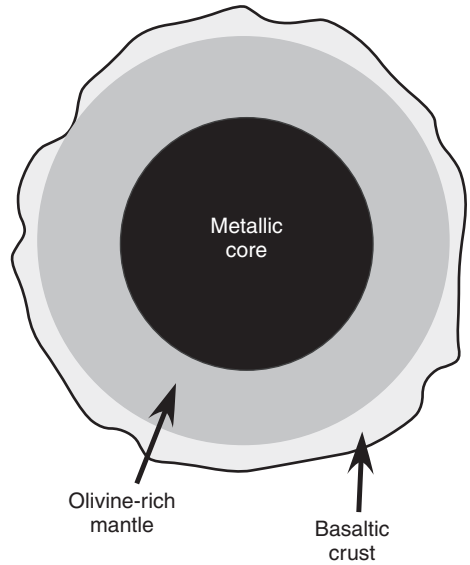

Fig. 11.14 **Sketch of the interior of a differentiated asteroid.**

Box 11.2 Iron meteorite cooling rates: a study of nickel diffusion

Nickel and iron form a solid solution at high temperatures, but an alloy on cooling will unmix to form oriented plates of low-Ni kamacite within high-Ni taenite. These plates constitute the familiar Widmanstatten pattern seen in many iron meteorites (see Fig. 6.8). Experiments indicate that both phases become more nickel-rich with further cooling, as kamacite plates grow thicker at the expense of taenite. Kamacite growth and taenite shrinkage occur by diffusion of nickel, the rate of which varies with temperature. Nickel diffusion in kamacite is rapid, so these plates tend to be homogeneous. However, at some point during cooling, diffusion becomes sluggish enough that nickel atoms in taenite begin to pile up at the margins of the plates, producing chemically zoned taenite in which the nickel content decreases toward the center of the grains. By approximately 450 °C, diffusion effectively grinds to a halt, and the zoning pattern becomes frozen in, as illustrated in Figure 11.15. Electron microprobe analyses of spots in a traverse across a taenite grain define a nickel profile that is often described as M-shaped (only half of the M is illustrated in Fig. 11.15).

Nickel diffusion profiles in taenite depend on nickel diffusion rates, the bulk nickel content, the nucleation temperature of kamacite, and the dimensions and cooling history of the system. The last parameter is the most interesting. Other things being equal, the more slowly an iron meteorite cooled, the greater the opportunity for nickel to diffuse to the interiors of the taenite crystals. By matching measured nickel profiles with calculated profiles, meteoriticists have estimated the cooling rates for iron meteorites. The most recent version of this method is given by Yang and Goldstein (2005). Iron meteorite cooling rates have been found to vary from less than one to several thousand degrees per million years.

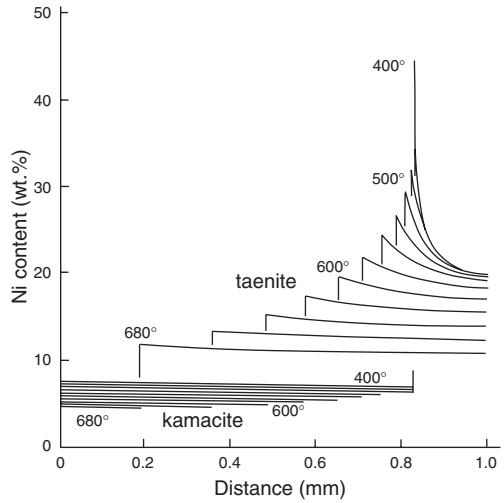

Fig. 11.15 **Computation of the development of nickel profiles in kamacite and taenite within an iron meteorite. The left edge of the figure represents the midpoint of a kamacite plate. The thickness of the plate expands and its nickel content increases as temperature falls. The right edge is the center of a residual taenite area. Its nickel content also increases with falling temperature, first throughout the crystal and later only at its edges, producing an M-shaped profile (only half of which appears in this sketch). Temperatures are given in °C.**

Cooling rates have important implications for the sizes of meteorite parent bodies. Because of its high thermal conductivity, a metallic core should have a uniform temperature, but its rate of cooling is controlled by outer silicate layers that act like insulation. Larger asteroids cool more slowly, and Haack *et al*. (1990) developed an approximate relationship between the radius of an asteroid R and the cooling rate CR of its metallic core:

$$R = 149(\mathrm{CR})^{-0.465}$$

Using this equation, the calculated radii of most iron meteorite parent bodies are found to have been ~10–100 km.

inside 2 AU and were then scattered into the main belt by interactions with growing planets (Bottke *et al*., 2005).

This pattern may be a natural consequence of the fact that accretion time increased with the density of materials in the swarm, and density decreased at greater solar distances. The planetesimals that accreted closer to the Sun and hence earlier would have had larger proportions of live ^{26}Al available to drive heating. A model summarizing this effect is illustrated in Figure 11.16 (Grimm and McSween, 1993). This diagram shows contours of peak temperature on a plot of asteroid size versus solar distance (the latter is equivalent to accretion time, shown at the top of the diagram). The vertical bar at 2.7 AU marks the approximate boundary between bodies that melted or were metamorphosed and those that

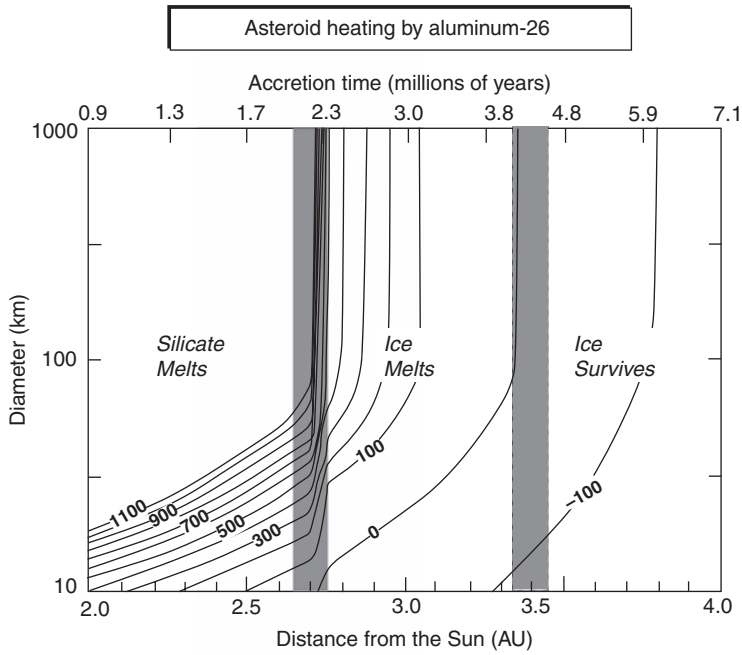

Fig. 11.16 **Contours of peak temperature (K) in asteroids as functions of size (diameter) and heliocentric distance. Accretion times corresponding to various solar distances are given at the top of the figure. Shaded vertical bars mark major divisions in the asteroid belt based on spectral interpretations of asteroid thermal histories. Modified from Grimm and McSween (1993).**

experienced melting of ice and subsequent aqueous alteration. The vertical bar at 3.5 AU denotes the transition to unaltered asteroids that might still contain ice. The accretion times at the top of Figure 11.16 produce peak temperatures appropriate for silicate melting (1375 K) and ice melting (273 K) for 100-km asteroids at the distances of the bars.

Ghosh *et al*. (2006) formulated a more complex model that incorporated incremental rather than instantaneous accretion. Because the timescale of accretion is comparable to that of ^{26}Al decay, asteroids were actually heated as they grew. By coupling a thermal model with an accretion model, they were able to calculate the stratification of asteroids in a more realistic way.

These models provide an explanation for the thermal structure of the asteroid belt that is probably correct in principle but not in its details. The recognition that differentiated asteroids formed earlier than chondrites, perhaps within the terrestrial planet region, requires models in which asteroid accretion was initiated earlier than 2 Myr after CAI formation.

Collisions among asteroids

Collisions among asteroids are commonplace, and impact craters occur on all asteroid surfaces (Fig. 11.1) (Chapman, 2002). Cratering rates within the main asteroid belt are a

hundred times greater than impact rates on the Moon. In general, impactors form craters roughly ten times their own diameters. However, the physics of cratering changes as crater diameters approach the diameters of the target asteroids themselves. In that case, both the impactor and the target asteroid may be catastrophically disaggregated. Commonly, most of the fragments do not exceed the escape velocity and instead they settle back, or reaccrete, to form a new asteroid. Such a body is called a "rubble pile" (Fig. 11.12b).

Evidence for rubble pile asteroids comes from a variety of observations. The low densities of many asteroids imply that they have high porosities, presumably resulting from the assembly of loose fragments. Spectral variations seen in some S-class asteroids as they rotate also support rubble piles. The variations suggest that portions of the surface have experienced different degrees of thermal metamorphism. Catastrophic collision and re-assembly has transformed bodies that formerly had onion shell structures into rubble piles.

Materials excavated by impact craters may become compacted and cemented together, forming "breccias." Meteorite breccias also reveal evidence of rubble pile parent bodies. For example, the Cangas de Onis ordinary chondrite breccia contains metal grains that cooled at rates varying from a few to a thousand K per million years (Fig. 11.17). (Metallographic cooling rates for chondrites are based on diffusion of nickel in iron, as discussed previously for iron meteorites in Box 11.2.) The slowest measured cooling rates could only have occurred in the center of the asteroid, so this one rock contains fragments that formed at various depths ranging from the center to the surface. Any impact that excavated materials

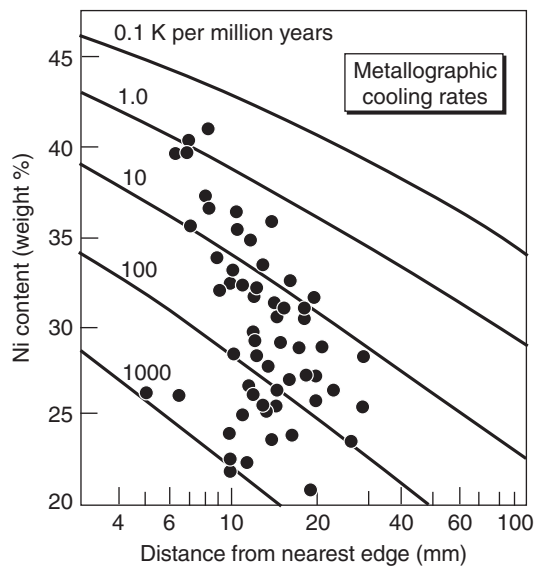

Fig. 11.17 Metal grain compositions in the Cangas de Onis chondrite breccia, and calculated metallographic cooling rates (curves). The cooling rates are estimated from modeling nickel diffusion profiles in metal grains. The slowest cooling rates of ~1 K per Myr require that those grains formed in the asteroid center, whereas cooling rates of ~1000 K per Myr must have formed near the surface. This huge range of metallographic cooling rates in one meteorite is evidence that the parent body was disrupted by impact and then reassembled to form a rubble pile.

from an asteroid center would certainly have disrupted it, so the formation of this breccia requires subsequent reaccretion.

When asteroid collisions are especially violent, sufficient kinetic energy may be imparted to launch fragments at greater than escape velocities. In that case, separate asteroids are formed. These fragments share similar orbital characteristics and are referred to as "families." The members of most asteroid families share the same spectral characteristics, further linking them together. Families composed of fragments of differentiated asteroids can potentially provide important information on their internal compositions.

When colliding objects are of comparable size, the impacts may be glancing blows rather than head-on collisions. In such a case, one body may strip the other of its outer layers, as discussed in Chapter 7. If the target asteroid were differentiated, this would provide a means of removing the crust and mantle, leaving behind a naked core. M-class asteroids may be the result of such impact stripping. This process may also explain the unusual cooling rates of several classes of iron meteorites. If metallic cores cooled slowly inside thermally insulating silicate mantles, the metallographic cooling rates of all samples of that core should be the same. However, the cooling rates of IVA irons vary from 90 to 7000 K per 10^6 yrs^{-1}, and IIIAB irons show smaller but still significant differences in cooling history. If their differentiated parent bodies were still molten when their mantles were stripped off by glancing impacts, the liquid cores could have cooled rapidly on the outside and more slowly in the center. Impact removal may also account for the fact that olivine-rich mantle materials are very uncommon among meteorites, whereas metallic cores are abundant. Repeated impacts could have ground the mantle materials to tiny particles over time.

Summary

Anhydrous planetesimals, and especially the meteorites derived from them, provide crucial cosmochemical data. Spectroscopic studies of asteroids do not provide chemical analyses, but the spectral similarities of several asteroid classes to known meteorite types provide indirect evidence of their compositions. The few chemical analyses of asteroids by spacecraft are consistent with ordinary chondrite or primitive achondrite compositions. Laboratory analyses of anhydrous meteorites – chondrites, achondrites, irons, and stony irons – allow us to study important chemical fractionations in early solar system bodies. Fractionations among chondrites occur mostly in elements with higher volatility, reflecting the accretion of various components whose compositions were determined by high- and low-temperature processes such as condensation and evaporation. Fractionations among achondrites and irons are more complex and involve partitioning of elements between melts and crystals during differentiation.

Thermal metamorphism in chondrites and melting in differentiated asteroids are driven by heat produced by the decay of short-lived radionuclides (especially ^{26}Al). Thermal models can reproduce the peak temperatures and cooling rates estimated for meteorites, as well as

explain the heliocentric distribution of asteroids with different thermal histories. Such models for chondrites produce onion-shell bodies, with more intensely metamorphosed materials at the center and materials of lower metamorphic grade near the surface. Models for differentiated bodies produce bodies with metallic cores, olivine-rich mantles, and basaltic crusts.

We now turn to ice-bearing planetesimals and asteroids that once contained ices. This will complete the inventory of chemically characterized small bodies, on which so much of cosmochemistry depends.

Questions

1. How are spectroscopic observations used to relate asteroids to various types of meteorites?
2. What is meant by a "geologic context" for interpretation of meteoritic data? Why is such a context important?
3. What are plausible heat sources for planetesimal differentiation?
4. Describe how various classes of asteroids are arrayed within the asteroid belt, and offer an explanation for this distribution.
5. What are onion shell and rubble pile asteroids, and how do they form?

Suggestions for further reading

Bottke, W. F., Cellino, A., Paolicchi, P. and Binzel, R. P., eds. (2002) *Asteroids III*, Tucson: University of Arizona Press, 785 pp. A wonderful, up-to-date resource on asteroids. The following chapters provide summaries of geology, taxonomy, and spectral interpretation, respectively:

Bus, S. J., Vilas F. and Barucci, M. A. (2002) Visible-wavelength spectroscopy of asteroids, pp. 169–182.

Burbine, T. H., McCoy, T. J., Meibom, A., Gladman, B. and Keil, K. (2002) Meteoritic parent bodies: their number and identification, pp. 653–665.

Sullivan, R. J., Thomas, P. C., Murchie, S. L. and Robinson, M. S. (2002) Asteroid geology from Galileo and NEAR Shoemaker data, pp. 331–350.

Haack, H. and McCoy, T. J. (2004) Iron and stony-iron meteorites. In *Treatise on Geochemistry, Vol. 1. Meteorites, Comets, and Planets*, ed. Davis, A. M. Oxford: Elsevier, pp. 325–345. This excellent review summarizes the compositions of iron meteorites.

Jarosewich, E. (1990) Chemical analyses of meteorites: A compilation of stony and iron meteorite analyses. *Meteoritics*, **25**, 323–337. A compilation of many years of painstaking wet-chemical analyses of representative chondrite powders. These analyses are especially useful because they distinguish the amounts of metallic iron and Fe^{2+}.

Mittlefehldt, D. W. (2004) Achondrites. In *Treatise on Geochemistry, Vol. 1. Meteorites, Comets, and Planets*, ed. Davis, A. M. Oxford: Elsevier, pp. 291–324. A superb review of achondritic meteorites, containing many high-quality analyses.

References

Bottke, W. F., Newvorny, D., Grimm, R. E., Morbidelli, A. and O'Brien, D. P. (2005) Iron meteorites as remnants of planetesimals formed in the terrestrial planet region. *Nature*, **439**, 821–824.

Brearley, A. J. and Jones, R. H. (1998) Chondritic meteorites. In *Planetary Materials, Reviews in Mineralogy* **36**, ed. Papike, J. J. Washington, D.C.: Mineralogical Society of America, pp. 3–1 to 3–398.

Chapman, C. R. (2002) Cratering on asteroids from Galileo and NEAR Shoemaker. In *Asteroids III*, eds. Bottke, W. F., Cellino, A., Paolicchi, P. and Binzel, R. P. Tucson: University of Arizona Press, pp. 315–330.

Clark, B. E., Hapke, B., Pieters, C. and Britt, D. (2002) Asteroid space weathering and regolith evolution. In *Asteroids III*, eds. Bottke, W. F., Cellino, A., Paolicchi, P. and Binzel, R. P. Tucson: University of Arizona Press, pp. 585–602.

Evans, L. G., Starr, R. D., Bruckner, J. et al. (2001) Elemental composition from gamma-ray spectroscopy of the NEAR-Shoemaker landing site on 433 Eros. *Meteoritics and Planetary Science*, **36**, 1639–1660.

Fujiwara, A., plus 21 coauthors (2006) The rubble-pile asteroid Itokawa as observed by Hayabusa. *Science*, **312**, 1330–1334.

Gaffey, M. J., Cloutis, E. A., Kelley, M. S. and Reed, K. L. (2002) Mineralogy of asteroids. In *Asteroids III*, eds. Bottke, W. F., Cellino, A., Paolicchi, P. and Binzel, R. P. Tucson: University of Arizona Press, pp. 183–204.

Ghosh, A. and McSween, H. Y. (1998) A thermal model for the differentiation of asteroid 4 Vesta, based on radiogenic heating. *Icarus*, **134**, 187–206.

Ghosh, A., Weidenschilling, S. J., McSween, H. Y. and Rubin, A. (2006) Asteroid heating and thermal stratification of the asteroid belt. In *Meteorites and the Early Solar System II*, eds. Lauretta, D. S. and McSween, H. Y., Jr. Tucson: University of Arizona Press, pp. 555–566.

Gradie, J. C. and Tedesco, E. F. (1982) Compositional structure of the asteroid belt. *Science*, **216**, 1405–1407.

Grimm, R. E. and McSween, H. Y. (1993) Heliocentric zoning of the asteroid belt by aluminum-26 heating. *Science*, **259**, 653–655.

Haack, H., Rasmussen, K. L. and Warren, P. H. (1990) Effects of regolith/megaregolith insulation on the cooling histories of differentiated asteroids. *Journal of Geophysical Research*, **95**, 5111–5124.

Herbert, F. and Sonnett, C. P. (1980) Electromagnetic inductive heating of the asteroids and moon as evidence bearing on the primordial solar wind. In *The Ancient Sun*, eds. Pepin, R. O., Eddy, J. A. and Merrill, R. B. New York: Pergamon, pp. 563–576.

Kallemeyn, G. W., Rubin, A. E., Wang, D. and Wasson, J. T. (1989) Ordinary chondrites: Bulk compositions, classification, lithophile-element fractionations, and composition-petrographic type relationships. *Geochimica et Cosmochimica Acta*, **53**, 2747–2767.

Keil, K., Stoffler, D., Love, S. G. and Scott, E. R. D. (1997) Constraints on the role of impact heating and melting in asteroids. *Meteoritics and Planetary Science*, **32**, 349–363.

Krot, A. N., Keil, K., Goodrich, C. A., Scott, E. R. D. and Weisberg, M. K. (2003) Classification of meteorites. In *Treatise on Geochemistry, Vol. 1. Meteorites, Comets, and Planets*, ed. Davis, A. M. Oxford: Elsevier, pp. 83–128.

Lauretta, D. S. and Killgore, M. (2005) *A Color Atlas of Meteorites in Thin Section*. Tucson: Golden Retriever Publications, 301 pp.

Lodders, K. and Fegley, B. Jr. (1998). *The Planetary Scientist's Companion*. New York: Oxford University Press, 371 pp.

McCoy, T. J. *et al*. (2001) The composition of 433 Eros: a mineralogical-chemical synthesis. *Meteoritics and Planetary Science*, **36**, 1661–1672.

McSween, H. Y., Ghosh, A., Grimm, R. E., Wilson, L. and Young, E. D. (2003) Thermal evolution models of asteroids. In *Asteroids III*, eds. Bottke, W. F., Cellino, A., Paolicchi, P. and Binzel, R. P. Tucson: University of Arizona Press, pp. 559–571.

McSween, H. Y. and Labotka, T. C. (1993) Oxidation during metamorphism of the ordinary chondrites. *Geochimica et Cosmochimica Acta*, **57**, 1105–1114.

Mittlefehldt, D. W., McCoy, T. J., Goodrich, C. A. and Kracher, A. (1998) Non-chondritic meteorites from asteroidal bodies. In *Planetary Materials, Reviews in Mineralogy* 36, ed. Papike, J. J., Washington: Mineralogical Society of America, pp. 4–1 to 4–195.

Mothe-Diniz, T., Carvano, J. M. and Lazzaro, D. (2003) Distribution of taxonomic classes in the main belt of asteroids. *Icarus*, **162**, 10–21.

Nittler, L. R. and 15 coauthors (2001) X-ray fluorescence measurements of the surface elemental composition of asteroid 433 Eros. *Meteoritics and Planetary Science*, **36**, 1673–1695.

Okada, T., Shirai, K., Yamanoto, Y. *et al*. (2006) X-ray fluorescence spectrometry of asteroid Itokawa by Hayabusa. *Science*, **312**, 1338–1341.

Pieters, C. M., Taylor, L. A., Noble, S. K. *et al*. (2000) Space weathering on airless bodies: resolving a mystery with lunar samples. *Meteoritics and Planetary Science*, **35**, 1101–1107.

Slater-Reynolds, V. and McSween, H. Y. (2005) Peak metamorphic temperatures in type 6 ordinary chondrites: an evaluation of pyroxene and plagioclase geothermometry. *Meteoritics and Planetary Science*, **40**, 745–754.

Tholen, D. J. (1984) *Asteroid Taxonomy from Cluster Analysis of Photometry.* Ph.D. thesis, University of Arizona, Tucson.

Tholen, D. J. and Barucci, M. A. (1989) Asteroid taxonomy. In *Asteroids II*, eds. Bottke, W. F., Cellino, A., Paolicchi, P. and Binzel, R. P. Tucson: University of Arizona Press, pp. 298–315.

Yang, J. and Goldstein, J. I. (2005) The formation of the Widmanstatten structure in meteorites. *Meteoritics and Planetary Science*, **40**, 239–253.

12 Chemistry of comets and other ice-bearing planetesimals

Overview

Ices, composed of water and other volatile compounds, are a very important component of the solar system. Whether formed by condensation in the nebula or imported from the interstellar medium, these frozen substances accreted with dust and rock beyond the snow-line to form vast swarms of planetesimals and some larger bodies. Most of the ice-bearing planetesimals have been swept out of the planetary region by gravitational interactions with the giant planets, and their distribution now extends out to the limits of the Sun's grasp. Occasionally these bodies careen into the inner solar system, where sunlight volatilizes their ices, revealing them to be comets. Other planetesimals that formerly contained ices have remained near their formation locations in the asteroid belt; most of these suffered aqueous alteration when ices were melted. In this chapter we consider what has been discovered about the chemistry of comets and hydrated asteroids. The importance of these objects to cosmochemistry is a consequence of their primitive compositions and remarkable state of preservation.

Icy bodies in the solar system

In Chapter 10, we briefly considered ices and how they trap noble gases and provide sites for the formation of organic matter in the ISM and the solar nebula. We now discuss the ices themselves, including how they originated, where they existed in the early solar system and where they exist today. Ice-bearing bodies are of considerable importance in understanding the early solar system, because the icy regions of the nebula constituted 99% of the area of the disk and ice rivals rock in abundance. Ices accreted, along with rocky materials, to form planetesimals and, ultimately, planets beyond the snowline. The objects that formed in this region include not only comets but also millions of other ice-bearing bodies that are stored at the fringes of the disk and blossom into cometary activity whenever they wander into the Sun's warming presence. Many icy bodies reside within the Kuiper belt, a disk-like distribution of planetesimals that begins beyond the orbit of Neptune. Kuiper belt objects are often referred to as "KBOs" or sometimes "TNOs" (trans-Neptune objects). More icy bodies are found within the Oort cloud, a spherical volume of planetesimals surrounding the

solar system at even greater distance. Comets are KBOs and Oort cloud objects whose orbits have been perturbed into the inner solar system.

Some classes of asteroids also contain, or formerly contained, ices. A comet is distinguished operationally from an asteroid if it displays cometary activity in the form of a bright coma of gas and dust around the nucleus and an elongated tail. Paradoxically, an asteroid that suddenly shows cometary activity can be reclassified as a comet, but a dead comet that no longer exhibits a coma and tail is not reclassified as an asteroid. It should be obvious that this observational definition, however serviceable it may be to astronomers, has little or no cosmochemical significance. Cometary activity results from the vigorous sublimation of ices as the nucleus is warmed by the Sun. If ice-bearing asteroids were to approach the Sun, they also would presumably produce comas and tails. Other classes of asteroids, specifically the parent bodies for CI and CM chondrites, might have been called comets if we had observed them billions of years ago. The ices in these bodies are now long gone, but their former presence is revealed by aqueous alteration caused by melted ice.

In this chapter we will consider the cosmochemistry of ice-bearing planetesimals. We will focus first on comets, because more is known about their chemistry than of the compositions of objects still in the Kuiper belt and Oort cloud. We will then explore asteroids whose ices melted long ago, and we will briefly consider some larger icy bodies, now represented by satellites of the giant planets. The importance of ice-bearing planetesimals to cosmochemistry stems from their primitive compositions, which have remained largely unchanged because of hibernation in a frozen state.

Orbital and physical characteristics

Although here we are most interested in the chemical compositions of ice-bearing planetesimals, we will first briefly review their orbital and physical characteristics, so as to provide some context for the discussion of chemistry to follow.

Orbits

The Kuiper belt begins beyond the orbit of Neptune, extending from ~30 to 50 AU. Most of these bodies lie near the ecliptic plane. As described in Box 12.1, Pluto and its moon Charon can actually be considered large KBOs, part of a group called "Plutinos" that have been captured into orbital resonances with Neptune. At distances beyond 30 AU, KBOs do not exhibit cometary activity. Because their surfaces are dark, there is a pronounced discovery bias in favor of larger objects. Discovered in 2005, Eris (~2400 km diameter, slightly larger than Pluto) has been described as the largest and most distant KBO so far (its semi-major axis of 67 AU actually falls outside the commonly defined outer limit of the Kuiper belt). The number of KBOs larger than 2 km has been estimated at 7 million. Gravitational interactions with the giant planets produce the so-called Jupiter family comets, which are in a transitional dynamical state between the Kuiper belt and the inner solar system.

The spherical Oort cloud is much larger, extending from ~3000 to 50 000 AU, some three orders of magnitude larger than the planetary region. Objects in this region are too distant to be observed directly. They are so weakly bound to the Sun that random passing stars can eject them from the solar system or perturb them into orbits that enter the planetary region. These so-called Halley family comets have long periods, but they can be modified into short-period comets by gravitational interactions with other bodies in the planetary region. The total number of objects in the Oort cloud has been estimated at 6 billion.

Where did the objects in the Kuiper belt and Oort cloud form? KBOs orbiting near 30 AU may have formed near their present orbital locations, and thus represent icy objects that formed an outer fringe of the original solar system. KBOs farther out may have been forced outward by gravitational interactions with Neptune. Oort cloud objects are thought to have formed inside the Kuiper belt region, perhaps closer to Jupiter or Saturn. They were subsequently scattered outward by gravitational interactions with the giant planets. So, paradoxically, the distant objects in the Oort cloud may represent planetesimals that originally formed closer to the Sun than the more proximal KBOs. The sheer numbers of gravitational interactions with these planetesimals may have caused Jupiter to migrate closer to the Sun, and may have forced Saturn, Uranus, and Neptune in the opposite direction. Simulations suggest that many of the ejected planetesimals escaped to interstellar space, especially those that formed near Jupiter. Some of these objects were also assembled into larger bodies and captured as moons of the giant planets.

Several classes of asteroids are also thought to contain ices presently, or contained them at some earlier time. The D- and F-class asteroids occur in the outmost main belt, and the C-, G-, B-, and F-class asteroids are concentrated within the central part of the belt. These asteroids probably formed near their present locations, in which case they represent ice-bearing planetesimals that accreted inside the orbit of Jupiter. A few asteroids exhibiting cometary activity also occur within the asteroid belt.

Appearance and physical properties

The activity that characterizes a comet is driven by solar heating. As the comet approaches the Sun, jets of dust and gas erupt from active areas (Fig. 12.1), as they periodically rotate into the sunlight. The nucleus becomes surrounded by a spherical "coma" formed by the emitted gas and dust. Emitted gas becomes ionized due to interaction with solar ultraviolet radiation, and the ions are swept outward by the solar wind to form the comet's ion tail. A separate dust tail commonly has a different orientation, reflecting variations in the velocities of solid particles and ions. A popular term describing comets is "dirty snowballs", although that description probably understates the proportion of rock and dust relative to ices.

Dust, representing less-volatile materials, is liberated from the comet and propelled outward by the expanding jets of gas. Appreciable quantities of dust are sometimes released; for example, the dust production rate from comet Hale-Bopp exceeded its gas production rate by a factor of five. Comet particles range in size from submicron dust to small rocks. Direct particle impacts onto spacecraft suggest that solid particles in the coma can be of at least millimeter size.

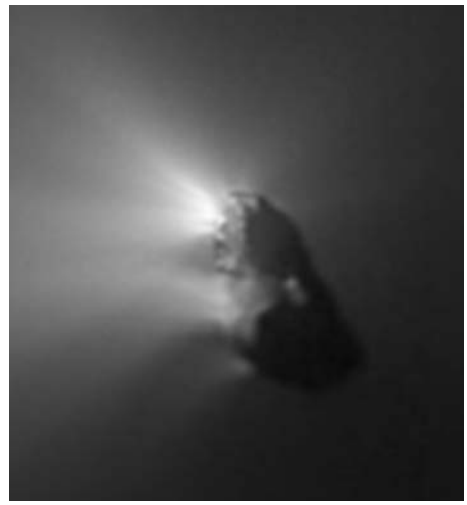

Fig. 12.1 **Image of comet Halley's nucleus, showing jets of dust and volatilized ices. This picture was taken by the Giotto spacecraft as it raced by in 1986. Image courtesy of ESA.**

Comets are generally considered to be weakly consolidated, and active comets are commonly observed to split into fragments. This is sometimes due to the tidal forces of a close planetary encounter, such as affected comet Shoemaker-Levy when it passed close to Jupiter in 1992 and broke into 21 pieces. More commonly, a comet spontaneously fragments multiple times over its orbit period, without any obvious cause. Disintegrating comets leave trails of small particles in their wakes. These trails are known as meteor streams, and when the Earth passes through such a meteor stream, as it does several times a year, a meteor shower occurs. Meter-sized rocks are known to occur within cometary meteor streams.

The densities of comets Halley and Tempel 2 were estimated to be ~0.3 g cm^{-3}, consistent with highly porous objects. However, comet 81P/Wild2, imaged by the Stardust spacecraft in 2004, appears to be a more coherent object, implying that it has a higher density, ~0.6 g cm^{-3}.

Images of comet nuclei taken during various spacecraft encounters illustrate both similarities and differences. Figure 12.2 compares images of comets Borrelly (taken by Deep Space 1 in 2001), Wild2 (taken by Stardust in 2004), and Tempel 1 (taken by Deep Impact in 2005). Despite being of comparable size, these objects have different shapes and varying proportions of smooth and rough areas. Tempel 1 shows visible layering. Comet Wild2 is especially interesting, with pinnacles more than 100 m high and numerous pockmarks, some of which may be impact craters.

For all comets visited by spacecraft, the measured albedo is <5%, making comet nuclei among the darkest objects in the solar system. This coloration is due to black crusts that cover most of the nuclei. The materials now comprising the crusts were presumably spewed out of the interior at speeds below the escape velocity, so they can be considered "lag" deposits. The parts of surfaces covered by such deposits are inert, and active areas releasing gas and dust constitute only a small percentage of a comet's total surface area.

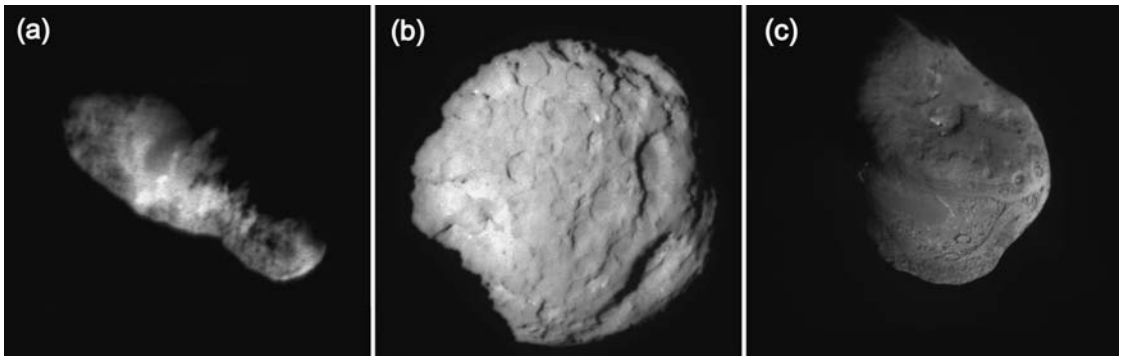

Fig. 12.2 **Images of comet nuclei taken by spacecraft. (a) Borrelly, imaged by Deep Space 1 in 2001, (b) Wild2, as seen by Stardust in 2004, and (c) Tempel 1, taken by Deep Impact in 2005. Images courtesy of NASA.**

Box 12.1 **Pluto and active, icy moons**

Pluto and some moons of the giant planets contain considerable amounts of ices and deserve special mention. In some cases they even exhibit active or recent processes that liberate liquids and gases derived from ices, suggesting a tentative link with cometary activity. These bodies, which are too large to be called planetesimals, include former KBOs now relocated into the planetary region, as well as objects that probably accreted in the giant planet region.

Pluto, with a diameter of 2300 km, has now been demoted from the smallest planet to one of the largest Kuiper belt objects. Pluto and its satellite Charon could be considered a binary system because they are closer in size than any other known celestial pair in the solar system and the barycenter of their orbits does not lie within either body. There are also two smaller moons, Nix and Hydra. All four bodies are likely KBOs with similar compositions. Pluto has a thin atmosphere containing N_2, with minor CH_4, CO, and Ar. Curiously, the face of Pluto oriented towards Charon contains more methane ice, and the opposite face contains more nitrogen and carbon monoxide ice.

Triton, Neptune's only large satellite, was first imaged by Voyager 2 (Fig. 12.3a) as the spacecraft rushed past in 1989 on its way out of the solar system. Triton's diameter is 2700 km. Its retrograde orbit and 29-degree tilt suggest that it may be a captured KBO, an inference bolstered by its spectral similarity to Pluto. Triton has a youthful surface estimated at only ~100 Myr old. Orbital capture would likely have caused intense tidal heating, which might account for its tectonically deformed surface. Perhaps an internal liquid ocean might even persist to this day. Triton's frigid crust contains a veneer of methane and nitrogen ices over a substrate of water ice, and it displays active geyser-like eruptions of volatiles and entrained organic molecules. This "cryovolcanism" is probably powered by sunlight, because eruptions appear only near the latitude that receives maximum solar illumination. Could Triton's geysers be a manifestation of cometary activity?

Europa, a moon of Jupiter with a diameter of 3210 km, has received considerable attention because of evidence that its icy crust hides a global ocean. Infrared spectra indicate abundant

water ice and some organic compounds on its surface. Spacecraft images reveal blocks of ice jumbled by swarms of rifts (Fig. 12.3b). The surface has low relief, and visible bands may be loci of volcanic water eruptions. Pits and spots may represent diapirs of warmer ice rising through the colder ice of the crust. Spectra from the Galileo spacecraft suggest that reddish features on Europa may be rich in hydrated silicates and salts such as magnesium sulfate, deposited from evaporating water.

On Enceladus (500 km diameter), a moon of Saturn, plumes of ice and gas rise from warm, active fractures (Fig. 12.3c) in its south polar region. This activity is probably the result of tidal heating. The Cassini spacecraft determined that water is the dominant plume constituent, although trace amounts of several organic compounds (acetylene and propane) were also measured. It is unclear whether the plumes are erupting as geysers or merely sublimating from the fractures, but in any case Enceladus is revealed as another active, partly frozen moon.

Titan, Saturn's largest satellite (5150 km diameter, approximately the size of Mercury), has a Europa-sized rock core enclosed within a mantle of water ice. It has a dense (1.5 bar) nitrogen–methane atmosphere that might be compositionally similar to Triton's surface ices; Triton is much colder, so all its nitrogen and methane have frozen onto the surface. Titan's orange-colored haze is believed to result from organic polymers derived from methane. The Cassini Huygens probe peered through Titan's obscuring atmosphere and revealed a young surface apparently sculpted by flowing liquids and winds. Hundreds of radar-dark areas in the northern hemisphere are interpreted to be lakes (Fig. 12.3d), and some are large enough to rightfully be called seas. Methane rain may feed rivers and ponds, and springs of liquid methane and ethane are predicted to bubble up from the crust. If the southern polar region contains lakes in comparable abundance to the north, Titan could contain hundreds of times more organic matter than the entire known oil and gas reserves on Earth. Dark materials (perhaps organic powders) have been blown across the surface to collect in dunes, and rounded rocks suggest erosion and transport.

We know very little about the physical properties of KBOs, and we can only surmise about Oort cloud objects. KBOs have probably not experienced the repeated solar heating that alters and eventually destroys active comets. The discovery of some rather large KBOs, coupled with their expected dynamical histories, suggests that smaller KBOs may be collisional fragments of larger objects. Limited spectral information suggests that KBOs contain methane ice and have surfaces that are dark and spectrally red. Reddened surfaces might result from changes in organic molecules resulting from exposure to cosmic rays. Laboratory irradiation experiments on frozen, carbon-containing mixtures produce complex hydrocarbons that become redder and darker as hydrogen is lost. The spectra of active and dead comets are less red than for KBOs, suggesting that cometary activity removes or obscures reddened surface materials.

Only one asteroid thought to have once contained ices has been imaged by spacecraft. A picture of the C-class asteroid 253 Mathilde was shown in the previous chapter (Fig. 11.1). This body has an extremely low albedo.

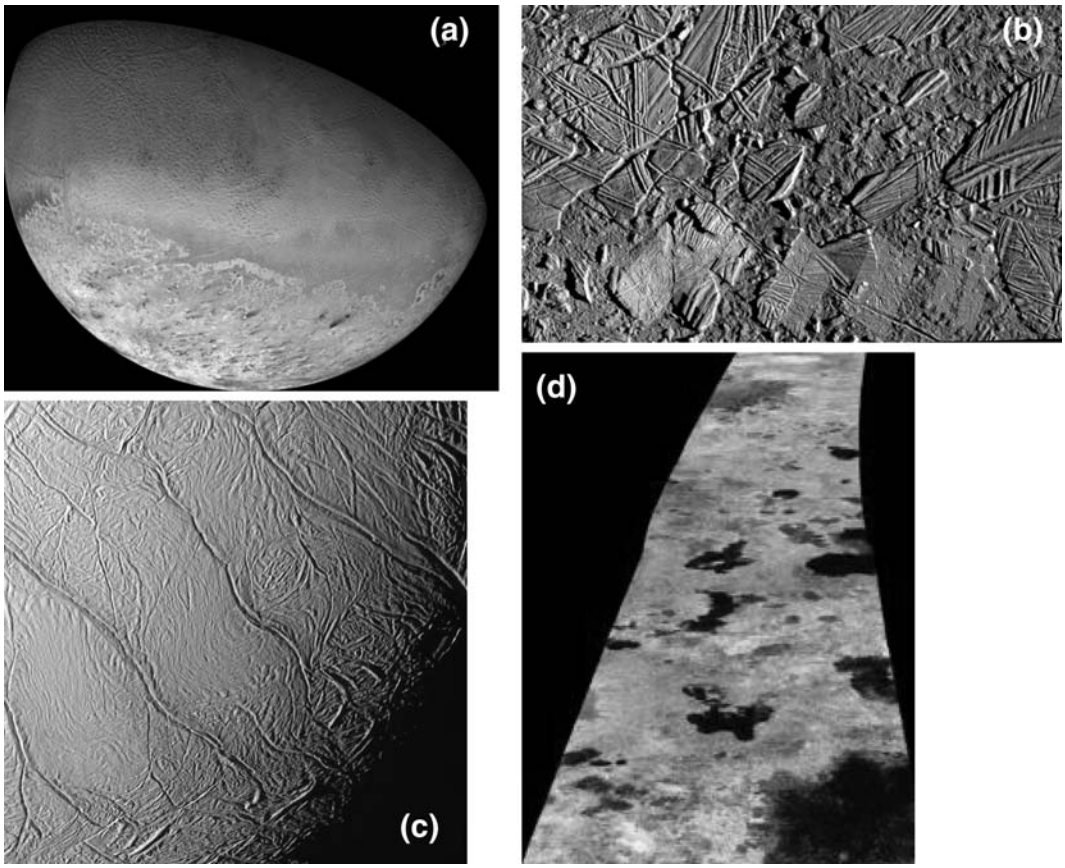

Fig. 12.3 Spacecraft images of icy moons. (a) Voyager 2 image of Triton, showing complex "cantaloupe" terrain and a polar cap of nitrogen ice; smooth areas near the equator may be frozen lakes. (b) Jumbled blocks (up to 13 km in size) of ice on the surface of Europa, revealed by Galileo imagery. Rafting of these plates suggests a substrate of water or soft ice. (c) Cassini image of Enceladus, showing fractures that are warmer than the surrounding terrain and from which volatiles are actively escaping. (d) Cassini radar image of Titan showing lakes (dark) interpreted to be liquid methane. Images courtesy of NASA.

Chemistry of comets

Comet ices

Depending on conditions, frozen substances in comet nuclei can be crystalline ices, amorphous ices, and clathrate hydrates (compounds in which cages in the water-ice lattice can host guest molecules). Compositions of the ices and associated organic materials in comets have been determined from both telescopic and spacecraft observations. Spectral line measurements of gases in a comet's coma allow the identification of molecules and radicals. An inherent difficulty in spectral measurements is that volatiles in the coma are commonly broken

apart by photolysis and photodissociation, so it is sometimes difficult to discern the parent species. Huebner (2002) has summarized spectroscopically determined volatile abundances in cometary comas. Compounds include H_2O, CO, CH_4, C_3H_6, HCN, NH_3, H_2CO, CH_3OH, and CH_4CN. Some of these compounds may have been formed by degrading more complex molecules. Spectroscopy of solid comet nuclei is more difficult owing to their faintness. Organic molecules and ices commonly have diagnostic spectral features in the near-infrared, but models of these spectra are complex and non-unique. The collision of the impactor from the Deep Impact spacecraft with comet Tempel 1 excavated material from the interior that contained higher concentrations of organic matter than the surface materials.

Several spacecraft that flew by comets carried mass spectrometers to identify gas molecules. However, identification is sometimes hampered by overlaps in the masses of certain species (for example, CO, N_2, and C_2H_4 all have 28 amu).

Water is clearly the most important volatile component in comets. Although it was surmised long ago that H_2O was the dominant volatile species, it was first detected only in 1985. H_2O that condenses below 120 K is amorphous, but on heating it crystallizes into cubic (above ~150 K) or hexagonal crystals (above ~200 K). Amorphous ice has a remarkable ability to accommodate other volatiles such as CO and noble gases; as much as 5% of its mass can be guest molecules. The transformation of amorphous to crystalline ice is exothermic, providing heat for sublimation and release of volatiles. Although models of cometary activity often assume that amorphous ice is present, there is some doubt that amorphous ice could actually have formed in the nebula. Even if amorphous ice was originally incorporated into comets, various heat sources (especially decay of short-lived radionuclides like ^{26}Al that might have been present in dust) may have caused the ice to crystallize.

Cometary activity occurring at great distance from the Sun (corresponding to temperatures <100 K) is probably controlled by ices more volatile than H_2O. For example, comet Hale-Bopp exhibited emission of highly volatile CO at great solar distances. Trapped CO was presumably released by crystallization of amorphous ice or sublimation of ice crystals at very low temperatures.

Other volatile species occur at lesser abundances. The most comprehensive analysis of cometary volatiles to date is for the long-period (Oort cloud) comet Hale-Bopp (Bockelee-Morvan and Crovisier, 2002). Hale-Bopp was the largest comet to pass through the inner solar system in the last 500 years. Its relative abundances of volatiles, expressed as production rates of molecules compared to H_2O, are given in Table 12.1. These compounds and their abundances are similar to those inferred for interstellar ices and molecular clouds. Such similarity suggests that the molecules comprising comets may have formed in extrasolar environments and were transported into the solar nebula, where they were trapped in condensing ices.

Comet dust: spectroscopy and spacecraft analysis

The mineralogical composition of coma dust has been inferred from telescopic measurements. Silicates were first detected from a 10 μm infrared emission feature resulting from the stretching of Si–O bonds. This silicate feature can only be observed in small (<2 μm) grains.

Table 12.1 Chemistry of comet Hale-Bopp, based on production rates of molecules, relative to water

Molecule	X/H_2O
H_2O	100
HDO	0.06
CO	23
CO_2	20
CH_4	0.6
C_2H_2	0.2
CH_3OH	2.4
H_2CO	1.1
HCOOH	0.09
NH_3	0.7
HCN	0.25
DCN	0.0006
HNCO	0.10
HNC	0.04
CH_3CN	0.02
HC_3N	0.02
NH_2CHO	0.015
H_2S	1.5
OCS	0.4
SO	0.3
CS	0.2
SO_2	0.2
H_2CS	0.02
NS	0.02
H_2O_2	<0.03
CH_2CO	<0.032
C_2H_5OH	<0.05
HC_5N	<0.003
Glycine I	<0.5

After Bockelee-Morvan and Crovisier (2002).

Fine structure on the silicate feature provides more specific mineralogical information. A small bump at 11.2 μm on the 10 μm feature (Fig. 12.4a), observed for several long-period comets, is generally interpreted as indicating crystalline olivine. Another shoulder at 11.9 μm and a slope change at 9.2 μm (Fig. 12.4a) are attributed to pyroxene or amorphous grains having pyroxene composition. The 11.2 μm feature is not seen in spectra of the interstellar medium and molecular clouds. A common astronomical interpretation is that amorphous ISM silicates were annealed to produce olivine crystals after they were incorporated into the solar nebula. A more likely possibility, strongly supported by new data (see below), is that olivine in comets formed within the solar nebula.

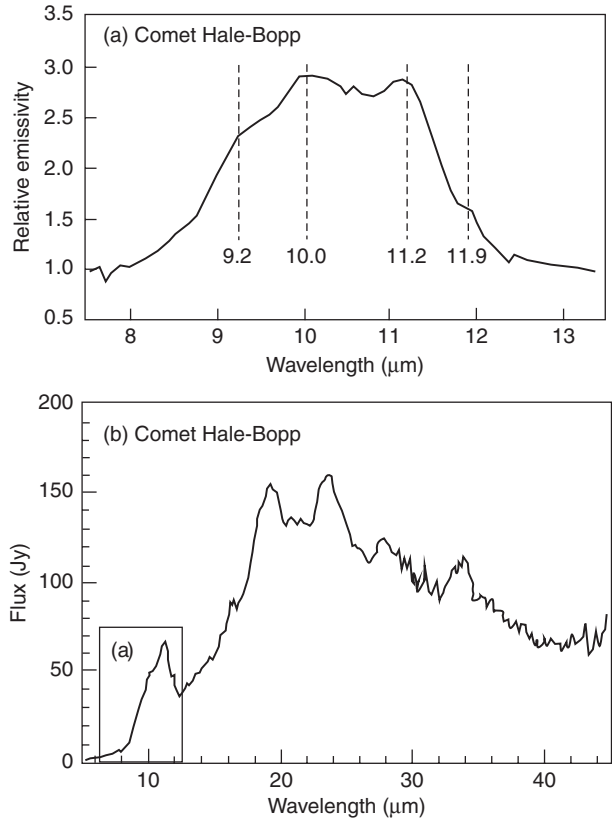

Fig. 12.4 **Spectra of comet Hale-Bopp, showing features attributable to silicate minerals. (a) Profile of fine structure in the 10 μm silicate emission feature; a peak at 11.2 μm and a shoulder at 11.9 μm are due to olivine, and a slope change at 9.2 μm results from pyroxene. (b) Expanded infrared spectrum exhibiting a number of sharp peaks due to magnesian olivine and pyroxene. The region of (a) is bounded by a small box. Modified from Crovisier *et al.* (2000) and Hanner and Bradley (2003).**

Figure 12.4b shows an expanded spectrum of comet Hale-Bopp (Crovisier *et al.*, 2000) covering the range from 16–45 μm, a region that is highly sensitive to mineralogy. Sharp peaks in this spectrum correspond to forsterite (Mg_2SiO_4), and minor features are attributed to enstatite ($Mg_2Si_2O_6$). Forsterite and enstatite are among the earliest silicate phases to form in condensation calculations, and it is difficult to see how magnesian end members could have formed by annealing of more iron-rich compositions. Condensation of these minerals is also suggested by the fact that forsterite and enstatite spectra are also measured around young stars.

Mass spectrometers were carried aboard the Vega and Giotto spacecraft that visited comet Halley and the Stardust spacecraft that encountered comet Wild2. Impacting dust particles generated ions whose masses were determined from their flight times in a drift tube. The particles were described as either "CHON" (composed mostly of carbon, hydrogen, oxygen, and nitrogen) or silicates (mainly of magnesium and iron in roughly chondritic proportions), or as mixtures of both. The continuum of compositions indicates

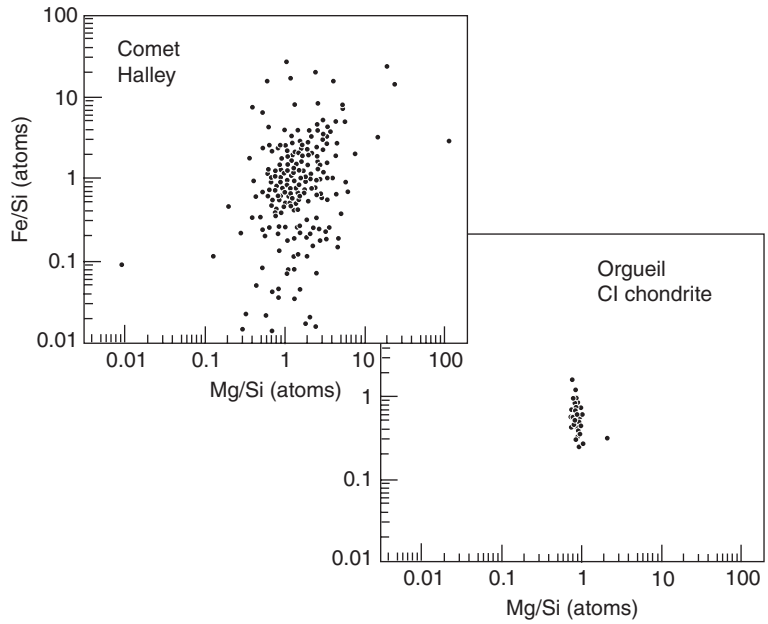

Fig. 12.5 **Fe/Si and Mg/Si ratios inferred from comet Halley dust spectra are significantly more scattered than analyses of comparably sized spots in the Orgueil CI chondrite. This scattering suggests lack of well-defined minerals in cometary dust. After Lawler *et al.* (1989).**

that carbonaceous and silicate material are mixed at the submicron scale, and that the bulk solid composition is close to chondritic except for higher abundances of carbon and nitrogen.

Mineralogical interpretations of Halley dust analyses remain controversial. Lawler *et al.* (1989) saw no clustering of compositions that might suggest crystalline minerals (Fig. 12.5), whereas Fomenkova *et al.* (1992) identified compositions that were consistent with a number of minerals, including pyroxene, phyllosilicate, carbonate, FeNi metal, iron sulfide, and iron oxide. The characterization of minerals in returned comet dust (see below) supports the identification of some of these primary minerals but calls into question the identification of those formed by alteration.

Interplanetary dust particles

Tiny particles less than ~100 μm in diameter entering the Earth's atmosphere are decelerated at high altitudes, and because of their large surface areas relative to their masses, aerodynamic ram pressures are insufficient to heat them to their melting points. These interplanetary dust particles, or IDPs (Fig. 12.6), consists of both cometary and asteroidal dust. IDPs have been collected in the stratosphere (at altitudes of ~20 km), adhering to collection pads on the wings of U2 aircraft. They occur in sizes ranging from 1 to >50 μm, although most are 5–15 μm. The larger IDPs, which commonly fragment on collection, often consist of many

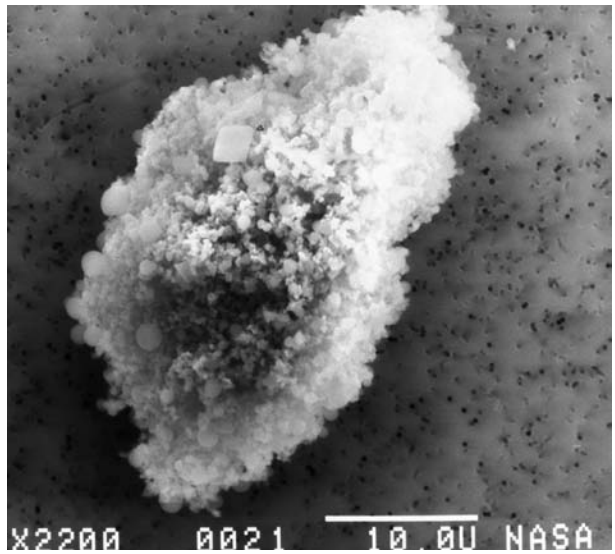

Fig. 12.6 Electron microscope image of a chondritic porous IDP. Image courtesy of D. Brownlee.

grains and are referred to as "cluster" particles. Some IDPs are almost certainly comet dust, especially particles less than 20 μm in size. The dusty trails shed by short-period comets are one potential source of IDPs, and dust from KBOs is also expected to spiral inwards towards the Earth. However, dust from long-period comets is an unlikely source because it is ejected on solar escape orbits, and objects within the Oort cloud are too distant to provide dust directly to the inner solar system. Asteroidal dust dominates the larger size fractions. Dust particles from ~100 μm to ~2 mm in diameter melt during atmospheric entry. The asteroidal particles are known as micrometeorites.

There are two distinct morphological classes of IDPs – smooth and porous. Because both classes have approximately chondritic bulk compositions, they are referred to as chondritic smooth (CS) and chondritic porous (CP). CS IDPs have compact textures and are thought to be particles from asteroids. CP IDPs are fluffy (porosities commonly exceed 30%, and values as high as 70% have been measured) and some texturally resemble bunches of grapes. Their densities vary considerably but can be as low as $0.3\,g\,cm^{-2}$. It is not obvious how grains having such high porosities could have survived compaction within kilometer-sized parent bodies unless ices were present, filling the volume between grains. Comet particles in space should have highly elliptical orbits and thus encounter the Earth at higher speeds than asteroid particles. Attempts to constrain atmospheric entry velocities for some CP IDPs, as inferred from their heating histories, give values consistent with their derivation from comets.

Advances in techniques for handling and analyzing very small particles have allowed detailed examination and characterization of IDPs. Especially useful instruments include the transmission electron microscope (TEM), synchrotron facilities, and the ion microprobe.

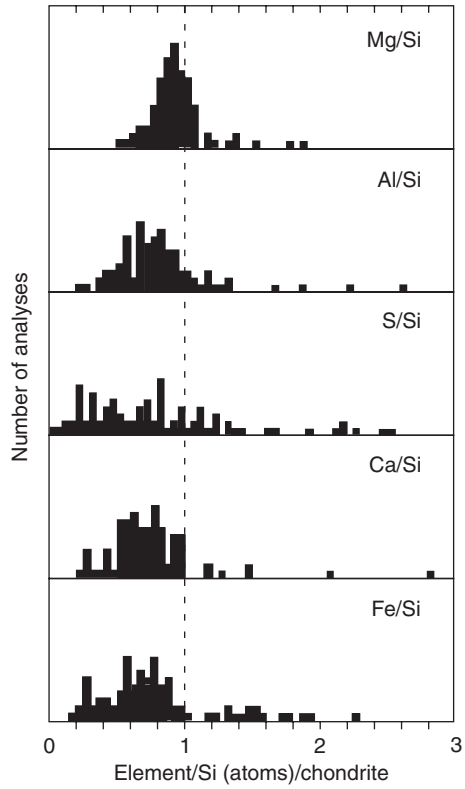

Fig. 12.7 **Chondrite-normalized element/silicon ratios measured in chondritic porous IDPs. CI chondrite ratios are shown by the vertical dashed line. Modified from Schramm *et al.* (1989).**

As implied by their names, chondritic IDPs have roughly cosmic bulk compositions. Element ratios for hundreds of analyzed particles are roughly chondritic (data for CP IDPs are shown in Fig. 12.7) (Schramm *et al.*, 1989). An exception, though, is carbon, which is significantly more abundant in IDPs. The mean carbon content of IDPs is ~10 wt.%, relative to 3.2 wt.% for CI chondrites (Bradley, 2004). The abundances of trace elements in bulk IDPs scatter from ~0.3 to ~3 times CI, and volatile elements especially tend to be enriched (Flynn and Sutton, 1992). Higher abundances of carbon and of volatile elements, relative to the most solar-like carbonaceous chondrites, support the contention that IDPs are among the most primitive materials known.

The CP and CS IDPs are mineralogically distinct (Rietmeijer, 1998; Jessberger *et al.*, 2001; Bradley, 2004). CS IDPs (Fig. 12.8a) are characterized by phyllosilicates (saponite) and carbonates. Their mineralogical similarity to CI and CM chondrites suggests derivation from asteroids that experienced aqueous alteration. In contrast, the CP IDPs (Fig. 12.8b) are anhydrous, consisting mostly of olivine, pyroxene, iron sulfides, FeNi metal, and glass. These phases, which occur as very small (generally submicron-size) grains, are mixed in various proportions to form heterogeneous aggregates. Olivine and pyroxene are usually magnesium-rich (forsterite and enstatite), although some grains are

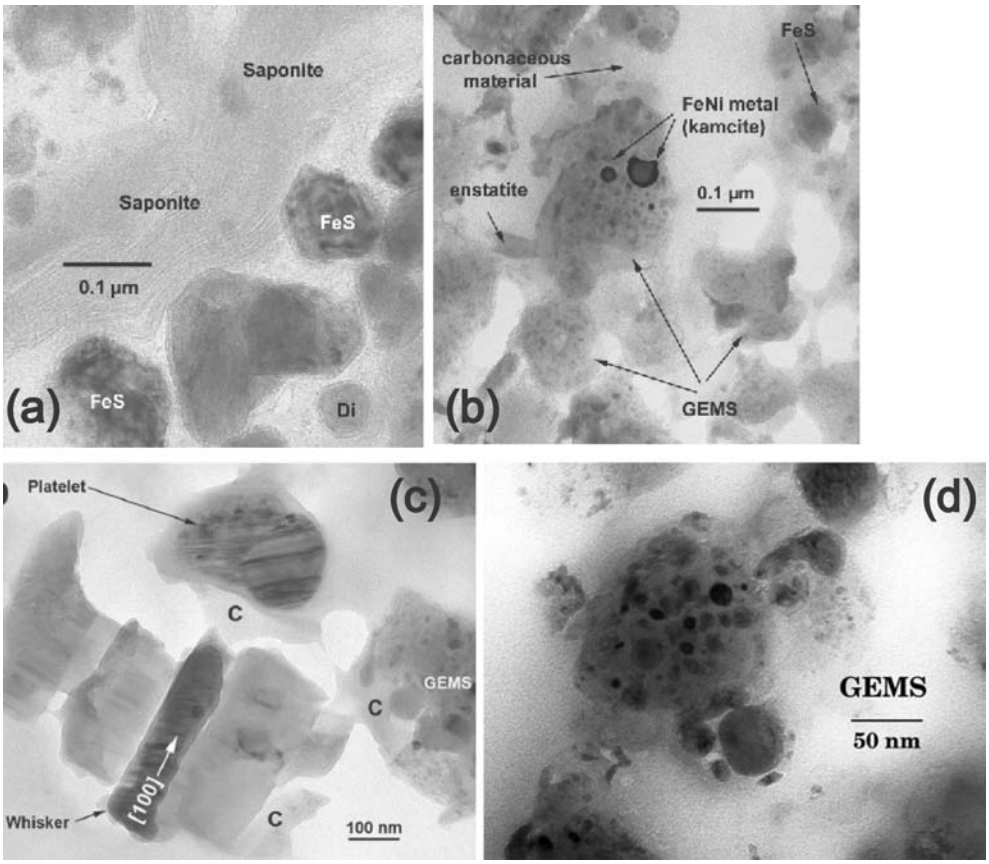

Fig. 12.8 TEM images of IDPs. (a) CS IDP, showing phyllosilicate (saponite), FeS, and diopside (Di). (b) CP IDP, containing pyroxene (enstatite), metal, FeS, GEMS, and organic matter. (c) Whisker and platelet morphologies of enstatite. (d) GEMS, composed of rounded metal and sulfide particles embedded in glass. Images courtesy of J. P. Bradley.

more iron-rich. Enstatite crystals have unusual platelet or whisker morphologies (Fig. 12.8c), consistent with growth from a vapor phase. Sulfides are mostly pyrrhotite, but other iron, nickel, and zinc sulfide minerals also occur. Some pyrrhotite has an unusual cubic crystal structure, unlike the more common hexagonal form. The cubic form, which has not been previously reported in nature, is metastable and transforms to hexagonal pyrrhotite when heated. A similar mineral has been produced in the laboratory by vapor phase growth, suggesting that the IDP sulfides may have formed by condensation from a gas.

The most exotic materials in CP IDPs are particles of glass with embedded metal and sulfides, identified by the acronym "GEMS" (Fig. 12.8d). Although GEMS are commonly described as having chondritic bulk compositions, that description applies only for aggregates of these submicron particles. The nanometer-sized FeNi metal (kamacite) inclusions and pyrrhotite are clearly out of equilibrium with the magnesium-rich silicate

glass. The eroded textures of mineral inclusions in GEMS suggest that they were exposed to ionizing radiation, as would be expected for interstellar dust. Some (but not all) GEMS have exotic oxygen isotopic compositions. In terms of their physical properties and compositions, GEMS are similar to interstellar silicates inferred from astronomical observations, and they were briefly mentioned when we discussed interstellar grains in Chapter 5.

Carbonaceous material (Fig. 12.8b) is intimately mixed with silicates and is very abundant (carbon abundance averages 13% and varies up to ~50%) in CP IDPs. Some carbon is elemental (graphite), but C–H stretching resonances in infrared spectra show that aliphatic hydrocarbons are also present. Polycyclic aromatic hydrocarbons (PAHs) also occur. Nanodiamonds have been identified in cluster IDPs, but not in smaller CP IDPs. Enormous D/H and $^{15}N/^{14}N$ anomalies have been measured in bulk IDPs, and the hydrogen isotopic anomalies are correlated with organic-rich domains. Ratios of D/H as high as 25 times the solar ratio suggest the presence of molecular cloud materials.

Returned comet samples

Particles collected from comet Wild2 (Fig. 12.9) were returned to Earth by the Stardust spacecraft (see Box 12.2). Most of the particles in the aerogel collectors were disaggregated during capture. Examination of these grains suggests that they were originally fine-grained, loosely bound aggregates, often containing some larger crystals (Zolensky *et al*., 2006). Care must be exercised in interpreting analyses of these grains, because impact heating during their collection has modified them in ways that cannot always be ascertained (Brownlee *et al*., 2006). Laboratory simulations have been critical in unraveling the effects of capture in aerogel.

Most of the larger particles consist of olivine, pyroxene, or FeNi sulfide (Zolensky *et al*., 2006; Ishii *et al*., 2008). Olivine grains exhibit a surprisingly large compositional range, from Fo_{100} to Fo_4, although most grains are magnesium-rich. Likewise, pyroxenes range from En_{100} to En_{52}, with most being magnesian, and they do not replicate the whisker morphologies seen in CP IDPs. Sulfides are either troilite or pyrrhotite (it is not possible to determine the exact stoichiometry of these tiny crystals) and pentlandite. Grains of FeNi metal also occur. This mineral assemblage resembles that of unaltered carbonaceous chondrites. Among the comet grains are also particles that superficially resemble GEMS, consisting of metal and sulfide embedded in glass. However, the glass is melted aerogel (the dust collection medium, described below). One grain curiously contained a phase having the composition of K-feldspar. Another particle, called “Inti” and consisting of anorthite, pyroxene, melilite, spinel, corundum, osbornite, and perovskite, has the same mineralogy as CAIs from meteorites. A few similar refractory IDPs have been described previously, but these were inferred to be asteroid rather than comet particles.

The oxygen isotopic compositions of comet silicate grains (Fig. 12.10) resemble those of chondrites, suggesting that they formed within the solar nebula (McKeegan *et al*., 2006). Only one grain was found with anomalous oxygen isotopes, demonstrating its extrasolar

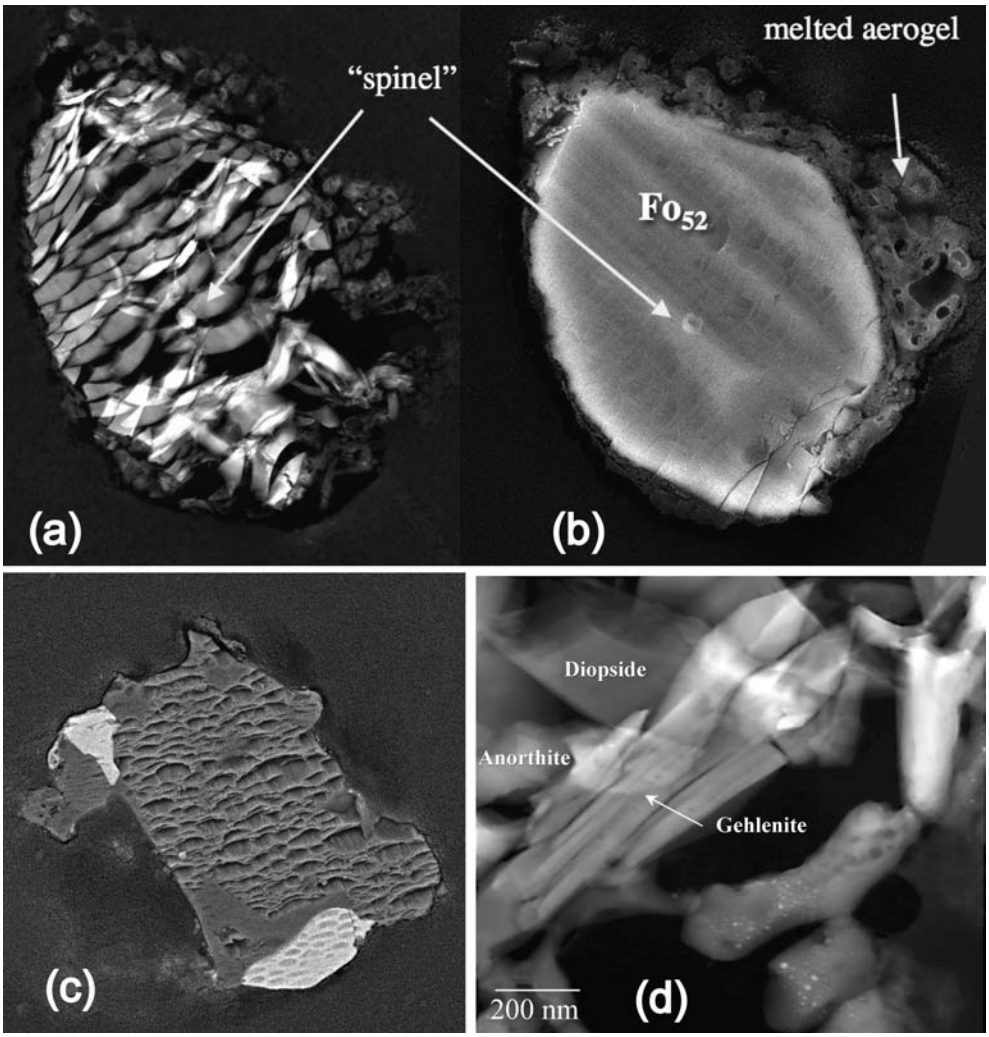

Fig. 12.9 Examples of comet particles collected and returned to Earth by the Stardust spacecraft. (a, b) Two ways to image a particle made of iron-rich olivine, with minor spinel; the left view is a thin section viewed through plane-polarized light, and the right view is an SEM image of the same grain, FOV = 4 μm. Fracturing in (a) is an artifact of the sectioning process. (c) Particle composed of pyroxene and sulfides, FOV = ~1 μm. (d) Particle composed of minerals that form CAIs. Images courtesy of D. Brownlee.

origin. Oxygen isotopes in the refractory inclusion particle Inti described above are like those of CAIs.

The bulk chemical composition of the dust, obtained by averaging the compositions of particles in numerous tracks (Fig. 12.11a) and impact crater residues (Fig. 12.11b), is chondritic for iron, silicon, titanium, chromium, manganese, nickel, germanium, and selenium, within the 2σ confidence level (Flynn *et al*., 2006). Copper, zinc, and gallium are

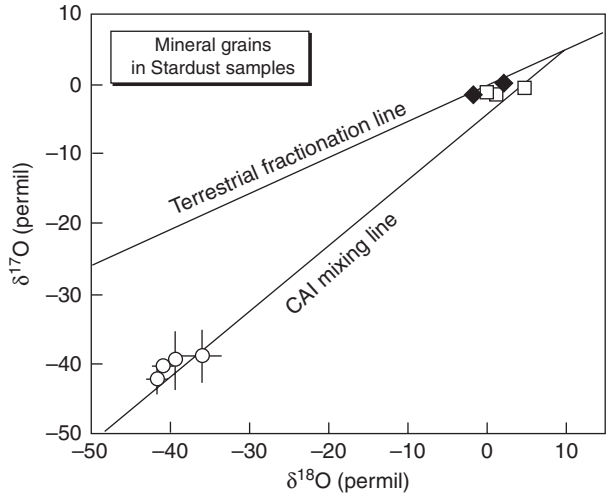

Fig. 12.10 **Oxygen isotopic compositions (relative to standard mean ocean water, SMOW) of several mineral grains in three Stardust particles, each grain denoted by a separate symbol. Open circles are from a CAI comet particle. After McKeegan *et al.* (2006).**

enriched in these particles, relative to CI chondrite values. These same chemical characteristics have been previously reported for CP IDPs.

The high abundance of crystalline minerals in comet dust was unexpected. Comets were expected to be dominated by interstellar grains, most of which are amorphous. Some comet crystals appear to be fragments of chondrules or refractory inclusions that presumably formed in the inner solar system and were transported outward. At least in the Kuiper belt where Wild2 formed, a large fraction of the material, probably a majority (Westphal *et al.*, 2009), had been cycled through the inner solar system before incorporation into the comet. Some Wild2 cometary grains appear to be loaded with noble gases that were probably implanted by energetic processes near the early Sun (Marty *et al.*, 2008). Radial transport of material over large distances in the early solar system seems to have been remarkably efficient. Several models contend with each other to explain this large-scale mixing, but one, the so-called X-wind model (Shu *et al.*, 1996), predicted the presence of inner solar-system material in the comet-forming regions years before the return of the Stardust samples.

The organic matter in these comet grains has also been characterized (Sandford *et al.*, 2006). In some grains PAHs consisting of one (benzene) and two (naphthalene) rings, without accompanying PAHs with greater numbers of rings, occur, which distinguishes them from the organic matter in chondrites. It is possible that these PAHs were synthesized by heating during collection. Other grains contain PAHs consisting of two-, three-, and four-ring compounds, many of which contain alkane functional groups. These resemble organic compounds in chondrites and may be indigenous to the comet. Other organic molecules include non-aromatic compounds with aliphatic, carboxylic,

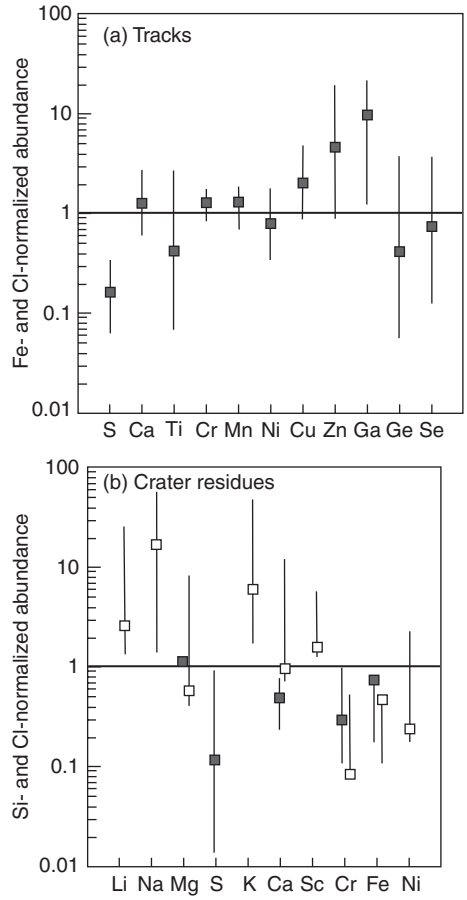

Fig. 12.11 Mean compositions of tracks and crater residues produced by Stardust particles, compared to CI chondrite ratios (horizontal lines). (a) Fe- and CI chondrite-normalized composition determined by averaging 23 track analyses by SXRM (filled squares). (b) Si- and CI- chondrite-normalized composition of seven crater residue analyses by SEM-EDX (filled squares), and TOF-SIMS analyses for five craters (open squares). Modified from Flynn *et al.* (2006).

and nitrogen-containing functional groups. Measurements of the atomic O/C and N/C ratios in functional groups are similar to those found in the organic matter of IDPs. Some amines were also detected, including one amino acid. All these organic compounds constitute a highly unequilibrated mixture, and they are much more labile than the insoluble organic matter in chondrites.

Hydrogen in these particles is correlated with carbon and is presumed to occur in organic matter. Analyses of the isotopic composition of hydrogen (McKeegan *et al.*, 2006) show D/H enrichments (Fig. 12.12). The D/H ratios overlap those of H_2O in comets but are well below those determined for organic matter in CP IDPs. Measurements of nitrogen isotopes show ^{15}N enhancements, suggesting an interstellar contribution.

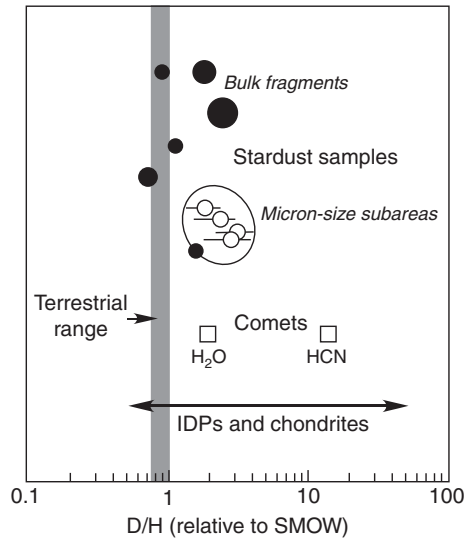

Fig. 12.12 **Measured D/H ratios in five bulk Stardust particles (black dots; sizes represent relative particle sizes), and in micron-size subareas in one particle (open circles enclosed by oval) measured by ion microprobe. The particle compositions overlap D/H ratios in comets, IDPs, and the insoluble organic matter in chondrites. Modified from McKeegan *et al.* (2006).**

Box 12.2 **The Stardust Mission: how to collect comet dust**

In 2004, the NASA Stardust spacecraft passed through the dust cloud surrounding the nucleus of comet Wild2 and captured more than 10 000 particles ranging from 1 to 300 μm in size (Brownlee *et al.*, 2006). These particles were returned to Earth for study in terrestrial laboratories in 2006. Initial results are described in the December 15, 2006, issue of *Science*.

At the time of encounter, Wild2 was at 1.86 AU, and thus was very active. Comets release thousands of tons of dust during cometary activity – the dust is there for the taking, the trick is to snatch it without destroying it or the spacecraft. Two technological achievements by scientists at the Jet Propulsion Laboratory made the collection of comet dust possible: the clever design of a trajectory that allowed the spacecraft to encounter the comet coma at a relatively modest speed (6.1 km s^{-1}), and the development of a capture medium that slowed and trapped the particles without destroying them.

The capture medium was aerogel (Tsou *et al.*, 2004), a highly porous silica foam with a density comparable to air. In order to slow the particles gradually, the aerogel collectors (Fig. 12.13a) were crafted to have densities varying from <0.01 g cm^{-3} at the surface to 0.05 g cm^{-3} at 3 cm depth. Impacts into the aerogel produced tapered cavities (tracks), some shaped like carrots and others like turnips with single or multiple roots (Fig. 12.13b). The thinner tracks were formed by particles that suffered little fragmentation on capture, and the bulbous tracks were formed from disaggregated particles. Although it is tempting to attribute the bulbous ends of tracks to impact vaporization of cometary ice, most particles

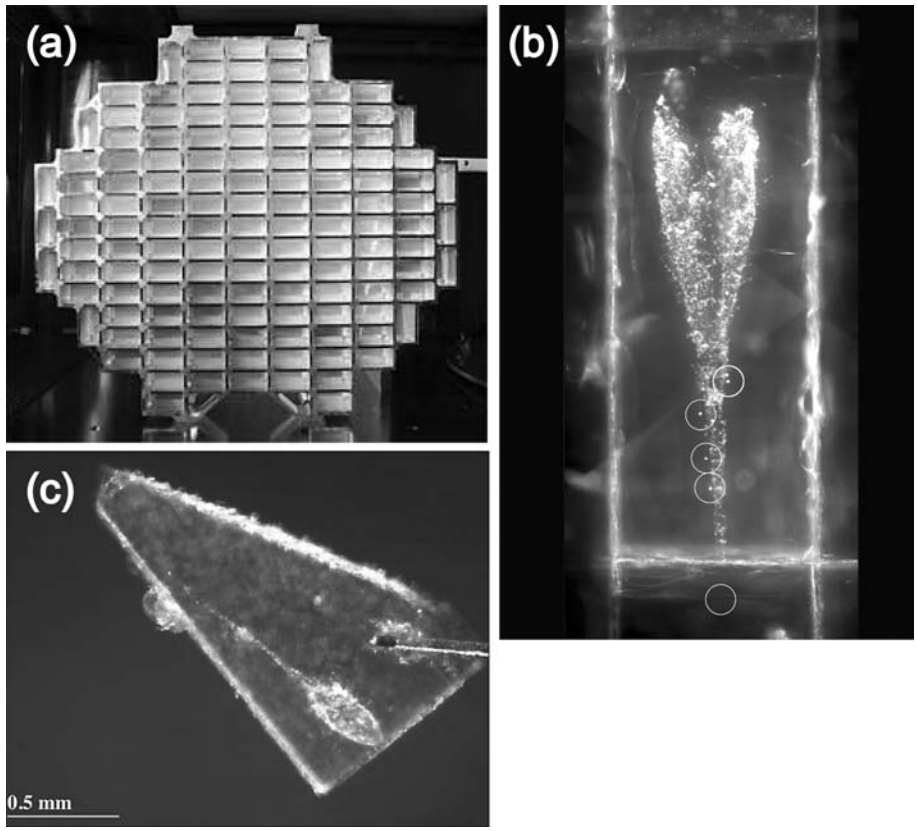

Fig. 12.13 **Images of aerogel used on the Stardust spacecraft. (a) A bank of aerogel collectors for cometary dust. (b) Tadpole-shaped track made by comet dust particles captured in aerogel. Impacting particles undergo devolatilization, producing the bulbous entryway. Large (2–15 μm) dust grains (circled) can be seen toward the end of a thin trail, and other finer material occurs along the track. (c) A keystone, containing a particle track, cut out of aerogel. Figures courtesy of D. Brownlee.**

are thought to have lost any icy component they may have had during their hours-long exposure to sunlight in space prior to collection. Terminal particles located at the ends of tracks represent intact cometary dust, whereas particles distributed along the tracks have usually been devolatilized, melted, or mixed with melted aerogel. All the particles were affected to some degree by capture, with the least effects in particles larger than a micron in size. The aluminum frame used to hold the aerogel was also impacted by dust particles, which produced tiny hypervelocity impact craters lined with melted projectile residue.

For particle handling, wedges of aerogel (Fig. 12.13c) containing entire tracks, called "keystones," were cut from the collection plates (Westphal *et al.*, 2004). From the keystones, individual particles and materials lining the tracks can be isolated and studied. The great advantage offered by these Stardust particles is the ability to bring to bear the analytical technology of Earth-based laboratories. Research on these cometary dust particles draws on the prior investments made in developing the cosmochemical techniques used for other microscopic samples, specifically IDPs and presolar grains.

Ice-bearing asteroids and altered meteorites

Some asteroids, thought to contain modest amounts of ices, might show cometary activity if they were to be perturbed into orbits that took them close to the Sun. Other asteroids originally accreted with ice components, which later melted. Such asteroids were then altered when fluids reacted with rock. Altered carbonaceous chondrites were discussed briefly in Chapter 6. Here we explore asteroid alteration in more detail.

Spectroscopy of asteroids formed beyond the snowline

Minerals containing bound water (OH) or water molecules (H_2O) adsorbed onto mineral surfaces give rise to prominent spectral absorptions near 3 μm that are observed in some asteroid classes (Rivkin *et al*., 2002). These absorptions have different shapes (Fig. 12.14) – the hydroxl feature is sharp and the H_2O feature is more subdued. Infrared spectra for asteroids with high albedos are generally characterized by the water feature, whereas spectra of low-albedo asteroids tend to have the sharp OH feature. Although the hydroxl band is partly obscured when viewed through the Earth's atmosphere (the dashed lines in Fig. 12.14), it is still an easily recognizable feature in the spectra of some asteroid classes.

The low-albedo C-, B-, G-, and F-class asteroids dominate the middle part of the main belt. The sharp ~3 μm feature in the spectra of these objects indicates that hydrous

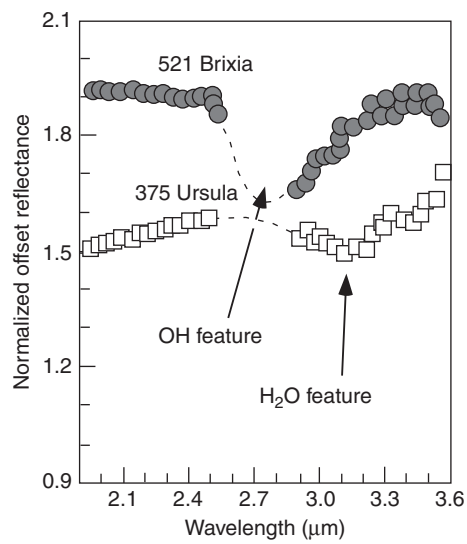

Fig. 12.14 Different shapes of the ~3 μm absorption feature in asteroid spectra. Low-albedo asteroid spectra show a sharp feature attributed to hydroxl-bearing minerals, whereas high-albedo asteroid spectra have a more subdued feature arising from adsorbed water molecules. Dashed lines in the middle of the spectra are regions obscured by the Earth's atmosphere.

phyllosilicates are present on their surfaces (Pieters and McFadden, 1994; Vilas *et al*., 1994). Another spectral characteristic that suggests alteration in these asteroids is an absorption feature near 0.7 μm, attributed to $Fe^{2+} \rightarrow Fe^{3+}$ charge transfer in phyllosilicates (Rivkin *et al*., 2002). Although a few other minerals can show a similar absorption feature, the presence of the 0.7 μm band usually correlates with the ~3 μm hydroxl feature in these asteroids (Vilas *et al*., 1994). These asteroid classes are thought to be the parent bodies for the hydrated carbonaceous chondrites (CI, CM). The C-, B-, G-, and F-class asteroids have actually been proposed to comprise an alteration sequence, varying from bodies showing considerable hydration to bodies that were dehydrated by later heating. Laboratory spectra of altered CM chondrites also show a prominent 3 μm feature, which is progressively obliterated by experimental heating.

The D- and P-class asteroids dominate the outer main belt and Trojan asteroids located in Jupiter's orbit. With only a few exceptions, the spectra of these asteroids show no 3 μm absorption bands (Jones *et al*., 1990). The D and P asteroids are thought to contain ice that has never been melted. However, it is also possible that D and P asteroids could contain hydrated silicates, and that the 3 μm feature is masked by an increasing abundance of elemental carbon with heliocentric distance. The unique carbonaceous chondrite Tagish Lake has a reflectance spectrum quite similar to D-class asteroids, and it has been hypothesized to be a sample of this class. However, Tagish Lake shows a significant 3 μm absorption.

Aqueous alteration of chondrites

The aqueous fluids formed by melting of ices in asteroids reacted with minerals to produce a host of secondary phases. Laboratory studies provide information on the identities of these phases. They include hydrated minerals such as serpentines and clays, as well as a variety of carbonates, sulfates, oxides, sulfides, halides, and oxyhydroxides, some of which are pictured in Figure 12.15. The alteration minerals in carbonaceous chondrites have been discussed extensively in the literature (Zolensky and McSween, 1988; Buseck and Hua, 1993; Brearley, 2004) and were most recently reviewed by Brearley (2006). In the case of CI chondrites, the alteration is pervasive and almost no unaltered minerals remain. CM chondrites contain mixtures of heavily altered and partially altered materials. In CR2 and $CV3_{oxB}$ chondrites, matrix minerals have been moderately altered and chondrules show some effects of aqueous alteration. For other chondrite groups such as CO and LL3.0–3.1, the alteration is subtle and secondary minerals are uncommon. In some CV chondrites, a later thermal metamorphic overprint has dehydrated serpentine to form olivine.

Heavily altered CI and CM chondrites exhibit a range of alteration assemblages. CI chondrites are composed mostly of phyllosilicates (serpentine interlayered with saponite). Magnetite with unusual morphologies (framboids and platelets) is common, along with carbonates and sulfides. Veins of sulfate in Orgueil have been cited as evidence for fluids percolating through the parent asteroid, but examination of old photographs suggests that the sulfates formed by interaction with water in the atmosphere after the

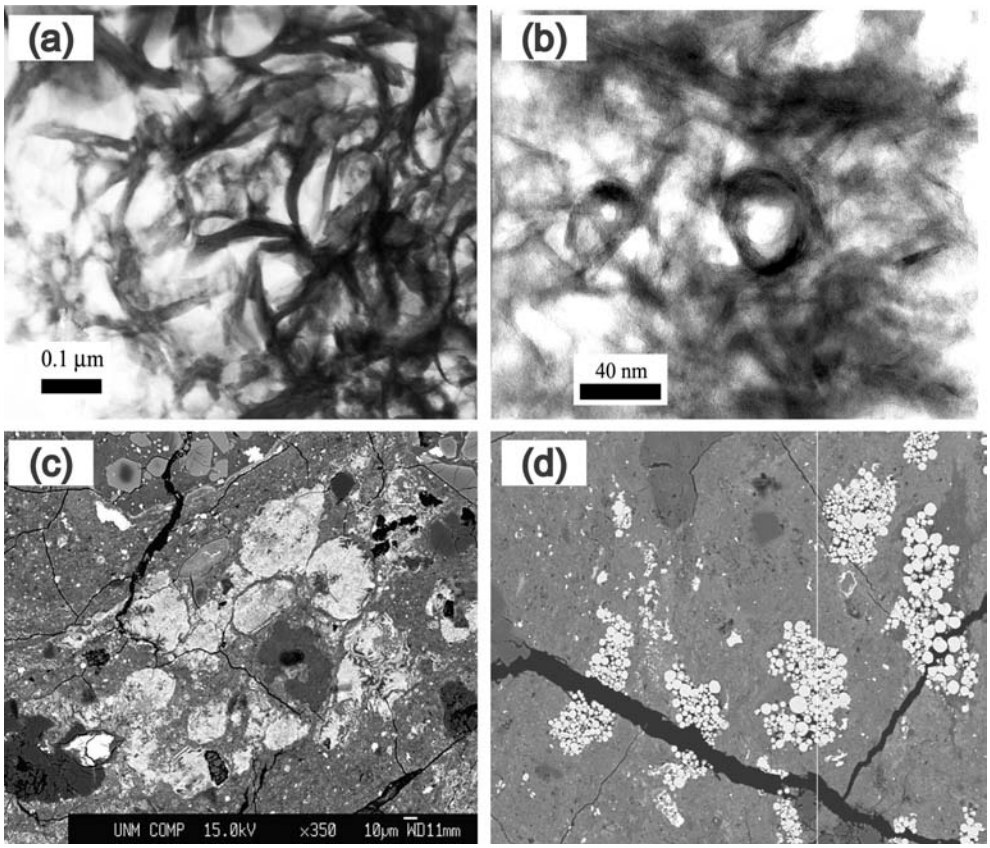

Fig. 12.15 Alteration minerals in carbonaceous chondrites. (a) TEM image of twisted phyllosilicate plates in the Ivuna CI chondrite. (b) TEM image of hollow serpentine tubes in the Murchison CM chondrite. (c) Backscattered electron image of intergrowths of tochilinite and cronstedite (light-colored clots) in the Y-791198 CM chondrite. (d) Clusters of spherical magnetite grains, called framboids, in the EET 93042 CR chondrite. Figures courtesy of A. Brearley.

meteorite fell to Earth. CI chondrites are classified as type 1 (recall from Chapter 6 that type 3 chondrites are least altered, type 2 are partly altered, and type 1 are pervasively altered).

The alteration mineralogy of CM2 chondrites consists of serpentine and amorphous materials, with sulfides and carbonates but not much magnetite or sulfate. An unusual but diagnostic mineral is tochilinite, a hydrated iron-magnesium sulfide that forms by alteration of FeNi metal (Fig. 12.15c). The degree of alteration among CM chondrites is quite variable, and several alteration indices based on their mineral assemblages and compositions have been proposed (Browning *et al.*, 1996; Rubin *et al.*, 2007). Bulk hydrogen contents increase and argon contents decrease with increasing alteration (Fig. 12.16), reflecting the incorporation of H_2O and destruction of the noble gas carrier as alteration advances. A few CM chondrites are pervasively altered and have been classified as CM1 chondrites.

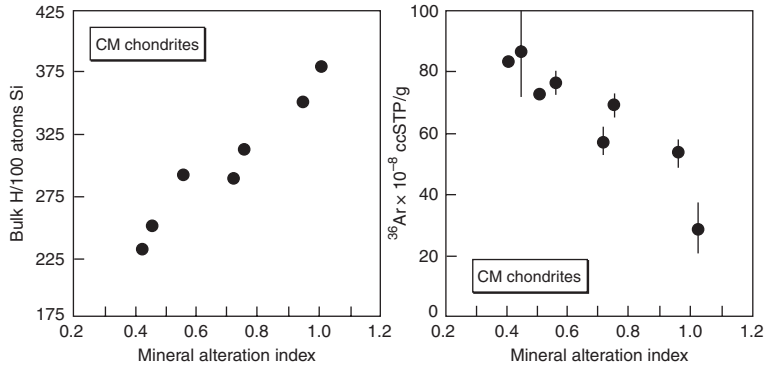

Fig. 12.16 **Bulk hydrogen and ^{36}Ar contents versus mineral alteration index for CM carbonaceous chondrites. These trends reflect progressive incorporation of water and destruction of the noble gas carrier as alteration advances. After Browning *et al.* (1996).**

These differences suggest that the compositions and amounts of fluids and the temperatures of reactions were quite variable. Temperatures and water/rock ratios have been constrained from oxygen isotope exchange between various minerals. Mass-dependent isotopic fractionation between coexisting calcite and phyllosilicates indicates that aqueous alteration of Murchison took place at ~0 °C, while alteration in CI chondrites apparently occurred at temperatures between 50 and 150 °C (Clayton and Mayeda, 1984, 1999). The CM chondrites show isotopic disequilibrium between the fluid phase and minerals that formed from the fluid and other minerals in the matrix. Residual mass-independent isotopic differences among phases permit estimates of the amount of water with which the rock reacted. Modeling of isotopic exchange during aqueous alteration between rock and fluid leads to estimated water/rock ratios for alteration of CM chondrites of 0.36–0.6, and similar modeling for CI chondrites gives water/rock ratios of ~2.5 (Clayton and Mayeda, 1999).

The CV, CO, and CR chondrites are mostly anhydrous and were considered in Chapter 11. However, the $CV3_{oxB}$ chondrites experienced significant aqueous alteration. The matrices of these meteorites are heavily altered and contain phyllosilicates, fayalite, Fe,Ni sulfides and carbides, Ca,Fe pyroxene, and andradite garnet. The CV_{oxA} chondrites were apparently also aqueously altered, but were subsequently dehydrated by thermal metamorphism. The matrices of CR2 chondrites contain alteration minerals that resemble those in CI chondrites, including phyllosilicates, magnetite (Fig. 12.15d), carbonates and sulfides, although the alteration is not as extensive. Chondrule mesostasis was affected in some CR chondrites. Minor phyllosilicates occur in the matrix of CO3 chondrites, but these meteorites contain no carbonates or sulfates.

The least metamorphosed ordinary chondrites (petrologic types 3.0–3.1) show evidence of minor aqueous alteration that primarily affected the matrix, but in some cases also affected chondrule mesostasis. In these meteorites, the amount of aqueous fluid was very small, limiting the degree of alteration.

Thermal evolution of ice-bearing bodies

Thermal evolution models for hydrated carbonaceous chondrite asteroids (Grimm and McSween, 1989; Young *et al*., 1999) are similar to those for anhydrous chondritic asteroids as discussed in Chapter 11, although there are a few important differences. Oxygen isotopic constraints suggest that alteration temperatures were within ~100 ºC of the melting temperature of water ice. The large heat of fusion of ice and the high heat capacity of water buffered temperature excursions when short-lived radionuclides decayed. Circulating water could also have enhanced heat loss, so that aqueously altered chondrites experienced alteration at low temperatures instead of thermal metamorphism. However, hydration reactions are exothermic and thus could have liberated large amounts of heat if reaction rates were rapid relative to ice melting. High vapor pressures associated with ice melting may also have caused fracturing and venting of gases.

The textures of a few unbrecciated CM chondrites suggest that they are accretionary rocks. Metzler *et al*. (1992) argued that altered rims around chondrules in these meteorites formed by hydration reactions in the nebula, rather than within hydrous asteroids. This proposal has led to controversy about the environment for aqueous alteration. Reactions of anhydrous minerals either with water vapor in the solar nebula or during passage of shock waves through regions with elevated ice/dust ratios might have produced aqueous-alteration minerals. More traditional models envision alteration occurring within parent bodies after accretion and melting of ice. Experimental and theoretical constraints on mineral stability and slow reaction rates in the nebula appear to support parent body alteration. Brearley (2006) has summarized the observations used in support of each model.

Chemistry of hydrated carbonaceous chondrites

The average chemical compositions of CI and CM chondrites are given in Table 12.2. We will illustrate some compositional differences among different groups using diagrams analogous to those used to describe the anhydrous chondrites in Chapter 11.

Figure 12.17a shows lithophile element abundances, and Figure 12.17b shows siderophile and chalcophile element abundances in CM chondrites, normalized to CI chondrites. Illustrated for comparison are the abundances in CO chondrites, which are the anhydrous carbonaceous chondrite group most closely allied to CM chondrites. As in other chondrites, the greatest differences are in volatile elements. The volatile and moderately volatile elements in CM chondrites are present at 50–60% of the abundances of the refractory elements. The volatile elements are primarily located in the matrix, and the matrix comprises 50–60% of CM chondrites. This implies that the matrix has essentially CI abundances of all elements, while the chondrules and refractory inclusions have CI relative abundances of refractory elements but are highly depleted in the volatile elements. The sloping transition in the region of moderately volatile elements indicates

Table 12.2 Average chemical compositions of hydrated carbonaceous chondrite groups

Element	CI	CM
H (mg g^{-1})	20.2	14
Li (μg g^{-1})	1.5	1.5
Be (μg g^{-1})	0.025	0.04
B (μg g^{-1})	0.87	0.48
C (mg g^{-1})	34.5	22
N (μg g^{-1})	3180	1520
O (mg g^{-1})	464	432
F (μg g^{-1})	60	38
Na (mg g^{-1})	5.0	3.9
Mg (mg g^{-1})	97	115
Al (mg g^{-1})	8.65	11.3
Si (mg g^{-1})	106.4	127
P (μg g^{-1})	950	1030
S (mg g^{-1})	54.1	27
Cl (μg g^{-1})	700	430
K (μg g^{-1})	550	370
Ca (mg g^{-1})	9.26	12.9
Sc (μg g^{-1})	5.9	8.2
Ti (μg g^{-1})	440	550
V (μg g^{-1})	55	75
Cr (μg g^{-1})	2650	3050
Mn (μg g^{-1})	1940	1650
Fe (mg g^{-1})	182	213
Co (μg g^{-1})	505	560
Ni (mg g^{-1})	11.0	12.3
Cu (μg g^{-1})	125	130
Zn (μg g^{-1})	315	180
Ga (μg g^{-1})	9.8	7.6
Ge (μg g^{-1})	33	26
As (μg g^{-1})	1.85	1.8
Se (μg g^{-1})	21	12
Br (μg g^{-1})	3.5	3.0
Rb (μg g^{-1})	2.3	1.6
Sr (μg g^{-1})	7.3	10
Y (μg g^{-1})	1.56	2.0
Zr (μg g^{-1})	3.9	7.0
Nb (μg g^{-1})	0.25	0.4
Mo (μg g^{-1})	0.92	1.4
Ru (μg g^{-1})	0.71	0.87
Rh (μg g^{-1})	0.14	0.16
Pd (μg g^{-1})	0.56	0.63
Ag (ng g^{-1})	200	160
Cd (ng g^{-1})	690	420

Table 12.2 (cont.)

Element	CI	CM
In (ng g^{-1})	80	50
Sn (μg g^{-1})	1.70	0.79
Sb (ng g^{-1})	135	130
Te (μg g^{-1})	2.3	1.3
I (μg g^{-1})	0.43	0.27
Cs (μg g^{-1})	0.19	0.11
Ba (μg g^{-1})	2.35	3.1
La (μg g^{-1})	0.235	0.320
Ce (μg g^{-1})	0.620	0.940
Pr (μg g^{-1})	0.094	0.137
Nd (μg g^{-1})	0.460	0.626
Sm (μg g^{-1})	0.150	0.204
Eu (μg g^{-1})	0.057	0.078
Gd (μg g^{-1})	0.200	0.290
Tb (μg g^{-1})	0.037	0.051
Dy (μg g^{-1})	0.250	0.332
Ho (μg g^{-1})	0.056	0.077
Er (μg g^{-1})	0.160	0.221
Tm (μg g^{-1})	0.025	0.035
Yb (μg g^{-1})	0.160	0.215
Lu (μg g^{-1})	0.025	0.033
Hf (μg g^{-1})	0.105	0.18
Ta (ng g^{-1})	14	19
W (ng g^{-1})	93	160
Re (ng g^{-1})	38	50
Os (ng g^{-1})	490	670
Ir (ng g^{-1})	465	580
Pt (μg g^{-1})	1.0	1.1
Au (ng g^{-1})	145	150
Hg (ng g^{-1})	310	
Tl (ng g^{-1})	142	92
Pb (μg g^{-1})	2.50	1.6
Bi (ng g^{-1})	110	71
Th (ng g^{-1})	29	41
U (ng g^{-1})	8	12

Data sources given by Lodders and Fegley (1998).

that the chondrules retain some fraction of these elements. The CO chondrites have both lower matrix abundances and lower volatile-element contents in their matrices compared to CM chondrites. The CI and CM chondrites are also more oxidized than other chondrite types.

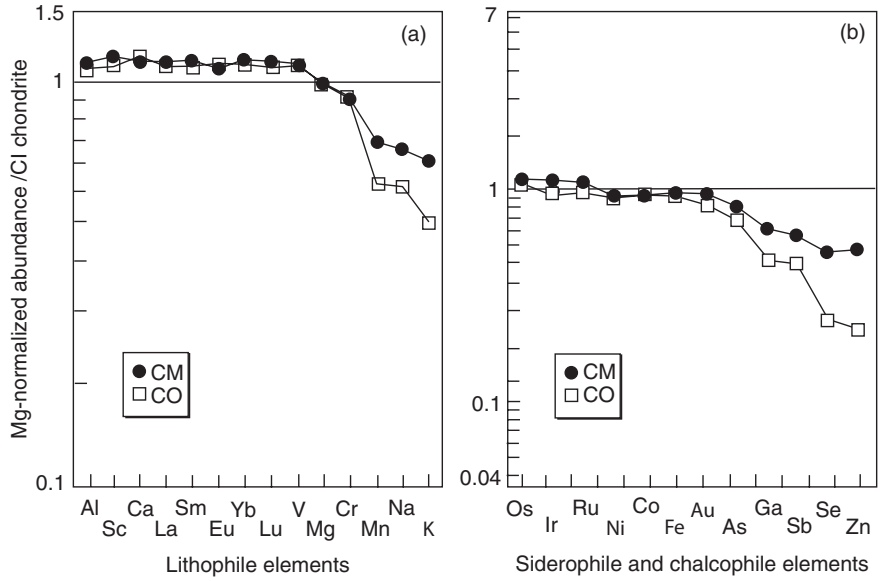

Fig. 12.17 **Differences in the abundances of (a) lithophile and (b) siderophile and chalcophile elements, all normalized to cosmic (CI chondrite) abundances, among altered carbonaceous chondrite groups. Normalizations as in Fig. 11.9. Modified from Krot *et al.* (2004).**

A perplexing observation is that aqueous alteration appears to have been largely isochemical. The CI chondrites, which provide the closest match to solar abundances, show the most extensive alteration. Likewise, the chemical compositions of CM chondrites are nearly uniform, despite significant differences in their degrees of aqueous alteration. Aqueous fluids can dissolve significant amounts of soluble materials during reactions, but there is little evidence in bulk CI and CM chondrites that the dissolved material was transported anywhere by the fluids. Why solidified mud should have retained its cosmic composition is a mystery.

Variations among ice-bearing planetesimals

Although planetesimals that formed beyond the snowline are composed of relatively primitive materials (chondritic solids and ices), their compositions are variable. That should not be surprising, because objects now in the asteroid belt, the Kuiper belt, and the Oort cloud formed in different parts of the outer solar system and were assembled at different temperatures. In a systematic study of the spectra of 41 comets, A'Hearn *et al.* (1995) recognized two compositional groups, one depleted in carbon-chain (C_2 and C_3) compounds and the other undepleted (Fig. 12.18). NH compounds in the same comets show no discernable trend. The depleted group represents comets derived from the Kuiper belt, whereas the undepleted group consists of Oort cloud comets.

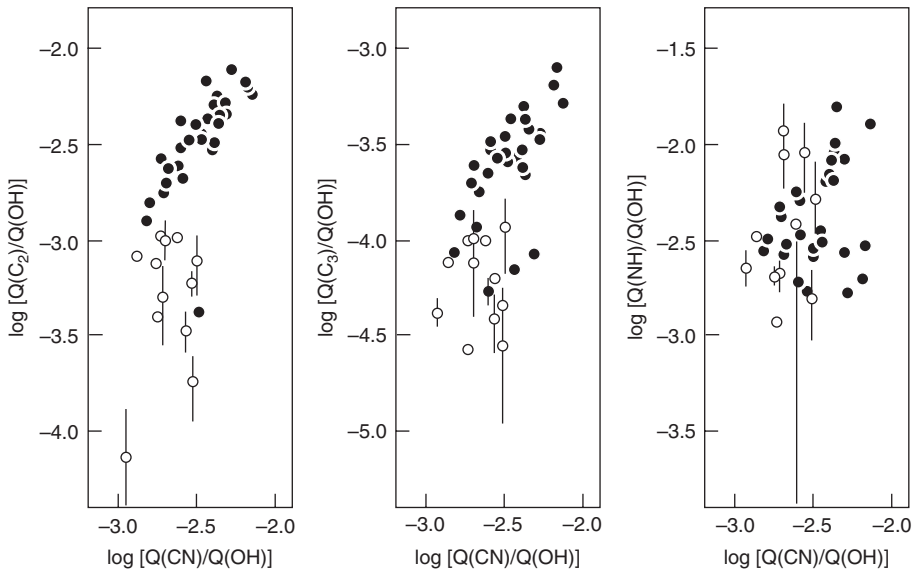

Fig. 12.18 **Compositional variations among comets, based on the production rates ("Q") of carbon-chain (C2 and C3) and NH molecules relative to water (OH). Filled symbols are Kuiper belt comets, and open symbols are Oort cloud comets. After A'Hearn *et al.* (1995).**

Asteroids in the outer asteroid belt show considerable spectral variability, due in part to differences in the degree of aqueous alteration. However, alteration alone is not sufficient to explain all the compositional variability observed in meteorites derived from these objects. Laboratory studies of carbonaceous chondrites show significant differences in the compositions and proportions of the various primary components, demonstrating that accreted materials in the asteroid belt were not uniform.

Although comets are not expected to have experienced the thermal processing that asteroids have, some of the larger KBOs and Oort cloud objects may have been heated by decay of radionuclides. The relative proportions of rock and ice may determine the amount of heating, as radionuclides occur in the rock fraction. Comets and asteroids may have had similar impact histories, and many of these bodies may now be collisional fragments.

Summary

Legions of ice-bearing planetesimals reside in the outer reaches of the solar system, within the Kuiper belt and more distant Oort cloud, although these are just the remnants of much larger populations of objects that formed originally. Occasionally these objects are perturbed into the planetary region, where sunlight causes ices to sublime and release dust particles. The compositions of comet ices are inferred from spectroscopic study of the molecules and molecular fragments given off by comets. Although spectra also provide some information about the chemistry of the dust, those materials are best characterized by laboratory analyses

of IDPs and comet samples returned by the Stardust spacecraft. These microscopic aggregates have broadly chondritic bulk compositions, and contain mostly anhydrous minerals with isotopic compositions that suggest they are mostly nebular materials rather than grains inherited from the interstellar medium. In comets, silicates, oxides, sulfides, metals, and glasses are intimately mixed with organic compounds that are more labile than those in chondrites. The organic matter has compositions that suggest formation in interstellar space. The tiny crystals, amorphous materials, and organic molecules in comets have been protected by sealing them in ices, so these aggregates represent the most primitive cosmochemical materials available for study. Despite their chondritic compositions, some chemical differences between comets may reflect formation at different solar distances (and hence temperatures).

Asteroids that formed beyond the snowline represent rock and ice accreted inside the orbit of Jupiter. The most distant asteroids may still contain ices, but many asteroids have been heated. Melting of ice produced aqueous fluids, which reacted with chondritic minerals at low temperatures to form secondary minerals (phyllosilicates, carbonates, sulfates, oxides). The alteration minerals can be discerned in asteroid spectra and characterized by analyses of chondrites derived from these bodies.

In the next chapter, we continue our examination of solar system objects through the geochemical exploration of larger bodies.

Questions

1. Distinguish between comets, Kuiper Belt Objects (KBOs), and Oort cloud objects.
2. What kinds of ices occur in comets, and how do they account for cometary activity?
3. What are interplanetary dust particles (IDPs) made of, and what do they tell us about the compositions of comets?
4. What kinds of asteroids and meteorites exhibit aqueous alteration, and how does that process manifest itself?
5. How might asteroids that experienced aqueous alteration relate to comets?

Suggestions for further reading

Bradley, J. P. (2004) Interplanetary dust particles. In *Treatise on Geochemistry*, Vol. 1. *Meteorites, Comets, and Planets*, ed. Davis, A. M. Oxford: Elsevier, pp. 689–711. This review provides an excellent summary of the voluminous literature that describes and interprets IDPs.

Brearley, A. J. (2006) The action of water. In *Meteorites and the Early Solar System II*, eds. Lauretta, D. S. and McSween, H. Y., Jr. Tucson: University of Arizona Press, pp. 587–624. The best available review of aqueous alteration processes and materials in chondritic meteorites.

Brownlee, D. E. (2004) Comets. In *Treatise on Geochemistry*, Vol. 1. *Meteorites, Comets, and Planets*, ed. Davis, A. M. Oxford: Elsevier, pp. 663–688. A comprehensive and thoughtful review of what is known about the composition and structure of comets and the bodies within the belts that supply comets.

Brownlee, D. and 181 coauthors (!) (2006) Comet 81P/Wild2 under a microscope. *Science* **314**, 1711–1716. This fascinating article, plus the more focused articles that follow it in the same issue, provide the first characterization of comet dust samples collected and returned by the Stardust spacecraft.

Lunine, J. I. (2006) Origin of water in the solar system. In *Meteorites and the Early Solar System II*, eds. Lauretta, D. S. and McSween, H. Y., Jr. Tucson: University of Arizona Press, pp. 309–319. An up-to-date review of water in the solar nebula.

References

A'Hearn, M. F., Millis, R. L., Schleicher, D. G., Osip, D. J. and Birch, P. V. (1995) The ensemble properties of comets: results from narrowband photometry of 85 comets, 1976–1992. *Icarus*, **118**, 223–270.

Bockelee-Morvan, D. and Crovisier, J. (2002) Lessons of comet Hale-Bopp for coma chemistry. *Earth, Moon, and Planets*, **89**, 53–71.

Brearley, A. J. (2004) Nebular vs. parent body processing of chondritic meteorites. In *Treatise on Geochemistry*, Vol. 1. *Meteorites, Comets, and Planets*, ed. Davis, A. M. Oxford: Elsevier, pp. 247–268.

Browning, L. B., McSween, H. Y. and Zolensky, M. E. (1996) Correlated alteration effects in CM carbonaceous chondrites. *Geochimica et Cosmochimica Acta*, **60**, 2621–2633.

Buseck, P. R. and Hua, X. (1993) Matrices of carbonaceous chondrite meteorites. *Annual Reviews of Earth and Planetary Sciences*, **21**, 255–305.

Clayton, R. N. and Mayeda, T. K. (1984) The oxygen isotope record in Murchison and other carbonaceous chondrites. *Earth and Planetary Science Letters*, **67**, 151–166.

Clayton, R. N. and Mayeda, T. K. (1999) Oxygen isotope studies of carbonaceous chondrites. *Geochimica et Cosmochimica Acta*, **63**, 2089–2104.

Crovisier, J. plus 13 coauthors (2000) The thermal infrared spectra of comets Hale-Bopp and 103 P/Hartley 2 observed with the Infrared Space Observatory. In *Thermal Emission Spectroscopy and Analysis of Dust, Disks, and Regoliths, ASP Conference 196*, eds. Sitko, M. L., Sprague, A. L. and Lynch, D. K., San Francisco: Astronomical Society of the Pacific, pp. 109–117.

Flynn, G. J. plus 79 coauthors (2006) Elemental compositions of comet 81P/Wild2 samples collected by Stardust. *Science*, **314**, 1731–1735.

Flynn, G. J. and Sutton, S. R. (1992) Trace elements in chondritic stratospheric particles: zinc depletion as a possible indicator of atmospheric entry heating. *Proceedings of the Lunar and Planetary Science Conference*, **22**, 171–184.

Formenkova, M. N., Kerridge, J. F., Marti, K. and McFadden, L. A. (1992). Compositional trends in rock-forming elements of comet Halley dust. *Science*, **258**, 266–269.

Grimm, R. E. and McSween, H. Y. (1989) Water and the thermal evolution of carbonaceous chondrite parent bodies. *Icarus*, **82**, 244–280.

Hanner, M. S. and Bradley, J. P. (2003) Composition and mineralogy of comet dust. In *Comets II*, eds. Festou, M., Keller, H. U. and Weaver, H. A., Tucson: University of Arizona Press, pp. 555–564.

Huebner, W. F. (2002). Compositions of comets: Observations and models. *Earth, Moon and Planets*, **89**, 179–195.

Ishii, H. A., Bradley, J. P., Dai, Z. R. *et al*. (2008) Comparison of comet 81P/Wild2 dust with interplanetary dust from comets. *Science*, **319**, 447–450.

Jessberger, E. K., Stephan, T., Rost, D. *et al*. (2001) Properties of interplanetary dust: information from collected samples. In *Interplanetary Dust*, eds. Grun, E., Gustafson, B. A. S., Dermott, S. F. and Fechteg, H. Berlin: Springer, pp. 253–294.

Jones, T. D., Lebofsky, L. A., Lewis, J. S. and Marley, M. S. (1990) The composition and origin of the C, P, and D asteroids: water as a tracer of thermal evolution in the outer belt. *Icarus*, **88**, 172–192.

Krot, A. N., Keil, K., Goodrich, C. A., Scott, E. R. D. and Weisberg, M. K. (2004) Classification of meteorites. In *Treatise on Geochemistry*, Vol. 1. *Meteorites, Comets, and Planets*, ed. Davis, A. M. Oxford: Elsevier, pp. 83–128.

Lawler, M. E., Brownlee, D. E., Temple, S. and Wheelock, M. M. (1989). Iron, magnesium, and silicon in dust from comet Halley. *Icarus*, **80**, 225–242.

Lodders, K. and Fegley, B., Jr. (1998). *The Planetary Scientist's Companion*. New York: Oxford University Press, 371 pp.

Marty, B., Palma, R. L., Pepin, R. O. *et al*. (2008) Helium and neon abundances and compositions in cometary matter. *Science*, **319**, 75–78.

McKeegan, K. D. plus 45 coauthors (2006) Isotopic compositions of cometary matter returned by Stardust. *Science*, **314**, 1724–1728.

Metzler, K., Bischoff, A. and Stoffler, D. (1992) Accretionary dust mantles in CM chondrites: evidence for solar nebula processes. *Geochimica et Cosmochimica Acta*, **56**, 2873–2897.

Pieters, C. M. and McFadden, L. A. (1994) Meteorite and asteroid reflectance spectroscopy: clues to early solar system processes. *Annual Reviews of Earth and Planetary Sciences*, **22**, 457–497.

Rietmeijer, F. J. M. (1998). Interplanetary dust particles. In *Planetary Materials, Reviews in Mineralogy* **36**, ed. Papike, J. J. Washington, D.C.: Mineralogical Society of America, pp. 2–1 to 2–95.

Rivkin, A. S., Howell, E. S., Vilas, F. and Lebofsky, L. A. (2002) Hydrated minerals on asteroids: the astronomical record. In *Asteroids III*, eds. Bottke, W. F., Cellino, A., Paolicchi, P. and Binzel, R. P. Tucson: University of Arizona Press, pp. 235–253.

Rubin, A. E., Trigo-Rodriguez, J. M., Huber, H. and Wasson, J. T. (2007) Progressive aqueous alteration of CM carbonaceous chondrites. *Geochimica et Cosmochimica Acta*, **71**, 2361–2382.

Sandford, S. A. plus 54 coauthors (2006) Organics captured from comet 81P/Wild2 by the Stardust spacecraft. *Science*, **314**, 1720–1724.

Schramm, L. S., Brownlee, D. E. and Wheelock, M. M. (1989) Major element composition of stratospheric micrometeorites. *Meteoritics*, **24**, 99–112.

Shu, F. H., Shang, H. and Lee, T. (1996) Toward an astrophysical theory of chondrites. *Science*, **271**, 1545–1552.

Tsou, P. plus 19 coauthors (2004) Stardust encounters comet 81P/Wind 2. *Journal of Geophysical Research*, **109**, E12S01, doi:10.1029/2004JE002317.

Vilas, F., Jarvis, K. S. and Gaffey, M. J. (1994) Iron alteration minerals in the visible and near-infrared spectra of low-albedo asteroids. *Icarus*, **109**, 274–283.

Westphal, A. J., Snead, C., Butterworth, A. *et al*. (2004) Aerogel keystones: extraction of complete hypervelocity impact events from aerogel collectors. *Meteoritics and Planetary Science*, **39**, 1375–1386.

Westphal, A. J., Fakra, S. C., Gainsforth, Z. *et al*. (2009) Mixing fraction of inner solar system material in comet 81P/Wild2. *Astrophysical Journal*, **694**, 18–28.

Young, E. D., Ash, R. D., England, P. and Rumble, D. (1999) Fluid flow in chondrite parent bodies: deciphering the compositions of planetesimals. *Science*, **286**, 1331–1335.

Zolensky, M. E. and McSween, H. Y. (1988) Aqueous alteration. In *Meteorites and the Early Solar System*, eds. Kerridge, J. F. and Matthews, M. Tucson: University of Arizona Press, pp. 114–143.

Zolensky, M. E. plus 74 coauthors (2006) Mineralogy and petrology of comet 81P/Wild2 nucleus samples. *Science*, **314**, 1735–1739.

13 Geochemical exploration of planets: Moon and Mars as case studies

Overview

The exploration of other planets increasingly involves combining the detailed chemical analyses of samples (laboratory or *in situ*) with chemical mapping by orbiting spacecraft to provide geologic context. In this chapter, we illustrate this approach to exploration by reviewing what has been learned about the Moon and Mars.

Lunar surface materials (Apollo and Luna returned samples and lunar meteorites) are classified into three geochemical end members – anorthosite, mare basalt, and KREEP. These components are clearly associated with the various geochemically mapped terrains of different age on the lunar surface. The composition of the lunar interior is inferred from the geochemical characteristics of basalts that formed by mantle melting, and geochemistry provides constraints on the Moon's impact origin and differentiation via a magma ocean.

Martian meteorites and Mars rover analyses suggest that it is a basalt-covered world, a conclusion supported by orbital measurements. Basalts of different ages appear to have distinct compositions. Since its original differentiation, the Martian mantle has remained geochemically isolated, although it is periodically melted to produce basalts. The core has an appreciable amount of sulfide, as inferred from trace elements in basalts. Water, once important in producing clays and sulfates, has now retreated into the subsurface.

Why the Moon and Mars?

The Moon and Mars are the only large bodies for which we have both samples for laboratory analysis and considerable chemical data from orbiting and landed spacecraft. Both bodies have experienced melting and differentiation. Following the distinction between cosmochemistry and planetary geochemistry made in Chapter 1, we will refer to efforts to describe the chemical compositions of these bodies as *geochemistry*. In the title of this chapter we also use the term *exploration*, to indicate that these studies involve spatial mapping of compositional differences and placing them into their proper geologic context.

Scientific literature on the geochemistry of the Moon and Mars is voluminous, and we can only provide overviews of some of the more recent data and current understanding. Lunar samples, lunar meteorites, and Martian (SNC) meteorites were briefly described in

Chapter 6. Here we combine what has been learned from detailed analyses of lunar samples with the results of geochemical mapping by orbiting spacecraft. Similarly, we compare the results from laboratory analyses of Martian meteorites with *in situ* geochemical analyses by the Mars rovers, as well as geochemical mapping by several Mars orbiters. Although mineralogy and petrology play important roles in this story, we will focus on chemistry, in keeping with the theme of this book.

Although the focus of exploration is on defining the composition of surface materials, we will also consider geochemical constraints on the compositions of the whole crusts, mantles, and cores of these bodies. Samples from the deep interiors of the Moon and Mars have not been analyzed directly, but inferences can be drawn from, or are limited by, analyses of some surface samples; trace element and radiogenic isotope data are particularly useful in constraining mantle and core compositions, and such measurements have so far been done only in laboratory settings. Accordingly, we will explore how the geochemistry of erupted basaltic magmas on the Moon and Mars may relate to the compositions of the mantle sources that partially melted to produce them. We will also explore how mantle depletions of siderophile (and sometimes chalcophile) elements caused by core formation are inherited by basalts. We do not consider how crust, mantle, and core compositions are combined to estimate the bulk compositions of planets – a topic to be considered in Chapter 14.

Global geologic context for lunar geochemistry

A gross subdivision of the Moon's surface is based on albedo. The bright regions are the *highlands*, which are clearly ancient because of their high densities of impact craters. The dark regions are younger *maria*, basaltic lavas that flooded the impact basins on the nearside of the Moon. Mare basalts are exposed over 17% of the lunar surface and probably comprise only 1% of the crustal volume.

The global stratigraphic framework for the Moon is based on using the ejecta blankets of large impact basins and craters as marker horizons. These ejecta units, called formations, are sufficiently widespread that their relative ages can be defined. Five major time intervals are identified, as summarized in Figure 13.1 (Wilhelms, 1987). Assigning absolute ages to these stratigraphic formations is controversial and depends on the proper assignment of returned samples to specific major impact events and the measurement of their radiometric ages.

The pre-Nectarian Period began with the formation of the Moon, and includes the solidification of its crust during a long period of intense impact bombardment. A critical concept in understanding the lunar geologic context is the magma ocean model. It is generally believed (based on geochemical evidence described below) that much, or perhaps all of the Moon was originally molten, resulting from its condensation following a giant impact with the Earth. Fractional crystallization of such a magma ocean could account for the feldspathic composition of the pre-Nectarian crust, and the complementary composition would represent the mantle.

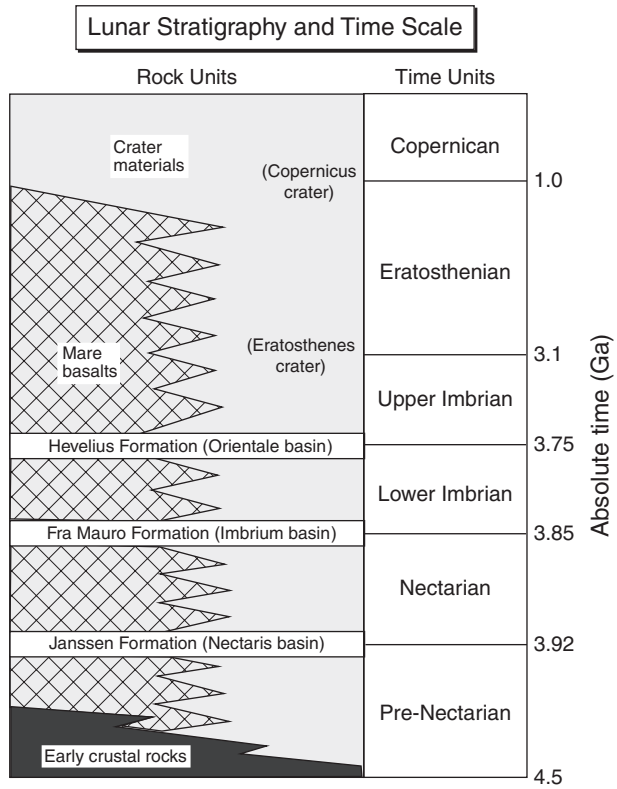

Fig. 13.1 **Schematic view of lunar stratigraphic and time units. The major rock and time periods are separated by Formations representing the ejecta of huge impact basins. Estimates of the absolute ages of these boundaries are shown on the right.**

The subsequent Nectarian Period was characterized by further bombardment that produced large basins and lasted only 0.7 Gyr. The Imbrian Period is subdivided into two intervals: the Early Imbrian Epoch included the formation of the Imbrium and Orientale basins, which had a profound effect on the present-day appearance of the Moon, and the Late Imbrian Epoch was marked by the cessation of giant impacts which allowed the voluminous extrusion of basalts into the basins, forming the maria. The Eratosthenian Period, which lasted 2.1 Gyr, was characterized by significantly declining volcanism and impact flux. The Copernican Period, representing the last 1.0 Gyr, marks the time during which rayed craters were preserved. Volcanism had ceased by this time.

The lunar surface is now covered by a thick regolith, formed by repetitive pulverization of rocks by meteors. Its depth may be tens of kilometers in places. Rock and mineral fragments and impact-melted glasses have been chaotically mixed and churned over time, producing a global layer of debris. Although smaller craters tend to homogenize the regolith, the stratigraphic framework provided by ejecta from huge impact basins survives.

Geochemical tools for lunar exploration

Instruments on orbiting spacecraft

The Lunar Prospector orbiter carried a gamma-ray/neutron spectrometer (GRS) that made precise measurements of the concentration and distribution of thorium (Lawrence *et al*., 1998) and hydrogen (Feldman *et al*., 2001). Subsequent spectral deconvolutions (Prettyman *et al*., 2006) have produced analyses of iron, titanium, potassium, magnesium, aluminum, calcium, and silicon. The principles of these analytical techniques are explained in Box 13.1.

The Clementine orbiter obtained high-resolution multispectral reflectance data. In comparing spectra with soil compositions at 39 locations sampled by Apollo astronauts, Blewett *et al*. (1997) determined a correlation between specific spectral features and chemical composition. This enabled Lucey *et al*. (1998) to develop an algorithm to estimate accurate FeO and TiO_2 abundances from Clementine spectra.

Global mapping of FeO, Th, and TiO_2 concentrations, especially, has allowed the abundance and distribution of different compositional regions of the lunar crust to be determined, and has provided new insights into heterogeneities in the mantle (Jolliff *et al*., 2000; Giguere *et al*., 2000).

Box 13.1 How gamma-ray and neutron spectroscopy works

Gamma-ray spectroscopy can determine some element concentrations from a spatially resolved portion of a planet's surface. Characteristic γ-ray line emissions for specific elements are produced by nuclear spallation reactions initiated by high-energy galactic cosmic rays hitting the planet's surface (Fig. 13.2). Spallation reactions are of two types: Inelastic scattering reactions occur when energetic (fast) neutrons produced by spallation lose energy to a target nucleus, leaving the nucleus in an excited state. The excited nucleus then produces γ-rays that can be used to identify that element. Neutron capture occurs when less energetic neutrons produced by spallation are absorbed by a target nucleus, again leaving the nucleus in an excited state. As with inelastic scatter, the nucleus de-excites and produces characteristic γ-rays. Elements that can be measured from spallation reactions include iron, titanium, magnesium, aluminum, calcium, silicon, and oxygen (the list of elements depends on what elements occur near to the instrument on the spacecraft). Finally, there are also a few naturally radioactive elements – thorium, uranium, and potassium – that on decay produce enough γ-rays that their abundances can be measured from an orbit (Fig. 13.2). Thorium has a very strong γ-ray signal, accounting for its ease of measurement on the Moon (see above).

Gamma-ray spectrometers use scintillator detectors. These spectrometers sense γ-rays from all directions, and hence have large "footprints" (commonly hundreds of kilometers diameter) with sizes determined by orbital elevation above the surface. The γ-rays come from depths of less than a meter in the target material.

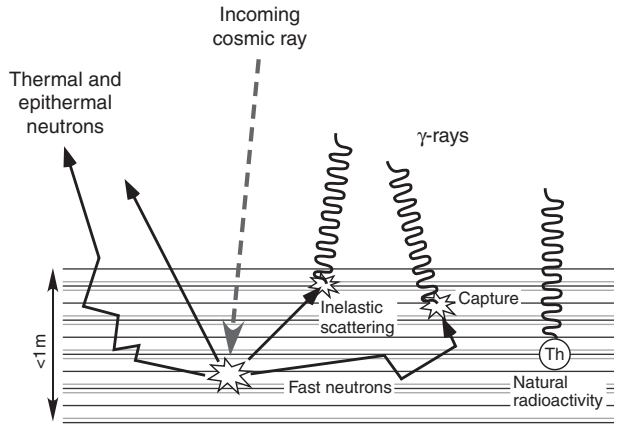

Fig. 13.2 **Production of γ-rays and neutrons used for *in situ* geochemical analysis. Galactic cosmic rays penetrate <1 m into the surface and collide with target atomic nuclei. Fast (energetic) neutrons are dislodged. These can be slowed by collisions with hydrogen atoms to produce thermal and epithermal neutrons, or undergo other kinds of nuclear reactions to produce γ-rays. Decay of natural radioactive isotopes (Th, U, K) also generates γ-rays.**

Neutrons generated by cosmic rays (Fig. 13.2) also provide a sensitive measurement of hydrogen in a planet's near-surface environment. The sensitivity stems from the fact that neutrons and protons (hydrogen nuclei) have essentially the same mass. When particles having the same mass collide, the energy transferred from the neutron to the proton is greater than in the case of a collision of the neutron with a heavier nucleus. (An analogy is colliding billiard balls, where significant energy is transferred to the target ball, in contrast to the collision of a billiard ball with a bowling ball, where the billiard ball retains its energy.) Consequently, neutrons impacting hydrogen atoms are slowed dramatically – they become "epithermal" neutrons that are easily absorbed. Thus the flux of epithermal neutrons that leak out of the planet's surface will be decreased in proportion to the hydrogen content. Measurements by orbiting neutron spectrometers of the epithermal neutrons that do escape can thus provide information on the distribution of hydrogen, commonly interpreted as water ice, in a planet's near-surface environment.

In some cases, thermal neutrons can also be used to measure the absolute abundances of other elements. Transforming the neutron spectrum into elemental abundances can be quite involved. For example, to determine the titanium abundances in lunar spectra, Elphic *et al*. (2002) first had to obtain FeO estimates from Clementine spectral reflectances and Th abundances from gamma-ray data, and then estimate the abundances of the rare earth elements gadolinium and samarium from their correlations with thorium. They then estimated the absorption of neutrons by major elements using the FeO data and further absorption effects by gadolinium and samarium, which have particularly large neutron cross-sections. After making these corrections, the residual neutron absorptions were inferred to be due to titanium alone.

Laboratory analysis of returned lunar samples and lunar meteorites

Six manned American Apollo missions have returned 382 kg of rocks and soils from the nearside of the Moon. Three automated Soviet Luna missions have also returned small amounts of soils. Most missions sampled maria; only the Apollo 14, 15, and 16 missions sampled highlands materials and basin ejecta as well as basalts. Descriptions and geologic significances of the various Apollo and Luna landing sites were given by Hiesinger and Head (2006).

The most informative geochemical analyses of highlands rocks are referred to as "pristine" (Warren and Wasson, 1977) to connote that they are coarse-grained plutonic rocks or large clasts (not brecciated mixtures of several rocks) and that there is no indication of contamination with siderophile elements (added by meteorite impact). Warren (1993) compiled a list of 89 pristine rocks, and another 171 possibly pristine rocks from the Apollo collection. Several suites of pristine highlands rocks are distinguished: the ferroan anorthosite (FAN) suite, the magnesian suite, the alkali suite, and KREEP. Ferroan (iron-rich) anorthosites, composed mostly of plagioclase with small amounts of pyroxene or olivine, are the dominant rock in the lunar highlands. They have very old ages (4.4–4.5 Ga) and represent cumulate crust formed from the magma ocean. Magnesian suite rocks contain much more pyroxene and olivine and are easily distinguished by their high Mg/Fe ratios and high concentrations of incompatible elements. Thus they have the unusual attribute that they are relatively unfractionated magmas but they have acquired high trace element abundances. They are thought to represent intrusions into the ancient FAN crust, and crustal assimilation may account for the trace element abundances. Their ages range from 4.5 to 4.1 Ga. Alkali suite rocks have sodium contents higher by a factor of four than those of ferroan anorthosites, and some small fragments have the compositions of granites. They are uncommon in the Apollo collection and absent from lunar meteorites, so they are unlikely to be a major crustal lithology. KREEP takes its name from high concentrations of potassium, rare earth elements, and phosphorus – all incompatible elements. The few pristine KREEP rocks are basalts, although a few small rock fragments are granitic and may have formed by fractionation of KREEP basalt. Because incompatible elements are concentrated in residual liquids, KREEP rocks might represent the last dregs of the magma ocean. More details about lunar crustal rocks can be found in Lucey *et al*. (2006) and Wieczorek *et al*. (2006).

Mare basalts include lavas that erupted from fissures and pyroclastic deposits that produced glass beads. Six of the nine missions to the Moon that returned samples included basalts. The mare basalts from different sites have distinctive compositions and are classified based on their TiO_2 contents, and to a lesser extent on their potassium contents (Fig. 13.3). A further subdivision is sometimes made, based on Al_2O_3 contents. Mare basalts are compositionally more diverse than their terrestrial counterparts. Volcanic glass beads, formed by fire fountains of hot lava erupting into the lunar vacuum, were found at several Apollo sites and eventually were shown to be a constituent of virtually every lunar soil. The glasses are ultramafic in composition and formed at very high temperatures.

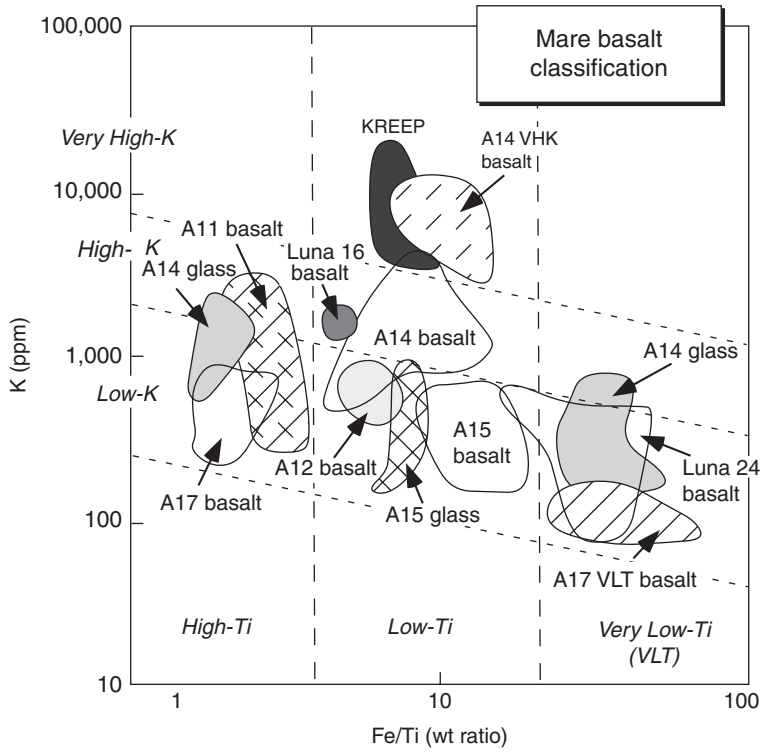

Fig. 13.3 **Lunar mare basalts from the various Apollo and Luna missions are classified by their titanium and potassium contents. After Lucey *et al.* (2006).**

Published geochemical studies of lunar rocks are voluminous. Compilations of lunar rock analyses can be found in *The Lunar Sourcebook* (Taylor *et al.*, 1991) and *Planetary Materials* (Papike *et al.*, 1998).

Lunar meteorites (see review by Korotev *et al.*, 2003) are mostly brecciated samples of highlands crust (FAN) and regolith, although a few mare basalts are included in this collection. It is likely that the source craters for the meteorites are randomly distributed and thus include materials from the lunar farside. As we will see, these meteorites provide a better estimate of the crustal composition than do the geographically biased samples returned by spacecraft.

Measured composition of the lunar crust

Sample geochemistry

Samples returned by the Apollo and Luna missions can be readily distinguished based on their contents of FeO and thorium. This may seem like an unlikely choice of chemical components for classification, but they nicely discriminate rock types and are easily measured by remote sensing. The FeO and thorium contents of ferroan anorthosites, mare basalts, impact melt breccias, and lunar meteorites are shown by various symbols in Figure 13.4.

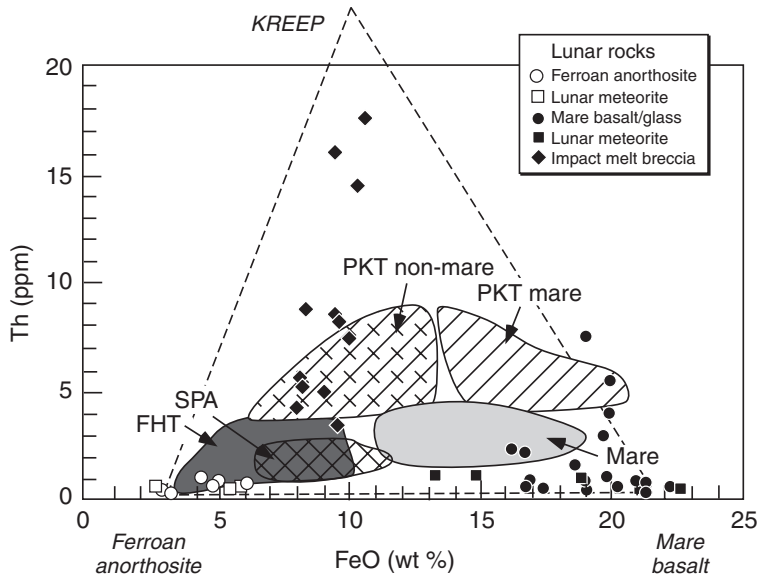

Fig. 13.4 Analyses of thorium and FeO in lunar rocks and lunar meteorites can be described by three compositional end members – ferroan anorthosite, KREEP, and mare basalt. The various lunar terranes defined by orbital measurements of Th and FeO, illustrated by shaded and hatched fields, can also be explained by mixtures of these components. Terrane abbreviations are: PKT (Procellarum KREEP Terrane); FHT (Feldspathic Highlands Terrane); SPA (South Pole-Aiken Terrane). Modified from Jolliff *et al*. (2000).

Anorthosites and basalts form two end members distinguished by FeO contents, and the impact melt breccias extend upward towards a KREEP end member with high thorium and intermediate FeO contents. Besides thorium, the KREEP end member is obviously enriched in the other incompatible elements that define its name. The impact melt breccias contain small clasts of KREEP basalt, which has not been sampled as large rocks.

The same ferroan anorthosite-mare basalt-KREEP components also define the compositions of lunar soils. The soils from each site contain different proportions of these end members. For example, Apollo 12 soils are mixtures of mare basalt and KREEP, whereas Apollo 15 soils contain all three components.

As noted earlier, lunar meteorites are mostly breccias of ferroan anorthosite and related early crustal rocks, although a few mare basalt meteorites are known. The lunar meteorites likely sample the whole Moon. The absence of KREEP-rich breccias so common among Apollo samples collected from the nearside in the lunar meteorite collection implies that KREEP-rich rocks cover only a small area on the Moon. In fact, the lunar highlands meteorites appear to provide a closer match to the average lunar crust than do the Apollo highlands samples (Fig. 13.5), as measured by geochemical mapping (see below).

Geochemical mapping by spacecraft

Orbital geochemical analyses since the Apollo and Luna sample return missions have revolutionized our understanding of the composition of the crust and mantle. As an example,

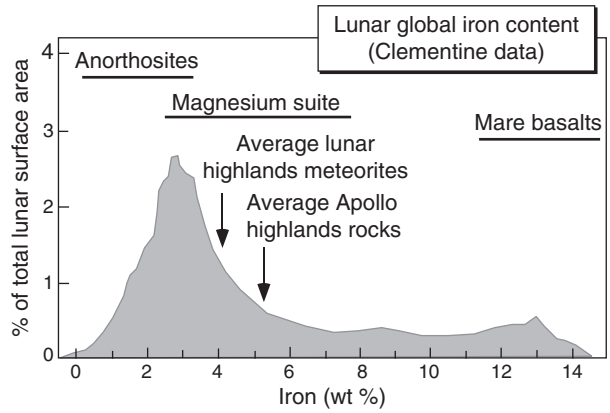

Fig. 13.5 Distribution of iron on the lunar surface, as measured by the Clementine spacecraft, compared with the average iron contents (arrows) of Apollo highlands crustal rocks and lunar highlands meteorites. The meteorites, which presumably come from the nearside and farside, more closely match the global iron peak. The compositional ranges for various lunar rock types are shown as horizontal bars.

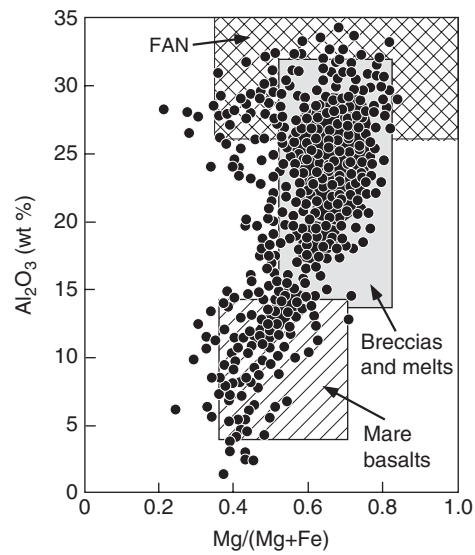

Fig. 13.6 Lunar prospector measurements of Al_2O_3 and magnesium number, Mg/(Mg+Fe) (black circles). These compositions are consistent with those of major lunar rock types from the Apollo collection (boxes). Modified from Prettyman *et al.* (2006).

Figure 13.6, which plots Al_2O_3 versus Mg/(Mg+Fe) from Lunar Prospector gamma-ray spectrometer data in 5° bins, shows that the global data overlap major rock types in the Apollo collection. Such comparisons give confidence that major geologic units have not been overlooked by biased sampling.

Global geochemical maps of the concentrations of FeO and thorium (Fig. 13.7) have proved to be especially informative. Using those data, Jolliff *et al.* (2000) identified three

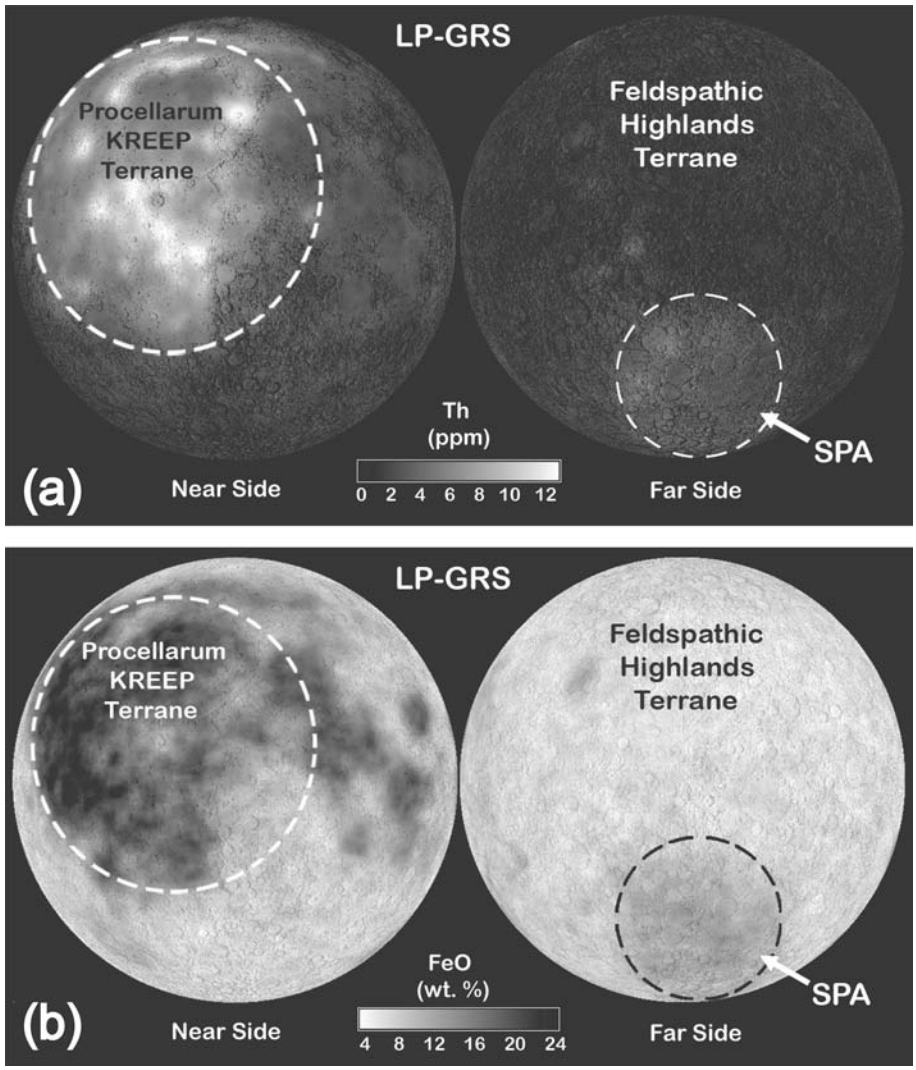

Fig. 13.7 Geochemical maps of the near and far sides of the Moon, for (a) thorium, and (b) FeO. Figures courtesy of B. Jolliff.

important lunar terranes based on their geochemical characteristics. (Choice of the term "terrane" rather than "terrain" is intentional; in terrestrial usage, terranes are broad regions of the crust that share a common geologic history.)

The Feldspathic Highlands Terrane (FHT) is characterized by its relatively low FeO and Th contents (Fig. 13.4), which are consistent with ferroan anorthosite. The FHT is the most extensive terrane and is concentrated on the lunar farside (Fig. 13.7). The Procellarum KREEP Terrane (PKT) occupies a large oval-shaped portion (Oceanus Procellarum) of the nearside (Fig. 13.7). The PKT has both light and dark areas, corresponding to highlands (non-mare) rocks and mare basalts. All of these materials

are characterized by high contents of thorium (Fig. 13.4) and other incompatible elements (KREEP). PKT non-mare materials include rugged mountain ranges representing basin ring structures and Imbrium ejecta. Accordingly, most of these materials are breccias. The PKT is also more FeO-rich than other highlands materials (Fig. 13.4), probably because of inclusion of magnesian suite rocks. The South Pole-Aitken Terrane (SPA) represents a gigantic (2600 km diameter) basin (Fig. 13.7). Its rocks have higher FeO contents than typical anorthositic crust (Fig. 13.4), probably because some lower crustal or mantle rocks are exposed.

All six Apollo missions landed near the boundaries between the two dominant terranes, the FHT and PKT. FHT and mare regions are fairly well represented in Apollo collections and among lunar meteorites (Fig. 13.4). The Apollo 14 mission provided the best sampling of rocks from the PKT (both non-mare and mare). Although thorium-rich igneous rocks such as alkali anorthosite and granite occur among Apollo samples, no 5° areas have compositions dominated by these kinds of rocks. The SPA terrane has apparently not been sampled by either the returned lunar samples or the lunar meteorites. Lunar soils collected during the Apollo missions are not plotted in Figure 13.4, but Jolliff *et al.* (2000) showed that soils from the various sites define elongated, overlapping fields that collectively cover the terranes defined by orbital data. The only exception is Apollo 14 soils, which plot near the KREEP apex.

In discussing global geochemical mapping thus far, we have made no distinction between mare basalts, although we learned in an earlier section that they are commonly subdivided by their TiO_2 contents. Titanium analyses of the nearside, where all the maria are, have been done using measurements based on Clementine reflectance spectra (Giguere *et al.*, 2000) and Lunar Prospector neutron spectra (Elphic *et al.*, 2002). Both studies produced similar maps (Fig. 13.8) showing variations attributed to different mare basalt compositions, although the TiO_2 concentrations from neutrons were lower than those from reflectance spectra (Fig. 13.9). More importantly, both global data sets demonstrated that there is a continuum between low-Ti and high-Ti basalt compositions, in contrast to the bimodal

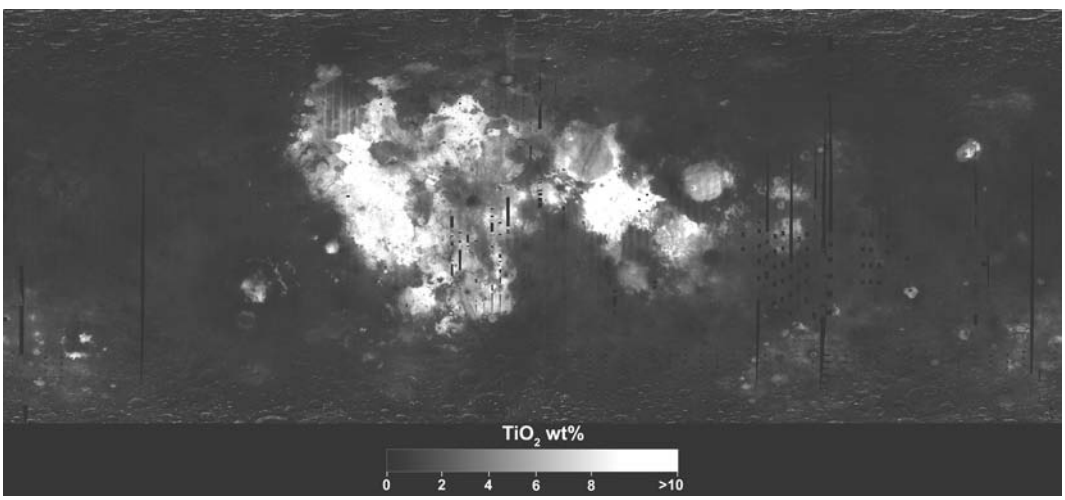

Fig. 13.8 TiO_2 concentration map of the lunar nearside generated from reflectance data collected by the Clementine mission. Adapted from Giguere *et al.* (2000), courtesy of J. Gillis-Davis.

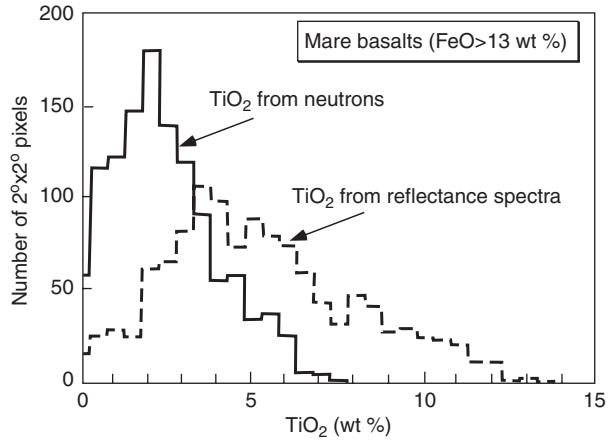

Fig. 13.9 Comparison of titanium contents of lunar mare basalts, as measured from neutrons by the Lunar Prospector gamma-ray spectrometer and from reflectance spectra by the Clementine spacecraft. After Prettyman *et al.* (2006).

distribution of the compositions of returned lunar samples. Although samples analyzed in the laboratory are invaluable, they can be geographically (and hence compositionally) biased.

Compositions of the lunar mantle and core

Even though the lunar crust has been thinned dramatically beneath large impact basins, no exposures of the mantle have been recognized. It is not surprising, then, that no mantle rocks have been found among returned samples. Consequently, the composition of the lunar mantle must be determined indirectly, from the basaltic magmas that represent partial melts of mantle sources.

Lunar basalts and glasses have major element compositions that are unique and require mantle sources that were not part of the primitive Moon but must be cumulates from the magma ocean (Shearer *et al.*, 2006). Relative to terrestrial basalts, they have lower CaO, Al_2O_3, and Na_2O contents (all components of plagioclase) and higher FeO and MgO contents. The glasses are ultramafic in composition, and the mare basalts formed by fractionating ultramafic magmas.

The major element compositions of these magmas determine what minerals crystallized as the magmas ascended and erupted. High-pressure experiments on these rocks can determine the pressures (depths) at which they are "multiply saturated," that is, in equilibrium with more than one mineral, as would be appropriate for a limited degree of melting. Such experiments indicate that the mantle sources consisted primarily of olivine and orthopyroxene, and suggest that lunar glasses may have originated at deeper levels than mare basalts. These experiments indicate considerable heterogeneity in mantle compositions, giving rise to magmas with varying titanium and aluminum contents.

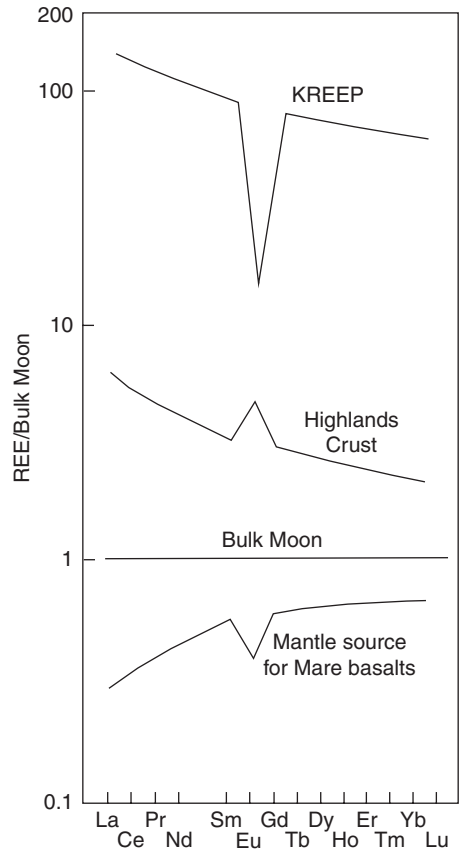

Fig. 13.10 **Rare earth element patterns, normalized to the bulk Moon composition, for various lunar materials. The highlands crust is enriched in REE over the bulk Moon because these rocks contain melts that concentrate incompatible elements, and its positive europium (Eu) anomaly indicates accumulation of plagioclase, which incorporates this element. The mantle would have a complementary REE pattern, depleted in abundance with a negative Eu anomaly, and this pattern was inherited by magmas generated from it, as represented by mare basalts. KREEP may represent the last dregs of the magma ocean, which would be extremely enriched in incompatible elements and exhibit a very large negative Eu anomaly because of the formation of the anorthositic crust.**

Rare earth element (REE) patterns of mare basalts and crustal rocks (Fig. 13.10) provide strong evidence for the former existence of a magma ocean, as described below. In Chapter 7, we discussed how large, trivalent REE ions are excluded from most rock-forming minerals. Divalent europium, however, is an exception, in that it fits comfortably into the structure of plagioclase. The low oxidation state of the Moon explains the high ratio of divalent to trivalent europium. REE patterns for the FAN suite (highlands crust) and mare basalts (which mimic the patterns of their mantle source) are complementary (Fig. 13.10), since they both formed from the same magma ocean. KREEP, representing the last residual melt from crystallization of the magma ocean, is very enriched in REE and has an even deeper negative europium anomaly (Fig. 13.10).

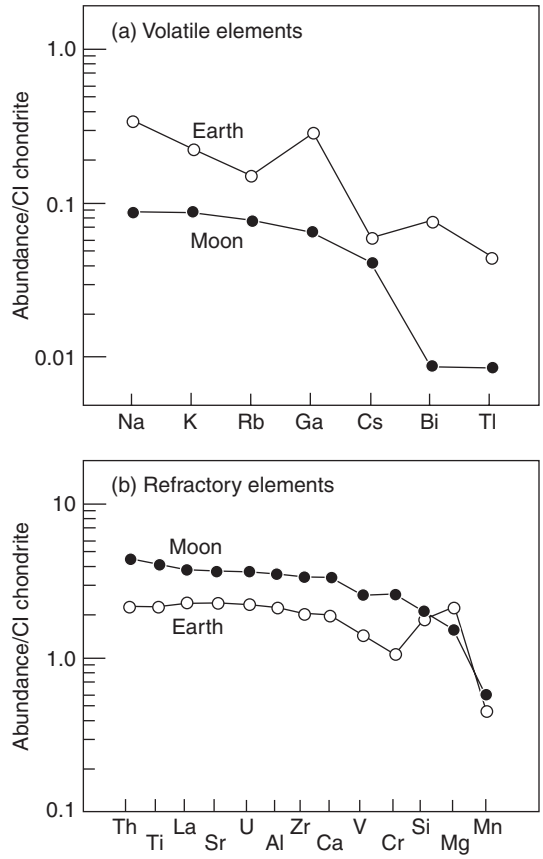

Fig. 13.11 **Comparison of the abundances of volatile and refractory elements, normalized to CI chondrites, for the Moon and the Earth. After Taylor *et al.* (2006a).**

Besides potassium, REE, and phosphorus, other trace elements that behave incompatibly in lunar basalts include strontium, barium, zirconium, niobium, tantalum, thorium, and uranium. The generally low incompatible-element concentrations in mare basalts indicate they come from already depleted sources, as appropriate for mafic cumulates from the magma ocean. Some trace elements are difficult to fractionate, and differences in their abundances can signal roles for specific minerals that incorporate one or the other. For example, fractionation of hafnium from zirconium may reflect crystallization of ilmenite, and the depletion of heavy REE relative to light in some volcanic glasses may suggest garnet was left behind in the deep mantle source region.

Trace element measurements in lunar basalts also indicate that the Moon is depleted in highly volatile elements (Taylor *et al.*, 2006a). Estimates of some of the Moon's volatile element concentrations are compared with the Earth in Figure 13.11a. The absence of water in lunar basalts suggests that the mantle is dry. The Moon may also be enriched in refractory elements (Fig. 13.11b). Volatile element depletion and refractory element enrichment are expected consequences of the giant impact origin and subsequent high-temperature accretion of the Moon.

Siderophile elements (cobalt, tungsten, nickel, molybdenum, gold, palladium, rhenium, iridium) are also depleted in lunar basalts (Righter and Drake, 1996). Geophysical evidence is inconclusive, being consistent with either presence or absence of a small metallic core. The depletion in siderophile elements clearly indicates segregation of metal somewhere, but it might simply reflect core formation in a precursor body that then impacted the Earth and lost its core. The formation of a lunar core depends critically on the degree to which the early Moon was molten.

Geochemical evolution of the Moon

There is now consensus that the Moon formed following a collision of the early Earth with a Mars-sized impactor (as summarized in the 1986 book *Origin of the Moon*). The timing of the impact and subsequent assembly of the Moon are not tightly constrained, but models of radiogenic isotopes suggest an age of 40 to 50 Myr after solar system formation (Halliday, 2004). The identical oxygen isotopic compositions of the Earth and Moon (Wiechert *et al.*, 2001) might suggest that the impactor was derived from the inner solar system, but equilibration of oxygen isotopes might also have occurred in a hot silicate atmosphere surrounding the Earth and proto-lunar disk (Pahlevan and Stevenson, 2007). Computer simulations indicate that the core of the impactor mostly accreted to the Earth, and the Moon formed mostly from silicate material in the impactor's mantle. This would account for the lack of a large lunar core. Vaporization and recondensation of material in Earth's orbit could account for the Moon's depletion in volatile elements. Condensation occurred in an environment with higher pressure than the ambient nebula, possibly allowing liquids to form (Pahlevan and Stevenson, 2007). Accretion of the solid and liquid materials produced a Moon that was largely, or at least partially, molten – in effect, a magma ocean (Taylor *et al.*, 2006b).

Crystallization models for a completely molten and half molten Moon are contrasted in Figure 13.12. In both models, olivine and orthopyroxene crystals formed early and sank to produce a cumulate mantle. Approximately 70% of the magma ocean formed mantle cumulates. Once fractionation of olivine and pyroxene had increased the Al_2O_3 content of the magma ocean, plagioclase crystallized and floated upward, forming a thick, feldspathic cumulate crust with a globally averaged thickness of 42 to 53 km (Wieczorek *et al.*, 2006). These simplified models do not take into account complications from the complex dynamics of a molten ocean cooling by convection and radiation from its top (Shearer *et al.*, 2006). The amount of crystallization of the magma ocean before plagioclase begins crystallizing is shown by tick marks for both models in Figure 13.12. Radiometric ages of FAN rocks range from 4.3 to 4.5 Ga, suggesting that solidification and cooling of the magma ocean required several hundred million years. The last dregs of the magma ocean were very rich in iron, titanium, and incompatible trace elements (KREEP), which were sandwiched between the crystallized mantle and crust. Subsequent mixing could have resulted from sinking of the dense KREEP layer or rising of plumes of magnesium-rich mantle cumulates. The degree of melting would have controlled the formation of a core; with a half melted Moon, a core is not possible.

The pronounced asymmetry of the lunar crust, with PKT dominating the nearside and FHT dominating the farside, is apparently a result of magma ocean crystallization. Some

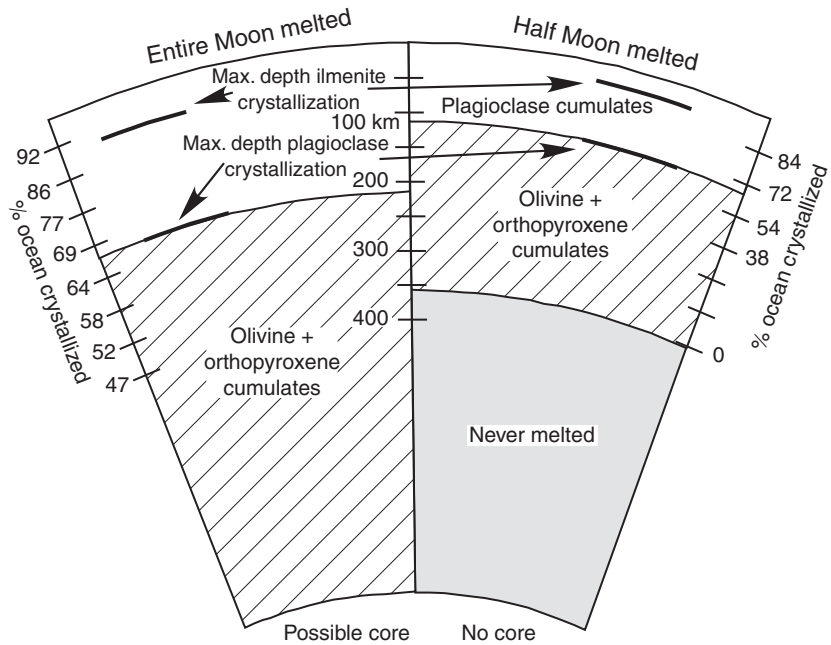

Fig. 13.12 **Two scenarios for the crystallization of the lunar magma ocean, involving different amounts of melt. In both models, olivine and orthopyroxene cumulates sink and plagioclase floats, but the thickness of the plagioclase-rich crust is greater for a completely melted Moon. Ilmenite crystallizes late in both models, but mixing of dense, ilmenite-rich rocks with early magnesium-rich cumulates could result from convection. After Ryder (1991).**

workers have advocated an anorthosite continent (FHT), with residual liquid (PKT) concentrated at its edge, and others have proposed that the PKT represents a mantle hotspot where thorium and other heat-producing elements were concentrated. The heat generated by their radioactive decay caused melting of upper mantle and KREEP materials to produce plutons of the magnesian and alkali suites. The radiometric ages of the highlands crustal rocks range from 4.5 to 3.9 Ga.

The so-called "late heavy bombardment," discussed more fully in Chapter 14, was a period of intense impacts by large planetesimals, concentrated in the Nectarian and Early Imbrian periods. The Procellarum and Imbrium impacts exposed subsurface rocks in the PKT. The SPA terrane formed during this time and represents not only the largest impact basin on the Moon, but also the biggest basin in the solar system. It exposes lower crust and perhaps mantle materials.

Following the late heavy bombardment, mare basalts formed by partial melting of the deep mantle, especially in the PKT region. Beginning at about 3.85 Ga, these magmas filled impact basins on the nearside over perhaps 2.5 Gyr. Most mare basalt activity occurred during the Late Imbrian, and decreased significantly during the Eratosthenian period.

Schematic cross-sections of the various lunar terranes are illustrated in Figure 13.13 (Jolliff *et al*., 2006). These sketches illustrate current thinking about the complexities of the crust and mantle in these regions.

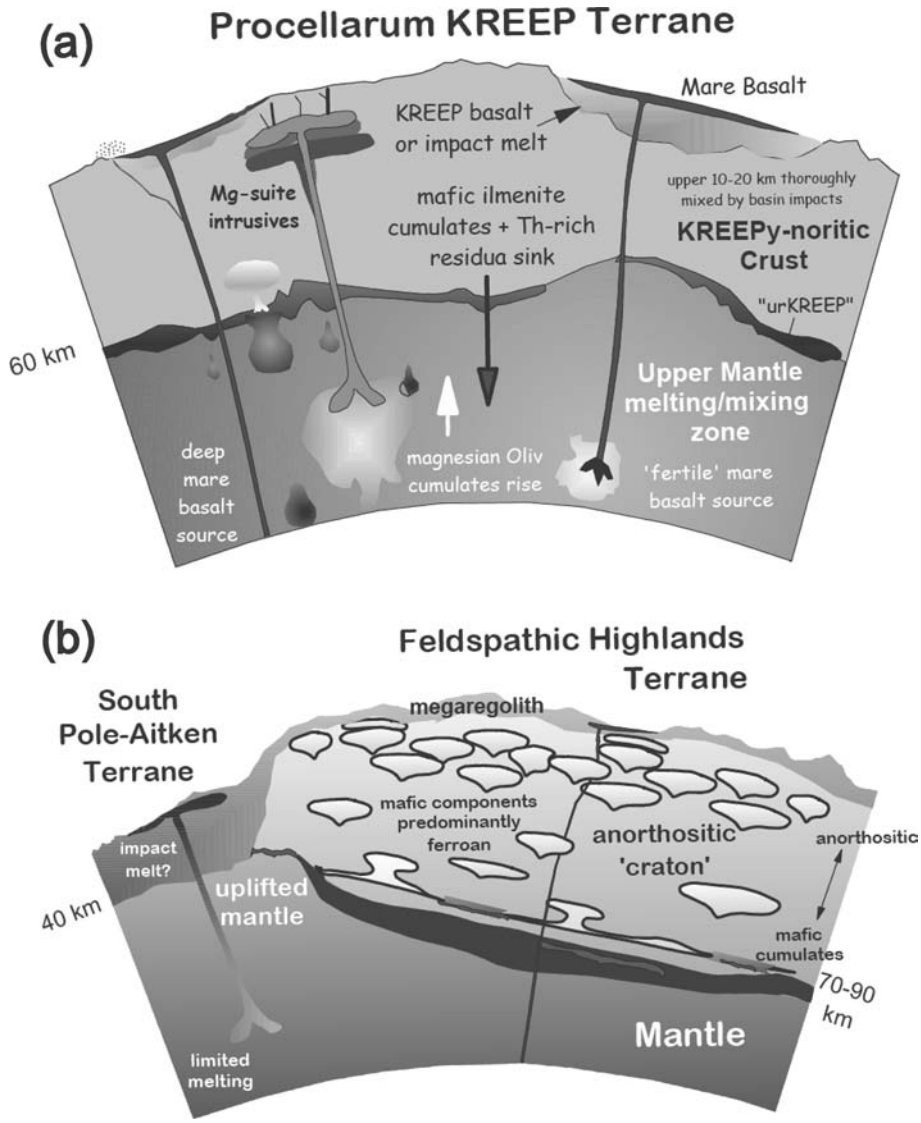

Fig. 13.13 Sketches of cross-sections of lunar terranes, illustrating processes that produced these terranes. (a) Procellarum KREEP Terrane, and (b) Feldspathic Highlands Terrane and South Pole-Aitken Terrane. Figures courtesy of B. Jolliff.

Box 13.2 **Geochemical exploration of asteroid 4 Vesta**

In most respects, asteroid 4 Vesta is geochemically similar to the Moon. As judged from howardite-eucrite-diogenite (HED) meteorites (see Chapter 6), Vesta is an ancient, basalt-covered world (Keil, 2002). Its rocks are highly reduced, and its depletions in volatile and siderophile element abundances resemble those of lunar basalts. And like the Moon, Vesta is hypothesized to have had an early magma ocean. The exploration of Vesta is now in progress, and within a few years we may have enough data to discuss it in a similar way that we have considered the Moon.

The connection between the HEDs and Vesta is based primarily on similar reflectance spectra. Spectral measurements obtained by the Hubble Space Telescope as Vesta rotated reveal different regions dominated by eucrite-, diogenite-, and howardite-like lithologies (Fig. 13.14a), and the petrologic properties of these meteorites suggest basaltic eucrite lava flows and howardite regolith cover a crust of cumulate eucrite and diogenite (Fig. 13.14b). A huge crater at Vesta's south pole (Fig. 13.14c) likely excavated numerous smaller asteroids ("Vestoids") having spectra similar to HEDs, distributed mostly between Vesta and a nearby orbital resonance with Jupiter. Objects broken off Vestoids and entering this escape hatch can be delivered into Earth-crossing orbits, providing a means of explaining this voluminous achondrite group.

Although the exact petrologic processes relating eucrites and diogenites are uncertain, the HEDs are linked by similar oxygen isotopic compositions (see Fig. 6.12). Eucrites are depleted in siderophile elements, suggesting that their parent asteroid has a core. Most HEDs are older (4.43–4.56 Ga, Wadhwa *et al.*, 2006) than most lunar rocks, indicating that Vesta's geologic evolution was rapid and of limited duration, probably fueled by decay of the short-lived radioisotope ^{26}Al (Ghosh and McSween, 1998). The melting of Vesta may have produced a magma ocean, and its crystallization formed a cumulate mantle of olivine, spinel, and orthopyroxene (Righter and Drake, 1997). After 80% crystallization, the remaining liquid was concentrated at the surface to produce a basaltic eucrite crust. No KREEP-like samples have been found among the HEDs, perhaps indicating more thorough convection and mixing in the Vesta magma ocean than on the Moon. The geochemistry of HEDs has been thoroughly described by Mittlefehldt *et al.* (1998) and Mittlefehldt (2004).

NASA's Dawn spacecraft is now in transit to Vesta, scheduled to arrive in 2011 (Russell *et al.*, 2006). Dawn carries a Gamma-ray and Neutron Detector (GRaND) that measures element abundances in a similar manner to the GRS instrument on Lunar Prospector. Dawn will be placed into three different orbits at progressively lower altitudes, and GRaND can function effectively only at the lowest orbit. However, it may measure the abundances of silicon, titanium, aluminum, iron, magnesium, calcium, potassium, hydrogen, and perhaps thorium, and provide some information on their global distributions. Because the GRaND footprints on Vesta will be large, it will be necessary to use the compositions of HEDs to unmix the measured abundances into their eucrite and diogenite end members (Usui and McSween, 2007). These chemical data will complement mineral mapping by a visible-infrared spectrometer.

Global geologic context for Mars geochemistry

Mars has a global dichotomy, separating the southern highlands, which stand well above the reference (average) surface elevation, and the northern lowlands. The north–south dichotomy is also expressed as differences in crater density (reflecting differences in age, with the northern plains being younger than the highlands) and in crustal thickness (with the lowlands crust being thinner than the highlands). Orbital spectra suggest that the ancient highlands are predominantly basaltic, although numerous deposits of clays and sulfate salts occur locally. In contrast, the spectra of the northern lowlands are consistent with partly altered basalts (although this is debated, as discussed below).

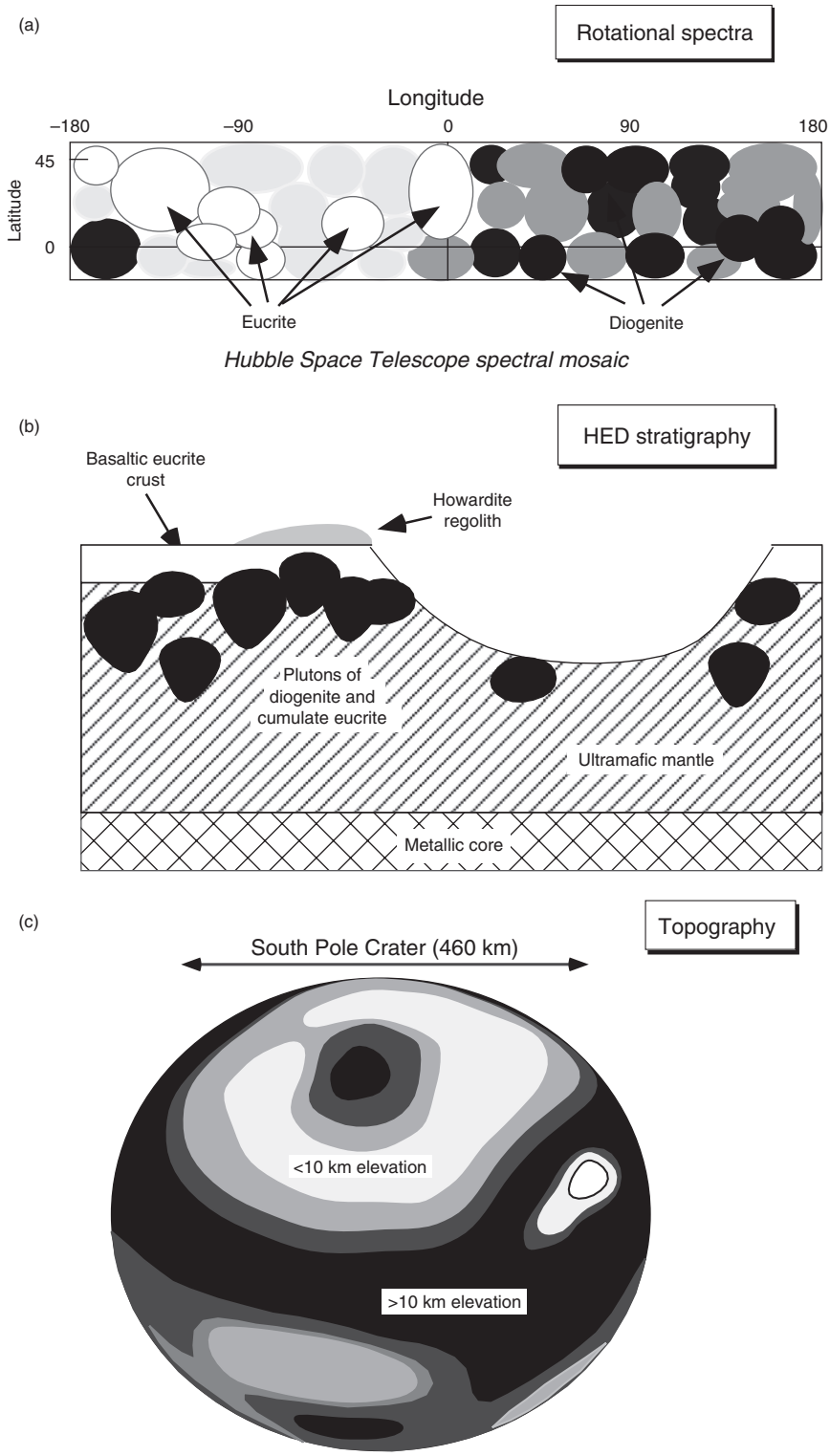

Fig. 13.14 Geologic data for asteroid 4 Vesta. (a) Spectral map of a part of the surface of Vesta as it rotates, showing the distribution of HED-like lithologies, modified from Binzel *et al.* (1997). (b) Interpretive geologic cross-section of Vesta, illustrating how HED meteorites might be distributed in the interior. (c) Topographic map of Vesta (Thomas *et al.*, 1997) showing a huge crater at its south pole. Rocks ejected from this crater are likely to have supplied most of the HED meteorites.

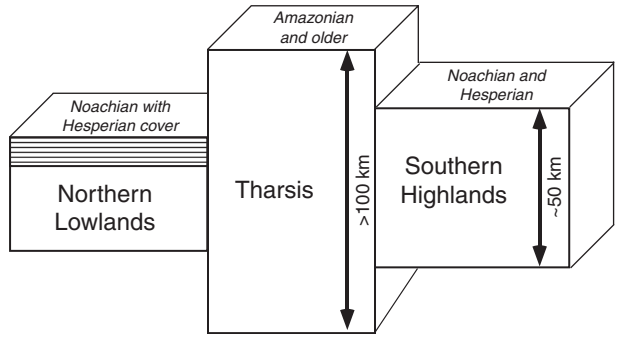

Fig. 13.15 **Illustration of the different ages and thicknesses of major parts of the Martian crust.**

The Tharsis bulge is a huge volcanic center located near the dichotomy boundary (Fig. 13.15). Its crustal thickness is significantly greater than the rest of Mars. The Tharsis hot spot formed during early Mars history and has been volcanically and tectonically active ever since. It is the locus of Mars' towering shield volcanoes and numerous radial fractures extend outward. A smaller bulge, called Elysium, represents a second locus of recent volcanism.

The global stratigraphic system for assigning ages to various parts of the Martian surface is based on the density of impact craters. The following time periods have been defined: Noachian (the earliest period, dating from ~4.5 to ~3.7 Ga), Hesperian (between ~3.7 and ~3.0 Ga), and Amazonian (postdating ~3.0 Ga). To first order, the southern highlands are dominated by Noachian rocks with some Hesperian cover, while in the northern lowlands, the Noachian basement is almost completely buried by Hesperian-age materials. The surface rocks of Tharsis and Elysium are Amazonian (Fig. 13.15).

The best available source for details about Mars geology is *The Surface of Mars* (Carr, 2006). Solomon *et al*. (2005) provided an excellent review of the geological evolution of Mars, and various chapters in *The Martian Surface: Composition, Mineralogy, and Physical Properties* (Bell, 2008) give up-to-date summaries of Mars geochemistry.

Geochemical tools for Mars exploration

Instruments on orbiting spacecraft

Gamma-ray/neutron spectrometers have been flown on the Soviet Phobos-2 and US Mars Odyssey orbiters. Because of their high orbiting altitudes, these instruments have larger footprints than for Lunar Prospector data, and only the data from the Gamma-Ray Spectrometer (GRS) on Mars Odyssey are useful. The principles of this instrument are as already described in Box 13.1. GRS has provided analyses of hydrogen, silicon, iron, calcium, potassium, chlorine, aluminum, and thorium, as well as low-resolution geochemical maps of global element distributions (Boynton *et al*., 2008; Feldman *et al*., 2008).

Mars Global Surveyor carried a Thermal Emission Spectrometer (TES), which provided thermal infrared spectra. Lattice vibrations in many minerals absorb thermal energy, so the

emitted radiation is missing those bands. Although designed as a mineral identification tool, several groups (Hamilton *et al*., 2001; Wyatt *et al*., 2001) have explored the use of these data in calculating bulk chemical compositions. Because thermal emission spectra for minerals combine linearly, a TES spectrum can be deconvolved into its constituent minerals, giving information on their relative proportions. When mineral proportions are combined with chemical compositions of those minerals in the spectral library, as measured in the laboratory, this gives the bulk chemical composition. Wyatt and his colleagues compared the chemical compositions of a variety of terrestrial lavas analyzed in the laboratory with those calculated from TES spectra, and concluded that the derived element abundances were generally within 10% of analyzed values. However, Martian terrains covered with even thin coatings of fine-grained dust (basically, the equatorial region of Mars) emit blackbody radiation and are not decipherable in terms of mineralogy or chemistry.

Various TES-derived estimates of Mars surface chemistry, based on mineral deconvolutions using different spectral libraries, were compiled by McSween *et al*. (2003). A subsequent spectral study identified 11 compositionally different regions on Mars (Rogers and Christensen, 2007).

A major difference between the GRS and TES-derived chemical datasets is that γ-rays penetrate and measure to 20–30 cm depth, whereas TES spectra sample only the outermost micron of surface grains. As we will see, surface alteration of rocks and soils has modified their compositions to such an extent that the TES data no longer give bulk sample chemistry, although they still provide valuable information on chemical alteration.

Instruments on landers and rovers

The Viking landers provided X-ray fluorescence (XRF) data for a limited number of Martian soils at two landing sites. These data were compiled by Clark *et al*. (1982).

The Mars Pathfinder rover carried an Alpha Proton X-ray Spectrometer (APXS), and the two Mars Exploration Rovers (MER – Spirit and Opportunity) carried Alpha Particle X-ray Spectrometers (also called APXS, but in this case more precise versions of the Pathfinder instrument, though without the ability to monitor protons for light element analyses). These instruments contained radioactive curium sources (Fig. 13.16) whose decay produced α-particles, which irradiated target rocks and soils. The resulting characteristic X-rays provided measurements of major and minor element abundances. The MER rovers also carried Mossbauer spectrometers, which yielded information on iron oxidation state.

Mars Pathfinder analyzed six rocks and five soils (Wänke *et al*., 2001; Foley *et al*., 2008). Although the Pathfinder rocks were coated with varying amounts of sulfur-rich dust, plots of other elements versus sulfur were extrapolated to zero sulfur to obtain the dust-free rock compositions (McSween *et al*., 1999; Wänke *et al*., 2001). To minimize the problem of dust-coated rocks, each MER rover carried a Rock Abrasion Tool (RAT) (Fig. 13.16), capable of brushing away dust or grinding away the outer portions of rocks to expose fresh interiors. The two MER rovers, together, have analyzed more than 250 rocks and 100 soils. Compilations of MER geochemical analyses were given by Gellert *et al*. (2006), Ming

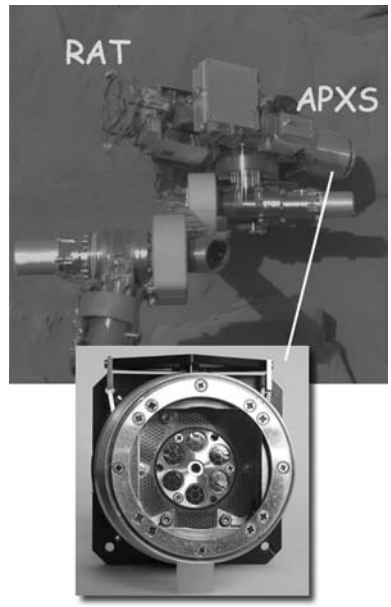

Fig. 13.16 Pancam image of the end of the MER arm, showing its APXS (used for chemical analyses) and RAT (used for abrading or brushing rock surfaces). A photograph of the APXS (bottom) shows radioactive curium α-particle sources surrounded by detectors.

et al. (2006), and Bruckner *et al*. (2008). Some representative analyses of Mars Pathfinder and MER rocks are given in Table 13.1.

Laboratory analyses of Martian meteorites

Martian meteorites (McSween, 2008) were described briefly in Chapter 6, and their chronology was described in Chapter 9. We learned previously that Mars launch ages for these meteorites (the sums of cosmic-ray exposure and terrestrial ages) generally clump into groups having the same petrographic characteristics and classifications (refer to Fig. 9.22). Each group presumably represents one impact event at one site that launched meteorites, so collectively the Martian meteorites may sample 6 or 7 separate sites – more locations than those studied by landers and rovers. The young crystallization ages ($\geq$1.3 Ga) of all but one Martian meteorite indicate that they are geographically biased, probably reflecting the fact that only impacts into young, coherent targets may be able to launch rocks to escape velocity. Most Martian meteorites may be derived from Tharsis or Elysium. The old (~4.5 Ga) ALH 84001 meteorite represents the ancient crust of Mars.

Chemical and isotopic analyses of many of the meteorites are remarkably complete. Compilations can be found in Treiman *et al*. (1987) and Lodders (1998). Analyses of representative meteorites are given in Table 13.2.

Table 13.1 Representative rock compositions from in-situ measurements by Mars rovers

Mars Pathfinder rocks[a]							
Oxide (wt.%)	A-3	A-7	A-16	A-17	A-18	Dust-free Rock	Unc[b]
Na_2O	1.69	1.19	2.30	2.03	1.78	2.46	40%
MgO	4.58	6.71	4.56	3.50	3.91	1.51	10%
Al_2O_3	11.02	9.68	10.24	10.03	10.94	11.0	7%
SiO_2	53.8	49.7	48.6	55.2	51.8	57.0	10%
P_2O_5	1.42	0.99	1.00	0.98	0.97	0.95	20%
SO_3	2.77	4.89	3.29	1.88	3.11	0.30	20%
Cl	0.41	0.50	0.41	0.38	0.37	0.32	15%
K_2O	1.29	0.87	0.96	1.14	1.10	1.36	10%
CaO	6.03	7.35	8.14	8.80	6.62	8.09	10%
TiO_2	0.92	0.91	0.95	0.65	0.82	0.69	20%
Cr_2O_3	0.10	n.d.	n.d.	0.05	n.d.	n.d.	50%
MnO	n.d.	0.47	0.65	0.49	0.52	0.55	25%
Fe_2O_3	16.2	16.7	18.9	14.8	18.1	15.7	5%

MER rocks[c]										
	Adiron	Hump	Mazat	Clov	Wish	Peace	Guad	Esch	Bounc	Unc
Na_2O	2.4	2.5	2.8	3.6	5.0	0	1.7	1.6	1.7	0.3
MgO	10.83	10.41	9.72	11.52	4.50	21.53	8.45	8.37	6.84	0.14
FeO	18.8	18.8	18.9	15.6	11.6	20.4	14.8	15.7	14.4	0.12
Al_2O_3	10.87	10.68	10.70	8.95	15.03	2.24	5.85	6.06	10.48	0.13
SiO_2	45.7	45.9	45.8	42.2	43.8	37.3	36.2	36.5	51.6	0.4
P_2O_5	0.52	0.56	0.65	1.05	5.19	0.49	0.97	1.01	0.92	0.07
SO_3	1.23	1.28	1.48	7.53	2.20	10.6	24.9	23.0	0.56	0.03
Cl	0.20	0.26	0.23	1.63	0.35	0.72	0.50	0.78	0.10	0.04
K_2O	0.07	0.10	0.16	0.35	0.57	0.00	0.53	0.57	0.11	0.05
CaO	7.75	7.84	8.02	6.04	8.89	4.90	4.91	5.00	12.1	0.06
TiO_2	0.48	0.55	0.59	0.84	2.59	0.45	0.65	0.75	0.74	0.06
Cr_2O_3	0.61	0.60	0.54	0.17	0.00	0.75	0.17	0.18	0.11	0.06
MnO	0.41	0.41	0.42	0.30	0.22	0.47	0.30	0.24	0.40	0.02
Ni ppm	165	164	132	735	67	774	589	564	81	39
Zn ppm	81	112	75	118	64	64	324	314	38	11
Br ppm	14	52	161	239	22	71	30	425	39	17

[a] Wänke *et al*. (2001), total Fe as Fe_2O_3.

[b] Average error, in relative %.

[c] MER-A (Spirit) rocks Adirondack, Humphrey, Mazatzal, Clovis, Wishstone, and Peace from Gellert *et al*. (2006); MER-B (Opportunity) rocks Guadalupe, Escher, and Bounce Rock from Bruckner *et al*. (2008), total Fe as FeO.

Table 13.2 Representative elemental abundances in SNC meteorites[a]

Element	Shergotty	QUE 94201	ALH 77005	ALH 84001	Nakhla	Chassigny
Li (ppm)	4.5±0.9		1.5±0.2		3.9	1.4±0.2
B (ppm)					4.6	63
C (ppm)	530±130		140±90	580	300±100	847
F (ppm)	46±6	40	22		57	15
Na (%)	1.03±0.14	1.17±0.19	0.35±0.06	0.10±0.02	0.34±0.05	0.09±0.01
Mg (%)	5.58±0.11	3.77±0.04	17.0±0.8	15.1±0.5	7.3±0.2	19.2±0.5
Al (%)	3.64±0.27	5.81±0.58	1.52±0.15	0.68±0.05	0.89±0.11	0.42±0.15
Si (%)	24.0	22.4	19.8±0.4	24.7±0.1	22.7±0.8	17.5±0.5
P (ppm)	3230±230		1750±150	61	500±45	275±35
S (ppm)	1270±760		510±200	110	260±80	260±130
Cl (ppm)	108	91	14	8.0±4.5	80	34
K (ppm)	1440±110	375±80	250±40	140±50	1070±190	300±110
Ca (%)	6.86±0.39	8.14±0.01	2.26±0.23	1.30±0.27	10.5±0.5	0.47±0.07
Sc (ppm)	52±7	48±2	21±1	13±1	51±4	5.3±0.4
Ti (ppm)	4,900±430	1 1000±900	2340±440	1240±70	2020±250	480±90
V (ppm)	290±40	113±15	162±6	201±6	192	39±9
Cr (ppm)	1,350±100	950±85	6670±520	7760±670	1770±280	5240±1,050
Mn (ppm)	4010±130	3480±150	3470±80	3560±100	3820±310	4120±840
Fe (%)	15.1±0.5	14.4±0.4	15.6±0.3	13.6±0.4	16.0±1.2	21.2±0.6
Co (ppm)	40±7	24±1	72±4	47±3	48±5	123±17
Ni (ppm)	79±12	<20	290±85	58	90	500±70
Cu (ppm)	16±9		5.1±6		12±6	2.6
Zn (ppm)	69±9	110	60±8	92±9	54±11	72±4
Ga (ppm)	16.0±1.3	27±1	7.3±1.2	2.9±0.5	3.0±0.5	0.7
Ge (ppm)	0.73±0.06		0.58	1.8	3.0	0.011
As (ppb)	25	770	22	<30	15	8
Se (ppm)	0.38±0.08		0.15	<0.16	0.08±0.02	0.037
Br (ppm)	0.88±0.2	0.35	0.077±0.011		4.5±0.2	0.088±0.031
Rb (ppm)	6.4±0.6		0.7±0.08	0.83	3.8±0.8	0.73±0.5
Sr (ppm)	48±8	70±15	14±3	4.5	59±10	7.2
Y (ppm)	19	31	6.2	1.6	3.3±1.1	0.64
Zr (ppm)	57±14	100±7	19.5	5.9	8.8±1.0	2.1±0.9
Nb (ppm)	4.6	0.68	0.65±0.11	0.42	1.57	0.34±0.03
Mo (ppm)	0.37		0.20		0.086	
Pd (ppb)	1.7				30±12	0.15
Ag (ppb)	11.4±5.1		4.4		40	2.6
Cd (ppb)	28±16		2.1	77	93±31	14
In (ppb)	26±4		11		20±7	3.9
Sn (ppm)	0.011		0.24		0.58	
Sb (ppb)	5.2±3.6		69		40±30	0.87
Te (ppb)	3.3±0.9		0.5		<4.3	50
I (ppb)	43±10	4600	1720		180	<10
Cs (ppb)	440±50		53±26	43±4	390±90	37
Ba (ppm)	34±5	<15	4.2±1.5	4.0	29±6	7.6±0.6

Table 13.2 (cont.)

Element	Shergotty	QUE 94201	ALH 77005	ALH 84001	Nakhla	Chassigny
La (ppm)	2.16±0.32	0.40±0.06	0.34±0.03	0.19±0.06	2.06±0.33	0.53±0.12
Ce (ppm)	5.45±0.86	1.47±0.23	0.91±0.15	0.59±0.14	5.87±0.37	1.12
Pr (ppm)	0.81±0.10		0.13	0.06	0.67	0.13
Nd (ppm)	4.2±0.5	2.2±0.4	0.95±0.17	0.265	3.23±0.52	0.62±0.11
Sm (ppm)	1.47±0.14	2.3±0.4	0.49±0.07	0.12±0.03	0.77±0.08	0.14±0.03
Eu (ppm)	0.60±0.11	1.04±0.07	0.22±0.02	0.035±0.008	0.235±0.030	0.045±0.007
Gd (ppm)	2.54±0.26	4.3	0.92	0.14	0.86±0.08	0.11
Tb (ppm)	0.48±0.05	0.87±0.09	0.17±0.01	0.038±0.005	0.12±0.01	0.03±0.02
Dy (ppm)	3.50±0.64	5.8±0.4	1.08±0.08	0.28±0.03	0.77±0.06	0.20±0.11
Ho (ppm)	0.71±0.10	1.19	0.25±0.03	0.076±0.007	0.155±0.020	0.044±0.020
Er (ppm)	1.88±0.02		0.66	0.21	0.37±0.05	0.09
Tm (ppm)	0.30±0.04		0.088±0.010	0.036	0.047	
Yb (ppm)	1.63±0.15	3.3±0.3	0.59±0.03	0.29±0.03	0.39±0.02	0.11±0.01
Lu (ppm)	0.26±0.03	0.50±0.06	0.078±0.004	0.049±0.006	0.055±0.007	0.015±0.004
Hf (ppm)	2.0±0.3	3.41±0.02	0.62±0.11	0.14±0.03	0.27±0.03	<0.1
Ta (ppb)	250±40	23	33±7	32	90	<20
W (ppb)	460±53		84	79	120±80	46
Re (ppb)	0.044		0.102	0.002	0.036±0.005	0.063±0.012
Os (ppb)	0.4		4.4	0.010	0.007±0.004	1.58±0.31
Ir (ppb)	0.057±0.025	<3	3.9±0.3	0.08	0.22±0.10	2.1±0.4
Pt (ppb)	0.16				0.5	
Au (ppb)	0.92±0.08	<0.5	0.21±0.02	0.009	0.72±0.20	0.73±0.3
Hg (ppb)					0.7	
Tl (ppb)	12.8±1.3		1.7		3.5±0.5	3.7
Pb (ppm)				72		
Bi (ppb)	1.1±0.6		<0.7			0.37
Th (ppb)	380±75	<50	57±3	35	198±13	57
U (ppb)	105±20	<50	15±3	11±2	52±9	18±4
H_2O (ppm)	280±120			550	570±120	740±70

[a] Source: Lodders (1998); Shergotty and QUE94201 are basaltic shergottites, ALH 77005 is a lherzolitic shergottite, ALH 84001 is an orthopyroxenite, Nakhla is a nakhlite, and Chassigny is a chassignite. Analytical uncertainties are 1*s* deviations for multiple analyses.

Measured composition of the Martian crust

The composition of Martian surface materials can be assessed using laboratory analyses of Martian meteorites, *in situ* APXS analyses from Mars Pathfinder and the Mars Exploration Rovers, and orbital geochemistry analyzed by GRS and derived from TES spectra.

Composition of the crust

Although the rocks in Meridiani Planum analyzed by the Opportunity rover are fascinating (see below), they are unusual. Therefore, we will focus on the rocks and soils in Gusev crater analyzed by the Spirit rover, which are spectrally similar to the bulk of the Martian crust. We will compare these compositions with those of Martian meteorites and Bounce Rock in Meridiani, which is similar to shergottites. We will also consider orbital geochemical data obtained by GRS.

Figure 13.17 shows a plot of Na_2O+K_2O versus SiO_2, which is commonly used to classify terrestrial volcanic rocks. The diagram is divided into fields labeled with rock names. Martian meteorites and geochemically similar Bounce Rock plot in the basalt field, as do most Gusev rocks and soils. GRS provided silica analyses (the width of the cross-hatched box represents the average silica abundance and standard deviations). GRS analyzed potassium but not sodium, so in constructing the vertical dimension of the box we have assumed the average Na_2O/K_2O ratio of Gusev soils. The GRS analyses also plot in the basalt field, indicating that the Martian crust is dominantly basaltic. The chemical compositions derived from orbital TES mineralogy, however, are higher in silica (Fig. 13.17). These compositions probably reflect surface weathering

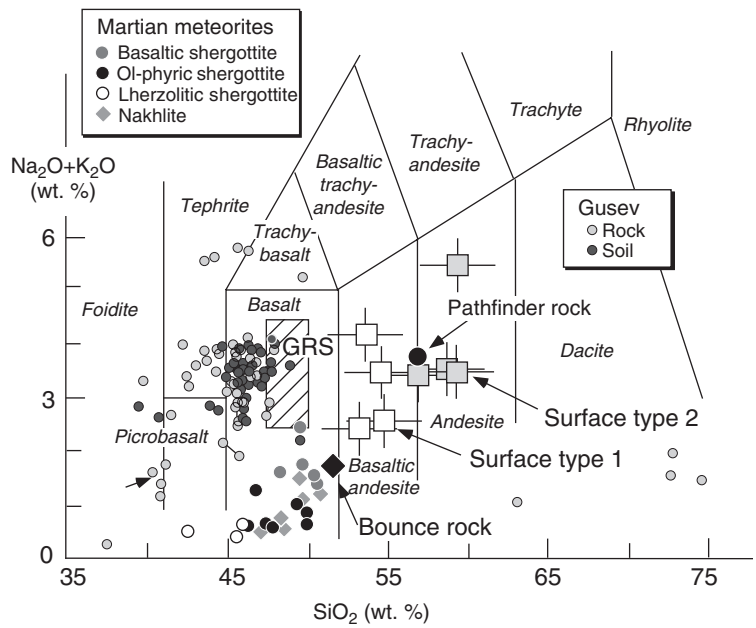

Fig. 13.17 Alkalis versus silica diagram used for geochemical classification of volcanic rocks. Martian meteorites, Gusev crater rocks and soils analyzed by the Spirit rover, and Bounce Rock analyzed by the Opportunity rover generally plot in the field of basalts, as does the average Mars Odyssey GRS analysis. Compositions derived from TES spectra (Surface Types 1 and 2) and the Mars Pathfinder dust-free rock plot in the basaltic andesite and andesite fields. After McSween *et al.* (2009).

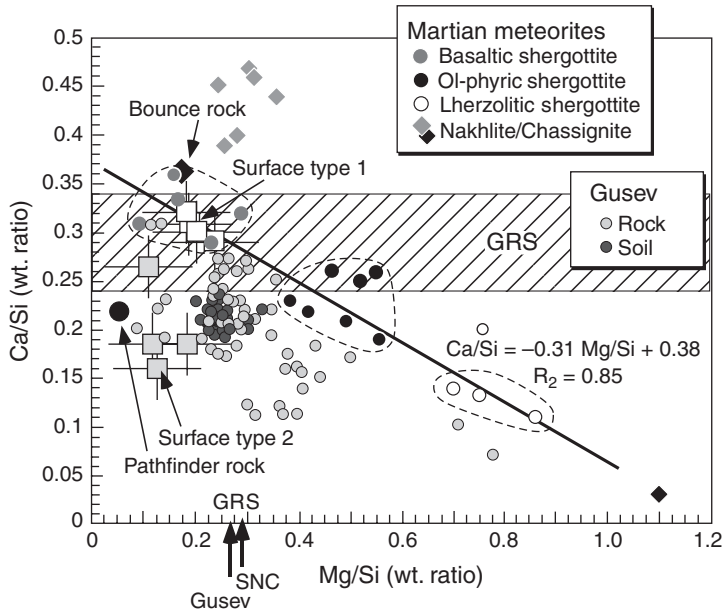

Fig. 13.18 **Ratios of Ca/Si and Mg/Si in various kinds of Mars rocks and soils. Shergottites form a linear trend. GRS measured calcium and silicon, but not magnesium. However, Mg/Si can be estimated from the intersection of the GRS Ca/Si line with the shergottite regression line (arrow labeled SNC) or from the average Mg/Si for Gusev rocks and soils (arrow labeled Gusev), which give nearly identical results. After McSween *et al.* (2009).**

processes that leached some other components and concentrated silica. The Pathfinder dust-free rock composition is also silica-rich and may represent an alteration rind on the rocks.

A plot of these compositions on a Ca/Si versus Mg/Si diagram is illustrated in Figure 13.18. A similar diagram has been used previously for geochemical classification of Martian meteorites (Ouri *et al.*, 2003). The various classes of shergottites (enclosed by dashed ovals) exhibit an inverse correlation between these ratios (Fig. 13.18). The nakhlites have higher Ca/Si, and the Gusev rocks and soils have lower Ca/Si ratios. GRS has provided data on calcium and silicon, and the average Ca/Si ratio and standard deviation are indicated by the cross-hatched field. Although GRS did not analyze magnesium, we can estimate the global Mg/Si ratio from the intersection of the GRS average Ca/Si ratio with the SNC regression line, or from the average Mg/Si of Gusev rocks and soils. Both methods give essentially the same results, as indicated by arrows at the bottom of the figure.

The FeO*/MgO (where * indicates total iron expressed as FeO) versus SiO_2 diagram (Fig. 13.19) is useful in discriminating various fractionation paths. Rocks plotting above the diagonal line show tholeiitic (TH) trends (nearly vertical black arrows, exhibited by dry magmas), whereas those plotting below the line show calc-alkaline (CA) trends (gray arrows, due to hydrous melting and fractionation). Virtually all the meteorites and Gusev data plot in the tholeiitic field. TES-derived compositions plot in the calc-alkaline field, but

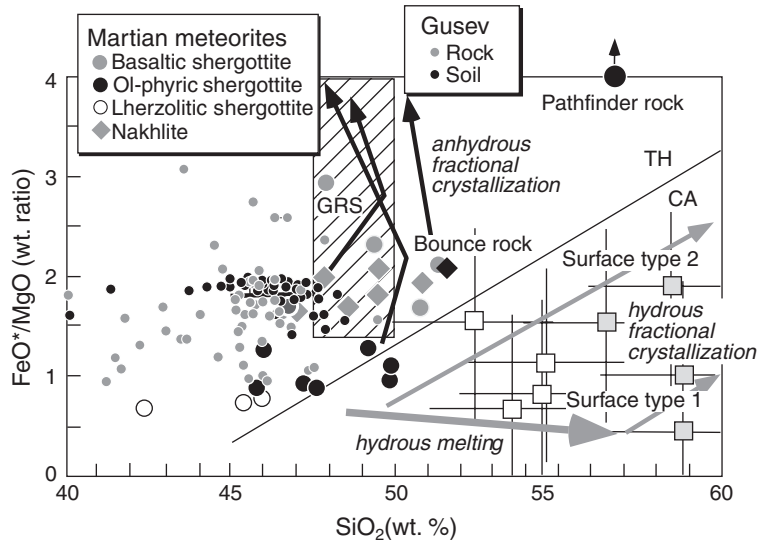

Fig. 13.19 Ratios of FeO* (total iron expressed as FeO) to MgO versus silica in Mars rocks and soils. A diagonal line separates tholeiitic (TH) from calc-alkaline (CA) rocks; tholeiitic magmas are anhydrous and calc-alkaline magmas are hydrous. All the Mars rocks plot in the tholeiitic field, as do GRS data (MgO was calculated from the Mg/Si ratio in Fig. 11.19). TES-derived data plot in the calc-alkaline field, but this is an artifact of alteration. After McSween *et al.* (2009).

this is apparently an artifact of weathering. Using the estimated Mg/Si ratio from Figure 13.18 and the GRS-measured iron contents, we can calculate the GRS FeO*/MgO ratio. The average value and standard deviation, indicated by the cross-hatched box, support the tholeiitic compositions.

Several global geochemical maps for specific elements analyzed by GRS (Boynton *et al.*, 2007, 2008) are illustrated in Figure 13.20. Differences in the abundances of silica and iron are relatively modest and consistent with a basaltic surface composition. Of particular interest is the global K/Th ratio map (Taylor *et al.*, 2007). These elements are both incompatible and thus should be fractionated together during igneous processes. However, potassium is mobile during aqueous weathering, whereas thorium is relatively immobile. Thus, unvarying K/Th ratios would normally be expected on a surface dominated by igneous rocks, and varying ratios would characterize a surface affected by chemical weathering. The K/Th ratio map for Mars indicates only modest variations, consistent with a basaltic surface.

Water, chemical weathering, and evaporites

Unlike the Moon, Mars has clearly had water on its surface, at least in the distant past. The amount of water in the Martian interior, which was presumably delivered to the surface by volcanic outgassing, has been controversial. Wänke and Dreibus (1988) proposed that Mars

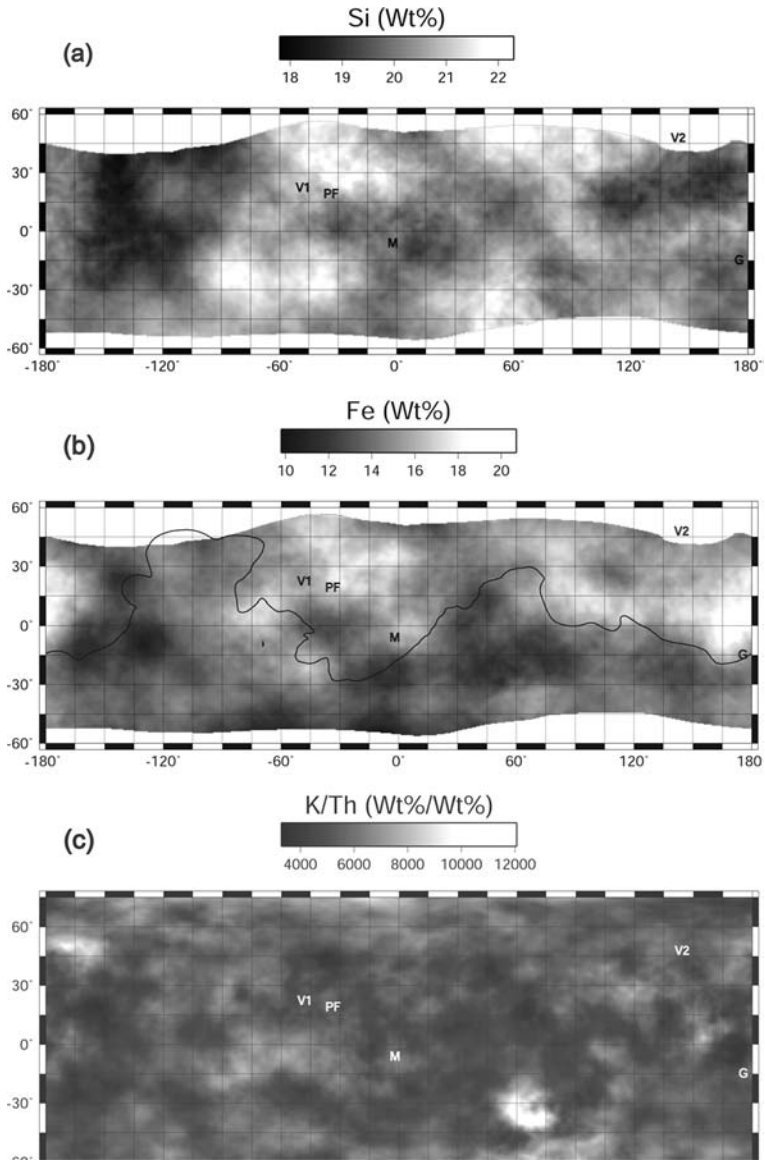

Fig. 13.20 **Global GRS maps of Mars, for (a) silicon, (b) iron, and (c) K/Th. Letters represent spacecraft landing sites: V1 and V2 Viking, PF Mars Pathfinder, M Merdiani (Opportunity), and G Gusev (Spirit). The line in (b) separates the southern highlands from the northern lowlands. White areas above 50° N and S were not analyzed.**

was very dry, based on the low water contents of Martian meteorites. However, McSween *et al*. (2001) suggested that several shergottites had lost significant quantities of water, based on concurrent loss of soluble trace elements.

Deuterium-enriched water in Martian meteorites (Leshin *et al*., 1996; Leshin, 2000) indicates that some water has been lost from the atmosphere, but the fate of most of the

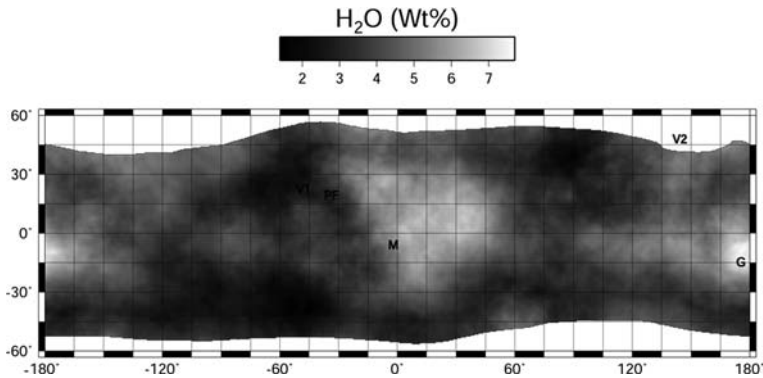

Fig. 13.21 Global GRS map of H, expressed as H_2O equivalent, on Mars. Symbols as in Fig. 13.20.

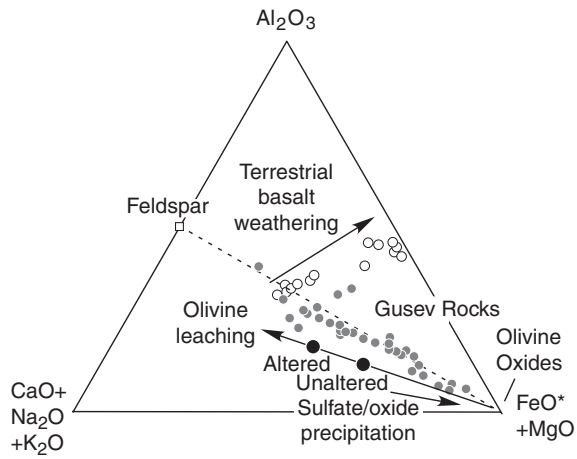

Fig. 13.22 Molar chemical diagram showing different weathering trends for terrestrial basalts (small black circles) and Martian basalts (gray circles), resulting from differences in acidity of fluids. Experiments (large black circles) demonstrate that olivine is leached under acid conditions. Modified from Hurowitz *et al.* (2006).

water that carved valleys and channels during the Noachian and early Hesperian is unclear. A GRS global map of hydrogen (Feldman *et al.*, 2002), expressed as equivalent H_2O and illustrated in Figure 13.21, provides information on the locations of water in the subsurface. Hydrogen concentrations at high latitudes are thought to reflect the presence of ice in the form of permafrost, whereas hydrogen near the equator might occur as OH in hydrous minerals.

Rocks analyzed by the Spirit rover in Gusev crater provide an interesting insight into Martian weathering reactions. This insight is provided by chemistry, as seen in Figure 13.22 (Hurowitz *et al.*, 2006). Unlike weathering of basalt on the Earth, which leaches soluble CaO, Na_2O, and K_2O while enriching the weathering profile in insoluble Al_2O_3 and Fe_2O_3,

weathered rocks on Mars form an array leading away from the FeO+MgO vertex. This difference is controlled by pH; Mars weathering occurs under acidic conditions, whereas terrestrial weathering occurs under neutral to basic conditions. Experiments conducted on the Mars Pathfinder basalt composition at low pH show preferential dissolution of olivine (Fig. 13.22). Weathered Gusev rocks also show some precipitation of iron oxide and iron sulfate.

Among the most interesting Martian data sets are rocks in Meridiani Planum analyzed by the Opportunity rover (Grotzinger *et al*., 2005; Ming *et al*., 2008). These ancient rocks are altered basaltic sandstones cemented by large quantities of salts and containing hematite concretions and possibly secondary silica. Interest in these rocks derives from the evidence they provide for evaporation processes on Mars. APXS measurements indicate large, varying proportions of sulfur and chlorine and modest amounts of bromine (Clark *et al*., 2005). Sulfates and halides formed by evaporation of acidic waters that had interacted with basalts (Tosca *et al*., 2005). An extended diagenetic history, with multiple episodes of cementation and dissolution, indicates a chemically evolving groundwater system (McLennan *et al*., 2005).

The occurrence of significant quantities of smectite clay minerals has been documented by spectral observations by instruments on the Mars Express and Mars Reconnaissance orbiters. Where mapped, these minerals appear to be concentrated in stratigraphically low deposits, probably of Noachian age. It has been suggested that clays formed early in Mars history, and that they were not stable during later periods (Bibring *et al*., 2005). Acidic groundwaters, as documented at Meridiani Planum and inferred from other sulfate-bearing units elsewhere on Mars, would inhibit the formation of clays. Although no geochemical data are yet available for clay-bearing sedimentary deposits, we can infer that aqueous chemical weathering occurred during early Mars history. Clay-bearing deposits are not obvious from global GRS maps and must be largely covered by basaltic lavas and sediments derived by their physical weathering. High proportions of highly soluble sulfates and chlorides in soils imply a climatic change from wet to arid in later Martian history.

Compositions of the Martian mantle and core

Geochemical models for the silicate portion of Mars (mantle plus crust, which is approximately equal to the mantle composition) are mostly based on, or constrained by SNC meteorites. One estimate (Wänke and Dreibus, 1988) was calculated from element ratios in SNCs, and two others (Lodders and Fegley, 1997; Sanloup *et al*., 1999) are combinations of various chondrite types in proportions that reproduce SNC oxygen isotope compositions. The composition of the Wänke–Dreibus Mars mantle is compared with the Earth's mantle in Figure 13.23. The Mars mantle is enriched in moderately volatile elements like manganese, sodium, potassium, and zinc. Based on SNC meteorites, at one time it was thought that the mantle was very different in composition from that of the Earth; however, newer data, such as MER analyses of nickel and magnesium in rocks and soils from Gusev crater (Fig. 13.24), indicate many similarities. Nevertheless, differences in volatile element

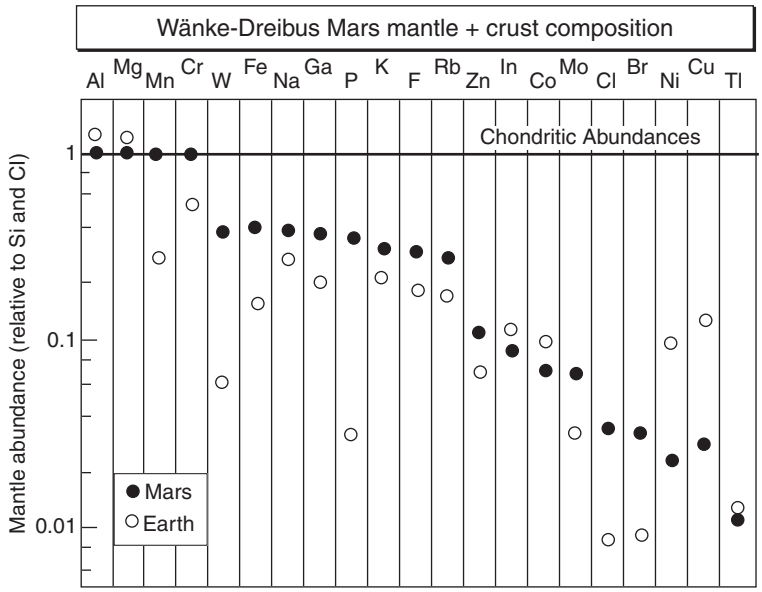

Fig. 13.23 Mars bulk silicate (mantle + crust) composition, estimated from Martian meteorites by Wänke and Dreibus (1988). This composition differs from the bulk silicate of Earth, because of differences in volatile element abundances and core differentiation.

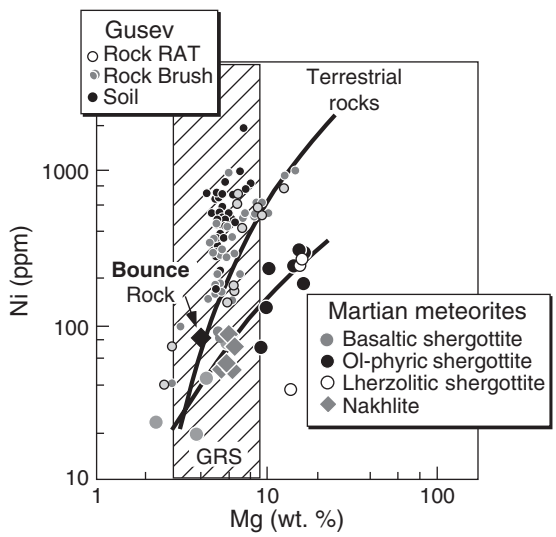

Fig. 13.24 Plot of nickel versus magnesium in Martian rocks and meteorites. GRS-estimated Mg content is also shown. After McSween *et al.* (2009).

abundances, as reflected in global K/Th, and total oxidized iron are distinct (Taylor *et al*., 2008), and several different mantle source regions are indicated by radiogenic isotopic compositions.

Estimates of the Mars core composition by the authors listed above suggest it is made of metal plus iron sulfide, the latter varying from 29 to 44 wt.%. Abundances of siderophile (tungsten, phosphorus, cobalt, molybdenum, nickel) and chalcophile (indium, copper) elements in the mantle (Fig. 13.23) are consistent with equilibrium between sulfide, metal, and mantle silicate at high temperature and pressure (Righter and Drake, 1996).

Geochemical evolution of Mars

Mars is more volatile-rich than Earth, reflecting a higher proportion of accreted volatile-bearing planetesimals. It is also more highly oxidized than Earth, so that twice as much of its iron has remained as Fe^{2+} in the mantle rather than in the metallic core. Wänke and Dreibus (1988) suggested that oxidation occurred during accretion, as water in accreted planetesimals reacted with iron metal.

Both short-lived (^{182}Hf–^{182}W, ^{146}Sm–^{142}Nd) and long-lived (^{87}Rb–^{87}Sr, ^{147}Sm–^{143}Nd, U–Pb, ^{176}Lu–^{176}Hf, ^{187}Re–^{187}Os) radiogenic isotope systems in Martian meteorites indicate early planetary differentiation, within a few tens of millions of years of accretion (Taylor *et al*., 2008, and references therein). Planetary differentiation on Mars produced a depleted mantle and a crust comprising ~4% of the planetary volume, a much greater proportion of crust than on Earth. It is likely that Mars, like the Moon, may have had an early magma ocean. Since its formation, the Martian mantle has been geochemically isolated, because there is no plate tectonics to recycle crust back into the mantle.

The crust of Mars is basaltic, with only small amounts of other rock compositions. Most volcanism was ancient but some eruptions, especially in Tharsis and Elysium, may extend to the present day.

Early on, water existed at least periodically on the Martian surface. The formation of clay minerals in the Noachian and precipitation of sulfates and chlorides in the Hesperian were consequences of this water. Some fraction of the water evaporated and was lost to space, as indicated by the high D/H ratios in SNCs. Other water was apparently sequestered at the poles or underground as permafrost. The surface of Mars is effectively dry now, and chemical weathering of crustal rocks is minimal.

Summary

The Moon and Mars have very different compositions and have had very different geologic histories. However, the geochemical techniques applied to both bodies are similar, and the results illustrate the power of chemical data in planetary exploration. Combinations of

laboratory analyses of meteorites or returned samples, sometimes coupled with *in situ* analyses by rovers, provide the most detailed geochemical information. Geochemical mapping by orbiting spacecraft provide global or regional geologic context for those analyses.

The compositions of the crusts of the Moon and Mars are distinct – one is dominated by feldspathic cumulates from an early magma ocean, and the other by basaltic lavas. Regional patterns reflect differences in subjacent mantle compositions. The compositions of the mantles and cores of these bodies can be constrained by chemical analyses of mantle-derived basalts. The interiors of both bodies have remained geochemically isolated, because of the absence of plate tectonics.

Having worked our way through the parts of the solar system for which we have significant cosmochemical or geochemical data, we will now see how what we have learned can constrain models for solar system formation.

Questions

1. Describe some analytical tools used on orbiting and landed spacecraft to analyze materials on the surface of the Moon and Mars.
2. Briefly describe the major groups of lunar rocks returned by Apollo astronauts and how they relate to groups determined from orbital measurements.
3. What are the major geochemical characteristics of the lunar mantle and crust?
4. How does the chemical composition of the Martian crust differ from that of the Moon?
5. How has water affected the surface of Mars?
6. What are the major geochemical characteristics of the Martian mantle and crust?

Suggestions for further reading

The following publications provide excellent summaries of the geologic and geochemical evolution of Mars:

Bell, J. (2008) *The Martian Surface: Composition, Mineralogy, and Physical Properties*. Cambridge: Cambridge University Press, 636 pp. This up-to-date book contains excellent chapters on chemical analyses by Pathfinder and MER APXS, Mars Odyssey GRS analyses, Martian meteorites, and geochemical interpretations of rocks and soils.

Carr, M. (2006) *The Surface of Mars*. Cambridge: Cambridge University Press, 307 pp.

Solomon, S. C., plus 16 coauthors (2005) New perspectives on ancient Mars. *Science*, **307**, 1214–1220.

These publications provide excellent summaries of the geologic evolution of the Moon:

Jolliff, B. L., Wieczorek, M. A., Shearer, C. K. and Neal, C. R., eds. (2006) *New Views of the Moon, Reviews in Mineralogy and Geochemistry* **60**, Washington, D.C.: Mineralogical Society of America and Geochemical Society.

Taylor, S. R. and McLennan, S. M. (2009) *Planetary Crusts: Their Composition, Origin and Evolution*. Cambridge: Cambridge University Press, 378 pp.

Wilhelms, D. E. (1987) *The Geologic History of the Moon*. U.S. Geological Survey Professional Paper 1348.

References

Bibring, J.-P., Langevin, Y., Gendrin, A. *et al*. (2005) Mars surface diversity as revealed by the OMEGA/Mars Express observations. *Science*, **307**, 1576–1581.

Binzel, R. P., Gaffey, M. J., Thomas, P. *et al*. (1997) Geologic mapping of Vesta from 1994 Hubble Space Telescope images. *Icarus*, **128**, 95–103.

Blewett, D. T., Lucey, P. G. and Hawke, B. R. (1997) Clementine images of the lunar sample-return stations: Refinement of FeO and TiO_2 mapping techniques. *Journal of Geophysical Research*, **102**, 16 319–16 325.

Boynton, W. V. plus 27 coauthors (2007) Concentration of S, Si, Cl, K, Fe, and Th in the low- and mid-latitude regions of Mars. *Journal of Geophysical Research*, **112**, E12S99, doi:10.1029/2007JE002887.

Boynton, W. V., Taylor, G. J., Karunatillake, S., Reedy, R. C. and Keller, J. M. (2008) Elemental abundances determined via the Mars Odyssey GRS. In *The Martian Surface: Composition, Mineralogy, and Physical Properties*, ed. Bell, J. F. Cambridge: Cambridge University Press, pp. 105–124.

Bruckner, J., Dreibus, G., Gellert, R. *et al*. (2008) Mars Exploration Rovers: Chemical composition by the APXS. In *The Martian Surface: Composition, Mineralogy, and Physical Properties*, ed. Bell, J. F. Cambridge: Cambridge University Press, pp. 58–101.

Clark, B. C., Baird, A. K., Weldon, R. J. *et al*. (1982) Chemical composition of Martian fines. *Journal of Geophysical Research*, **87**, 10 050–10 067.

Clark, B. C. plus 23 coauthors (2005) Chemistry and mineralogy of outcrops at Meridiani Planum. *Earth and Planetary Science Letters*, **240**, 73–94.

Elphic, R. C., Lawrence, D. J., Feldman, W. C. *et al*. (2002) Lunar Prospector neutron spectrometer constraints on TiO_2. *Journal of Geophysical Research*, **107** (E4), doi:10.1029/2000JE001460.

Feldman, W. C., Maurice, S., Lawrence, D. J. *et al*. (2001) Evidence for water ice near the lunar poles. *Journal of Geophysical Research*, **106** (E10), 23 231–23 251.

Feldman, W. C. plus 12 coauthors (2002) Global distribution of neutrons from Mars: results from Mars Odyssey. *Science*, **297**, 75–78.

Feldman, W. C., Mellon, M. T., Gasnault, O., Maurice, S. and Prettyman, T. H. (2008) Volatiles on Mars: Scientific results from the Mars Odyssey Neutron Spectrometer. In *The Martian Surface: Composition, Mineralogy, and Physical Properties*, ed. Bell, J. F. Cambridge: Cambridge University Press, pp. 125–148.

Foley, C. N., Economou, T. E., Clayton, R. N. *et al*. (2008) Martian surface chemistry: APXS results from the Pathfinder landing site. In *The Martian Surface: Composition, Mineralogy, and Physical Properties*, ed. Bell, J. F. Cambridge: Cambridge University Press, pp. 35–57.

Gellert, R., Rieder, R., Brückner, J. *et al*. (2006) The Alpha Particle X-Ray Spectrometer (APXS): results from Gusev crater and calibration report. *Journal of Geophysical Research*, **111**, E02S05, doi:10.1029/2005JE002555.

Giguere, T. A., Taylor, G. J., Hawke, B. R. and Lucey, P. G. (2000) The titanium contents of lunar mare basalts. *Meteoritics and Planetary Science*, **35**, 193–200.

Ghosh, A. and McSween, H. Y. (1998) A thermal model for the differentiation of asteroid 4 Vesta, based on radiogenic heating. *Icarus*, **134**, 187–206.

Grotzinger, J. P. plus 19 coauthors (2005) Stratigraphy and sedimentology of a dry to wet eolian depositional system, Burns formation, Meridiani Planum, Mars. *Earth and Planetary Science Letters*, **240**, 11–72.

Halliday, A. N. (2004) The origin and earliest history of the Earth. In *Treatise on Geochemistry, Vol. 1. Meteorites, Comets and Planets*, ed. Davis, A. M., New York: Elsevier, pp. 509–557.

Hamilton, V. E., Wyatt, M. B., McSween, H. Y. and Christensen, P. R. (2001) Analysis of terrestrial and Martian volcanic compositions using thermal emission spectroscopy: 2. Application to Martian surface spectra from the Mars Global Surveyor thermal emission spectrometer. *Journal of Geophysical Research*, **106**, 14,733–14,746.

Hartmann, W. K. *et al*., editors (1986) *Origin of the Moon*. Lunar and Planetary Institute.

Hiesinger, H. and Head, J. W. (2006) New views of lunar geoscience: an introduction and overview. In *New Views of the Moon, Reviews in Mineralogy and Geochemistry* **60**, eds. Jolliff, B. L., Wieczorek, M. A., Shearer, C. K. and Neal, C. R. Washington, D.C.: Mineralogical Society of America and Geochemical Society, pp. 1–18.

Hurowitz, J. A., McLennan, S. M., Tosca, N. J. *et al*. (2006) *In situ* and experimental evidence for acidic weathering of rocks and soils on Mars. *Journal of Geophysical Research*, **111**, E02S19, doi:10.1029/2005JE002515.

Jolliff, B. L., Gillis, J. J., Haskin, L. A., Korotev, R. L. and Weiczorek, M. A. (2000) Major lunar crustal terranes: Surface expressions and crust-mantle origins. *Journal of Geophysical Research*, **105** (E2), 4197–4216.

Keil, K. (2002) Geological history of asteroid 4 Vesta: The "smallest terrestrial planet." In *Asteroids III*, eds. Bottke, W., Cellino, A., Paolicchi, P. and Binzel, R. P. Tucson: University of Arizona Press, pp. 473–585.

Korotev, R. L., Jolliff, B. L., Zeigler, R. A., Gillis, J. J. and Haskin, L. A. (2003) Feldspathic lunar meteorites and their implications for compositional remote sensing of the lunar surface and the composition of the lunar crust. *Geochimica et Cosmochimica Acta*, **67**, 4895–4923.

Lawrence, D. J., Feldman, W. C., Barraclough, B. L. *et al*. (1998) Global elemental maps of the Moon: the Lunar Prospector gamma-ray spectrometer. *Science*, **281**, 1484–1489.

Leshin, L. A. (2000) Insights into Martian water reservoirs from analysis of Martian meteorite QUE 94201. *Geophysical Research Letters*, **27**, 2017–2020.

Leshin, L. A., Epstein, S. and Stolper, E. M. (1996) Hydrogen isotope geochemistry of SNC meteorites. *Geochimica et Cosmochimica Acta*, **60**, 2635–2650.

Lodders, K. (1998) A survey of shergottite, nakhlite and chassigny meteorites whole-rock compositions. *Meteoritics and Planetary Science*, **33**, A183–A190.

Lodders, K. and Fegley, B. (1997) An oxygen isotope model for the composition of Mars. *Icarus*, **126**, 373–394.

Lucey, P. G., Blewett, D. T. and Hawke, B. R. (1998) Mapping the FeO and TiO_2 content of the lunar surface with multispectral imagery. *Journal of Geophysical Research*, **103**, 3679–3699.

Lucey, P. G., plus 17 coauthors (2006) Understanding the lunar surface and space-Moon interactions. In *New Views of the Moon, Reviews in Mineralogy and Geochemistry* **60**, eds. Jolliff, B. L., Wieczorek, M. A., Shearer, C. K. and Neal, C. R. Washington, D.C.: Mineralogical Society of America and Geochemical Society, 83–219.

McLennan, S. M. plus 31 coauthors (2005) Provenance and diagenesis of the evaporite-bearing Burns formation, Meridiani Planum, Mars. *Earth and Planetary Science Letters*, **240**, 95–121.

McSween, H. Y. (2008) Martian meteorites as crustal samples. In *The Martian Surface: Composition, Mineralogy, and Physical Properties*, ed. Bell, J. F. Cambridge: Cambridge University Press, pp. 383–395.

McSween, H. Y. and 14 coauthors (1999) Chemical, multispectral and textural constraints on the composition and origin of rocks at the Mars Pathfinder landing site. *Journal of Geophysical Research*, **104**, 8679–8715.

McSween, H. Y., Grove, T. L., Lentz, R. C. F. *et al*. (2001) Geochemical evidence for magmatic water within Mars from pyroxenes in the Shergotty meteorite. *Nature*, **409**, 487–490.

McSween, H. Y., Grove, T. L. and Wyatt, M. B. (2003) Constraints on the composition and petrogenesis of the Martian crust. *Journal of Geophysical Research*, **108** (E12), 5135, doi:10.1029/2003JE002175.

McSween, H. Y., Taylor, G. J. and Wyatt, M. B. (2009) Elemental composition of the Martian crust. *Science*, **324**, 736–739.

Ming, D. W., plus 16 coauthors (2006) Geochemical and mineralogical indicators for aqueous processes in the Columbia Hills of Gusev crater, Mars. *Journal of Geophysical Research*, **111**, E02S12, doi:10.1029/2005JE002560.

Ming, D. W., Morris, R. V. and Clark, B. C. (2008) Aqueous alteration on Mars. In *The Martian Surface: Composition, Mineralogy, and Physical Properties*, ed. Bell, J. F. Cambridge: Cambridge University Press, pp. 519–540.

Mittlefehldt, D. W. (2004) Achondrites. In *Treatise on Geochemistry, Volume 1. Meteorites, Comets, and Planets*, ed. Davis, A. M. Oxford: Elsevier, pp. 291–324.

Mittlefehldt, D. W., McCoy, T. J., Goodrich, C. A. and Kracher, A. (1998) In *Planetary Materials, Reviews in Mineralogy* **36**, ed. Papike, J. J. Washington, D.C.: Mineralogical Society of America, pp. 4–1 to 4–195.

Ouri, Y., Shirari, N. and Ebihara, M. (2003) Chemical composition of Yamato (Y)980459 and Y000749: Neutron-induced prompt gamma-ray analysis study. *Antarctic Meteorite Research*, **16**, 80–93.

Pahlevan, K. and Stevenson, D. J. (2007) Equilibrium in the aftermath of the lunar-forming giant impact. *Earth and Planetary Science Letters*, **262**, 438–449.

Papike, J. J., Ryder, G. and Shearer, C. K. (1998) Lunar samples. In *Planetary Materials, Reviews in Mineralogy* **36**, ed. Papike, J. J. Washington, D.C.: Mineralogical Society of America, pp. 5–1 to 5–234.

Prettyman, T. H., Hagerty, J. J., Elphic, R. C. *et al*. (2006) Elemental composition of the lunar surface: analysis of gamma ray spectroscopy data from Lunar Prospector. *Journal of Geophysical Research*, **111**, E12007, doi:10.1029/2005JE002656.

Rieder, R., Gellert, R., Anderson, R. C. *et al*. (2004) Chemistry of rocks and soils at Meridiani Planum from the alpha particle X-ray spectrometer. *Science*, **306**, 1746–1749.

Righter, K. and Drake, M. J. (1996) Core formation in the Earth's Moon, Mars and Vesta. *Icarus*, **124**, 513–529.

Righter, K. and Drake, M. J. (1997) A magma ocean on Vesta: core formation and petrogenesis of eucrites and diogenites. *Meteoritics and Planetary Science*, **32**, 929–944.

Rogers, A. D. and Christensen, P. R. (2007) Surface mineralogy of Martian low-albedo regions from MGS-TES data: implications for upper crustal evolution and surface alteration. *Journal of Geophysical Research*, **112**, E01003, doi:10.1029/2006JE002727.

Russell, C. T., plus 20 coauthors (2006) Dawn Discovery mission to Vesta and Ceres: present status. *Advanced Space Research*, **38**, 2043–2048.

Ryder, G. (1991) Lunar ferroan anorthosites and mare basalt sources: the mixed connection. *Journal of Geophysical Research*, **118**, 2065–2068.

Sanloup, C., Jambon, A. and Gillet, P. (1999) A simple chondritic model of Mars. *Earth and Planetary Science Letters*, **112**, 43–54.

Shearer, C. K., plus 15 coauthors (2006) Thermal and magmatic evolution of the Moon. In *New Views of the Moon, Reviews in Mineralogy and Geochemistry* **60**, eds. Jolliff, B. L., Wieczorek, M. A., Shearer, C. K. and Neal, C. R. Washington, D.C.: Mineralogical Society of America and Geochemical Society, pp. 365–518.

Taylor, G. J., Warren, P., Ryder, G., Delano, J. and Pieters, C. (1991) Lunar rocks. In *Lunar Sourcebook: A User's Guide to the Moon*, eds. Heiken, G. H., Vaniman, D. T. and French, B. M. Cambridge: Cambridge University Press, pp. 183–284.

Taylor, G. J., plus 26 coauthors (2007) Variations in K/Th on Mars. *Journal of Geophysical Research*, **111**, E03S06, doi:10.1029/2006JE002676.

Taylor, G. J., McLennan, S. M., McSween, H. Y., Wyatt, M. B. and Lentz, R. C. F. (2008) Implications of observed primary lithologies. In *The Martian Surface: Composition, Mineralogy, and Physical Properties*, ed. Bell, J. F. Cambridge: Cambridge University Press, pp. 501–518.

Taylor, S. R., Pieters, C. M. and MacPherson, G. J. (2006a) Earth-Moon system, planetary science, and lessons learned. In *New Views of the Moon, Reviews in Mineralogy and Geochemistry* **60**, eds. Jolliff, B. L., Wieczorek, M. A., Shearer, C. K. and Neal, C. R. Washington, D.C.: Mineralogical Society of America and Geochemical Society, pp. 657–704.

Taylor, S. R., Taylor, G. J. and Taylor, L. A. (2006b) The Moon: a Taylor perspective. *Earth and Planetary Science Letters*, **70**, 5904–5918.

Thomas, P. C., Binzel, R. P., Gaffey, M. J. *et al*. (1997) Impact excavation on asteroid 4 Vesta: Hubble Space Telescope results. *Science*, **277**, 1492–1495.

Tosca, N. J., McLennan, S. M., Clark, B. C. *et al*. (2005) Geochemical modeling of evaporation processes on Mars: insight from the sedimentary record at Meridiani Planum. *Earth and Planetary Science Letters*, **240**, 122–148.

Treiman, A. H., Jones, J. H. and Drake, M. J. (1987) Core formation in the shergottite parent body and comparison with the Earth. *Journal of Geophysical Research*, **92**, E627–E632.

Usui, T. and McSween, H. Y. (2007) Geochemistry of 4 Vesta based on HED meteorites: prospective study for interpretation of gamma-ray and neutron spectrometer for the Dawn mission. *Meteoritics and Planetary Science*, **42**, 255–269.

Wadhwa, M., Srinivasan, G. and Carlson, R. W. (2006) Timescales of planetesimal differentiation in the early solar system. In *Meteorites and the Early Solar System II*, eds. Lauretta, D. S. and McSween, H. Y., Jr. Tucson: University of Arizona Press, pp. 715–731.

Wänke, H. and Dreibus, G. (1988) Chemical composition and accretion history of terrestrial planets. *Philosophical Transactions of the Royal Society of London*, **A325**, 545–557.

Wänke, H., Bruckner, J., Dreibus, G., Rieder, R. and Ryabchikov, I. (2001) Chemical composition of rocks and soils at the Pathfinder site. *Space Science Reviews*, **96**, 317–330.

Warren, P. H. (1993) A concise compilation of petrologic information on possibly pristine nonmare Moon rocks. *American Mineralogist*, **78**, 360–376.

Warren, P. H. and Wasson, J. T. (1977) Pristine nonmare rocks and the nature of the lunar crust. *Proceedings of the 8th Lunar Science Conference*, 2215–2235.

Weichert, U., Halliday, A. N., Lee, D-C., Snyder, G. A. *et al*. (2001) Oxygen isotopes and the Moon-forming giant impact. *Science*, **294**, 345–348.

Wieczorek, M. A., plus 15 coauthors (2006) The constitution and structure of the lunar interior. In *New Views of the Moon, Reviews in Mineralogy and Geochemistry* **60**, eds. Jolliff, B. L., Wieczorek, M. A., Shearer, C. K. and Neal, C. R. Washington, D.C.: Mineralogical Society of America and Geochemical Society, pp. 221–364.

Wyatt, M. B., Hamilton, V. E., McSween, H. Y., Christensen, P. R. and Taylor, L. R. (2001) Analysis of terrestrial and Martian volcanic compositions using thermal emission spectroscopy: 1. Determination of mineralogy, chemistry, and classification strategies. *Journal of Geophysical Research*, **106**, 14,711–14,732.

14 Cosmochemical models for the formation of the solar system

Overview

Cosmochemistry places important constraints on models for the origin of the solar nebula and the formation and evolution of planets. We explore nebula constraints by defining the thermal conditions under which meteorite components formed and examine the isotopic evidence for interaction of the nebula with the ISM and a nearby supernova. We consider how planetary bulk compositions are estimated and how they are used to understand the formation of the terrestrial and giant planets from nebular materials. We review the differentiation of planets, focusing especially on the Earth. We also consider how orbital and collisional evolution has redistributed materials formed in different thermal and compositional regimes within the solar system.

Constraints on the nebula

Understanding the formation of the solar system requires that we delve into processes for which there are no counterparts in terrestrial experience. Grand models for the formation and evolution of the solar nebula are mostly exercises in the physics of gravitational collapse and orbital mechanics. However, cosmochemistry imposes critical constraints on nebular conditions, events, and chronology. In this chapter, we consider how astrophysical models for the formation of the Sun and its accretion disk can be reconciled with cosmochemistry. Theories about how the planets were assembled in the nebula are likewise dominated by physical models of accretion, but cosmochemistry provides information about the nature of precursor materials and the timescales for planet assembly and differentiation. In this chapter we focus on chemical processes and fractionations that occurred during and after the formation of the terrestrial and giant planets and led to their compositional diversity. We will also discuss how orbital and collisional evolution has changed the locations and distributions of planets, which complicates discerning spatial cosmochemical patterns.

From gas and dust to Sun and accretion disk

Stars form when dense regions of cold molecular clouds undergo gravitational collapse. In dense molecular cloud cores, the temperature is in the order of 10–20 K and the gas density

is in the order of 10^6 particles per cm^3. Under these conditions, the gas phase consists mostly of molecular hydrogen, helium, and a few other very volatile compounds, while the rest of the atoms are in the solid phase as dust and ice. The dust includes mineral grains that formed in the atmospheres of dying stars, some of which we have identified as presolar grains, along with amorphous dust formed through many cycles of evaporation by shock waves and UV light and by recondensation under non-equilibrium conditions in interstellar space.

The process of star formation takes on the order of a few million years. This time scale is constrained both by astronomical observations and by the chronology of early solar system materials (meteorites). The stages of star formation were discussed in Chapter 9 and illustrated in Figure 9.7. A majority of stars form as binary systems, which makes the Sun somewhat unusual. Most stars, perhaps 70–90%, form in regions of cluster star formation where thousands of stars form approximately simultaneously. The star-forming region in Orion is a classic example of such an environment. During cluster star formation, the intense radiation generated by the first massive stars to form opens up a bubble of low-density hot gas around the stars. The radiation drives a shock front into the molecular cloud, which may trigger additional star formation. As the shock front overruns these newly forming systems, especially dense regions containing the protostars are left behind, first as "pillars" of molecular gas still connected to the main cloud, and eventually as evaporating gaseous globules (EGGs). It is this sequence of events that accounts for the spectacular images of molecular clouds such as that shown in Figure 14.1. The EGGs then evaporate, revealing the new stellar system. Shortly thereafter, the massive star explodes as a supernova, dispersing the surrounding cloud further and generally terminating star formation in the local region. But farther away, as the expanding supernova bubble slows down by piling up molecular cloud material ahead of the expanding shock front, new dense regions form that can initiate another round of star formation.

Based on the probabilities, we might infer that the Sun originated in such a setting of cluster star formation. Cosmochemistry provides ways to test this idea. As discussed in Chapter 9, the short-lived radionuclides in the early solar system carry a record of nucleosynthesis in the galaxy and in the immediate environment where the solar system formed. The abundances of rapidly decaying ^{41}Ca, ^{36}Cl, ^{26}Al, and ^{60}Fe in the early solar system were much too high to have been inherited from the interstellar medium. Production of these nuclides just before or during solar system formation is required. Even in the early days just after the discovery of ^{26}Al (Lee *et al*., 1977), a supernova was recognized as a strong candidate for its source. Cameron and Truran (1977) proposed a model in which the expanding shock front from a nearby supernova explosion compressed the gas and dust in the Sun's parent molecular cloud and triggered gravitational collapse, simultaneously seeding the solar system with newly synthesized material. The discovery that CAIs are ^{16}O rich compared to most solar system material (Clayton *et al*., 1973, 1977) and the first isotope anomalies in heavy elements discovered in CAIs (Wasserburg *et al*., 1977; McCulloch and Wasserburg, 1978a, 1978b) were thought to be explained by this model. Stellar sources of various kinds have been considered since that time, with supernova and AGB stars getting the most attention.

The discussion changed with the discovery that the short-lived radionuclide ^{10}Be was abundant in CAIs (McKeegan *et al*., 2000). Because ^{10}Be can only be produced by particle

Fig. 14.1 Hubble Space Telescope image of gas and dust in the star-forming region of the Carina nebula. A massive star to the upper left is evaporating the surrounding molecular cloud, leaving pillars of gas pointing at the star. Dense knots of cloud material are evaporating gas globules (EGGs) containing new stellar systems. The bright star in the center is a foreground star not associated with the molecular cloud.

irradiation and not by stellar nucleosynthesis, serious attention was given to the idea that all of the short-lived nuclides might have been produced by irradiation in the nebula. This idea had been explored in the late 1970s to explain the presence of ^{26}Al, but had been abandoned because the conditions inferred for the solar nebula at that time did not permit the high fluxes of high-energy particles required to make ^{26}Al, and the irradiation as modeled should have produced huge isotopic anomalies in other elements that were not observed. But a new model for production of CAIs close to the Sun, known as the X-wind model (Shu *et al.*, 1996; see below), provided a way to get the high particle fluxes required. Gounelle *et al.* (2001) formulated an energetic particle irradiation model that reproduced the relative initial abundances of ^{10}Be, ^{41}Ca, ^{26}Al, and even ^{53}Mn in CAIs. However, their calculations depend on special assumptions about target chemistry and rather extreme conditions for the energy

and composition of solar cosmic rays. The discovery that ^{60}Fe was much more abundant in the early solar system than previously thought (Tachibana and Huss, 2003) changed the game again because ^{60}Fe cannot be made by irradiation. If a stellar source is required for ^{60}Fe, then that source is likely to have contributed other short-lived radionuclides.

A model consistent with the observations is that most of the ^{41}Ca, ^{36}Cl, ^{26}Al, and all of the ^{60}Fe in the early solar system were contributed by a stellar source, most likely a nearby supernova of mass >20 $M_{\odot}$. A supernova is indicated because it can more efficiently produce ^{60}Fe, and the higher-mass supernova is indicated because it may avoid the overproduction of actinides. The ^{10}Be and some of the ^{41}Ca, ^{36}Cl, and perhaps even some of the ^{26}Al and ^{53}Mn were produced by particle irradiation in the solar system. The requirement for a high particle flux in the region where CAIs formed constrains the radiation environment of the early solar system. The longer-lived radioactive nuclides were likely inherited from the interstellar medium. The apparent requirement that a supernova produced the short-lived nuclides supports the inference from probabilities that the Sun formed in a region of cluster star formation. Debate now centers on how the short-lived nuclides could have gotten into the early solar system from the stellar source.

The original supernova trigger model by Cameron and Truran (1977) proposed that the short-lived radionuclides were injected into the parent molecular cloud by the supernova that triggered the gravitational collapse of the solar system. Over the years, increasingly detailed models have tried to simulate this, without much success. The problem is that extremely hot gas, like that behind an expanding supernova shock, does not mix with cold molecular cloud gas. The two regimes interact across a shock front, and it is easier to assimilate the cold gas into the hot region than the other way around. For supernova ejecta to efficiently mix into a molecular cloud, the gas must cool, and the characteristic time scale for such cooling is a million years. Models have successfully gotten some supernova material into a collapsing cloud, but the range of conditions where this occurred was extremely limited.

A recent model suggests that the way to get around the mixing problem is to inject the short-lived nuclides in the form of dust directly into the already-formed accretion disk (Ouellette *et al*., 2005). The model builds on the picture described above where the first massive stars trigger formation of additional stars and then uncover them by evaporating the surrounding molecular material, after which the massive star explodes as a supernova, pummeling the newly formed star systems with fast-moving gas and dust ejecta (Fig. 14.2). Once the protostar and accretion disk have formed, they are too dense to be evaporated by the supernova ejecta. Dust in the ejecta goes through the bounding shock and into the newly formed system. Although the dust evaporates in the bounding shock, it deposits its atoms into the accretion disk and thus seeds the disk with short-lived nuclides from the supernova. Numerical models seem to show that this works, but the probability for the right conditions to occur is again low.

Another idea under investigation can be labeled “self enrichment” of the molecular cloud. The idea uses the observation that in a giant molecular cloud, serial star formation may occur, where the massive stars in the first batch of stars to form explode as supernova and trigger a second round of star formation, the massive stars of which explode and trigger yet another round of star formation. As each supernova explodes, it dumps short-lived nuclides

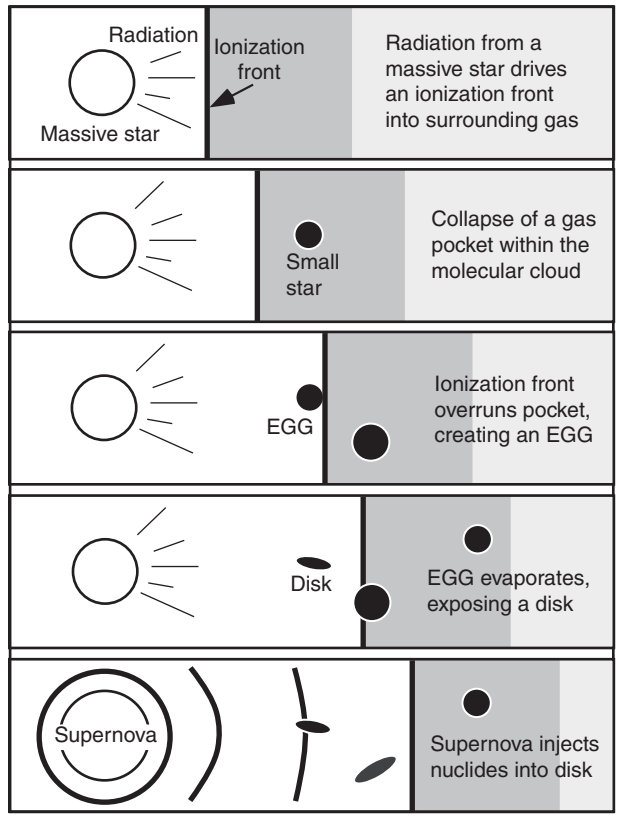

Fig. 14.2 **Sequence of events (top to bottom) affecting low-mass stars like our Sun, formed in the vicinity of high-mass stars within molecular clouds. After Hester and Desch (2005).**

into the interstellar medium that can be mixed into the surrounding molecular cloud on few-million-year time scales. If this happens repeatedly, the abundances of the short-lived nuclides will increase throughout the cloud. If the solar system formed late, then it would have inherited high abundances of the short-lived nuclides. While this idea is attractive, the predictions of the model in detail do not match the observations very well. Because the time scale for mixing newly synthesized material into a dense molecular cloud is at least a few million years, the abundances of ^{41}Ca and ^{36}Cl ($t_{1/2}$ = 1–3 × 10^5 years) would be orders of magnitude lower than inferred for the early solar system (see Chapter 9 and Fig. 9.5), even if mixing times were at the short end of the range of possible mixing times.

Although additional work clearly is required to sort out the details, it seems likely that a supernova was involved in the formation of the solar system and that the Sun originated in a region of cluster star formation. One avenue of future work will be to investigate the potential contributions to stable isotopes from a late supernova. It is difficult to establish the level of such a contribution from observations because there are no labels on the atoms of stable isotopes produced in the last supernova as there are for the short-lived radioactive isotopes. It might be possible to infer the contribution by comparing solar system

abundances with the composition of the galaxy in the solar neighborhood at ~4.57 Ga. This will require a major improvement in our knowledge of galactic abundances, but based on the amazing things we have learned to date, there is no reason to believe that we cannot eventually get the required information.

Temperatures in the accretion disk

By the late 1960s it was almost universally accepted that the inner solar system went through a hot nebula stage where all pre-existing solids had evaporated. This conclusion was based on modeling by Cameron (1962) that showed very high temperatures in the disk and on the conclusion from isotope measurements that all matter that scientists had access to had the same isotopic compositions (previously identified isotopic anomalies had all been shown to be experimental artifacts). From the late 1960s to the early 1990s, most cosmochemical data was interpreted in terms of a hot solar nebula. However, even in the early days, there were hints that this model was not correct. Reynolds and Turner (1964) identified isotopic anomalies in xenon that could not be explained by known processes operating on a homogeneous composition in the solar system. Black and Pepin (1969) identified a neon component consisting of nearly pure ^{22}Ne, which they called Ne-E, that they attributed to decay of short-lived ^{22}Na ($t_{1/2}$ = 2.6 years). Because of this short half-life, they proposed that Ne-E was probably located in a carrier that condensed in the atmosphere of a dying star where ^{22}Na was produced. Then came the discovery of mass-independent oxygen isotopic variations in chondrites (Clayton *et al*., 1973, 1977). In the years that followed, isotopic anomalies that could not be explained in the context of a hot solar nebula turned up with increasing regularity. By the mid 1980s, new nebula models showed that the accretion disk at the radius of the asteroid belt probably was never hot enough to vaporize all solids. Then in the late 1980s, presolar grains were discovered (Lewis *et al*., 1987), and by 1990 they were known to be present in all classes of primitive chondrites (Huss, 1990). The hot solar nebula model that had appeared to explain so much was in serious trouble.

Can a hot solar nebula be reconciled with the observations summarized above? Presolar grains are located in the matrix material of the chondrites, material that was never melted. One possibility is that the presolar grains (and much of the matrix itself) might be a late addition to the region where chondrites formed. Perhaps they were added after the high temperatures that produced the volatility fractionations and the transient events that produced the chondrules had subsided. The main problem with this idea is that the presolar grains in each meteorite class record a heating event that closely tracks the event that depleted volatile elements in the bulk meteorites. While the two events for each class could have been separated in time (to allow the nebula to cool), it is more plausible that the presolar grains and the bulk compositions record the same events. Even if the late addition did solve the problem with the presolar grains, it does not address the isotopic anomalies found in both high-temperature components of chondrites, such as CAIs, and in bulk meteorites, including differentiated bodies. Bulk isotopic anomalies in titanium,

molybdenum, ruthenium and other elements in both chondrites and differentiated meteorites (Dauphas *et al*., 2002a, 2002b; Trinquier *et al*., 2009) show that the bulk nebular material was not homogenized on an atomic scale. So it does not appear that the hot solar nebula model can be reconciled with the observations.

How can we then account for the large number of observations that appear to be explained by a hot solar nebula? For example, what about the idea that all of the materials to which we have access seem to have formed from the same well-mixed isotopic reservoir? Everything that happens to matter after it is ejected from stars works to homogenize its composition. Dust and gas from a wide variety of sources are mixed by turbulence, stellar winds, and supernova explosions. If dust grains are evaporated by supernova shocks, the atoms are scattered and likely recondense along with atoms with completely different histories as amorphous material or into ices. By the time the solar system formed, its materials were likely very well mixed, although individual grains that had not evaporated would still be isotopically and chemically anomalous. Within the solar system, any process that melts a representative sample of this well-mixed material will be isotopically very similar. This brings up two questions: (1) How well can we measure the isotopic compositions of different materials? The better we get at measuring, the more we find isotopic anomalies that were previously too small to detect. (2) How large a sample is required for it to be representative? This question feeds back on question 1, because the larger the sample, the better it will approximate the whole, and the better we measure, the better we can detect when it does not. The answer to this question may also depend on which element we are considering. A major element may be easy to sample representatively, while a trace element may require a lot of material to get a representative sample because of where the element is sited. Overall, then, the observations are consistent with formation of most solar-system objects out of processed, but not completely evaporated, molecular cloud material. The close similarity between the isotopic compositions of most objects does not require a hot solar nebula.

Let us consider another example. The bulk chemical compositions of high-temperature materials in chondrites, that is, the CAIs, AOAs, and chondrules, appear to follow approximately the calculated path for solids arising from equilibrium condensation (Fig. 14.3) (MacPherson *et al*., 2005). As we discussed in Chapter 7, equilibrium condensation is an end member of a continuum of volatility-based gas–solid fractionation processes. The equilibrium calculations tell us, to a first approximation, what the outcome of all of these processes is likely to look like. For example, moving from an equilibrium condensation regime to a regime where kinetic fractionations dominate is not going to make a CAI composition volatile. It might raise the temperature for complete evaporation of moderately volatile elements, but it will not make them less volatile than refractory elements. So general agreement with the prediction of equilibrium calculations is to be expected, almost independently of the details of the actual process that took place. Also, the precursors of CAIs, AOAs, and chondrules could have formed in a wide variety of places, both within and outside of the solar system, under conditions that ranged from near-equilibrium (in a stellar atmosphere or during a transient high-temperature event in the nebula, for example) to very far from equilibrium. Thus, Figure 14.3 does not provide a compelling argument that equilibrium condensation in a hot solar nebula controlled the

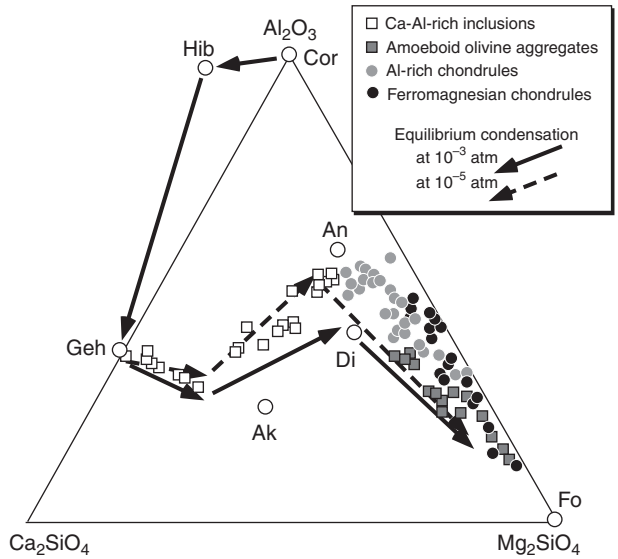

Fig. 14.3 **Bulk chemical compositions of CAIs, AOAs, and chondrules, compared to trends for calculated total condensed solids formed by equilibrium condensation of a hot solar gas at two different pressures. Condensed minerals are corundum (Cor), hibonite (Hib), end members of melilite series gehlenite (Geh) and akermanite (Ak), anorthite (An), diopside (Di), and forsterite (Fo). Modified from MacPherson *et al.* (2005).**

compositions of these objects. We already discussed in Chapter 7 how the heating of molecular cloud dust could explain the differences in volatile depletions and mixtures of presolar grains among chondrite classes. Other observations once thought to require equilibrium condensation have similar explanations. So, while there is clear evidence for transient high-temperature events affecting inner solar system materials, there is no compelling evidence recorded in the meteorites or terrestrial planets of a global hot stage when the pre-existing solids were evaporated.

So how hot was the solar nebula? There is a need for new models of the Sun and accretion disk that take into account new astronomical observations, new physical understanding, and the tremendous improvement in computing power that we have seen over the last decade. Current models indicate that during the main accretion stage of the Sun, temperatures at the midplane of the accretion disk were likely hot enough to vaporize silicates within a few AU from the star (e.g. Humayun and Cassen, 2000), but this high-temperature phase was short-lived and, as matter moved through the disk and accreted onto the Sun, the temperature in the disk dropped. According to one model, the temperature at 2 AU would have dropped below 1000 K within ~20 000 years of the start of accretion (Gammie and Johnson, 2005). Because matter was moving inward through the disk to accrete onto the protostar, it is unlikely that material from the high-temperature epoch would be a major component of the material in the asteroid belt. Low ambient temperatures are consistent with the widespread survival of isotopic anomalies in meteorite components and bulk meteorites and of presolar grains in primitive chondrites.

Localized heating: nebular shocks and the X-wind model

Chondrules comprise the major portion of most chondrites, the most abundant type of meteorites. If the achondrites and terrestrial planets formed from chondrite-like precursors, then much, perhaps most of the solid matter in the inner solar system once existed as chondrules. Even if chondrules were restricted to the chondrites, the process that formed them was important in that region. The origin of chondrules is an important unsolved problem in cosmochemistry. Chondrules formed in the Sun's accretion disk through some sort of transient flash-heating event(s). Some CAIs apparently also were melted in the disk. What was the process (or processes) that melted the chondrules and CAIs? Whatever it was, it dominated the disk for at least a few million years.

When Henry Sorby first studied chondrites with the petrographic microscope, he correctly inferred that they had crystallized from molten droplets. In 1877 he wrote, "melted globules with well-defined outlines could not be formed in a mass of rock pressing against them on all sides, and I therefore argue that some at least of the constituent particles of meteorites were originally detached glassy globules, like drops of fiery rain." Sorby thought that the molten droplets that crystallized to form chondrules were likely pieces of the Sun, and the idea that the droplets condensed from hot gas was popular for a long time.

We now know that the vast majority of chondrules formed by melting of solid precursors in some sort of flash heating event (see Grossman *et al*., 1988, for a review of chondrule properties). Evidence includes relict grains that did not melt during chondrule formation and the porphyritic textures of most chondrules, which require the presence of residual solid nuclei to guide the formation of large crystals. The source of heat to melt chondrules is among the most perplexing questions in cosmochemistry. Temperatures were not uniformly high enough to melt silicates on a nebular scale, and the cooling time for a hot nebula is many orders of magnitude too slow to explain quenched chondrule textures. A localized heating process is required. Proposed mechanisms have included impact, lightning, heating by the Sun, and passage of shock waves, among others.

The formation of chondrules by impact was investigated after samples returned from the Moon were found to contain round glassy droplets of a size similar to chondrules. The idea lost favor because the production efficiency of glassy droplets in an impact (at least on the Moon) is very low, so a concentration mechanism would also be required. This idea is still discussed in the context of collisions between molten planetesimals, but the unfractionated chemical compositions of chondrules in bulk would seem to preclude this mechanism because molten bodies should either have differentiated or be in the process of differentiation. Impact is thus not widely considered to be the mechanism of formation of the vast majority of chondrules. A subset of chondrules in the rare CB and CH chondrites might have formed through impact. These chondrules all have the same unusual composition, the same texture, and the same oxygen-isotope composition. They are thought to have been formed by condensation of liquid droplets from the vapor plume produced by the impact of two large asteroids late in nebular history.

Lightning received considerable attention the 1980s and 1990s (Whipple, 1966; Love *et al*., 1995). A lightning discharge potentially carries plenty of energy. The heating time scale is rapid and the cooling time scale depends on ambient conditions, but could match that of chondrules. Lightning is expected to have occurred in a turbulent nebula. The event is localized, but perhaps too localized to produce huge numbers of chondrules. The idea has lost favor because the conditions necessary to produce sufficiently energetic lightning bolts are limited and may not match average nebular conditions and because the efficiency of such a process is expected to be low.

Solar heating has been discussed in a number of contexts. For example, Huss (1988) suggested that the intense radiation of the FU-Orionis eruptions known to occur in young stellar objects (see Chapter 9) could have both melted dust aggregates to form chondrules and helped them to rapidly accrete to form chondrites. Liffman and Brown (1995) suggested that liquid droplets melted close to the Sun by solar radiation could be lifted by bipolar outflows and deposited in the asteroid belt. They suggested that traveling through the thin gas above the disk could sort the droplets according to size, thus explaining why chondrite classes have unique and narrow size ranges for their chondrules. Neither these nor other similar models have gained much of a following.

A model that incorporated both the lightning concept and the energy of the Sun is the X-wind model proposed by Frank Shu and his colleagues in 1996. In this model, the magnetic fields of the young Sun and the surrounding disk interacted, producing a gap between the Sun and the disk (Fig. 14.4). When materials spiraling inward reached the inner edge of the disk (called the X-region), they took one of two paths. Rapidly orbiting materials were flung outward along magnetic field lines (producing the X-wind), whereas less rapidly moving materials fell onto the star (Fig. 14.4). Intense solar heating in the X-region was proposed as the source of heat to melt CAIs and chondrules, which were then ejected out of the nebular plane and re-accreted onto the nebula disk at greater solar distance. A modification of the model added production of short-lived radionuclides by irradiation in the reconnection ring.

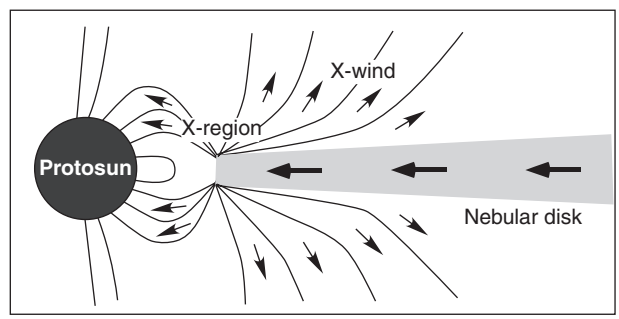

Fig. 14.4 Sketch of the X-wind model, showing a gap between the protosun and the inner edge of the nebular disk caused by interfering magnetic fields. Materials migrating inward in the disk reach the X-region, where they either accrete onto the star or are ejected outward above the disk (X-wind), only to be accreted back onto the disk farther out. After Shu *et al*. (1996).

The passage of shock waves through the nebula potentially has the power to melt dust aggregates and form chondrules (e.g. Desch and Connolly, 2002). In this model, the dust aggregates are heated both by gas drag as they pass through the shock and by radiation from the hot gas behind the shock. Shocks could be generated either by gravitational instabilities in the outer accretion disk or by the passage of giant protoplanets through the disk.

None of these models has been universally accepted as the mechanism to form chondrules. All of them have their problems. It is possible that we have not yet conceived of the true mechanism that formed chondrules, but whatever it was, it operated pervasively at least in the area where chondrites accreted.

Formation of CAIs also requires transient high-temperature events in the early solar system. However, the textural and mineralogical diversity of CAIs is much greater than in chondrules and it is likely that a variety of processes, including condensation, evaporation, sintering, and melting were involved to varying degrees. The Type B CAIs and compact Type A CAIs, which appear to have been almost completely melted, have a different thermal history than chondrules. These CAIs were heated to a lower temperature (~1700 K versus 1770–2120 K for chondrules), but remained at elevated temperatures for considerably longer than chondrules (also see Chapter 7). They also apparently formed earlier in the history of the accretion disk than did the chondrules (see Chapter 9). And their bulk compositions suggest that the ambient temperature was higher when the transient melting event occurred. Thus, it is not clear if the same types of events that produced chondrules also melted the CAIs.

The X-wind model was explicitly designed to explain the production of both CAIs and chondrules. In this model, both CAIs and chondrules were melted by radiative heating very close to the Sun and were lifted by a bipolar wind and sent out to the asteroid belt. In the original model, CAIs were considered to have formed first, during a higher temperature phase, with chondrules forming later. This is consistent with the more refractory compositions of the CAIs, but not with the higher peak temperatures reached by the chondrules. The model was later coupled to an irradiation model for the production of short-lived radionuclides, and in this model, the CAIs were exposed to both a higher radiation flux and a higher particle flux. The chondrules formed in a more shielded region at approximately the same time. Thus, in this version of the model, the difference in abundance of ^{26}Al between CAIs and chondrules has no temporal significance. The X-wind model runs into serious problems in detail not only with the thermal profiles, but also with preserving the bulk compositions of chondrites and explaining the textural and size differences between the CAIs of different meteorite groups.

The shock-wave model may also be applicable to CAIs. Shocks operating under different nebula conditions when the CAIs formed could generate a different temperature profile. Details of this type of model have not been worked out.

To summarize, chondrules and CAIs formed by transient heating events that processed a large fraction of the matter in the accretion disk. These heating events appear to overprint the thermal processing that produced the volatile element depletions among chondrites. The exact nature of these events is unknown, although shock waves in the nebula and the X-wind model are currently receiving the most attention.

Accretion and bulk compositions of planets

Agglomeration of planetesimals and planets

Settling towards the midplane of the nebula and coagulation of solid grains could have produced kilometer-size objects on timescales of a few thousand orbital periods, corresponding to less than 10^4 years (Cuzzi and Weidenschilling, 2006). However, dynamical models have focused on non-turbulent accretion disks. Nebular turbulence would have slowed or prevented settling and delayed accretion. In a turbulent disk, the motions would bring dust grains into contact with one another, resulting in efficient formation of centimeter- to meter-sized objects, with the larger objects forming in eddies where particles were concentrated.

It is not at all clear how these meter-sized objects got together to form larger bodies, but once bodies reached the sizes of planetesimals (1–10 km), they were no longer controlled by nebular gas drag. Thereafter they grew by mutual collisions, and became bound by gravity. Eventually, a few dominant bodies would have emerged, large enough that their gravity focused more collisions onto them. This would have resulted in runaway growth, forming planets. Smaller objects not accreted into planets would eventually be gravitationally scattered by close encounters, and perhaps were lost from the solar system. Bodies in the asteroid belt partly escaped this fate, but models suggest that as much as 99% of the original mass of the main belt has been removed, probably through gravitational interactions with Jupiter.

The formation of the terrestrial planets is constrained by their bulk chemical compositions, but determining the compositions of entire planets is challenging. Because planets are differentiated into crust, mantle, and core, there is no place on or within a planet that has the composition of the entire body. Before considering the formation of the terrestrial planets, let's review how we go about estimating their bulk compositions.

Constraints on planet bulk compositions

To illustrate how a planetary bulk composition is estimated, let's begin with the Earth, about which we have the most information. For this analysis, we need estimates of the compositions of the crust, mantle, and core. Several widely accepted crust compositions have been determined by estimating the relative proportions of continental and oceanic crustal rocks and averaging their compositions. The crust comprises only a small fraction (~0.4%) of the Earth's mass, as judged from seismic data, but it is important to estimate its composition correctly as it contains a significant proportion of the planet's incompatible elements. Mantle compositions are obtained by analyzing mantle inclusions brought up in lavas or mantle blocks exposed by tectonic forces. Many mantle samples are residues from partial melting that produced basaltic magma, and some proportion of basalt can be added to residue compositions to reconstruct the chemistry of the primitive mantle (before basaltic magma was extracted). The mantle composition is especially important, because the mantle

Table 14.1 Bulk chemical composition of the Earth (Kargel and Lewis, 1993)

Element	Abundance	Element	Abundance	Element	Abundance
H (ppm)	36.9	Cu (ppm)	82.7	La (ppm)	0.434
Li (ppm)	1.69	Zn (ppm)	47.3	Ce (ppm)	1.114
Be (ppm)	0.052	Ga (ppm)	4.42	Pr (ppm)	0.165
B (ppm)	0.292	Ge (ppm)	10.2	Nd (ppm)	0.836
C (ppm)	44	As (ppm)	1.73	Sm (ppm)	0.272
N (ppm)	0.59	Se (ppm)	3.16	Eu (ppm)	0.1035
O (wt%)	31.67	Br (ppm)	0.13	Gd (ppm)	0.363
F (ppm)	15.8	^{84}Kr (ppm)	3.7×10^{-6}	Tb (ppm)	0.0671
^{20}Ne (ppm)	2.7×10^{-5}	Rb (ppm)	0.76	Dy (ppm)	0.448
Na (ppm)	2450	Sr (ppm)	14.4	Ho (ppm)	0.1027
Mg (wt%)	14.86	Y (ppm)	2.88	Er (ppm)	0.294
Al (wt%)	1.433	Zr (ppm)	7.74	Tm (ppm)	0.0447
Si (wt%)	14.59	Nb (ppm)	0.517	Yb (ppm)	0.300
P (ppm)	1180	Mo (ppm)	1.71	Lu (ppm)	0.0449
S (wt%)	0.893	Ru (ppm)	1.31	Hf (ppm)	0.203
Cl (ppm)	264	Rh (ppb)	227	Ta (ppb)	28.1
^{36}Ar (ppm)	6.5×10^{-5}	Pd (ppb)	831	W (ppb)	171
K (ppm)	225	Ag (ppb)	99	Re (ppb)	67.4
Ca (wt%)	1.657	Cd (ppb)	68	Os (ppb)	898
Sc (ppm)	11.1	In (ppb)	4.9	Ir (ppb)	889
Ti (ppm)	797	Sn (ppb)	340	Pt (ppm)	1.77
V (ppm)	104	Sb (ppb)	61	Au (ppb)	157
Cr (ppm)	3423	Te (ppb)	390	Hg (ppb)	6.5
Mn (ppm)	2046	I (ppb)	36	Tl (ppb)	7.35
Fe (wt%)	32.04	^{132}Xe (ppb)	4.0×10^{-4}	^{206}Pb (ppb)	172
Co (ppm)	779	Cs (ppb)	55	Bi (ppb)	5.72
Ni (wt%)	1.72	Ba (ppm)	4.33	Th (ppb)	54.3
				U (ppb)	15.2

constitutes the largest portion of the planet. The size of the core is inferred from the bulk density of the Earth and from its geophysical properties, while its chemistry is estimated from solar system elemental abundances (iron is so abundant that it must dominate the core) and knowledge of how siderophile elements partition between metal and silicate from high-pressure experiments. Estimates of the compositions of the Earth's crust, mantle, and core compiled from various sources have been tabulated by Lodders and Fegley (1998). The Earth's bulk composition, as derived from combining these compositions and relative proportions, is given in Table 14.1.

In estimating the bulk compositions of the other terrestrial planets, there are not nearly so many constraints. Determination of a planet's mass (obtained from its gravitational effect on the orbits of moons or nearby spacecraft) and volume (calculated from its diameter as measured by telescopes) enables the calculation of its mean density. A meaningful comparison of planet mean densities requires that we correct for the effects of self-compression due

to gravity – massive planets are more internally compressed than less massive ones. The "uncompressed mean densities" (in g cm^{-3}) of the terrestrial planets are shown in Figure 14.5. To first order, these density variations reflect differences in the relative proportions of metal (core) and silicate (mantle plus crust), also illustrated in Figure 14.5. Because iron is by far the most abundant element in metal, these proportions depend on how iron is partitioned between its different oxidation states. The terrestrial planets show an inverse relationship between the mass fractions of metallic iron in cores and oxidized iron (FeO) in mantles (Fig. 14.6). Oxidation state appears to be related to heliocentric distance. A planet's moment of inertia (obtained from the observed degree of flattening as it rotates, or from precise measurements of the precession of its rotational axis over time) provides

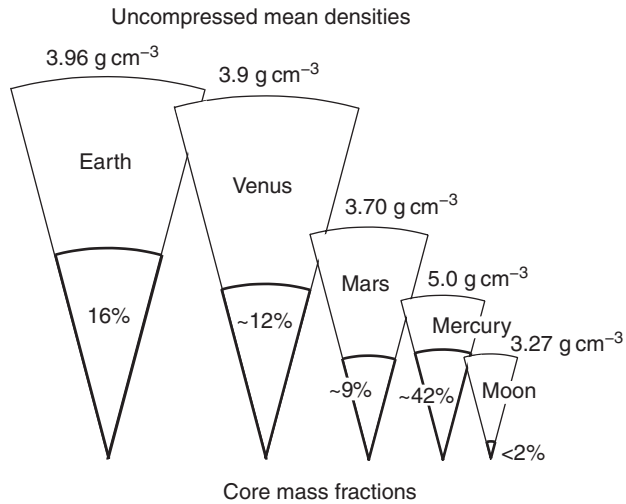

Fig. 14.5 Uncompressed mean densities of the terrestrial planets and the Moon (Taylor and McLennan, 2009) vary with the relative volume proportions of cores and mantles.

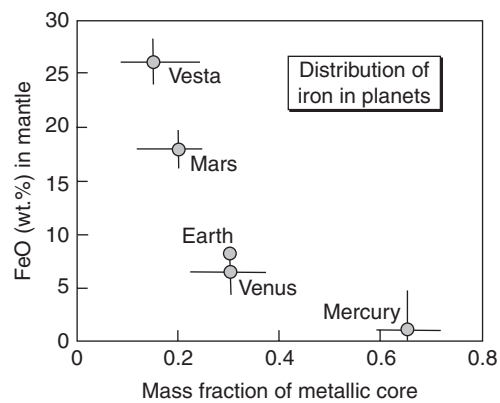

Fig. 14.6 Mass fractions of cores (metallic iron) versus concentrations of FeO in mantles (oxidized iron) in the terrestrial planets and asteroid Vesta. After Righter *et al.* (2006).

information on how mass is distributed within its interior. Estimates of the bulk chemical compositions of planets are used (with assumptions about internal temperature and pressure variations) to calculate how plausible minerals with different densities are distributed with depth. These mineral distributions can then be used to calculate mean densities and moments of inertia, for comparison with the measured values.

The giant planets are composed mostly of hydrogen and helium. Uncompressed mean densities provide constraints on the proportion of rock to ice or gas, although the enormous internal pressures in some of these planets produce phase changes in hydrogen that complicate this determination (discussed below).

Models for estimating bulk chemistry

In keeping with the theme of this book, we are most concerned with estimating planet bulk compositions, which then can be recast into mean density and moment of inertia. A number of different cosmochemical models have been attempted to estimate the bulk compositions of planets for which we have very few, or more likely no samples.

The *equilibrium-condensation model* assumes that solids thermally equilibrated with the surrounding nebular gas, and any uncondensed elements were somehow flushed from the system. Planets accreted from these solids would then have compositions dictated by condensation theory. Because temperature and pressure decreased away from the Sun, the condensed solids would have varied with heliocentric distance. Figure 14.7 shows planets

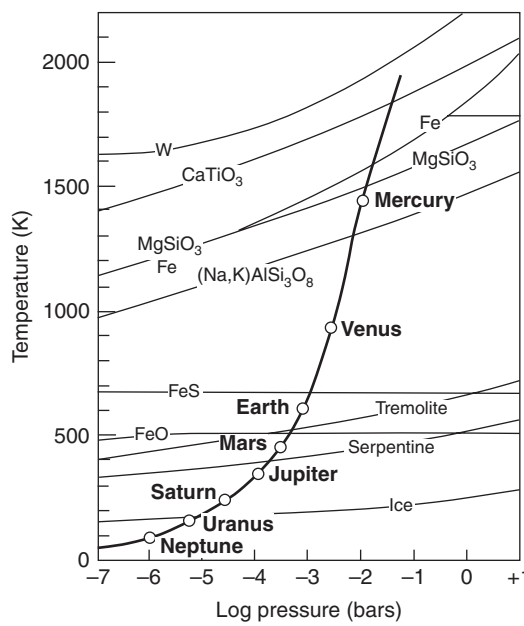

Fig. 14.7 Equilibrium condensation model for planet bulk compositions, assuming that temperature and pressure decreased outward from the Sun, as shown by the heavy curved line. Modified from Barshay and Lewis (1976).

arranged along a presumed nebular temperature–pressure profile, with important condensation curves illustrated. In this model, Mercury and Venus would contain high proportions of refractory elements and all their iron would be metallic, resulting in high uncompressed mean densities. Earth formed in a cooler region, where some iron had reacted to form sulfide and ferrous silicates. Mars formed at a still lower temperature, permitting more oxidation of iron and possibly the formation of some phyllosilicates, decreasing its mean density. Further outward, ices condensed and were mixed with silicates to form the giant planets. This model is now mostly of historical interest, given the evidence discussed above against a hot nebula where equilibrium condensation would be widespread.

Most modern models can be characterized as *heterogeneous accretion models*. Heterogeneous accretion envisions the material progressively accreting to form the planets as changing in composition and oxidation state with time. For example, based on the distribution of siderophile and moderately siderophile elements in the Earth's mantle, Wänke (1981) suggested that the first 80–90% of the Earth accreted from very reduced materials. The siderophile and moderately siderophile elements would have been quantitatively extracted into the core. The next 10–20% of the material accreting to the Earth would have been more oxidized, so all but the most highly siderophile elements would have remained in the mantle. The last ~1%, a so-called "late veneer" was so oxidized that all iron was present in oxidized form. The late veneer would have brought water to the Earth.

The origin of the components that were accreted to make up the planets is the subject of intense discussion. *Chondrite-mixing models* attempt to build the planets using known chondritic materials. These models are constrained by the mean densities, moments of inertia, and, to the extent that they are known, the bulk chemical and isotopic compositions of the planets. Mars and 4 Vesta can be modeled reasonably well by known types of chondritic material (Righter *et al*., 2006). However, the Earth seems to have formed, at least in part, from materials that are not represented in our collections of chondritic meteorites (see below).

Some estimates of the bulk chemical compositions of the other terrestrial planets are compared with the Earth's in Table 14.2. In this compilation, the compositions and relative proportions of the silicate (mantle plus crust) and core fractions are separated.

Estimated compositions of the giant planets are given in Table 14.3, normalized to the solar composition. The relative proportions of rock and volatiles are estimated from mean densities, the rock compositions are assumed to be chondritic, and the ratios of hydrogen to helium are derived from spectroscopic or spacecraft measurements of atmosphere compositions.

Formation of the terrestrial planets

Planetesimal building blocks

We have already seen that the various chondrite groups have distinct compositions, and we might expect that these compositions would have varied systematically with solar distance. The asteroids show a rough radial gradient in composition, with E and S asteroids concentrated nearer the Sun, C asteroids farther outboard, and P and D asteroids at still greater

Table 14.2 Selected major element compositions for bulk silicate and core components of the terrestrial planets

	Mercury	Venus	Earth	Mars
Mantle plus crust				
MgO	34.5	38.0	35.1	30.2
Al_2O_3	18.1	3.9	3.64	3.02
CaO	14.6	3.2	2.89	2.45
SiO_2	32.1	45.9	49.9	44.4
TiO_2	0.7	0.3	0.16	0.14
Na_2O	———	0.1	0.34	0.50
K_2O	0	0.015	0.02	0.038
FeO	0	8.1	8.0	17.9
Cr_2O_3	———	0.3	———	0.76
MnO	———	0.1	———	———
Core				
Fe	88–91	86.2	90.6	77.8
Ni	6.5–7.5	4.8	7.9	7.6
Co	———	———	0.5	0.36
S	0.5–5	1.0		14.24
Relative masses				
Mantle plus crust	36	71.8	67.5	78.3
Core	64	28.2	32.5	21.7

Data sources: Mercury (Fegley and Cameron, 1987; Goettel, 1988), Venus (Basaltic Volcanism Study Project, 1981), Earth (Taylor, 1992), Mars (Taylor, 1992).

Table 14.3 Abundances of major elements and molecules in the atmospheres of the giant planets, relative to solar abundances (Lunine, 2004)

	Jupiter	Saturn	Uranus	Neptune
Helium	0.8	0.8	1	1.3
Methane, CH_4	2.5–3.5	6	30–60	30–60
Ammonia, NH_3	3–4	0.5–3	>1?	20–40 as N_2
Water, H_2O	>1?			
Phosphine, PH_3	>0.2	6		
H-sulfide, H_2S	2.2–2.9			
Arsine, AsH_3	0.6–3	2–8		
Germane, GeH_4	0.1	6		
Neon	0.2			
Argon	2.0–3.0			
Krypton	2.2–3.2			
Xenon	1.8–3.0			

heliocentric distances (Chapter 11, see Fig. 11.7). The C-type asteroids are generally associated with CI and CM2 carbonaceous chondrites because of their low albedos and spectral signatures of hydrated silicates. The S-type asteroids may be a mixture of primitive bodies such as chondrites, and differentiated objects. The E-type asteroids, which are rare, have been associated with enstatite chondrites. In detail, however, the concentrations of volatile, moderately volatile, and refractory elements, and the relative abundances of lithophile and siderophile elements among chondrites are not correlated in any straightforward way. This probably reflects the dynamic nature of the nebula where, at any given location, temperature and oxidation state changed (probably independently) with time, and material moved inward and outward through that location. In such a dynamic system, only a general correlation between properties of the final objects and heliocentric distance would be expected.

High-resolution chronometers (Wadhwa *et al*., 2006), especially that based on the ^{182}Hf–^{182}W system (Kleine *et al*., 2005), indicate that the earliest planetesimals were differentiated and that they formed 1–2 Myr before the chondrite parent bodies, as discussed in Chapter 9. Objects that accreted earlier would have contained more live ^{26}Al, and logically would have been heated to higher temperatures than objects that accreted later. Bottke *et al*. (2006) argued on dynamical grounds that the differentiated asteroids actually formed well inside the region of the present asteroid belt, probably within the terrestrial planet region. Accretion within this region was probably rapid, because of a higher density of planetesimals. Differentiated asteroids not swept up by planets subsequently drifted outward or were perturbed by encounters with planets into their present orbital locations in the main belt. This dynamical shuffling of objects would also blur original correlations between properties of bodies and heliocentric distance.

The ratios of various isotopes and elements in the Earth are roughly chondritic, explaining why chondrites have normally been considered as planetary building blocks. However, a detailed comparison of the Earth's composition with chondrites reveals some inconsistencies (Righter *et al*., 2006). For example, a plot of Mg/Si versus Al/Si, shown in Figure 14.8,

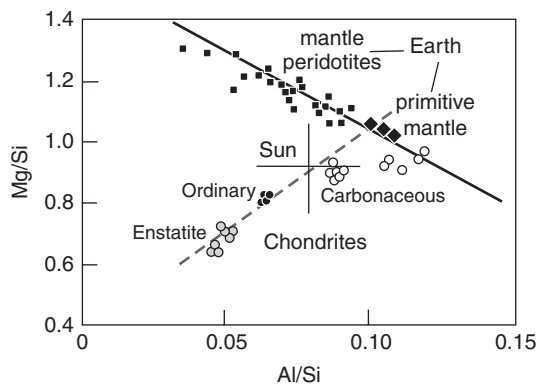

Fig. 14.8 **Major-element compositions (weight ratios of Mg/Si and Al/Si) for mantle rocks (peridotites) and estimates of the primitive mantle composition of the Earth compared with various groups of chondrites and the Sun. No mixture of chondrite types provides an exact match to the primitive mantle composition, although some carbonaceous chondrites provide the closest match. Modified from Righter *et al*. (2006).**

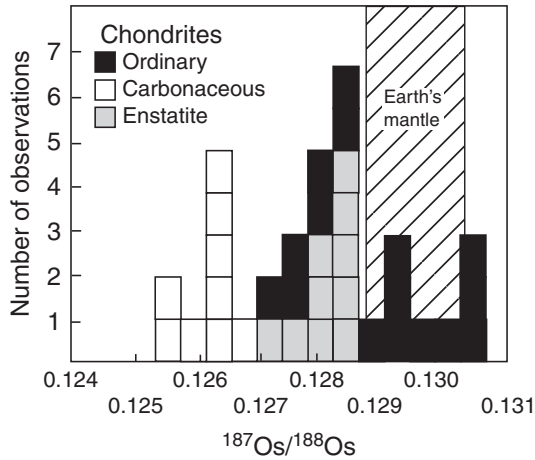

Fig. 14.9 **Osmium isotopic ratio of the bulk silicate Earth overlaps measurements of ordinary chondrites but is distinct from other chondrite groups. Adapted from Righter *et al.* (2006).**

reveals that no mixture of known chondrite types has the exact composition of the bulk silicate Earth (mantle plus crust), although carbonaceous chondrites provide the closest match. However, the $^{187}Os/^{188}Os$ ratio in carbonaceous chondrites is distinct from that measured for the Earth's mantle (Fig. 14.9); ordinary chondrites provide a better match for osmium. But neither carbonaceous nor ordinary chondrites can match the Earth's oxygen isotopic composition – instead, enstatite chondrites plot on the Earth's fractionation line. Thus, none of these chondrite types consistently matches the composition of the Earth.

Perhaps this is not surprising, given that recent chronologic data (Chapter 9) have raised questions about the approach of using chondrites as building blocks. Differentiated planetesimals formed earlier than chondritic planetesimals, and differentiated bodies probably dominated the terrestrial planet region. These bodies would have had different elemental fractionation patterns relative to the bulk solar system composition than objects formed further from the Sun. Dynamical models suggest that the feeding zones for large bodies during much of their accretion were relatively narrow, implying that the majority of the Earth accreted from planetesimals from the same region of the solar system, not from the asteroid belt. It then follows that differentiated planetesimals, not chondrites, were building blocks for the terrestrial planets. This idea has much to recommend it, but we should note that the bulk compositions of differentiated planetesimals were probably chondritic in terms of many element ratios. The differences between achondrites and chondrites are primarily in the proportions of the moderately volatile elements, with differentiated materials being significantly more depleted than chondrites. The Earth, and probably Venus and Mercury, share this chemical characteristic, inherited from their planetesimal building blocks.

Delivery of volatiles to the terrestrial planets

If the terrestrial planets were assembled from differentiated, volatile-depleted planetesimals located well inside the snowline, how did these planets obtain their water and other volatiles? During the early stages of accretion, models suggest that the feeding zones for planets were fairly narrow. However, during the later stages of accretion, feeding zones widened substantially and extensive mixing of nebular materials occurred. Thus the composition of accreting materials likely varied with time, as planets grew larger. Even though the terrestrial planets formed mostly from already differentiated planetesimals, they probably incorporated some chondritic material with higher volatile element contents as veneers later in their assembly.

The Earth's oceans reveal an abundance of water that corresponds to ~1/1000 of the planet's mass. Mars, too, once had liquid water that sculpted its surface, and water ice still resides at its poles and in its subsurface at high latitudes. The high D/H ratio in the atmosphere of Venus suggests that it once may have contained water in similar abundance to the Earth. Even Mercury, baking in the Sun's glare, appears to have water ice at its poles. The amounts of water in the terrestrial planets are modest, relative to the amounts of water in gas- and ice-rich planets in the outer solar system, but the importance of water for planetary habitability demands that we discuss how the inner planets got their water.

Gravitational stirring of icy planetesimals by the giant planets could have sent many comets careening into the inner solar system, providing a mechanism for late addition of water to the terrestrial planets. Comets impacting the Earth and the other terrestrial planets would have delivered water as ice (Owen and Bar-Nun, 1995; Delsemme, 1999), whereas the accretion of already altered carbonaceous chondrite asteroids would have delivered water in the form of hydroxl-bearing minerals (Morbidelli *et al*., 2000; Dauphas *et al*., 2000).

Noble gases may provide a constraint on the source of water and other volatiles. The abundance pattern of noble gases in planetary atmospheres resembles that of chondrites, perhaps arguing against comets. However, there are some differences, especially in the abundance of xenon. Relative to solar system abundances, krypton is more depleted than xenon in chondrites, but in the planets, krypton and xenon are present in essentially solar relative abundances (Fig. 10.11). This observation has been used to support comets as the preferred source of volatiles (even though measurements of xenon and krypton in comets are lacking). A counter-argument is that the Ar/H_2O ratio in comets (if the few available measurements are accurate and representative) limits the cometary addition of volatiles to the Earth to only about 1%.

Another possibly problematical observation is that the D/H ratio of the Earth's oceans is roughly half that measured in comets, but is similar to that for carbonaceous chondrites (Fig. 14.10). For this reason, Dauphas *et al*. (2000) calculated that no more than 10% of our planet's H_2O was accreted as comet ice, a conclusion consistent with dynamical constraints (Morbedelli *et al*., 2000). Despite the importance that D/H measurements have been given in recent publications, fractionation of these isotopes when ice is sublimated has been demonstrated experimentally. Consequently, the measurements of D/H in comet comae may not

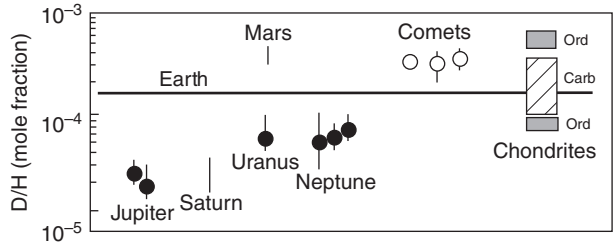

Fig. 14.10 **Hydrogen isotopic compositions, expressed as molar D/H ratios, of solar system bodies. The relatively low D/H values in the atmospheres of Jupiter and Saturn are similar to those in the early Sun, whereas D/H ratios for Uranus and Neptune are intermediate between the Jupiter-Saturn values and those of comets and chondrites. The Earth's oceans have D/H shown by the horizontal line. Mars values are from SNC meteorites. Modified from Righter *et al.* (2006) and Lunine (2004).**

accurately reflect the D/H ratio in comet ice. We have also seen that not all comets are alike, so some as-yet-unrecognized comet reservoir might have an Earth-like hydrogen isotopic composition.

It is also possible that neither of these mechanisms for providing water to the inner planets is correct. Another hypothesis is that absorption of water onto dust particles in the accretion disk might account for the Earth's oceans (Drake, 2005). As already mentioned, the amount of water required to explain Earth's water is not large on a per-gram basis. Regardless of whether comets, asteroids, or nebular particles were the source of our planet's oceans, the water likely came from more distant regions of the nebular disk.

Planetary differentiation

Differentiation is among the most important geochemical processes that affected planets. We have already discussed the differentiation of planetesimals in Chapter 11; here we will consider differentiation in large planets, which differs because of longer duration and the effects of significantly higher pressures. Specifically, we will focus on the Earth, since we know most about it. A complete discussion of the Earth's differentiation is beyond the scope of this book, and readers are referred to reviews of this topic (e.g. Halliday, 2004; Tolstikhin and Kramers, 2008; Halliday and Wood, 2009) for more detailed information.

The time scale for Earth's differentiation was discussed in Chapter 9. We learned that tungsten isotopes constrain the time interval between nebula formation and core separation as less than 30 Myr (Yin *et al.*, 2002). Differentiation must have been complete before the giant impact that formed the Moon, currently constrained to have occurred 40–45 Myr after the solar system formed (Halliday, 2004 and references therein).

The Earth's core is composed of iron–nickel alloy, with an inner solid core surrounded by a molten outer core. A mismatch between the inferred density of the outer core and that predicted for iron–nickel metal at high pressure suggests that some light element(s) must dilute the iron in the molten core. Some possibilities are oxygen, sulfur, silicon, and hydrogen, all elements with high cosmic abundances that can alloy with iron at very high

pressures. Core formation required that the Earth was sufficiently molten that metal droplets could coalesce and sink through the silicate mantle. There is a growing consensus that the early Earth was largely melted, forming a magma ocean, although no direct evidence for that is apparent. A Moon-forming impact (described below) would have produced planet-wide melting, but even without such a catastrophic collision, short-lived radionuclides could have caused widespread melting in the early stages of accretion. In fact, magma oceans might have been commonplace on all planets. The accretion of already differentiated planetesimals would also have increased the efficiency of core separation, since large masses of metal sink more readily than small droplets.

Knowledge of the behavior of siderophile elements in iron meteorites is not necessarily a good guide to their behavior deep within the Earth, because the pressures inside asteroids are negligible. Experiments indicate that element partitioning between metal and silicate melts varies, depending on pressure. Siderophile element abundances in the mantle do not match predictions from experiments at low pressures and moderate temperatures (Fig. 14.11). Righter *et al*. (1999) reviewed partitioning behavior at high pressures and suggested that fractionation of metals near the bottom of a magma ocean might account for the observed partitioning. Chabot *et al*. (2005) found that variations in redox state might allow partitioning experiments for various elements to be reconciled. Another interesting observation is that the moderately and highly siderophile elements each show relatively constant depletions (Fig. 14.11), unlike the depletions expected from experiments. Some workers have suggested that equilibrium between silicate melts and metal alloys did not occur during core formation, and others hypothesize that highly siderophile elements were added as a chondritic veneer after core separation. Regardless of the exact partitioning behavior and conditions, the Earth's mantle has clearly been depleted in siderophile elements relative to chondritic abundances.

Crystallization of the magma ocean would have allowed fractionation of high-pressure silicate and oxide minerals that dominate the Earth's deep interior. The olivine-rich

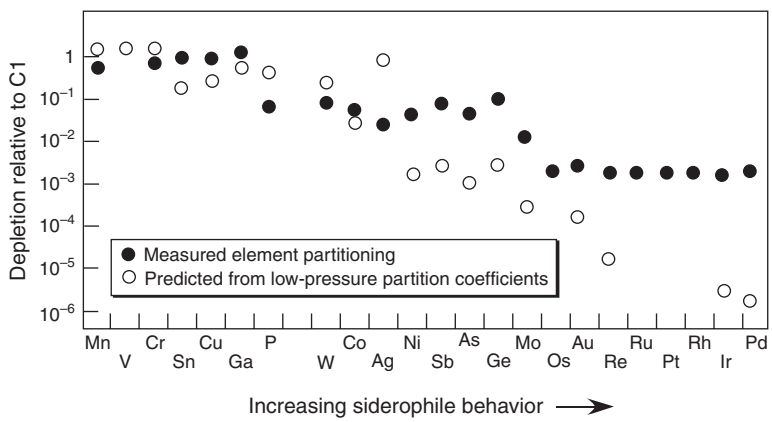

Fig. 14.11 **Chondrite-normalized abundances of siderophile elements in the Earth's mantle. The measured concentrations do not match those expected from low-pressure metal-silicate partition coefficients determined by experiments. Modified from Tolstikhin and Kramers (2008).**

(silica-poor) upper mantle may owe its non-chondritic composition to fractional crystallization of the high-pressure form of $MgSiO_3$, which is called Mg-perovskite in the literature because its structure is like that of $CaTiSiO_5$ (perovskite). Crystallization and settling of Mg-perovskite would produce a complementary, silica-rich lower mantle (Agee and Walker, 1988). However, the strong and uniform fractionation of some element ratios that would be expected from crystallization of a magma ocean is not apparent on Earth. Perhaps our planet's magma ocean was vigorously stirred by convection, obliterating such geochemical effects.

Formation of the crust required repeated episodes of mantle melting, which concentrated incompatible elements to a remarkable degree. The continental crust, especially, represents the geochemical complement to the upper mantle (Fig. 14.12). The composition of the continents is nearly equivalent to andesite, the common magma type produced in subduction zones (Taylor and McLennan, 2009), implying that subduction is largely responsible for that material. The oceanic crust is basaltic in composition. Subduction recycles oceanic crust back into the mantle. In the process, partial melting produces andesitic volcanism, which concentrates incompatible elements in the granitic continental crust that remains at the surface. Crust formation was probably accompanied by outgassing, as mantle-derived magmas carried dissolved gases to the surface.

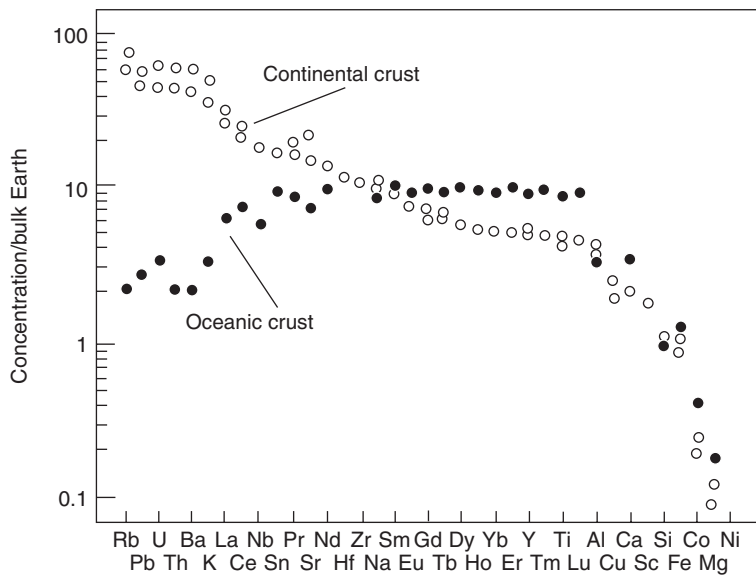

Fig. 14.12 Comparison of element concentrations in the continental crust and oceanic crust. Elements are ordered from left to right by increasing compatibility, so the greatest differences are among the most incompatible elements. The highly and moderately incompatible elements in both crustal components are enriched relative to the bulk Earth, but the concentrations of the most highly incompatible elements show complimentary abundance patterns. Oceanic basalts are derived from the upper mantle, which has been significantly depleted in incompatible elements by the extraction of magmas that made the continental crust over billions of years.

Differentiation of other terrestrial planets must have varied in important ways from that of the Earth, because of differences in chemistry and conditions. For example, in Chapter 13, we learned that the crusts of the Moon and Mars are anorthosite and basalt, respectively – both very different from the crust of the Earth. Neither has experienced recycling of crust back into the mantle, because of the absence of plate tectonics, and neither has sufficient water to help drive repeated melting events that produced the incompatible-element-rich continental crust (Taylor and McLennan, 1995). The mantles of the Moon and Mars are compositionally different from that of the Earth, although all are ultramafic. Except for these bodies, our understanding of planetary differentiation is rather unconstrained and details are speculative.

Nevertheless, we can make some general statements about the geochemistry of differentiated planets. The planetesimals from which they accreted had compositions determined largely by element volatility. Once assembled into a planet and heated, the partitioning of elements into cores and mantles was governed by their siderophile or lithophile affinities. Further differentiation of mantles to form crusts was controlled by the compatible or incompatible behavior of elements.

Formation of the giant planets

There are two competing theories for the formation of giant planets – Jupiter, Saturn, Uranus, and Neptune. In the *gravitational instability* model, a gravitationally unstable accretion disk fragments directly into self-gravitating clumps of gas and dust that then contract to become giant gaseous protoplanets (Cameron, 1978; Boss, 2004). This model permits the rapid formation of the gas giant planets. The main drawbacks are that it works best in disks that are much more massive than the one thought to have produced the solar system, and it does not easily lead to planets with compositions that differ significantly from the accretion disk from which they formed. An alternative mechanism, called *core accretion*, is generally viewed as more plausible for forming the giant planets (Lunine, 2004). This idea assumes that rocky cores accreted first from planetesimals, and once they became large enough they attracted nebular gas or ices. Core accretion is a slower process than gravitational instability. Some models indicate that the nebula might have dissipated before cores sufficiently massive to capture gas from the nebula could accrete. Can cosmochemistry provide constraints on these models?

The giant planets were assembled from materials in the solar nebula, which had a bulk composition as illustrated in Figure 14.13. The "metals" component, comprising all elements except hydrogen and helium, can be expressed in terms of ices (water, methane, and ammonia) and rock (everything else), as illustrated on the right side of this figure. Let's see how these abundances compare to the bulk compositions of the giant planets.

To the accuracy of the measurement of molecular weights for the giant planets, only hydrogen and helium have significant abundances. The relative proportions of these elements, expressed as the molar fraction He/H, are 0.068±0.002 for Jupiter, 0.068±0.013 for Saturn, 0.076±0.016 for Uranus, and 0.100±0.016 for Neptune (Lunine, 2004). None of these ratios are like those of the nebula (0.085, Table 4.1).

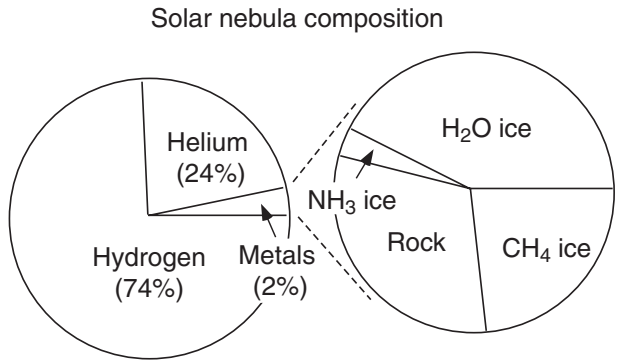

Fig. 14.13 **Diagram on the left shows the composition of the solar nebula (abundances in wt. %). Diagram on the right expands metals (astronomical jargon) into ices (water, methane, and ammonia) and rock (all other remaining elements). Jupiter and Saturn formed mostly from nebular gases, Uranus and Neptune formed mostly from ices, and the terrestrial planets formed primarily from rock.**

The proportions of nebular gas incorporated into the giant planets, relative to accreted solids (ice plus rock), appear to decrease monotonically from Jupiter outward to Neptune. At one time it was thought that the giant planets had solar compositions and thus had formed directly from nebular gases. However, the abundances of elements heavier than hydrogen and helium are clearly enriched relative to solar abundances. Heavy elements certainly comprise the rocky cores of these planets, but they are also dispersed in other layers. The Galileo probe, which was sent down into the atmosphere of Jupiter, found that helium, neon, argon, krypton, and xenon were all enriched by about a factor of three relative to solar abundances. The total abundances of heavy elements in Jupiter and Saturn are estimated to be equivalent to 10–20 Earth masses (Guillot *et al*., 2003), considerably greater than would be appropriate for bodies of solar composition. The overabundances of heavy elements support a core accretion model.

The outer layers of the atmospheres of Jupiter and Saturn show depletions in helium relative to hydrogen, but those of Uranus and Neptune do not (Table 14.3). This pattern may be explained by considering the equation of state of hydrogen and helium at the high pressures that are obtained inside giant planets. A possible phase diagram for hydrogen is illustrated in Figure 14.14. At pressures above about 3 Mbar, which are appropriate for the deep interiors of massive Jupiter and Saturn, hydrogen changes from molecular to metallic form. (In this case, "metallic" refers to a material in which electrons flow freely.) The presence of electrically conducting metallic hydrogen, along with planetary rotation, provides a natural dynamo mechanism to create the magnetic fields of those planets. Once the stability field for metallic hydrogen is reached, hydrogen and helium become immiscible, causing drops of helium to form and rain downward. This process, somewhat analogous to core separation in the terrestrial planets, fractionated hydrogen and helium and can explain the lower atmospheric helium abundance in Jupiter and Saturn. Uranus and Neptune are smaller planets, with interior pressures that do not exceed about 2 Mbar. Consequently, hydrogen and helium remain miscible throughout and their outer layers do not show helium depletions (Table 14.3).

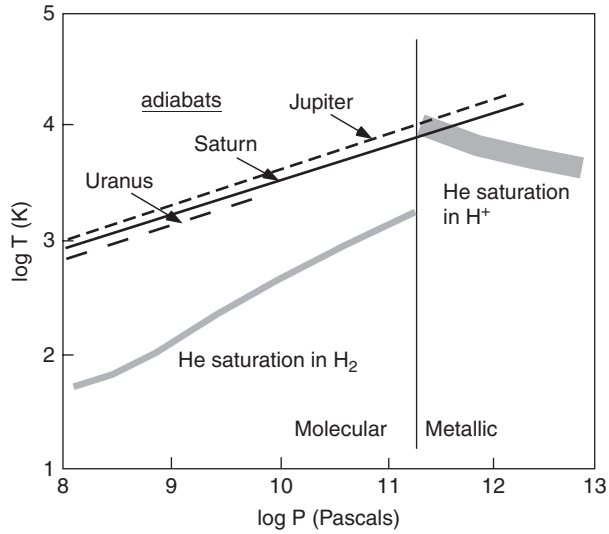

Fig. 14.14 **Phase diagram for hydrogen, showing the conditions under which hydrogen changes from molecular (H_2) to metallic (H^+). Below the gray He saturation curves, He and H are immiscible. Adiabats for Jupiter and Saturn cross the saturation curve once H becomes metallic, but the Uranus (and presumably Neptune) adiabats do not reach such high pressures.**

Models of the interiors of the giant planets depend on assumed temperature–pressure–density relationships that are not very well constrained. Models for Jupiter and Saturn feature concentric layers (from the outside inward) of molecular hydrogen, metallic hydrogen, and ice, perhaps with small cores of rock (rocky cores are permissible but not required by current data). Uranus and Neptune models are similar, except that there is no metallic hydrogen, the interior layers of ice are thicker, and the rocky cores are relatively larger.

The interior compositions of giant planets are speculative, but we can actually measure the chemical compositions of their atmospheres (Lunine, 2004). However, detailed measurements from spacecraft only exist for Jupiter. Because hydrogen dominates, the other elements occur in reduced molecular forms – carbon as CH_4, nitrogen as NH_3, oxygen as H_2O, sulfur as H_2S, and so forth (Table 14.3). However, less reduced molecules like CO have also been detected, perhaps dredged up from more highly oxidized regions in the interior or produced by photochemistry in the atmosphere. Photochemical reactions also produce some hydrocarbons such as ethane (C_2H_6) and acetylene (C_2H_2). The atmospheres of the giant planets are highly reducing because of their high hydrogen abundances, so complex organics are recycled back to methane on time scales that are short relative to the age of the planets. Consequently, organic molecules in the giant planets cannot provide information on their sources, nor do they increase in complexity over time. The overabundance of noble gases in the atmosphere, mentioned earlier and shown in Table 14.3, also demonstrates that Jupiter does not have solar composition.

Isotopic abundances for hydrogen have been measured in giant planet atmospheres, as shown in Figure 14.11. The D/H ratios in Jupiter and Saturn are similar to those in the Sun, but lower than those in the Earth's oceans or in comets. D/H ratios in Uranus and Neptune

fall between the Jupiter–Saturn values and comet values. The decrease in the amount of gas accreted relative to ice plus rock from Jupiter to Neptune appears to be reflected in the varying D/H ratios, assuming that the accreted ice component had a hydrogen isotopic composition similar to comets.

Box 14.1 Exoplanets

We now have the ability to identify and determine the properties of bodies orbiting around other stars (known as "exoplanets"). These planetary systems provide interesting comparisons with our own solar system. Astronomers have catalogued more than 300 exoplanets, mostly by observing the wobbles of these stars caused by massive planets orbiting around them. Direct imaging of a few exoplanets around nearby stars is a recent development.

One way to begin to make sense of exoplanets is to plot their estimated masses versus the mean distances from the stars around which they orbit, as illustrated in Figure 14.15. In this diagram, distance is given as thermal equivalent radius (AU normalized to the Sun's luminosity), which corrects for different stellar properties. Several populations of planets can be identified. On the left side of the diagram are "Hot Jupiters," which circumnavigate their stars in hours or days. Skimming above the surfaces of these stars, they experience enormous tides that mold their orbits into circular shapes. The sizes of these planets can sometimes be measured as they transit in front of the stars. Their radii are generally somewhat larger than Jupiter, and their masses imply that they are composed mostly of gases but contain rocky cores. A second group of planets, sometimes called "Eccentric Giants," orbits farther away from their parent stars. At greater distances tidal circularization is not important, so these bodies have elliptical orbits. The Eccentric Giants discovered so far tend to be larger than Hot Jupiters. For comparison, planets in our solar system are indicated by open symbols and labeled by their initials in Figure 14.15.

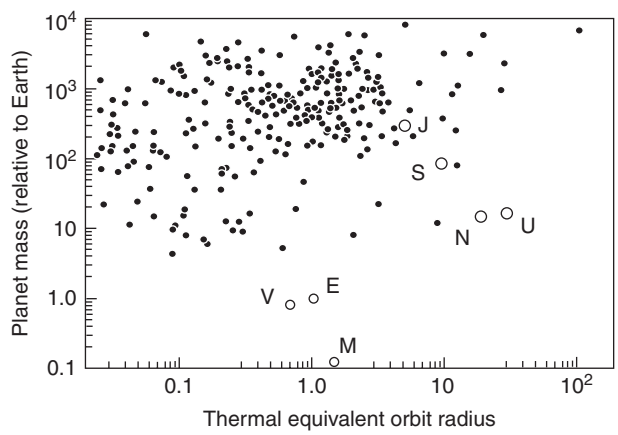

Fig. 14.15 Masses (relative to Earth) versus thermal equivalent radii for extrasolar planets. Thermal equivalent radii are the mean orbital distances from their stars normalized to the Sun's luminosity, which corrects for different stellar properties. Planets in our solar system (open circles) are identified by their first letters. Modified from Lunine *et al.* (2009).

Neither Hot Jupiters nor Eccentric Giants have counterparts in our own solar system. It might be tempting to jump to the conclusion that our solar system is unique, or at least unusual. That might be true, but we should note that the known extrasolar planets are only those that can be observed with present technology. We know nothing of the planetary retinues that might accompany the 90% of stars in our neighborhood for which extrasolar planets have not yet been discovered. Numerical simulations suggest that huge numbers of planets lie outside the limits of detection and probably fill the bottom of the diagram.

A particularly interesting observation, from the perspective of cosmochemistry, is that extrasolar planets are most likely to be found around stars with high proportions of heavy elements. Recall that astronomers refer to elements heavier than hydrogen and helium in stars as "metals." We know that metals comprise approximately 2% by mass of our Sun. Stars with metallicities comparable to the Sun have about a 5% chance of harboring a detectable planet, whereas nearly 30% of stars having three times the Sun's metallicity have observable planets (Fischer and Valenti, 2005). Given that all the extrasolar planets found so far are gas giants, this connection to stellar metallicity suggests that rocky cores are important constituents of giant planets everywhere. This observation also may support the hypothesis that core accretion is the common mechanism by which gas giants form.

Orbital and collisional evolution of the modern solar system

No description of our solar system's formation would be complete without a discussion of the profound changes wrought by its orbital and collisional evolution. Although these physical processes may not seem to be related to cosmochemistry, they have changed the spatial distribution of planets and small bodies of differing compositions within the solar system, and in some cases, even the bulk compositions of large bodies. Understanding these processes can help us appreciate how some of the cosmochemical conundrums and complexities of the solar system arose.

First let's consider major collisional events. One such impact is thought to have affected the early Earth. As mentioned in Chapter 13, a glancing blow to the Earth from a Mars-sized body produced a huge volume of fragments and vaporized materials that went into orbit around the Earth and rapidly reaccreted to form the Moon. Cosmochemical evidence in support of this giant impact hypothesis includes the Moon's bulk depletion in iron (estimates of its abundance vary between 8 and 12%) relative to the Earth (31% iron). Models suggest that the metallic core of the impactor would have accreted to the Earth, and the Moon would have been formed primarily from silicates from the impactor and dislodged from the Earth's mantle. The identical oxygen isotopic composition of the Earth and Moon is also frequently cited as evidence for a close relationship. Oxygen isotopes may have equilibrated via a hot silicate atmosphere surrounding the Earth and proto-lunar disk (Pahlevan and Stevenson, 2007). The high pressures in this disk may have allowed liquid to condense, so that the newly accreted Moon was largely molten.

Incomplete recondensation of vaporized materials could also account for the Moon's depletion in volatiles and its virtual absence of water.

Another example of an impact with cosmochemical consequences may be Mercury. The abnormally massive core of that planet may result from a large collision that stripped off mantle material and left a planet with non-chondritic abundances of siderophile versus lithophile elements.

Collisions can either result in net accretion, as demonstrated by the assembly of planets from planetesimals, or disruption, as in the case of the formation of the Moon. Even accretional collisions can redistribute materials far and wide, altering and perhaps blurring the distributions of compositionally distinct surface materials and exposing subsurface compositions.

The huge basins that occur on the lunar surface are the result of the "late heavy bombardment." There has been considerable debate about whether this bombardment was a punctuated event at about 4 Ga, or whether it represents the waning of solar system-wide, protracted accretion. However, there is a growing consensus for a singular event, when many large planetesimals were perturbed into the inner solar system. The impact records of Mercury, Venus, and Mars show similar size distributions of impactors, all thought to have come from the main asteroid belt (Strom *et al*., 2005). A recent model suggests that as the orbits of Jupiter and Saturn evolved, due to gravitational interactions between them and with a massive disk or planetesimals, they passed through a state where Jupiter orbited the Sun exactly twice for each orbit of Saturn (known as a 1:2 mean motion resonance). This resonance caused their orbits to become eccentric and brought them closer to Uranus and Neptune. This migration of the giant planets in turn disrupted the disk of planetesimals, sending them careening into the inner solar system and impacting the terrestrial planets (Tsiganis *et al*., 2005; Gomes *et al*., 2005). Such an event could have left a record in the form of the craters that we assign to the late heavy bombardment.

Orbital migration of the giant planets may likewise have stirred the legions of icy planetesimals in the outer solar system into a frenzy, scattering those that originated near Jupiter and Saturn outward to form the Oort cloud and causing the mean radius of the Kuiper belt to increase. Perhaps the dark, organic-rich bodies of the outer asteroid belt may even be interlopers that were scattered inward by migrating giant planets, complicating the meaning of the snowline. If the locations and distributions of objects in the present solar system are not original but have been modified by changes in the orbits of giant planets, this would have profound implications for any inferences drawn from the chemical compositions, radioisotope chronologies, and geologic histories of planets and asteroids at different heliocentric distances. Planetary dynamics calculations are providing a new paradigm for how the early solar system evolved and that, in turn, affects how the discoveries of cosmochemistry are interpreted.

Summary

Our general understanding of how the solar system came to be comes from a variety of different sources. Astronomical observations and theoretical modeling provide a broad picture of how stars form. Elemental and isotopic abundances in the solar system,

interpreted in the context of models of galactic nucleosynthesis over time, tell us the approximate age of the elements. These models and the abundances of short-lived radionuclides inferred for the early solar system tell us about the environment in which the solar system formed. Based on the above considerations, the Sun probably formed in an environment of cluster star formation in association with one or more nearby supernovae.

The evolution of the accretion disk to form our solar system can be modeled theoretically, but the models depend on constraints from astronomical observations and cosmochemistry. It now seems likely that the material that comprises asteroids (and meteorites) did not experience global temperatures in the nebula high enough to evaporate all pre-existing solids. The chemical fractionations observed in meteorites thus likely reflect processing of molecular cloud dust within the solar system. High temperature components such as chondrules and CAIs require transient high-temperature heating events that post-date the general chemical fractionations observed in meteorites. The nature of these transient events is currently unknown, but the X-wind model and the shock-wave model offer interesting possibilities.

The formation of the terrestrial planets is significantly constrained by knowledge of their bulk chemical compositions. Obtaining these data is challenging because planetary differentiation ensures that no samples have the composition of the whole. The Earth's composition has been estimated by integrating analyses of crust and mantle samples with inferences about the composition of the core, as constrained by seismic data. For planets other than the Earth, we rely on chemical models constrained by bulk density and moment of inertia. Although planet bulk compositions are commonly modeled using chondrites as building blocks, new chronology suggests that planetesimals in the terrestrial planet region were differentiated. Thus, the terrestrial planets may have accreted from already differentiated objects. Relative to chondrites, differentiated meteorites are depleted in volatile elements. Late accretion of volatile-enriched materials (chondritic bodies or comets) may be required to account for water on the terrestrial planets. Differentiation of the planets involved complex geochemical fractionations under varying conditions, leading to a variety of core, mantle, and crust compositions.

The giant planets are composed mostly of hydrogen and helium along with elements accreted as gas, ices, and dust. Their bulk compositions are not well constrained, but limited analyses and inferences from bulk densities suggest that all of them have lower H/He ratios than the nebula gas and are enriched in heavy elements relative to solar system abundances. Exoplanets so far discovered are all giant planets and reveal great diversity in composition and distribution. Orbital migrations of the giant planets probably led to the late heavy bombardment in the inner solar system and ejection of icy planetesimals into the outer reaches of the solar system, changing the primordial cosmochemical distributions with heliocentric distance.

Questions

1. What is the evidence that our Sun formed in the vicinity of other stars and was influenced by a nearby supernova?
2. Discuss the evolution of ideas about temperatures in the solar nebula, and how that relates to the formation of CAIs.

3. What constraints do we have on the bulk chemical compositions of planets?
4. Describe the building blocks that accreted to form the terrestrial planets, and explain how that may relate to their volatile element depletions.
5. How do the chemical compositions of the giant planets differ from those of the terrestrial planets, and from each other?

Suggestions for further reading

Halliday, A. N. (2004) The origin and earliest history of the Earth. In *Treatise on Geochemistry, Vol. 1, Meteorites, Comets, and Planets*, ed. Davis, A. M. Oxford: Elsevier, pp. 509–557. A thoughtful summary of a very large topic.

Hester, J. J. and Desch, S. J. (2005) Understanding our origins: Star formation in H II region environments. In *Chondrites and the Protoplanetary Disk, ASP Conference Series*, **341**, eds. Krot, A. N., Scott, E. R. D. and Reipurth, A. San Francisco: Astronomical Society of the Pacific, pp. 107–130. A clear and up-to-date review of astronomical observations that constrain models for solar system formation.

Lunine, J. I. (2004) Giant planets. In *Treatise on Geochemistry, Vol. 1. Meteorites, Comets, and Planets*, ed. Davis, A. M. Oxford: Elsevier, pp. 623–636. This chapter nicely summarizes how the physical and chemical properties of the giant planets are determined and discusses models for the origin of these bodies.

Taylor, S. R. (1992) *Solar System Evolution: A New Perspective*. Cambridge: Cambridge University Press, 307 pp. A thorough treatise that covers ideas about the origin and evolution of the terrestrial planets.

References

Agee, C. B. and Walker, D. (1988) Mass balance and phase density constraints on early differentiation of chondritic mantle. *Earth and Planetary Science Letters*, **90**, 144–156.

Barshay, S. S. and Lewis, J. S. (1976) Chemistry of primitive solar material. *Annual Reviews of Astronomy and Astrophysics*, **14**, 81–94.

Basaltic Volcanism Study Project (1981) *Basaltic Volcanism on the Terrestrial Planets*. New York: Pergamon Press, 1286 pp.

Black, D. C. and Pepin, R. O. (1969) Trapped neon in meteorites, II. *Earth and Planetary Science Letters*, **6**, 395–405.

Boss, A. P. (2004) Convective cooling of protoplanetary disks and rapid giant planet formation. *Astrophysical Journal*, **610**, 456–463.

Bottke, W. F., Nesvorny, D., Grimm, R. E., Morbidelli, A. and O'Brien, D. P. (2006) Iron meteorites as remnants of planetesimals formed in the terrestrial planet region. *Nature*, **439**, 821–824.

Cameron, A. G. W. (1962) The formation of the sun and planets. *Icarus*, **1**, 13–69.

Cameron, A. G. W. (1978) Physics of the primitive solar accretion disk. *Moon and Planets*, **18**, 5–40.

Cameron, A. G. W. and Truran, J. W. (1977) The supernova trigger for formation of the solar system. *Icarus*, **30**, 447–461.

Chabot, N. L., Draper, D. S. and Agee, C. B. (2005) Conditions of core formation in the Earth: constraints from nickel and cobalt partitioning. *Geochimica et Cosmochimica Acta*, **69**, 2141–2151.

Clayton, R. N., Grossman, L. and Mayeda, T. K. (1973) A component of primitive nuclear composition in carbonaceous meteorites. *Science*, **182**, 485–487.

Clayton, R. N., Onuma, N., Grossman, L. and Mayeda, T. K. (1977) Distribution of the presolar component in Allende and other carbonaceous chondrites. *Earth and Planetary Science Letters*, **34**, 209–224.

Cuzzi, J. N. and Weidenschilling, S. J. (2006) Particle-gas dynamics and primary accretion. In *Meteorites and the Early Solar System II*, eds. Lauretta, D. S. and McSween, H. Y., Jr. Tucson: University of Arizona Press, pp. 353–381.

Dauphas, N., Robert, F. and Marty, B. (2000) The late asteroidal and cometary bombardment in water deuterium to protium ratio. *Icarus*, **148**, 508–512.

Dauphas, N., Marty, B. and Reisberg, L. (2002a) Molybdenum evidence for inherited planetary scale isotope heterogeneity of the protosolar nebula. *Astrophysical Journal*, **565**, 640–644.

Dauphas, N., Marty, B. and Reisberg, L. (2002b) Molybdenum nucleosynthetic dichotomy revealed in primitive meteorites. *Astrophysical Journal Letters*, **569**, L139–L142.

Delsemme, A. H. (1999) The deuterium enrichment observed in recent comets is consistent with the cometary origin of seawater. *Planetary and Space Science*, **47**, 125–131.

Desch, S. J. and Connolly, H. C. (2002) A model of the thermal processing of particles in solar nebula shocks: application to the cooling rates of chondrules. *Meteoritics and Planetary Science*, **37**, 183–207.

Drake, M. J. (2005) Origin of water in the terrestrial planets. *Meteoritics and Planetary Science*, **40**, 519–527.

Fegley, B. F. and Cameron, A. G. W. (1987) A vaporization model for iron/silicate fractionation in the Mercury protoplanet. *Earth and Planetary Science Letters*, **82**, 207–222.

Fischer, D. A. and Valenti, J. (2005) The planet-metallicity correlation. *Astrophysical Journal*, **622**, 1102–1117.

Gammie, C. F. and Johnson, B. M. (2005) Theoretical studies of gaseous disk evolution around solar mass stars. In *Chondrites and the Protoplanetary Disk, ASP Conference Series*, **341**, eds. Krot, A. N., Scott, E. R. D. and Reipurth, A. San Francisco: Astronomical Society of the Pacific, pp. 145–164.

Goettel, K. A. (1988) Present bounds on the bulk composition of Mercury: implications for planetary formation processes. In *Mercury*, eds. Vilas, F., Chapman, C. R. and Matthews, M. S. Tucson: University of Arizona Press, pp. 613–621.

Gomes, R., Levison, H. F., Tsiganis, K. and Morbidelli, A. (2005) Origin of the cataclysmic late heavy bombardment period of the terrestrial planets. *Nature*, **435**, 466–469.

Gounelle, M., Shu, F. H., Shang, H. *et al*. (2001) Extinct radioactivities and protosolar cosmic-rays: self-shielding and light elements. *Astrophysical Journal*, **548**, 1051–1070.

Grossman, J. N., Rubin, A. E., Nagahara, H. and King, E. A. (1988) Properties of chondrules. In *Meteorites and the Early Solar System*, eds. Kerridge, J. M. and Mathews, M. S. Tucson: University of Arizona Press, pp. 619–659.

Guillot, T., Stevenson, D. J. and Hubbard, W. B. (2003) The interior of Jupiter. In *Jupiter*, eds. Bagenal, F., Dowling, T. and McKinnon, W. Cambridge: Cambridge University Press, pp. 35–58.

Halliday, A. N. and Wood, B. J. (2009) How did Earth accrete? *Science*, **325**, 44–45.

Humayan, M. and Cassen, P. (2000) Processes determining the volatile abundances of the meteorites and terrestrial planets. In *Origin of the Earth and Moon*, eds. Canup, R. M. and Righter, K. Tucson: University of Arizona Press, pp. 3–23.

Huss, G. R. (1988) The role of presolar dust in the formation of the solar system. *Earth, Moon, and Planets*, **40**, 165–211.

Huss, G. R. (1990) Ubiquitous interstellar diamond and silicon carbide in primitive chondrites: abundances reflect metamorphism. *Nature*, **347**, 159–162.

Kargel, J. S. and Lewis, J. S. (1993) The composition and early evolution of Earth. *Icarus*, **105**, 1–25.

Kleine, T., Mezger, K., Palme, H., Scherer, E. and Munker, C. (2005) Early core formation in asteroids and late accretion of chondrite parent bodies: Evidence from ^{182}Hf-^{182}W in CAIs, metal-rich chondrites and iron meteorites. *Geochimica et Cosmochimica Acta*, **69**, 5805–5818.

Lee, T., Papanastassiou, D. A. and Wasserburg, G. J. (1977) Aluminum-26 in the early solar system: fossil or fuel? *Astrophysics Journal*, **211**, L107–L110.

Lewis, R. S., Tang, M., Wacker, J. F., Anders, E. and Steel, E. (1987) Interstellar diamonds in meteorites. *Nature*, **326**, 160–162.

Liffman, K. and Brown, M. (1995) The motion and size sorting of particles ejected from a protostellar accretion disk. *Icarus*, **116**, 275–290.

Lodders, K. and Fegley, B. F. (1998) *The Planetary Scientist's Companion*. New York: Oxford University Press, 371 pp.

Love, S. G., Keil, K. and Scott, E. R. D. (1995) Electrical discharge heating of chondrules in the solar nebula. *Icarus*, **115**, 97–108.

Lunine, J. I., Macintosh, B. and Peale, S. (2009) The detection and characterization of exoplanets. *Physics Today*, May issue, pp. 46–51.

MacPherson, G. J., Simon, S. B., Davis, A. M., Grossman, L. and Krot, A. N. (2005) Calcium-aluminum-rich inclusions: major unanswered questions. In *Chondrites and the Protoplanetary Disk, ASP Conference Series*, **341**, eds. Krot, A. N., Scott, E. R. D. and Reipurth, A. San Francisco: Astronomical Society of the Pacific, pp. 225–250.

McCulloch, M. T. and Wasserburg, G. J. (1978a) Barium and neodymium isotopic anomalies in the Allende meteorite. *Astrophysical Journal*, **220**, L15–L19.

McCulloch, M. T. and Wasserburg, G. J. (1978b) More anomalies from the Allende meteorite: samarium. *Geophysical Research Letters*, **5**, 599–602.

McKeegan, K. D., Chaussidon, M. and Robert, F. (2000) Incorporation of short-lived ^{10}Be in a calcium-aluminum-rich inclusion from the Allende meteorite. *Science*, **289**, 1334–1337.

Morbidelli, A., Chambers, J., Lunine, J. I. *et al*. (2000) Source regions and timescales for the delivery of water to the Earth. *Meteoritics and Planetary Science*, **35**, 1309–1320.

Ouellette, N., Desch, S. J., Hester, J. J. and Leshin, L. A. (2005) A nearby supernova injected short-lived radionuclides into our protoplanetary disk. In *Chondrites and the Protoplanetary Disk, ASP Conference Series*, **341**, eds. Krot, A. N., Scott, E. R. D. and Reipurth, A. San Francisco: Astronomical Society of the Pacific, pp. 527–538.

Owen, T. and Bar-Nun, A. (1995) Comets, impacts, and atmospheres. *Icarus*, **116**, 215–226.

Pahlevan, K. and Stevenson, D. J. (2007) Equilibrium in the aftermath of the lunar-forming giant impact. *Earth and Planetary Science Letters*, **262**, 438–449.

Reynolds, J. H. and Turner, G. (1964) Rare gases in the chondrite Renazzo. *Journal of Geophysical Research*, **69**, 3263–3281.

Righter, K., Drake, M. J. and Scott, E. R. D. (2006) Compositional relationships between meteorites and terrestrial planets. In *Meteorites and the Early Solar System II*, eds. Lauretta, D. S. and McSween, H. Y., Jr. Tucson: University of Arizona Press, pp. 803–828.

Righter, K., Drake, M. J. and Yaxley, G. (1999) Prediction of siderophile element metal-silicate partition coefficients to 20 GPa and 2800 °C: the effects of pressure, temperature, oxygen fugacity, and silicate and metallic melt compositions. *Physics of the Earth and Planetary Interiors*, **100**, 115–134.

Shu, F. H., Shang, H. and Lee, T. (1996) Toward an astrophysical theory of chondrites. *Science*, **271**, 1545–1552.

Sorby, H. C. (1877) On the structure and origin of meteorites. *Nature*, **15**, 495–498.

Strom, R. G., Malhotra, R., Ito, T., Yoshida, F. and Kring, D. A. (2005) The origin of planetary impactors in the inner solar system. *Science*, **309**, 1847–1850.

Tachibana, S. and Huss, G. R. (2003) The initial abundance of ^{60}Fe in the solar system. *Astrophysical Journal*, **588**, L41–L44.

Taylor, S. R. and McLennan, S. M. (1995) The geochemical evolution of continental crust. *Reviews of Geophysics*, **33**, 241–265.

Taylor, S. R. and McLennan, S. M. (2009) *Planetary Crusts: Their Composition, Origin and Evolution*. Cambridge: Cambridge University Press, 378 pp.

Tolstikhin, I. and Kramers, J. (2008) *The Evolution of Matter from the Big Bang to the Present Day Earth*. Cambridge: Cambridge University Press, 521 pp.

Trinquier, A., Elliott, T., Ulfbeck, D. *et al*. (2009) Origin of nucleosynthetic isotope heterogeneity in the solar planetary disk. *Science*, **324**, 374–376.

Tsiganis, K., Gomes, R., Morbidelli, A. and Levison, H. F. (2005) Origin of the orbital architecture of the giant planets of the solar system. *Nature*, **435**, 459–461.

Wadhwa, M., Srinivasan, G. and Carlson, R. W. (2006) Timescales of planetesimal differentiation in the early solar system. In *Meteorites and the Early Solar System II*, eds. Lauretta, D. S. and McSween, H. Y., Jr. Tucson: University of Arizona Press, pp. 715–732.

Wänke, H. (1981) Constitution of terrestrial planets. *Philosophical Transactions of the Royal Society of London*, **A325**, 545–557.

Wasserburg, G. J., Lee, T. and Papanastassiou, D. A. (1977) Correlated O and Mg isotopic anomalies in Allende inclusions II: magnesium. *Geophysical Research Letters*, **4**, 299–302.

Whipple, F. L. (1966) Chondrules: suggestion concerning their origin. *Science*, **153**, 54–56.

Yin, Q. Z., Jacobsen, S. B., Yamashita, K. *et al*. (2002) A short timescale for terrestrial planet formation from Hf-W chronometry of meteorites. *Nature*, **418**, 949–952.

Appendix: Some analytical techniques commonly used in cosmochemistry

The purpose of this appendix is to present some additional information on various analytical techniques and methods that are used in cosmochemistry. This is not an exhaustive review. The goal is to give the reader an idea of the techniques that are available and their capabilities and limitations. References to more detailed discussions are provided.

Chemical compositions of bulk samples

There are a variety of methods for determining the bulk chemical composition of a sample. Each has its strengths and weaknesses. The choice of which technique to use depends on the elements of interest, the methods to which you have access, and the funding that is available for the analysis, among other things. The minimum sample requirement of the technique is an important consideration, but it can be very misleading. The true minimum sample size is the size that adequately accounts for the chemical and mineralogical complexity of the sample.

Wet chemical analysis

The traditional method of determining the bulk chemical compositions of meteorites is by wet chemical analysis. The process is time consuming and requires skill and patience to obtain quality results. The best meteorite data were obtained by Hugo Wiik (e.g. Wiik, 1956) and Eugene Jarosewich (e.g. Jarosewich, 1990). The procedure for analyzing a chondrite can be summarized as follows. A sample is first crushed and divided into two fractions by passing it through a 100-mesh sieve. The coarse fraction is primarily metal, while the fine fraction consists primarily of silicate. This division permits accurate assignment of iron to metal and oxide. Six different aliquots of the homogenized sample are analyzed to determine different subsets of elements. A typical analysis gives concentrations of 16 elements, along with the amount of iron present as metal and the amount of bound water. A detailed discussion of the methodology is provided by Jarosewich (1990).

The format for reporting chemical data comes from wet chemical analyses. Major and minor element abundances are normally reported as wt. % oxides, although oxygen is not actually measured and oxides are calculated based on stoichiometry. Units of weight are the "natural" units for chemical analysis because the amount of each element is determined by weighing the samples. Atomic % element would probably make more sense, but is not commonly used. Weight % oxide must be converted to atomic % element in order to calculate mineral structural formula, and many modern analytical techniques count atoms rather than weigh the samples. Unfortunately, because of the wt. % convention, a cosmochemist must become adept at converting published analyses to atomic % element.

X-ray fluorescence (XRF)

X-ray fluorescence uses secondary (fluorescent) X-rays emitted from a material that has been bombarded with high-energy X-rays. The sample is ground into a fine powder, homogenized, and pressed into a pellet. The pellet is irradiated by a monochromatic X-ray beam. Atoms in the sample absorb some of the X-rays, causing electrons to be ejected. The ejection of an electron causes other electrons to drop to lower energy levels to fill the vacancy, and fluorescent X-rays are emitted. The X-rays are characteristic of the element from which they were emitted. The secondary X-rays are either detected simultaneously with one of the various types of energy-dispersive, solid-state detectors, including lithium-drifted silicon, lithium-drifted germanium, and PIN-diode detectors, or sequentially with wavelength-dispersive spectrometers. This method can, in theory, measure elements heavier than beryllium, but in practice elements lighter than sodium are difficult to quantify unless background corrections and comprehensive inter-element absorption corrections are made. The XRF technique was popular in the 1960s and 1970s for analyzing bulk compositions of meteorites. XRF instruments were part of the instrument package on the Viking landers that operated on Mars in 1976.

Neutron activation analysis

During the late 1960s and early 1970s, neutron activation analysis provided a new way to measure bulk chemical composition. Neutron activation analysis utilizes (n,γ) reactions to identify elements. A sample is placed in a nuclear reactor where thermal neutrons are captured by atoms in the sample and become radioactive. When they decay, the radioactive isotopes emit characteristic γ-rays that are measured to determine abundances. Approximately 35 elements are routinely measured by neutron activation analysis. A number of others produce radioactive isotopes that emit γ-rays, but their half-lives are too short to be useful. Unfortunately, silicon is one of these elements. Other elements do not produce γ-ray-emitting isotopes when irradiated with neutrons. There are two methods of using neutron activation to determine bulk compositions, instrumental neutron activation analysis (INAA) and radiochemical neutron activation analysis (RNAA).

In INAA, a rock or mineral sample is irradiated in the reactor. The irradiated sample is removed from the reactor, and the dangerous radioactivities are allowed to decay. Then the sample is placed into a counter and the γ-rays emitted by each element in the sample are counted. A variety of counters are used, including scintillation counters, gas ionization counters, or semi-conductor counters. For the most precise results, background counts in the detectors produced by electronic noise, cosmic rays, and other radioactive decays must be eliminated. The technique is very sensitive, and samples as small as a few tens of milligrams can be measured.

In RNAA, the sample is irradiated as for INAA. But after irradiation, the sample is chemically processed to separate elements with γ-rays whose energies cannot be resolved by the detectors and to concentrate the element of interest to improve sensitivity. Typically RNAA involves larger samples in order to facilitate chemical processing.

The extreme sensitivity of neutron activation analysis can be both an advantage and disadvantage. The obvious advantage is that one can obtain data on small and precious

samples. However, a danger is that one might measure a sample that is too small to be representative of the material of interest. For example, 50-mg samples of chondrites do not adequately sample all of the components in the rock, so either larger samples must be measured or multiple samples must be measured and the results combined to get a good measurement.

Petrology, mineralogy, mineral chemistry, and mineral structure

Optical microscopy

The polarizing microscope is an important tool for investigating the mineralogy of a sample and the textural relationships between minerals. The microscope can be used with either transmitted light or reflected light. The light sources are designed to illuminate the sample from either directly below or directly above, using the microscope lens to focus the light.

In order to use transmitted light, samples are prepared as standard thin sections, 30 μm thick, thin enough for light to be transmitted through rock samples. The light is first passed through a polarizer to generate plane-polarized light. The minerals in the sample rotate the direction of polarization of the light to varying degrees. When a second polarizer, oriented at 90 degrees to the first, is inserted between the sample and the observer the minerals appear with different colors. These "interference colors" (birefringence) are used, along with other properties such as shape, cleavage, twinning, etc., to identify the minerals. Transmitted light is used to identify silicates, carbonates, and some oxides. The textural relationships are also easy to study. Transmitted light microscopy is not able to investigate materials with grain sizes smaller than the 30-μm thickness of the thin section, because the grain boundaries scatter the light. Material with a mean grain size of less than a few microns will appear opaque in transmitted light due to this scattering.

Reflected light microscopy can be used either on thin sections or thicker polished sections. Reflected light is used primarily for identifying opaque minerals such as metals, sulfides, and some oxides. Each of these minerals has a unique appearance in reflected light.

Electron-beam techniques

When a high-energy electron beam strikes a sample, the electrons undergo elastic and inelastic scattering that generate a number of signals that can be used for imaging and for investigating the chemical and structural properties of a sample. The signals originate at different places in the sample, as illustrated schematically in Figure A.1. *Auger electrons* are generated when the primary electron beam hits and ejects an electron from an inner shell of an atom of the sample. The vacancy is filled by an electron from an outer shell, a process that generates energy that is carried away by either an auger electron or an X-ray photon (see below). Auger electrons have energies characteristic of the element from which they are emitted and originate within 1–3 nm of the surface. Electrons generated deeper in the sample are scattered by sample atoms and lose energy. *Secondary electrons*, the most commonly used imaging signal, are generated in a volume just below the surface when an incident electron passes near enough to an atom to impart some of its energy to one or more of the

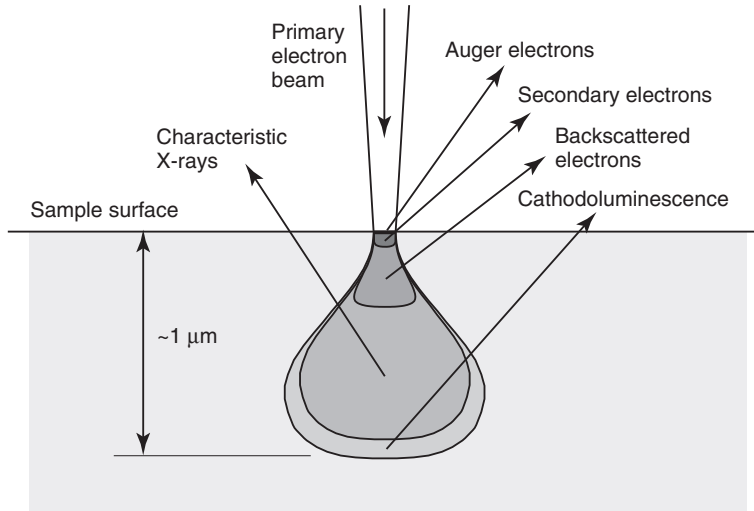

Fig. A.1 When an high-energy electron beam strikes a sample, interactions occur that produce a variety of types of radiation that can be used for analysis. Different signals come from different parts of the interaction volume (see text). At the sample surface, auger electrons are produced. At slightly greater average depth, secondary electrons are generated, followed at greater depth by backscattered electrons. Characteristic X-rays are generated over a volume of ~1 μm^3 (the exact volume depends on the impact energy of the electrons). Auger electrons are also produced at this depth, but they do not leave the sample because of interactions and scattering with other atoms. Cathodoluminescence requires somewhat less energy to produce and thus can be generated from a slightly larger volume than for X-rays.

outer electrons. Some of these electrons leave the sample at low energy, becoming secondary electrons. Secondary electrons sample the outer ~10 nm of the sample. *Backscattered electrons* are generated over a somewhat larger volume when an incoming electron impacts an atom directly and is scattered backward in the direction that it came with little or no loss of energy (an elastic collision). Backscattered electrons are generated from a larger region than secondary electrons (Fig. A.1). *Characteristic X-rays* are generated when an electron from the primary electron beam ejects an electron from an atom in the sample. In order for another electron to fill the vacancy, it must lose energy, which is removed by an X-ray with an energy that is characteristic of the element from which it was emitted. The volume of the sample from which characteristic X-rays (and to a lesser extent backscattered electrons) are generated is a function of the accelerating voltage of the primary electron beam, with higher accelerating voltages resulting in a larger interaction volume in the sample. *Cathodoluminescence* (CL) is visible light that is generated when the electron beam excites the outermost electrons in an atom to a higher state. When the electron drops back into its original orbital, it emits a photon that can be detected. The volume from which CL is generated is larger than those of the other signals (Fig. A.1).

Modern instruments use all of these signals to extract information about a sample. These include the scanning electron microscope, the transmission electron microscope, the electron microprobe, and the auger nanoprobe. For many of these techniques, a conductive

coating (carbon or sometimes gold) is put on the sample to permit the charge imparted to the sample by the electron beam to be dissipated.

Scanning electron microscope

A scanning electron microscope (SEM) consists of a source that produces a beam of electrons accelerated to high-energy (accelerating voltages can range from ~5 to ~30 keV), a column of electrostatic lenses and apertures to focus the beam, and one or more detectors. In standard operation, a focused beam of high-energy electrons is rastered across a rectangular area of a sample and an image is constructed from signals generated in the sample using a computer. Information about the position of the primary beam as a function of time is used to generate the image. Scanning electron microscopes use secondary electrons and backscattered electrons for imaging. Secondary electrons produce higher quality images because they originate closer to the surface of the sample and because more of them are produced per incoming primary electron. Secondary electron images are used to obtain morphological information about a sample. Backscattered electrons provide information on the mean atomic weight of the sample. In a backscattered-electron image, the brighter areas have a higher mean atomic weight, and an experienced analyst can often determine the mineralogy of a sample from a backscattered-electron image.

The spatial resolution of a scanning electron microscope is governed by a combination of the size of the primary electron beam and the size of the interaction volume. For secondary electrons, the size of the electron beam dominates. Two types of electron guns are in current use, the thermionic gun and the field emission gun (FEG). The thermionic gun is the most common source. It is easier and cheaper to operate and maintain than the field emission gun. Electrons are emitted from a heated filament and then accelerated toward an anode. The electrons emerging from the anode are focused into a beam by a set of electrostatic lenses. The field emission gun uses a very strong electric field to extract electrons from a metal filament. It operates at a much lower temperature than the thermionic gun and is a much brighter source. However, it requires a much better vacuum and tends to be harder to operate. The field emission source permits a much smaller primary electron beam to be generated, resulting in much higher spatial resolution. A modern field emission SEM can image features down to ~10 nm in size.

Scanning electron microscopes are often equipped with energy-dispersive X-ray detectors for semi-quantitative and quantitative chemical analysis. These detectors are typically lithium-doped silicon detectors that are operated at liquid nitrogen temperature. The electronics recognize the energy of each incoming X-ray and produce an X-ray spectrum from which the composition of the sample can be determined. Modern instruments are equipped with sophisticated software that estimates the composition without the use of standards. The resulting compositions are reasonably accurate. Precise chemical compositions require careful standardization. If precise compositions are required, the electron microprobe is a better instrument to use. Chemical information can be obtained from a spot or from an area, and compositional maps can be generated.

Scanning electron microscopes can be equipped with a CL detector. Cathodoluminescence provides information on the mineralogy of a sample. An electron backscatter

diffraction (EBSD) detector can also be mounted on an SEM to permit investigation of the structures of minerals. To use an EBSD detector, the sample is carefully polished to produce a damage-free surface. It is then mounted in the SEM at a high tilt angle so that the primary electron beam arrives almost parallel to the sample surface. The electrons are scattered by the atoms in the sample based on their positions, and the crystal structure of the mineral can be determined. The principal advantage of this technique over classical X-ray diffraction is that the petrographic context of the sample is maintained. Crystal orientation maps can be generated with an EBSD detector.

Transmission electron microscope

Transmission electron microscopy (TEM) uses high-energy electrons to probe the structure and composition of materials at high spatial resolution. Electrons are accelerated from 60 to 400 KeV, focused to a very small spot, and directed onto the sample. The sample must be thinned to electron-beam transparency; the thickness depends on the "electron density" of the material, but <200 nm is a good guide and 50 nm or less is best for high-resolution TEM (HRTEM) and electron energy-loss spectroscopic (EELS) studies. TEMs come in two varieties – conventional (CTEM) and scanning (STEM). CTEM uses a fixed, stationary probe on the sample, whereas STEM rasters a fine probe across the area of interest. The spatial resolution of the TEM is limited primarily by spherical aberration, but software correction of such aberration for the HRTEM gives spatial resolutions of < 0.1 nm, allowing individual atomic columns to be investigated.

The electrons passing through the thin sample comprise three types: (1) Electrons that do not interact with the sample as they pass through give information on thickness and mean atomic weight. Thicker samples and areas of higher mean atomic weight will appear darker on the imaging screen. The contrast in the images is caused by absorption of electrons in the sample. At lower magnifications, this so-called "bright-field image" gives information on shapes and morphologies of samples being studied. (2) Elastic scattering gives rise to diffraction effects and is the basis for the atomic scale information in HRTEM images and selected area electron diffraction (SAED) patterns. (3) Inelastic scattering occurs where the incident monochromatic electron beam loses energy through interaction with the electrons in the solid. Inelastically scattered electrons form the basis of electron-energy-loss spectroscopy (EELS), where the incident monochromatic electrons lose energy through interaction with core electrons. For example, interaction of a 100 000 eV electron with a carbon 1s electron (with a binding energy of ~290 eV) will reduce the final energy of the transmitted electron to <99 710 eV. The incident electron beam can also "interact" with the atoms in the sample generating backscattered, secondary, and auger electrons, and X-rays. One of the great advantages of TEM is the ability to generate images, structure-specific HRTEM and SAED data, chemical and bonding EELS data, and energy-dispersive X-ray spectra, from the same nanometer-sized region. For a detailed review of TEM instrumentation and techniques, see Williams and Carter (2009).

The TEM has found wide use in studying presolar grains, IDPs, and Stardust samples, and in analyzing the fine-grained alteration minerals in carbonaceous chondrites.

Electron microprobe

An electron microprobe (EMP) non-destructively analyzes the chemical composition of small volumes of minerals or glasses (Reed, 1993; Goldstein *et al*., 2003). The electron beam is generated in the same way as in a scanning electron microscope. However, for EMP analysis, the beam is focused on a single spot and the characteristic X-rays are counted for a few seconds to a few minutes using wavelength-dispersive spectrometers. Each wavelength-dispersive spectrometer consists of one of several types of crystal that is used to diffract the X-rays of interest (using the principle of Bragg diffraction) into a gas-filled counter. A wavelength-dispersive spectrometer is better able to separate X-rays of different energy and is more sensitive than the energy-dispersive detector commonly found on SEMs, but it can only measure one element at a time. An electron microprobe typically has several spectrometers to permit analysis of multiple elements simultaneously. Major, minor, and some trace elements can be measured with a modern electron probe. Some electron microprobes are also equipped with energy-dispersive detectors to help with choosing points for analysis and to otherwise support the wavelength-dispersive analysis.

Electron microprobes can be used in spot mode to measure the chemical compositions of individual minerals. Mineral grains with diameters down to a few microns are routinely measured. The chemical composition of the sample is determined by comparing the measured X-ray intensities with those from standards of known composition. Sample counts must be corrected for matrix effects (absorption and fluorescence). The spatial resolution of the electron microprobe is governed by the interaction volume between the electron beam and the sample (Fig. A.1). An electron probe can also be operated in scanning mode to make X-ray maps of a sample. You will often see false-color images of a sample where three elements are plotted in different colors. Such maps allow rapid identification of specific minerals. EMP analysis has become the standard tool for characterizing the minerals in meteorites and lunar samples.

Auger nanoprobe

Auger electron spectroscopy (AES) uses the auger electrons, which are generated at the surface of the sample by the impacting primary electron beam (Fig. A.1). The primary electrons eject an electron from an inner shell of an atom in the sample. An electron from an outer shell fills the vacancy and either another electron, the auger electron, or an X-ray photon carries away the excess energy. The energy of the auger electron is governed by the energy levels of the electrons and is thus characteristic of the element. The detector uses an electrostatic analyzer to steer electrons of a specific energy into the detectors. Because only electrons of a single energy can be measured at one time, an analysis can take a long time.

Auger electrons are generated in the top 1–3 nm of the sample. The spatial resolution is controlled entirely by the size of the primary electron beam, which is very small, resulting in spatial resolution of a few tens of nanometers. Auger spectroscopy cannot detect hydrogen or helium but is sensitive to all other elements. It is most sensitive to elements of low atomic number. The analysis must be done at high vacuum because the auger electrons emerge with low energy and, because auger spectroscopy is a surface technique, the sample must be free

of adsorbed oxygen and the carbon coat must be removed at the point of analysis. Modern auger nanoprobes are equipped with an ion beam (typically using argon) to sputter clean the surface before analysis.

As with the electron microprobe, the chemical composition is determined through comparison with standards. Corrections for interactions with different elements are also necessary. However, the standardization and correction procedures for the AES are much less mature than those for the electron probe. In cosmochemistry, the auger nanoprobe is used primarily to determine the chemical compositions of presolar grains. It is ideal for this application because it is a surface technique and has the same spatial resolution as the NanoSIMS (see below), which is used to identify presolar grains *in situ* in meteorite samples and IDPs.

Other techniques for determining chemical composition and mineral structure

Proton-induced X-ray emission (PIXE)

PIXE is a technique that uses a MeV proton beam to induce inner-shell electrons to be ejected from atoms in the sample. As outer-shell electrons fill the vacancies, characteristic X-rays are emitted and can be used to determine the elemental composition of a sample. Only elements heavier than fluorine can be detected due to absorption of lower-energy X-rays in the window between the sample chamber and the X-ray detector. An advantage of PIXE over electron beam techniques is that there is less charging of the sample from the incoming beam and less emission of secondary and auger electrons from the sample. Another is the speed of analysis and the fact that samples can be analyzed without special preparation. A disadvantage for cosmochemistry is that the technique is not as well quantified as electron beam techniques. PIXE has not been widely used in cosmochemistry.

Inductively coupled-plasma atomic-emission spectroscopy (ICP-AES)

Emission spectroscopy utilizes the characteristic line emission from atoms as their electrons drop from the excited to the ground state. The earliest version of emission spectroscopy as applied to chemistry was the flame test, where samples of elements placed in a Bunsen burner will change the flame to different colors (sodium turns the flame yellow; calcium turns it red, copper turns it green). The modern version of emission spectroscopy for the chemistry laboratory is ICP-AES. In this technique rocks are dissolved in acid or vaporized with a laser, and the sample liquid or gas is mixed with argon gas and turned into a plasma (ionized gas) by a radio frequency generator. The excited atoms in the plasma emit characteristic energies that are measured either sequentially with a monochromator and photomultiplier tube, or simultaneously with a polychrometer. The technique can analyze 60 elements in minutes.

X-ray diffraction (XRD)

X-ray diffraction uses the elastic scattering of X-rays from structures that have long-range order. Diffracted waves from different atoms in the structure can interfere with each other

and the resulting intensity distribution is directly related to the atomic distances in the structure. For a given set of lattice planes with an inter-plane distance of d, the condition for a diffraction peak is $2d\sin\theta = \lambda$, where λ is the wavelength of the incident X-rays and θ is the angle between the incident X-ray beam and the sample surface. This relationship is known as Bragg's law.

Two types of diffraction measurements are typically made on cosmochemical samples. Powder diffraction, where a sample powder is mounted on the end of a fiber and placed in the X-ray beam, is most commonly used. The term "powder" in this usage means that the crystal lattice domains are randomly oriented. Powder diffraction is used to identify unknown materials and to determine their basic crystal structure. Single-crystal X-ray diffraction is used to solve the complete structure of crystalline materials. For more details, see Cullity (1978).

Synchrotron techniques

Several analytical techniques are based on X-rays emitted from high-energy synchrotron electrons. These have been used to study IDPs and are an important part of the analytical arsenal being used on the Stardust samples. Three of these are discussed here.

Micro-XRF

Micro-XRF uses a monochromatic X-ray beam focused to a few microns in diameter. The principle is the same as for the XRF system discussed earlier. A typical analytical mode is to raster the sample under the X-ray beam to produce element maps of the samples. This technique is used to determine bulk compositions of IDPs and the material in the Stardust tracks.

Scanning transmission X-ray microscopy

Scanning transmission X-ray microscopy (STXM) employs a monochromatic X-ray beam focused to a very small spot using a Fresnel zone plate and a pinhole aperture. Spot sizes of 30–35 nm are typical. The image is formed by scanning the sample through the focal spot of the beam in X and Y. A detector records the total transmitted intensity for each pixel. A map of the distribution of a single element can be made by setting the X-ray energy to the "absorption edge" of the element. An absorption edge is a sharp discontinuity in the absorption of X-rays as a function of energy that occurs when the energy of the X-ray photon corresponds to the energy of an electron shell of an atom. The absorption edge of each element is at a different X-ray energy. By changing the energy of the X-ray beam, maps of different elements can be obtained with a spatial resolution of 30–35 nm.

X-ray absorption near-edge spectroscopy

X-ray absorption near-edge spectroscopy (XANES) uses the STXM beam line. Instead of holding the X-ray wavelength constant and moving the sample, the sample stays fixed and the X-ray energy is varied around the absorption edge of the element of interest. The details of the shape of the absorption edge depend on the bonding environment of the atom. XANES has been used to investigate the carbon, nitrogen, and oxygen of organic compounds in primitive meteorites and IDPs. Because the absorption edge for iron shifts slightly

in energy as a function of oxidation state, XANES is also a good way to determine the oxidation state of a sample; it has been used to investigate the oxidation state of iron in the Stardust samples.

Mass spectrometry

Mass spectrometers are used primarily as tools for measuring isotopic compositions, although some kinds can also be used to determine elemental abundances. Mass spectrometers have three basic components: (1) a means of ionizing the sample; (2) a mass analyzer that separates atoms based on their masses; and (3) a detector. Most of the time, the mass spectrometer is identified by its source, although the mass analyzer can also be identified. In the next few paragraphs, we will describe the various sources, the different mass analyzers, and the detectors, and then describe the most common configurations used in cosmochemistry. For more details, see Gross (2008).

Ion sources

Gas-source

Gas-source mass spectrometers work with elements in the gaseous state. The elements of interest are extracted from the samples either by chemical means or by heating and are introduced into the mass spectrometer source as a gas. The gas is ionized by a beam of electrons passing through the sample gas with an energy of ~70 eV. The electrons in the beam knock an electron out of a gas atom, creating an ion that can be accelerated by a high-voltage plate into the mass spectrometer. For this reason, a gas source is also called an electron-impact source. Gas-source mass spectrometers are used primarily to measure hydrogen, carbon, nitrogen, oxygen, and noble gases. Gas-source mass spectrometers can also be coupled to a laser that vaporizes the sample. The vaporized sample is transferred as a gas to the mass spectrometer and measured. This technique permits measurements of samples while retaining the petrographic context. The spot size is typically a few tens of microns.

Thermal-ionization

Thermal-ionization mass spectrometers use a hot filament to ionize the sample. The element of interest is first purified using wet chemistry and then is loaded onto a source filament, often along with another substance that makes ionization easier and a more stable function of temperature. The filament is heated and as the sample evaporates, it is ionized. Both positive and negative ions can be created by thermal ionization, depending on the electronegativity of the element to be measured. Thermal-ionization mass spectrometers are used to measure a wide variety of elements, including magnesium, calcium, titanium, iron, nickel, rubidium, strontium, neodymium, samarium, rhenium, osmium, uranium, lead, and many others.

Inductively coupled plasma

Inductively coupled plasma (ICP) mass spectrometers use a hot plasma to ionize the sample. The plasma is generated by electromagnetic induction. The plasma source operates at

several thousand degrees and the sample is fully ionized. The ions are then extracted into the mass spectrometer. The ICP source is very stable and mass spectrometers using this technique can produce results with high precision and accuracy. However, relatively large amounts of sample are required. The ICP source can also be coupled to a laser that vaporizes the sample. The gas is then transferred to the ICP source and measured. This approach retains the petrologic context of the sample, but does not produce the same level of precision as the standard technique.

Secondary-ion mass spectrometry

An ion beam is used to sputter atoms from a sample surface and ionize them for mass spectrometry. The ion beam can be aimed very precisely at the sample of interest, preserving the petrologic context. Depending on the instrument, the primary ion beam can be focused to as small as a hundred nanometers or can be defocused to a larger area. These secondary ions are pulled into a mass spectrometer and analyzed. Thus, the technique is known as secondary ion mass spectrometry (SIMS) and the instrument is typically called an ion probe. An ion beam sputtering a sample produces every species imaginable, including neutral atoms, positive and negative ions of various charges, molecular species, etc. For this reason, the sputter source is typically coupled to a high-performance mass spectrometer.

Laser-resonance

Laser-resonance mass spectrometers use a tuned laser beam to preferentially ionize the element of interest from gas or a plume of atoms vaporized by another laser or an ion beam. In some cases, two lasers are used for ionization, with the first one raising an outer-shell electron to an excited state and the second one adding enough additional energy to ionize the atom. This method can be extremely efficient at ionizing the element of interest and extremely selective against all other elements in the gas. Laser resonance ionization can be used on a wide variety of elements, but instruments using this technique are currently much more expensive and complicated to operate than most other types of sources. This may change in the future.

Mass analyzers

The mass analyzer is the heart of the mass spectrometer. Several types of mass analyzers are commonly used and several other types may see use in the future. The performance of a mass spectrometer is typically discussed in terms of its mass-resolving power. Mass-resolving power is defined as $M/\Delta M$, where M is the mass of the species and ΔM is the width of the peak that can separate that mass from an adjacent mass. Implicit in the mass-resolving power is a definition of what it means to separate a mass peak from an adjacent peak. A commonly used definition is that the signal decreases to 10% of the maximum between the two peaks (the 10% height). Other definitions include the 50% height or full width at half maximum. In addition, a given mass resolving power at low mass will give a lower mass-resolving power at high mass, because the fractional difference in mass between two isotopes is smaller at higher mass. So in order to interpret a number given for mass-resolving power, one must understand the definition that is being used and the mass range of the elements being measured.

Magnetic sector

Magnetic sector mass spectrometers are the most common type used in cosmochemistry. In these devices, ions are separated based on their mass-to-charge ratio. The equation governing the magnetic sector mass analyzer is

$$\frac{m}{q} = \frac{B^2 r^2}{2V}$$

where m is the mass of the ion, q is its charge, B is the magnetic field, r is the radius of curvature of the magnetic sector, and V is the accelerating voltage. At a constant accelerating voltage, each value for the magnetic field corresponds to a unique mass-to-charge ratio. The radius of the magnetic sector governs the mass dispersion of the instrument and the mass-resolving power. In general, bigger instruments have higher mass-resolving power. The mass-resolving power can be increased by adding slits before and after the magnetic sector to limit the size of the beam going into the magnet and to block masses that are off axis from reaching the detector. The performance of a magnetic sector instrument can be improved by coupling the magnetic sector with an electrostatic sector, which filters the ions based on their energy.

Time of flight

Time of flight analyzers use an electric field to accelerate ions to the same kinetic energy and then measure the time it takes for the ions to reach the detector. The velocity of the ions, and thus the time of flight to the detector, depends only on the mass-to-charge ratio

$$t = L\sqrt{\frac{m}{q} \times \frac{1}{2V}}$$

where t is the time of flight, L is the length of the flight path, m is the mass of the ion, q is its charge, and V is the accelerating voltage. A pulsed ion source is required for a time-of-flight instrument. The mass resolving power is governed by the length of the flight path and the speed of the electronics at the detector end. Most time of flight mass spectrometers have an electrostatic mirror called a reflectron in the flight path so that the detector can be placed near the source and the overall length of the instrument can be minimized. Time of flight instruments are used in a wide variety of applications, including on spacecraft.

Quadrupole

Quadrupole mass analyzers consist of four rods that produce a radio frequency quadrupole field. Only a single mass-to-charge ratio has a stable trajectory through the mass analyzer, but the electric potentials can be swept rapidly, either continuously or in discrete steps to measure a variety of masses. Quadrupole mass spectrometers are used in a wide variety of applications, but are not widely used in cosmochemistry.

Quadrupole ion traps

Quadrupole ion traps are closely related to quadrupole mass analyzers, but in the ion trap the fields are manipulated so that the ions of interest are trapped, rather than passed through to a detector. Instruments of this type are being investigated for space-flight applications.

Detectors

There are two basic types of detectors used to measure ion signals, current detectors and ion counters. Each type has different implementations. A third type of detector is an imaging detector. In some SIMS instruments, the mass spectrometer is also an ion microscope, which transmits a stigmatic image of the sample to a detector plane.

Faraday cup

A Faraday cup is a current detector consisting of a conductive cup designed to catch charged particles in a vacuum. The charged particles transfer their charge to the metal cup, which is connected to a current-measuring device. In most systems, measurements are made by a high-precision voltmeter that measures the voltage developed across a resistor from the conducting lead to ground. In most systems the Faraday cup has a repeller plate in front of the cup to prevent secondary ions from leaving the cup and changing the reading.

Daly detector

A Daly detector is an ion detector that consists of a metal "doorknob", a scintillator (typically a phosphor screen), and a photomultiplier. Incoming ions hit the doorknob and release secondary electrons. The electrons are attracted to the scintillator by a high voltage (~20 keV), where they are converted to photons. The photons are detected by the photomultiplier. An advantage of the Daly detector is that the photomultiplier tube can be placed outside the vacuum system of the mass spectrometer, separated by a window. This extends the life of the detector and permits use of a higher voltage between the doorknob and the scintillator, potentially improving sensitivity for high-mass ions.

Electron multiplier

An electron multiplier is an ion detector that consists of a series of plates or channels that dramatically amplify the incoming signal. An incoming ion strikes the conversion dynode of the electron multiplier and ejects one to three secondary electrons. These electrons are accelerated into the multiplier where they strike another surface, with each electron ejecting one to three more electrons. Each of these is again accelerated to strike another surface. This process continues until a single incoming ion has generated a pulse of 10^6 to 10^7 electrons. This pulse then passes through a discriminator that rejects smaller noise pulses, shapes the pulse, and then sends it to a counter. While the system is amplifying and counting each pulse, it cannot respond to another incoming ion. This is known as the dead time. The electron multiplier has a dead time on the order of 10–15 nanoseconds, but because the length of the dead time depends on the size of the electron pulse, the electronics actually constrain the dead time to be a fixed length, longer than the longest electron pulse. Typical values of the overall system dead time range from ~18 to as much as 60 ns, depending on the details of the counting system. The dead time is accounted for in the data reduction, but if it is too large, the uncertainty in the dead time can begin to dominate the measurement uncertainty. The maximum practical count rate for an electron multiplier system is around 10^6 counts per second.

Electron multipliers can also be operated in analog mode as current detectors. In this mode, they have a lower gain and measure higher signals than in pulse-counting mode. This

was the normal way to run an electron multiplier until fast digital electronics came along. In analog mode, the electron multiplier output may not be linear with input signal, so calibration curves must be established to get accurate data. In GCMS systems (see below), electron multipliers are typically run in analog mode.

Imaging detectors

Some mass spectrometers, such as the ims series Cameca ion microprobes, are also ion microscopes. They can project a stigmatic ion image of the sample surface on a two-dimensional imaging detector. This capability was originally intended for use in tuning the instrument (and that is a tremendous advantage), but, after a few years, operators began making quantitative ion maps of their samples. The original imaging detector on the Cameca ion microprobes was a channel plate and phosphorescent screen, with the output captured on a video camera. This system was adapted to produce semi-quantitative isotope ratio maps that were used to search for presolar grains (which exhibit highly unusual isotopic compositions).

Recently, a Japanese group has developed a solid-state imaging detector for Cameca ion microprobes called SCAPS (Nagashima *et al*., 2001). This CMOS-type detector has a sensitivity of about three ions and is linear over a range of ~5×10^4. Adaptive electronics that read individual pixels as they reach saturation can increase that range significantly. This detector has been used to identify presolar grains in primitive chondrites and to investigate oxygen isotope variations within CAI minerals. This detector is much more robust than an electron multiplier, can measure high currents without dead time, and yet can also measure extremely low ion signals. This detector and the next generation of solid state detectors will certainly have a greater role as ion detectors in the future.

Mass spectrometer systems used in cosmochemistry

Stable-isotope mass spectrometers

The mass spectrometers used to measure isotopic compositions of hydrogen, carbon, nitrogen, oxygen, and sometimes sulfur are gas-source machines with simple magnetic-sector mass spectrometers. Both single and multiple detector systems can be used; modern instruments are multi-detector instruments. Faraday Cups are the most common detectors. To make a measurement, the element of interest must be extracted from the sample in an extraction line and converted to a chemical compound that is suitable for measurement. The mass spectrometer typically has relatively low mass-resolving power, so the sample must be effectively cleaned before measurement. The mass spectrometer is designed to compare the sample to a standard. The source has two inlets, one for the standard and one for the sample. First the standard is introduced into the source and measured, and then the inlet is switched to the sample and it is measured. By switching back and forth between sample and standard, instrumental effects can be minimized. The results are typically reported as parts per thousand (permil, ‰) deviation relative to a standard composition. Oxygen analyses can be done with laser fluorination, where a laser is used to extract the gas from a specific portion of a sample in the presence of fluorine. The purified gas is then introduced into the mass spectrometer and measured. The sensitivity of stable-isotope mass spectrometers

has been improved with the introduction of a gas chromatograph inlet system. These systems use a carrier gas to bring the sample to the mass spectrometer and the gas chromatograph helps to purify the sample. These systems are orders of magnitude more sensitive than conventional stable-isotope mass spectrometers.

Noble gas mass spectrometers

The mass spectrometers used to measure noble gases are also gas-source machines, typically with magnetic sector mass analyzers. However, unlike the stable-isotope machines, noble gas machines are run in static mode. Noble gas mass spectrometers have low mass resolving power (~180 to ~600), so gases must be purified before measurement to eliminate interferences. Electron multiplier detectors are common for many applications, but Faraday cups are also used in some situations. The exact protocol for measuring the noble gases depends on the goal of the study. We give an example protocol here. The noble gases are released from the sample by heating or oxidation. Chemically active gases are removed by chemical reactions with various types of "getters". The noble gases are then frozen onto a cold finger at liquid nitrogen temperature, which quantitatively removes argon, krypton, and xenon from the gas phase. The helium and neon are then admitted to the mass spectrometer, the valve is closed, and the gases are measured. At the end of the measurement, the helium and neon are pumped from the mass spectrometer. The cold finger is warmed somewhat to release argon, which is cleaned with getters and then admitted to the mass spectrometer for measurement. The mass spectrometer is again pumped out and krypton is released from the cold finger and measured. After krypton is pumped out of the spectrometer, xenon is released from the cold finger, introduced into the mass spectrometer and measured. Protocols are designed to minimize noble gas blank and interferences from various compounds and to ensure high sensitivity. In recent years, laser extraction systems have been added to noble gas mass spectrometers so that gases can be selectively extracted from just the grains of interest.

Thermal-ionization mass spectrometers

Thermal-ionization mass spectrometers (TIMS) combine a hot-filament source with a magnetic-sector mass spectrometer. The mass spectrometers are operated at low to moderate mass-resolving power. A large number of elements can be measured with thermal ionization mass spectrometry. Special care is taken to purify the samples using ion exchange columns. Samples are loaded onto the filaments along with an emitter, and a typical run may take several hours. Modern systems have multiple collectors so that several isotopes can be measured simultaneously. High-precision measurements are done with Faraday cup detectors, but low-abundance isotopes can be measured on electron multipliers. Modern machines are capable of precisions of 0.1 to 0.01 permil.

Inductively coupled-plasma mass spectrometers

Inductively coupled-plasma mass spectrometers (ICPMS) are relatively new to cosmochemistry, although they have been widely used in other fields. The plasma source makes most of the periodic table accessible to measurement, so several radioactive isotope systems that used to be impractical to use for chronology are now routinely used (see Chapters 8 and 9).

Most machines used for cosmochemistry are magnetic sector instruments, often including an electrostatic sector to minimize the spread in energy. Both single collector and multi-collector machines are used. Single collector machines coupled to a laser source are used to measure trace elements. Multicollector machines are used for high-precision isotope work. The ICP source is very stable, permitting precise correction for instrumental mass fractionation. Multi-collector ICPMS has helped to revolutionize isotope geochemistry over the last decade by improving the measurement precision by about an order of magnitude. The higher precision has meant that issues of sample preparation and analysis that used to be hidden in the noise are now important. Some workers have had to learn the hard way that high precision does not necessarily equate with high accuracy.

Magnetic-sector ion microprobes

Magnetic sector ion microprobes are becoming increasingly important in isotopic analysis of extraterrestrial materials as spot size decreases and the precision and accuracy of the measurements improve. The first of the commercially available ion microprobes used in cosmochemistry were the Cameca ims 3f–7f series machines, which initially became available in the mid-1980s. These multipurpose instruments are able to measure isotopic compositions of most elements of interest in cosmochemistry and can also be used to measure trace element abundances. Their main drawback is that the relatively small mass spectrometer can only be operated at mass-resolving powers below about 9000, and at this mass resolving power, the transmission of the mass spectrometer is very low.

To remedy this problem the large-geometry SHRIMP machines, made by Anutech, an arm of the Australian National University, and the Cameca ims 1270–1280 series were created. These instruments have much larger magnetic-sector mass spectrometers and much higher sensitivity at high mass-resolving power. The initial application for large-geometry ion probes was uranium–lead dating, and this is still a major thrust of the work done on these machines. But recent improvements in ion optics, electronic stability, and automation has made the Cameca ims 1280 a highly versatile instrument capable of high-precision isotope ratio measurements that rival the capabilities of traditional mass spectrometers of the 1970s. This may not sound like much, but in the 1970s people generally believed that ion microprobes would never be quantitative instruments. The high-precision measurements coupled with retaining petrographic context make these ion probes very popular, even though they are very expensive.

The Cameca ims 1280 is an ion microscope as well as an ion microprobe. That means that it can transmit direct ion images to an image detector. This capability has now been adapted for semi-quantitative and quantitative ion imaging. Direct ion imaging does not depend on the size of the primary ion beam for its spatial resolution. The new solid-state SCAPS detector has a spatial resolution of less than a micron, close to that of the NanoSIMS (see below).

Another new development in ion microprobes is the NanoSIMS, which was originally designed as an imaging machine for biological applications, but which has now been adapted to cosmochemistry. The primary ion beam can be focused to less than 100 nm, about a factor of three smaller than the ims 1280. NanoSIMS is a true multicollector instrument and has high transmission at high mass-resolving power. It was originally

brought into cosmochemistry to study presolar grains, but its applications are expanding rapidly to include stable isotope work and radiochronology. Its main weakness is that it cannot generate high enough ion currents to measure trace elements in natural samples.

Time of flight ion probes

Time of flight ion probes (TOF SIMS) have unique capabilities not found in other mass spectrometers. A pulsed ion beam, typically either cesium or gallium, ejects atoms and molecules from the sample. Ionized species are accelerated down the flight tube and the arrival time in the detector is recorded, giving the mass of the species (see discussion of time-of-flight mass analyzers above). TOF SIMS instruments used in cosmochemistry have spatial resolutions of <1 μm. They are used to determine elemental abundances in IDPs and Stardust samples. The spatial distribution of elements within a small sample can also be determined. TOF SIMS instruments can obtain good data with very little consumption of sample.

Resonance-ionization mass spectrometry

Resonance-ionization mass-spectrometry is still in the development stage in terms of its application to cosmochemistry. The Charisma instrument, which is operated by Argonne National Laboratories, uses multiple lasers to resonantly ionize only the elements of interest, which are then analyzed with a time-of-flight mass spectrometer. The Charisma instrument has made isotopic measurements of molybdenum, zirconium, strontium, ruthenium, barium and other elements in presolar grains. These measurements are made possible by the high ionization efficiency of the RIMS technique and its ability to completely eliminate isobaric interferences. Work is now underway to build a RIMS instrument that can be operated by an individual investigator in a university laboratory. If this succeeds, RIMS will play an increasing role in analysis of extraterrestrial materials.

Gas chromatography-mass spectrometry

Gas chromatography-mass spectrometry (GCMS) systems are a mainstay of organic chemical analysis in cosmochemistry. These systems are used even more widely in other fields such as environmental monitoring, criminal forensics, security, and monitoring food and beverage quality. A GCMS system consists of two parts, a gas chromatograph, which separates molecules based on chemical properties, and a mass spectrometer, which measures the chemicals separated by the GC by breaking them into ionized fragments and measuring their mass-to-charge ratio. The combined system permits a much finer degree of substance identification than either system used alone. A GCMS system flew on the Mars Viking landers as part of the instrument package to search for evidence of life.

Raman spectroscopy

Raman spectroscopy is a non-destructive technique that is used in cosmochemistry for identification of minerals and to evaluate the bonding and composition of organic molecules. The technique does not require special sample preparation; raw rock samples, polished sections, fine-grained powders, and liquids can be analyzed. Raman spectroscopy is the basis for several instruments that are under consideration for upcoming NASA missions.

As we discussed for electron, protons, and X-rays, the photons of visible and infrared light interact with molecules to induce transitions between electron energy states. Most photons are elastically scattered, and the emitted photon has the same wavelength or energy as the absorbing photon. Inelastic scattering of photons by molecules produces the Raman effect. It comprises a very small fraction of the incident photons (~1 in 10^7). In Raman scattering, the energies of the incident and scattered photons are different. The difference is equal to the energy of a vibration of the scattering molecule. Thus, Raman spectroscopy measures the vibrational energies of molecules created by the inelastic scattering of light. A laser provides a monochromatic light source that is much more powerful than ambient light. The inelastic scattering by the different materials in the sample produces characteristic shifts in wavelength that can be measured by a spectrometer. Different wavelengths of laser light can be used to better couple with the elements in the sample or to minimize fluorescence. Infrared spectroscopy, also sensitive to the vibrational state of a molecule, yields complementary information.

A confocal Raman microscope couples a Raman spectrometer with a confocal microscope. The confocal microscope uses a point illumination and an appropriately placed pinhole in front of the detector to eliminate out-of-focus signals. The laser light is passed through the pinhole to create the point illumination and the return Raman scattered light is passed to the spectrometer. This significantly lowers the background signal in comparison to a classic system and permits acquisition of Raman data from very small regions both on the sample surface and within a transparent sample. When the microscope is equipped with an automated stage, Raman maps of natural samples that have a spatial resolution of close to 1 μm can be obtained. For a detailed discussion of Raman spectroscopy, see Smith and Dent (2005).

Flight instruments

Chemical analyses by spacecraft are spectroscopic techniques. Some techniques used successfully on spacecraft (X-ray fluorescence, mass spectrometers) have been discussed previously. Here we focus on some important remote sensing techniques that have not already been presented.

Gamma-ray and neutron spectrometers

The principles of γ-ray and neutron spectrometry were previously described in Box 13.1. Both kinds of radiation, produced in the target by cosmic rays, are non-directional, so the instruments sense them coming from the target as well as from the spacecraft itself (which is why, when possible, the instruments are mounted on a boom). Although γ-rays and neutrons are measured by separate instruments, they are commonly used together and the data are complementary. The measurements depend critically on counting statistics, which are functions of integration time and distance from the source. For normal spacecraft orbital altitudes, integration times for most detected elements are measured in months. Elements vary considerably in detection sensitivity and abundance, and only a few elements can usually be measured.

A neutron spectrometer separates detected neutrons into different energy ranges (thermal, epithermal, fast). Proportional counters containing ^{3}He are commonly used for

thermal and epithermal neutron detection, whereas some other material such as a scintillator made of borated plastic is used for fast neutrons. Neutrons are sensitive to light elements, especially hydrogen, or elements with especially high neutron capture cross-sections.

There are a number of possible sensor options for a γ-ray spectrometer. These include a germanium sensor or scintillators made of various synthetic materials. Elements that are routinely analyzed with γ-rays include silicon, iron, titanium, magnesium, calcium, and aluminum, plus the radioactive elements potassium and thorium (uranium concentrations are usually too low).

Alpha-particle X-ray spectrometer

All Mars rovers to date have carried alpha-particle X-ray spectrometer (APXS) instruments for chemical analyses of rocks and soils (see Fig. 13.16). The source consists of radioactive curium, which decays with a short half-life to produce α-particles, which then irradiate the sample. Secondary X-rays characteristic of specific elements are then released and measured by a silicon drift detector. The Mars Pathfinder APXS also measured the backscattered α-particles, for detection of light elements, but the Mars Exploration Rovers measured only the X-rays.

Mössbauer spectrometer

Mössbauer spectroscopy is a technique based on the resonant emission and absorption of γ-rays in solids. A sample is exposed to γ-radiation, and a detector measures the intensity of the beam transmitted through the sample. The atoms in the γ-ray source must be of the same isotope as the atoms in the sample absorbing them. In this case, the emitted γ-rays will not lose energy to recoil and thus will have the right energy to be absorbed by the target atoms. The minor differences are attributable to the chemical environment of the target atoms, which is what we wish to measure. In cosmochemistry, ^{57}Fe is the isotope normally studied by Mössbauer spectroscopy. Three kinds of nuclear interactions (isomer shift, quadrupole splitting, and hyperfine splitting) are observed. These three parameters can often be used to identify a particular iron-bearing mineral, and this is also an important method for determining iron oxidation states. Mössbauer instruments were included on the Mars Exploration Rovers.

Sample preparation

Thin-section preparation

Preparing thin sections of rocks and minerals is not conceptually difficult, but it is challenging to make high-quality thin sections. Thin sections are made either on standard rectangular glass slides (the dimensions differ in the US and in Europe) or on one-inch round glass slides. The latter are used if electron-probe or ion microprobe analysis is planned because of the sample requirements of the instruments. First, a suitably sized chip of the rock is prepared. It is ground flat on one side and polished to a high polish. The polished surface is then glued to the glass slide using a suitable epoxy that has the same refractive index as glass. Sometimes the glass is "frosted" first by grinding with a coarse grit to give the epoxy

a rough surface for bonding. The glass with the sample on it is put into a precision saw and the rock is cut off parallel to the surface of the glass within half a millimeter or so. The sample is then ground to near the official thickness of 30 μm and then polished with various grades of diamond polish to achieve both the standard thickness and a high polish (1 μm diamond polish or better is the final step). The thickness is determined by checking the birefringence of known minerals in the section. In terrestrial samples, quartz is ideal for this purpose, but in meteorites, olivine is often used. A top quality thin section has a uniform thickness across the section, a very high polish, and a very low degree of "plucking" of softer and more fragile materials. Although thin sections used for petrography in a petrographic microscope often have cover slips on them, if the sections are to be used for analytical work, a cover slip cannot be used. Cover slips are seldom seen on sections in cosmochemistry research.

Sample preparation for EBSD

The EBSD technique measures the top few monolayers of a sample to determine its crystal structure. However, most polishing techniques leave a damaged layer on the samples. Even 1 or 0.25 μm diamond polish is not sufficient. For EBSD work, a final polish with colloidal silica (grain size 0.05 μm) is often required to remove the damaged surface layers.

Sample preparation for the TEM

The TEM has relatively strict sample requirements. As discussed above, the sample must be thinned to electron-beam transparency, typically less than 200 nm and in some cases as thin as 50 nm. In addition, the sample must be small enough to fit into the TEM, on the order of <3 mm wide. There are several techniques used to thin samples to electron transparency. Ion milling is often used. An ion mill uses a beam of argon accelerated to high energy to sputter-thin the sample. The main drawback of this technique is that the thinned areas are on the edges of holes in the sample, and it is often impossible to choose a specific spot to make thin. Another way to obtain electron-transparent samples is to use a microtome. This device uses a very sharp, strong knife to cut slices from the sample of interest. Often the sample is mounted in epoxy prior to slicing in order to provide a substrate to control and keep track of the sample. A microtome can produce 50–200 nm slices. The slices are then mounted on copper-grids for transfer to the TEM.

A new way of preparing electron transparent sections of small grains, such as presolar grains from meteorites, is the focused ion beam (FIB) lift-out technique. This technique permits the preparation of a section of a specific micron-sized grain. First, a mask of platinum is laid down over the grain of interest. The FIB then uses a tightly focused gallium beam to dig a trench on either side of the sample, leaving the thin, electron-transparent section behind. A micromanipulator attaches a probe to the platinum mask, lifts the sample out, and transfers it to a TEM grid. This technique is very time consuming, but it is the only way to get a specific grain into the TEM for analysis. Note that a 100-nm-thick section can be produced with a 500 nm ion beam because the FIB removes the material from around the material of interest. Curf loss (the material lost to cutting) is quite high, and in fact a single section is all one can get from a micron-sized grain.

Preparing aerogel "keystones"

The return of the Stardust mission with its treasure of comet dust posed a major challenge in sample preparation. The sample particles are dispersed along tracks in the aerogel, a material that is notoriously hard to work with. Westphal *et al*. (2004) came up with a very clever way to extract complete particle tracks from the aerogel. This system uses a high quality binocular microscope and a programmable micro-manipulator. A very fine glass needle is prepared and given the required shape. It is inserted into a clamp in the arm of the micromanipulator. The micromanipulator is programmed to poke a series of closely spaced holes in the aerogel to cut out the track. It turns out that poking with a fine needle breaks the individual strands of the aerogel silica in a controlled way and leaves a clean trench around the track. A small silica "pickle fork" is inserted into the remaining aerogel around the track to serve as a handle. The aerogel "keystone" with the track inside is then lifted out of the aerogel block, ready for analysis (see Fig. 12.13).

Preparation of samples for TIMS and ICPMS

Because the mass spectrometers used for TIMS and ICPMS measurements typically do not have the mass-resolving power required to separate the elements of interest from each other and from other elements and molecules, careful chemical separations must be carried out. Details of chemical procedures used by various laboratories are available in the published literature, although some level of specialized knowledge derived from experience is necessary to implement the published procedures. To a first approximation, the initial step in all of these procedures is to get the sample into solution. Various acids, bases, and organic chemicals are used, sometimes in controlled environments. In some cases, in order to get everything into solution, high temperatures or high-pressure bombs must be used. This chemistry must be very clean so as not to introduce atoms of the element of interest from the surroundings. Ultra-pure water, acids, and bases are produced and used for this chemistry.

Once the sample is fully into solution, it is then necessary to separate the components. Distillation is one means of separating volatile components from refractory ones. Ion-exchange columns are also important tools. Very effective ion-exchange resins are commercially available. Ion-exchange resins take advantage of reversible chemical reactions. For example, a resin with hydrogen ions available will exchange those ions for magnesium ions from solution according to the following reaction:

$$2(\text{R-SO}_3\text{H}) + \text{Mg}^{2+} = (\text{R-SO}_3)_2\text{Mg}^{2+} + 2\text{H}_3\text{O}^+$$

The R indicates the organic portion of the resin. Synthetic resins are produced as small porous beads, which are packed into a glass tube to make an ion-exchange column. The sample solution is poured into the top of the column and moves slowly down the column. The column is set up to have many more active sites than there are atoms of the element of interest in the solution so that all of the atoms are absorbed in the column. The magnesium in the above example can be recovered from the resin by increasing the concentration of H_3O^+ in the solution, that is, by passing an acid solution through the column. A wide variety of resins are available and can be used to retain both positive and negative ions. A well-designed

chemical procedure coupled with the right ion exchange resins can produce clean chemical separations with high recovery (>90%). The resulting chemical separates are ready for mass spectrometry.

Details of radiometric dating systems using neutron activation

^{40}Ar–^{39}Ar dating

The ^{40}Ar–^{39}Ar system was developed to avoid the necessity of making a separate measurement of the potassium content, which must be done on a separate aliquot of the sample. In ^{40}Ar–^{39}Ar dating, the sample is irradiated with fast neutrons and a portion of the ^{39}K is converted to ^{39}Ar. The sample is then placed in an ultra-high-vacuum system and the argon is extracted by heating the sample in a series of increasing temperature steps. The argon released at each step is purified and admitted to a mass spectrometer for measurement. With this technique, the ^{40}Ar from the irradiation and the ^{40}Ar from decay of ^{40}K are directly associated, minimizing the corrections for unrelated ^{40}Ar. By extracting the argon at different temperature steps, the argon in different minerals can be extracted separately, giving information about the thermal history of the rock and allowing isotopic disturbance of the sample to be recognized.

In order to obtain a date from the measurement of an irradiated sample, it is necessary to know the proportion of ^{39}K that was converted to ^{39}Ar. The number of ^{39}Ar atoms formed by irradiation of the sample is given by

$$^{39}\mathrm{Ar} = {}^{39}\mathrm{K}\Delta T \int \phi(\varepsilon)\sigma(\varepsilon)d\varepsilon \tag{A.1}$$

where ^{39}K is the number of ^{39}K atoms in the sample, ΔT is the duration of the irradiation, $\phi(\varepsilon)$ is the neutron flux density at energy ε, and $\sigma(\varepsilon)$ is the capture cross-section of ^{39}K for neutrons of energy ε. The integration is carried out over the entire neutron energy spectrum. However, the neutron flux density and capture cross-sections for ^{39}K are not well known. To calculate the date from the irradiated sample, it is useful to introduce a parameter J, defined as

$$J = \frac{\lambda_e}{\lambda}\frac{^{39}\mathrm{K}\Delta T}{^{40}\mathrm{K}} \int \phi(\varepsilon)\sigma(\varepsilon)d\varepsilon \tag{A.2}$$

where λ_e is the decay constant for electron capture and λ is the combined decay constant. The value of J can be determined by including a sample of known age in the irradiation as a flux monitor. Because the decay constant of ^{40}K is known and the number of ^{40}Ar* and ^{39}Ar atoms in the flux monitor can be measured, the value of J can be calculated as follows:

$$J = \frac{e^{\lambda t_m} - 1}{\left(^{40}\mathrm{Ar}^*/^{39}\mathrm{Ar}\right)_m} \tag{A.3}$$

where t_m is the known age of the flux monitor. The date for each step of the ^{40}Ar–^{39}Ar measurement can then be calculated from

$$t = \frac{1}{\lambda}\ln\left(\frac{^{40}\mathrm{Ar}^{*}}{^{39}\mathrm{Ar}}J + 1\right) \tag{A.4}$$

As with all radiometric dating systems, the ^{40}Ar–^{39}Ar system gives a valid age if several conditions are satisfied. In addition to the conditions given in Chapter 8, there are several conditions that apply specifically to the ^{40}K–^{40}Ar and ^{40}Ar–^{39}Ar systems and to extra-terrestrial samples: (1) The abundance of ^{40}K in natural potassium is assumed to be constant. This assumption is required because ^{40}K is almost never measured directly and must be inferred from the total potassium content. Small shifts in the potassium isotopic abundances due to mass-dependent fractionation can occur, but these are limited to <3%. In extraterrestrial samples, cosmic-ray-induced spallation reactions on ^{40}Ca can produce ^{40}K and alter the isotopic abundance. However, in most cases, the cosmic-ray exposure occurred late in the history of the object and the additional ^{40}K has not had time to significantly affect the abundance of ^{40}Ar*. In these cases, the additional ^{40}K can be ignored. (2) The radiogenic ^{40}Ar* measured in the sample must have been produced *in situ* by the decay of ^{40}K. (3) Suitable corrections can be made for non-radiogenic ^{40}Ar present in the object being dated. Argon-40 is the dominant argon isotope in the Earth's atmosphere. Atmospheric ^{40}Ar can be accounted for by measuring ^{36}Ar and subtracting an amount of ^{40}Ar equal to the $^{36}\mathrm{Ar}_{\mathrm{measured}} \times (^{40}\mathrm{Ar}/^{36}\mathrm{Ar})_{\mathrm{air}}$. Extraterrestrial samples may have non-radiogenic ^{40}Ar from other sources, but in most cases satisfactory corrections can still be made. (4) The sample must have remained a closed system since the event being dated. No addition or loss of potassium or ^{40}Ar* can have occurred. Many samples do not entirely meet this requirement, particularly if they have had a complex thermal history. But the ^{40}Ar–^{39}Ar technique permits the scientist to extract not only the formation age, but also additional information about the thermal history of many such objects. A good review of the ^{40}Ar–^{39}Ar technique is given by McDougall and Harrison (1988).

^{129}I–^{129}Xe dating

Iodine-129 was the first short-lived radionuclide shown to have been present in the early solar system. It was difficult to prove that the excess ^{129}Xe found by Reynolds (1960) in meteorites was due to the decay of ^{129}I. A means had to be found to show that the excess ^{129}Xe was associated with iodine. Jeffery and Reynolds (1961) solved the problem by irradiating a meteorite sample with thermal neutrons in order to convert ^{127}I to ^{128}Xe. They were then able to show that the radiogenic ^{128}Xe* from the irradiation of ^{127}I and the radiogenic ^{129}Xe* from the decay of ^{129}I were in the same crystallographic sites. The parent isotopes of ^{128}Xe* and ^{129}Xe* had both been iodine.

It has been difficult to establish the ^{129}I–^{129}Xe system as a chronometer in part because iodine is quite mobile in the environment. The neutron irradiation method has turned out to be the only practical way of distinguishing the primordial iodine in a sample as associating it with the ^{129}Xe*. In addition, it is only necessary to measure the xenon isotopic abundances, to derive the abundances of both the parent element and the daughter isotope. Even though xenon is present in very low abundances in most samples, it is easily extracted and purified for measurement by a gas-source, isotope-ratio, mass spectrometer. By coupling neutron irradiation with stepped heating to extract the xenon, iodine that is in different sites from the radiogenic ^{129}Xe in the sample can be identified and excluded from the final result.

If the iodine in a system is isotopically homogeneous, then a suite of objects forming at the same time from that system will have the same $^{129}I/^{127}I$ ratio. If the system remains closed, then $^{129}Xe^*$ from the decay of ^{129}I will remain in association with ^{127}I. In an iodine-bearing phase, the measured ^{129}Xe consists of radiogenic $^{129}Xe^*$ from the decay of ^{129}I and the ^{129}Xe that was originally trapped in the sample ($^{129}Xe_t$). In the same way, the measured ^{128}Xe consists of $^{128}Xe^*$ produced by irradiation from ^{127}I and the $^{128}Xe_t$ originally trapped in the sample. Thus, both ^{129}Xe and ^{128}Xe will be two-component mixtures between a trapped component and an iodine-derived component, and, if the assumptions of radiometric dating have been met, measured samples of the same age will plot on a single line. The xenon isotope ratios are calculated with respect to either ^{132}Xe, the most abundant isotope, or to ^{130}Xe, an isotope shielded from production by fission. In the case where the xenon isotopes are normalized to ^{132}Xe, the equation of the isochron on a $^{129}Xe/^{132}Xe$ versus $^{128}Xe/^{132}Xe$ plot such as Figure 8.26 is:

$$\frac{^{129}Xe}{^{132}Xe} = M \times \frac{^{128}Xe}{^{132}Xe} + \left[\left(\frac{^{129}Xe}{^{132}Xe}\right)_t - M \times \left(\frac{^{128}Xe}{^{132}Xe}\right)_t\right] \quad \text{(A.5)}$$

where M is the slope ($^{129}Xe^*/^{128}Xe^*$) and the term in brackets is the trapped component represented by the end point of the line at the lower left on Figure 8.26 (analogous plots and equations can be created if ^{130}Xe is used for normalization). The trapped component is typically the dominant noble-gas component in chondrites, known as Xe-P1 or Q-xenon. Although the measurements must be corrected for blank in the mass spectrometer and for small amounts of adsorbed air, these corrections are usually very small and the composition of atmospheric xenon has similar isotopic ratios to the trapped component, so uncertainties in the corrections do not affect the slope of the isochron.

It turns out to be quite difficult to determine the absolute ^{127}I abundance through the neutron irradiation method. This is because typical iodine-bearing minerals have iodine concentrations many orders of magnitude larger than the meteorite samples of interest, which results in non-linear activation behavior in the reactor (e.g. Hohenberg and Pravdivtseva, 2008). Thus, the absolute $^{129}I/^{127}I$ ratio for the early solar system is not very well known. In practice, this does not affect ^{129}I–^{129}Xe dating because the Shallowater aubrite is used as a flux monitor. In this meteorite, the iodine is sited in enstatite and thus is tightly bound, and the igneous history of the meteorite means that all samples of the meteorite have the same $^{129}Xe/^{127}I$ ratio. A piece of Shallowater is included in every irradiation, so the initial $^{129}I/^{127}I$ ratios of the unknown samples are determined relative to the ratio for Shallowater (Fig. 8.26). Over the last few years, the absolute age of the Shallowater meteorite (4563.3±0.4 Ma) has been determined through use of several isotope chronometers. This has placed the ^{129}I–^{129}Xe ages determined relative to Shallowater on an absolute scale.

Suggestions for further reading

Cullity, B. D. (1978) *Elements of X-ray Diffraction*. Reading, Massachusetts: Addison-Wesley, 555 pp.

Goldstein, J., Newbury, D., Joy, D. *et al*. (2003) *Scanning Electron Microscopy and X-ray Microanalysis*. New York: Springer, 689 pp.

Gross, J. H. (2008) *Mass Spectrometry: A Textbook*. Berlin: Springer-Verlag, 538 pp.

Hohenberg, C. M. and Pravdivtseva, O. V. (2008) I-Xe dating: From adolescence to maturity. *Chemie der Erde*, **68**, 339–351.

Jarosewich, E. (1990) Chemical analyses of meteorites: A compilation of stony and iron meteorite analyses. *Meteoritics*, **25**, 323–337.

Jeffery, P. M. and Reynolds, J. H. (1961) Origin of excess Xe^{129} in stone meteorites. *Journal of Geophysical Research*, **66**, 3582–3583.

McDougall, I. and Harrison, M. T. (1988) *Geochronology and Thermochronology by the $^{40}Ar/^{39}Ar$ Method*. Oxford Monographs on Geology and Geophysics No. 9. Oxford: Oxford University Press, 212 pp.

Nagashima, K., Kunihiro, T., Takayanagi, I., Nakamura, J., Kosaka, K. and Yurimoto, H. (2001) Output characteristics of stacked CMOS-type active pixel sensor for charged particles. *Surface and Interface Analysis*, **31**, 131–137.

Reed, S. J. B. (1993) *Electron Microprobe Analysis*. Cambridge: Cambridge University Press, 322 pp.

Reynolds, J. H. (1960a) Determination of the age of the elements. *Physical Reviews Letters*, **4**, 8–10.

Sharp, Z. (2007) *Principles of Stable Isotope Geochemistry.* Upper Saddle River, New Jersey: Pearson Prentice Hall, 344 pp.

Smith, E. and Dent, G. (2005) *Modern Raman Spectroscopy, A Practical Approach*. West Sussex, England: John Wiley and Sons, 210 pp.

Wiik, H. B. (1956) The chemical composition of some stony meteorites. *Geochimica et Cosmochimica Acta*, **9**, 279–289.

Westphal, A. J., Snead, C., Butterworth, A. *et al*. (2004) Aerogel keystones: extraction of complete hypervelocity impact events from aerogel collectors. *Meteoritics and Planetary Science*, **39**, 1375–1386.

Williams, D. B. and Carter, C. B. (2009) *Transmission Electron Microscopy: A Textbook for the Material Sciences*. New York: Springer, 832 pp.

Index